

Recent Intraplate Earthquakes in Northwest Germany
—
**Glacial Isostatic Adjustment and/or a Consequence of
Hydrocarbon Production?**

Von der Naturwissenschaftlichen Fakultät
der Gottfried Wilhelm Leibniz Universität Hannover

zur Erlangung des Grades
DOKTOR DER NATURWISSENSCHAFTEN
Dr. rer. nat.

genehmigte Dissertation
von
M. Sc. Philipp Uta

2017

Referentin: Prof. Dr. rer. nat. Jutta Winsemann

Korreferent: Prof. Dr. rer. nat. Manfred Joswig

Tag der Promotion: 20.06.2017

*Zufall ist ein Wort ohne Sinn.
Nichts kann ohne Ursache existieren.*

Voltaire

Für Madlen
und meine Familie

ABSTRACT

Though northern Germany is regarded as a low-seismicity area, the region was affected by 77 earthquakes with magnitudes between 0.5 and 4.3 M_L within the time period of January, 1st 1993 to December, 31st 2016. The aim of this thesis is to analyse trigger mechanisms for the recent earthquakes in NW Germany in order to better differentiate between potential anthropogenic and natural tectonic drivers. Possible trigger mechanisms are stress changes related to either the extraction of natural gas and/or processes of the ongoing glacial isostatic adjustment. This study is divided into three major parts; (i) seismological analyses; (ii) geological 3-D subsurface modeling and (iii) numerical simulations of the glacial isostatic adjustment.

In a novel approach, two differently scaled 3-D P -wave-velocity models were used in NonLinLoc to relocate earthquakes. The vast majority of epicenters is located in the vicinity of hydrocarbon fields in northern Germany. Their focal depths are in a range of 3.5 to 9 km. Five earthquakes show hypocenter depths of more than 13 km and four of them are located far away from hydrocarbon fields. Fault plane solutions derived for 16 significant events trend mainly NW-SE, NNW-SSE or roughly N-S. With just three exceptions, all of the focal mechanisms indicate normal fault movement.

Based on the hypocenter locations in combination with the geological 3-D models, earthquakes in the vicinity of active hydrocarbon fields were most probably caused by movements along major Permian rift-related faults, which today are located below the base Zechstein. These faults mainly trend NW-SE, NNW-SSE, roughly N-S and in some cases WNW-ESE. Altogether, 25 potential seismogenic faults were identified that are characterized by normal fault movements.

The GIA simulations were carried out by Holger Steffen (Landmäteriet, Gävle, Sweden) for a compressive and an extensional stress field. In a compressive stress regime, each fault location in the study area indicates the possibility of fault movement due to stress changes, which are induced by the deglaciation of the Weichselian ice sheet up to the present day. For an extensional stress regime, models with 1-D and 3-D viscosity structures as well as varying lithosphere thicknesses between 70 km and 90 km show stable fault conditions at present day. Only models with lithosphere thicknesses of 120 km or 140 km indicate the potential of fault movements due to GIA-induced stress perturbations at present day.

Most of the seismic events in NW Germany, which are ranging in depths between 5 and 9 km are concentrated along the Rotliegend rift normal faults in close proximity to the natural gas fields. Due to their spatio-temporal occurrence and their similarities to other anthropogenic seismicity all over the world, they are most likely caused by gas extraction and reservoir depletion.

Driving forces for slightly stronger earthquakes ($M_L \geq 4.0$) of greater depth seem to be more complex. The Rotenburg mainshock from 2004 is possibly related to an interaction between major GIA-induced stress changes and a minor depletion triggered component.

Controlling factors for the deep earthquakes in northern Germany are difficult to derive. However, the results clearly indicate that also GIA-induced stress changes as a result of the melting of the Late Pleistocene ice sheet play a role in case of fault reactivation in the study area.

Key words: Earthquakes, NW Germany, induced seismicity

KURZZUSAMMENFASSUNG

In den letzten 25 Jahren traten in Norddeutschland 77 seismische Ereignisse mit einer Magnitude zwischen 0.5 und 4.3 M_L auf, obwohl die ganze Region als eher aseismisch betrachtet wird. Die Lage der Epizentren in der unmittelbaren Umgebung zu den Erdgasfeldern zwischen Cloppenburg im Westen und Salzwedel im Osten legten den Schluss nahe, dass die meisten von ihnen anthropogen entstanden sind. Eine geringe Anzahl an historisch überlieferten Ereignissen und einige sehr tiefe, rezente Erdbeben deuten jedoch auch auf einen natürlichen Auslöser hin. Das Ziel dieser Arbeit ist es, die seismischen Ereignisse auf Grundlage ihrer Auslösemechanismen zu charakterisieren und voneinander unterscheiden zu können. Zu den wahrscheinlichsten Ursachen die rezenten Ereignisse zählen Spannungsfeldänderungen im Untergrund. Zum einen aufgrund der Entleerung von Gasreservoirien durch Extraktion und/oder zum anderen durch anhaltende glazial-isostatische Ausgleichbewegungen. Die Arbeit setzt sich aus drei wesentlichen Teilen zusammen: (I) seismologischen Analysen, (II) geologischen 3-D Untergrundmodellierungen und (III) der numerischen Simulation der glazial-isostatischen Ausgleichsbewegungen.

In einem neuartigen Ansatz mit zwei unterschiedlich groß skalierten 3-D P -Wellengeschwindigkeitsmodellen wurden die seismischen Ereignisse mit NonLinLoc relokalisiert. Die Ergebnisse zeigen, dass die meisten seismischen Ereignisse in Tiefen zwischen 3,5 km und 9 km in unmittelbarer Nähe zu den Erdgasfeldern liegen. Nur fünf Erdbeben wurden in größeren Tiefen (> 13 km) relokalisiert. Die meisten berechneten Herdmechanismen zeigen Abschiebungskinetiken mit zumeist NW-SO, NNW-SSO und zum Teil N-S streichenden Störungsflächen.

Durch die Verknüpfung der relokalierten seismischen Ereignisse mit den Untergrundstrukturen konnten die permischen Störungen des Rotliegend Rift als möglicher Ursprung der Seismizität in Norddeutschland identifiziert werden. Die 25 potentiell seismogen aktiven Störungen streichen zumeist NW-SO, NNW-SSO oder N-S und vereinzelt WNW-OSO.

Die Ergebnisse der numerischen GIA-Simulation über die finite Elementmethode von ABACUS© (durchgeführt von Holger Steffen, Landmåteriet, Gävle, Schweden) zeigen, dass parallel zum ehemaligen Eisrand orientierte Störungen (etwa WNW-OSO, als optimal orientiert bezeichnet) in einem kompressiven Spannungsfeld durch die glazial-isostatischen Ausgleichsbewegungen bis in die heutige Zeit reaktiviert werden können. Für ein extensionales Spannungsfeld zeigt sich jedoch, dass alle Störungen, die mit den Modellen der geringmächtigeren Lithosphäre getestet wurden (70 km und 90 km) in der heutigen Zeit stabil sind. Die Modelle mit den Lithosphärenmächtigkeiten von 120 km und 140 km deuten darauf hin, dass Bewegungen entlang von parallel zum ehemaligen Eisrand verlaufenden Störungen bis in die heutige Zeit möglich sind.

Die charakteristischen Merkmale anthropogen induzierter Seismizität, insbesondere die räumlich-zeitliche Definition, lassen sich auf fast alle seismischen Ereignisse Norddeutschlands anwenden. Die flachen seismischen Ereignisse mit Magnituden $M_L \leq 3.9$, die in unmittelbarer Nähe zu den Erdgasfeldern liegen, konzentrieren sich entlang von Störungen mit einer Abschiebungskinetik des permischen Rotliegend Riftsystems. Diese NNW-SSO oder N-S streichenden Störungen sind nicht optimal orientiert, um ein erhöhtes Reaktivierungspotential durch die glazial-isostatischen Ausgleichsbewegungen zu erhalten. Aus diesen Gründen wird für die schwachen Ereignisse in Norddeutschland die Erdgasförderung als höchstwahrscheinlichster Auslösemechanismus angenommen.

Leicht stärkere Ereignisse ($M_L \geq 4.0$) aus größeren Tiefen, wie zum Beispiel das Rotenburg Beben von 2004 haben vermutlich einen komplexeren Auslösemechanismus. Die Störungen, an denen diese Ereignisse liegen sind für die induzierten Spannungen, der glazial-isostatischen Ausgleichsbewegungen nicht optimal orientiert. Spannungsänderungen, die die Störung nahe an das Bruchkriterium bringen, sind möglich. Neben den glazial-isostatischen Ausgleichsbewegungen könnte auch eine geringe Druckabsenkung in einem sehr nahe gelegenen Reservoir ausreichen, um eine Bewegung an der vermutet seismogen aktiven Störung auszulösen.

Der Ursprung der fünf tiefen Erdbeben ist schwierig zu bestimmen, da sehr wenige Daten über die Untergrundgegebenheiten vorliegen. Allerdings bilden die Spannungsänderungen, hervorgerufen durch die glazial-isostatischen Ausgleichsbewegungen, einen möglichen Mechanismus, um diese tiefen Erdbeben auszulösen. Weitere Untersuchungen sind jedoch erforderlich.

Schlagwörter: Erdbeben, NW Deutschland, induzierte Seismizität

CONTENT

ABSTRACT	v
KURZZUSAMMENFASSUNG	vi
1. INTRODUCTION	10
2. GEOLOGICAL SETTING	13
2.1 The Central European Basin System	13
2.2 State-of-the-art seismicity in NW Germany	17
3. HYDROCARBON FIELDS IN NW GERMANY	20
4. PLEISTOCENE GLACIATIONS IN NW GERMANY AND THE GLACIAL ISOSTATIC ADJUSTMENT	22
4.1. The glacial isostatic adjustment	23
4.1.1 GIA-related phenomena and investigations	24
4.1.2 GIA-induced stress changes and associated seismicity	25
4.1.3 Observations of GIA-induced seismicity	27
5. DATABASE AND METHODS	30
5.1 General workflow	30
5.2. Relocalization of earthquakes in NW Germany	32
5.2.1 1-D pre-localization	33
<i>Selection classes</i>	35
5.2.2 3-D relocalization	36
3-D velocity models	36
a) the CRUST1.0 model	37
b) the WEG model	38
5.2.3 The software package NonLinLoc	40
<i>Vel2Grid(3D)</i>	40
<i>Grid2Time</i>	41
<i>Time2EQ</i>	41
<i>NLLoc</i>	42
<i>Preliminaries and limitations of NonLinLoc</i>	43
5.2.4 3-D travel time grids	44
5.2.5 Uncertainty estimation and associated quality criteria	45
5.2.6 Synthetic tests of travel time grids	47
<i>Implications of synthetic tests</i>	50
5.3 Fault plane solutions	51
5.4 Synthetic seismograms	54
5.5 Amplitude spectra and corner frequencies	57
5.6. Geological 3-D subsurface modeling	59
5.6.1 Modeling workflow	61
5.6.2 „Geotektonischer Atlas von Nordwest-Deutschland und dem Deutschen Nordsee-Sektor“	62
5.6.3 Digitization and 3-D modeling with GOCAD©	62

5.7. Glacial isostatic adjustment – Numerical simulations	65
5.7.1 Coulomb Failure Stress	65
5.7.2 Three-dimensional finite element modeling and model geometry	67
<i>Ice and Earth models for the 3-D finite element modeling</i>	69
5.7.3 Modeling of Coulomb Failure Stress	73
6. RESULTS	75
6.1. 3-D relocalization	75
6.1.1 Hypocenter accuracy	75
<i>Localization improvements</i>	78
6.1.2 Spatial distribution of relocated seismic events in NW Germany	80
<i>Earthquake location shift</i>	83
6.2. In-depth seismological analyses of relocated events	85
6.2.1 Fault plane solutions	85
6.2.2 Synthetic seismograms	89
6.2.3 Amplitude spectra and corner frequencies	97
6.3. 3-D relocalization results of prominent seismic events in NW Germany in comparison with former earthquake studies	103
6.3.1 Soltau 1977	103
6.3.2 Rotenburg 2004 mainshock	105
6.3.3 Völkersen 2012	106
6.3.4 Syke 2014	107
6.3.5 Emstek 2014	108
6.4. Geological 3-D subsurface models	110
6.4.1 Region Cloppenburg	111
6.4.2 Region north of Cloppenburg	113
6.4.3 Region Syke	115
6.4.4 Region Sulingen/Nienburg	117
6.4.5 Region Langwedel/Völkersen	119
6.4.6 Region Rotenburg/Söhlingen	121
6.4.7 Region Walsrode	123
6.4.8 Limitations of the GTA and the 3-D models	125
6.5. Hypocenter linking	126
6.5.1 Cloppenburg	126
6.5.2 North of Cloppenburg	128
6.5.3 Syke	130
6.5.4 Sulingen/Nienburg	131
6.5.5 Langwedel/Völkersen	133
6.5.6 Rotenburg/Söhlingen	135
6.5.7 Walsrode	136
6.6. Glacial isostatic adjustment	138
6.6.1 GIA in an assumed compressional stress regime	141
6.6.2 GIA in an assumed extensional stress regime	144
7. INTRAPLATE SEISMICITY	146
7.1 Seismicity of NW Germany in comparison to seismicity in other intraplate regions of the world	146

8. DISCUSSION	150
8.1. Quality of the 3-D relocalization	151
8.1.1 Improvement of hypocenter localization	151
<i>Influence of V_p/V_s on the focal depth</i>	154
8.2. Possible trigger mechanisms for intraplate earthquakes in NW Germany	156
8.2.1 Induced seismicity due to reservoir depletion	156
8.2.2 Glacial isostatic adjustment and stress field	163
9. CONCLUSIONS	168
REFERENCES	171
APPENDIX.....	cc
ACKNOWLEDGEMENTS.....	ccliii
CURRICULUM VITAE	ccliv

1. INTRODUCTION

Altogether, 77 earthquakes (except quarry blasts) with magnitudes between M_L 0.5 - 4.3 affected Northwest Germany (Fig. 1) in the time period from January, 1st 1993 to December, 31st 2016 (e.g. Leydecker, 2011, Bischoff et al., 2013, 2014, 2015). northern Germany is regarded as an area of low seismicity (e.g. Leydecker and Kopera 1999, Leydecker, 2011) and average macroseismic intensities (European Macroseismic Scale, EMS98, Grünthal, 1998) did not exceed an intensity of IV, which means no damage to buildings and no injury to people occurs (Grünthal and Bosse, 1997, Grünthal et al., 1998, Tyagunov et al., 2006). The majority of the epicenters determined by the routine analysis of the Federal Institute for Geosciences and Natural Resources (BGR) are located in the vicinity of natural gas fields and events like the Rotenburg 2004 earthquake with a magnitude of $M_W = 4.4$ were therefore interpreted as the consequence of hydrocarbon recovery (Dahm et al., 2007, 2015). In addition, there were also earthquakes of undoubted tectonic origin like a number of historic events that took place over the last 1200 years (Leydecker, 2011) and also a few more recent deep events of mostly small magnitude in the Northwest German Basin. A possible trigger mechanism for the natural earthquakes could be lithospheric stress changes due to glacial isostatic adjustment (GIA, Brandes et al., 2012, 2015). The possible occurrence of anthropogenically and naturally triggered earthquakes side-by-side requires a re-evaluation of the seismicity in northern Germany.

Seismic activity related to hydrocarbon production is a well-known phenomenon (e.g. Milne and Berry, 1976). There are two different ways to trigger earthquakes during the production process. Fluid injection leads to reduction of normal stress in the reservoir, while the shear stress remains constant (Grasso, 1992). This can cause movements almost instantly along pre-existing fractures (Edelmann, 2006, Mukuhira et al., 2013), which may be accompanied by seismic events (Davis and Pennington, 1989). The second trigger mechanism is related to extraction of fluids (Yerkes and Castle, 1976, Segall, 1989). It is typical that the seismic activity in this case is concentrated above, below or in the peripheral region of the reservoir (e.g. Segall, 1989, Grasso, 1992 or McGarr et al., 2002). The surface deformation, faulting and fault mechanisms vary with respect to the seismic event location in the vicinity of the reservoir (Segall, 1989, Odone et al., 1999). Recent studies on seismicity related to reservoir depletion deal with gas fields in the Netherlands (e.g. van Eck et al., 2006, van Eijs et al., 2006 and Bommer et al., 2016), with a sour gas field in Alberta/Canada (Wetmiller, 1986, Eaton and Mahani, 2015) and with the Lacq gas field in France (Bardainne et al., 2008). A comprehensive summary of world-wide seismicity related to hydrocarbon fields is given by Suckale (2009, 2010).

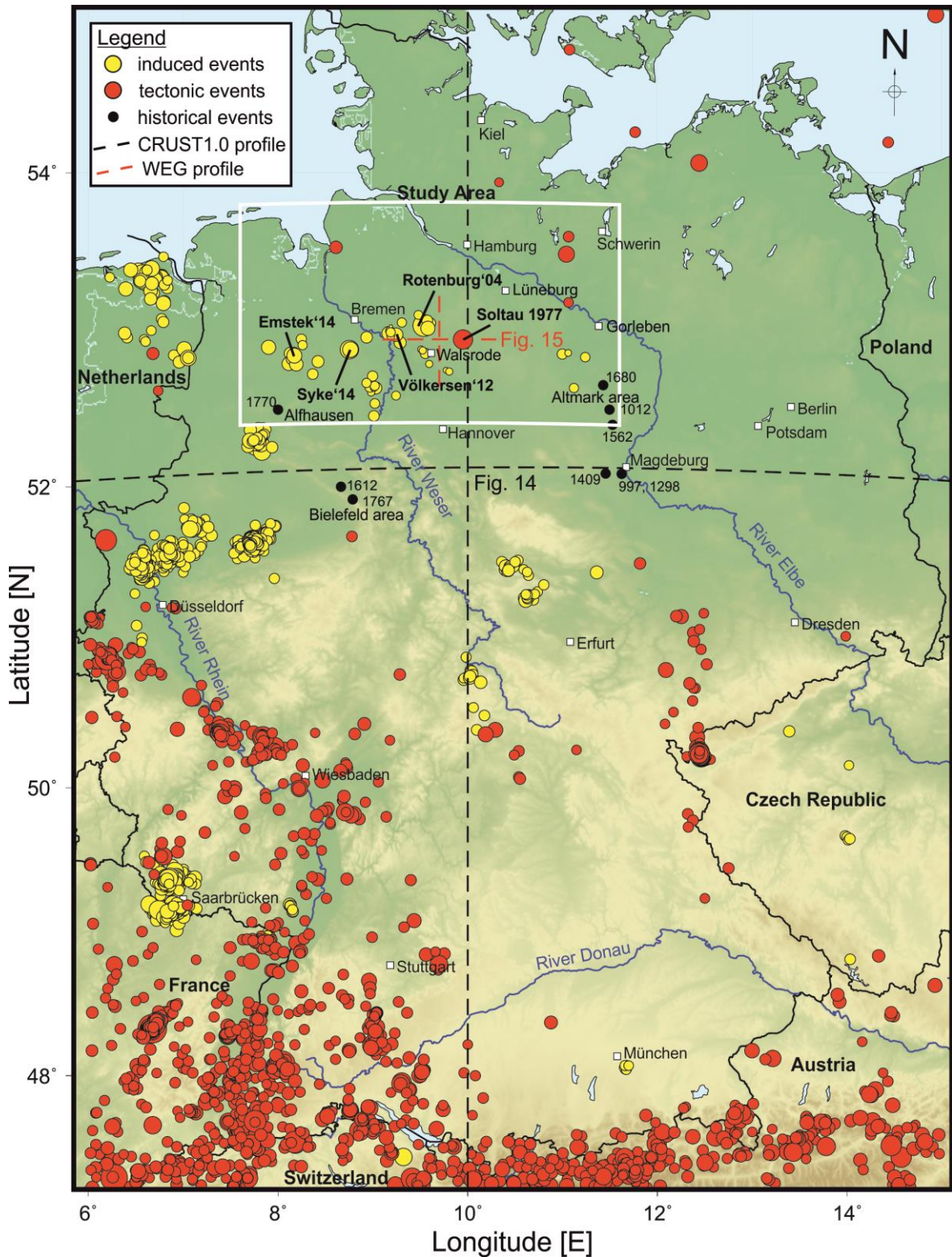


Figure 1. Location of the study (white box) including epicenters of seismic events in Germany and adjacent areas. The map shows earthquakes, which occurred during a time period from 1993 to 2016. The epicenter locations and classifications (yellow circle = induced; red circle = tectonic) were adopted from the data catalogue of the BGR. The circle diameter indicates the earthquake magnitude. The black and red dashed lines show profile lines belonging to the two differently scaled velocity models – CRUST1.0 model and WEG model, respectively. Vertical cross sections are shown in Figures 14 and 15. In addition, black dots label important historical events (including annual figures) in the vicinity of the study area (modified after Leydecker, 2011 and Vogt and Grünthal, 1994).

Natural triggers are changes in the stress field due to erosion (Calais et al., 2010), variations in the subsurface fluid pressure (Costain et al., 1987, Costain and Bollinger, 2010), stress perturbations by salt movements (Koupriantchik et al., 2007) and stress changes due to the loading and unloading of large ice sheets (Wu and Johnston, 2000, Bungum et al., 2010). The deglaciation of the Scandinavian ice sheet caused earthquakes in the intraplate region of Scandinavia (Wu et al., 1999). Recent studies from Brandes et al. (2012), Brandes and Winsemann, (2013) and Brandes et al. (2015) show evidence for a postglacial seismicity in northern Central Europe, a region, which was not covered by the Late Pleistocene ice sheet (Ehlers et al., 2011, Hughes et al., 2016).

Historical earthquakes (Intensity up to VII, Leydecker, 2011) in northern Germany, such as the strong earthquake at the Osning Thrust in A.D. 1612 (Vogt and Grünthal, 1994) are most likely related to the melting of the Scandinavian Late Pleistocene ice sheet, although they are located about 250 km away from the ice margin (Brandes et al., 2015). The study area (Fig. 1) is located between the Osning Thrust in the south and the former ice margin.

The main goal of this thesis is to better analyse the recent intraplate earthquakes in northern Germany. The study is subdivided into three major steps: 1) relocalization of the hypocenters and analysis of the focal parameters, 2) construction of 3-D subsurface models to link the hypocenters and the fault pattern and 3) numerical simulations of GIA-related stress build up (that were carried out by Holger Steffen) to analyse the reactivation potential of the faults. Therefore, this thesis is structured as follows:

Chapter two gives an overview of the geological framework and a brief summary of state-of-the-art seismicity in NW Germany. In chapter three, a short overview of natural gas production and hydrocarbon field locations in NW Germany is given. Late Pleistocene (de)glaciation as well as the theory of the glacial isostatic adjustment are described within chapter four. Chapter five deals with the applied methodologies such as the 3-D relocalization approach, in-depth seismological analyses, the geological 3-D subsurface modeling and the numerical simulations to reveal the postglacial reactivation potential based on GIA in the study area. In section six, the results are presented, namely 3-D relocalizations, fault plane solutions, synthetic seismograms, geological 3-D models and hypocenter linking as well as the glacial isostatic adjustment. Chapter seven deals with a qualitative comparison between the newly derived seismicity pattern of northern Germany and intraplate seismicity distributed all over the world. The final part is devoted to a critical discussion and resulting conclusions on the new relocalization approach and on the topic of tracking down the causes for recent intraplate earthquakes in northern Germany.

2. GEOLOGICAL SETTING

2.1 The Central European Basin System

The study area is situated within the Northwest German Basin (Lohr et al., 2007), which belongs to the Central European Basin System (CEBS, Littke et al., 2008). This nearly NW-SE trending basin evolved on top of the Carboniferous Variscan foreland basin (Betz et al., 1987). The CEBS is composed of several en echelon subbasins such as the Polish Basin, the North German Basin (divided into Northwest German and Northeast German Basin) and the Norwegian-Danish Basin (Lohr et al., 2007, Fig. 2). These basins cover the area of the North Sea, Denmark, parts of Great Britain, the Netherlands, northern Germany and Poland (Fig. 2).

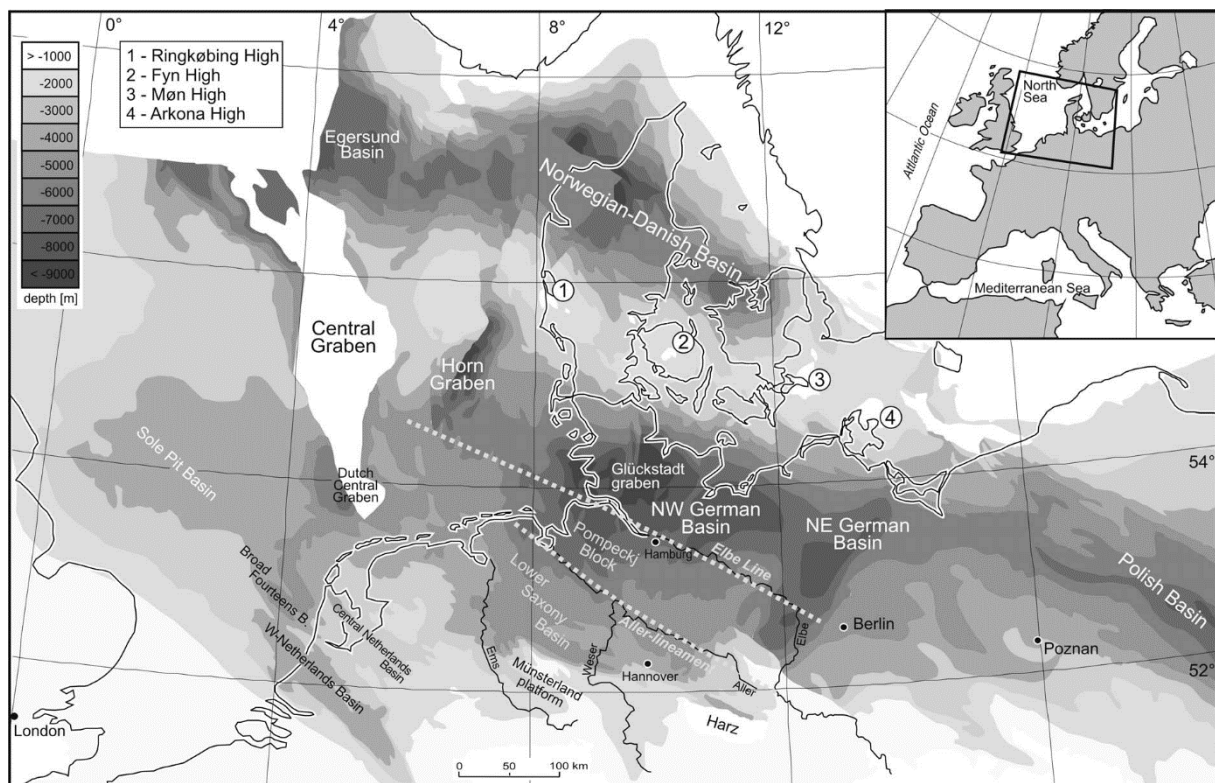


Figure 2. Zoom into the Central European Basin System. Depth map of the CEBS. Post-Permian sub-basins within the Central European Basin System (modified after Lohr et al., 2007).

The CEBS has its origin in the latest Carboniferous to earliest Permian times (Maystrenko et al., 2008). The composition of the CEBS basement is a result of the Caledonian and Variscan orogenies (Krawczyk et al., 2008).

Due to a broad igneous activity during the Permian, a thermal relaxation of the lithosphere, resulting in E-W extension (Bachmann and Grosse, 1989, Ziegler, 1990) led to a wide continental rift basin that had dominated the central part of the CEBS (e.g. Scheck and Bayer, 1999 or van Wees et al., 2000). The superimposed so-called Northwest German Basin (Ziegler, 1990) is characterized by north-south trending horst and graben structures (Fig. 3) (Gast, 1988, Gast and Gundlach, 2006), which were filled by terrestrial sediments under semi-arid to arid climate conditions and a low sea-level (Glennie, 1983). These Rotliegend clastics form the most important gas reservoir rocks in the basin (Drong, 1979, Schöner and Gaupp, 2005).

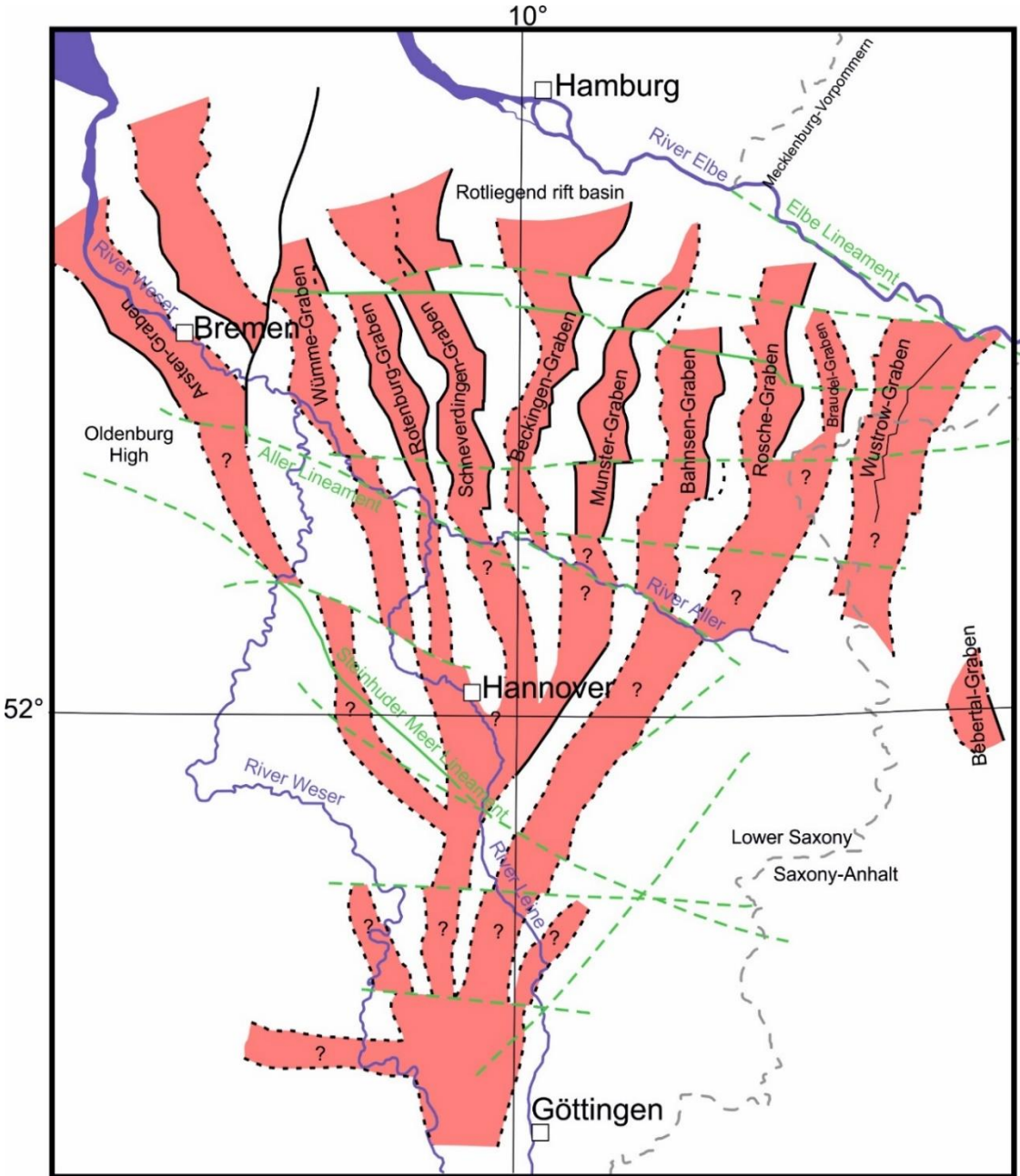


Figure 3. Rotliegend rift (red) in northern Germany including graben boundary faults (black lines) assumed graben boundary faults (dashed black lines) and major fault systems (dashed green lines). The question marks indicate the assumed course of graben structures (modified after Gast, 1988).

In the Late Permian, several southward directed marine transgressions occurred and subsequently thick layers of Zechstein salt were accumulated in the CEBS (Mazur and Scheck-Wenderoth, 2005, Stollhofen et al., 2008), summing up to more than 2,000 m of salt in the basin centre (Maystrenko et al., 2005).

In Late Triassic to Early Jurassic times the ongoing break-up of Pangaea (Seton et al., 2012) led to the drift of the CEBS further to the north. Thereby, the Triassic E-W trending extension formed NNE-SSW directed graben systems such as the Horn or Glückstadt graben (Fig. 2) in the north of the study area (Scheck and Bayer, 1999, Maystrenko et al., 2005, Lohr et al., 2007).

In the Mesozoic and Cenozoic a large number of Permian Zechstein salt structures (salt diapirs, pillows and walls) developed in the study area. The salt movements were initially triggered by an extensional stress regime in the Triassic (Mohr et al., 2005, Brandes et al., 2013). Several salt structures were later modified under a compressional horizontal stress field during the Late Cretaceous tectonic inversion phase (e.g. Best and Zirngast, 2002, Brandes et al., 2012, Brandes et al., 2013, Tanner et al., 2015).

Due to a distinct tectonic inversion phase in Late Cretaceous to Early Paleocene times (Baldschuhn et al., 1991, Kockel, 2003, Mazur et al., 2005), several local sub-regions were tectonically developed in the study area. Distinct regions were differently subsided or uplifted, respectively – the Lower Saxony Basin and the Pompeckj Block evolved separately (Fig. 2; Betz et al., 1987, Baldschuhn et al., 2001, Lohr et al., 2007). The underlying inversion was caused by changes in the regional stress field, possibly induced by the rotation of the Iberian Peninsula (Kley and Voigt, 2008). The Lower Saxony Basin is dominated by NW-SE trending faults, whereas the main strike directions in the Pompeckj Block is N-S or NNW-SSE (Lohr et al., 2007).

The orientation and kinematics of faults within the study area are summarized in Lohr et al. (2007), who identified altogether five deformation phases: Early Permian E-W extension that created N-S trending normal faults, Late Triassic NNW-SSE extension, causing WNW-ESE oriented normal faults and Middle Jurassic E-W transtension. Subsequently, during the Cretaceous, E-W and N-S oriented contraction took place (Lohr et al., 2007), and WNW-ESE or NW-SE trending reverse faults were created (Kley and Voigt, 2008). Superordinate fault systems like the Aller Lineament or the Elbe Lineament trend WNW-ESE or NW-SE (Figs. 2 and 3) whereas prominent Rotliegend graben faults trend mainly NNW-SSE, N-S or NNE-SSW (Fig. 3). In the study area, the recent subsidence rate is about 1 – 2 mm/a (Reicherter et al., 2005).

The present-day stress field is influenced by the Alpine orogeny and the North–Atlantic ridge push (Ziegler et al., 1995, Ziegler and Dèzes, 2006, Reicherter et al., 2008). After Heidbach et al. (2010) the maximum horizontal stress (S_{Hmax}) in northern Germany trends NW-SE. Marotta et al. (2002) compared the stress pattern with a fan in which S_{Hmax} deviates in directions between NW-SE in the western part to NE-SW in the eastern part of northern Germany. In contrast to the direction of the principle stress, values of stress magnitudes are hardly investigated (Röckel and Lempp, 2003). A small database for the stress tensor in northern Germany leads to different interpretation of the recent stress field. After Kaiser et al. (2005) a compressive stress field is dominant in northern Central Europe, whereas Röckel and Lempp (2003) show that there is evidence for an extensional stress regime in the North German Basin.

2.2 State-of-the-art seismicity in NW Germany

The complex fault pattern in northern Germany is the source for a distinct seismicity that affected the area during the last 1200 years (Fig. 4). The regional historic record starts in NE Germany with seismic events that took place in the Magdeburg area in 997 (macroseismic intensity, $I_0 = 6.0$) and in the Altmark in 1012 ($I_0 = 6.0$) (Leydecker, 2011). Additional earthquakes in 1298 ($I_0 = 4.0$) and 1409 ($I_0 = 6.0$) close to Magdeburg, as well as events 1562 ($I_0 = 4.5$) and 1680 ($I_0 = 4.5$) in the Altmark (Leydecker, 2011), underline the tectonic significance of this region. Ongoing seismicity in the Altmark area with low magnitude events ($2.2 \leq M_L \leq 2.6$) was recorded in the 1980s by the monitoring network for seismic risks in the Gorleben storage site for radioactive waste.

In NW Germany, important historic earthquakes occurred in the Bielefeld area 1612 ($I_0 = 6.0 - 7.0$) and 1767 ($I_0 = 6.0$) (Vogt and Grünthal, 1994, Grünthal and Bosse, 1997), as well as near Alfhausen 1770 ($I_0 = 6.0$) (Meier and Grünthal, 1992, Leydecker, 2011) (Fig. 4). The first instrumentally recorded event in northern Germany was the Soltau earthquake of 1977 with a magnitude of $M_L = 4.0$ and a focal depth in a range between 4 to 13 km (Leydecker et al., 1980). In 2004, a significant earthquake with the magnitude of $M_L = 4.4$ took place between two hydrocarbon fields near Rotenburg. Both events are interpreted as consequence of hydrocarbon recovery (Dahm et al., 2007). The Rotenburg 2004 earthquake was the first observed event in NW Germany, for which also 3 aftershocks could be recorded. Two aftershocks with magnitudes of $M_L 2.2$ and 2.0 occurred some hours after the main shock and a third one 4 days later. According to present knowledge, only the Rotenburg event in the study area revealed aftershocks.

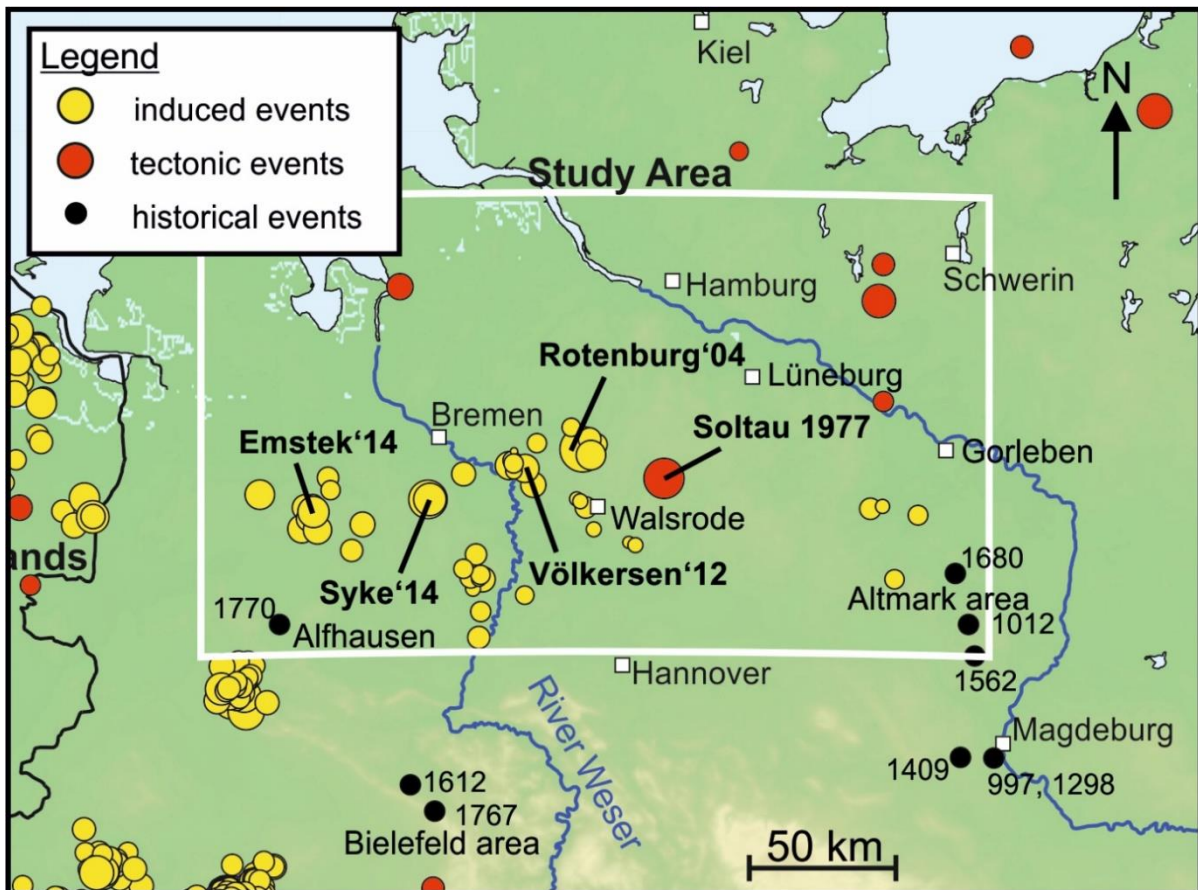


Figure 4. Historical and recent seismic events within and in the proximity of the study area. Significant historical earthquakes, which occurred during the last centuries are labeled (black circles). The circle diameter indicates the earthquake magnitude. Mapped earthquakes are classified in induced (yellow circle) and natural, tectonic (red circle) events. Soltau'77 and Rotenburg'04 with magnitudes of $M_L \sim 4.0$ and $M_L \sim 4.4$, respectively, are the strongest events in this region. Locations, classifications and earthquake magnitudes (see different diameters) were adopted from the earthquake catalog of the BGR (Gernot Hartmann, pers. communication).

Due to the advent of the German Regional Seismic Network (GRSN) in 1991, online data is provided to monitor the entire seismicity of Germany in almost real-time (Stammler, 2002). Up until now and in the future, the GRSN is extended by BGR and new temporal networks are installed in cooperation between BGR, the State Authority for Mining, Energy and Geology (LBEG) and some universities (e.g. Bischoff et al., 2013). In addition, the so-called WEG seismic network (Association of German Oil and Gas Producers, now referred to as BVEG, Bundesverband Erdgas, Erdöl und Geoenergie e.V.) was established in the region of Völkersen, Söhlingen and Soltau to monitor possible seismic activity in the vicinity of the hydrocarbon fields. An extension of this first network was completed in 2016 to monitor the seismicity in the regions of Cloppenburg, Syke and Sulingen/Nienburg. The improved seismic station coverage resulted in a decrease of the detection threshold and the registration of several earthquakes with magnitudes below M_L 2.0 was available. Furthermore, significant seismic events like Völkersen 2012 ($M_L = 2.9$), Syke 2014 ($M_L = 3.2$) and Emstek 2014

($M_L = 3.1$) occurred that were examined in detail. Hypocenters, which were calculated for these events, indicate focal depths between 4 - 5 km ($\pm 1 - 2$ km) and mostly NW-SE or WNW-ESE striking normal fault focal mechanisms (Bischoff et al., 2013, 2014, 2015).

In contrast to the assumed shallow and distinctly clustered seismic events in NW Germany, deep earthquakes (below 10 km) are sparsely distributed and rarely evaluated. Only two seismic events were located by BGR in the north of the Elbe river with hypocenter depths between 10 and 30 km (Hitzacker'12 and Zarrentin'14). After Bock et al. (2002) in 2000, another deep earthquake occurred near Wittenburg with M_W 3.1. They determined a focal depth between 16 and 17 km. However, reliable geological and structural data of the subsurface in these depth ranges is more or less not available. Therefore, the driver for these deep-seated earthquakes are not investigated yet. Until now, deep earthquakes were not registered in the vicinity of active hydrocarbon fields in NW Germany.

3. HYDROCARBON FIELDS IN NW GERMANY

For more than 100 years, hydrocarbon production, mainly of conventional natural gas, is established in NW Germany (WEG, 2008). More than 95 % of the natural gas production in Germany is originated in Lower Saxony (LBEG, 2016), where the gas is extracted from an E-W trending reservoir belt between Salzwedel (Altmark area) and Cloppenburg (Fig. 5). In this region, the reservoirs are mainly situated within the Rotliegend, Zechstein or Buntsandstein sedimentary rocks, in depths between 3,000 and 5,000 m. The different reservoir depths are indicated by the colour-coded reservoir shapes in Figure 5. Thereby, the western hydrocarbon reservoirs are mainly situated in greater depth, according to the Rotliegend sedimentary rocks, in contrast to the shallower more western reservoirs belonging to the Zechstein and Buntsandstein layers. Table 1 shows the production value of the fields, their cumulative output since the beginning of production and the number of active production wells (LBEG, 2016, Final Report "Erdöl und Erdgas in der Bundesrepublik Deutschland 2015).

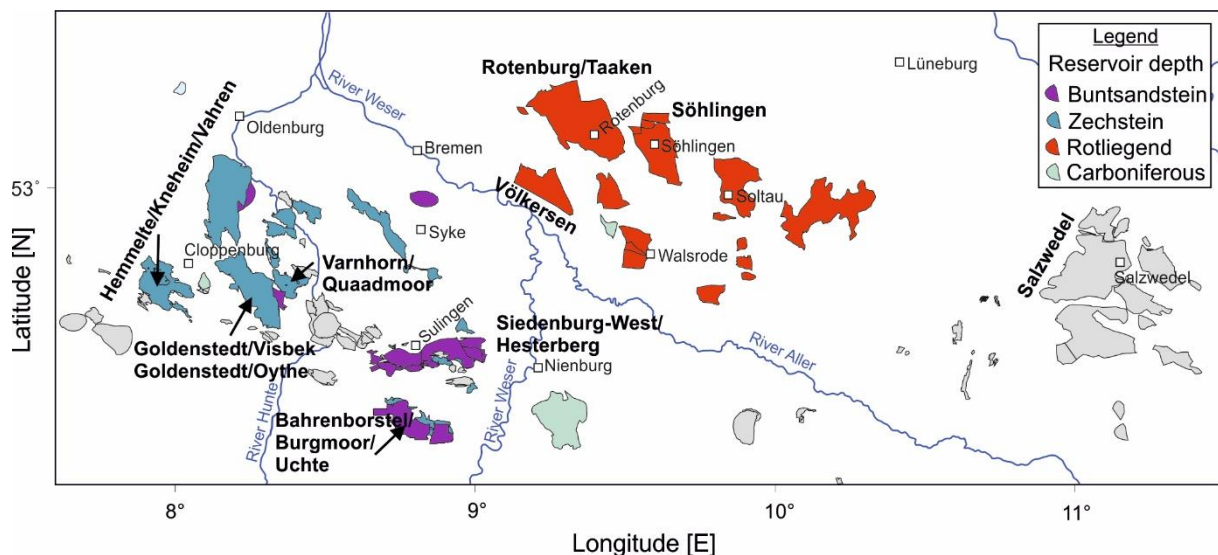


Figure 5. Active hydrocarbon fields in NW Germany. The most important reservoirs, concerning my study, are colour-coded (see legend). The different colours highlight the geological unit, where most parts of the reservoir are situated (Nibis Server, LBEG, 2016 and DMT, 2016). In addition, ten of the most productive gas fields are named (LBEG, 2016).

Within the Northwest German Basin, the complex fault pattern and several different salt structures form traps in which the natural gas was accumulated (Baldschuhn et al., 2001, Lohr et al., 2007, Maystrenko et al., 2013). Main source rocks for hydrocarbons are Upper Carboniferous coal seams (Kosinowski et al., 1997). The roughly N-S trending horst and graben structures control the sediment thickness distribution within the Northwest German Basin (e.g. Gast, 1988, Gast and Gundlach, 2006) and thus, the thickness of the reservoirs.

In the Söhlingen area, the thicknesses of the most productive reservoirs vary in a range of 350 m (Havel Subgroup, Guadalupian) and a few tens of meters (Wustrow sandstone, Hannover Formation, Guadalupian to Lopingian). The regions of Cloppenburg and Syke are characterized by reservoir thicknesses of 150 m (Staßfurt Carbonates, Lopingian) (Schröder et al., 1995).

Details on the reservoir characteristics are summarized in Plein (1978), Gast (1988), Schröder et al. (1995), Schwarzer and Littke, (2007), Bischoff et al. (2013, 2014, 2015) and in the annual reports of “Erdöl und Erdgas in der Bundesrepublik Deutschland...”.

Table 1. Production value, the cumulative output since the beginning of production and the amount of active production wells for ten of the most productive fields in NW Germany in 2015 (after LBEG, 2016).

Hydrocarbon field	Production 2015		Cumulative production		Production wells in 2015
	1000 m ³ (V _n)	%	1000 m ³ (V _n)	%	
Rotenburg/Taaken	1,171,182	12.6	60,453,789	5.9	28
Völkersen	1,092,418	11.7	21,044,985	2.0	16
Goldenstedt/Visbek	979,002	10.5	62,943,131	6.1	22
Varnhorn/Quaadmoor	543,614	5.8	28,137,445	2.7	13
Hemmelte/Kneheim/Vahren	448,430	4.8	35,277,304	3.4	11
Söhlingen	442,947	4.8	41,512,280	4.0	20
Bahrenbor./Burgmoor/Uchte	441,981	4.7	18,722,589	1.8	9
Siedenburg-West/Hesterberg	414,459	4.4	29,332,350	2.9	10
Salzwedel	399,501	4.3	210,755,435	20.5	135
Goldenstedt/Oythe	279,114	3.0	4,327,364	0.4	5

4. PLEISTOCENE GLACIATIONS IN NW GERMANY AND THE GLACIAL ISOSTATIC ADJUSTMENT

During the Pleistocene, three prominent glaciations affected the area of northern Germany – the Elsterian, Saalian and Weichselian glaciation (Fig. 6). These Middle and Late Pleistocene glaciations and subsequent deglaciations had an influence on the present-day surface of northern Germany (Gibbard, 1988, Sirockko et al., 2008, Ehlers et al., 2011). The periods with alternating glaciations and deglaciations impacted the surface, the near subsurface temperatures (Grassmann et al., 2010), affected also salt structures (Sirockko et al., 2008, Lang et al., 2014) and the stress in the subsurface (Steffen and Wu, 2011).

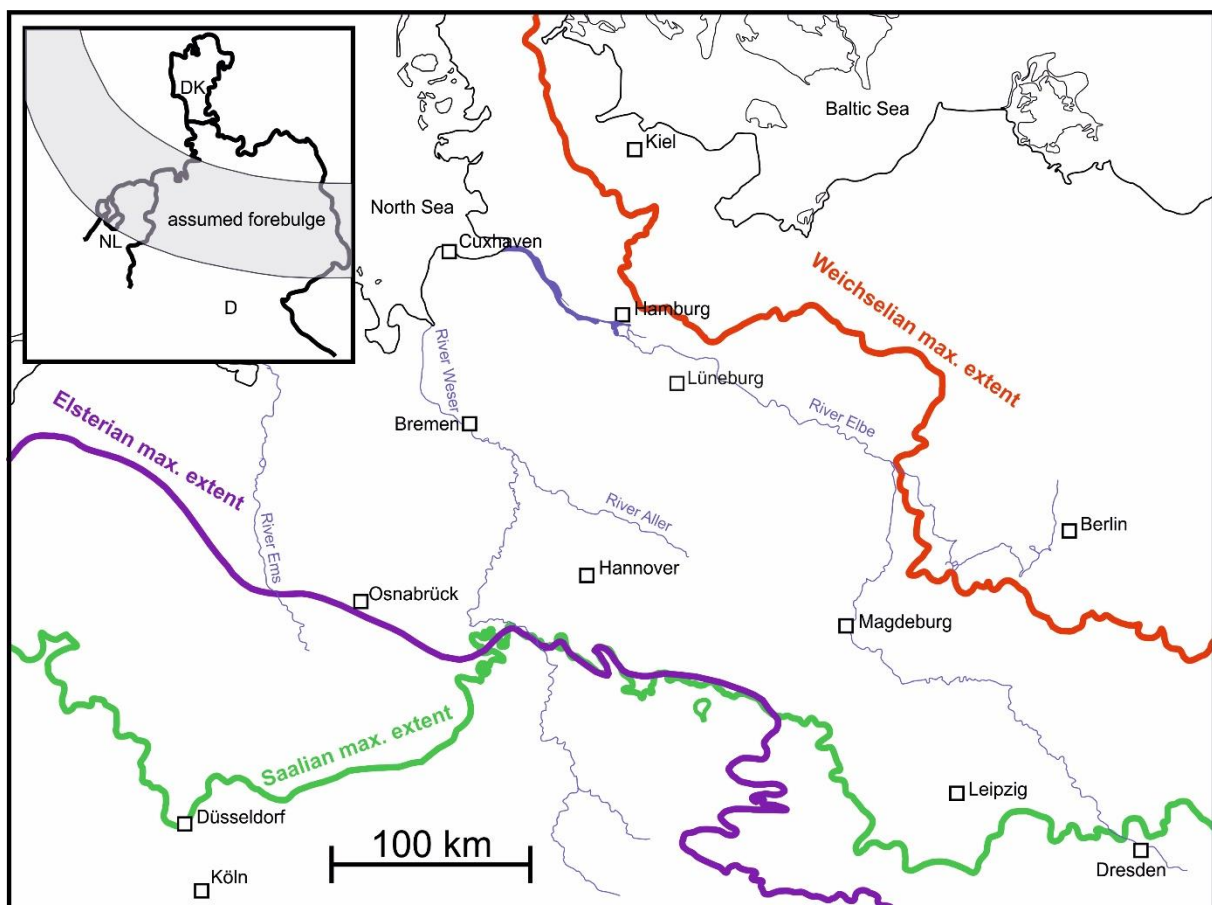


Figure 6. Maximum ice sheet extent of the last three major ice advances. The three major glaciations are drawn here from old to young - Elsterian glaciation (purple), Saalian glaciation (green) and Weichselian glaciation (red). Ice margins are modified from Ehlers et al. (2011). The little sketch in the upper left corner shows the assumed forebulge area after Kiden et al. (2002).

The Late Pleistocene Glacial Maximum occurred during Marine Isotope Stage (MIS) 2 (Lüthgens and Böse, 2012). The maximum extent of the Late Pleistocene ice sheet probably occurred at around 21 ka BP covering an area of approximately 5.5 Mio. km² (Hughes et al., 2016). In northern Germany, the maximum ice extent was reached at about 23 to 22 ka BP (Hughes et al., 2016).

The maximum thickness of the Scandinavian ice sheet at around 21 ka BP (central Sweden, over Ångermanland) was about 2,800 m (Lambeck et al., 2010). Near the German coast of the Baltic sea, the assumed ice thickness was about 750 m going parabolically down to 0 m at the ice margin (Peltier et al., 2015).

Depending on different dating approaches, the onset of the ice retreat in northern Germany is ranging from about 24 (Reimer et al., 2004) to 20 ka BP (Heine et al., 2010). The complete deglaciation of northern Germany was reached between 16.4 to 13.7 ka BP (Lüthgens et al., 2011, Rinterknecht et al., 2014).

More detailed information, referring to Pleistocene ice sheets, extents and thicknesses for different time-slices, which were used in the numerical simulation approach of GIA (carried out by Holger Steffen) can be found among others in Lambeck et al. (2010), Ehlers et al. (2011), Lüthgens and Böse (2011), Marks (2011) and Hughes et al. (2016).

4.1. The glacial isostatic adjustment

In general, the isostatic adjustment is referred to surface mass loading/unloading on the elastic lithosphere floating on top of the lower viscosity media of the mantle. If weight is added to the Earth's crust, the response will be subsidence, and when weight is removed, the crust will rebound (Jamieson, 1865). In addition to that the different rheologies between the lithosphere and underlying mantle are responsible for a time-depending behavior while the system tries to reach the gravitational equilibrium state. The rigid lithosphere is not able to react elastically at once because of the interconnection with the viscous mantle, which prevents an almost instant response (Nansen, 1928). The redirected viscous flowable mantle material leads to a delay time of crustal response (Peltier, 1974).

Mass load and accompanying subsidence was observed by the development and advance of large ice sheets (Jamieson, 1865). On the basis of the surface load (water, ice or sediments), an imbalance was created due to the movement of water from the oceans towards the growing ice sheets, where also a portion of the water-mass was bonded (Williams et al., 1998). According to this mass transfer, two resulting processes were responsible for the subsequent Earth's crust and mantle deformation: (1) the superimposed load of the ice sheet weight depressed the surface down into the viscous mantle, (2) the bottom of the ocean rose slightly due to the missing water load (Steffen and Wu, 2011). During deglaciation, reversing effects can be observed. Prominent driving forces, concerning mass unloading uplift are associated with erosion (Brown and Oliver, 1976) or deglaciation (Jamieson, 1865). Depressed areas rebound in many thousands of years and peripheral areas are often related to subsidence due

to the previously created flexural forebulge in glaciated times (Daly, 1920, see sketch in Figure 6).

The theory of GIA, first mentioned by Haskell (1935, 1936), covers all of the dynamic responses of the Earth to the surface loading events during glaciation and mass unloading during deglaciation (Steffen and Wu, 2011). The whole procedure of subsidence and uplift during ice sheet advances and retreats, with each associated phenomena is described by GIA (Steffen et al., 2014c).

4.1.1 GIA-related phenomena and investigations

The glacial isostatic adjustment describes many Earth's phenomena such as ice age induced changes in the Earth's rotation vector (Mitrovica et al., 2005, Mitrovica and Wahr, 2011), respectively, changes in the length of the day based on pole variations (Ricard et al., 1993), true pole wander (Spada et al., 1992), time-depending variations within the global and regional gravitational field of the Earth (Peltier, 2004) and influences of ice sheets on global climatic change (Clark et al., 1978, Church et al., 2013). In this study, important for the numerical simulations are the relation between GIA and sea-level changes (e.g. Peltier and Tushingham, 1989) as well as GIA and stress changes relating to seismicity (e.g. Stewart et al., 2000, Grollmund and Zoback, 2001).

The modeling of GIA was initially used to determine variations in the relative sea-level (Woodward, 1888, Farrell and Clark, 1976). Peltier and Tushingham (1989) investigated interactions between the ocean, the solid Earth and the cryosphere to install a realistic ice model for reliable GIA modeling approaches. Significant effects of sea-level changes were observed by Peltier (1994, 1996), who showed impacts on the Earth's structure during the last millennia. Sea-level variations can be derived by paleo-strandlines, tide gauges and satellite altimetry measurements. Instrumental observations of global sea-level changes (mainly sea-level rise) have to be corrected by the influence of GIA because the water mass transfer from the ice to oceans and – vice versa – the storage of water within the ice sheets are one of the main origin of regional sea-level changes (Milne et al., 2009). Thus, the history of the past sea-level and recent sea-level variations can be interpreted (Spada, 2016). Furthermore, a forecast of sea-level rise must contain investigations of the Earth's response such as the return of the surface to its isostatic equilibrium (Slangen, 2012). As long as this equilibrium is not reached, GIA responses, referring to surface mass load/unloading, are able to deform the surface below and also in front of the former ice sheets (Stewart et al., 2000, King et al., 2010).

The deformation of the lithosphere and mantle is also responsible for induced stress variations within the viscous mantle and elastic crust, which is able to cause seismicity (Stewart et al., 2000, Grollmund and Zoback, 2001, Steffen and Wu, 2011, Brandes et al., 2012, 2015).

4.1.2 GIA-induced stress changes and associated seismicity

Vertical stress in the lithosphere is induced by the weight of an ice sheet during glaciated times. In addition to the effects on the vertical stress vector, after Johnston (1987), all components of the stress tensor are affected due to the horizontal bending stresses, which are induced by the elastic flexure of the lithosphere.

Figure 7 shows effects of surface loading and unloading during a glacial cycle within an idealized compressional stress regime area. The Mohr diagram describes the influence of glaciation and deglaciation on fault stability. Before a glaciation (BG), in an area, which is dominated by thrust fault movements, the maximum (σ_1) and intermediate principal stress are nearly horizontally oriented and the minimum principal stress (σ_3) is near-vertically oriented. The black Mohr circle (Fig. 7a) is situated next to the failure envelope, which indicates a fault that is close to failure. During the advance of an ice sheet (Fig. 7b), all three principal stresses increase by nearly the same proportion and the Mohr circle is shifted in the direction of positive normal stresses, whereas the radius remains constant (ice blue circle, Fig. 7b). Thus, faults are stabilized and fault slip is suppressed because the Mohr circle is more distant to the line of failure than before. After deglaciation (Fig. 7c), when the ice had melted, the vertical load decreases and the surface rebounds. However, due to the viscous behaviour of the mantle, the rebound of the lithosphere is slowed down. The vertical (minimum, σ_3) principal stress decreases and the radius of the Mohr circle increases significantly because of the almost constant remaining lithospheric bending stress (σ_1 maximum principal stress). The red Mohr circle in Figure 7c touches or crosses the failure envelope and the fault movements are possible. Stress can be released in form of an earthquake.

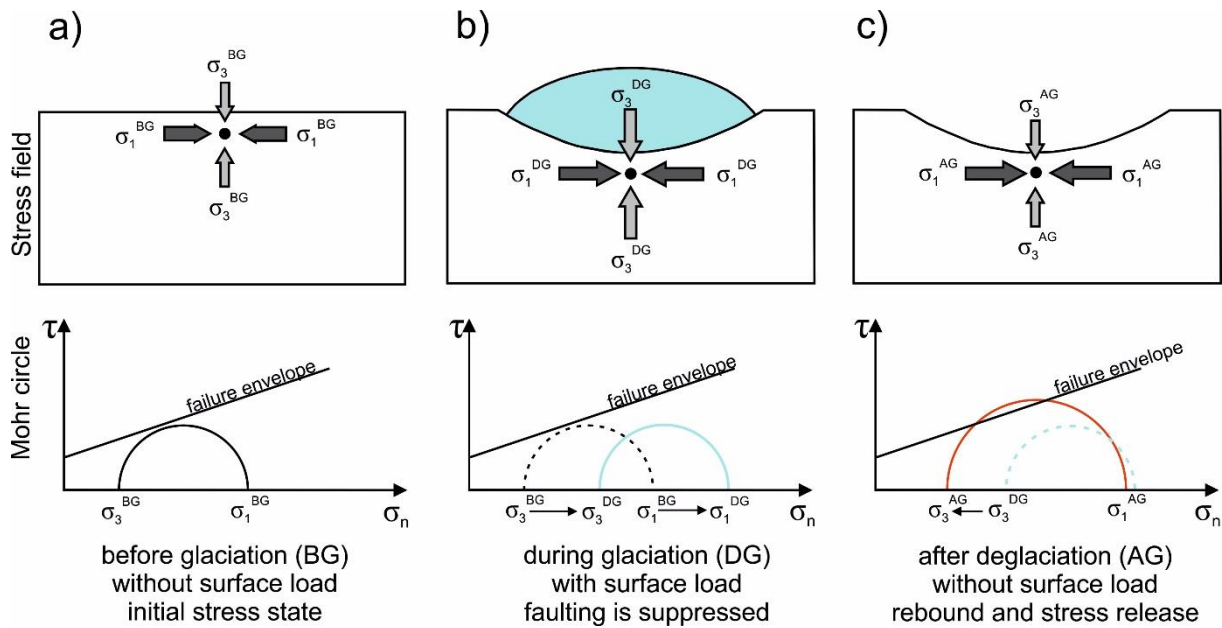


Figure 7. Fault stability for a compressional stress regime resulting in thrust or reverse movement of faults during a glacial cycle. Stress field conditions at a point in the crust are shown in the three top pictures. Relating Mohr circle behavior is given in the three diagrams below the according stress field conditions. Each Mohr circle indicates the maximum (σ_1) and minimum (σ_3) principal stresses on the normal stress (σ_n) axis. The black Mohr circle illustrates stress settings **a)** before glaciation, the blue Mohr circle **b)** during glaciation and the red circle **c)** after deglaciation. The dashed lines highlight Mohr circles with related principal stresses from the previous situation. Details are described within the text above (modified after Steffen et al., 2014b).

Hence, applying this concept on an optimally oriented fault, slip is triggered. Optimally oriented means nearly parallel to the former ice margin (Brandes et al., 2015). Pre-existing faults that were reactivated at the end of a glaciation by the glacial isostatic adjustment are called postglacial faults. The reactivation of these faults was often observed in regions, where a compressional stress regime, resulting in thrust or reverse fault kinematics, is dominant (Mazzotti and Townend, 2010, Steffen et al., 2012 for North America and Steffen and Wu, 2011, for Fennoscandia). However, the reactivation is not limited to thrust or reverse faults. Further evidence for reactivated normal or strike-slip faults, according to GIA was found in North America and Canada (Stein et al., 1979, 1989, Quinlan, 1984, Zoback, 1992), in Scandinavia and on the Baltic Shield (Slunga, 1991, Muir-Wood, 1993, Arvidsson, 1996, Lund and Zoback, 1999). Postglacial faults were formed in times near the end of deglaciation (Steffen and Wu, 2011) and exhibit throws of more than 30 m (Lundqvist and Lagerbäck, 1976).

Glacially-induced earthquakes are originated at postglacial faults in high latitude areas, especially on the northern hemisphere in Scandinavia and North America, eastern Canada (summarized in the following studies among others, Johnston et al., 1998, Plag et al., 1998, Wu et al., 1999, Muir-Wood, 2000, Stewart et al., 2000, Jakobssen et al., 2014, Smith et al., 2014, Berglund and Dahlström, 2015, Sandersen and Jørgensen, 2015, Mikko et al., 2015, Palmu et al., 2015 and Malehmir et al., 2016). Postglacial seismic activity in North America

and eastern Canada is associated with the decay of the Laurentide ice sheet (Hobbs, 1927, Wu and Hasegawa, 1996a, b, Wu, 1998, Wu and Johnston, 2000, Grollmund and Zoback, 2001).

In this study, the interaction between GIA-related stress perturbations, the reactivation of faults, the earthquake occurrence and the influence of ice sheet growth and decay in Scandinavia, a key area of GIA research (Steffen and Wu, 2011) plays a major role to find evidence for a trigger mechanism of the recent seismic events in northern Germany. Therefore, a brief research history of GIA-induced seismicity in Scandinavia and the non-ice-sheet covered region of NW Germany is given in the following.

4.1.3 Observations of GIA-induced seismicity

Scandinavia was covered by the last Late Pleistocene ice sheet, which has completely melted about 9,000 a BP (Muir-Wood, 1989, Mörner et al., 2000, Harbor et al., 2006, Hughes et al., 2016). In contrast to the intraplate region of NW Germany, Scandinavia had experienced remarkably high seismicity in times right after deglaciation, concentrated in certain areas (Fjeldskaar et al., 2000, Mörner, 2004). After deglaciation, the early postglacial rebound was activated and led to earthquakes with moment magnitudes up to M_w 8.2 (Arvidsson, 1996). The magnitude was estimated by Arvidsson (1996) on the basis of an observed fault length up to 160 km with an average rupture displacement of up to 15 m. Moreover, a significant breakout of larger earthquakes at pre-existing faults was observed for this period of initial and fast uplift (Muir-Wood, 1989, Lagerbäck, 1990, Dehls et al., 2000).

However, today, the seismicity is low to moderately low (Mörner, 2004). Recent earthquakes, showing largest magnitudes of $M = 4 - 5$, are concentrated along the border between

southern Norway and southern Sweden, the east coast of Sweden around the northern part of the Gulf of Bothnia and mid Finland (Fjeldskaar et al., 2000). In contrast to the offshore seismicity, the onshore activity is lower and magnitudes are even smaller (Fjeldskaar et al., 2000). Kvale (1960) and Bath (1978) pointed out that earthquakes along the Norwegian coast are mostly driven by tectonic forces, whereas postglacial uplift due to the vanished ice load caused seismic activity at postglacial faults and along the Bothnian Bay (Fig. 8).

The postglacial faults in Scandinavia and related earthquakes, caused by GIA-induced stress changes, were located below the former glaciated intracontinental regions. However, recent studies show evidence for a postglacial seismicity also in front of former great ice sheets. For example, Grollmund and Zoback (2001) stated that the retreat of the Laurentide ice sheet had changed the stress field in the New Madrid seismic zone (eastern-central US), which is

located in front of the former ice sheet and as a consequence the remaining stress variations are still able to trigger earthquakes in this zone. Other possible driving forces for earthquakes in the New Madrid seismic zone are Late Pleistocene erosion by river incisions (Calais et al., 2010), a lithospheric weak zone in combination with the ridge push as the tectonic driving force (Liu and Zoback, 1997, Kenner and Segall, 2000), or the downward movement of a high-density mafic body in combination with deglaciated-induced stress perturbations (Pollitz et al., 2001), which have been proposed and reveal the difficulty to identify trigger mechanisms in a complex crustal region.

Brandes et al. (2012, 2015) and Brandes and Winsemann (2013) found evidence for a postglacial seismic activity along the Cretaceous WNW-ESE trending Osning thrust which is located outside the former ice front relative to the LGM of the Weichselian ice sheet (Fig. 8). The Osning thrust is located near Bielefeld, approximately 70 km south of the study area. Other major Cretaceous WNW-ESE or NW-SE trending reverse faults in northern Germany such as the Aller Valley Fault or the Gardelegen and the Haldensleben Fault in the Altmark area and Magdeburger Börde, respectively (Fig. 8), reveal also historic seismic activity, which is most probably related to postglacial faulting and seismicity (Fig. 8, Brandes et al., 2015).

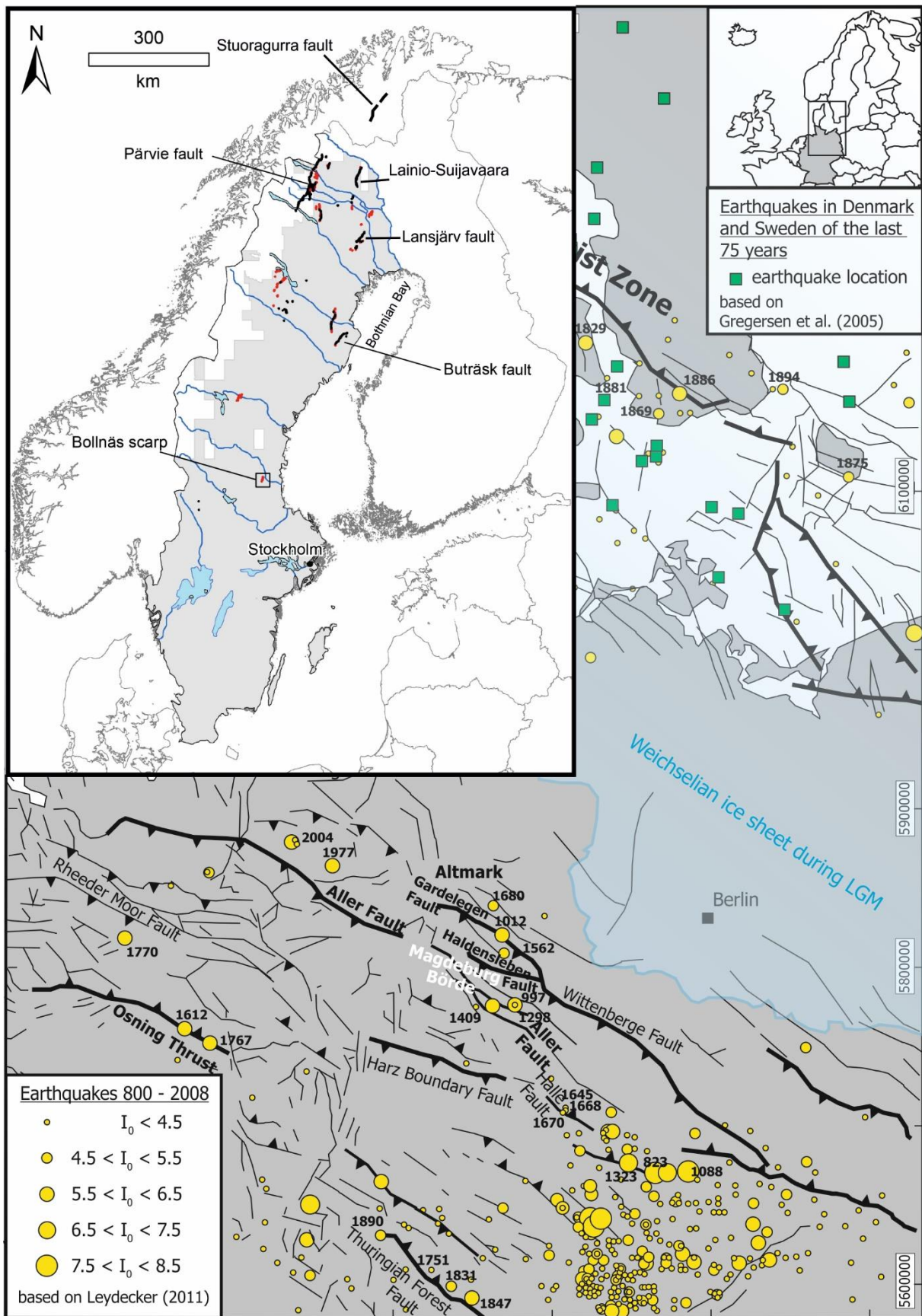


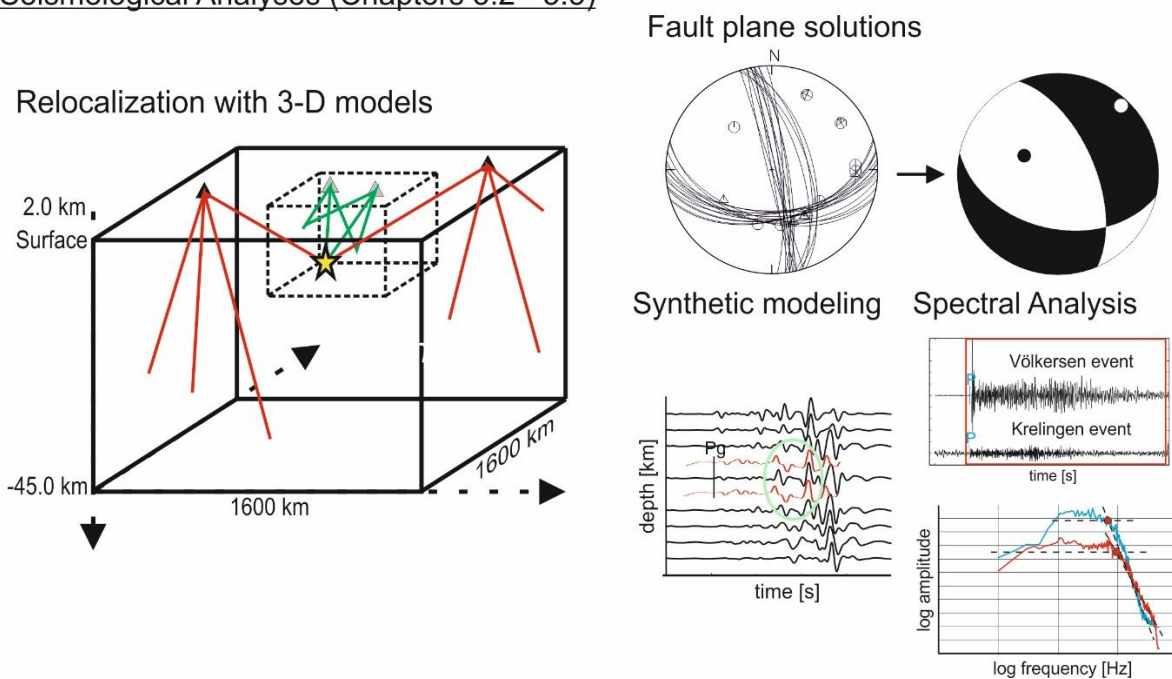
Figure 8. Prominent Cretaceous reverse faults in northern Germany and investigated postglacial faults in Scandinavia (see sketch in the upper left corner). Epicenters of historic earthquakes are also shown (yellow dots). Map based on Kley and Voigt (2008), (modified after Brandes et al., 2015, sketch in the upper left corner is modified after Malehmir et al., 2016).

5. DATABASE AND METHODS

5.1 General workflow

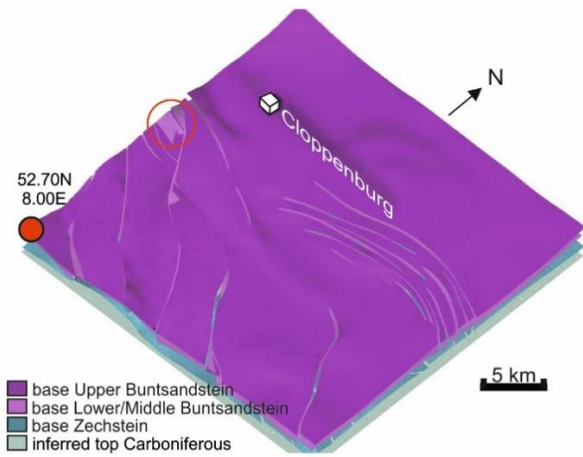
Three major analytical parts were performed in this study (Fig. 9): (I) Seismological analyses, (II) geological 3-D subsurface modeling and (III) the numerical simulations of the glacial isostatic adjustment. Seismological analyses are important to gain a reliable focal parameter database. These precise and highly resolved hypocenter locations were subsequently transferred to the created 3-D geological subsurface models to identify potential seismogenic faults in the study area. Numerical simulations are performed afterwards to figure out the glacial isostatic adjustment and reactivation potential of these faults.

I. Seismological Analyses (Chapters 5.2 - 5.5)

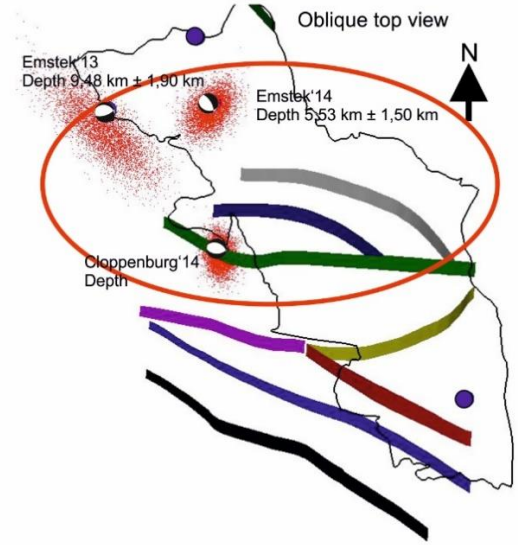


II. 3-D subsurface modeling (Chapter 5.6)

Lithostratigraphic unit modeling

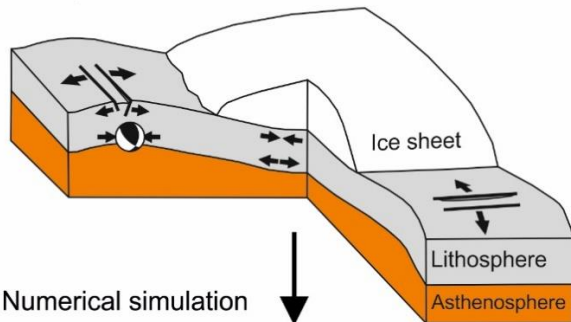


Fault modeling / linking hypocenter

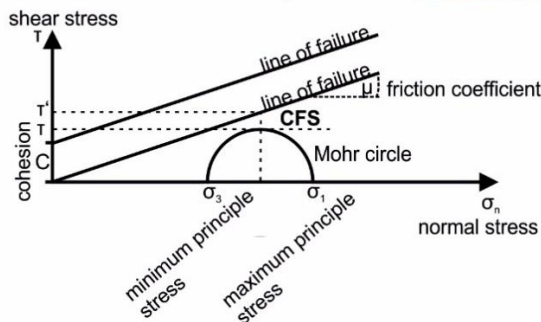


III. Glacial isostatic adjustment (Chapter 5.7)

Theory



Numerical simulation



Coulomb failure stress

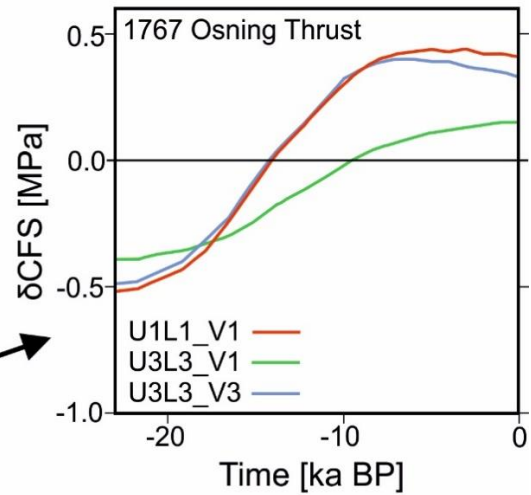


Figure 9. The three major steps in my approach to find possible causes of recent intraplate earthquakes in NW Germany. The chapters where you can find more detailed information, concerning each step are also marked. In part III, the picture of the GIA theory is modified after Stewart et al. (2000) and the Osning Thrust curves on the right are modified after Brandes et al. (2015).

5.2. Relocalization of earthquakes in NW Germany

The relocalization of earthquakes in NW Germany using 3-D velocity models and improving the seismicity pattern is one of the major topic of the seismological analyses and is therefore described in detail. In general, earthquake location is regarded as one of the basic problems in seismology (e.g. Pujol, 2004, Gajewski and Tessmer, 2005) and can be divided into two main parts, a forward computation of theoretical travel times and an inverse search for the unknown hypocenter parameters (Wittlinger et al., 1993). Both, the forward computation and the inversion were applied in this study.

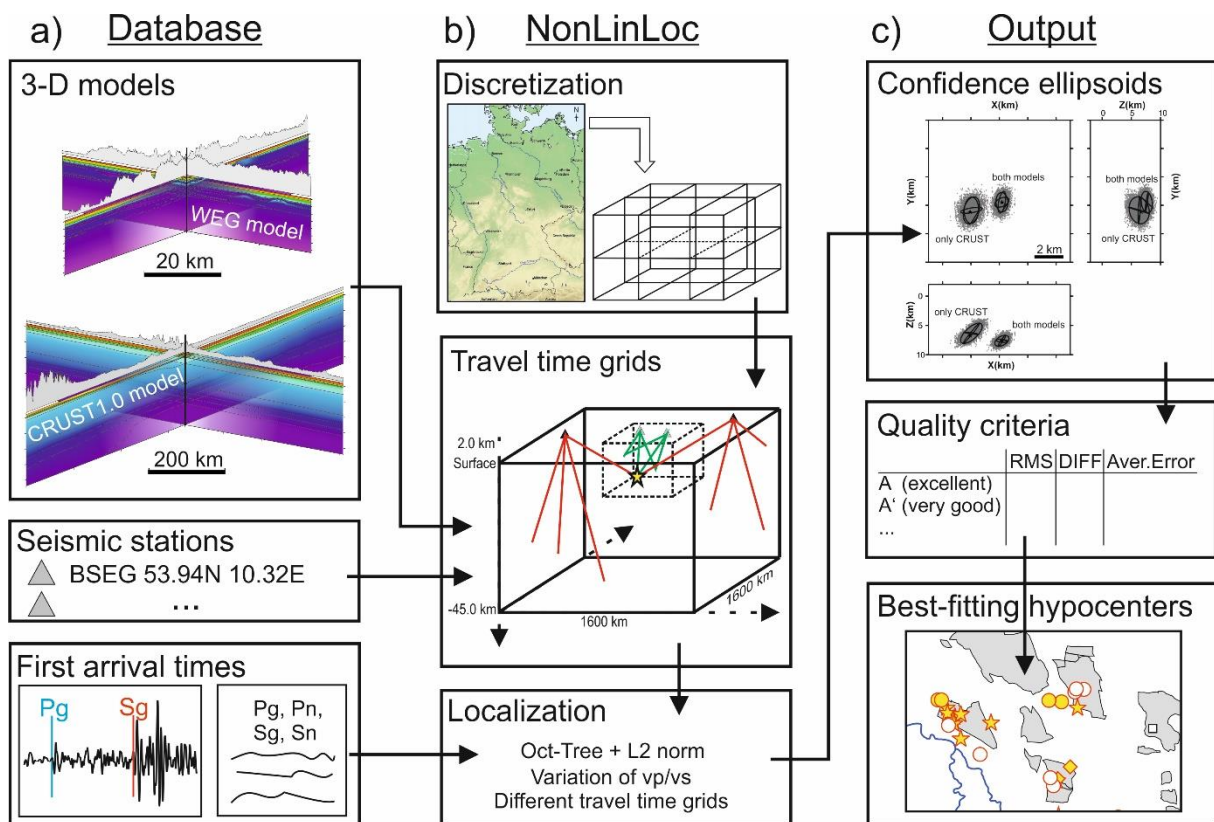


Figure 10. Organigram of the three major steps in the relocalization approach. **a)** The creation of the database comprising repicked first arrival time observations and 3-D velocity models. **b)** The software package NonLinLoc in which 3-D travel time grids were generated on the basis of the 3-D velocity models and the subsequent localization was handled with. **c)** NonLinLoc output parameters were used to derive quality criteria resulting in the best-fitting hypocenters.

The relocalization approach conducted in this study is divided into three main parts (Fig. 10). First, I have picked first arrivals of *P* and *S* phases for all events (77) during the so-called 1-D pre-localization and used them as database for subsequent relocalizations (Fig. 10a). Second, I generated different travel time grids using two differently scaled 3-D *P*-wave-velocity models and relocated selected seismic events with NonLinLoc and varying V_p/V_s ratios (Fig. 10b). In the last step (Fig. 10c), uncertainties derived by the probabilistic relocalization results were

estimated, rated and the best-fitting hypocenters were plotted. The aim was to generate a re-evaluated hypocenter database of earthquakes in NW Germany.

5.2.1 1-D pre-localization

Prior to the 3-D relocation, the establishment of a reliable and consistent phase time database was essential. Since 1991, the German Regional Seismic Network (GRSN) is operated by the Federal Institute for Geosciences and Natural Resources (BGR). During their routine analysis seismologist reviewed available online data to locate local, regional and teleseismic events. However, continuously varying analysts and the iterative-linearized localization algorithm of LocSAT (Bratt and Bache, 1988; Nagy, 1996) in combination with simple 1-D layered velocity models restrain more or less a consistent phase time picking (Husen and Smith, 2004) for most of the earthquakes in Germany. To avoid inconsistencies during the picking process due to different approaches, in the present study I analysed each of the 77 seismic events. In this so-called pre-localization approach the waveform analysis tool Seismic Handler (SHM, Stammer, 1993) and two different 1-D velocity models (Fig. 11) were used to gather accurate seismic phase picks for the first arrival time database.

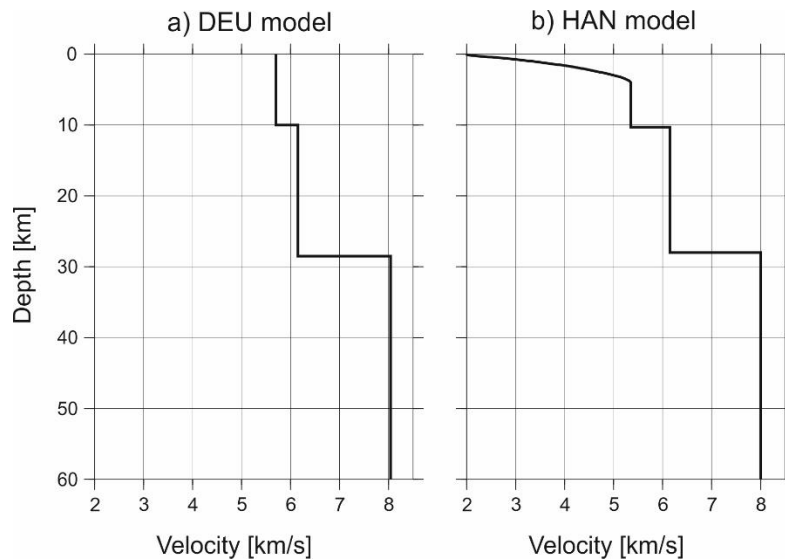


Figure 11. Simple 1-D layered *P*-wave-velocity models, which were applied during the pre-localization to gather phase time picks for the consistent database. Both models were also used in the scope of the routine earthquake analysis at BGR. **a)** DEU model (SZO, pers. communication): A simple two-layer model over half-space with average crustal velocities for Germany. **b)** HAN model (SZO, pers. communication): A slow velocity gradient model in the uppermost layers up to 4 km in depth to simulate the sediment and sedimentary rocks in the upper crust. Below 10 km, the velocity structure is similar to the DEU model.

Diehl and Kissling (2009) provided recommendations for a consistent phase picking procedure, which is tailored to my specific needs:

- 10 s time window around the *P* or *S* onset (kept constant)
- only well constrained onsets (mostly impulsive)
- broadband channel BH (20 Hz sample rate) until 2004, HH (100 Hz sample rate) for the permanent GRSN stations and since 2012 DH-channel (250 Hz sample rate) for stations operated by German Montan Technology (DMT) as well as temporary stations of BGR (EH-channel, 200Hz sample rate)
- Butterworth filter (2. order) 1 - 8 Hz and 5 – 20 Hz ($M_L < 2.0$)

Figure 12 displays typical seismograms from a recent earthquake in northern Germany (Syke, May, 1st 2014) created with Seismic Handler. Highlighted phase picks are *P_g*, *P_n*, and *S_g*, which defines the first arrival time observations of the different seismic waves.

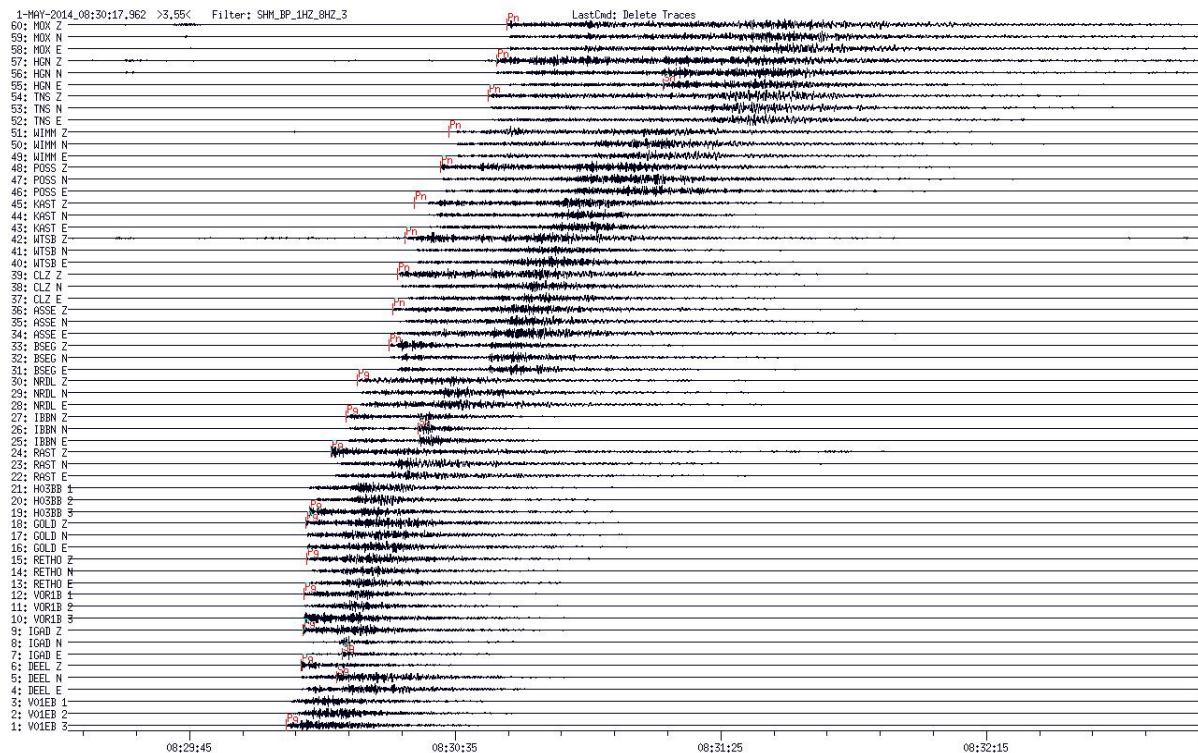


Figure 12. Seismograms from a local earthquake on May, 1st 2014 in the region of Syke. In the diagram the seismic waves propagate from the stations on the bottom to the top.

Altogether, 1102 phases (744 *P* phases and 358 *S* phases) were repicked in filtered seismograms (example in Figure 12) of 108 seismic stations distributed over Germany (see GTSRCE in NLL control-file Appendix I, GRSN and WEG, now referred to as BVEG network stations) and adjacent countries (Luxemburg, Netherlands, Denmark, Sweden, Czech

Republic, Austria and Switzerland). Retained phases, containing direct phases like *Pg*, *Sg* and also the Moho refracted phases *Pn* and *Sn*, served as database for the applied relocalization approach.

Selection classes

Recent studies of Husen et al. (2003), Husen and Smith (2004) or Diehl et al. (2014) pointed out that a high hypocenter location accuracy can be achieved by using only those events for which several preconditions are fulfilled. Following the recommendations of Deichmann et al. (2004) and Diehl et al. (2014), I adopted selection classes on the basis of four defined criteria (Tab. 2 and Fig. 13).

Table 2. Selection classes, which were defined by station network criteria and location uncertainties. Within the amount of seismic events, there is a lack of 12 very small magnitude seismic events. These 12 events were only located by the DMT and adopted from the official website of the WEG (now referred to as BVEG). Abbreviations: GAP = greatest azimuthal distance between two observations; DM = distance from the epicenter to the closest observation; H = horizontal and Z = depth.

Selection class	Seismic network criteria		Location uncertainties		Amount of seismic events
	GAP (degrees)	DM (km)	H (km)	Z (km)	
I	≤ 180	≤ 1,5 x depth	≤ 2	≤ 3	11
II	≤ 200	≤ 25	≤ 5	≤ 10	20
III	≤ 270	≤ 60	≤ 10	> 10	10
IV	> 270	> 60	> 10	> 10	25

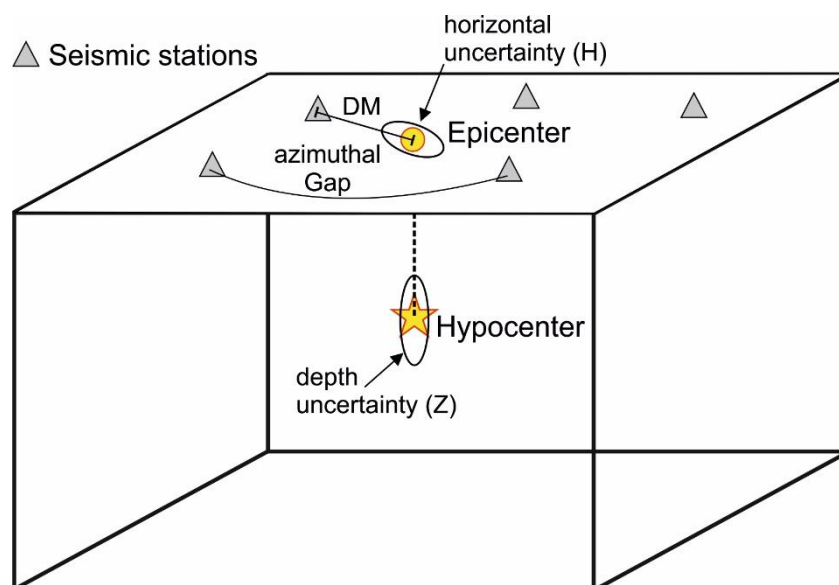


Figure 13. Drawing of the selection class definitions as mentioned above in Table 2. Abbreviations are described in the caption of Table 2.

All seismic events with the best ratings (I and II) inferred from the selection classes (Tab. 2) had been relocated. In case of an almost complete assessment of the recent intraplate seismicity in NW Germany, nine significant events were added, although their data quality is limited (selection classes: III and IV). Most of them were registered before 2012. The ongoing debate, concerning the cause of the Soltau event (June, 2nd 1977, Leydecker et al., 1980, Dahm et al., 2007) prompted me to include also phase picks of the Soltau event from the BGR database and to invert them by using my 3-D relocation approach. Altogether, 40 out of 78 seismic events had been relocated with NonLinLoc. Due to the limitation of NLL (only first arrival observations are used), I had to evaluate and reduce the phase pick database by 95 *Pg* and 65 *Sg* phases. Finally, the relocation of the 40 seismic events was performed using 507 *P* phases and 195 *S* phases.

5.2.2 3-D relocation

My applied technique differs widely from the routinely used 1-D earthquake localization approach of Seismic Handler (Stammler, 1993) in combination with the implemented iterative-linearized algorithm of LocSAT (Bratt and Bache, 1988, Nagy, 1996) and is also hardly comparable with further prominent 1-D localization programs like Hypo71 (Lee and Lahr, 1975), Hypoinverse (Klein, 1978) or Hypoellipse (Lahr, 1980).

Wittlinger et al. (1993) already stated the importance of applying new localization methods that incorporate complex 3-D velocity structures as had been observed for subduction zones, volcanoes and hydrocarbon fields. In the following, I describe both 3-D velocity models used in this study, the probabilistic earthquake localization approach imprinted within the applied software package of NonLinLoc and the evaluation of hypocenters as well as their uncertainties.

3-D velocity models

Two differently scaled 3-D *P*-wave-velocity models are the basis for the relocation: a) Crust1.0 model (Laske et al., 2013) and b) the so-called WEG model (made available by the Association of German Oil and Gas Producers, WEG, now referred to as BVEG, but in this study, the model is still named WEG model). Before 2012, northern Germany had a very limited seismic station coverage. To analyse earthquakes older than 2012, solely distant seismic stations would be taken into account and further the applied velocity model has to be large enough like the Crust1.0 to span these stations. Younger events that occurred after the installation of the new networks in 2012 can be analysed with the more detailed, smaller and

fine-meshed WEG velocity model. Both velocity models were combined to allow an analysis of the two different datasets.

a) the CRUST1.0 model

The model Crust1.0 is a one-degree crustal model for the entire world and is evolved from previous models - CRUST5.1 (Mooney et al., 1998) and CRUST2.0 (Bassin et al., 2000). Crust1.0 has nine depth layers with different depth values. Each layer has defined *P*- and *S*-wave velocities as well as densities as a function of depth. Information about topography, depths and velocities were taken from a sediment model (Mooney et al., 1998), the model ETOPO1 (Amante et al., 2009), the model LITHO1.0 (Pasyanos et al., 2014) and were finally combined with 170 distinct velocity functions (Laske et al., 2013). The data of the initial CRUST1.0 model was adapted for the study area by an interpolation of the *P*-wave velocity over 0.5 degree cells in latitude and longitude, each in 1 km depth steps. The determination was handled with MATLAB© (MATLAB and Statistics Toolbox Release 2012b, The MathWorks, Inc., Natick, Massachusetts, United States). Figure 14 displays the coverage of this modified model including topographic profile lines. The modified CRUST1.0 model covers the entire crust of Germany and adjacent areas up to a depth of 45 km. It encompasses a region from the Alps in the south to Denmark in the north and from the Netherlands in the west to Poland in the east, respectively. This great model extent was necessary to assure that each seismic station, which was used for the localization (108 seismic stations) was entirely enclosed in this model and the determination of seismic travel times to each node of the model grid was possible.

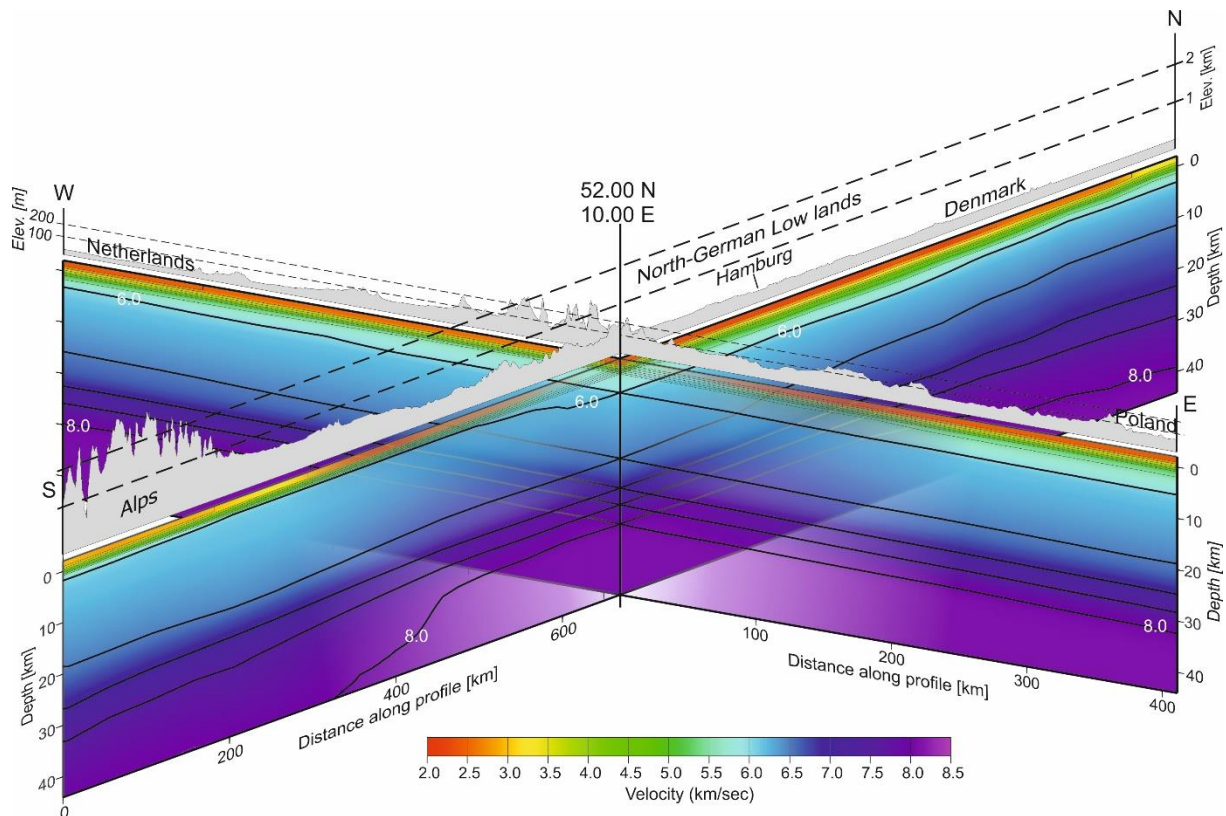


Figure 14. Vertical cross-sections of the modified Crust1.0 3-D *P*-wave-velocity model (see black dashed profile lines in Fig. 1). End point coordinates of the profiles are 46.00N 10.00E, 58.00N 10.00E; 52.00N 4.00E, 52.00N 16.00E. This model covers 1600 x 1600 x 45 km (L x W x H). The grey colored topographic profiles are used for orientation inside the model. Significant features are e.g. the Alps or the North-German Low lands. Furthermore, below the Alps, the descending Moho forming the crustal root is visible.

b) the WEG model

The WEG model is a more detailed velocity model for an area of 88 x 73 x 15 km (L x W x H). Since 2012, a monitoring seismic network with 6 borehole and 15 surface stations is operated by the German Montane Technology (DMT) in the region of Völkersen, Rotenburg/Söhlingen in the west, and Walsrode to Lüneburg in the east (red dashed lines in Figure 1 and vertical cross-sections in Figure 15). Each of these seismic stations is entirely located within the WEG velocity model. The waveforms were made available by industry partners. Furthermore, most of the temporary stations installed by BGR and universities as well as some additional GRSN stations are also situated in the distinct WEG model area. The WEG velocity model is based on components of smaller-scaled velocity models, which were developed from seismic subsurface experiments (Fritschen and Kremers, 2013). For a reliable hypocenter localization significant features are well resolved in this model: (1) salt structures, (2) laterally distributed zones of high and low velocities. To my knowledge, this is the most realistic model for this distinct area.

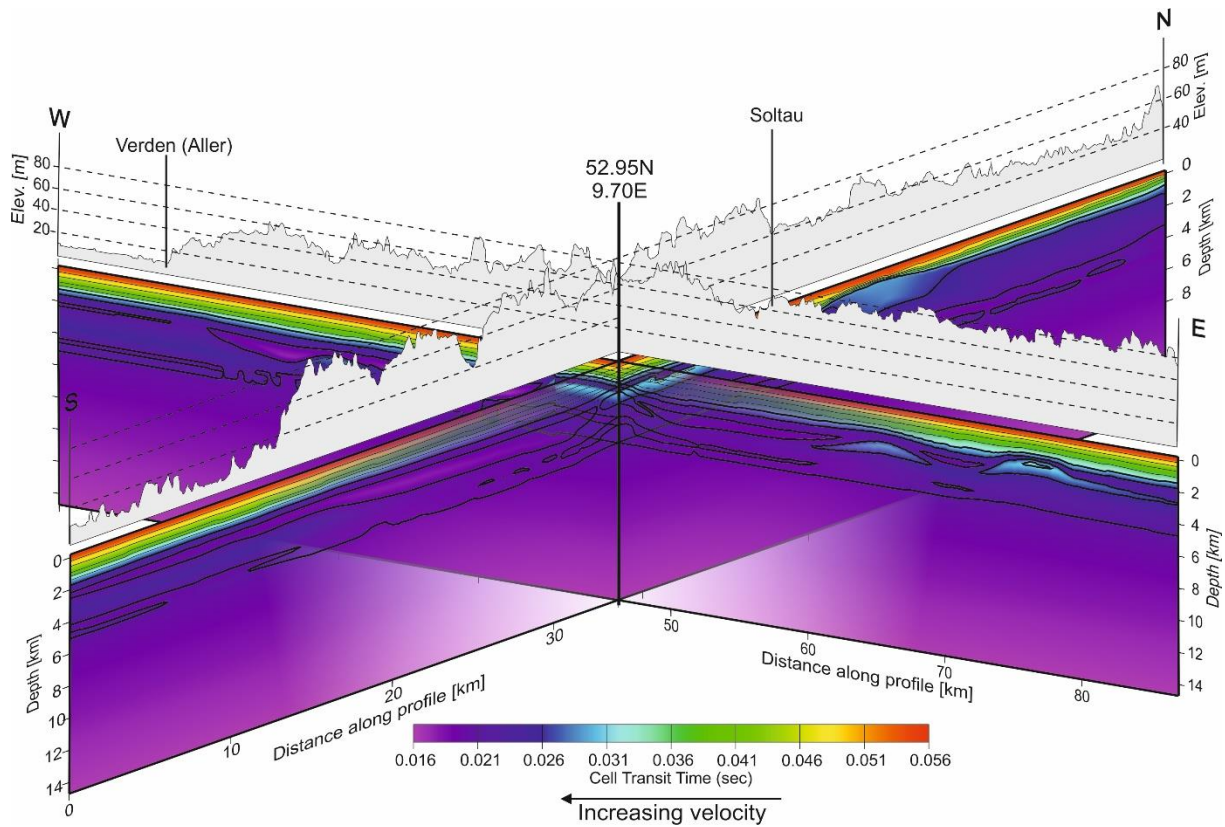


Figure 15. Vertical cross-sections of the WEG 3-D *P*-wave-velocity model (see the short red dashed profile lines within the study area in Figure 1). End point coordinates of the profiles are 52.65N 9.70E, 53.25N 9.70E; 52.95N 9.10E, 52.95N 10.30E. The grey colored topographic profiles are used for orientation inside the model.

In Figure 16 the dimensions of the two velocity models are shown. The WEG model is totally embedded in the modified CRUST1.0 model. An advantage of this configuration is the strong reduction of computational time for the 3-D models, because the size of the very detailed model is limited and the amount of grid nodes is manageable.

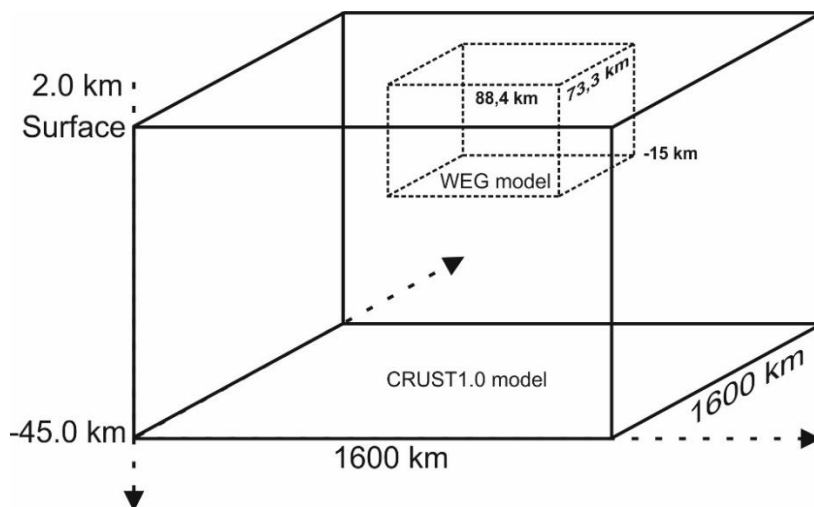


Figure 16. Dimensions of the two applied 3-D velocity models. The WEG model is entirely embedded in the modified CRUST1.0 model. Both models consist of different detailed velocity information. Note: Dimension of the WEG model is exaggerated for a better visualization.

It has to be taken into account that short wave paths suffer strongly from heterogeneous media (Aki, 1968). Thus, the high sediment thickness (Littke et al., 2008) as well as velocity anomalies like salt structures (Scheck-Wenderoth et al., 2008), fluids/brines saturated sediment layers (Gaupp et al., 2008, Shillington et al., 2008), which are present in the Northwest German Basin (Ziegler, 1990) had the major influence on wave paths and seismic velocities. These velocity anomalies, especially salt structures, showing high velocity gradients are well resolved within the more detailed WEG velocity model. In contrast, long travel paths, passing through a coarse grid (CRUST1.0 model) were hardly influenced by these velocity changes. NonLinLoc provides the possibility to incorporate different 3-D velocity models. In the next subchapter, the different program packages of NonLinLoc are described in more detail.

5.2.3 The software package NonLinLoc

The 3-D relocalization approach in this study was carried out with the software package NonLinLoc (NLL), (Lomax et al., 2000, Lomax et al., 2001, Lomax et al., 2009). NonLinLoc is able to solve the non-linear inversion problem formulated by Tarantola and Valette (1982a, b) by using probability density functions (PDF) to determine a complete non-linear (3-D) hypocentral solution including location uncertainties. There are two different localization modes called: global and non-global search. I used the non-global search for the localization of local earthquakes in NW Germany. In this setting, NLL applied a left-handed, rectangular, x-, y-, z-coordinate system, where east is in positive x-direction, north is in positive y-direction and the depth is in positive z-direction. Units are in kilometers. The software package consists of four main programs - Vel2Grid(3D), Grid2Time, Time2EQ and NLLoc. So-called generic control statements and program parameters are stored in one control file (see Appendix I). In this chapter, I describe briefly how these individual program parts work, what boundary conditions, input parameters and limitations had to be considered prior to the re-localizations and how the output files can be used to evaluate the uncertainties.

Vel2Grid(3D)

This program processes different dimensional velocity models. In a first step, a region or rather the extent of the used velocity grid (VGGRID = control file statement) and the grid origin had to be defined. The study area was discretized by a finite number of nodes in x-, y- and z-direction with certain edge lengths. It is important that the length of the edge is in equal size, because only square cells will be used for travel time determinations (slowness-vectors). In the next step, the user had to define parameters for the velocity model, like layer depth, P -

wave (and/or S-wave) velocities and/or densities for each layer. This is simple for 1-D velocity layers over a half-space.

In case of 3-D velocity models, the program was modified - Vel2Grid 3D (Stephan Husen, pers. communication, and recently available in the NonLinLoc beta version). Information about depth and corresponding velocities for certain layers have to be written in the input format of SIMULPS12 (Thurber, 1987). As described above, MATLAB© was used to interpolate the data of the CRUST1.0 model and also fit them into this pattern. Vel2Grid or Vel2Grid 3D converted the input parameters into 3D-velocity-grid-files, which were used for the next subprogram.

Grid2Time

Within the previously generated 3D-velocity-grid-files, containing velocity information of a certain model, Grid2Time is able to calculate travel times from selected seismic stations to each node in the defined grid. The seismic stations are listed in the control file with information about latitude, longitude and elevation (negative value for depth). The travel times were determined by the scheme of the Eikonal finite differences algorithm, which was developed by Podvin and Lecomte (1991). This numerical method supports the determination of only first arrival times but provides accurate first travel times in the presence of extremely severe, arbitrarily shaped velocity contrasts (Podvin and Lecomte, 1991), as resolved within the detailed WEG velocity model. The algorithm calculates the length of slowness vectors (values in seconds) through square cells. It is striking that the computation time increases significantly with the used grid dimension and amount of grid points.

Time2EQ

Synthetic model tests can be carried out with this subprogram. Therefore, predicted arrival times and/or predicted take-off angles were determined. Input parameters are a synthetic hypocenter including x-, y- and z-coordinates and several seismic stations for which the predicted times were calculated using formerly created travel time grids. This forward calculation is also based on the Eikonal finite differences algorithm of Podvin and Lecomte (1991). Results were written in a so-called observation file to use them in the subsequent inversion, which is described in the next subprogram.

NLLoc

In this subprogram, the previously determined travel times (Grid2Time) were combined and compared with the picked phases of each seismic event. In this case, an observation file had to be written in a certain pattern. An example of the used NLL-format is shown in Table 3.

Table 3. Example of a part of an observation file in the supported NLL-format. Question marks in the “Phase”-column define further onset parameters such as the first motion (compressive or dilative), or phase onset (emergent or impulsive) and others. These are not taken into account during the localization procedure.

Stationcode	Phase	Date (yyyymmdd)	Time (hhmm)	Onset time (ss.sss)	Error
NRDL	? ? ? P ?	20141219	0412	54.117	GAU 0 0 0 0
SEVE	? ? ? S ?	20141219	0412	35.668	GAU 0 0 0 0

As mentioned before, the non-linear inversion problem formulated by Tarantola and Valette (1982a, b) is approximated by the determination of probability density functions (PDF). For each inversion, a priori information was considered to solve the PDF. Mistakes within the observations or errors in the predicted travel times are normally distributed. Therefore, each error is arbitrarily distributed and not subjected to systematic errors. The localization algorithm follows the L2-norm to determine the PDF and is described with the formula below:

$$pdf(x, t_0) \propto k \times \exp \left(-\frac{1}{2} \sum_{obs_i} \frac{[T_{obs_i}(x) - T_{calc_i}(x)]^2}{\sigma_i^2} \right)$$

Therein, the x defines a point in the three dimensional space, t_0 marks the estimated origin time, k is a scaling factor; T_{obs} and T_{calc} are the observed, respectively predicted travel times, which are squared (L2-norm). Three different methods for searching seismic events within the predefined study area are available - two analytic and one stochastic approach. In this study, the analytic Oct-Tree Importance Sampling method (Lomax et al., 2000) was used. It is similar to a normal grid-search, but approximately ten times faster (Lomax and Curtis, 2001). The Oct-Tree mode uses an initial grid, which is defined in the control file. This grid is subdivided into 8 new equal size cells at the point with the highest probability (respectively the minimum misfit value). The subdivision will proceed until the lowest cell-size or the maximum amount of subdivisions is reached (Fig. 17). In contrast to a normal grid search, the Oct-Tree search did not raster the complete grid.

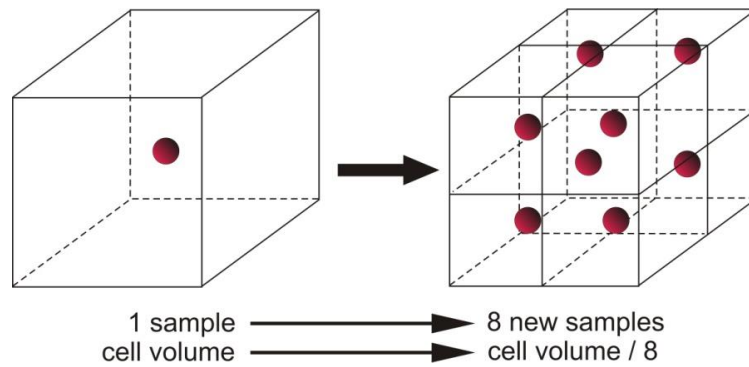


Figure 17. Oct-Tree search method: One initial cell with a predetermined point of the probability density function (red dot), which was subdivided into 8 uniform cells, where the algorithm of Tarantola and Valette (1982a, b) calculated eight new probabilities (modified after <http://alomax.free.fr/nlloc/>).

Preliminaries and limitations of NonLinLoc

As mentioned before, the finite difference algorithm of Podvin and Lecomte (1991) imprinted in NonLinLoc supports only the determination of the first arrival times. Therefore, NLL is not able to differentiate between different P (P_g , direct wave or P_n , Moho refracted wave) and S (S_g or S_n) phases. In contrast, LocSAT (Bratt and Bache, 1988) is equipped with predicted travel time tables of each local seismic phase for its iterative and linearized localization approach. In case of the pre-localization procedure, direct and Moho refracted phases were stored together within the observation files, which should be used in the inversion. However, in a distance of about 140 km between a seismic station and an epicenter, the first arrival phase is changing from P_g to P_n or S_g to S_n , respectively because of a higher Moho refracted wave velocity (Bormann, 2012, Fig. 18). Due to this limitation of NLL, I had to evaluate and reduce the phase pick database.

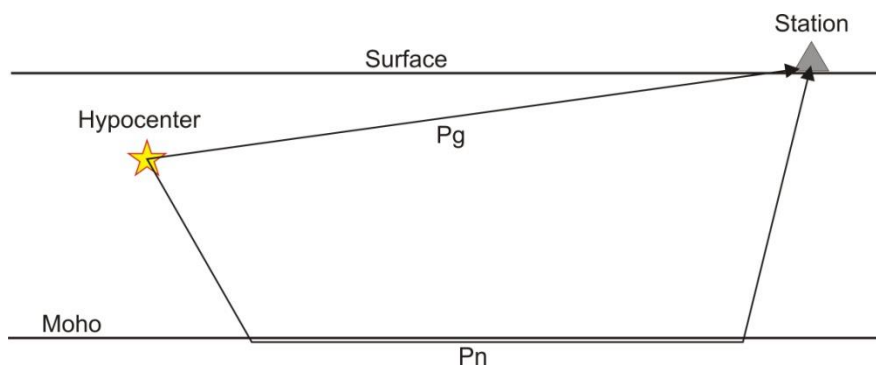


Figure 18. Different travel paths of emitted phases from the hypocenter. P_g defines the direct wave and P_n describes the refracted wave, which moves directly beneath the Moho with a higher velocity in contrast to the direct wave (modified after Bormann, 2012).

Reliable hypocenter depth determinations are very important to achieve an accurate picture of the seismicity pattern. However, there is a distinct uncertainty in hypocenter depth determination if there is no station, which is close to the analysed seismic event. A well-

constrained determination of hypocenter depth is possible if at least one seismic station is located not more than approximately 1.5 times of focal depths distance from the epicenter (e.g. Gomberg et al., 1990, Steinberg and Rabinowitz, 2003, Deichmann et al., 2004). Another opportunity to get reliable hypocenter coordinates is the observation (modeling) of depth phases (pP) (Dahm et al., 2007). During the pre-localization approach with Seismic Handler the focal depth was fixed, if the seismic stations were too far away from the epicenter. This option is not available in the software package NLL and requires the formation of an additional criterion in the selection of the processed earthquakes. The quality criteria are shown in Table 4 (chapter 5.2.5).

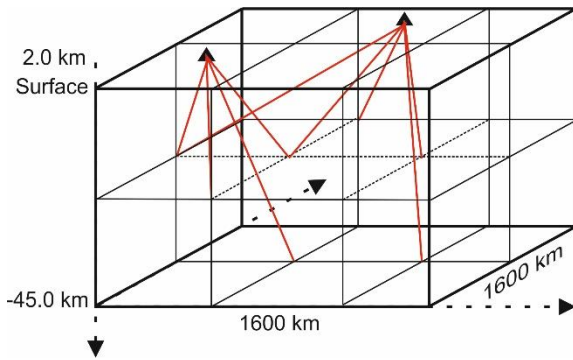
5.2.4 3-D travel time grids

The implemented Eikonal finite differences algorithm of Podvin and Lecomte (1991) calculates predicted travel times from selected seismic stations to each node in the 3-D grid, which encompasses the predefined and discretized extension of the chosen input velocity model. Altogether, three travel time grids, which are shown and described in Figure 19, had been generated:

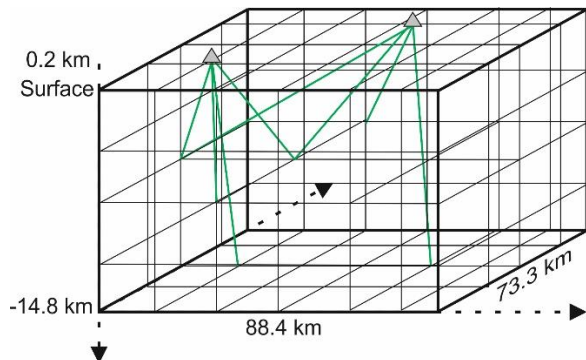
- the 3-D P -wave CRUST1.0 velocity model for Germany and adjacent areas (Fig. 19a)
- the 3-D P -wave WEG velocity model for the region of Völkersen, Söhlingen and Walsrode (Fig. 19b)
- a combined P -wave-velocity model, comprising velocity information of both models (Fig. 19c)

Because of the absence of an accurate S -wave-velocity model the ratio between compressional (V_p) and shear (V_s) wave velocity (V_p/V_s) had been set by hand as a fixed value for each relocalization run. The common V_p/V_s ratio usually assumed for crustal layers is about 1.73 ($=\sqrt{3}$). I applied a variation between 1.65 to 1.95 (with a step of 0.01). The lower threshold is based on results of e.g. Gregory (1976), Hamada (2004) or Shillington et al. (2008) who identified a decrease of 10 - 20 % in V_p/V_s due to the presence of hydrocarbons in the subsurface. The upper limit of 1.95 is somewhat arbitrary. However, it is based on some vertical seismic profile (VSP) measurements in the Northwest German Basin that shows an average V_p/V_s ratio of about 2.0 within the first 2,000 m depth (Dr. Thomas Bartels, DEA Deutsche Erdoel AG, pers. communication).

a) large-scaled CRUST1.0 travel time grid



b) fine-meshed WEG travel time grid



c) combination of both grids

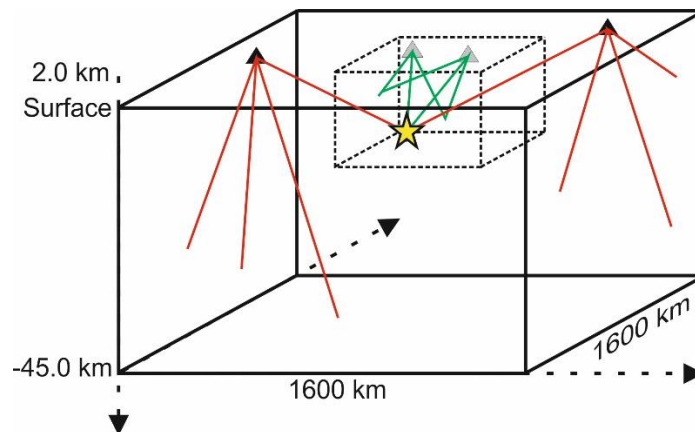


Figure 19. Schematic layout of the separately calculated travel time grids. **a)** The created CRUST1.0 model was subdivided by the Vel2Grid 3D subprogram of NonLinLoc into cubes with edge length of 1 km. Grid2Time interpolates and converts the velocity information to slowness vectors considering each cube. **b)** The same procedure was done for the WEG model, however, with a more closely meshed grid using an edge length of 100 m for the very limited region of Völkersen, Rotenburg/Söhlingen, and Soltau. **c)** Both determined travel time grids were combined within one new travel time grid, in which each station only exists once. For example, the seismic event (yellow star) was located by different travel time information, which includes velocity information of the CRUST1.0 model for distant stations (red ray paths) and for short travel times containing the more detailed velocity information of the WEG model (green ray paths). No ray path cut through the other velocity model. This type of combination helps to avoid velocity artifacts within the travel time grids.

5.2.5 Uncertainty estimation and associated quality criteria

Hypocenter uncertainties are evaluated by output parameters provided by NonLinLoc such as the root mean square value (RMS), the density scatter-plot obtained by samples from the PDF and the 68% Gaussian estimated confidence ellipsoid. The shape of the density scatter cloud depends on the azimuthal distribution of seismic stations (network geometry), measurement errors of the observations (e.g., phase misidentification or delay) and errors within the determination of predicted travel times (e.g., velocity model errors) (Husen and Smith, 2004). After Husen and Smith (2004) a well constrained hypocenter solution should have the following criteria:

- ellipsoidal shape of the scatter cloud
- small extent of the confidence ellipsoid
- well matching scatter cloud within the confidence ellipsoid (avoid different local minima)
- determined hypocenter close to the midpoint of the ellipsoid (short distance between expected and determined hypocenter)

Figures 20a and 20b display the differences between a well constrained hypocenter solution (Fig. 20a) and a hypocenter solution, which depends on a poor, respectively limited database. In most cases, the greater uncertainty domains in x and y direction (Fig. 20b) are caused by a limited station coverage resulting almost in a high GAP (greatest azimuthal distance without observation), whereas the length of the z-axis (depth uncertainties) depends on the lack of at least one seismic station within the critical focal depth distance (1.5 times of focal depth, Deichmann, 2003; Deichmann et al., 2004).

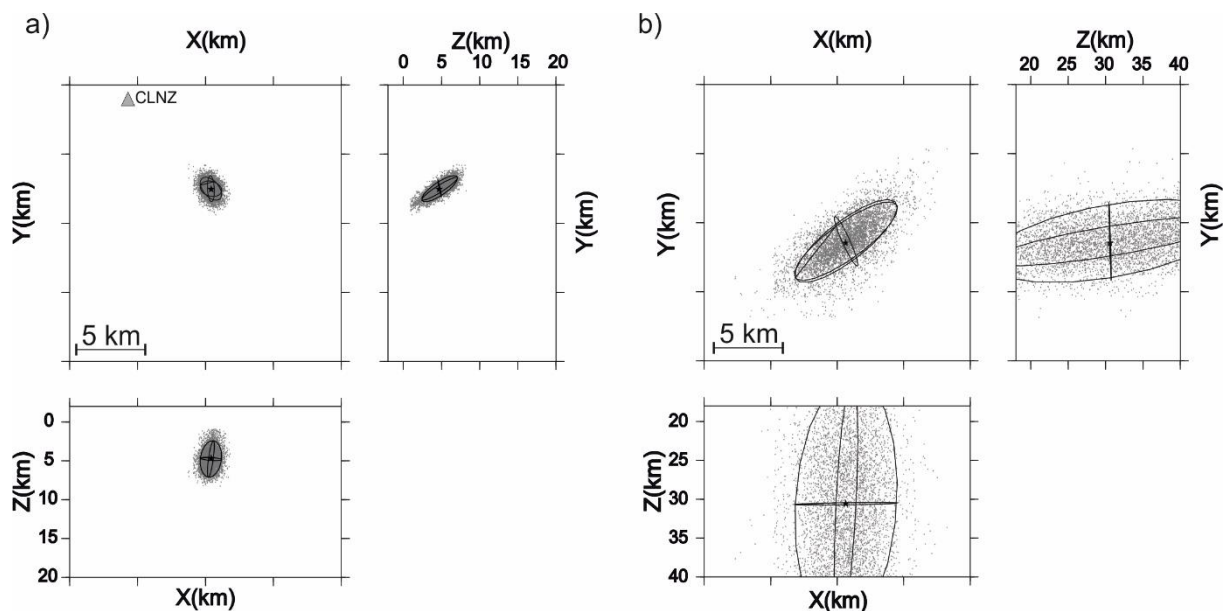


Figure 20. Differences of a well-constrained hypocenter location and a poorly-constrained hypocenter. These are shown by different extents of the 68 % confidence ellipsoid including the scatter cloud obtained from samples of the PDF, one horizontal view in x and y direction and two cross-sections (xz and yz). **a)** A well-constrained hypocenter, which is defined by a small extent of the confidence ellipsoid, a well-matching scatter cloud within the ellipsoid and a very small distance between the maximum likelihood hypocenter and the expected one. **b)** A poorly-constrained hypocenter solution. Details are given in the text.

The quality class definitions (Tab. 4) are based on statistical output parameters provided by NonLinLoc. The RMS value is determined during the relocalization procedure, whereas the difference between the maximum likelihood and the statistically expected hypocenter location in a x, y, z medium (DIFF value) and the average error had to be calculated manually. The discrimination of these values is described afterwards while defining the quality classes (the complete table is given in Appendix II).

Table 4. Definition of the five qualities to classify the relocated events and figure out the best-fitting hypocenter location if different parameters were used during the localization procedures (modified after Husen and Smith, 2004). Abbreviations: RMS = root-mean-square value; DIFF = distance between expected and determined hypocenter; Average error = sum of each axis of the confidence ellipsoid divided by 3.

Quality class	RMS (s)	DIFF (km)	Average error (km)
A (excellent)	< 0.5	< 0.5	< 2.0
A' (very good)	< 0.55	< 0.5	< 2.0
B (good)	< 0.7	< 0.5	≥ 2.0
C (questionable)	< 0.7	≥ 0.5	≥ 2.0
D (poor)	≥ 0.7	≥ 0.5	≥ 2.0

The differentiation between both best quality classes A and A' by increasing the RMS value from 0.5 s to 0.55 s is somewhat arbitrary, but necessary for my purpose. Some of the relocated events derived RMS values, which are slightly higher than 0.5 s because of using a high amount of observations, mostly more than 18 *P* and *S* phases for the relocation. This increases the probability of receiving a higher phase time error occurred during the picking process, which affects directly the RMS value. Nevertheless, the hypocenter is very well constrained due to its very small uncertainty domains. In turn, this weakens the impact of the RMS value, which is often regarded as the major quality factor to classify the hypocenter accuracy.

5.2.6 Synthetic tests of travel time grids

My relocation approach is based on the combination of two differently scaled 3-D *P*-wave-velocity models: the interpolated coarse CRUST1.0 velocity model (Fig. 14) and the small-scale WEG velocity model (Fig. 15). In order to test the efficiency of this approach, synthetic travel time grid tests were conducted. Firstly, to examine if the application of two differently scaled travel time grids in combination with NonLinLoc is properly working and secondly, to investigate how strong the bias on the hypocentral parameters is, by using a simplified model and a more detailed velocity model for inversion. The geometry of the network, the calculation of the travel times as well as the three tested synthetic scenarios are as follows:

Prior to the inversion, I created an artificial station network consisting of 11 near-epicentral (WEGx) and 14 far-epicentral (CRUSTx) seismic stations being embedded in the area of the WEG and of the CRUST1.0 model, respectively. This station configuration was approximately adopted by a simplified station network geometry in Germany and follows

recommendations of Diehl et al. (2014) or Deichmann et al. (2004) for station network geometry. A hypothetical seismic event (named SYN) was placed somehow in the middle of the WEG model area (Fig. 21) at a hypocentral depth of 5 km.

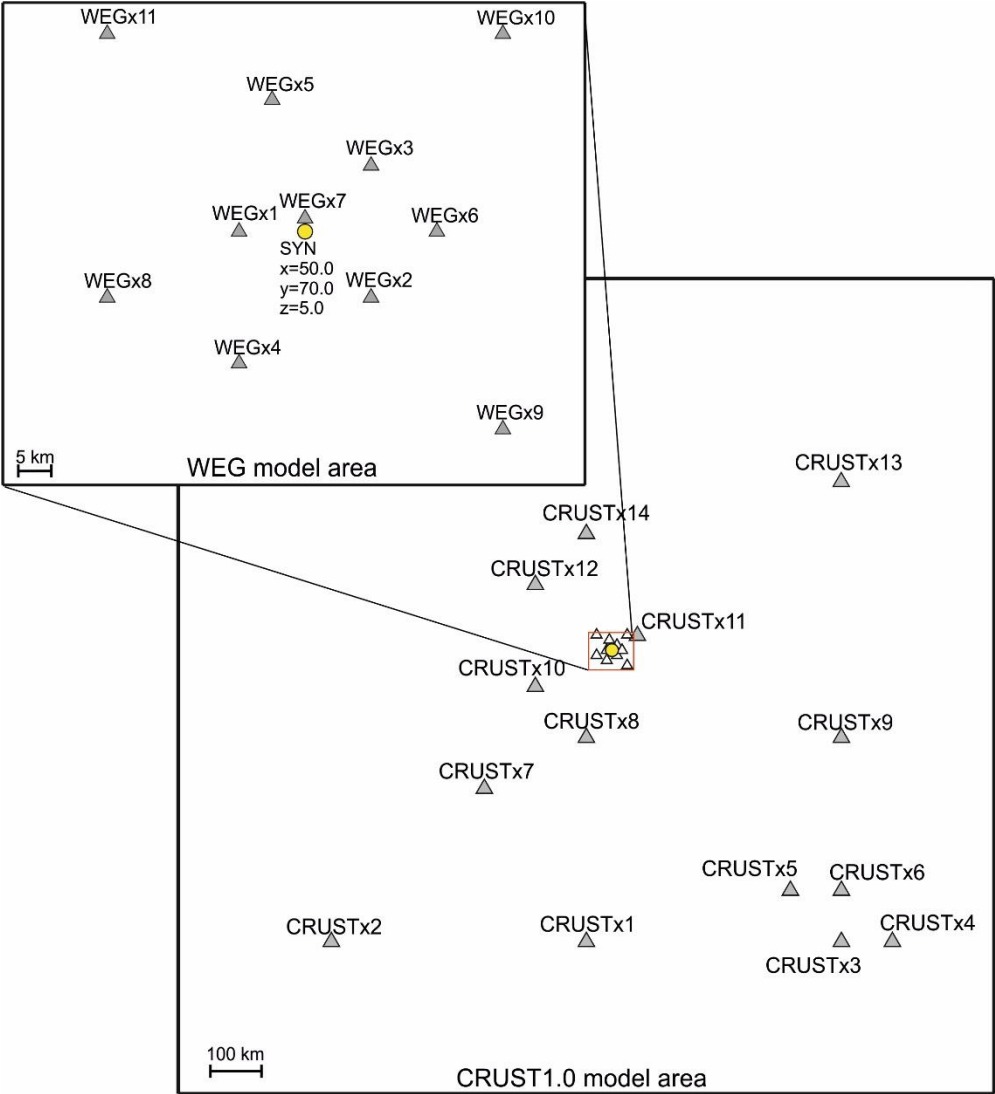


Figure 21. Extent of the WEG and CRUST1.0 model area comprising the created synthetic station distribution and the event location (SYN) used for the forward calculation of predicted arrival times within different travel time grids.

The predicted arrival times from the hypothetical hypocenter to the stations were calculated by the NonLinLoc subprogram Time2EQ, which determines arrival times at different seismic stations using the formerly generated travel time grids (see Figures 19a-c) by applying the Eikonal finite differences algorithm of Podvin and Lecomte (1991). The forward calculation of *P* phases was done in two steps: (1) predicted arrival times were calculated from the hypocenter to the WEGx stations using the WEG travel time grid, (2) predicted arrival times from the hypocenter to the CRUSTx stations were computed with the CRUST1.0 travel time grid. Then, both synthetic arrival time datasets were stored within one observation file and

subsequently inverted using several individual travel time grids described in three scenarios below:

Scenario a: This so-called ideal inversion was conducted with the combined velocity model grid. Thereby, WEGx arrival times were inverted with the WEG travel time grid and CRUSTx arrival times were inverted using the CRUST1.0 travel time grid. The determined hypocenter of the inversion for this ideal test is shown in Figure 22 together with the uncertainties (red scatter cloud and 68 % confidence ellipsoid). As expected, the hypocenter was located nearly at the same point as the synthetic event and thereby almost exactly retrieved (rms = 0.001 s). On the basis of this computation, the proper function of NonLinLoc for the purpose was confirmed and I was able to continue to further tests.

Scenario b: The second inversion was conducted on the basis of the predicted arrival times now exclusively inverted with the coarser CRUST1.0 travel time grid, this meant also for the near epicentral stations (WEGx). As shown in Figure 22, the extent of the confidence ellipsoid is nearly the same as for the ideal case in Scenario a, only a small epicentral shift was observed (green colored scatter cloud). However, the focal depth was shifted about 5 km deeper in comparison to the given synthetic hypocenter. Moreover, the root-mean-square value of 0.46 s is considerably higher than in Scenario a.

Scenario c: This third scenario was similar to the second one. Instead of the CRUST1.0 travel time grid a grid for a simple 1-D layered velocity model (DEU model, Fig. 11a) was applied and also used within the scope of the routine earthquake analysis of BGR. The result of the inversion is shown in Figure 22, where confidence regions are highlighted in yellow. The hypocenter clusters beneath station WEGx7. An epicentral shift of about 2 km in the direction of the y-axis was observed with respect to the given synthetic epicenter. The confidence regions in the z-axis are very large and the RMS value of 1.26 s is very high, both indicating a poorly-constrained focal depth.

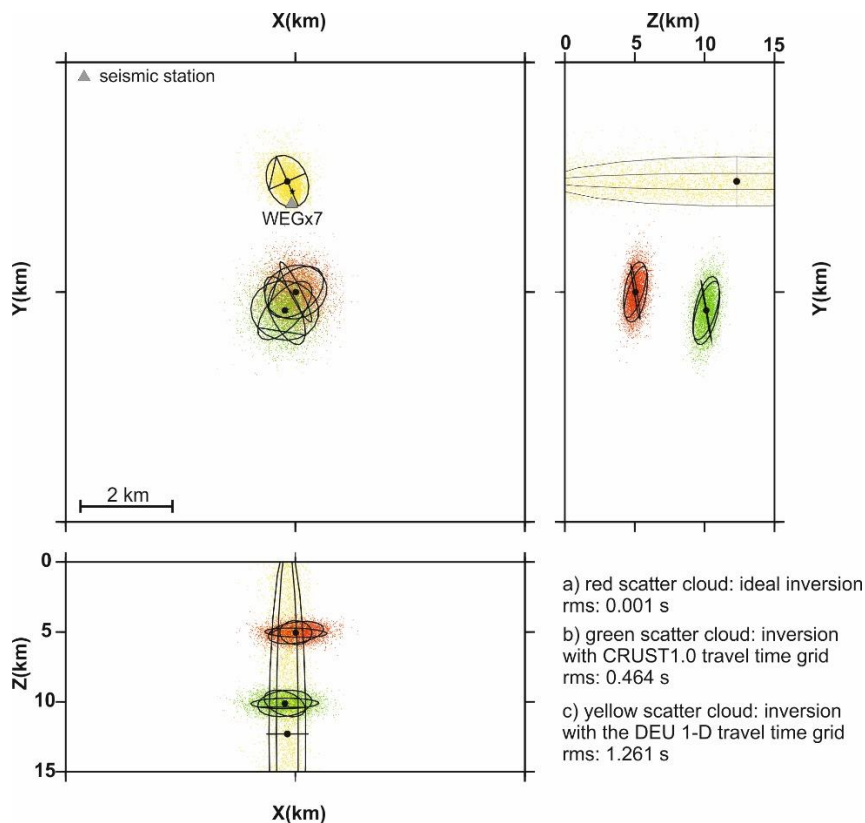


Figure 22. Scatter clouds and associated 68 % confidence ellipsoids of the three inversion results. The different inversion approaches (a - c) are described in the text above.

In further synthetic tests (not shown here), I had reduced the number of stations or observations, respectively. In these tests, the uncertainties for the inversion with the 1-D layered model significantly increased. The same was observed for the coarse CRUST1.0 model. However, only from a station reduction of more than 30 % the uncertainties became larger. These tests demonstrate that the 3-D models are more robust than the 1-D one.

Implications of synthetic tests

The synthetic tests show that a combination of two differently scaled velocity grids in combination with the NonLinLoc hypocenter inversion yield reasonable results. These tests also reveal that the near-epicentral seismic stations in combination with different velocity grids have the major impact on the hypocenter determination and its uncertainty domains. Especially, a 1-D velocity model is not sufficient to provide a reliable focal depth in a heterogeneous crustal region. Without an accurate velocity model, which is able to reflect the crustal structure beneath seismic stations in detail, the effect of average velocities (faster than the velocities in the detailed model) on the hypocenter are very large, especially concerning the focal depth. Therefore, if there is a heterogeneous subsurface structure around the hypocenter, a fine meshed 3-D velocity model in the vicinity of the analysed event is strongly demanded to determine a reliable focal depth.

5.3 Fault plane solutions

At the source point, an earthquake releases seismic waves and causes deformation. Fault-related earthquakes refer to faulting that can be described by different slip orientations. End-members of these slip orientations are strike-slip, normal faulting and reverse/thrust faulting. Thereby, fault plane solutions (also referred to as focal mechanisms) define the spatial orientation of a planar fault surface and a slip along this fault. In addition to the location and magnitude of an earthquake, the fault plane solution is an important focal parameter to correlate investigated seismic events with the predominant tectonic regime. They are very important to define the radiation pattern of seismic waves to identify seismogenic faults and to serve as input parameters for calculations of theoretical seismograms (see chapter 5.4).

For NW Germany, only a very limited number of fault plane solutions were determined and published in studies and reports (Tab. 5). However, to better understand the seismicity in a distinct area, it is important to achieve more and reliable focal parameters.

Table 5. List of published focal mechanisms for earthquakes in northern Germany.

Event name	Date	Focal mechanism	Nodal plane	Reference
Soltau	02 June 1977	oblique reverse fault	NNW-SSE	Leydecker et al. (1980)
Rotenburg	20 October 2004	oblique normal faulting	roughly N-S	Dahm et al. (2007)
Völkersen	22 November 2012	normal faulting	WNW-ESE	Bischoff et al. (2013)
Syke	01 May 2014	oblique normal fault	WNW-ESE or N-S	Bischoff et al. (2014)
Emstek	19 December 2015	oblique normal fault	NNW-SSE or NNE-SSW	Bischoff et al. (2015)

Therefore, the database of focal mechanisms is extended by the following approach: Parameters, which were created during the relocalization with NonLinLoc and the two 3-D velocity models form the basis of the determination. Especially, the take-off angles, calculated on the basis of the 3-D velocity models were different to those using simple one-dimensional layered models.

The double-couple focal mechanisms were determined using a grid search algorithm provided by the software package FOCMEC (Snoke et al., 1984, Snoke, 2009). FOCMEC, written in Fortran 77 code, uses polarities (P , SV and SH) and/or amplitude ratios (SV/P , SH/P and SV/SH) to search for the best-fitting nodal planes over a focal sphere projection (lower hemisphere), in increments of 1 to 5 degrees. Additional parameters for the calculations are station codes, azimuth of seismic stations and take-off angles (depending on the source depth

and chosen velocity model) (example see Table 6) based on the solutions of the hypocenter inversion with NLL and 3-D velocity models.

Table 6. Input file (extract) example for the FPS calculation using FOCMEC. The first column shows user information, which will not be taken into account during the calculation of the focal mechanisms. Abbreviations: *P* polarities, D = Dilatation (onset down on z-component), C = Compression (onset up on z-component); *SH* polarities, < = first motion to left (back to event, facing station), > = first motion to right (back to event, facing station) (modified after Snoke, 2009).

Emstek'14, 19.12.2014, depth: 5,533 km, velomod: CRUST1.0, P-Pol without filter			
Station code	Azimuth	Take-off angle	Polarities
FAH	338.17	113.7	D
SYK	85.36	80.3	C
CLZ	126.71	48.6	C
CLZ	126.71	48.6	<
BSE	41.71	44.7	>

Phase polarities were taken from unfiltered seismograms - *P* polarities on z-component and additional *SH* polarities on the rotated seismogram transversal component were picked. Each polarity was rated with a quality value from 5 - very good (impulsive) over 3 - moderate to 1 - suspected (mostly emergent). *P* polarities with a quality of 5 and only, if it was needful the quality of 3 were used for the determination of the focal mechanisms. In this case, *P* polarities of lower quality were taken into account if the station coverage was limited. Thereby, results should be interpreted with caution. Furthermore, a second experienced analyst had picked the polarities independently. In the next step, both solutions were compared to minimize uncertainties and to derive high quality input parameters for FOCMEC. In addition, to gain a more robust and reproducible fault plane solution for each selected event, four common 1-D *P*-wave-velocity models (Fig. 23) were also used for the determination. The FPSs were only calculated for events with the following criteria:

- magnitude $M_L \geq 2.0$
- magnitude ≤ 2.0 but observations ≥ 15
- source depth, which was determined with NLL and 3-D models
- $GAP \leq 180$

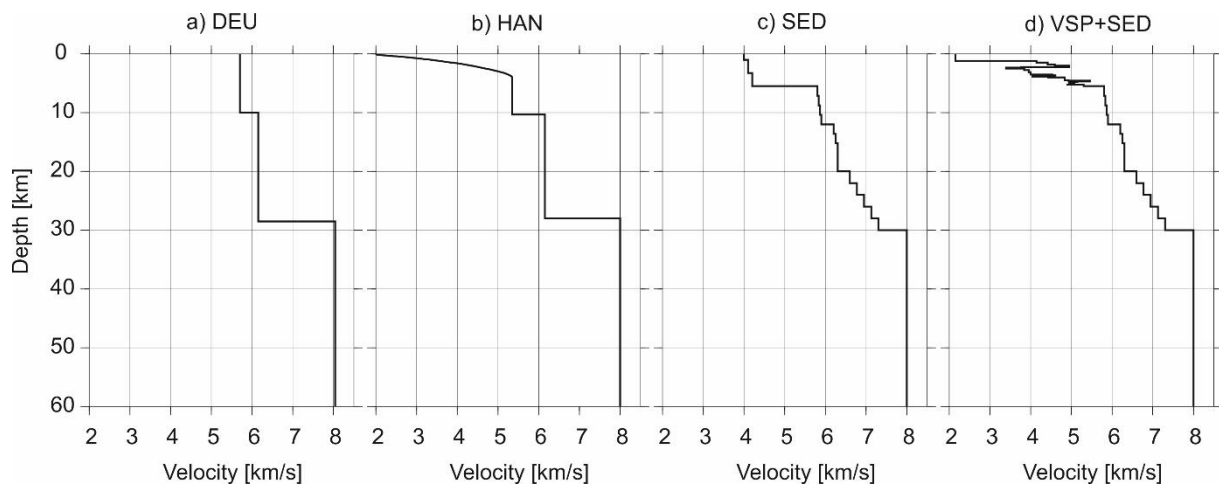


Figure 23. 1-D *P*-wave-velocity models, which were used during the determination of FPS. **a)** A simple two layer over half-space model with average crustal velocities for Germany; **b)** A slow velocity gradient model in the uppermost layers up to 4 km in depth to simulate the sediment and sedimentary rocks in the upper crust, after 10 km it is similar to the DEU model; **c)** A more detailed layer model adapted from Dahm et al. (2007); **d)** A combination of *P*-wave velocities adapted from a vsp-processing near Völkersen (Dr. Thomas Bartels, DEA Deutsche Erdoel AG, pers. communication) followed by data from the aforementioned SED model.

However, additional significant earthquakes like Rotenburg'04, Bassum'05, Langwedel'08 and Emstek'13, which do not fulfill all the requirements, are also considered for calculating the fault plane solutions. The results of these older events have to be handled with care due to their relatively small database. Fault plane solution results are given in chapter 6.2.1.

5.4 Synthetic seismograms

Synthetic seismograms are a powerful tool to model earthquake source parameters, as for example the hypocenter depth or the focal mechanism. Under the assumption of a source model and a media between the source and the receiver, full seismic waveforms can be calculated via wave propagation theory. A subsequent comparison between the synthetic seismograms and the observed ones allows conclusions on the used source parameters in the model.

In the present study, synthetic seismograms are calculated on the base of the reflectivity method, which was introduced by Fuchs and Müller (1971). In particular, the extended reflectivity method is used, in which reflection and transmission coefficients are calculated recursively in a horizontal, layered model. A detailed description is given in e.g., Kennett (1983) and Müller (1985). The applied program code is PSWELLdLC (modified by Lars Ceranna, pers. communication). It calculates synthetic seismograms for a layered medium along a vertical velocity profile from a predefined source depth up to the Earth surface.

The main input parameters for the calculation of the synthetic seismograms are a) the velocity model of the media b) the moment tensor or the earthquake focal mechanism, respectively c) the source signal and the frequency range under consideration and finally d) the hypocenter and the spatial distribution of seismic stations.

In the following, the choice of the relevant parameters for my application is described:

a) Velocity model: Firstly, CRUST 1.0 model was used. However, it became apparent, that for the calculation of the synthetics the CRUST1.0 depth profile is too coarse. Therefore, I changed to the SED model (sediment layered model, Dahm et al., 2007, see Figure 23c) which was also applied during the evaluation of the fault plane solutions. S-wave velocities are calculated for a constant V_p/V_s -value of $\sqrt{3}$ (~ 1.73). Subsurface layer densities are adopted from the literature (e.g., Landolt and Börnstein, 1982, Blundell et al., 1992). The values are averaged over typical material properties for each stratigraphic unit. The attenuation, quantified by Q (seismic quality factor) for P and S waves is depending on the depth. In most cases, the Q-factor increases with depth (e.g., Roecker et al., 1982, Gagnepain-Beyneix, 1987). I follow a recommendation of Leydecker et al. (1980) that the Q-factor for the P wave in the first 5 km has a value of 80 and the Q-factor for P waves below 5 km has a value of 200. The Q-factor for the S waves is set to 4/9 of the Q-factor for P waves.

b) Moment tensor: The orientation of the double-couple represented by strike, dip and slip, is strongly affecting the amplitudes of the different crustal phases. For the calculation of the synthetics, the double-couple solutions calculated and provided in chapter 6.2.1 are used and transformed into moment tensor notation.

c) Source signal and frequency range: Specifications of the source signal and the frequency band defined the seismogram length as well as the dominating period and the frequency window. As source signal a Küpper-wavelet with the dominant period of 1 Hz was used in the calculation of the synthetic seismograms. The Küpper-wavelet has been chosen due to its simple waveforms (Emoto et al., 2010). In a further step, the synthetics as well as the observed seismograms were filtered with a 1 Hz lowpass filter. The application of the lowpass filter leads to more simple waveforms, which are more convenient to model. The application of the filter improves the visualization of the key phases without significant information loss. Furthermore, a detailed fine-gridded 3-D velocity model is not available for the broader region, which however is necessary to model the higher frequencies.

d) Hypocenter and station distribution: The hypocenters are adopted from the 3-D localizations with NonLinLoc presented in chapter 6.1.2 and station distributions are reproduced by real observations. An example of an input-file is shown in Table 7.

Table 7. Input-File for the program PSWELLdLC.

Input-File	Description
1000110010 DEU Modell Mai-2015, Syke-Beben 2014	program execution switches / header
1.00 0.000	reference frequency / exponent
0.00 5.700 3.290 2.780 400.0 300.0 0 30.00 5.700 3.290 2.780 400.0 300.0 1 30.00 8.050 4.620 3.300 500.0 300.0 0	velocity model layer depth/vp/vs/density/Q-value1/2 /gradient description
	blank line
1 1	source position / no. of point sources
0.0000 0.0000 5.0000 0.0000 1.0000	coordinates and strength of source
1 16384 0.0100 1.0000 0.0250 0.0500 3.0000 6.0000	data of source signal and frequency band
65.000	suppression of time domain aliasing
0.600 0.600 0.750 20.000 25.000 25.000 1500	data of integration over slowness
0.000 0.000 0	reduction velocity and minimum time
1.0000 0.0000 0.0000 0.0000 1.0000 0.0000	definition of double couple
5	total number of receivers
5.000 360.0000 90.000 360.0000 90.000 90.0000 120.000 360.0000 120.000 90.0000	receiver coordinates distance / azimuth

After processing each seismogram datasets, I compared significant sections of the complete synthetic seismograms with parts of the real waveforms to constrain the hypocenter depth and to verify or improve the fault plane solutions. The workflow approach was the following:

- Calculation of complete waveform synthetic seismograms (particle velocity, cm/sec) for selected seismic stations defined by the distance and azimuth. These seismograms were calculated on the basis of different source depths and a fixed fault plane solution or two varying focal mechanisms (Rotenburg example).
- Loading the real waveform seismogram within Seismic Handler (Stammler, 1993). Pay attention, in which sample rate the traces are.
- Transferring each synthetic seismogram to Seismic Handler and plotting them within the same figure.
- Identification of the first onset. The zero point on the timeline is tagged by the origin time of the investigated earthquake.
- Filtering each seismogram with a 1 Hz lowpass filter.
- Identification of characteristic features within the real seismogram.
- Comparison of time-dependent characteristic features, which were located at the same time in both waveforms to find the best-fitting hypocenter depth and/or fault plane solution.

Two significant earthquakes were used to test this complex and new qualitative approach – the seismic event near Syke (May, 01st 2014) and the Rotenburg mainshock from October, 20th 2004. For both, focal parameters such as the hypocenter depth and/or the fault plane solution are not reliable and provided higher uncertainties. The Syke'14 seismic event was used to describe this approach in detail. For the Syke'14 event, synthetic seismograms of focal depths between 3 – 8 km were determined for the seismic station IBBN (Ibbenbüren) using the fixed focal mechanism, which was derived from the FPS determination. The simulation of the older Rotenburg earthquake was more difficult, because the hypocenter depth and the focal mechanism remain unclear after the evaluation. Therefore, several hypocenter depths (3 – 13 km) and two different fault plane solutions (normal and thrust faulting) were theoretically calculated for the seismic stations NRDL (Niedersachsen-Riedel) and BSEG (Bad Segeberg). Each synthetic seismogram was calculated for the vertical, and both horizontal – transversal and radial – component. A detailed description and challenges are given in the results (chapter 6.2.2).

5.5 Amplitude spectra and corner frequencies

From the spectrum of seismic waves, seismic source parameters such as fault length, rupture velocity and stress drop can be derived (Aki, 1967). Thus, the shape of the amplitude spectra and their associated corner frequency depend on the magnitude and seismic moment (M_0), respectively (Bormann, 2012). More information about source spectra, corner frequencies and impacts of seismic source parameters on the spectra were given in Bormann, 2012). In this study, the evaluation of amplitude spectra and the determination of corner frequencies formed an additional and advanced approach to create possible discrimination criteria between induced seismicity and natural tectonic earthquakes for the region of NW Germany.

The waveform analyses tool Seismic Handler Motif (SHM, Stammer, 1993) provides the option to calculate and visualize the spectral content of a selected section of a seismogram in form of amplitude spectra based on a Fast Fourier Transformation (FFT). For a better visualization, the spectra were stacked ten times. This allowed the identification of distinct frequency peaks or amplitude values within the different seismograms. Figure 24 represents a typical log/log amplitude spectrum (displacement spectrum), where the amplitude is plotted against the frequency. The two main elements of the curve are marked with dashed lines - named the plateau and the decreasing amplitude part. The intersection point between these two straight lines, called the corner frequency (f_c), is highlighted by a red dot. After Bormann (2012), the plateau-section is defined as a constant ground displacement for frequencies smaller than f_c . Its amplitude depends on the seismic moment M_0 . Each amplitude with $f > f_c$ is subjected to a decrease with an almost constant factor (sloping section, Fig. 24). This decay of spectral displacement amplitude is decreasing until half of the sample rate is reached. For comparison, each amplitude spectrum of the selected seismic events was taken at the same seismic station - CLZ (Clausthal-Zellerfeld, z-component, sample rate 100Hz) with a seismogram recording of about one minute. The selection window, defining the time period, covers almost the entire waveform (signal) of the seismic event and starts about one second before the first onset occurs.

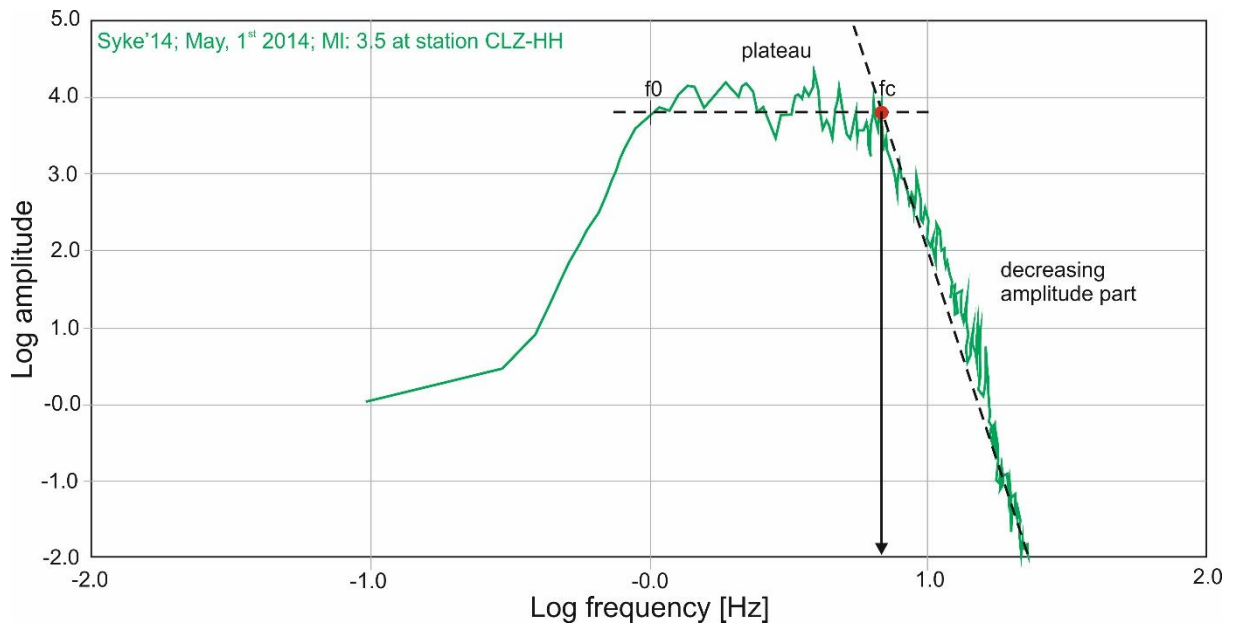


Figure 24. Example of an amplitude spectrum (displacement spectrum), generated with SHM. It is taken from the z-component at CLZ for the Syke-event (May, 1st 2014). The amplitude is plotted on the y-axis and the frequency on the x-axis, both in logarithmic scale.

Some parameters of the different seismic events like the hypocentral depth, the focal mechanism or the propagation path parameters, which varied along the travel path, influence the seismogram shape and therefore the spectral characteristics. A qualitative interpretation of these amplitude spectra was carried out by plotting the plateau and the decreasing amplitude part, which is suspended to higher frequencies until half of the sampling rate is reached. Distinct corner frequencies and the seismic moments were determined by an additional program called Qopen (Eulenfeld and Wegler, 2016). It estimates seismic moments, the separation of intrinsic and scattering attenuation and the determination of the corner frequency by an envelope inversion of the S wavelet. The corner frequency f_c minus f_0 (plateau range = pr), and in addition the gradient of the decreasing part was determined to find differences between the earthquakes in northern Germany, in contrast to usually used discrimination parameters such as spatial and temporal variations. At least, for two seismic events with similar magnitudes located in the distinct regions of Cloppenburg, Syke, Völkersen and Rotenburg and in addition all natural earthquakes in the study area, amplitude spectra were processed with this approach. Results see chapter 6.2.3.

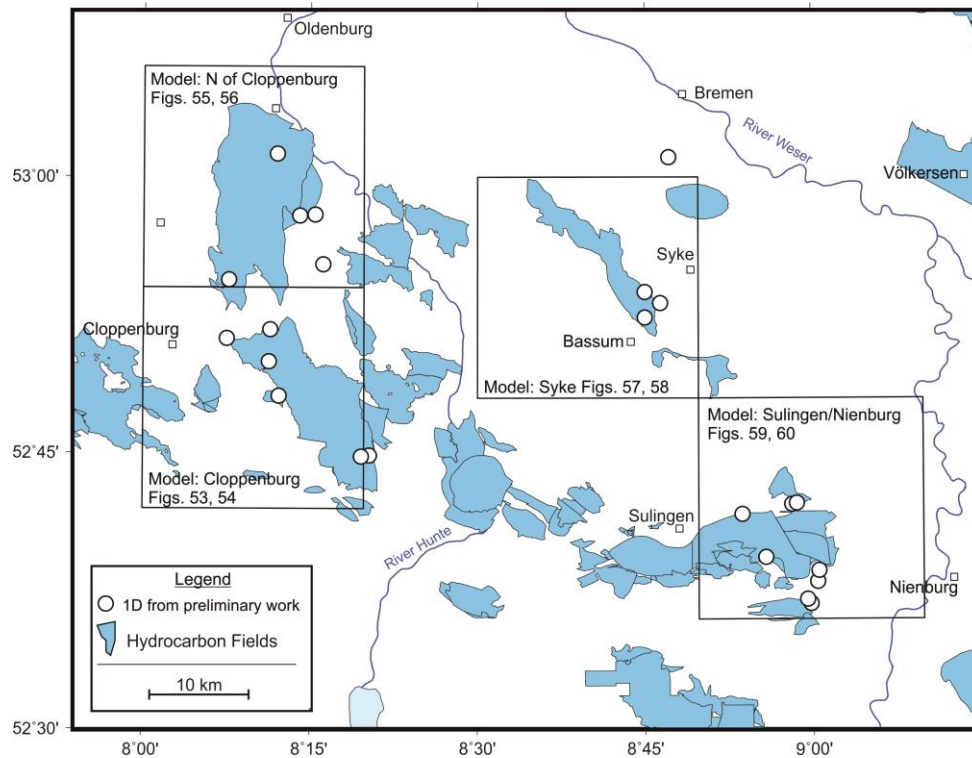
5.6. Geological 3-D subsurface modeling

The second part of my study comprises a broad 3-D geological subsurface modeling with GOCAD®. Ford et al. (2010) pointed out that the geoscientific understanding has benefited from the construction of 3-D models. These models integrate different data sets and allow e.g. a comprehensive visualization of subsurface geometries (Blendinger et al., 2004), enhanced aquifer characterization (e.g. Schulz et al., 2007, Schulze, 2009) as well as a risk reduction in exploration of mineral resources (De Kemp, 2007) and hydrocarbon systems (Hantschel and Kauerauf, 2009).

The application of 3-D models enables an accurate visualization of complex subsurface structures, where 2-D sections are too simplistic or fail. In this thesis, 3-D models were used to link earthquake hypocenters and fault planes to carry out potential seismogenic faults. 3-D subsurface models for the regions Langwedel/Völkersen, Rotenburg/Söhlingen, Walsrode, Cloppenburg (split into two models), Syke and Sulingen/Nienburg were constructed. These areas have well constrained hypocenters with relatively low uncertainties. Figures 25a and b display the modeled areas. The 1-D pre-located seismic event locations are also shown.

The models are based on contour line plots (depth maps) of the “Geotektonischer Atlas von Nordwest-Deutschland und dem Deutschen Nordsee-Sektor” (GTA, Baldschuhn et al., 2001) as well as on significant fault traces, which are visible in 3-D seismics provided by industry partners (Fig. 25b).

a)



b)

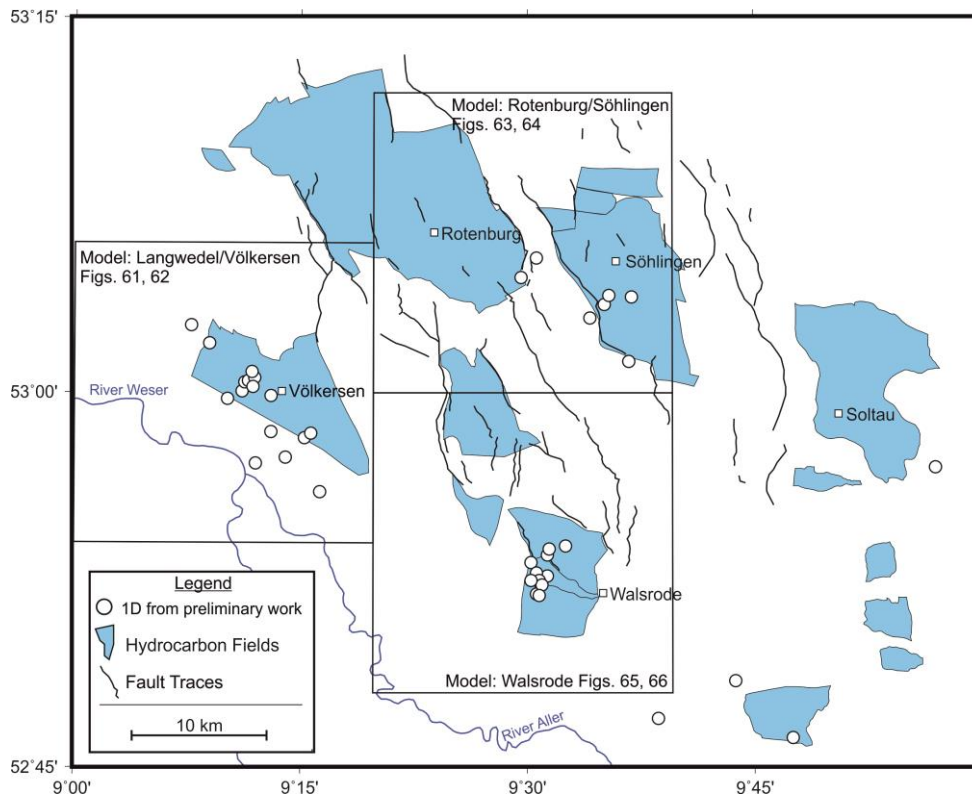


Figure 25. Location of the seven model areas (black boxes) situated in the study area. Seismic events are highlighted by white points (earthquake catalogue of the BGR). First order faults (black lines) in the regions of Söhlingen, Soltau and Walsrode are visible in 3-D seismics provided by industry partners, are also shown. **a)** Model extents in the western part and **b)** model areas of the eastern part.

5.6.1 Modeling workflow

As mentioned above, data such as contour line plots and cross-sections derived from the GTA (Baldschuhn et al., 2001) are the basis for the modeling approach. I focused on the base Zechstein, the base Lower or Middle Buntsandstein and the base Upper Buntsandstein. Geological units in the footwall like the Rotliegend or the Carboniferous could only be considered in areas where data is available. Among others, Lohr et al. (2007) or Schwarzer and Littke (2007) identified the top Carboniferous reflectors in a depth of about 6,000 m for the regions Völkersen and Söhlingen. In the fault modeling workflow, this surface is used to construct inferred Permian basement faults, which might be the source of earthquakes below 5 km. Figure 26 shows the modeling workflow, which was used in this study.

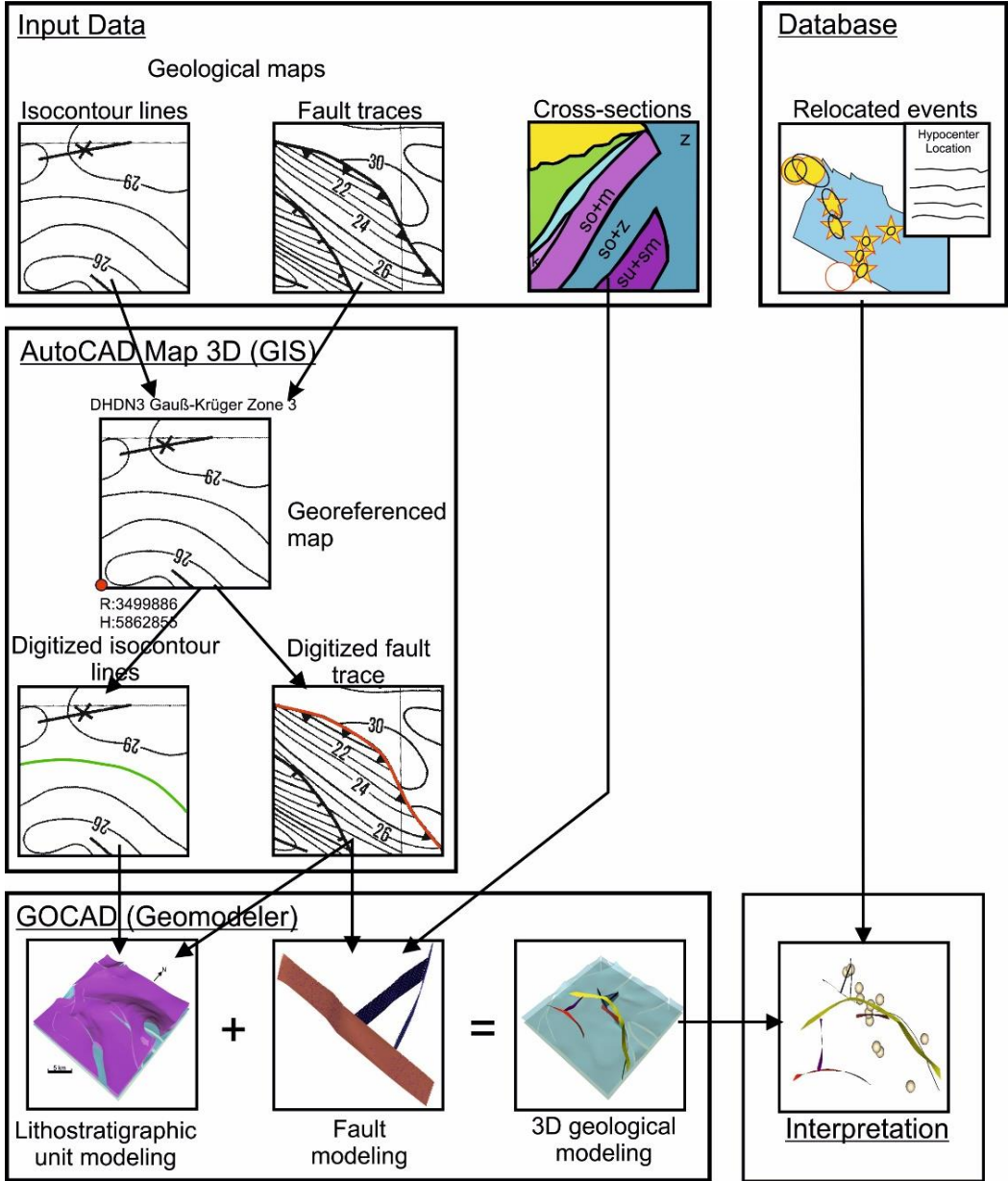


Figure 26. Workflow of the modeling approach. Details are explained in the following text.

5.6.2 „Geotektonischer Atlas von Nordwest-Deutschland und dem Deutschen Nordsee-Sektor“

The GTA of NW Germany is an extensive collection of 14 structural contour maps and geological cross-sections, subcrop maps and lithostratigraphic tables (Baldschuhn et al., 2001). This dataset is based on about 75,000 deep wells, which were drilled in exploration campaigns. Additionally, more than 500,000 km of reflection seismic lines, in the vast majority made available by oil companies/hydrocarbon industry were integrated into the GTA. Reflectors were interpreted, correlated and digitized as isocontour lines in intervals of 100 m in each case. Each depth value is given in meter below sea level. To find the accurate time to depth transformation, a uniform seismic velocity concept was applied based on about 1,200 velocity measurements from boreholes (Jaritz et al., 1991). The material is available as a collection of maps (Baldschuhn et al., 1996), or in digital forms on 3 CD-ROMs (Baldschuhn et al., 2001) and since 2007 as 3-D models (GOCAD©-objects). The digital data for the 3-D models was not used. Firstly, because of several overlapping problems including some incorrectly labeled isocontour lines and secondly, because of the oversized extent. Furthermore, the large number of faults within each model is not necessary for my purpose. I focus on an array of more reliable, “first order” faults. Faults of the base Zechstein may reach deeper geological units like the Rotliegend or the Carboniferous. Therefore, in the following, they are also called and summarized as Permian basement faults.

5.6.3 Digitization and 3-D modeling with GOCAD©

The three selected geological units are represented by isocontour line maps at a scale of 1:300,000. Each set of depth maps for all modeled study areas were scanned and converted into tiff-files with a resolution of 300 dpi and an edge length of 75 mm. For each tiff-file, a separate so-called tfw world-file with scaling details for the tiff picture had to be generated. This procedure was necessary to digitize the isocontour lines, faults and salt structures in a uniform way (geo-referencing). The digitization was performed with the program AutoCAD Map 3D©. Each model area, encompassing about 400 km², was georeferenced within the DHDN3 Gauß-Krüger Zone 3 coordinate system and has the origin in the lower left corner. The isocontour lines and faults were digitized and coded with elevation values in meters. Fault traces and isocontour lines were separately stored for the subsequent modeling with GOCAD©. A total number of 2,047 isocontour lines, 327 faults as well as 23 salt dome outlines and countless support points were digitized.

The GOCAD© (Geological Object Computer Aided Design) software was developed for modeling complex geological objects in connection with geophysical, geological and reservoir engineering applications. A detailed description is given by Mallet (1992). I used the 14.1 SKUA GOCAD© (Subsurface Knowledge Unified Approach GOCAD©) version.

Prior to the modeling with SKUA GOCAD©, the following initial parameters had to be adjusted. The DHDN3 Gauß-Krüger Zone 3 coordinate system was used because it also served as reference frame in AutoCAD Map 3D©. Area and depth units are in meters and defined as positive values downwards on the z-axis. The AutoCAD Map 3D© dxf-output file had to be converted from cultural, unassigned data into assigned SKUA GOCAD© 3-D objects, defined as horizons and faults (pic. 1, Fig. 27). To generate smooth surfaces, I interpolated the isocontour lines (curves) with the GOCAD© DSI-algorithm (Discrete Smooth Interpolator, Mallet, 1992, 2002) on the basis of a Delaunay triangulation to create surfaces with the lowest roughness. A smooth interpolation with nearly equilateral triangles can only be achieved, if the control points form a regular grid over the entire model. However, the control points within my model area were defined by the GTA derived isocontour line curves and were consequently very unevenly distributed.

To cope with this, an envelope curve (closed curve) around the model area was created, where the control points are equidistantly distributed with a distance of 250 m (pic. 2, Fig. 27). This envelope also encompasses salt dome outlines and the fault related footwall and hanging wall cutoffs in the depth maps. This provided the possibility to create a reliable fault geometry. To avoid artifacts, the envelope and the separately stored fault traces were projected on the average depth of the modeled horizon. I applied the “Border and Faults” GOCAD© option (pic. 3, Fig. 27) to interpolate the initial flat surface. After the generation of the initial surface, I had to work manually on that. Thereby, links between the aforementioned surface cutoffs and further untouched fault structures within the model area were generated to prepare reliable horizon-to-fault and fault-to-fault contacts.

Subsequently, the isocontour line depth information of the created curves were used to connect control points with the initial subsurface. Each previously digitized point was then linked by blue lines (pic. 4, Fig. 27) with the surface. On this basis, the surface was smoothed with the DSI-algorithm (pic. 5, Fig. 27).

The modeling of fault planes (pic. 6, Fig. 27) was carried out in two different ways. In case of faults, which cut through more than one geological unit (e.g. from Lower to Upper Buntsandstein), the footwall in one horizon and the hanging wall in the other were identified. Both fault traces were digitized as GOCAD© “curves” and connected by interpolating a new surface, which was then defined as the fault surface. In some cases, base Zechstein faults were constructed using a supplementary level – top Carboniferous in a depth of 6,000 m (cf.

Lohr et al., 2007). However, these faults had to be constructed as vertical planes because information of the dip angle lacks. The strike direction was adopted from the fault traces in the base Zechstein. The horizon-to-fault and fault-to-fault contacts were modeled by using the “structural modeling” workflow in GOCAD©. Salt domes were not integrated into the subsurface model because their geometry was most likely irrelevant for the hypocenter-fault correlation. However, salt dome bounding faults were integrated in the 3-D models. Additionally, for the regions of Rotenburg/Söhlingen and Walsrode “first order” fault traces, which are visible in 3-D seismics provided by industry partners. In the last step, the relocated earthquake locations within each region were converted from Lat/Lon into Gauß-Krüger coordinates and then uploaded as “cultural data” into the GOCAD© model (pic. 7, Fig. 27).

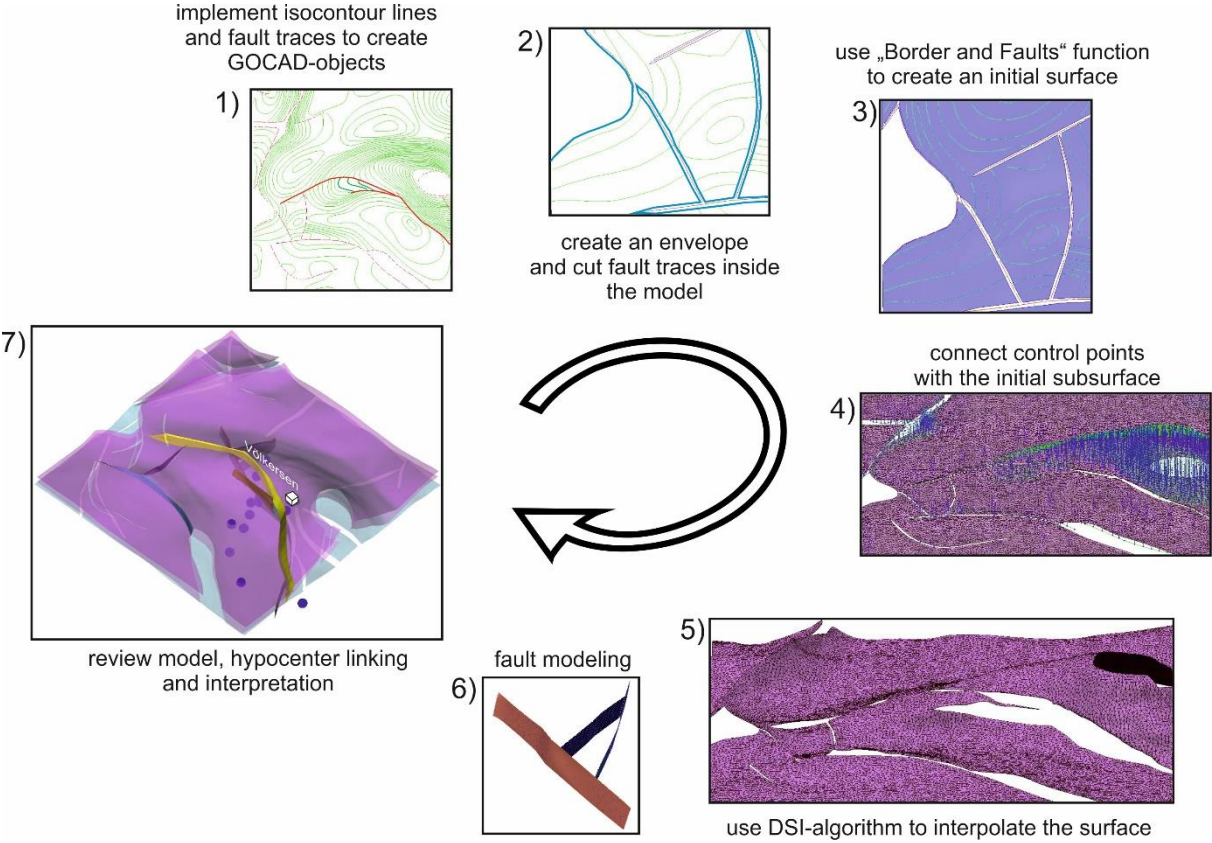


Figure 27. Workflow of the 3D geological subsurface modeling with GOCAD©. The detailed description is given in the text above.

5.7. Glacial isostatic adjustment - Numerical simulations

The numerical simulation approach in this study is performed with different ice and earth models. The determinations were thankfully conducted by Holger Steffen (Landmäteriet, Gävle, Sweden). The description of the Coulomb Failure Stress, which is the calculated quantity to show an eventual fault activation, follows Steffen et al. (2014a, b).

5.7.1 Coulomb Failure Stress

The Mohr circle in a Mohr diagram, in which the shear stress (τ) is plotted against the normal stress (σ_n , see Figure 28) represents the total stress field at a certain point in an investigated area (Brandes et al., 2015). This total stress field comprises, first, the time independent ambient stress, including tectonic stresses and the vertical normal stress, and secondly, the time dependent glacially induced rebound stress, which superimposes the first one (Steffen et al., 2014a). Movement along a significant fault is possible when the state of stress is perturbed and the Mohr circle touches or crosses the failure envelope (King et al., 1994). This failure envelope is practically approximated by the following linear equation (Harris, 1998):

$$|\tau_c| = C + \mu\sigma_n.$$

Thereby, the critical value (τ_c) defines the shear stress along a fault plane (Brandes et al., 2015). In this equation, μ is the internal coefficient of friction, σ_n defines the normal stress related to the fault plane and C is the cohesion strength. After Ranalli (1995), the strike direction of a fault plane is given if the Mohr circle reaches the line of failure by:

$$\tan(2\theta) = 1/\mu.$$

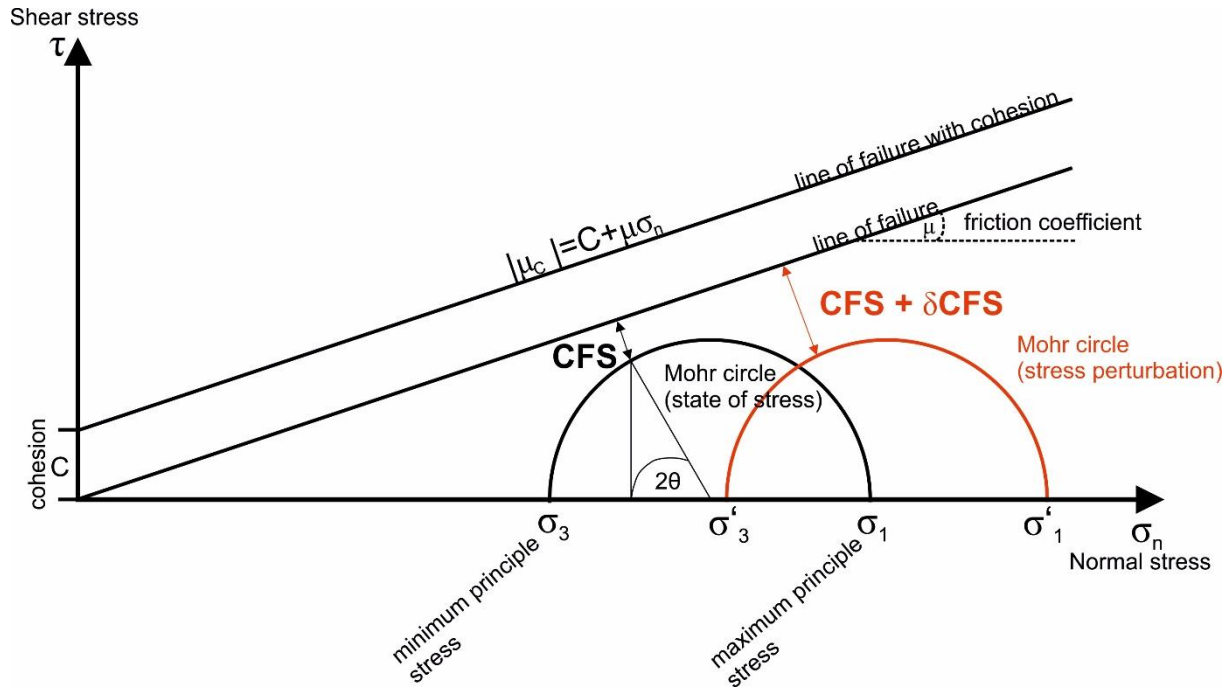


Figure 28. Diagram of the relationship between the shear stress τ and the normal stress σ_n . The Mohr circle, which is defined by the minimum principle stress (σ_3) and the maximum principle stress (σ_1) describes the state of stress at a point in an investigated area. To initiate movement along a fault, the vertical distance between the Mohr circle and the line of failure, which is called Coulomb Failure Stress (CFS) have to be vanished. This can be done by shifting σ_3 and σ_1 to more negative values on the normal stress axis or by increasing the radius. Due to changes in the CFS (δCFS), the red half-circle indicates a perturbed state of stress, which leads to more stable conditions (modified after Scholz, 2002, Steffen et al., 2014a, c and Brandes et al., 2015).

The vertical distance between the Mohr circle and the failure envelope is called the Coulomb Failure Stress (CFS) (Harris, 1998). Stress changes resulting in changes of the Coulomb Failure Stress, which may lead to failure or more stable fault conditions are described by the δCFS value. During stress evolution, the potential for fault (re)activation or inhibition is defined by an increasing or decreasing of the δCFS value, which means an increase or decrease of the distance between the Mohr circle and the failure envelope, respectively. A fault becomes more stable if the Mohr circle is shifted in positive normal stress direction, and if the Mohr circle is shifted towards the failure envelope the potential of fault movement is higher. Time-dependent changes in the Coulomb Failure Stress are determined by

$$\delta CFS(t) = CFS(t) - CFS(t_0),$$

where t_0 is the initial state of stress (Brandes et al., 2015). According to Wu and Hasegawa (1996a, b) and Harris (1998), simplifying the determination, the cohesion C is neglected and the approach is based on the principle compressive stresses. Taking this into account, stress changes can be defined as:

$$\delta CFS(t) = \tau(t) - \tau(t_0) + \mu(\sigma_n(t) - \sigma_n(t_0)).$$

Prior to the determination of δCFS , the following assumptions are made for the numerical simulations in this study:

- During a glacial cycle, stress evolves continuously and so does the CFS value with time (Brandes et al., 2015).
- Only optimally oriented pre-existing faults (nearly parallel to the former mass load, Brandes et al., 2015) can be reactivated. These faults have to be close to failure and the Cohesion C is neglected.
- These pre-existing faults have no influence on the state of stress, so they are called “virtual faults” (Steffen et al., 2014a, Brandes et al., 2015).
- The determination of fault (re)activation can be affected by changes in lithostatic pressure and fluid pressure. After Wu and Hasegawa (1996a, b) these values are difficult to calculate. They are taken into account though, but only as time independent parameters.
- Changes in the Coulomb Failure Stress revealed a similar behavior inside the former ice sheet as well as in front of the former ice sheet (up to 500 km radius) (Brandes et al., 2015).

For the evaluation of δCFS , knowledge about the stress evolution below and in front of the ice sheet is important. Furthermore, the three different main fault regimes - normal, strike-slip and thrust faulting will be distinguished. The differentiation is done by defining the maximum, intermediate and minimum principal stress, accordingly in each case.

5.7.2 Three-dimensional finite element modeling and model geometry

In this study, the finite element software ABAQUS (Dassault Systèmes, 2015) was used to solve the Boussinesq problem (Pedlosky, 1987) for a layered, three-dimensional, viscoelastic half space with isotropic, compressional material properties. This problem describes the phenomenon of convection in a viscous incompressible flow (Pedlosky, 1987). On basis of the viscous flow in the mantle, after deglaciation, the deformed ice-free surface must be able to return to its initial equilibrium state within the model (Steffen et al., 2006). Therefore, the ABAQUS finite element modal was modified to include pre-stress advection (after Wu, 1992a, b, 2004) and to allow the deformed free surface to reach its initial equilibrium via viscous flow. Stress and displacement are results of the finite element modeling, using ABAQUS, which are subsequently transferred to δCFS determinations.

The initial model geometry, important depth values and related depth layers are shown in Figure 29. The three-dimensional flat earth model covers a total area of 60,000 x 60,000 x 2,891 km (L x W x H). It consists of a 90 x 90 x 17 elements central part (4,500 x 4,500 x 2,891 km) and a frame with 10 elements, encompassing together 27750 km, that are added at each

side of the inner section, respectively (Fig. 29a) (Steffen et al., 2006). The 4,500 km wide inner part is more fine-meshed (edge length 50 km horizontally per element) than the frame (horizontal edge length increases towards the outside using the BIAS optional parameter of the ABAQUS node generation commands, Steffen et al., 2006) because the ice load is only on the center allowing stress change determination in higher resolution. The added 27,750 km broad peripheral area in each direction is needed because the viscoelastic mantle material requires an (infinite) horizontal extent enabling flow out of the area underneath a load (Steffen et al., 2006). Following the recommendation of Steffen et al. (2006) the peripheral frame is added with more than 10 times of dimension of the central part to simulate this infinite extent. Vertical edge length is 5 km for the six uppermost crustal layers to increase resolution here. Edge length in deeper layers is larger than those following the Earth's structure.

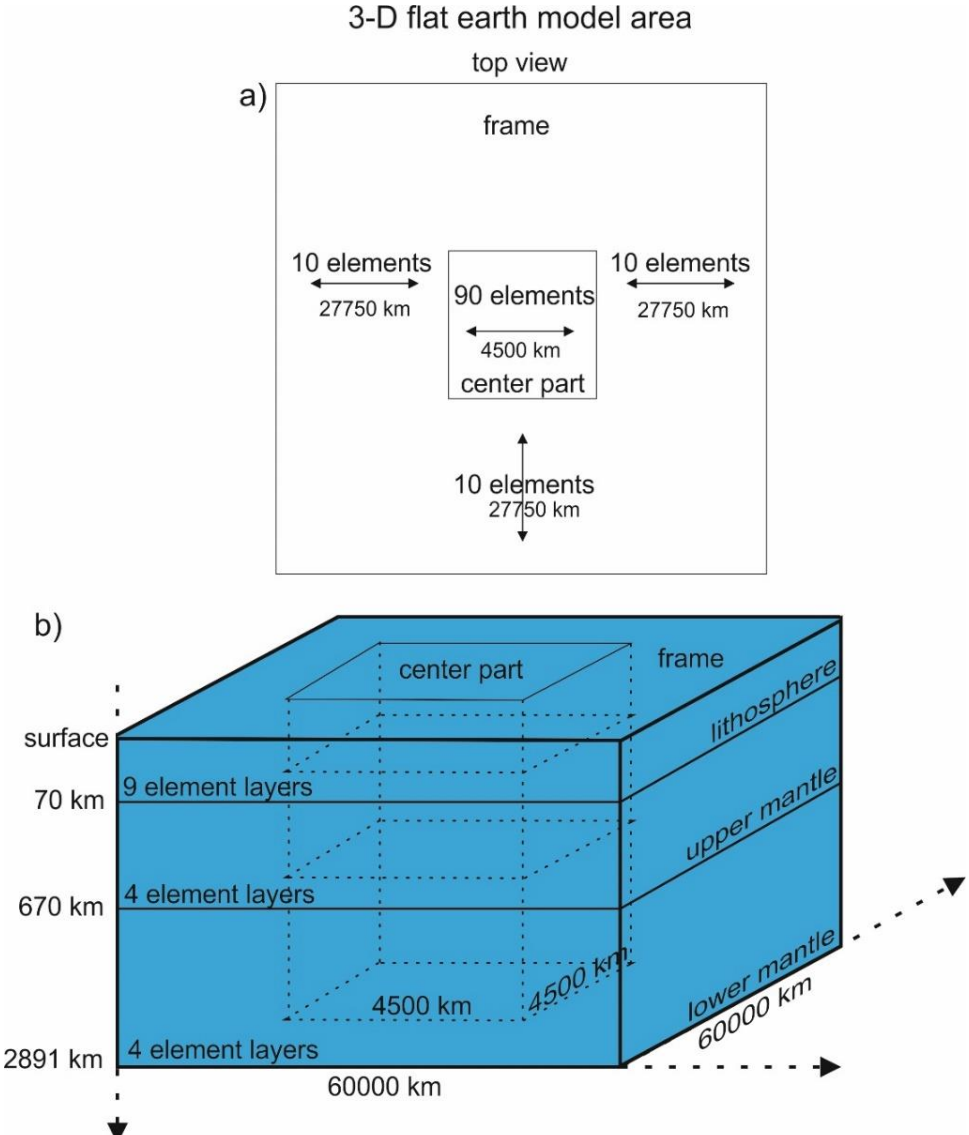


Figure 29. Model geometry of the 3-D flat earth model. **a)** Top view of the element arrangement for the broader frame and the more fine-meshed central part. **b)** 3-D model geometry comprising lithosphere, upper mantle and lower mantle with according depth values and number of element layer for the three major Earth structural layers, (modified after Wu, 2004 and Steffen et al., 2006).

Further parameters about the model geometry and the Earth model are based on the modeling approach used in Steffen et al., 2006 (and in addition, Holger Steffen, pers. communication). In reference to the Earth's structure, the whole model, comprising central part and peripheral frame area is divided into three major layers – the lithosphere, the upper mantle and the lower mantle - which are further subdivided into 9, 4 and 4 layers in the vertical direction, respectively. Depending on the different models used for the simulations, the lithosphere thickness varies between 70 to 140 km. Variations of lithosphere thickness are based on several publications (Wang and Wu, 2006, Vink et al., 2007 and a list of publications in Table 3 in Steffen and Wu, 2011). In addition, Geissler et al. (2010) used S receiver functions to calculate the lithosphere thickness. They show variations in the lithosphere of northern Germany between 80 and 120 km. The boundary between upper and lower mantle is in a depth of 670 km. Each model consists of 110 x 110 x 17 hexahedra blocks, comprising 205,700 elements (Holger Steffen pers. communication).

Ice and Earth models for the 3-D finite element modeling

In general, two models are needed for the numerical simulation of GIA-induced stresses – an ice model, defining the surface load and an Earth model. On the basis of the applied surface load (defined by the ice model), responses triggered by glacially-induced perturbations are given by the solid Earth models (Steffen et al., 2006).

Ice models contain the time-dependent surface load of built-up and retreat of a continental-scale ice sheet. Many ice models, especially for Fennoscandia, were developed in the last decades (e.g. global models, ICE, Peltier and Andrews, 1976; ICE-2, Wu and Peltier, 1982; ICE-3G, Tushingham and Peltier, 1991; ICE-4G Peltier, 1994; ICE-5G, Peltier, 2004). The more recently derived global ice model ICE-6G_C from Peltier et al. (2015), which is based on its precursor ICE-5G (Peltier, 2004) is used in this study. It is a refined model, in which the thickness of local ice cover and timing of retreat is constrained by using all available and most recently Global Positioning System (GPS) measurements of vertical motion (Peltier et al., 2015). This model contained the ice history of the last deglaciation event in the Late Quaternary for the whole world. Concerning northwestern Europe and Eurasia, it is referred to as the Weichselian ice age. Important information for the numerical simulation in this study, taken from this model, is the predicted rate of vertical motion of the crust, which is derived from GPS measurements (see Figure 11 in Peltier et al., 2015). Contrary to the uplift region around the former glaciated area in Scandinavia (see Figure 30), subsidence dominates NW Germany.

Rates of about 2 mm/year are predicted on the basis of the ICE-6G_C (VM5a) model (Peltier et al., 2015). VM5a refers here to the best-fitting Earth model structure found by Peltier et al. (2015). The subsidence in the study area is related to the collapse of the forebulge (Fjeldskaar, 1994, Fjeldskaar et al., 2000, Kiden et al., 2002). The forebulge, also called peripheral or flexural bulge is defined by an uplifted area due to the flexure of the rigid lithosphere, which is affected by mass load (Nansen, 1928, Daly, 1934). The collapse occurs after the deglaciation, when the elastic lithosphere tries to reach the isostatic equilibrium (Daly, 1934). A more detailed description of the ICE-6G_C (VM5a) model is given in Peltier et al. (2015).

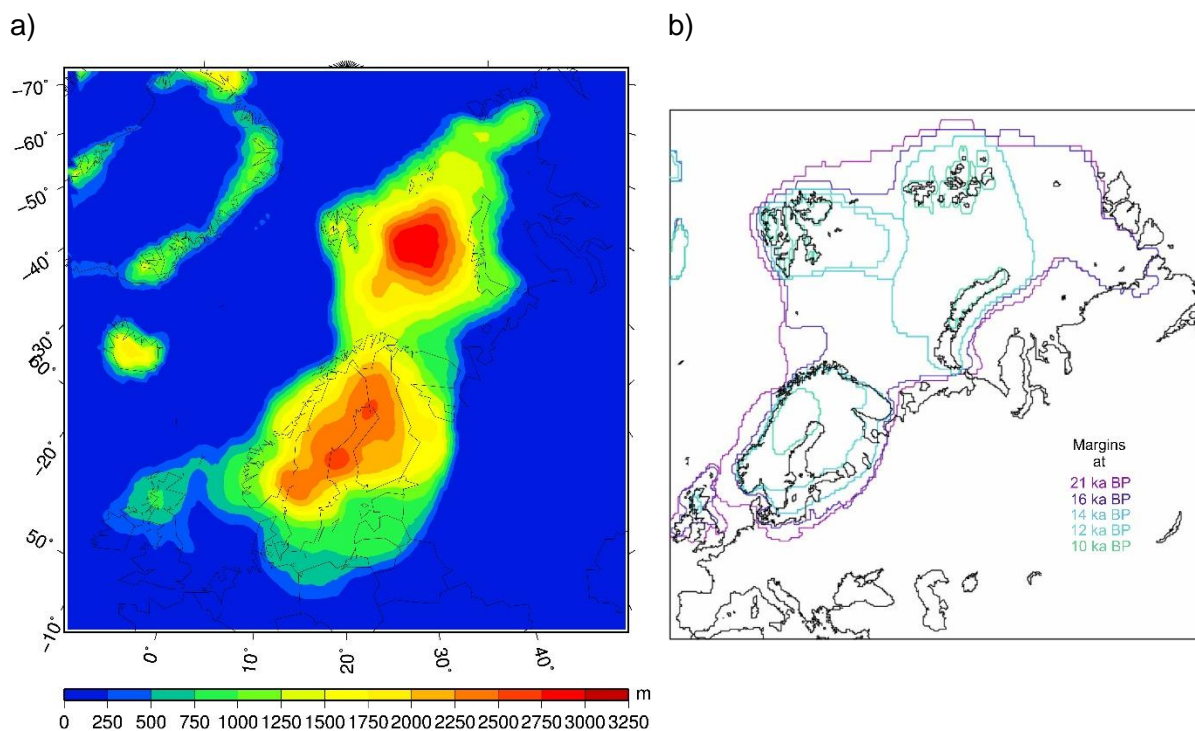


Figure 30. Model parameters included in the ICE-6G_C (VM5a) ice model. **a)** Ice thickness of the Scandinavian ice sheet at 22,000 years before present. Figure courtesy of Holger Steffen **b)** Ice sheet retreat of the Scandinavian ice sheet complex from LGM to present day (after Gyllencreutz et al., 2007). Figure taken and modified from Peltier et al. (2015).

The GIA-induced stress perturbations on the basis of the ice load history derived by the ICE-6G_C model influence the chosen Earth models in different ways, according to the different parameterizations. Density, Young's modulus and Poisson ratio for different layers are obtained using the Preliminary Reference Model (PREM, Dziewonski and Anderson, 1981). An example for the parameterization of the 17 layers in one Earth model is given in Table 8.

Table 8. Exemplary parameterization of one Earth model (120 km thick lithosphere) used for the finite element modeling.

Layer	Thickness (km)	Depth (km)	Density (kg/m ³)	Young's modulus GPa	Poisson's ratio	
I	5,0	5,0	2600	67,9	0,2822	Lithosphere
II	5,0	10,0	2600	67,9	0,2822	
III	5,0	15,0	2669	77,7	0,2761	
IV	5,0	20,0	2900	110,2	0,2561	
V	5,0	25,0	2997	123,1	0,2610	
VI	5,0	30,0	3380	173,5	0,2800	
VII	30,0	60,0	3378	172,8	0,2801	
VIII	30,0	90,0	3375	169,4	0,2832	
IX	30,7	120,7	3371	165,5	0,2871	
X	125,7	246,4	3390	171,7	0,2903	Upper mantle
XI	204,0	450,4	3595	213,2	0,2994	
XII	120,6	571,0	3869	272,3	0,2964	
XIII	100,0	671,0	3986	309,2	0,2950	
XIV	553,8	1224,8	4578	471,7	0,2764	Lower mantle
XV	588,3	1813,1	4889	562,3	0,2880	
XVI	519,2	2332,3	5168	645,3	0,2965	
XVII	553,2	2885,5	5435	728,0	0,3037	

Elastic properties of the lithosphere are defined for the first nine layers I - IX. The upper mantle with a total thickness of about 550 km and the lower mantle with a total thickness of about 2,200 km, comprising four layers, respectively, are represented by the layers X to XVII. In case of a reliable stress determination and the subsequent δ CFS calculation, the differentiation of rheology between upper and lower mantle is applied (Steffen et al., 2006). However, lower mantle viscosities play a minor role during the simulation because the lower mantle is hardly deformed by the ice mass load (Mitrovica, 1996, Wu et al., 1999).

For the finite element modeling, altogether, 6 models were created – four models with a 3-D viscosity structure and two models with a 1-D viscosity structure. The first four models were generated by using certain lithosphere thicknesses (lith = 70 km, 90 km, 120 km and 140 km). Each of these models comprises four mantle layers, which are defined by lateral variations of viscosity values for the following depth structure: varying end of lithosphere to 420 km, 420 to 670 km, 670 to 1,330 km and 1,330 to 2,891 km. The initial model subdivision into the 17 different element layers still remains. Therefore, two element layers within the upper and lower mantle, respectively, contain the same viscosity distribution (Fig. 31). The 3-D viscosity information is derived from a global seismic tomography model by Grand et al. (1997) and is adapted from Kierulf et al. (2014).

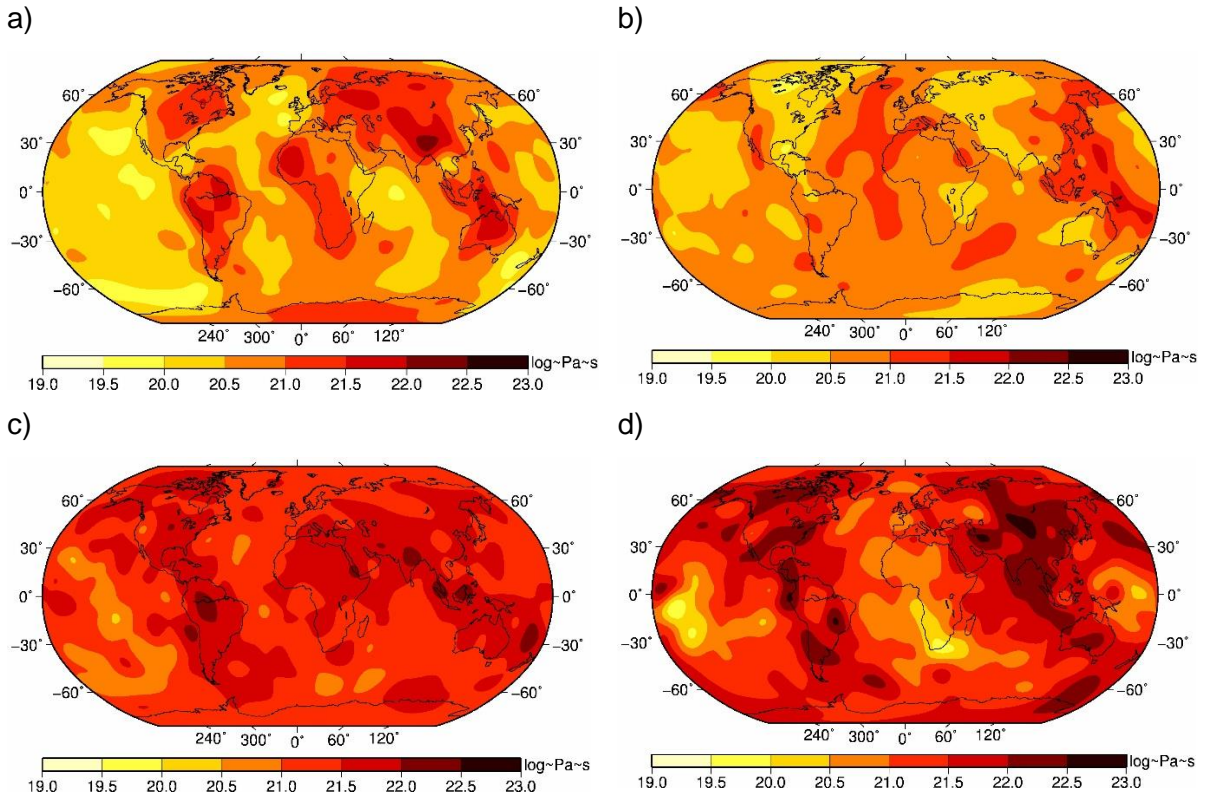


Figure 31. Laterally varying viscosity structure in the upper and lower mantle, which was used within the numerical simulations. **a)** in depth between 150 to 420 km. **b)** in depth between 420 to 670 km. **c)** in depth between 670 to 1330 km and **d)** in depth between 1330 to 2891 km (after Kierulf et al., 2014).

The fifth model has a lithosphere thickness of 90 km and a 1-D viscosity structure that varies only radially. Two fixed viscosity values for the upper and lower mantle, respectively were adopted and no asthenospheric layer below the lithosphere is considered. The sixth model is similar to the fifth but has a laterally varying lithosphere thickness, which was adapted from Wang and Wu (2006). Model names and descriptions are given in Table 9.

Table 9. Parameters of the six GIA-models used in this study. The composition of the first four model names are defined as follows: ICE6G describes the applied ice model, L... includes the thickness of the lithosphere, Llat means lateral variations in lithosphere thickness adapted from Wang and Wu (2006), and GRAND_V1 defines the 3-D viscosity structure adapted from Kierulf et al. (2014). The fifth model has a 90 km thick lithosphere without any asthenosphere parameterization (A000000, means no thickness and no viscosity) and a 1-D viscosity structure, which is only divided into an upper (U520) and lower mantle viscosity value (L221), respectively. The sixth model is similar to the fifth but has a laterally varying lithosphere thickness.

Name	ICE-model	Lithosphere thickness [km]	Upper mantle viscosity [Pa*s]	Lower mantle viscosity [Pa*s]
ICE6G_L070_GRAND_V1	ICE-6G_C	70	see global plots in Figure 32a-d above this table 3-D viscosity structure adapted from Kierulf et al. (2014)	
ICE6G_L090_GRAND_V1	ICE-6G_C	90		
ICE6G_L120_GRAND_V1	ICE-6G_C	120		
ICE6G_L140_GRAND_V1	ICE-6G_C	140		
ICE6G_L090_A000000_U520_L221	ICE-6G_C	90	5 x 10E20	2 x 10E21
ICE6G_Llat_A000000_U520_L221	ICE-6G_C	laterally varying, adapted from Wang and Wu (2006)	5 x 10E20	2 x 10E21

5.7.3 Modeling of Coulomb Failure Stress

The reactivation potential of the identified seismogenic active faults, derived from the geological 3-D subsurface modeling compared with the relocated hypocenters (see chapter 6.6.), is tested on basis of the ice unloading after the last glaciation (Weichselian).

The complex stress field in northern Germany is mainly controlled by the North-Atlantic ridge push and ongoing continent-continent collision of Africa and Eurasia (e.g. Grünthal and Strohmeier, 1992, Reicherter et al., 2005, Heidbach et al., 2010). After Kaiser et al. (2005), Central Europe exhibits a compressional stress regime, whereas Röckel and Lempp (2003) show that the vertical stress exceeds mostly the maximum horizontal stress in the North German Basin, which indicates a recent normal fault tectonic regime on a regional scale. On the basis of the relatively sparse database, especially of vertical stress values, both stress regimes are taken into account for the numerical simulations of stress changes due to the glacial isostatic adjustment.

Brandes et al., (2015) show that stress changes in front of the former ice sheet (up to 500 km) behave in a way similar to locations inside the former ice mass load. Therefore, this behavior is used as one of the framework conditions in the simulations.

Assuming that the faults were close to failure before glaciation, during deglaciation, changes in the Coulomb Failure Stress are observed. The δCFS value indicates possible fault (re)activation when positive values are reached. Figure 32 shows an example to describe the development of the δCFS value over time and how it affects fault (in)stability in a compressional stress regime. δCFS is plotted against time and displays the evolution of the thrust from past to present.

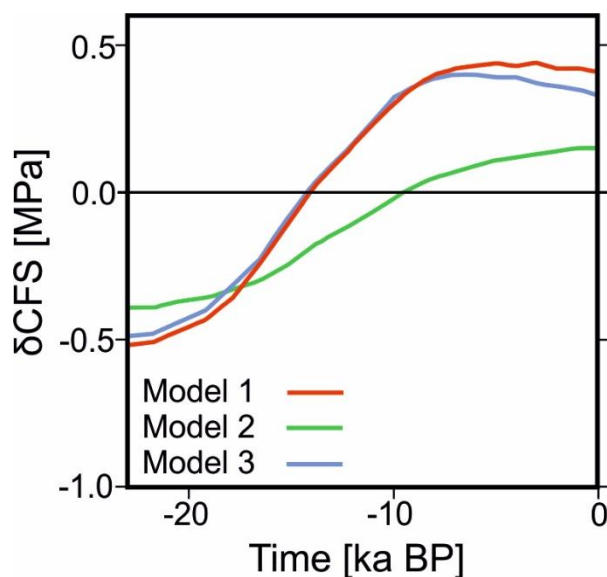


Figure 32. Example of changes in the Coulomb Failure Stress (δCFS) induced by the last glaciation (Weichselian). δCFS is calculated and plotted against the time (last 23 ka) for a theoretical fault in a compressive stress regime. Three models with different rheology conditions are exemplarily plotted. Details are given in the text below (modified after Brandes et al., 2015).

A fault is stable for negative δCFS values, while instable conditions yield for positive δCFS . If the curve reaches the zero line, a movement along the fault is therefore possible. Hence, in Figure 33, models 1 and 3 (red and blue lines) would point to a possible fault activation at about 15 ka BP, while model 2 (green line) would suggest 10 ka BP as activation time. Fault slip due to GIA-induced earthquakes is not calculated in this study due to the application of virtual faults (because, this is not possible as there are no faults included in the model). However, in recent studies, slip evolution is determined using finite-element models (Turpeinen et al., 2008, Hampel et al., 2009, 2010a, b, Steffen et al., 2014a). Their results indicate that faults become more stable during ice loading in a layered medium, but reveal unstable conditions if the ice retreats. Results of the numerical simulations are presented in chapter 6.6.

6. RESULTS

6.1. 3-D relocation

6.1.1 Hypocenter accuracy

For the relocation of all 40 selected seismic events (selection classes see chapter 5.2.1), I used the efficient and fast Oct-Tree importance sampling (see Lomax and Curtis, 2001) because of the short computing time relative to a usually used grid-search algorithm (factor 1/100; Lomax and Curtis, 2001; Husen et al., 2003) and its reliable representation of location uncertainties, which are shown by density scatter plots. The best-fitting results of each localization approach including the varying travel time grids, mentioned before, are stored within the table of Appendix III. The complete table of all 78 analysed seismic events (40 3-D relocated and 38 only 1-D pre-located) in northern Germany is given in Appendix IV.

Table 10. Definition of the five qualities to classify the relocated events and figure out the best-fitting hypocenter solution if different parameters were used during the localization procedures. Modified after Husen and Smith, 2004. Abbreviations: RMS = root-mean-square value; DIFF = distance between expected and determined hypocenter; Average error = sum of each axis of the confidence ellipsoid divided by 3.

Quality Class	RMS (s)	DIFF (km)	Average error (km)	Events
A (excellent)	< 0.5	< 0.5	< 2.0	17
A' (very good)	< 0.55	< 0.5	< 2.0	4
B (good)	< 0.7	< 0.5	≥ 2.0	15
C (questionable)	< 0.7	≥ 0.5	≥ 2.0	4
D (poor)	≥ 0.7	≥ 0.5	≥ 2.0	-

Each of the 40 selected seismic events had been relocated several times by using the different travel time grids and varying V_p/V_s ratios between 1.65 to 1.95 (using 0.1 steps). Thereby, up to 90 relocation runs can be performed for each seismic event. With some minor changes, I followed recommendations of Husen and Smith (2004), in order to figure out the best-fitting hypocenter location obtained by the highest hypocenter accuracy. Table 10 contains the quality classes, the differentiation criteria and the associated amount of relocated events. Examples of the four quality classes are shown in Figures 33a - d by density scatter plots including the 68% Gaussian estimated confidence ellipsoid. Any other derived density scatter plot is stored within Appendix V.

The quality class definitions (Tab. 10) are based on statistical output parameters provided by NonLinLoc. The RMS value was determined during the relocation procedure, whereas the

distance (in km) between the maximum likelihood and the statistically expected hypocenter location in a 3-D medium (DIFF value) and the average error had to be calculated manually. The discrimination of these values is described afterwards while defining the quality classes (the complete table is given in Appendix III).

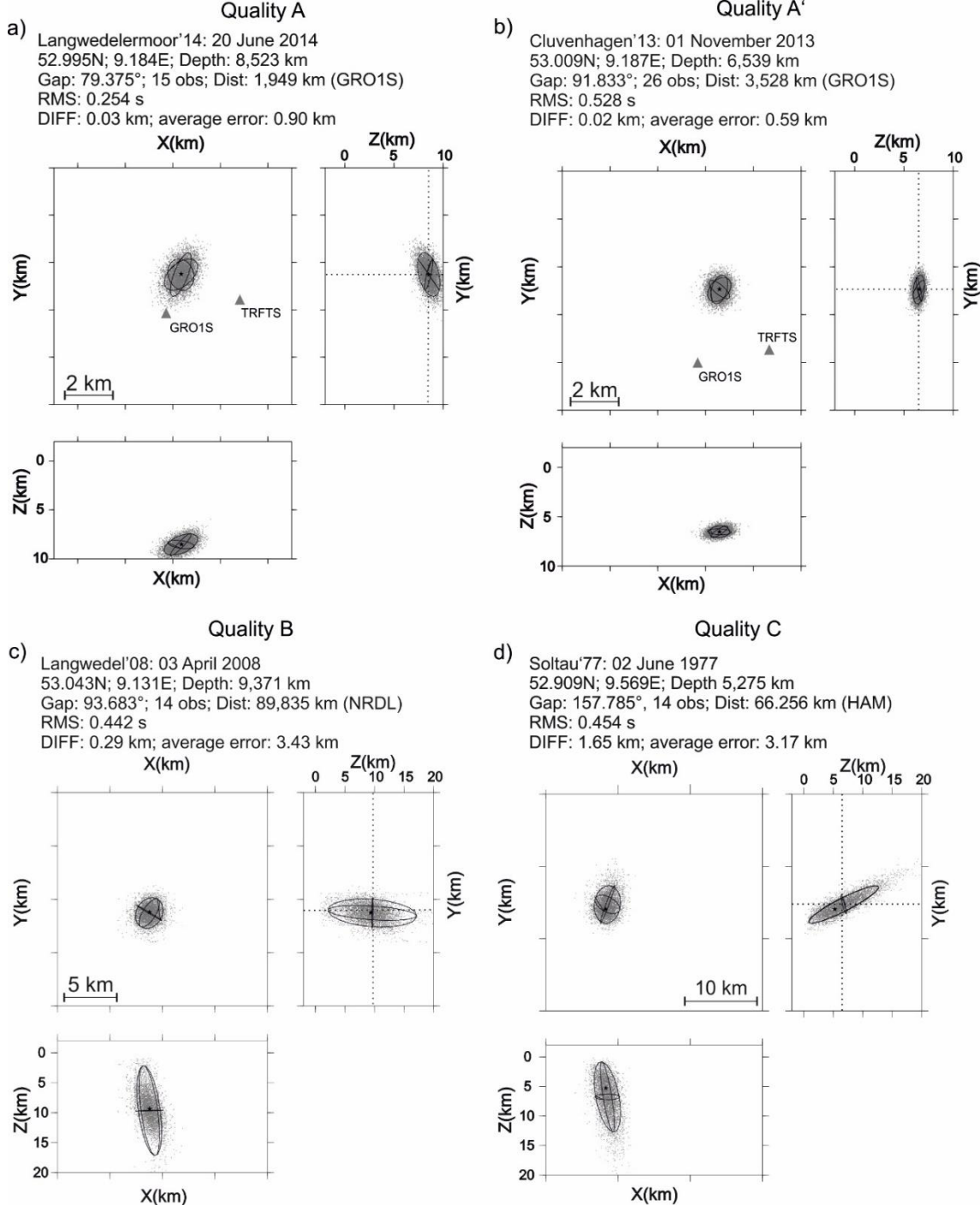


Figure 33. The four quality classes A, A', B and C derived by the evaluation of the relocation results. Hypocenters are shown in one plane view (xy-direction) and two cross-sections (xz and zy). The maximum likelihood hypocenter (star) is enclosed by the scatter cloud obtained by samples of the probability density function (grey cloud) and the projected 68% confidence ellipsoid (black lines). The intersection point of the black dashed lines marks the expected hypocenter determined by NLL. Note the different scaling factors. Differences between the four quality classes **a) – d)** and their differentiation criterion are given in the text.

The differentiation between both best quality classes A and A' by increasing the RMS value from 0.5 s to 0.55 s was somewhat arbitrary, but necessary in my purpose. Some of the relocated events resulted in RMS values, which are slightly higher than 0.5 s because of using a high amount of observations, in most cases more than 18 *P* and *S* phases for the relocalization. This increases the probability of receiving a higher phase time error during the picking process, which affects directly the RMS value. Nevertheless, the hypocenter was very well constrained due to its very small uncertainty domains. In turn, this weakens the impact of the RMS value, which is often regarded as the major quality factor to classify the hypocenter accuracy.

The DIFF value defines the difference between the maximum likelihood and the statistically expected hypocenter location in a *x*, *y*, *z* medium. The determination is based on a simple distance calculation of two points in the 3-D space. This DIFF value is important because it may indicate a possible ill-conditioned location problem (Lomax et al., 2000; Husen et al., 2003) as long as more than one local minimum in the scatter cloud of the density plot is determined within the Gaussian estimation of the probability density function. Except one evaluation (seismic event on November, 11th 2014, Vehmsmoor'14), each of the best-fitting relocated hypocenter is distinctly defined by only one local minimum.

The semi-minor, semi-intermediate and semi-major axis of the 68 % Gaussian estimated confidence ellipsoid is not exactly oriented in the corresponding *x*, *y* and *z* direction. Therefore, the length of these axis has to be proportionally allocated to one spatial direction in the *x*, *y*, *z* media, regarding to longitude, latitude and depth, respectively. The so-called average error for each seismic event is then defined by the quotient of the length of these three axis. It is evident that this quality class criterion is highly influenced by the major axis of the ellipsoid, which corresponds mostly to the *z*-axis (depth uncertainty). Especially, the seismic events, which were relocated only with the coarser CRUST1.0 velocity model, showed mostly high depth uncertainties and were therefore not taken into account for the best-fitting hypocenters. In most cases, the relocalization including the combination of both velocity models (CRUST1.0 and WEG) lead to the best-fitting hypocenters.

Table 11. Influence of the station network described by the GAP as well as the importance of having at least one station within the critical focal depth distance, on the average error and the length of the z-axis. Each of the 40 relocated seismic events was evaluated. Abbreviation: GAP: greatest azimuthal distance between two observations.

Quality criteria	At least one station within 1.5 times of focal depth		Without a station within 1.5 times of focal depth	
Quality criteria	GAP < 100°	GAP > 100°	GAP < 100°	GAP > 100°
Average error [km]	1.08	1.94	1.48	2.07
Average length of z-axis [km]	1.31	1.48	2.75	3.61

Table 11 shows the influence of the station network, which is hereby defined by the GAP and the importance of having at least one seismic station within 1.5 times of focal depth on the location uncertainties. Relocated events with a GAP < 100° and at least one station within 1.5 times focal depth showed very small uncertainty domains (Tab. 11, average error ± 1.08 km). Altogether, 25 out of the 40 relocated seismic events showed that their depth uncertainty had the main impact on the extent of the confidence ellipsoid. This relationship defines also the main difference between quality class A or A' and B. The Epicenter locations of earthquakes in quality class B (15 events) are mostly well constrained, whereas the focal depth is less well defined. In addition to the use of the coarser CRUST1.0 velocity model, the lack of stations within the critical focal depth distance stretched significantly the extent of the z-axis (Tab. 11) and resulted in a poorly constrained focal depth (Figs. 33c and d). Especially events, which were registered before 2012 (June 2012, establishing of temporary stations of BGR and December 2012, establishing of the WEG seismic network, now referred to as BVEG) were subjected to quality classes B and C, because of the limited station coverage in northern Germany at that time (Tab. 11, GAP > 100). Only four events are categorized as questionable (quality class C). Their calculated distance between the expected and the determined hypocenter exceeded the defined threshold of 0.5 km. This might indicate the existence of more than one local minimum or very high uncertainty domains. Class D is neglected because within this study no seismic event was poorly relocated. The proportion of the z-axis length to the average uncertainty error calculated from the 3 axis of the 68 % confidence ellipsoid is 52 %, whereas the horizontal uncertainties sharing 48 % among themselves divided into latitude and longitude error.

Localization improvements

For the 40 best-fitting relocated hypocenters, the associated uncertainty variations and localization improvements were investigated in more detail. In this case, I used the average error quality criteria mentioned before. The impact of the different travel time grids using a fixed

V_p/V_s ratio of 1.8 and higher and the amount of observations due to the increase of seismic stations in the study area on the hypocenter location uncertainties is shown in Figure 34a.

Due to the absence of seismic stations (and observations) within the small WEG model area until the end of 2012, the interpolated coarse CRUST1.0 was the only 3-D velocity model, which was available for my relocalization approach. The first bar in Figure 34a shows the lowest hypocenter accuracy belonging to the highest average error of 6.77 km for the three axis of the 68 % Gaussian estimated confidence ellipsoid. This average error is based on 12 relocated seismic events using CRUST1.0 with an average number of 15 observations. The increase of station density in the region of Völkersen, Söhlingen and Soltau since 2012 allowed for a significant decrease of uncertainties. The average length of the confidence ellipsoid axis was reduced by nearly 3.0 km to 3.56 km. The use of the combined travel time grid for the events after 2012 had reduced the total uncertainties again from 3.56 km to 2.99 km. Altogether, the increased number of stations in northern Germany and the application of the two differently scaled 3-D P -wave-velocity models had reduced the earthquake uncertainties by almost one half.

Moreover, Figure 34b displays hypocenter depth uncertainties obtained by using different travel time grids. The estimated focal depth uncertainties were decreased from about 2.0 km for nearly 40 % to below 1.2 km. The reduction of the uncertainty in the z-axis had the main impact on the total average error by about 58 %. Remaining uncertainties are attributed to the horizontal errors in latitude (y-axis) and longitude (x-axis) direction.

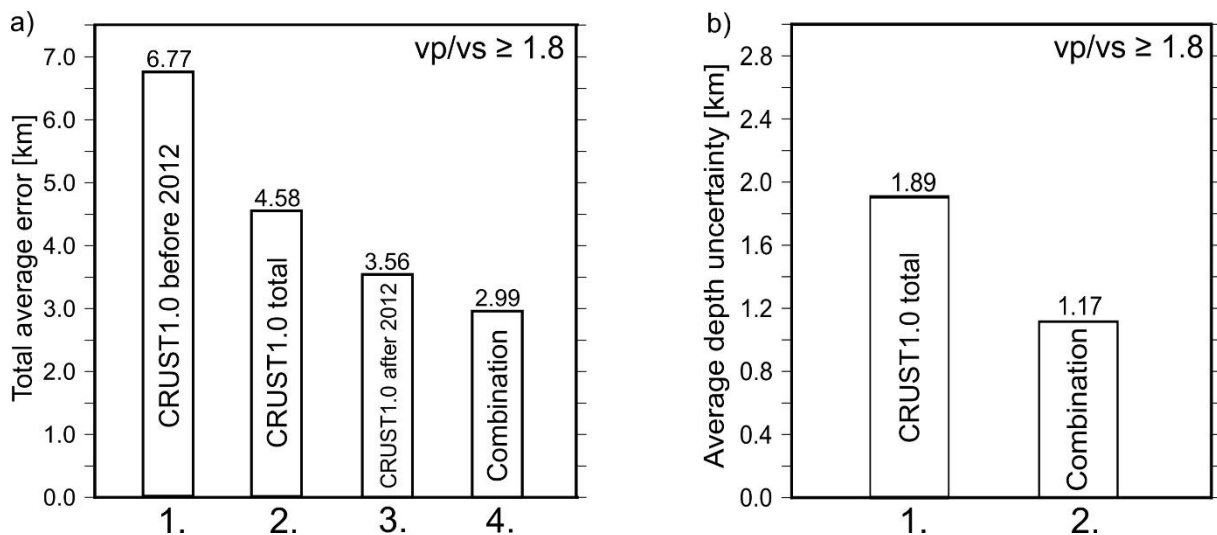


Figure 34. Localization improvements related to the use of different travel time grids. **a)** The total average error considering the length of the three axis of the 68 % confidence ellipsoid to determine the best suitable velocity model for the study area. 1. only CRUST1.0 before the establishment of the WEG network; 2. only CRUST1.0 total; 3. only CRUST1.0 including observations from WEG stations; 4. combination of both models. **b)** Impact of the different travel time grids on the average length of the z-axis (hypocenter depth uncertainty). 1. CRUST1.0; 2. combination of both models.

6.1.2 Spatial distribution of relocated seismic events in NW Germany

Figure 35 maps the (epicentral and hypocentral) locations of the 40 best-fitting relocated seismic events (yellow symbols with red outline). The remaining 38 events, which were only located with the 1-D pre-localization approach are shown as white circles with red outline. In addition to that Figure 36 shows a more detailed view into seven regions with increased seismicity including the 3-D relocated and 1-D pre-located (white circles with red outline) seismic events. The results are drawn with their horizontal uncertainty ellipse. The best-fitting solutions were derived by applying the quality criteria introduced in the previous chapter. Different symbols define the quality differences between the relocated events. The yellow star marks the highest hypocenter accuracy related to the quality classes A and A' (excellent and very good) containing 21 out of 40 relocated earthquakes (52.5 %). Class B (yellow circle, good) consists of 15 events (37.5 %). Their earthquake epicenters are also well constrained, however, the focal depth should be handled with care, because of the higher uncertainties due to the greater extent of the z-axis. The smallest group of the relocated earthquakes, class C, contains 4 out of 40 events (10 %). They were questionably relocated and are marked on the map by a yellow diamond symbol.

The relocated earthquakes are not arbitrary distributed in Northwest Germany. They clearly cluster in distinct areas, in a relatively narrow east to west trending corridor between 52.5N and 53.1N in the vicinity of hydrocarbon fields (Fig. 35). In particular, these events occurred mostly at the margin and only some of them inside of the fields (Figs. 36a-g). Furthermore, seismicity is more or less restricted in certain parts of these fields. Though many earthquakes were located in NW Germany, most of the active hydrocarbon fields lack seismicity. Only four seismic events are located far away (more than 30 km) from these natural gas fields (highlighted with blue circles, Fig. 35).

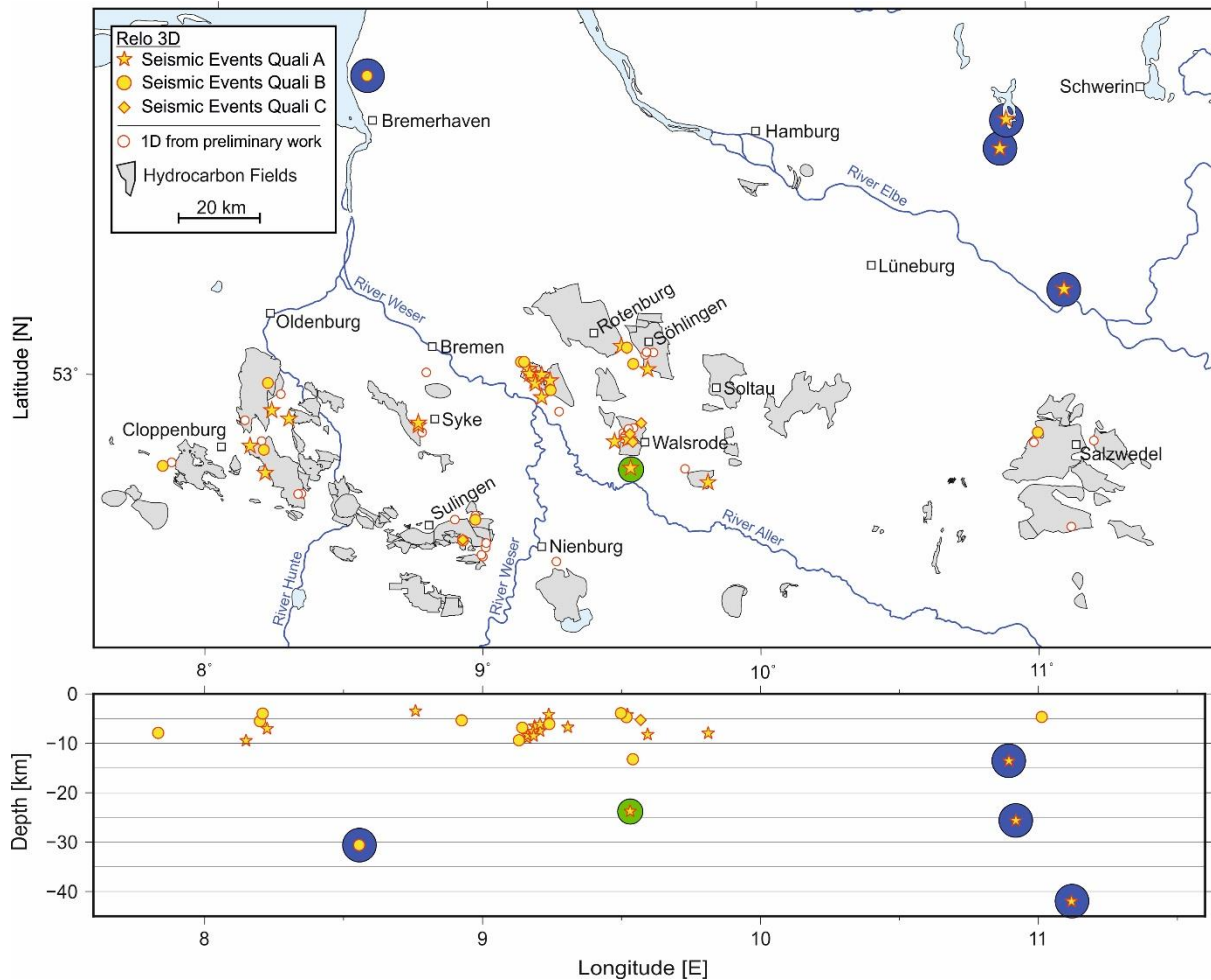


Figure 35. Epicenter map of the 3-D relocated earthquakes divided into the quality classes and the pre-located events (empty circles). Only the best-fitting earthquake hypocenters were plotted. The evaluated event quality for the 3-D solutions is marked by different symbols from “excellent” to “questionable” (A and A' summarized = yellow star, B = yellow circle and C = yellow diamond). In addition, each relocated event is displayed in a vertical cross-section through the study area to show the improved depth distribution. Blue circles indicate deep earthquakes, which were located far away from the hydrocarbon fields, whereas the green circle highlights one event, which is also located in the vicinity of a hydrocarbon field, but in much greater depth.

In addition, the 40 relocated seismic events are displayed within a vertical cross-section in depth and longitude direction. The most reliable hypocenters (Class A and A') are located between 3.5 and 9.0 km in depth, whereas only one single seismic event is located in much greater depth at about 23 km (highlighted by a green circle in Figure 35). In the northern part of the study area, towards the coastlines of Germany, four earthquakes lie much deeper (marked by blue circles, Fig. 35, 13.0 - 42.0 km). The depth distribution indicates a seismicity gap between 13 and 23 km. The hypocenter depth of the relocated earthquakes, belonging to quality classes B and C should be handled with care. For five seismic events, NonLinLoc only calculated a high accurate epicentral location because of an undefined problem during the focal depth determination.

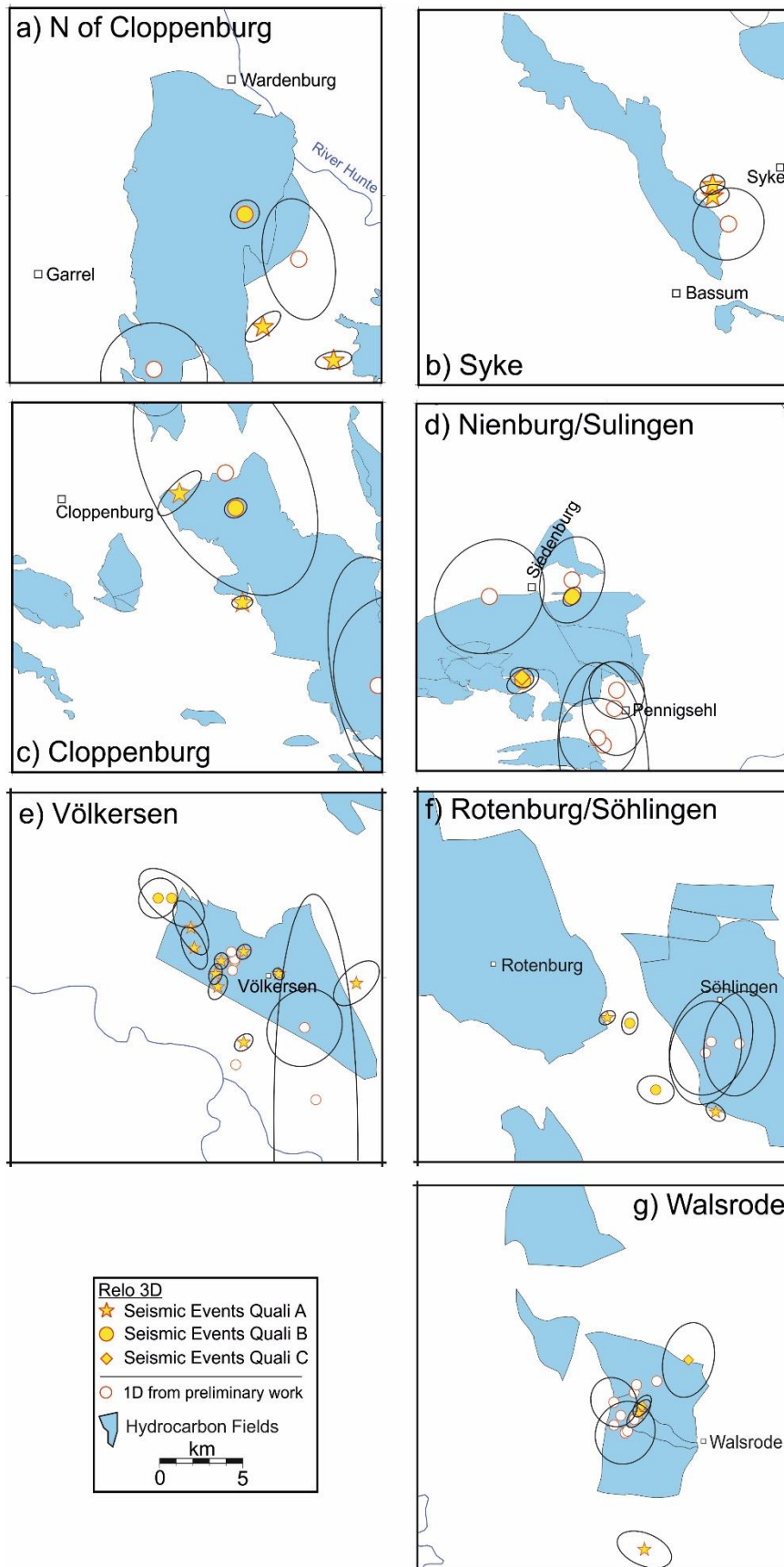


Figure 36. Detailed view of regions with higher seismic activity. The 3-D relocated seismic events are displayed as yellow symbols and the 1-D pre-located events are highlighted by white circles. In addition, uncertainty domains are also shown (black ellipses). **a)** region N of Cloppenburg, **b)** region Syke, **c)** region Cloppenburg, **d)** region Nienburg/Sulingen, **e)** region Völkersen, **f)** region Rotenburg/Söhlingen and **g)** region Walsrode.

Earthquake location shift

A systematic comparison between the BGR routine locations obtained by linearized localization techniques and the new 3-D located hypocenter locations is difficult because of the very differently used input parameters, techniques and velocity models as well as the distinct Gaussian estimated output parameters of both approaches (1-D LocSAT, 95% confidence interval, Bratt and Bache, 1988 vs. 3-D, NLL, 68% confidence interval, Lomax et al., 2000). Nevertheless, I compared the spatial localization results: Figure 37 displays the differences in latitude, longitude and depth (each in m) between the newly derived seismicity pattern and the routine analyses of the BGR. Furthermore, the quality classes obtained from the relocation are also highlighted as yellow stars, circles and diamonds.

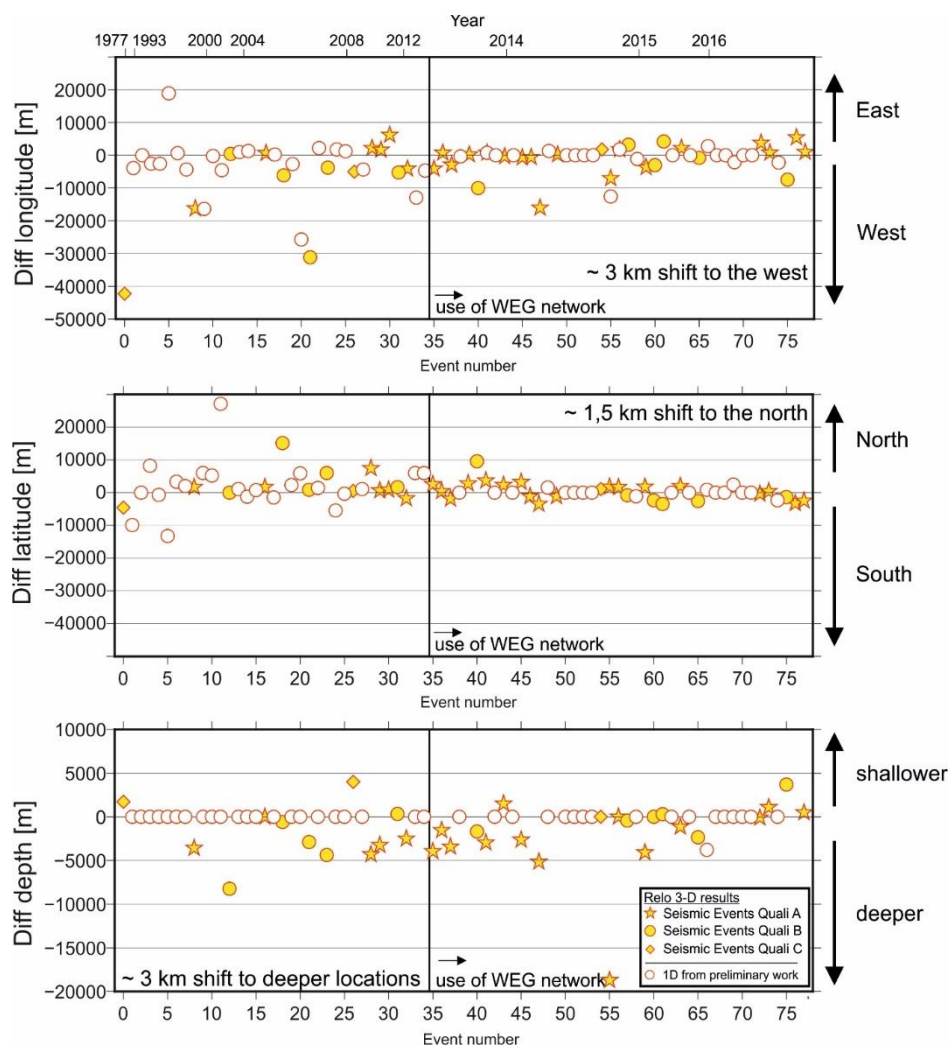


Figure 37. Differences in latitude, longitude and depth (each in m) between my relocated earthquake locations and the earthquake locations obtained from the BGR routine analysis catalogue. Arrows on the right side show the shift direction of NonLinLoc earthquake locations relative to the BGR database earthquake locations. The 1-D located events obtained from the pre-localization are marked as white circles, whereas the relocated events are divided into the three quality classes A (A'): yellow star, B: yellow circle and C: yellow diamond (details see Appendix II, III). The vertical black line marks the starting point where observations from new stations, including WEG network and BGR stations served as additional input parameter for the relocation. In the depth determination graph, each circle on the zero difference line indicates either the same fixed depth, which was used also in the BGR catalogue or the lack of depth determinations by NonLinLoc.

Including outliers, an average epicentral shift of about 1.5 km to the north and 3 km to the west was observed. Earthquakes, which occurred after the establishment of the WEG seismic network in 2012, have only minor individual shifts in latitude and longitude, if the hypocenters were located inside the network. An increase of the station coverage leads to the reduction of the azimuthal GAP, in most cases below a value of 100° . Large individual shifts were observed for earthquakes with the quality rating of B and C, which were mostly connected with a small amount of observations and a lack of a seismic station within the critical focal depth distance. Deviations in hypocenter depth between the earthquake locations determined by the routine analyses of the BGR relative to the relocated hypocenters revealed a slightly different picture. Most of the seismic events, which were determined in the 1-D pre-localization (white circles) show zero differences due to a fixed hypocenter approach. The high amount of excellent 3-D relocated seismic events, especially after the establishment of the WEG network showed a shift to deeper hypocenters of about 3 km relative to the routine solution of the BGR (fixed depth mostly at 5 km). Thus, it indicates a slightly underestimated assumed depth during their routine analyses.

6.2. In-depth seismological analyses of relocated events

In contrast to epicenter parameters, focal depths and focal mechanisms are more difficult to determine, especially if the database or in particular the station coverage is limited like in northern Germany. Spatial and temporal variations of the seismic events, which were based on these earthquake characteristics, are not sufficient to analyse and figure out reliable causes for intraplate earthquakes in NW Germany. Therefore, in-depth seismological analyses were carried out to support or contradict the formerly derived earthquake parameters. In the following, fault plane solutions for selected seismic events and calculated synthetic seismograms constraining hypocenter depth are shown. In addition, amplitude spectra and determined corner frequencies are investigated.

6.2.1 Fault plane solutions

The determination of fault plane solutions is exemplarily described for the seismic event near Syke (May, 1st 2014). After the application of the quality criteria, this event was rated with the second-best category, which referred to B (see chapter 6.1.1). The Syke'14 event with a local magnitude of $M_L = 3.5$ was located using 41 *P* observations, which were more or less properly distributed around the epicenter (GAP = 67 degrees). As described in chapter 5.3 the *P* polarities define the orientation of the onset on the z-component of the selected seismograms: Down = D = dilatation and up = C = compression. Four *Pg/Pn* and one *Sg* first motion onsets are shown in Figure 38. The first three z-component seismograms provide easily discernible impulsive *P* polarities, except IGAD (Garlstedt) transversal-component, which contributes one *SH* polarity for the analysis. The z-component of Station BUG (Bochum) presents an emergent onset, which is of low quality and was therefore not taken into account by plotting this onset direction into the lower-hemisphere of the focal sphere to determine the fault plane solutions.

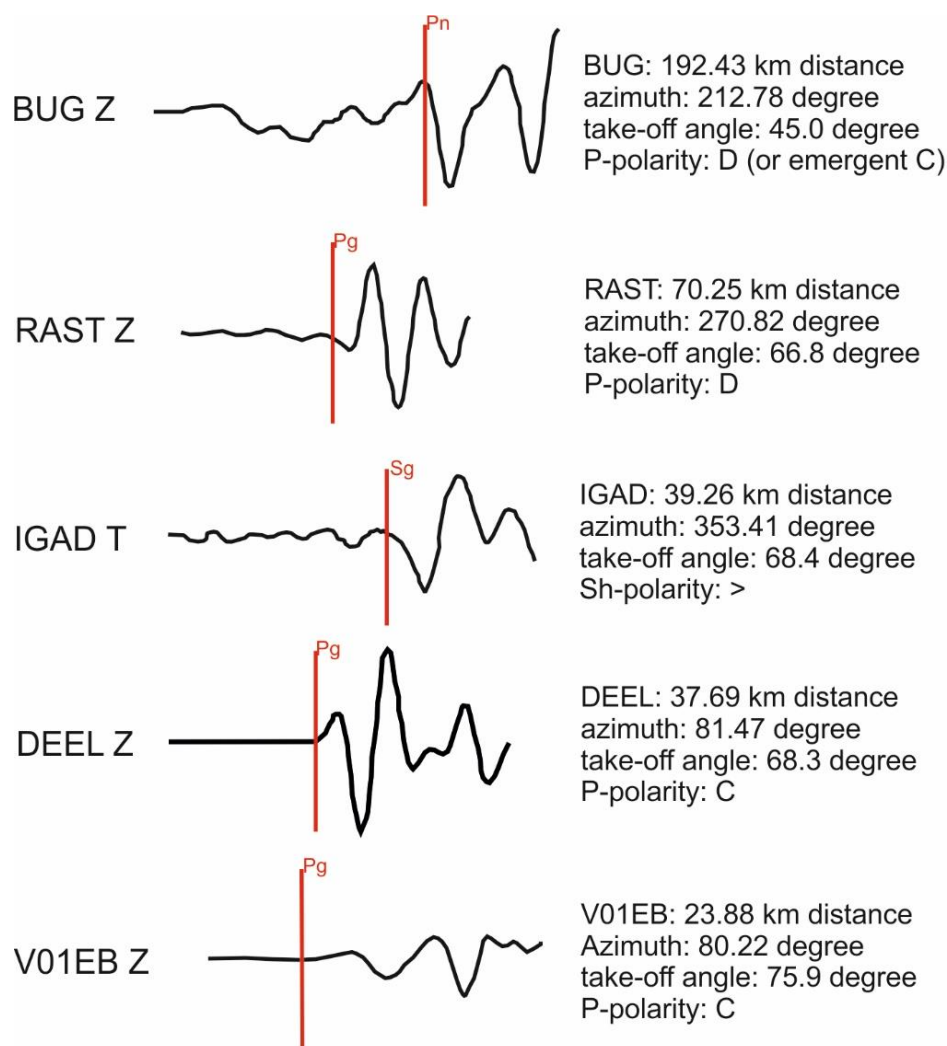


Figure 38. Non-filtered waveforms of real seismograms at five stations, including picked P and S onsets and descriptions of input parameters for FOCMEC. Azimuth and take-off angle were derived by the relocalization with NLL and 3-D velocity models.

Station-Codes, azimuths, take-off angles and first motion polarities served as input parameters for the determination with the program FOCMEC. Initially, the first calculation for focal mechanisms of the Syke'14 event was carried out with 41 P polarities and one additional SH polarity at station IGAD. To reduce uncertainties during the evaluation of P and SH polarities, two interpreters analysed the onsets independently. Both solutions were compared and the best-fitting one served as input parameter for FOCMEC. In addition, for a more robust and reproducible result of the FPS determination four common 1-D velocity models (Fig. 23, chapter 5.3) were also used for the calculation. The nodal plane solutions of each selected seismic event are shown in Appendix VI.

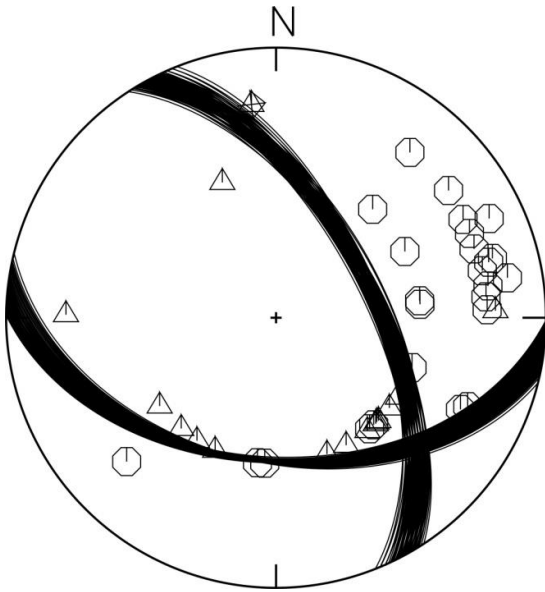


Figure 39. Nodal plane solution pairs (black lines) on lower hemisphere of the focal sphere by using input parameters, as mentioned above for the Syke'14 event. 41 *P* polarities expressed as octagon = compression and triangles = dilatation and one *SH* polarity expressed as an arrow.

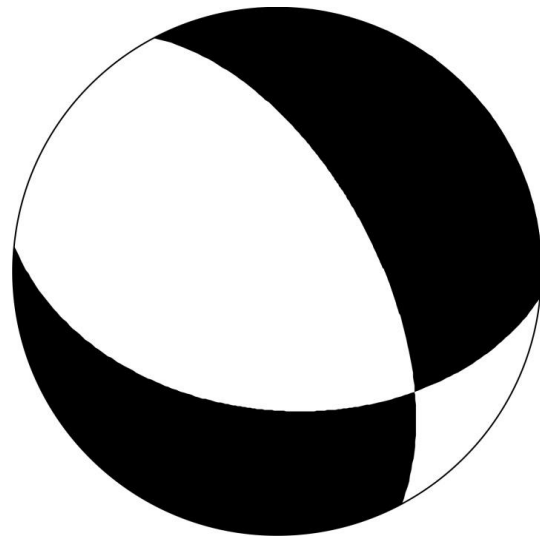


Figure 40. Best-fitting fault plane solution for the Syke'14 event. Beachball expressed in strike: 332.06, dip: 60.47 and slip: -53.22. Referred to the circles and triangles, the differently painted sections on the beachball marked compression (black) and dilatation (white).

The stereographic projection of all nodal plane pairs in Figure 39 shows all possible solutions on the lower hemisphere of the focal sphere for the Syke'14 event using data from the 3-D relocalization (station azimuth and take-off angles). Altogether, 78 fault plane solutions were determined with five or fewer polarity errors. The nodal plane solutions derived by the FOCMEC calculation vary less than 8 degrees from each other. Therefore, they provide a reliable and unambiguously fault plane solution. This best-fitting focal mechanism (median) is shown in Figure 40, displayed in a so-called beachball plot. The focal mechanism represents a NW-SE trending oblique normal fault. The unambiguous solution is attributed to the high amount of observations (42), the balanced azimuthal station distribution (GAP = 67 degree) and the well-constrained onsets of the first arrivals (mostly impulsive). Furthermore, the tapped polarities of the second analyst and each of the four used 1-D velocity models provided nearly the same focal mechanism (Appendix VI). Determined strike, dip and slip for the 18 selected seismic events are shown in Table 12 and displayed as beachballs with the best-fitting fault plane solutions in an epicenter map of the study area (Fig. 41).

Table 12. Focal mechanisms of the 18 selected seismic events with strike, dip and slip of the best-fitting solution. In some cases, there are two possible solutions (sol.), where the determination of fault plane solutions did not allow a unique classification.

Event	Date	Lat (N)	Lon (E)	Depth (km)	Strike	Dip	Slip
08. Wittenburg2000	19.05.2000	53.505	10.894	13.6	too many solutions		
12. Rotenburg'04 sol. 1	12.10.2004	53.039	9.541	13.2	165	58	59
12. Rotenburg'04 sol. 2					329	56	-53
*16. Bassum'05	15.07.2005	52.901	8.759	5.0 (fixed)	208	35	-30
18. Bremerhaven'05	11.08.2005	53.669	8.556	30.6	too many solutions		
23. Langwedel'08 sol. 1	03.04.2008	53.043	9.131	9.4	17	74	-37
23. Langwedel'08 sol. 2					214	52	64
29. Visselhövede'12 sol. 1	13.02.2012	53.027	9.594	8.2	180	64	56
29. Visselhövede'12 sol. 2					337	60	-54
30. Hitzacker'12	16.03.2012	53.193	11.119	42.0	183	68	-28
32. Völkersen'12	22.11.2012	52.970	9.207	7.5	282	66	-85
36. Cluvenhagen'13	01.11.2013	53.009	9.187	6.5	160	80	-69
39. Emstek'13	20.12.2013	52.851	8.149	9.5	287	28	-57
43. Syke'14	01.05.2014	52.907	8.759	3.5	332	60	-53
45. Nindorf'14	20.06.2014	53.002	9.182	7.6	78	44	-22
47. Zarrentin'14 sol. 1	20.07.2014	53.569	10.919	25.6	150	39	57
47. Zarrentin'14 sol. 2					113	40	82
*49. Cloppenburg'14	02.09.2014	52.792	8.205	5.0 (fixed)	291	42	-75
55. Krelingen'14	02.11.2014	52.810	9.531	23.7	32	35	-53
57. Emstek'14	19.12.2014	52.843	8.199	5.5	329	66	-72
72. Völkersen'16	22.04.2016	53.002	9.238	4,2	189	50	-90
73. Bothel'16	28.05.2016	53.078	9.498	3,9	183	65	-67

* Depth value were not calculated by NLL, so that these events were only determined by using 1-D velocity models to provide take-off angles.

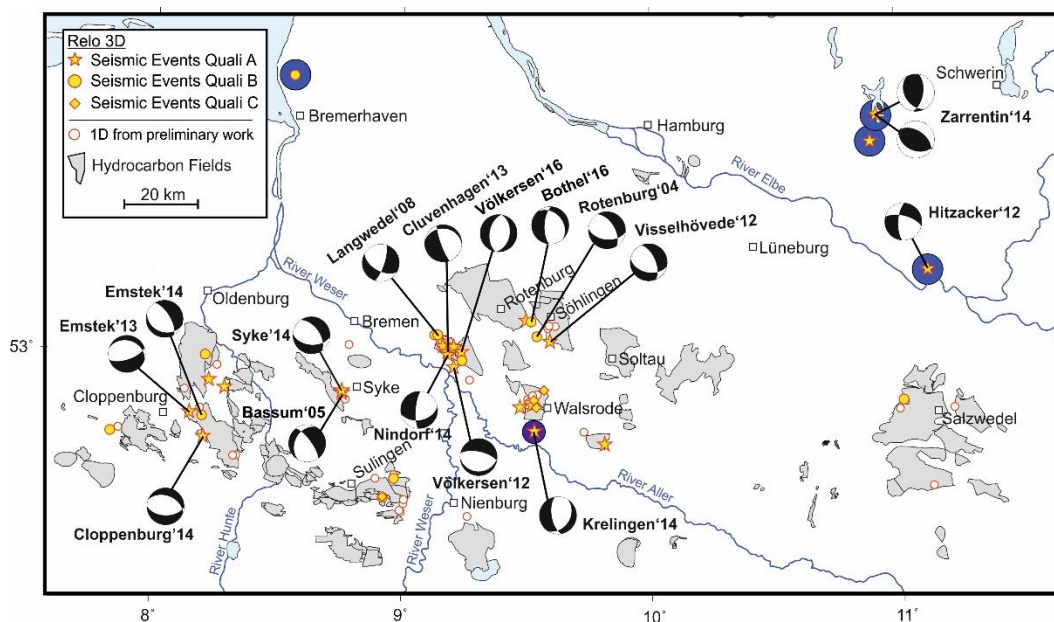


Figure 41. Epicenter map of the study area, including best-fitting fault plane solutions expressed as “beachballs” for the 18 selected seismic events, except 08. Wittenburg'2000 and 18. Bremerhaven'05. The identification numbers refer to Table 12.

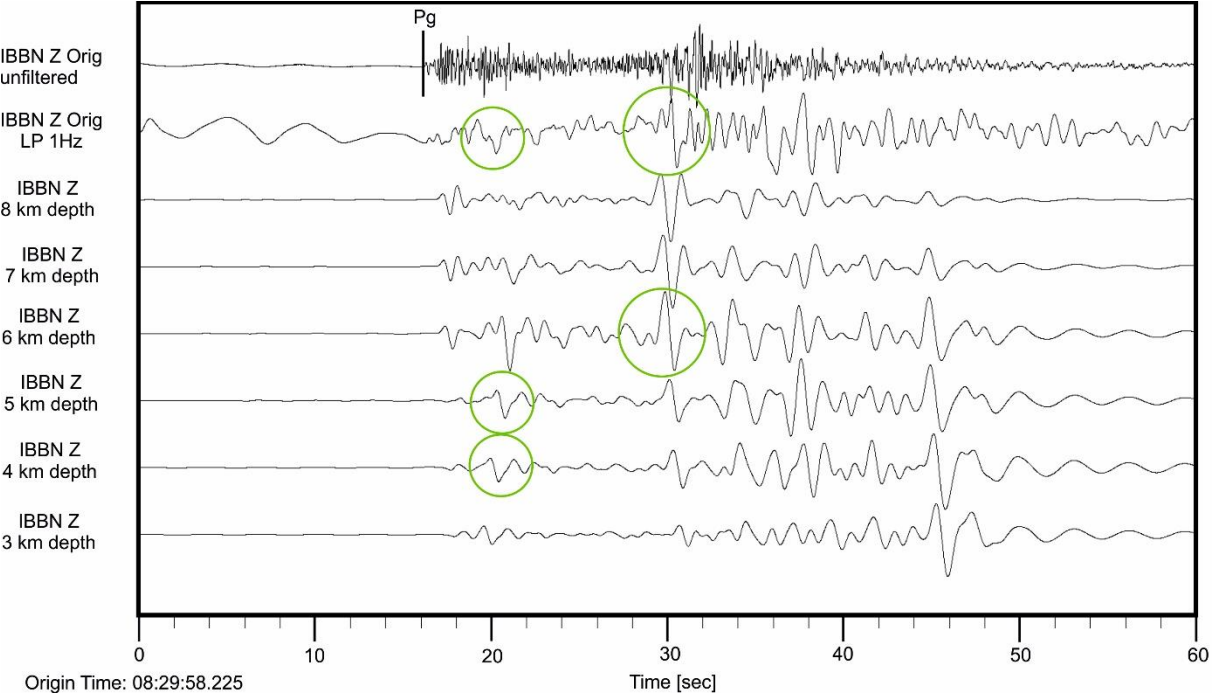
The number of observations and the limited station coverage, being available for the seismic events of Wittenburg 2000 and Bremerhaven'05, were not sufficient to derive a reliable fault plane solution. The analysis of most of the older events (no.12, 23, 29 and in addition 47) provides two different solutions. In case of the focal mechanism for Zarrentin'14, both derived mechanisms indicate thrust fault movement, whereas, the strike direction differed about 40 degrees from NW-SE to roughly N-S. However, for both events Rotenburg'04 (no. 12) and Visselhövede'12 (no. 29), two completely different mechanisms (oblique normal and thrust fault) were calculated, respectively. But, together the determined fault plane solutions are nearly the same for both seismic events. The focal mechanism for event no. 23 (Langwedel'08) was difficult to determine, because of very ambiguous and not reliable onsets. Only 7 out of 29 calculated solutions for the Langwedel'08 event provided a thrust fault movement, so that this case is less likely than the opportunity of normal fault solutions. Depending on the hypocenter depth, a clear correlation to a distinct focal mechanism may not be given, regarding to each selected seismic event. Most of the other fault plane solutions exhibit oblique normal faulting with WNW-ESE or NW-SE striking nodal planes, whereas the focal mechanisms of the tectonic events like Zarrentin'14 or Krelingen'14 show roughly N-S or NNW-SSE trending nodal planes. Oblique normal fault focal mechanisms (13 out of 18) were mostly determined for seismic events, which were previously interpreted as induced and located in shallower depth (3.5 – 9.0 km). Some hypocenter depths and/or fault plane solutions need to be reviewed by the modeling of synthetic seismograms, which are compared with the observed waveforms to constrain the derived solutions.

6.2.2 Synthetic seismograms

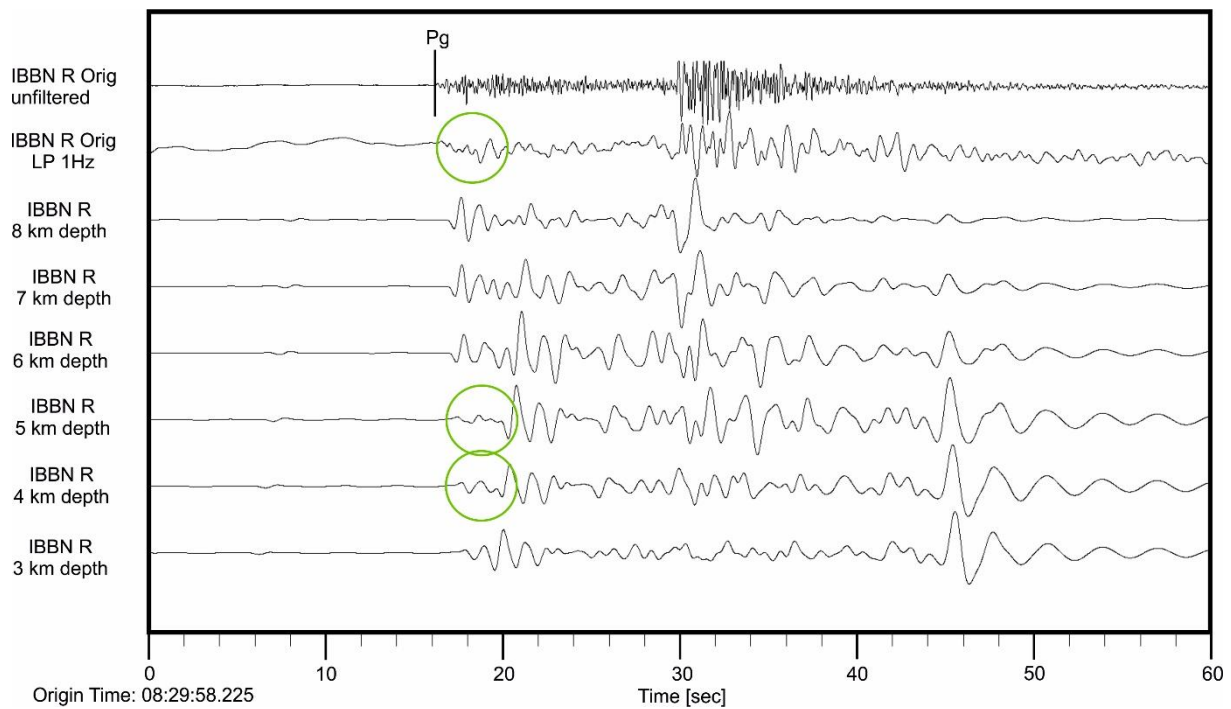
Similar to the presentation of the fault plane solution results, the seismic event on May, 1st 2014 near Syke served also as a good example for the determination of synthetic seismograms, constraining hypocenter depth, because it has a unique fault plane solution. Whereas, the depth uncertainty domain remains relatively high. According to NLL, the hypocenter was determined in depth of 3.5 ± 3.1 km. The closest station to epicenter, which was used for the relocalization, had a distance of approximately 24 km (V01EB - Klein Wulmstorf). This distance is still too far, concerning the recommendations of Deichmann et al. (2004) and Diehl et al. (2014), to maintain a reliable hypocenter depth calculation. For a better assessment of focal depths, I compared time-dependent characteristic waveforms and distinct shapes within real and synthetic seismograms at the seismic station IBBN (Ibbenbühen). In that case, time-dependent means that the distinct feature has to be situated nearly at the same time in both waveform sections (green ellipse in Figures 42a-c). In addition, the green ellipse covers the predicted depth range, in which the hypocenter is presumably located.

Figures 42a, b and c display complete synthetic seismograms (black), which were calculated at the station IBBN for all three components – vertical, radial and transversal. IBBN is located about 94 km away from the epicenter. For this distance, I assume that the influence of the 1-D velocity model, especially on the *S* minus *P* time is very low, because of the longer travel time. Using the SED velocity model (Dahm et al., 2007, see also Figure 23c, chapter 5.3), the simulated hypocenter depths are varied in a range of 3 to 8 km with steps of 1 km. The applied normal fault focal mechanism ($sds = 332\ 60\ -53$) is derived from the determination of fault plane solutions in this study. Further important parameters for each selected seismic event, which had been applied in the calculation of the theoretical seismograms are shown in Table 13.

a) Syke'14 at IBBN – vertical component seismograms



b) Syke'14 at IBBN – radial component seismograms



c) Syke'14 at IBBN – transversal component seismograms

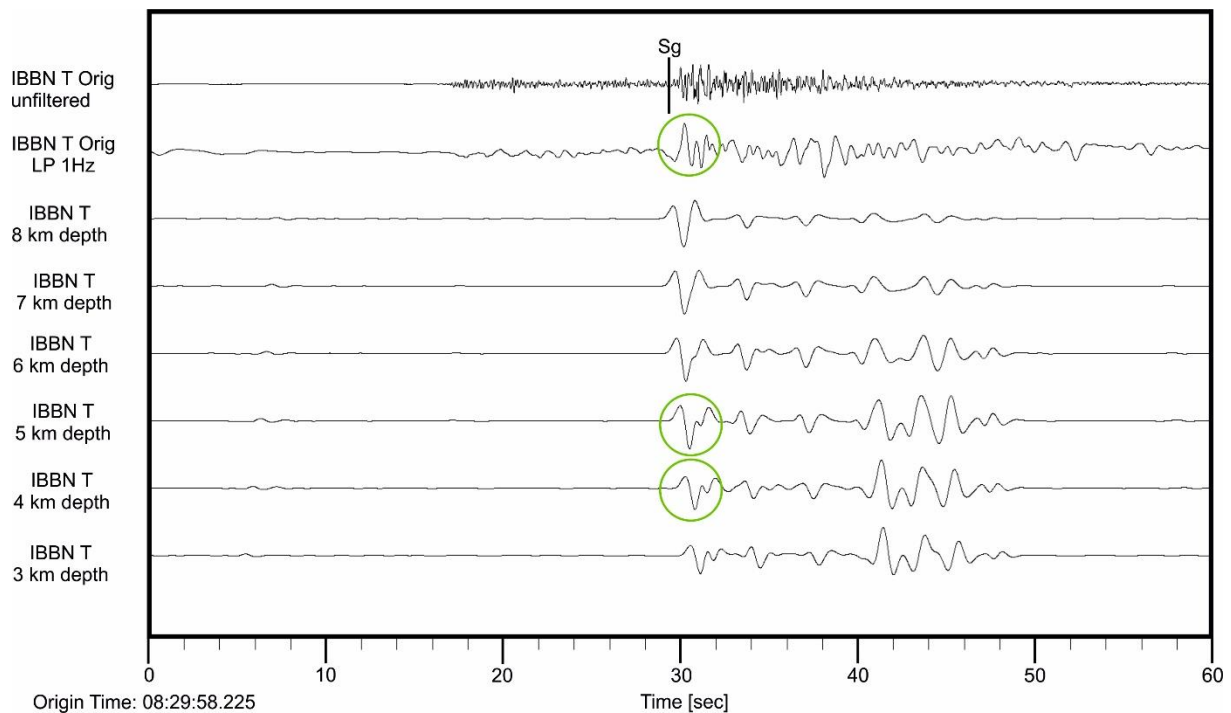


Figure 42. Real waveforms (Orig) and synthetic ones at the station IBBN for the **a)** vertical, **b)** radial and **c)** transversal component, generated for the seismic event on May, 1st 2014 near Syke. Within the figures, the predicted depth (3 – 8 km) is plotted against the time. Green circles in each figure highlights the characteristic feature that was unique in the selected seismogram section and which was used in comparison with the observed waveform to constrain hypocenter depths.

Table 13. Key parameters, which were used during the comparison of observed waveforms with synthetic seismograms. Abbreviations are: Dist. = distance from station to epicenter, Azim. = azimuth from epicenter to station (in easterly direction) and LP = lowpass filter.

Event	Date	Station	Dist. & Azim.	Filter	Model	Figures
12. Rotenburg'04	October, 20 th 2004	NRDL	71.78 km; 149.35 deg	LP 1 Hz	SED	43a, b
		BSEG	110.44 km; 26.44 deg			44a, b
42. Syke'14	May, 01 st 2014	IBBN	94.20 km; 226.17 deg	LP 1 Hz	SED	42a-c

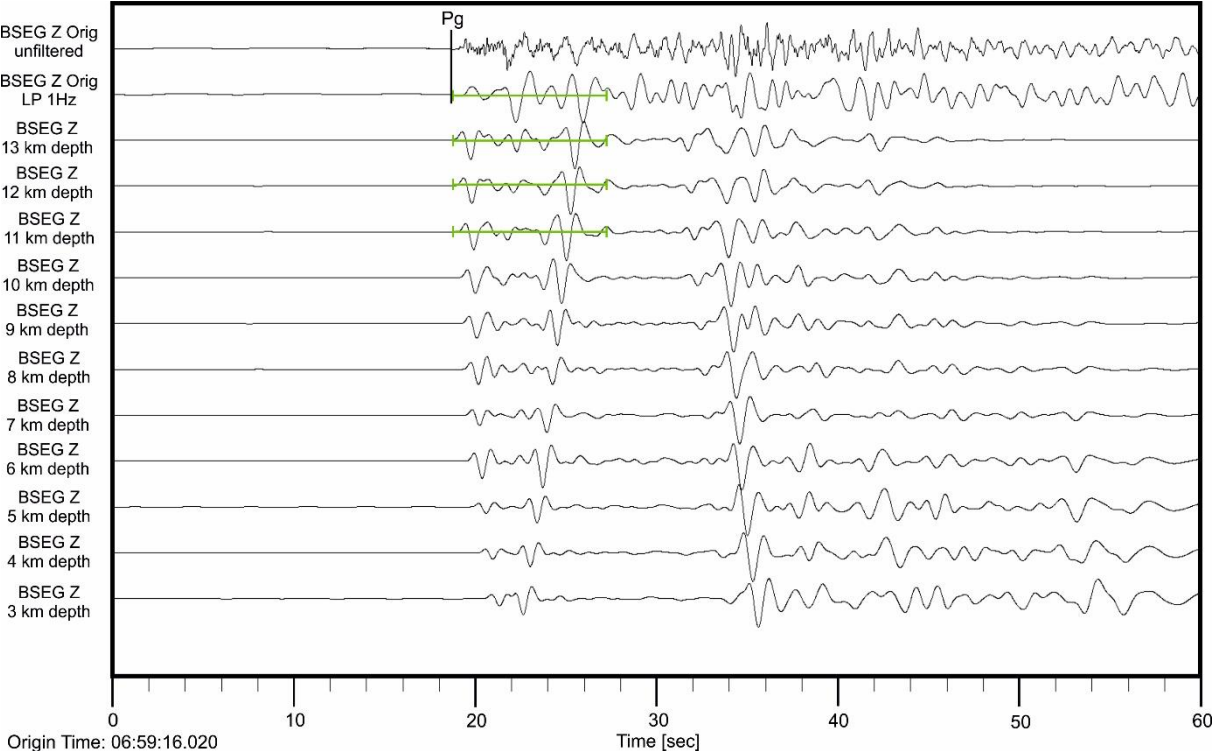
The calculation of synthetic seismograms is difficult because many input parameters, especially the velocity model have to be well evaluated in more detail to approximate the natural features providing reliable calculated waveforms. Therefore, it is difficult to find the best-fitting hypocenter depth by comparing the whole real waveforms with the synthetic ones using only a visual analysis. In this case, I searched for characteristic features within selected waveform sections and/or parts between significant peaks, which have the same time range in the predicted and observed traces, respectively.

For example, within the waveform of the vertical component at the station IBBN (Fig. 42a), the green ellipses highlight two characteristic features within the *P* and *S* wavelet. Both significant waveforms can be found within the synthetic seismograms according to the depths between 4 to 6 km. Likewise, at the radial component of station IBBN (Fig. 42b), the observed waveform had the most similarities with the synthetic ones between the depths of 4 - 6 km. In addition, the comparison of the *P*-wave energy on the radial component seems to be another characteristic feature to constrain the hypocenter depth. In synthetic seismograms for depths 6 – 8 km, the *P* onset is impulsive and the amplitude is not comparable with the more likely emergent *P* phase in the observed waveform. Therefore, hypocenter depth below 6 km are more or less excluded and the most probable focal depth is situated between 4 – 6 km. Similarities between the observed and predicted seismograms on the transversal component are difficult to see. However, as expected, the synthetic seismograms, belonging to the transversal component of the station IBBN (Fig. 42c) do not show any *P* phase energy and serve as indicator for a reliable synthetic seismogram modeling.

Synthetic seismograms for the Rotenburg event are simulated at two seismic stations with two different focal mechanisms (Figs. 43 and 44). This earthquake was the strongest event ever instrumentally recorded in NW Germany. A local magnitude of M_L 4.3 was observed (M_W 4.4, Dahm et al., 2007). NRDL (Niedersachsen-Riedel) was the closest station to epicenter (distance = 72 km), which had recorded this earthquake. However, the station was too far away to determine a reliable hypocenter depth and focal mechanism by using simple analysis methods. Applying the software FOCMEC, two different focal mechanisms were derived. Sds1 (strike-dip-slip = 329 56 -53) indicates a normal fault movement, whereas sds2 (165 58 59)

describes thrust faulting. For two stations - NRDL and BSEG (Bad Segeberg) - synthetic seismograms were calculated on all three components (vertical, radial and transversal). Both fault plane solutions were considered. The theoretical seismograms were calculated in a depth range between 3 to 13 km with 1 km steps. All traces had been 1 Hz lowpass filtered. For a better overview, only selected components for the station BSEG are shown (Figs. 43a, b and Figs. 44a, b). BSEG is located about 110 km away from the epicenter. For this distance, I assume that the influence of the 1-D velocity model, especially on the *S* minus *P* time is very low, because of the longer travel time. All other components and the example of NRDL are given in Appendix VII.

a) Rotenburg'04 at BSEG, sds1 = normal fault – vertical component seismograms



b) Rotenburg'04 at BSEG, sds2 = thrust fault – vertical component seismograms

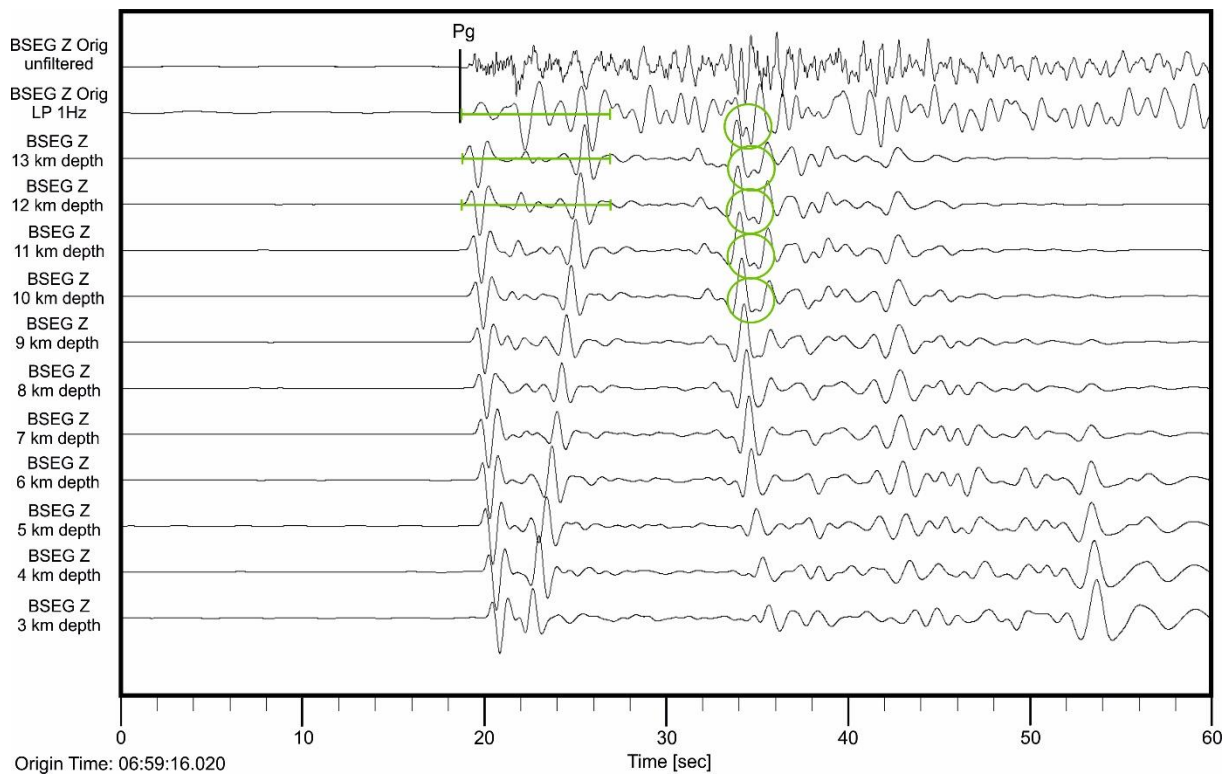
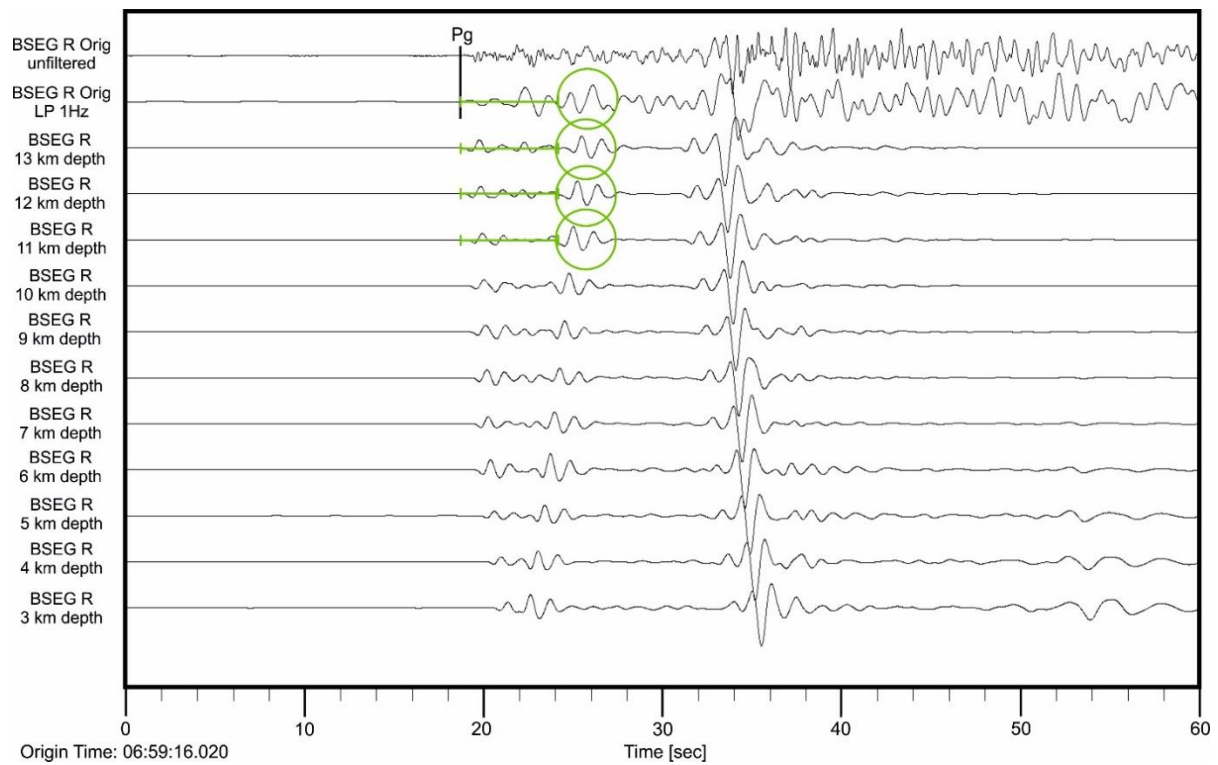


Figure 43. Comparison of synthetic and real waveform seismograms for the seismic event near Rotenburg from October, 20th 2004 located between the Söhlingen and Rotenburg/Taaken Rotliegend hydrocarbon fields. Observed and calculated waveforms are displayed at the station BSEG for the vertical component with **a)** the normal fault and **b)** the thrust fault focal mechanism. Except the unfiltered original seismogram, each seismogram was lowpass filtered at 1Hz. Green circles and green lines in each figure point out the characteristic features, which were unique in the selected seismogram section and which were used in comparison with the observed waveform.

Figures 43a and b display complete synthetic seismograms (black), which were calculated at the station BSEG for the vertical component. Both fault plane solutions show slightly different calculated waveforms. However, *P* and *S* phases and the time span between these significant phases are nearly the same for both focal mechanisms. Therefore, a criterion to distinguish between the normal (Fig. 43a) and the thrust fault focal mechanism (Fig. 43b) cannot be identified within modeling results of the vertical component. Constraining the hypocenter depth, the length of the *P* wavelet plays an important role (see green line in Figs. 43a and b). Within the observed waveform the *P* wavelet has an assumed time duration of about 9 s. In comparison to the calculated seismograms this fits very well for modeled focal depth greater than 10 km. For assumed shallower origins the distance between the significant *P* peaks is too short. In addition to that, a downgoing double peak within the *S* wavelet is highlighted by a green circle in Figure 43b. This double peak indicates that the hypocenter depth is located between 10 to 13 km.

a) Rotenburg'04 at BSEG, sds1 = normal fault – radial component seismograms



b) Rotenburg'04 at BSEG, sds2 = thrust fault – radial component seismograms

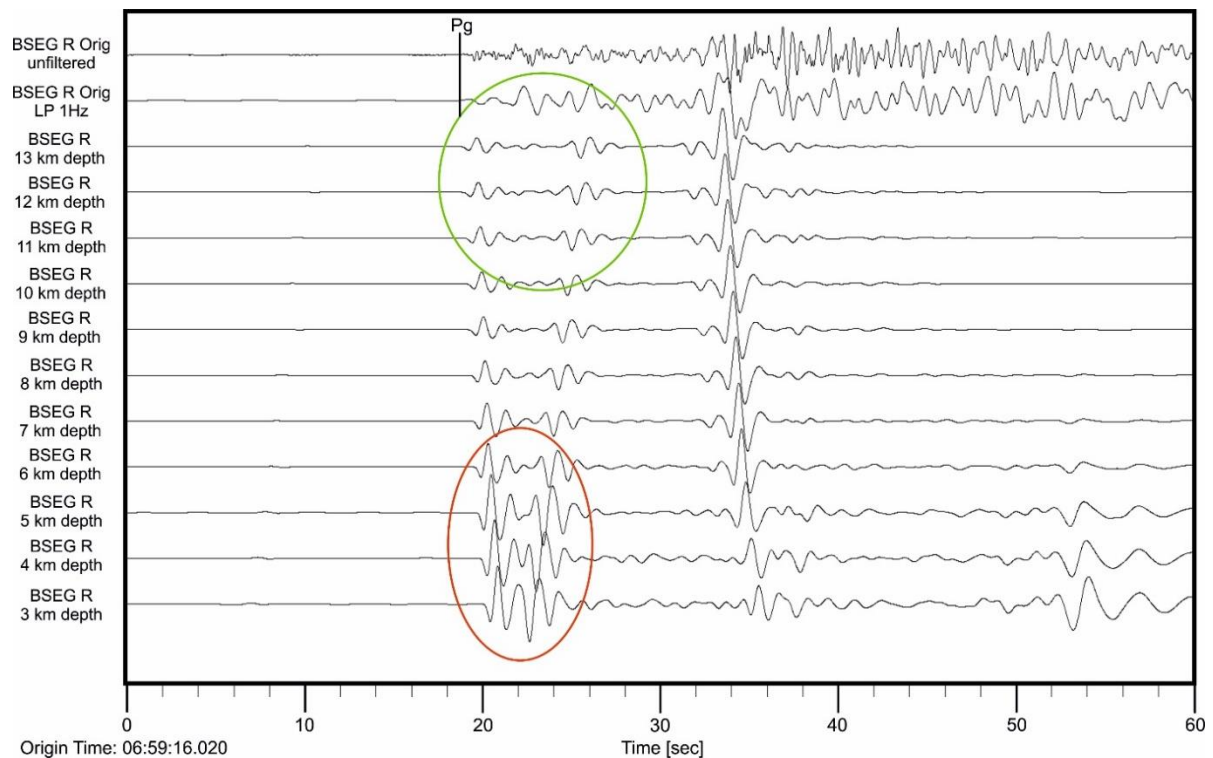


Figure 44. Comparison of synthetic and real waveform seismograms for the seismic event near Rotenburg from October, 20th 2004 located between the Söhlingen and Rotenburg/Taaken Rotliegend hydrocarbon fields. Observed and calculated waveforms are displayed at the station BSEG for the radial component with **a)** the normal fault and **b)** the thrust fault focal mechanism. Except the unfiltered original seismogram, each seismogram was lowpass filtered at 1Hz. Green circles and green lines in each figure point out the characteristic features, which were unique in the selected seismogram section and which were used in comparison with the observed waveform. The red ellipse in b) indicate a characteristic feature, which does not correspond to the observed waveform. Details see in the text below.

Figures 44a and b display the observed waveform and related synthetic ones at the seismic station BSEG for the radial component. Similar to the investigated vertical component above, a criterion to distinguish between the normal (Fig. 44a) and the thrust fault focal mechanism (Fig. 44b) could not be identified. However, another waveform feature is observed within the *P* wavelet (green circle in Figure 44). The time span from the first *P* onset and these peaks indicate an assumed focal depth greater than 10 km. In addition to that, the amplitude of the *P* wavelet in the radial component seismograms for the thrust fault example (red and green ellipses in Figure 44b) seems to be too high for shallower modeled focal depth in comparison with the observed waveforms. Amplitudes and amplitude ratios of the synthetic ones fit better for greater depth. All of these highlighted characteristic features contribute to the relatively deep relocalization result, which was derived by using NonLinLoc in combination with 3-D velocity models.

The differentiation between both, the thrust and normal fault focal mechanisms is more difficult than the hypocenter improvement. Unambiguous characteristic features within the observed waveform and the predicted seismograms cannot be carried out to distinguish between both fault plane solutions. Each result had to be handled with care due to the visual and qualitative approach.

6.2.3 Amplitude spectra and corner frequencies

Amplitude spectra were generated with the software Seismic Handler (Stammler, 1993). The procedure is exemplarily illustrated for two different events (the Völkersen event on November, 22nd 2012 and the Krelingen event on November, 02nd 2014 (Fig. 45a). Both were compared with each other. The spectrum (Fig. 45b) for the Völkersen event was generated from the z-component seismogram at the station CLZ (Clausthal-Zellerfeld, 100Hz sample rate) in a time window from 20:38:30 UTC to 20:39:30 UTC (60 sec.). In the same way, the waveform signal of the Krelingen event was taken over a period of 60 seconds from 11:34:56 UTC to 11:35:56. Both sections encompassed the entire *P* and *S* wavelet (signal) of these seismic events.

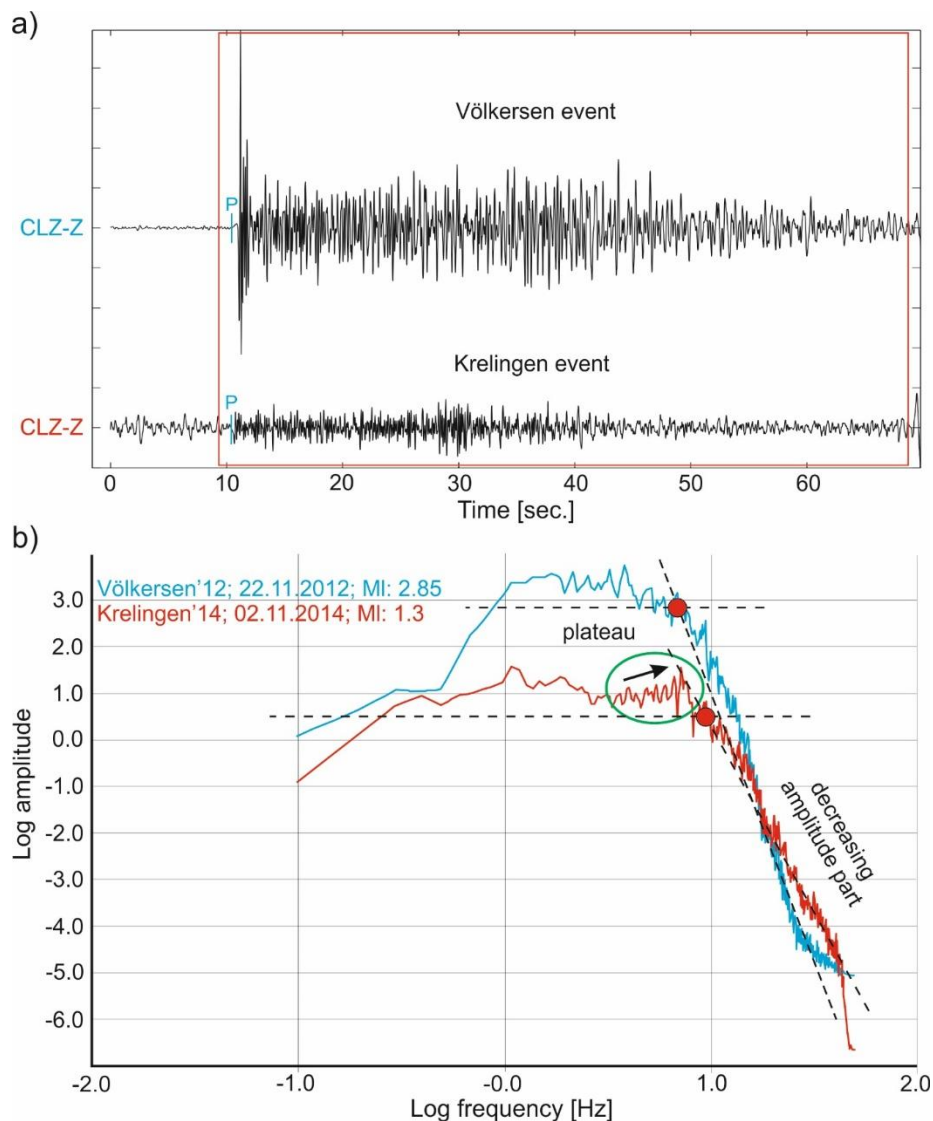


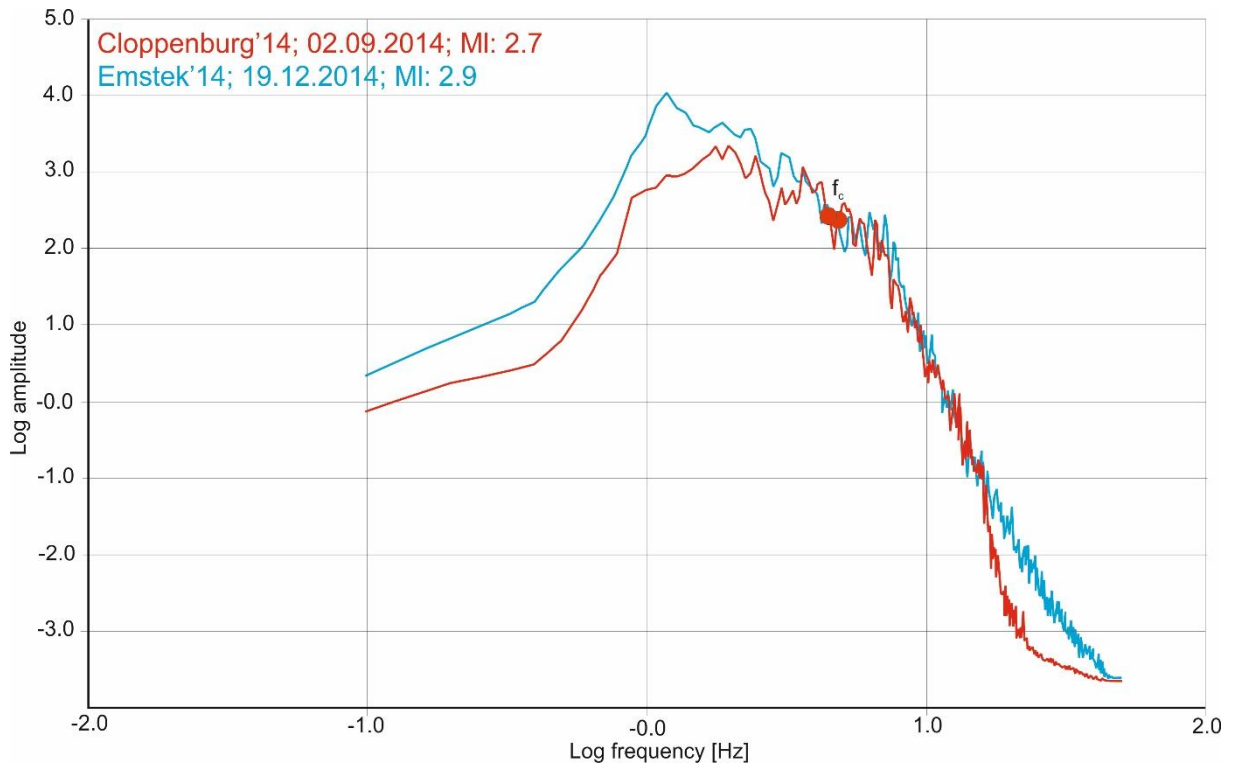
Figure 45. Seismograms and derived amplitude spectra generated with Seismic Handler. **a)** 70 seconds section received from the original seismograms of the Völkersen event (above) and of the Krelingen event (below) at the station CLZ. The red box marks the time window, in which the amplitude spectra were generated. **b)** log/log amplitude spectrum generated from the red marked area (see a.). The corner frequency for each spectrum is highlighted by a red dot. The plateau and the decreasing amplitude part are traced by the dashed black lines. Further details are mentioned in the text.

The Völkersen and Krelingen event, both located close to a hydrocarbon field, showed very different shapes of waveform signals (Fig. 45a). Völkersen had a local magnitude of $M_L = 2.85$, a very sharp (impulsive) P onset and was located in a shallow depth (7.5 km), whereas the hypocenter of Krelingen was situated in a depth of about 24 km. This deep event had a very small local magnitude ($M_L = 1.3$). Therefore, the waveform hardly differed from the background signal (noise). As shown in Figure 45b the different high magnitudes define the amplitudes in the amplitude spectra. Despite the amplitude, the style of both amplitude spectra, especially of the main characteristics (plateau and decreasing amplitude part) was roughly the same. However, in detail, the spectrum of the Krelingen event had a broader plateau range and the slope of the decreasing amplitude part was lower than the one of the Völkersen event. But, the significant anomaly in the spectrum of Krelingen, in contrast to the one of Völkersen was the slightly increasing amplitude section directly located a few frequency values before the decreasing part starts (green ellipse and arrow in Figure 45b). The highest amplitude seems to be shifted in the direction of higher frequencies. Based on the corner frequency, I defined a quantitative criterion to distinguish between these and other investigated spectra.

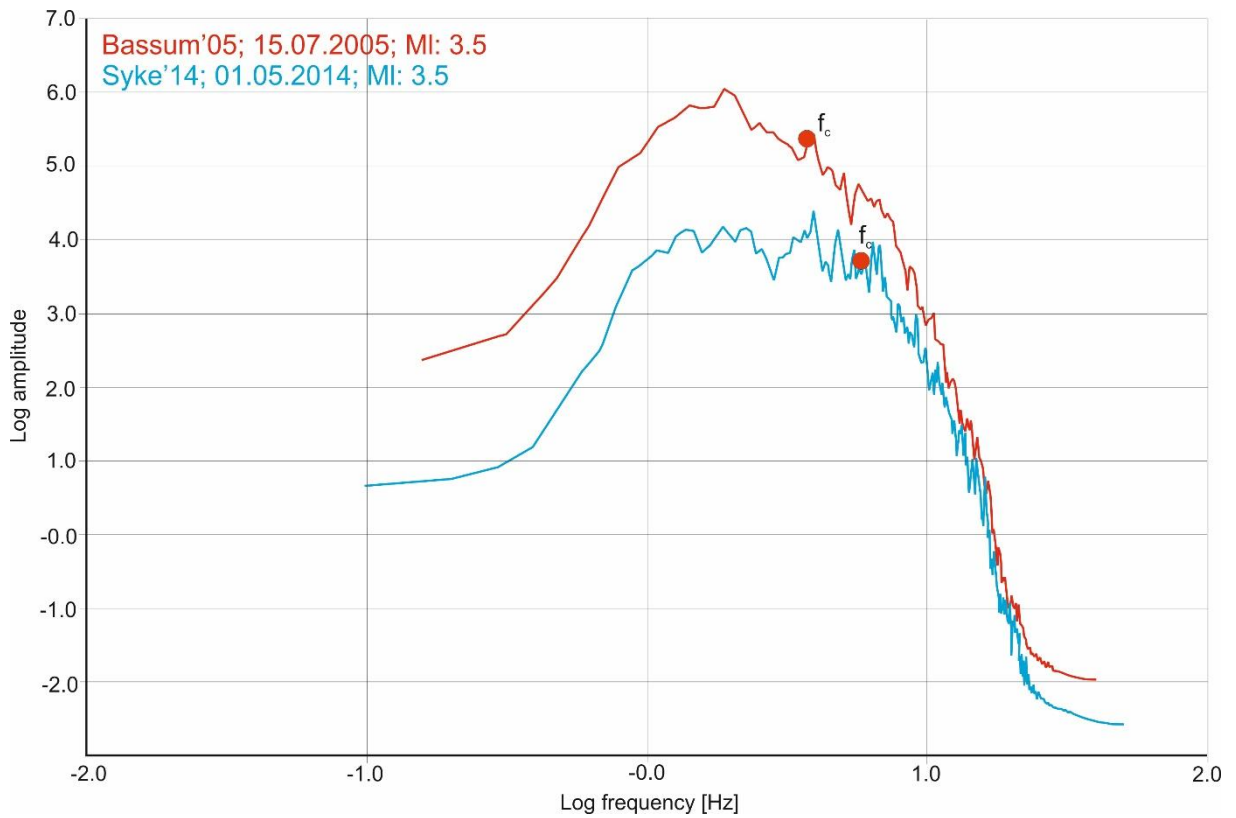
The corner frequency for each seismogram was calculated with the program Qopen (Eulenfeld and Wegler, 2016) and had a value of 5.8 Hz for the Völkersen event and 9.9 Hz for Krelingen (red dots in Figure 45b). The corner frequency defined the intersection point between the plateau and the decreasing amplitude part (see chapter 5.5). The plateau range value for Völkersen is 4.8 Hz ($f_c = 5.8$ minus $f_0 = 1.0$), whereas for Krelingen it had a broader range with 9.65 Hz.

Figures 46a-d show amplitude spectra of two seismic events for each selected region in the study area, in which significant earthquakes were clustered – a) Cloppenburg, b) Syke, c), Langwedel/Völkersen and d) Rotenburg/Söhlingen - whereas Figure 46e shows four earthquakes, which were presumably determined in deeper geological horizons (13 - 42 km).

a)



b)



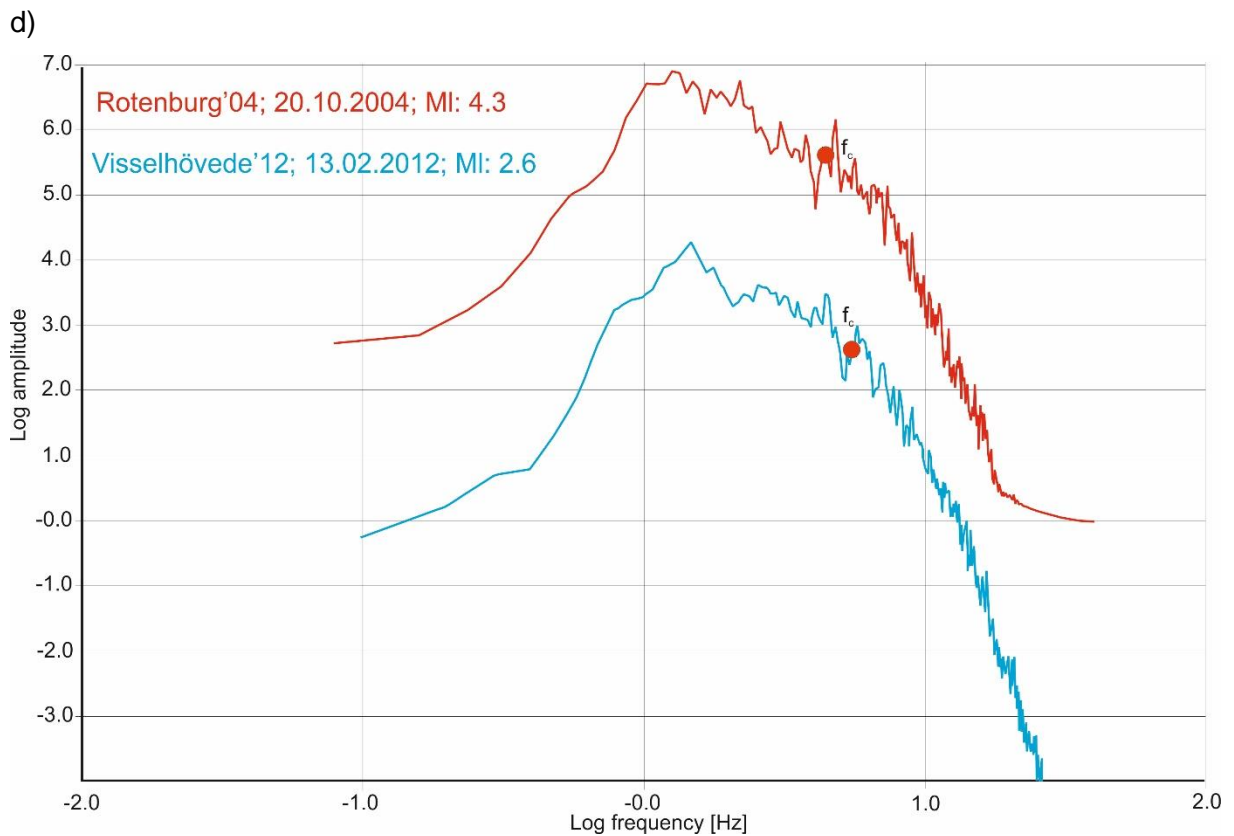
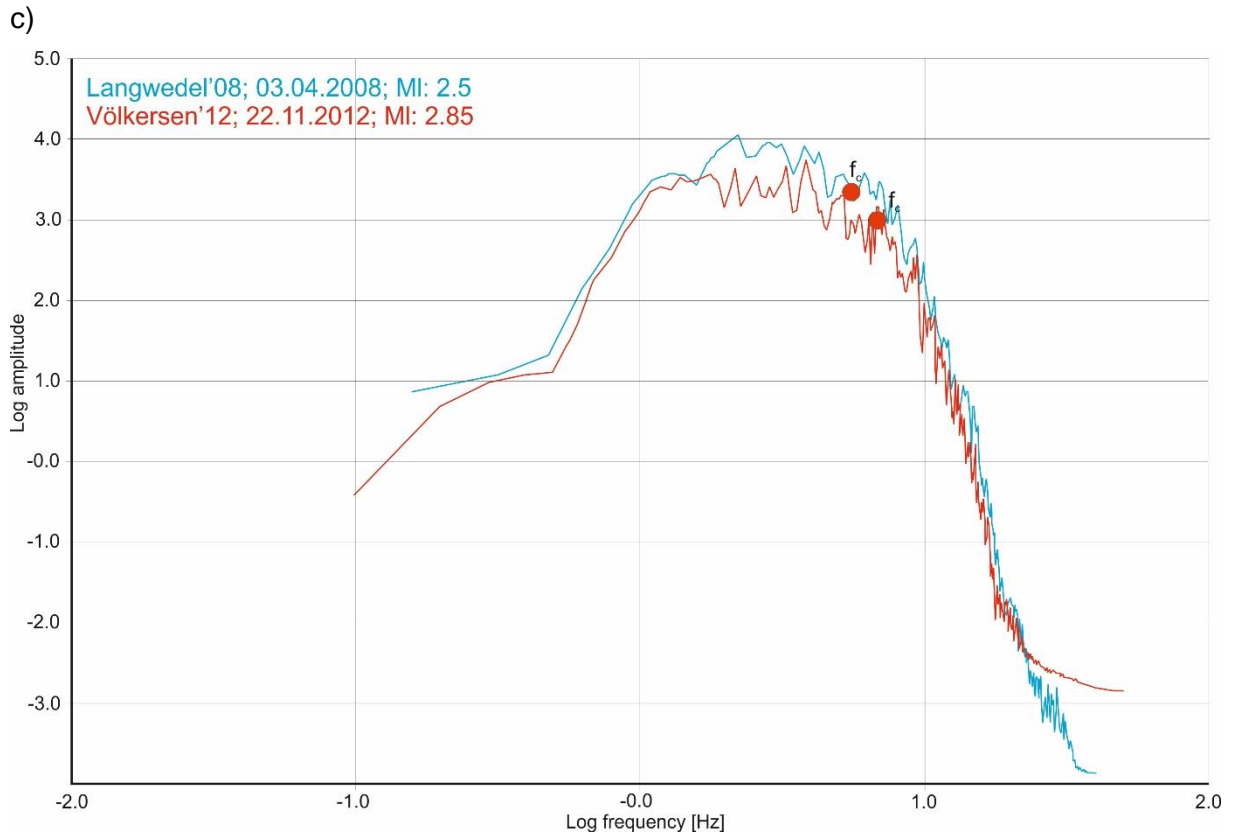


Figure 46. Log/log amplitude spectra of 8 seismic events in the study area. The spectra were generated with Seismic Handler. The corner frequency is highlighted by a red dot and f_c . **a)** region Cloppenburg, **b)** region Syke, **c)** region Langwedel/Völkersen, **d)** region Rotenburg/Söhligen.

The amplitude spectra in Figures 46a-d show nearly the same increasing amplitude tendency until a frequency value between one and two Hz was reached, because the lower frequency boundary was cut off at 1Hz. However, after this amplitude peak and without regarding the different high absolute amplitudes, the spectrum for earthquakes in each selected region looked nearly the same but the evolution was different. In general, the shape of the plateau is decreasing very slightly to f_c . From then on a higher slope within the spectrum indicated the beginning of the decreasing amplitude part. The determined parameters are given in Table 14.

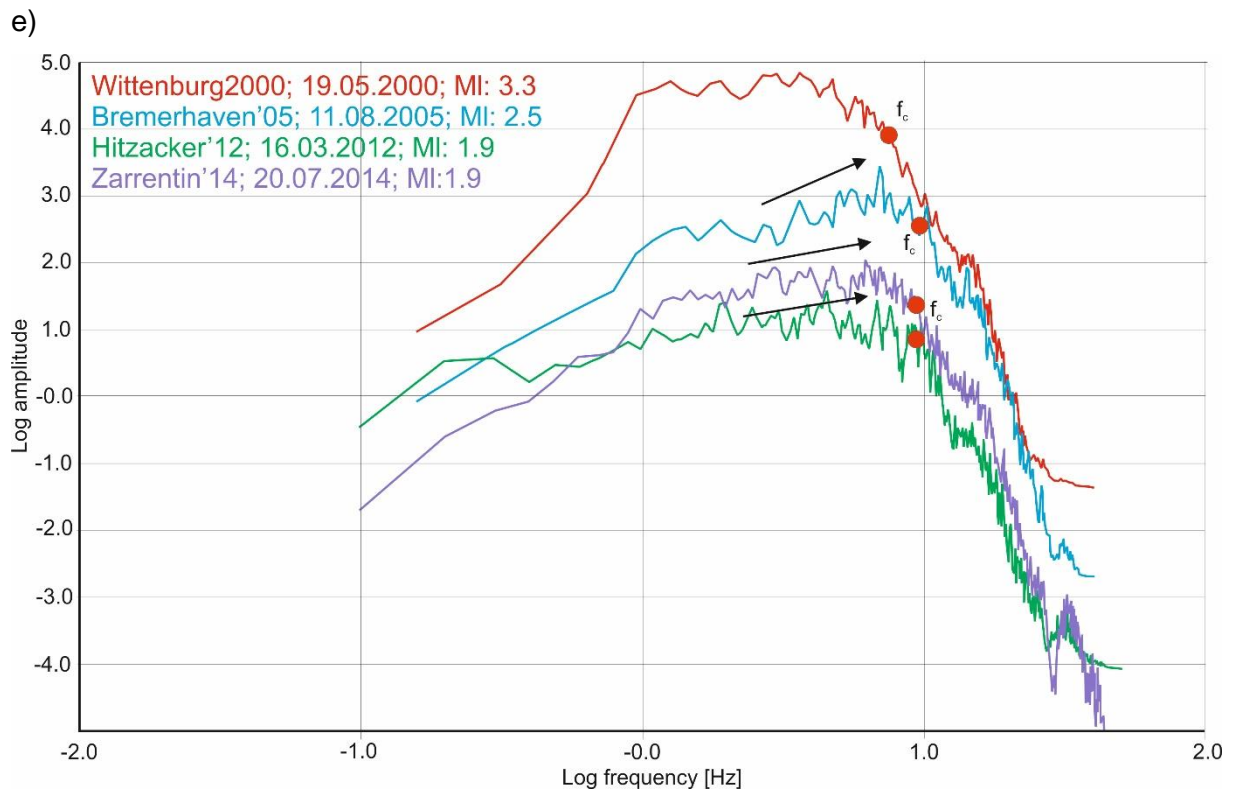


Figure 46e. Log/log amplitude spectra of four earthquakes with hypocenters located at depths between 13 to 42 km. Therefore, these events are defined as tectonic earthquakes. The corner frequency is highlighted by a red dot and f_c .

In contrast to the previously described amplitude spectra, which are displayed in Figures 46a-d, the four spectra in Figure 46e show a slightly different shape. The maximum amplitude value is reached towards higher frequencies, in particular near the corner frequency f_c . The plateau range is broader and as also mentioned for the Krelingen'14 event (Fig. 45b) there is a slightly increasing amplitude section within the spectra of Bremerhaven'05, Hitzacker'12 and Zarrentin'14 in the direction of higher frequencies (see arrows in Figure 46e). The Wittenburg'2000 earthquake is different, because the shape of the spectrum is similar to the spectra of the shallower earthquakes in Figures 46a-d. These observations were supported by quantifying the corner frequency for each spectrum, which is stored in Table 14 and displayed in Figure 47. Except Rotenburg'04, the seismic events with hypocenter depths less than 10 km

have a corner frequency of less than 6 Hz (yellow ellipse in Figure 47). The corner frequencies for earthquakes, which were located deeper than 20 km, have a value of approximately 9 Hz and higher (red ellipse in Figure 47). In addition, earthquakes with $M_L > 2.5$ show, in most cases smaller corner frequencies whereas smaller earthquakes with $M_L < 2.5$ indicate higher corner frequencies.

Table 14. Determined parameters for the spectral analysis of selected seismic events.

Event	Date	Depth (km)	M_L	f_c [Hz]	pr [Hz]	slope
08. Wittenburg2000	19.05.2000	13.565	3.30	7.5	6.70	-0.24
12. Rotenburg'04	12.10.2004	13.230	4.30	3.3	2.50	-0.38
*16. Bassum'05	15.07.2005	5.000 (fixed)	3.50	3.7	2.70	-0.38
18. Bremerhaven'05	11.08.2005	30.588	2.50	9.5	8.55	-0.23
23. Langwedel'08	03.04.2008	9.371	2.50	5.4	4.40	-0.35
29. Visselhövede'12	13.02.2012	8.241	2.60	4.3	3.50	-0.31
30. Hitzacker'12	16.03.2012	42.005	1.90	9.2	8.50	-0.21
32. Völkersen'12	22.11.2012	7.512	2.85	5.8	4.80	-0.35
43. Syke'14	01.05.2014	3.479	3.50	5.9	5.00	-0.34
47. Zarrentin'14	20.07.2014	25.648	1.90	9.2	8.00	-0.23
*49. Cloppenburg'14	02.09.2014	5.000 (fixed)	2.70	4.8	4.00	-0.22
55. Krelingen'14	02.11.2014	23.749	1.30	9.9	9.65	-0.21
57. Emstek'14	19.12.2014	5.533	2.90	4.2	3.40	-0.23

* Seismic events, for which no depth value was calculated by NonLinLoc.

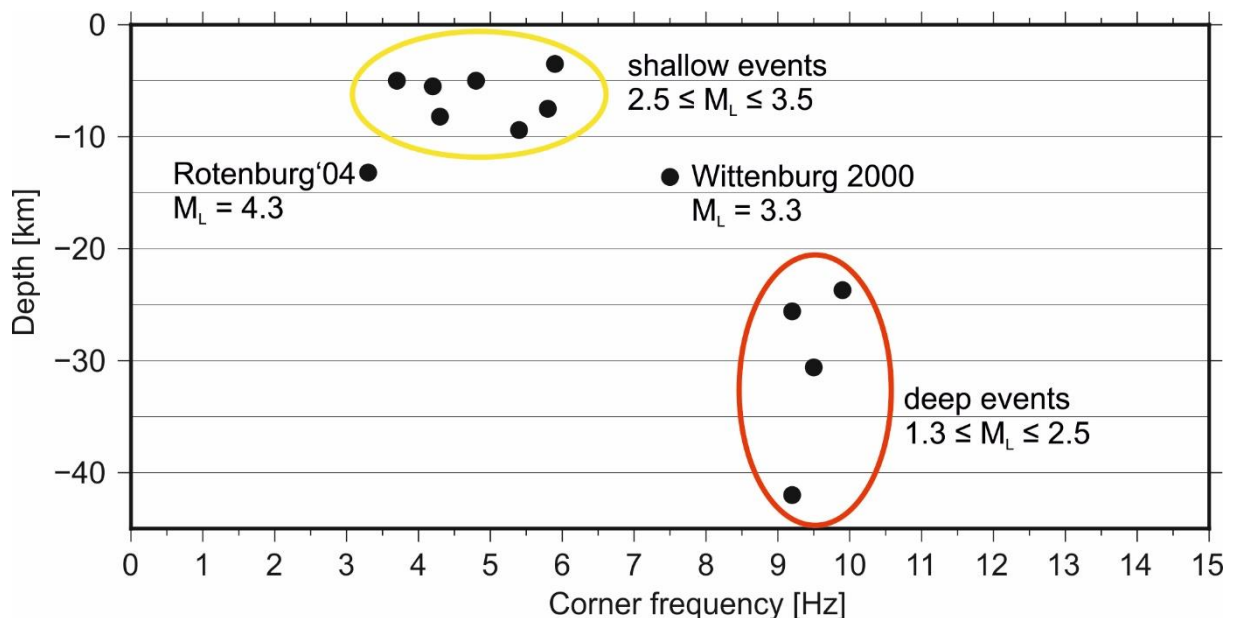


Figure 47. Corner frequencies depending on the hypocenter depth.

6.3. 3-D relocation results of prominent seismic events in NW Germany in comparison with former earthquake studies

Prominent earthquakes in NW Germany were investigated in the following studies: the Soltau earthquake from 1977 by Leydecker et al. (1980), the unusual deep Wittenburg 2000 earthquake (Bock et al., 2002), the Rotenburg main event in 2004 by Leydecker et al. (2006) and Dahm et al. (2007), the Völkersen'12 event by Bischoff et al. (2013), the Syke'14 event by Bischoff et al. (2014) and the Emstek'14 event by Bischoff et al. (2015). Another report, concerning the strongest event ever recorded at the Völkersen hydrocarbon field (M_L 3.1) on April, 22nd 2016 is currently being processed by BGR and LBEG (State Authority for Mining, Energy and Geology) and should be available during spring 2017. Except Wittenburg 2000, results of these studies are now chronologically compared with my estimated focal parameters such as epicenters, focal depths and fault plane solutions.

6.3.1 Soltau 1977

The database for the Soltau 1977 earthquake is very limited. At that time, only three Gräfenberg seismic stations provided digital seismic waveforms. The original data base, like analog notations (paper seismograms) was lost (G. Leydecker, pers. communication).

Due to the absence of digital seismograms, analyses of own phase picks were not possible. However, 16 observations of the first arrival (seismic phases) are stored in the BGR database. Thus, I was able to relocate the event with NLL and two 3-D velocity models. A detailed description of the relocation results is given in Figure 48 including the scatter cloud, quality and important input parameters as well as the 68 % Gaussian estimated confidence ellipsoid. The relocated earthquake belongs to the quality class C (questionable). The difference between expected and determined hypocenter and uncertainty domains are large. Thereby, especially the GAP and the distance to the nearest observation (Hamburg) have the main impact on the localization quality.

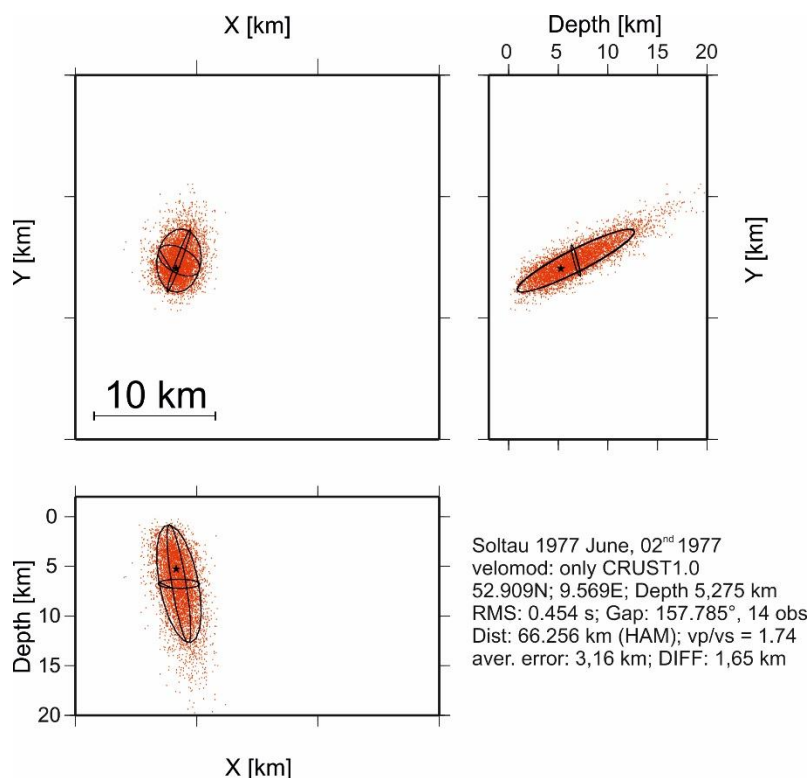


Figure 48. Scatter cloud of the relocated Soltau 1977 earthquake.

My relocation result shows that the epicenter is shifted significantly about 26 km to the west and is located now near the Walsrode hydrocarbon field (Fig. 49). In addition, the International Seismological Centre (ISC) also relocated this event more west, approximately 30 km (International Seismological Center, On-Line Bulletin, United Kingdom, 2012). Based on the results of the ISC, the event is located near the Söhlingen hydrocarbon field, where also the Rotenburg mainshock is assumed. The macroseismic evaluation by Leydecker et al. (1980) shows that the epicenter is located in the east of Soltau (Fig. 49). This analysis is based on information where the earthquake was felt and has a distinct uncertainty due to an unevenly distributed population. In case of the Soltau 1977 event, a macroseismic epicenter might have been placed in a wrong position. Iseismic lines on a map shown in Leydecker et al. (1980) display a greater extent in a westerly direction even as far as Verden (near the Völkersen hydrocarbon field), which fits better to the 3-D solution presented in this study (Fig. 49).

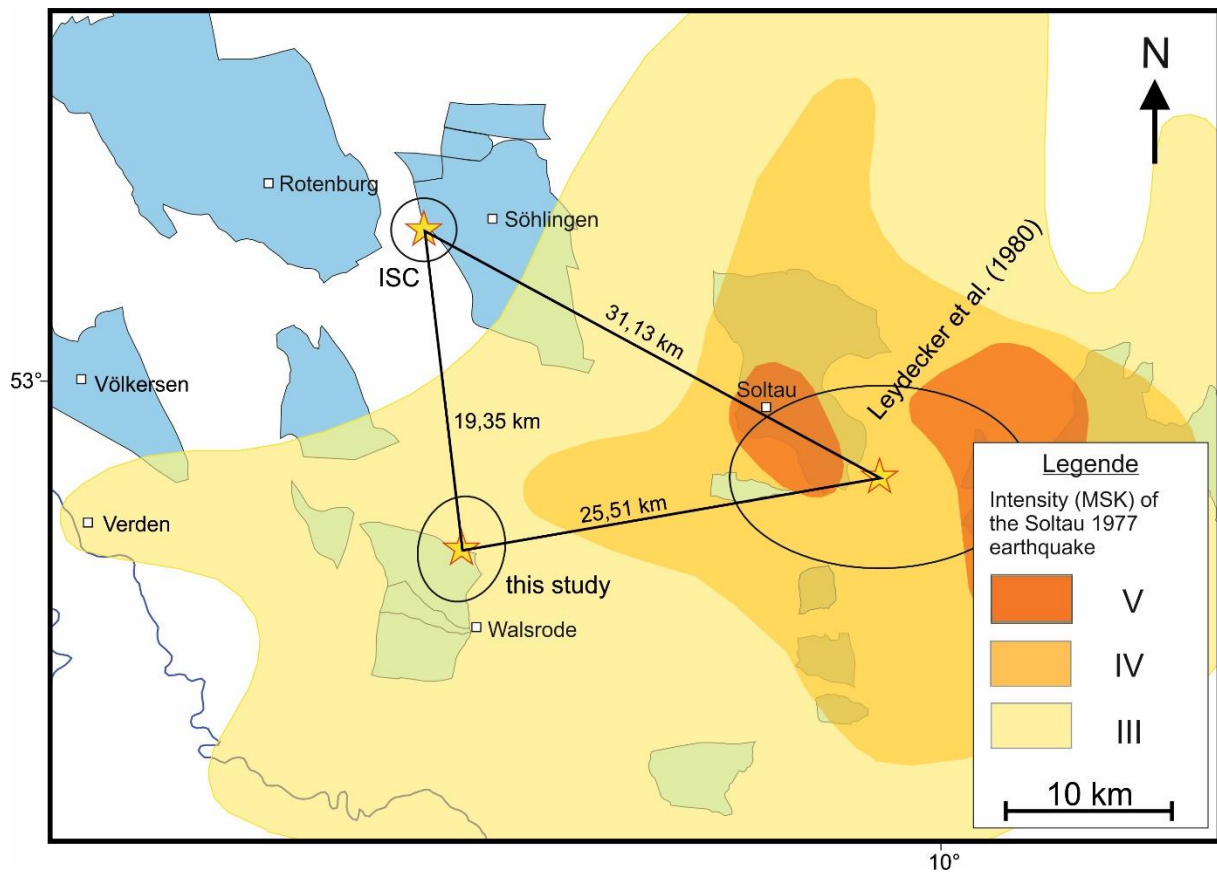


Figure 49. Different locations of the Soltau 1977 event including isoseismic lines of the macroseismic intensity evaluation modified and obtained from Leydecker et al. (1980).

6.3.2 Rotenburg 2004 mainshock

In contrast to the localization results obtained from Dahm et al. (2007), the epicenter location of the Rotenburg mainshock (October, 20th 2004, 06:59:17 UTC) is insignificantly shifted (8 km) to the east. Greater uncertainties of up to 7 km (Dahm et al., 2007) in the longitude direction include both localization results. Both epicenter locations are probably related to normal faults (see chapter 6.5.6) in the subsurface at the western margin of the Söhlingen natural gas field and furthermore, not inside the gas field. The hypocenter solution obtained from Dahm et al., (2007) is in a range between 5 to 7 km whereas the solution in the present study shows a hypocenter depth of about 13 ± 3.2 km. In addition to the determined normal fault focal mechanism for an assumed shallow hypocenter, an oblique reverse kinematic was derived by using FOCMEC and the hypocenter depth of 13 km. The solution for the shallow hypocenter fits very well with the focal mechanism obtained from Dahm et al. (2007). Many waveform inversions and modeling approaches from Dahm et al. (2007) contradict the greater depth determination and the possibility of an oblique reverse fault focal mechanism assessment.

The large magnitude of M_L 4.3 (or e.g. Dahm et al., 2007; M_L 4.5 or M_w 4.4) might be related to the reactivation of a pre-existing major fault below a reservoir. The aspect of serious damage, which can be expected for such a strong earthquake, does not really seem to be considered within these evaluations. As far as known, the amount of damage is close to zero (Leydecker et al., 2006). This could be an indication for a deeper source. According to the hypocenter solution, ranging in depths between 10 to 13 km, impacts on the surface may not be expected. After Leydecker et al. (2006), macroseismic evaluations support my assumption that the Rotenburg'04 event is situated in deeper layers than instrumentally registered by Dahm et al. (2007). In addition, the calculation of synthetic seismograms (see chapter 6.2.2) also supports the determination of a greater hypocenter depth below 10 km. However, it should be kept in mind, that the data quality of this event is almost insufficient for a reliable instrumental approach. Nevertheless, the Rotenburg event seems to be a special case and should be the main subject of further investigations, especially for a new hazard and risk assessment in northern Germany.

6.3.3 Völkersen 2012

Until December 2016, altogether 18 seismic events were registered inside or at the margin of the Völkersen hydrocarbon field. On November the 22nd in 2012, the prominent Völkersen'12 event occurred in the vicinity of this natural gas reservoir about 3 km south of the southern field concession limit. My 3-D relocation result and the location obtained from the report Bischoff et al. (2013) show nearly the same epicentral location (Fig. 50).

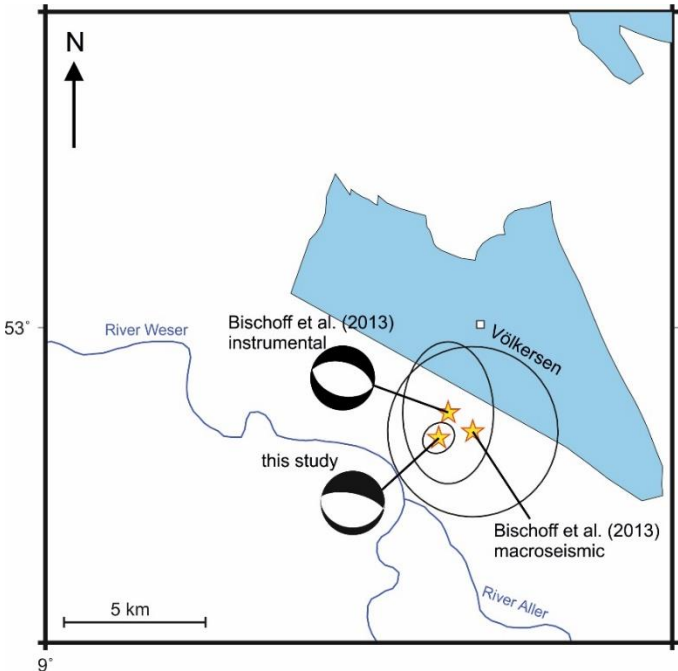


Figure 50. Different localizations and fault plane solutions of the Völkersen'12 event.

Bischoff et al. (2013) applied the localization software Hyposat (Schweitzer, 2001) with 42 observations and a 1-D homogeneous velocity model to determine the hypocenter in depth of 4.9 ± 1.6 km. Thus, the seismic event is situated in depth of the production horizon. My solution, derived by the 3-D relocalization using two-differently scaled *P*-wave-velocity models revealed a greater depth of about 7.51 ± 1.2 km. Both focal depths were reliably located by using at least one station within the critical focal depth (1.5 times of focal depth, Deichmann, 2003; Deichmann et al., 2004). The depth differences of about 2.5 km are potentially due to the different localization techniques and the different velocity models. The latter one served as the main factor to influence a hypocentral shift because near-field stations need well-resolved velocity information of the subsurface. Including lateral heterogeneities, the very small-scaled WEG velocity model represents the subsurface structure in the region of Völkersen in a more detailed and realistic way than a simple 1-D model. Therefore, my 3-D estimated hypocenter depth is potentially more reliable. Nevertheless, both solutions show very small uncertainty domains and gain an event location below the base Zechstein where this event was potentially caused by movements along major Permian basement faults. Moreover, Bischoff et al. (2013) and my determined focal mechanisms show a WNW-ESE trending nearly pure normal fault kinematic (Fig. 50).

6.3.4 Syke 2014

In the last 12 years, only three seismic events were instrumentally registered in the region between the villages Bassum and Syke at the hydrocarbon field Klosterseele/Kirchseele/Ortholz. Two events occurred in 2005 and after nine years of silence the prominent seismic event Syke'14 on May, 01st 2014 was felt by people up to 19 km away from the epicenter (e.g. in Bremen) (Bischoff et al., 2014). The seismological analysis by Bischoff et al. (2014), using a 1-D velocity model and 57 *P* and *S* observations offers only very small epicentral and slightly higher focal depth differences, in contrast to my 3-D relocalization approach with the CRUST1.0 model and 41 *P* observations (Fig. 51). The epicentral shift between my location and the location obtained from Bischoff et al. (2014) is about 2.5 km in a southern direction varying from outside the Klosterseele hydrocarbon field part inside the reservoir.

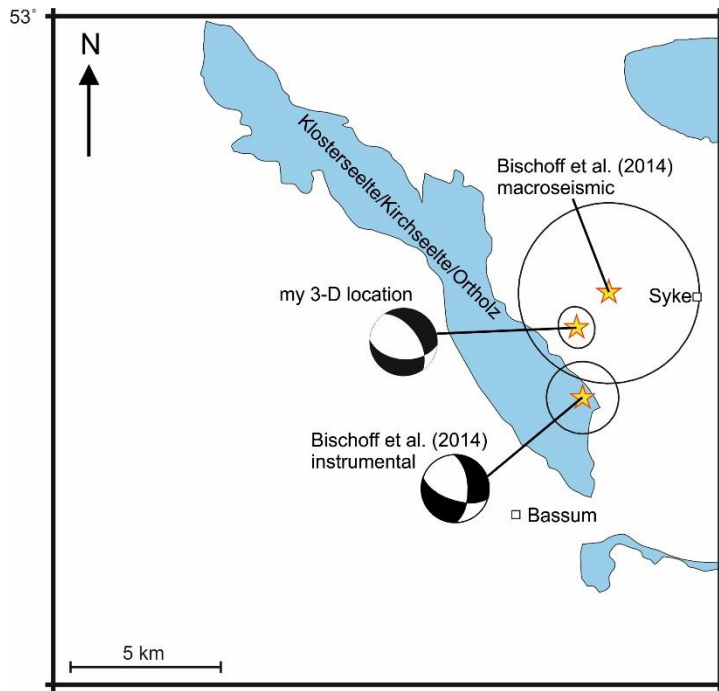


Figure 51. Different locations and fault plane solutions for the Syke'14 event.

The WEG-network station V01EB was the nearest observation used in both evaluations. The distance between station and epicenter is approximately 25 km, which results in greater depth uncertainties up to 3.0 km. Due to this uncertainty the calculation of focal mechanisms should be handled with care because it depends mostly on hypocenter depths and resulting take-off angles, which serve also as input parameter for the calculation of fault plane solutions. Nevertheless, Bischoff et al. (2014) and my determined focal mechanism are nearly the same for an assumed focal depth of 3.5 km. Both show NW-SE trending normal fault focal mechanisms (Fig. 51). Exceeding a local magnitude of $M_L > 3.0$ the Syke'14 event is one of only six earthquakes in the study area with such a “high” magnitude in the region of northern Germany.

6.3.5 Emstek 2014

Until 1993, the region of Cloppenburg and Emstek (a village in the east of Cloppenburg) was seismically quiescent. Historical earthquakes are not known for this area. Since 1993, altogether, 10 earthquakes were instrumentally registered mostly at the margins of the hydrocarbon fields Goldenstedt/Visbek, Hengstlage and Hemmelte. Their magnitude range is between $1.9 < M_L < 3.0$. One of these seismic events was the prominent and strongest event in the Cloppenburg area – the Emstek'14 event with a magnitude of $M_L \sim 3$. Bischoff et al. (2014) located this event within the Goldenstedt/Visbek hydrocarbon field in a depth of 5.1 ± 1.3 km. Figure 52 shows my 3-D location derived by NonLinLoc and one 3-D *P*-wave-velocity

model, including 19 *P* and *S* observations and the location obtained from Bischoff et al. (2014) with 27 *P* and *S* phases inverted with a 1-D regional velocity model using the LocSAT algorithm.

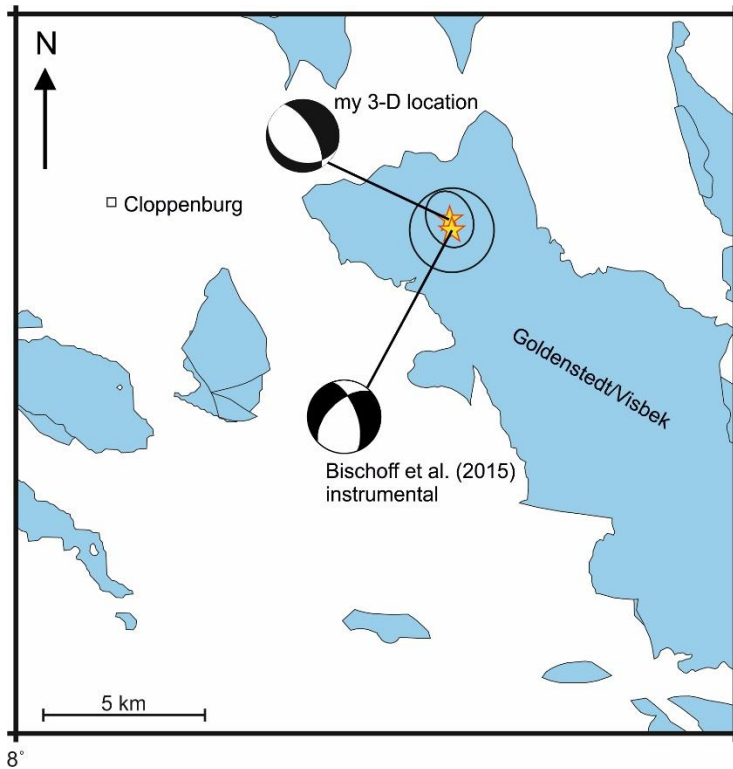


Figure 52. Different seismic event location, fault plane solutions and uncertainty domains of the Emstek'14 event.

Emstek'14 was nearly identically located, concerning epicenter, hypocenter and uncertainty domains, with different input parameters and localization techniques. However, the focal mechanism determined with FOCMEC and unequivocal *P* polarities at non-filtered seismograms indicate normal fault movement but reveal very different strike directions. The focal mechanism derived from Bischoff et al. (2014) trend NNE-SSW, whereas my solution trend NW-SE. The used *P* polarities in both fault plane evaluations were relatively impulsive and clear. Whereby, the velocity models differ significantly and provide very different take-off angles, which serve as input parameter in FOCMEC. These variations in the location of *P* polarities on the lower hemisphere of the focal sphere are potentially responsible for the different strike directions between my fault plane solution and that one of Bischoff et al. (2014). Due to the 3-D subsurface modeling, NW-SE trending normal faults were identified (see chapter 6.5.1) and support the normal fault focal mechanism.

6.4. Geological 3-D subsurface models

3-D subsurface models were constructed for the regions Cloppenburg (two models), Syke, Sulingen/Nienburg, Langwedel/Völkersen, Rotenburg/Söhlingen and Walsrode based on the GTA contour maps of the base Zechstein, the base Lower/Middle Buntsandstein and the base Upper Buntsandstein. For the models, the following color scheme was used: base Zechstein = blue; base Lower or Middle Buntsandstein = light purple; base Upper Buntsandstein = deep purple and in addition, the inferred top Carboniferous = light grey/green. Fault planes were constructed based on the GTA data.

In the following, each constructed model is displayed in an overview picture and two figures with the modeled fault traces. In addition, further subchapters include perspective views of the modeled fault arrays in combination with the relocated hypocenter locations.

6.4.1 Region Cloppenburg

Figure 53 shows an overview of the 3-D subsurface model of the region Cloppenburg. The left corner (red dot) marked the origin at 52.70N Latitude and 8.00E Longitude, which is near the village of Quakenbrück (Fig. 25a). The dimension of the model is about 22 km x 22 km x 3.8 km (LxWxH). The red circle in Figure 53 highlights a modeling artifact, where the Lower Buntsandstein overlaps the Upper Buntsandstein.

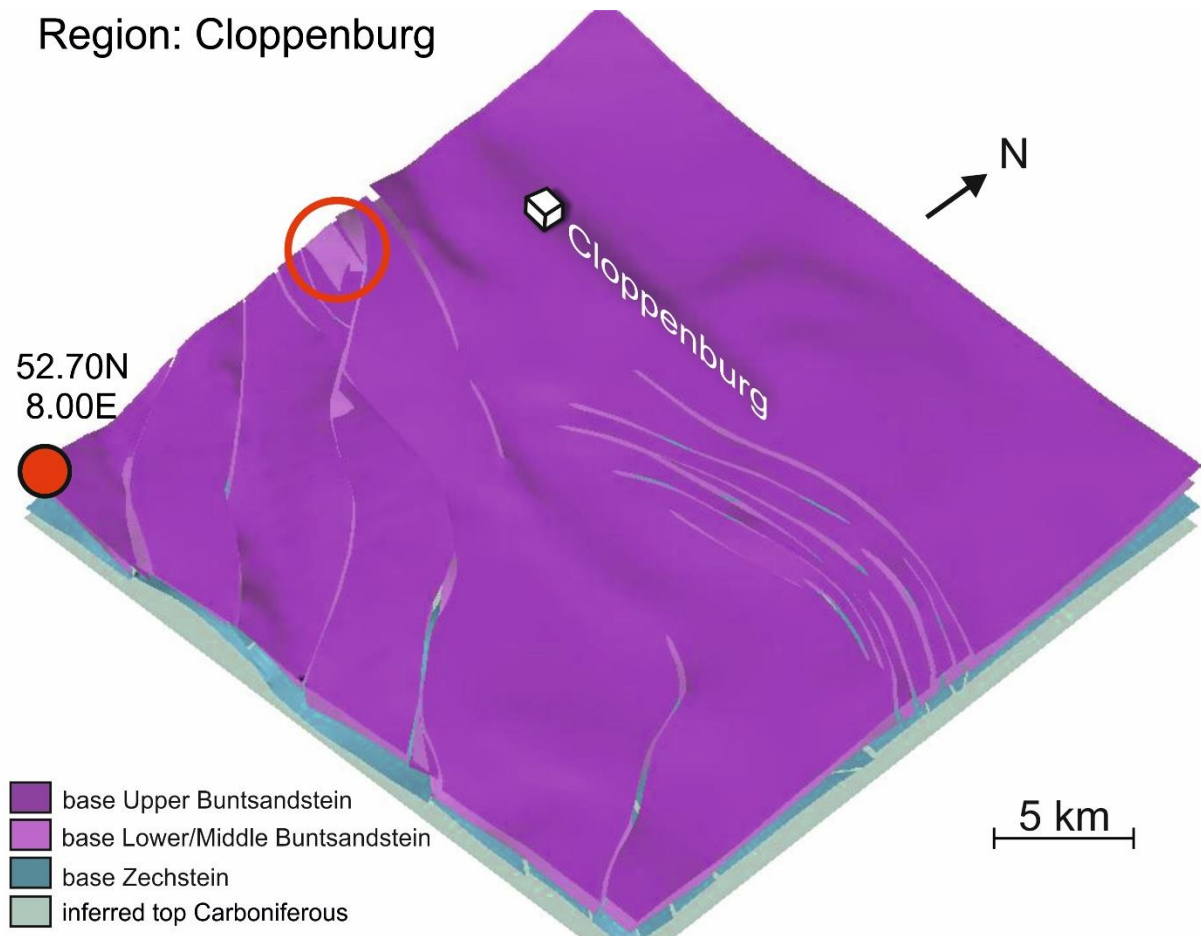


Figure 53. Geological 3-D subsurface model of the region Cloppenburg. The three digitized isocontour line maps of the base Zechstein, the base Lower/Middle Buntsandstein and the base Upper Buntsandstein were modeled. The underlying flat surface defines the inferred top Carboniferous. A detailed description of the structures (tagged by a red circle) is given in the text.

The average depth of the base Zechstein is about 3,900 – 4,500 m, the base Lower Buntsandstein is situated in an average depth of about 3,700 m, whereas the base Upper Buntsandstein is located in depth of about 2,600 – 3,200 m.

There are no salt diapirs developed in this region. Altogether, ten base Zechstein faults were modeled (Figs. 54a and b). The overlying Buntsandstein faults are not be considered because the earthquake hypocenters are clearly deeper than 4 km. The faults in the model

area trend mainly NW-SE and E-W. The dense anastomosing array (classification after van der Pluijm and Marshak, 2004) of NW-SE striking faults in the SW of the area is not relevant because of the absence of seismic events. With one exception, each of the modeled base Zechstein faults are normal faults.

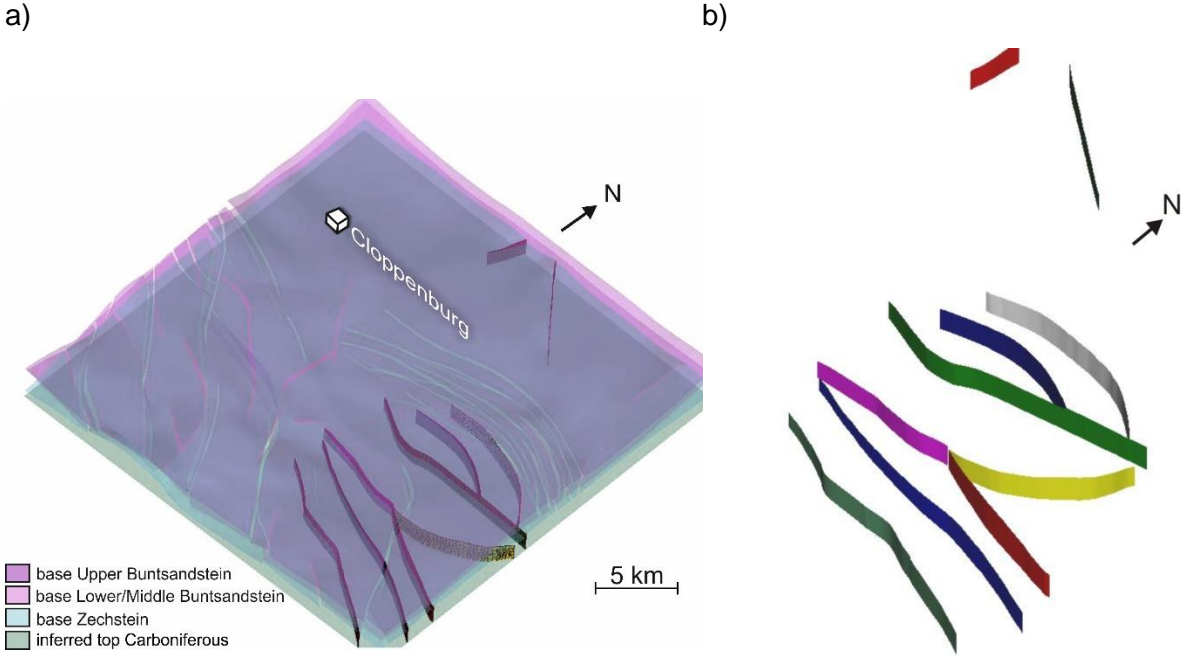


Figure 54. Modeled faults in the region of Cloppenburg. **a)** Inferred fault traces from the base Zechstein down to the top Carboniferous. Modeled layers are color-coded and named within the legend. **b)** 3-D model of the base Zechstein fault array.

6.4.2 Region north of Cloppenburg

Figure 55 shows an overview of the 3-D subsurface model of the region north of Cloppenburg. The SW corner (red dot) marks the origin at 52.90N Latitude and 8.00E Longitude, which is near the village of Varrelbusch (Fig. 25a). The dimension of the model is about 22 km x 22 km x 4.0 km (LxWxH). Artifacts are marked with red circles to show limitations of the GTA or interpolation mistakes by GOCAD©. The distinct light blue feature is a modeled diapir (GTA3D, Blatt C3114, Sagermeer Salzstockumhüllende, LBEG, Hannover, 2013).

Region: North of Cloppenburg

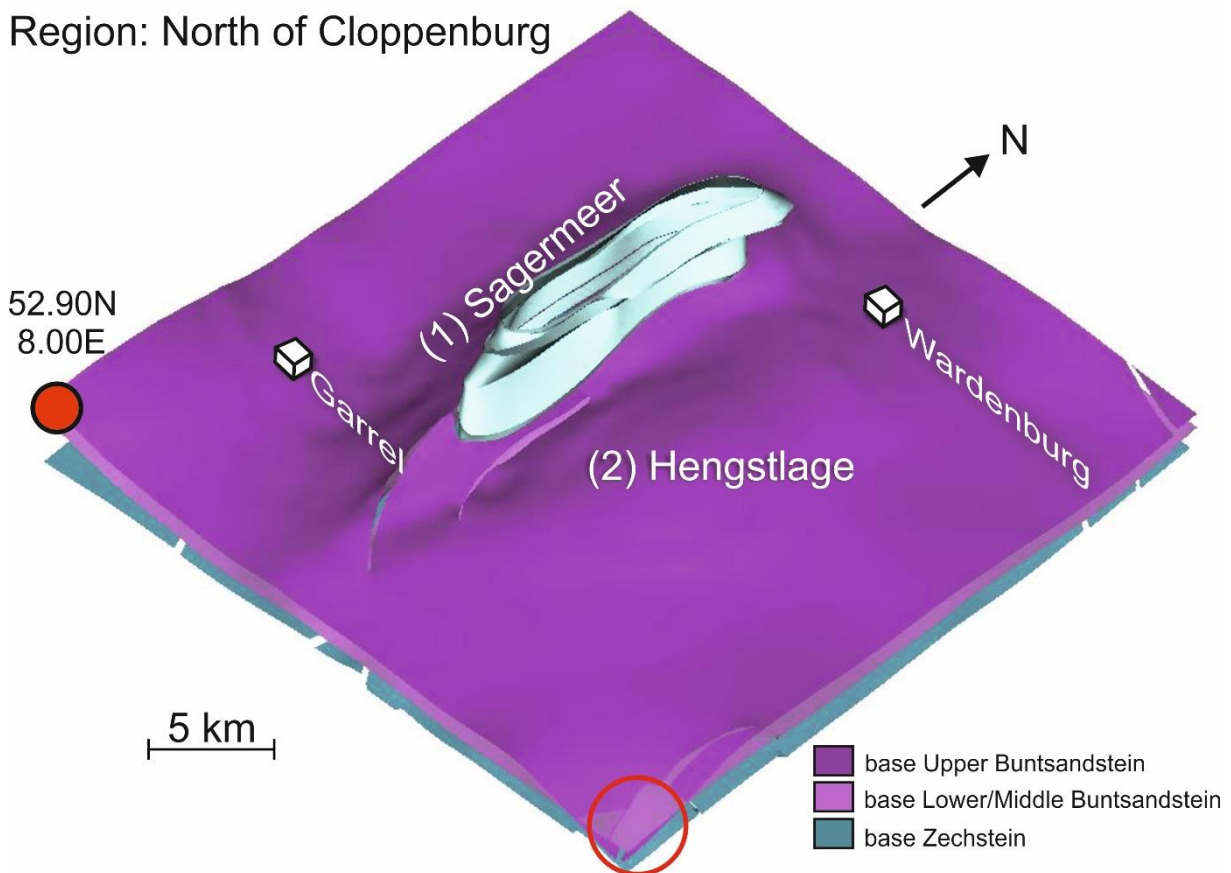


Figure 55. Geological 3-D subsurface model in the north of Cloppenburg. The three digitized isocontour line maps of the base Zechstein, the base Lower/Middle Buntsandstein and the base Upper Buntsandstein were modeled. The white cubes mark villages for the orientation within the model. A detailed description of the structures (tagged by white numbers and red circles) is given in the text.

The average depth of the base Zechstein is about 4,200 m, the base Lower/Middle Buntsandstein is situated in an average depth of about 4,400 m – 2,500 m, whereas the base Upper Buntsandstein is located in depth of about 3,400 m - 2,000 m. The Sagermeer diapir (1, Fig. 55) is the dominating feature within the model area. Close to this salt structure, the Buntsandstein layers are deformed and elevated. The eastern and western flanks are steeply

dipping. Another elevated feature is defined by the Hengstlage salt pillow (2, Fig. 55), which does not pierce the overburden layer.

Close to the salt domes, three base Zechstein faults (the red, yellow and green segment forms one fault) and one Buntsandstein fault (blue) were modeled and displayed in Figures 56a and b. In general, there are only a few Buntsandstein faults within the original data of the GTA. The faults in the model area trend mainly N-S, which is also the strike direction of the dominant salt diapir Sagermeer.

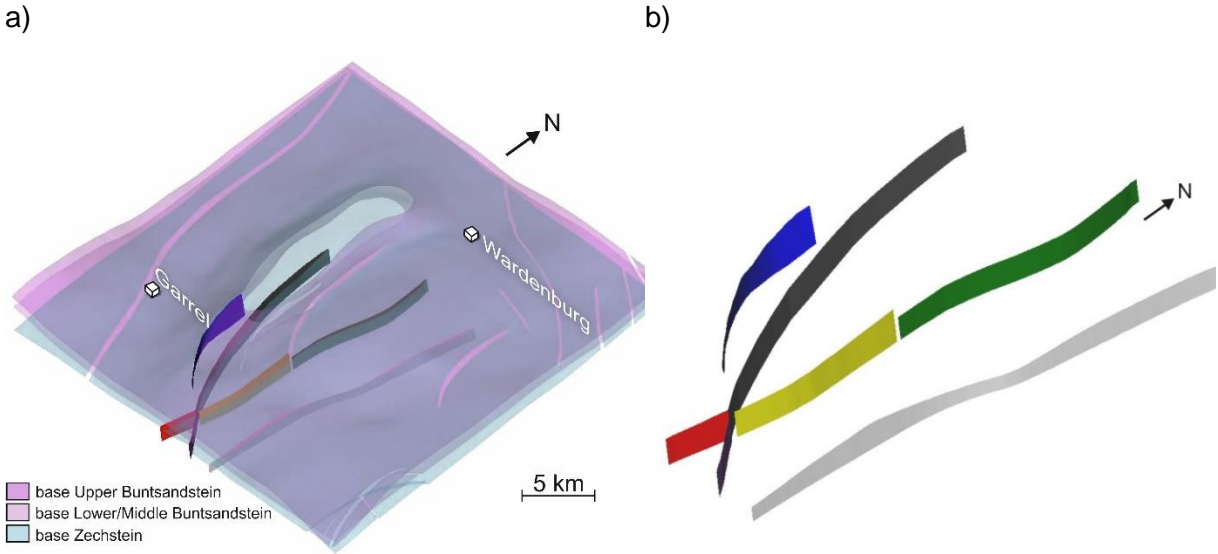


Figure 56. Modeled faults in the region north of Cloppenburg. **a)** 3-D geological model including the base Zechstein, the base Lower/Middle Buntsandstein and the base Upper Buntsandstein. **b)** Display of the three modeled Permian basement fault planes and one Buntsandstein fault (blue).

6.4.3 Region Syke

Figure 57 shows an overview of the geological 3-D subsurface model of the region Syke. The left corner (red dot) marks the origin at 52.80N Latitude and 8.50E Longitude, which is near the village of Goldenstedt (Fig. 25a). The dimension of the model is about 22 km x 22 km x 3.3 km (LxWxH). The three layers, the base Zechstein (blue), the base Lower/Middle Buntsandstein (light purple) and the base Upper Buntsandstein (deep purple) are shown in Figure 57. In addition, the top Carboniferous (light grey/green) forms a supplementary surface in depth of 6,000 m (cf. Lohr et al., 2007) to connect possible base Zechstein faults with deeper layers. The structures 1 to 3 within Figure 57 are less developed salt pillows called Hengsterholz (1), Barrien (2) and Bassum (3).

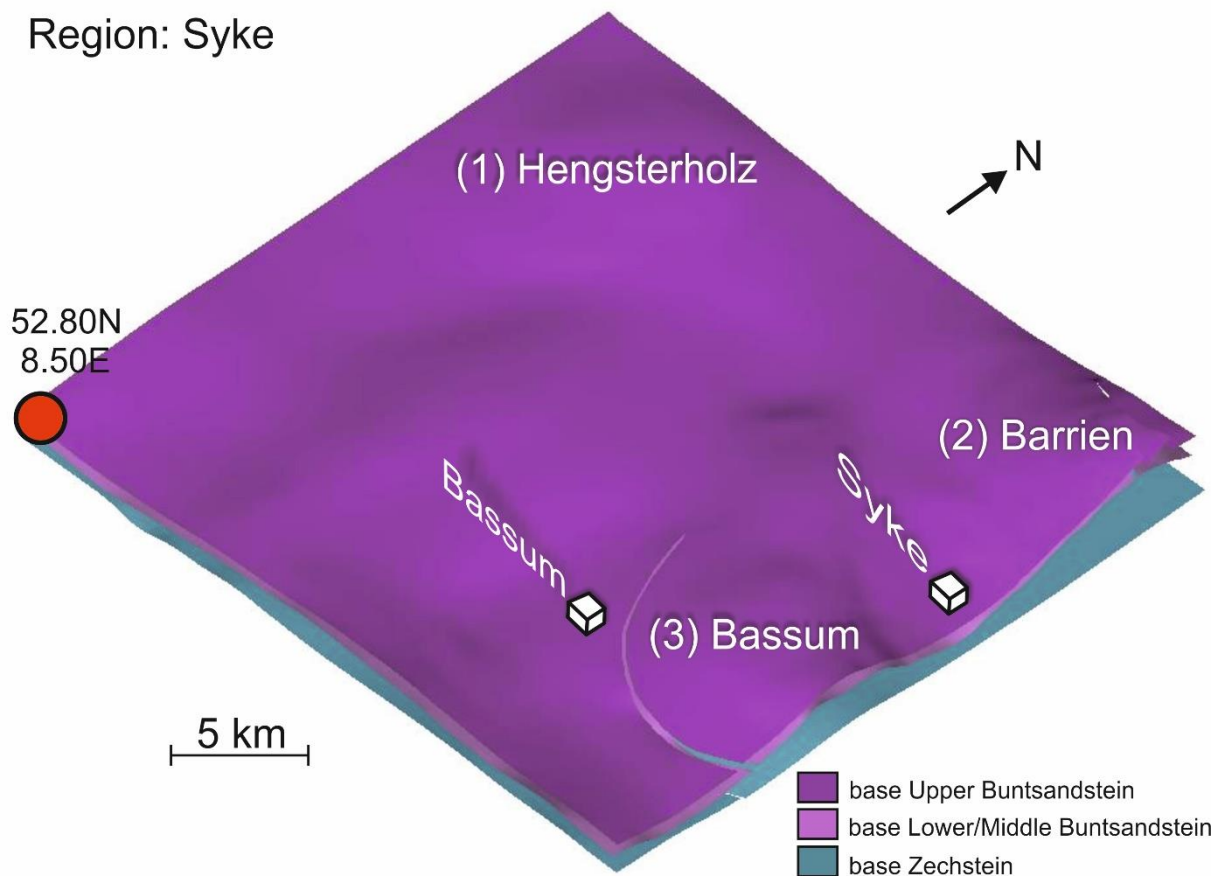


Figure 57. Geological 3-D subsurface model of the region of Syke. The three layers, the base Zechstein, the base Lower or Middle Buntsandstein and the base Upper Buntsandstein are shown. The white cubes mark villages for the orientation within the model. A detailed description of structures (tagged by white numbers) is given in the text.

The base Zechstein, in the region of Syke is situated in an average depth of about 4,400 m. The base Lower/Middle Buntsandstein has an average depth of 3,600 m, whereas the Base Upper Buntsandstein is located in a depth of about 2,900 m.

Based on data of the GTA, the region near Syke shows isolated faults (Figs. 58a and b). Only one Buntsandstein fault and four base Zechstein faults are situated within the area. Figures 58a and b display the base Zechstein (transparent blue), the Lower and Upper Buntsandstein (light purple and dark purple) and the five modeled faults (yellow, black, purple and grey are base Zechstein faults and the red one is a Buntsandstein fault).

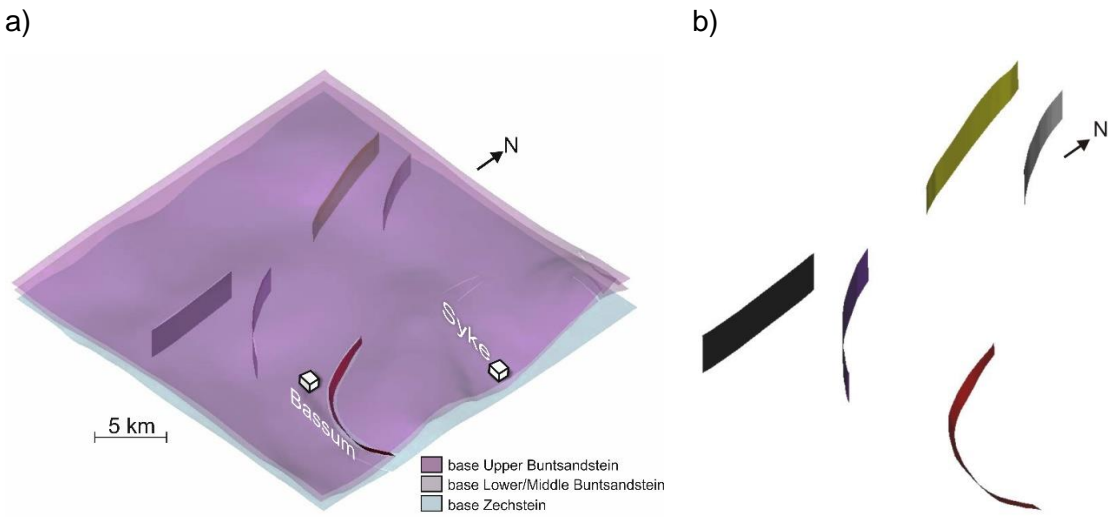


Figure 58. Fault planes within the area of Syke. **a)** 3-D geological model of the region of Syke including the base Zechstein, the base Lower/Middle Buntsandstein and the base Upper Buntsandstein. **b)** 3-D model of the four base Zechstein faults (black, dark purple, dark grey and yellow) and one Buntsandstein fault (red)

The base Zechstein faults trend mainly NNW-SSE or N-S and show normal fault movements, whereas the E-W striking Buntsandstein fault (red) turns in a more northerly direction along the Bassum salt pillow and indicates thrust or reverse fault kinematics (Fig. 58).

6.4.4 Region Sulingen/Nienburg

Figure 59 shows an overview of the 3-D subsurface model of the Sulingen/Nienburg region. The SW corner (red dot) marks the origin at 52.60N Latitude and 8.83E Longitude, which is near the village of Kirchdorf (Fig. 25a). The dimension of the model is about 22 km x 22 km x 3.8 km (LxWxH). Artifacts are marked with red circles to show limitations of the GTA.

Region: Sulingen/Nienburg

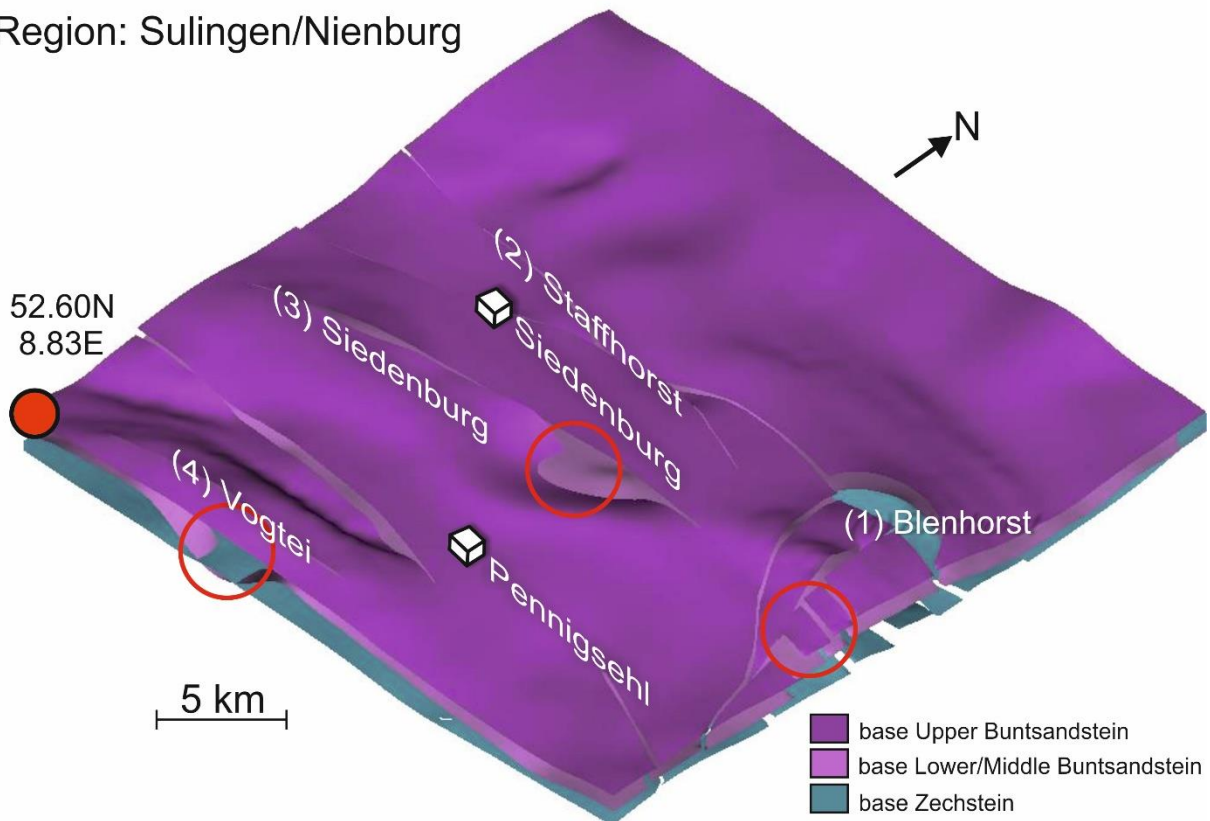


Figure 59. Geological 3-D subsurface model of the region Sulingen/Nienburg. The three digitized isocontour line maps of the base Zechstein, the base Lower/Middle Buntsandstein and the base Upper Buntsandstein were modeled. The white cubes mark villages for the orientation within the model. A detailed description of the structures (tagged by white numbers and red circles) is given in the text.

The average depth of the base Zechstein is about 3,700 m – 4,500 m, the base Lower/Middle Buntsandstein is situated in an average depth of about 3,400 m, whereas the base Upper Buntsandstein is located in depth of about 2,700 m. Four salt structures are developed within the observed region. In the east the Blenhorst diapir is located (1, Fig. 59). The salt structures continue to the west with the E-W trending Staffhorst (2) and Siedenburg (3) salt pillows and walls. The structure 4 within Figure 59 was also caused by salt mobilisation and is called Vogtei (4). The structures 2 – 4 in Figure 59 do not pierce the overburden layer - the Buntsandstein horizons. Red circles mark artifacts within the modeled horizons, resulting from missing or

incorrect depth information within the GTA. The artifacts often occur at the flanks of salt structures.

Ten major faults, comprising four faults (dark blue, red, yellow and dark green) situated within the Buntsandstein units and six Permian basement faults (orange, aqua, purple, black, dark grey and grey) were modeled and displayed in Figures 60a and b. The faults in the model area trend mainly E-W and except one Buntsandstein fault (yellow, thrust fault kinematic), each show normal fault movements. In general, the model area shows a dense fault array. However, the Buntsandstein faults are decoupled from the Zechstein unit.

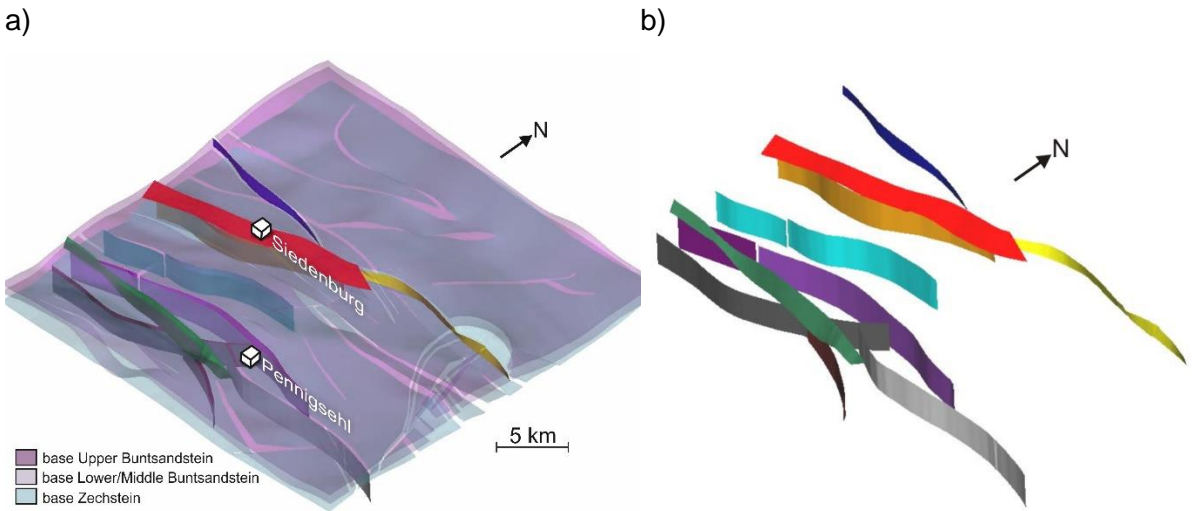


Figure 60. Modeled faults in the region of Sulingen/Nienburg. **a)** 3-D geological model including the base Lower and Upper Buntsandstein (purple) and the base Zechstein (transparent blue). **b)** Display of the six modeled Permian basement fault planes (orange, aqua, purple, black, dark grey and grey) and the four Buntsandstein faults (dark blue, red, yellow, and dark green).

6.4.5 Region Langwedel/Völkersen

Figure 61 shows an overview of the 3-D subsurface model of the region Langwedel/Völkersen. The left corner (red dot) marks the origin at 52.89N Latitude and 8.99E Longitude, which is near the village Schwarne (Fig. 25b). The dimension of the model is about 22 km x 22 km x 4.5 km (LxWxH). The red circle in Figure 61 highlights a modeling artifact, where the Lower Buntsandstein seems to be situated above the Upper Buntsandstein.

Region: Langwedel / Völkersen

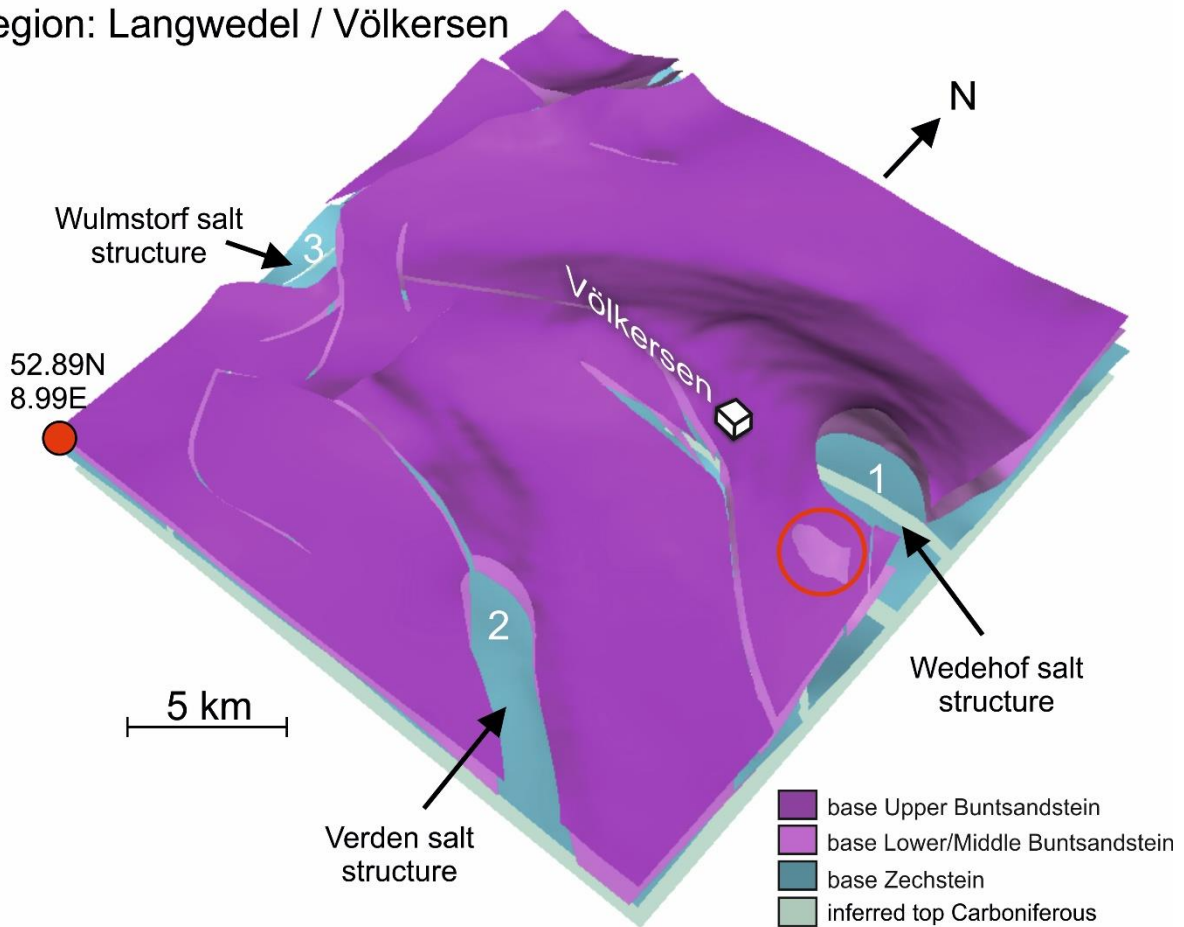


Figure 61. Geological 3-D subsurface model of the region Langwedel/Völkersen. The three digitized isocontour line maps of the base Zechstein (blue), the base Lower/Middle Buntsandstein (light purple) and the base Upper Buntsandstein (deep purple) were modeled. The light grey/green flat surface defines the inferred top Carboniferous. A detailed description of the structures (tagged by black numbers and a red circle), is given in the text.

The average depth of the base Zechstein is about 4,500 – 5,000 m, the base Lower Buntsandstein is situated in an average depth of about 4,400 m, whereas the base Upper Buntsandstein is located in depth of about 3,600 – 4,000 m. Three salt structures are developed in the region, (1) Wedehof in the E, (2) Verden in the SE and (3) Wulmstorf from W to NW (Fig. 61).

Altogether, eight faults were modeled (Figs. 62a and b). The green and the black faults are situated below the base Zechstein. In addition to the salt domes, one of the significant structure in the model is the yellow fault. In general, the faults in the model area trend mainly NW-SE, but four faults (yellow, red, brown and green, Figs. 62a and b) curve into an E-W direction. Only the fault displayed in yellow (Fig. 62) may reach below the base Zechstein. All other faults are developed within the Buntsandstein.

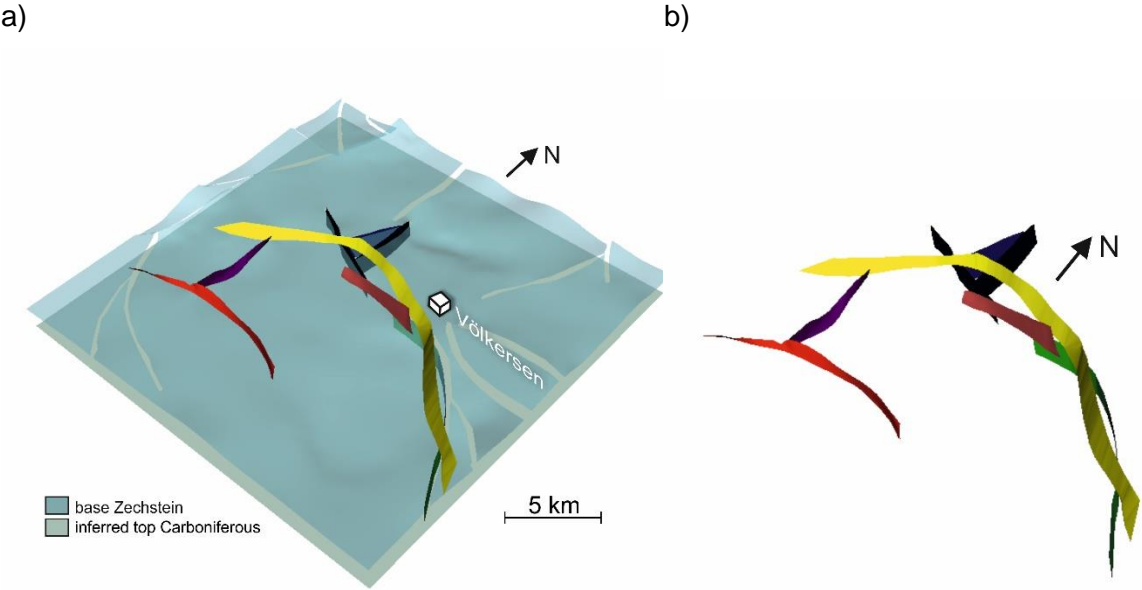


Figure 62. Modeled faults in the region of Langwedel/Völkersen. **a)** Faults between the base Lower and the base Upper Buntsandstein together with the base Zechstein (transparent blue) and inferred fault traces down to the top Carboniferous (light grey/green). **b)** 3-D model of the fault array. The green fault and the black faults are situated below the base Zechstein. All the others are Buntsandstein faults.

6.4.6 Region Rotenburg/Söhlingen

Figure 63 shows an overview of the 3-D subsurface model of the Rotenburg/Söhlingen region. The SW corner (red dot) marks the origin at 53.00N Latitude and 9.33E Longitude, which is near the village Holtum (Fig. 25b). The dimension of the model is about 22 km x 22 km x 5.0 km (LxWxH). Artifacts are marked with red circles to show limitations of the GTA. In addition to that, the digitization of the Upper Buntsandstein had to be performed a second time. Some contour line values within the GTA are unclear at relative steep structures, where the density of contour lines is very high.

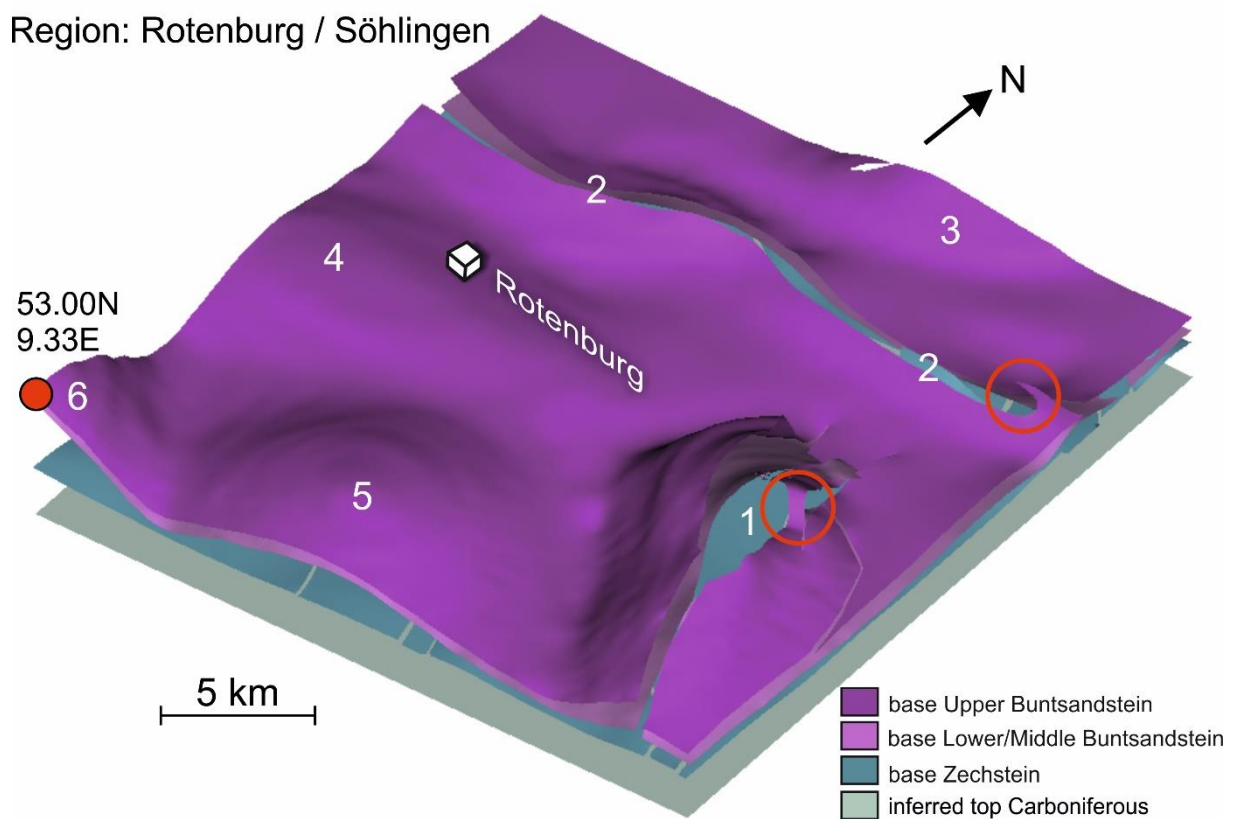


Figure 63. Geological 3-D subsurface model of the region Rotenburg/Söhlingen. The three digitized isocontour line maps of the base Zechstein (blue), the base Lower/Middle Buntsandstein (light purple) and the base Upper Buntsandstein (deep purple) were modeled. The light grey/green surface defines the inferred top Carboniferous. A detailed description of the structures (tagged by white numbers and red circles) is given in the text.

The average depth of the base Zechstein is about 4,600 m, the base Lower or Middle Buntsandstein is situated in an average depth of about 4,300 m, whereas the base Upper Buntsandstein is located in depth of about 4,000 m. Six salt structures are developed within the analysed region. In the SE the Söhlingen diapir is located (1, Fig. 63) and in the north, trending from E to W the Ostervesede, respectively the Scheeßel salt dome (2, Fig. 63). The

structures 3 to 5 within Figure 63 are salt pillows called Stemmen (3), Rotenburg (4) and Lüdingen (5), respectively. Feature 6 (Fig. 63) forms the NE flank of the Wedehof diapir, which is mainly situated within the Langwedel/Völkersen region and described in more detail within chapter 6.4.5. Red circles highlight artifacts within the modeled base Upper Buntsandstein, resulting from missing depth information within the GTA.

The Söhlingen diapir (1, Fig. 63) has steeply dipping flanks. The measured major offset between Lower/Middle and Upper Buntsandstein in this area is about 1,080 m for the southern fault and about 1,680 m for the northern fault, close to the salt dome. Figures 64a and b show the base Zechstein (transparent blue), the inferred top Carboniferous (light grey/green) in depth of 6,000 m, six major fault planes including the modeled fault-to-fault contact and the fault traces (black dots) in this region. The faults in the model area trend mainly NNW-SSE. Because of their length, the green and the aqua fault are the most significant fault structures within the Rotenburg/Söhlingen region.

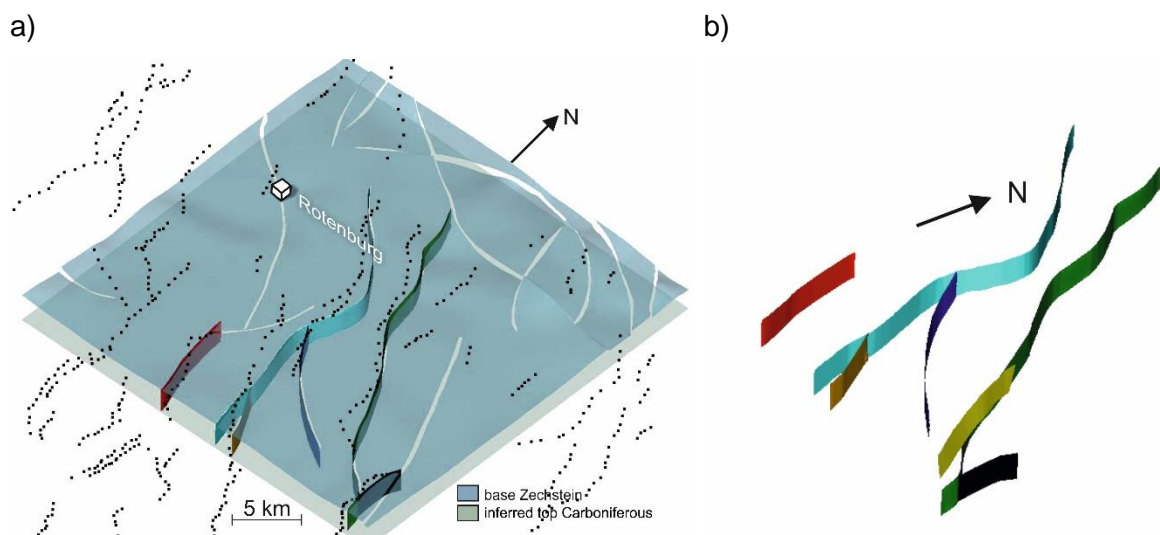


Figure 64. Modeled faults in the region of Rotenburg/Söhlingen. **a)** 3-D geological model including the base Zechstein (transparent blue) and the flat surface of the inferred top Carboniferous. The faults were modeled based on the GTA and on the fault traces (black dots), which are visible in 3-D seismics provided by industry partners. **b)** Display of the six modeled Permian basement fault planes.

The own modeled faults derived from the GTA database and the interpreted 3-D seismic fault data (black dots) are very consistent in the middle of the model, but differs significantly towards the boundary areas. Some fault traces, which are visible in 3-D seismics provided by industry partners don't belong to the database of the GTA.

6.4.7 Region Walsrode

Figure 65 shows an overview of the geological 3-D subsurface model of the region Walsrode. The left corner (red dot) marks the origin at 52.80N Latitude and 9.33E Longitude, which is near the village Dörverden (Fig. 25b). The dimension of the model is about 22 km x 22 km x 4.8 km (LxWxH). The three layers, the base Zechstein (blue), the base Lower/Middle Buntsandstein (light purple) and the base Upper Buntsandstein (deep purple) are shown in Figure 65. In addition, the top Carboniferous (light grey/green) forms a supplementary surface in depth of 6,000 m (cf. Lohr et al., 2007) to connect possible base Zechstein faults with deeper layers. The red circles in Figure 65 marks modeling artifacts, which were generated during the repeated DSI interpolation. Near structure (1), the lack of isocontour lines lead to a misinterpretation of the elevated surface. Furthermore, the control points of the isocontour lines of the base Lower/Middle Buntsandstein near the structure (2) seem to be wrongly connected to the interpolated surface. This forms a kind of uplifted structure, which most likely does not reflect the natural geometry.

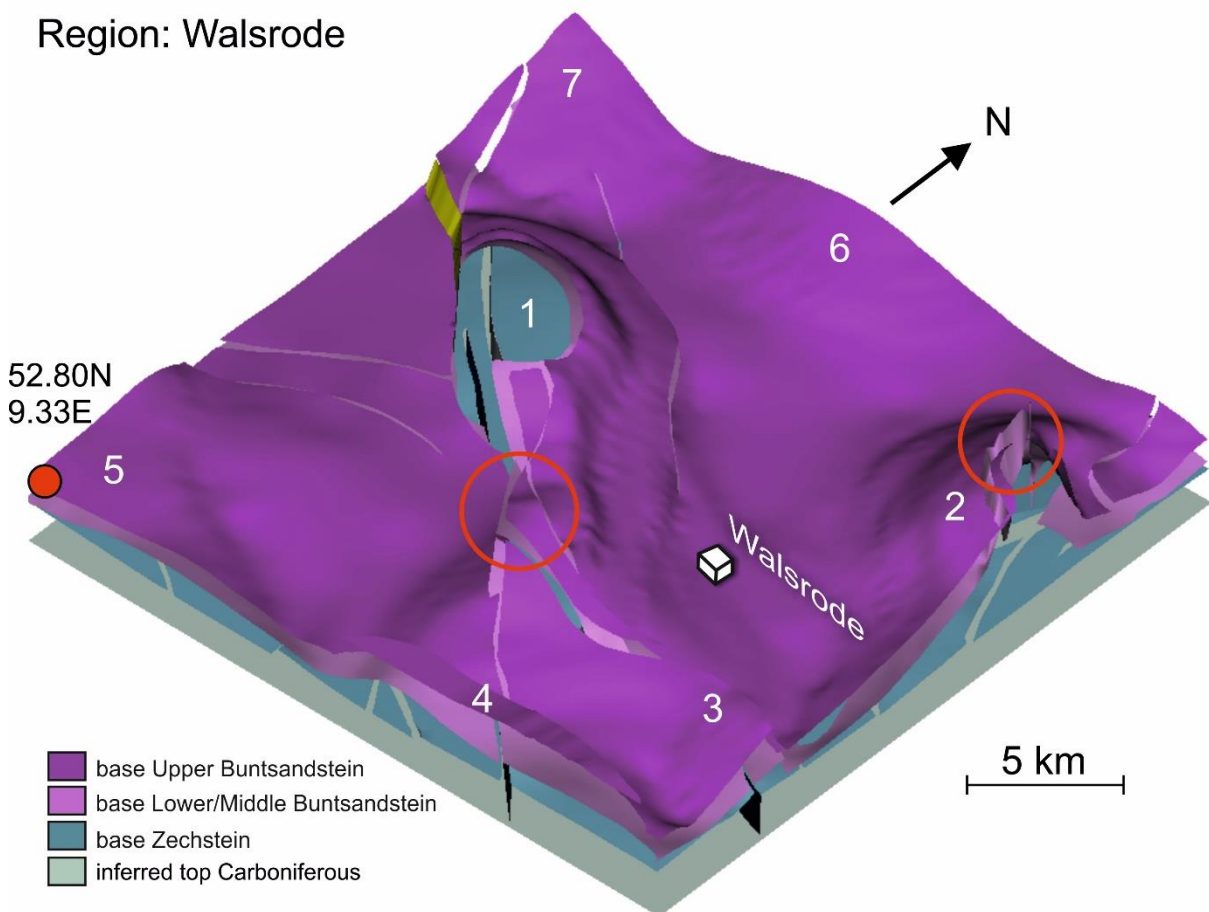


Figure 65. Geological 3-D subsurface model of the region of Walsrode. The three layers, the base Zechstein (blue), the base Lower/Middle Buntsandstein (light purple) and the Base Upper Buntsandstein (deep purple) are shown. The light grey/green surface defines the inferred top Carboniferous for the fault plane modeling between the base Zechstein and deeper layers. A detailed description of structures (tagged by white numbers and red circles) is given in the text.

The base Zechstein, in the region of Walsrode is situated in an average depth of about 4,600 m. The base Lower/Middle Buntsandstein has an average depth of 4,200 m, whereas the Base Upper Buntsandstein is located in a depth of about 3,900 m. Close to salt structures these layers can be elevated. Seven salt structures are developed within the modeled region: Hamwiede (1), Bommelsen (2), Düşhorn (3), Hodenhagen (4), Rethem (5), Lüdingen (6) and Wedehof (7) (Fig. 65).

Seven Permian basement faults and one Buntsandstein fault (yellow) were constructed using the GTA data and the fault traces (black dots), which are visible in 3-D seismics provided by industry partners. Figures 66a and b display the base Zechstein (transparent blue), the inferred top Carboniferous (light grey/green) in a depth of 6,000 m, seven major Permian basement faults (blue, black, dark grey, red, green, purple and aqua) and the fault traces (black dots) of this region.

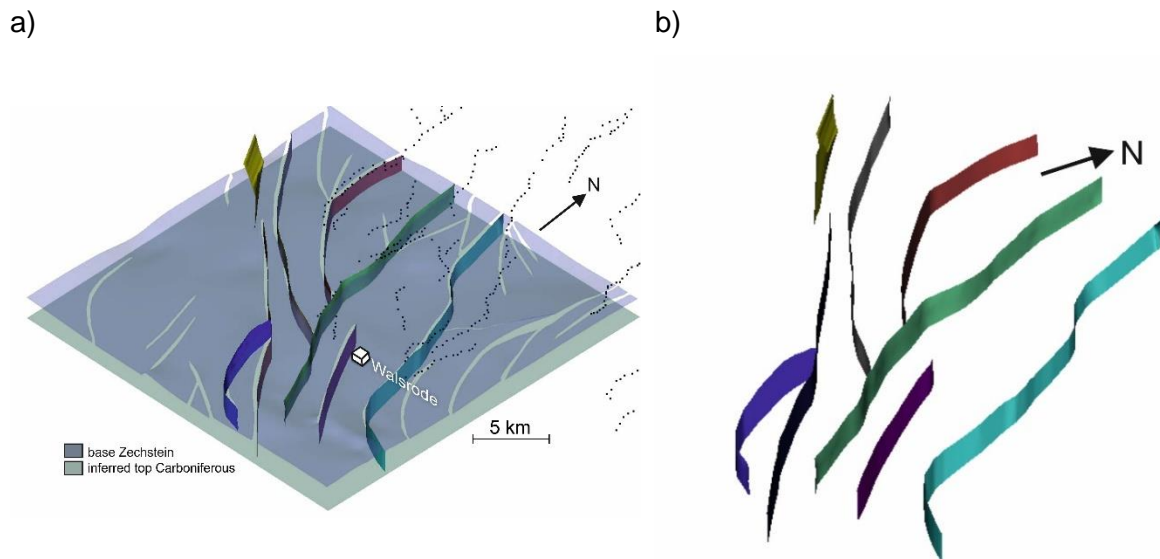


Figure 66. Fault planes within the area of Walsrode. **a)** 3-D geological model in the region of Walsrode including the base Zechstein (transparent blue) and the flat surface of the inferred top Carboniferous. The faults were modeled based on the GTA and on the polygon traces (black dots), which are visible in 3-D seismics provided by industry partners. **b)** 3-D model of the fault array comprising one Buntsandstein fault (yellow) and seven Permian basement faults.

Faults in the Zechstein unit trend NNW-SSE or roughly N-S.

6.4.8 Limitations of the GTA and 3-D models

The modeling workflow (described in chapter 5.6., Figs. 26 and 27) is easy to handle but also slightly time consuming. In case of sparse datasets, it is necessary, that this data is reviewed and validated manually to avoid artifacts and misinterpretations within the model. However, some challenges still occur during the construction of the 3-D subsurface models. Artifacts within the 3-D models may reflect e.g. misinterpretations or mislabeling of isocontour line values, as well as isolated isocontour lines without any connection occur in some model areas. This lack of depth information is characteristic for the vicinity of salt structures, where the interpretation of isocontour line values can be difficult. Furthermore, the missing data below the base Zechstein prevents conclusive observations, or a reliable modeling of fault planes reaching below the Permian basement. Therefore, these structures were only modeled as vertical planes. Most of the relocated hypocenters in the region of Langwedel/Völkersen are located deeper than 6,000 m, below the base Zechstein. Considering the hypocenter depth uncertainties, a connection between these seismic events and the Permian basement faults is difficult, but possible.

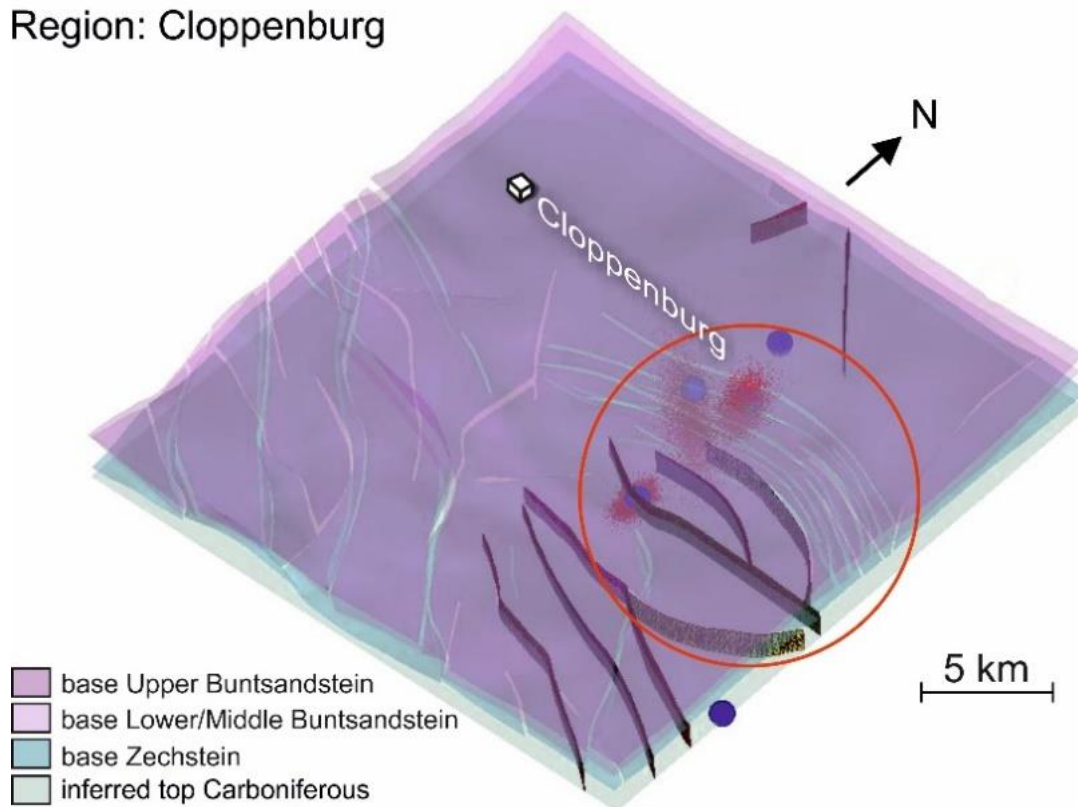
6.5. Hypocenter linking

Each modeled and analysed region is characterized by several salt structures and fault arrays. The strike directions of the modeled faults differ significantly between the several regions – Cloppenburg: mostly NW-SE; north of Cloppenburg: N-S; Syke: mostly N-S, Sulingen/Nienburg: E-W, Langwedel/Völkersen: NW-SE and curve into an E-W direction, Rotenburg/Söhlingen: NNW-SSE and Walsrode: NNW-SSE. To identify seismogenic faults, the relocated hypocenters are implemented into the 3-D geological subsurface models. In addition, the black dots within the models of the regions Rotenburg/Söhlingen (Fig. 64) and Walsrode (Fig. 66) indicate fault traces, which are visible in 3-D seismics provided by industry partners. The combination of the GTA database and the data from DEA establish a robust structural model. In each analysed region most of the hypocenters are located below the base Zechstein (depth > 4,000 m), where data is rare or even not available. The determined focal mechanisms, shown in chapter 6.2.1 are also plotted as rotated “beachballs”.

6.5.1 Cloppenburg

a)

Region: Cloppenburg



b)

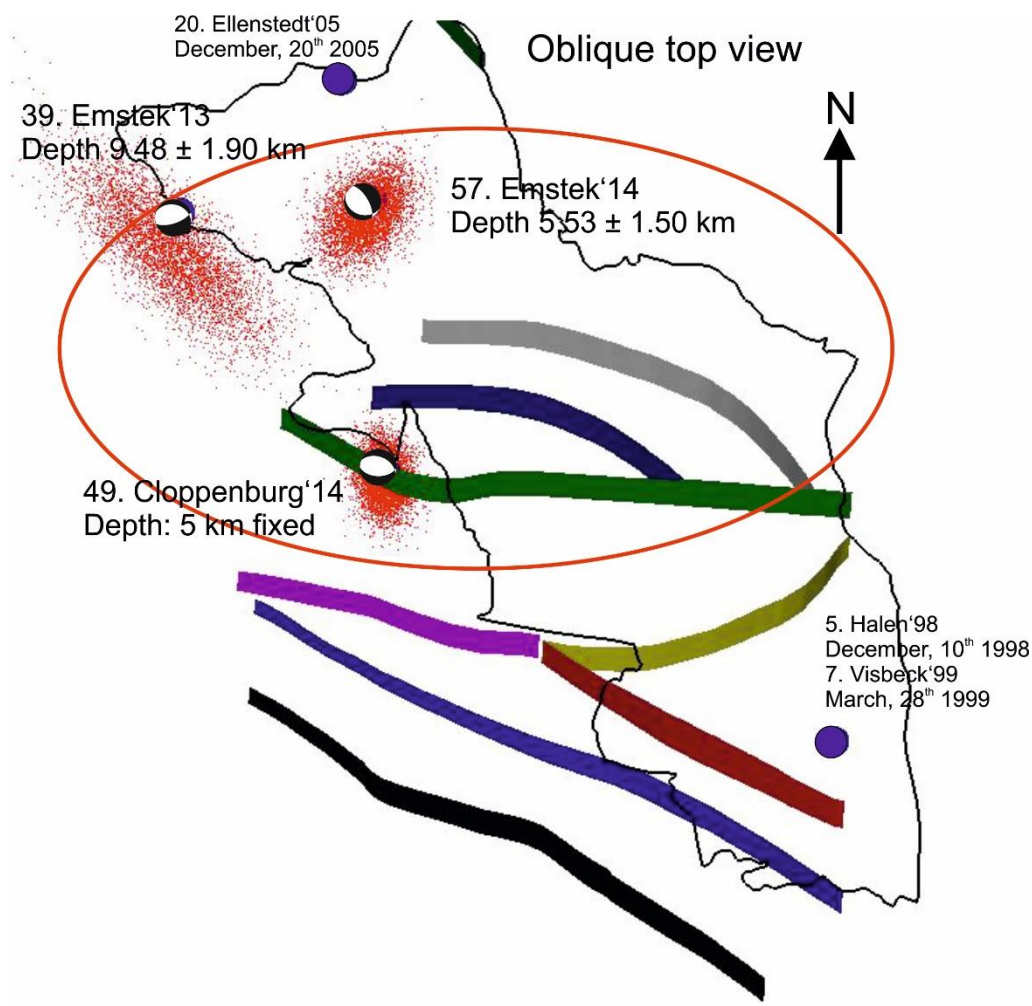


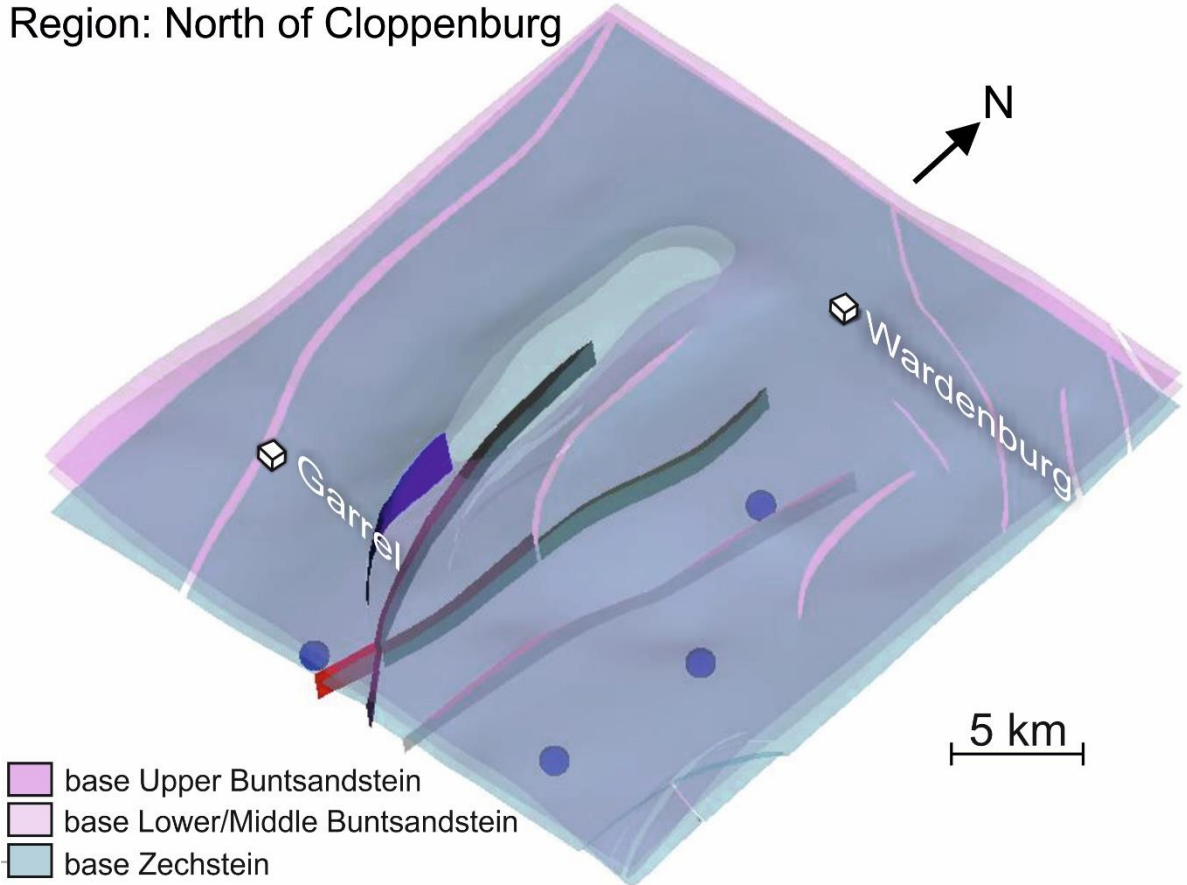
Figure 67. Hypocenter location and fault planes in the region of Cloppenburg. **a)** 3-D geological subsurface model of the base Zechstein (transparent blue), the base Lower/Middle Buntsandstein (transparent light purple), the base Upper Buntsandstein (transparent deep purple). The modeled fault planes and the hypocenter locations are also shown. The light grey/green surface defines the inferred top Carboniferous. **b)** Simple top view of the ten modeled base Zechstein fault planes together with hypocenters (blue spheres and "beachballs"). The red dots define the scatter clouds of the probability density function. The prominent hydrocarbon field Goldenstedt/Visbeck is also shown (black shape). Details are described within the text. In addition, details for the labeled seismic events are given in Appendix IV.

Figures 67a and b show an overview of the region Cloppenburg, with five relocated earthquake hypocenters (blue spheres, "beachballs" and the scatter cloud of the probability density function). Besides the two seismic events, which were fixed in depth of 5 km for the purpose of the 1-D pre-localization, the other (3-D relocated) hypocenters are located in depth between 6 and 9 km. Note the low hypocenter accuracy of Emstek'13 ($9.48 \text{ km} \pm 2.00 \text{ km}$). Figure 67b displays a simple top view of the major faults and the hypocenters including three normal fault focal mechanisms. Bischoff et al. (2015) determined a comparable normal fault focal mechanism for the Emstek event from December 2014. The hypocenter depth and the determined normal fault movements indicate a possible seismogenic active normal fault array in the Permian basement (red ellipse in Figure 67b). In the region of Cloppenburg, four faults are assumed to be seismogenic.

6.5.2 North of Cloppenburg

a)

Region: North of Cloppenburg



b)

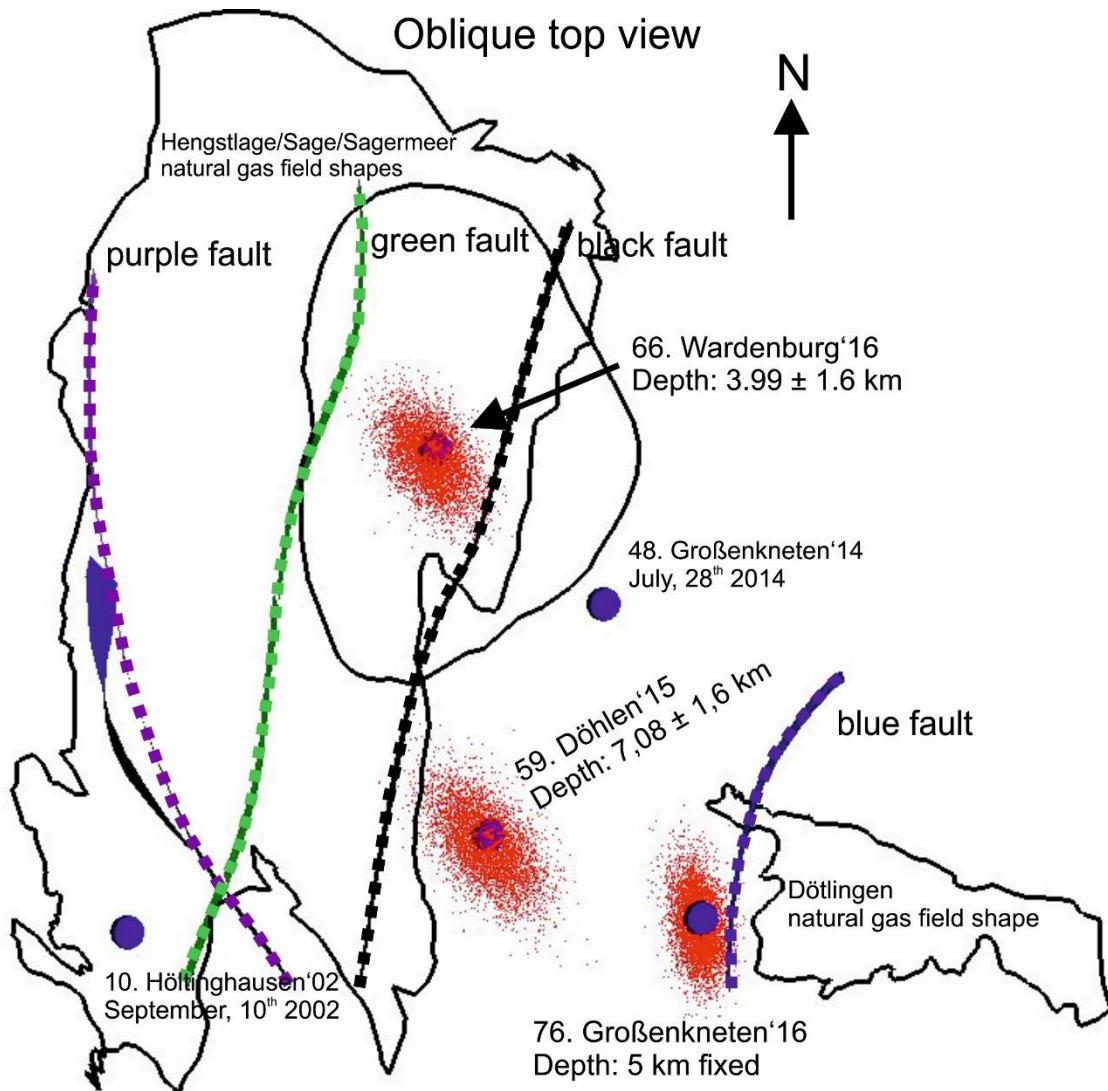
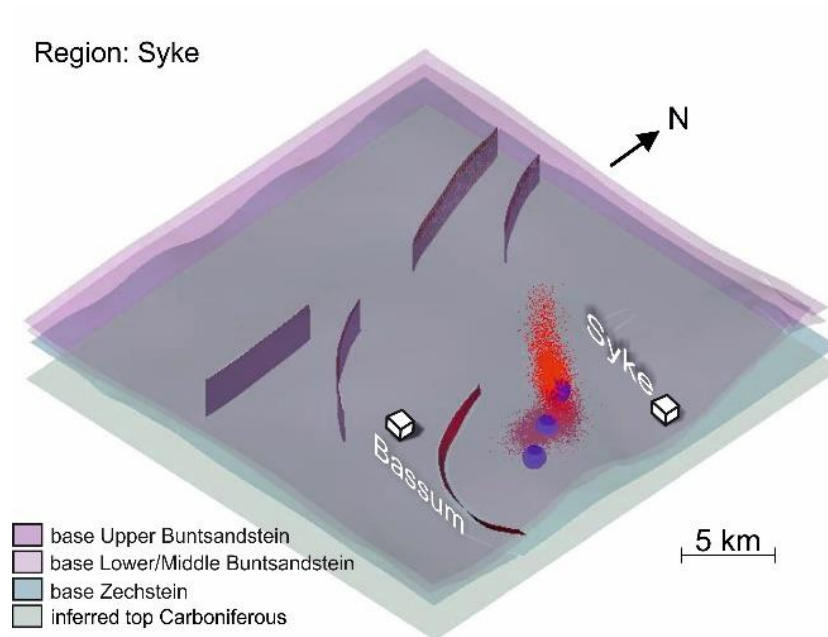


Figure 68. Hypocenter location and fault planes North of Cloppenburg. **a)** 3-D geological subsurface of the base Zechstein (transparent blue), the base Lower/Middle Buntsandstein (transparent light purple), the base Upper Buntsandstein (transparent deep purple) and Permian basement faults in combination with hypocenter locations (blue spheres). **b)** Oblique top view of the four modeled Permian basement fault planes (purple, green, black and blue) and one Buntsandstein fault (dark blue) in connection with hypocenters (blue spheres) as well as the extent of the Hengstlage/Sage/Sagermeer and Dötlingen hydrocarbon fields is shown. Details are described within the text. In addition, details for the labeled seismic events are given in Appendix IV.

Figures 68a and b show perspective views of four Permian basement faults, one Buntsandstein fault as well as five located seismic events (blue spheres) in the region north of Cloppenburg. Each of these five seismic events can be assigned to one of the NNW-SSE or NNE-SSW trending Permian basement normal faults. Most of the hypocenters were relocated in depths between 5 and 7 km. Similar to the region of Cloppenburg, I assume that the earthquakes were mostly caused by Permian basement faults below the base Zechstein based on their hypocenter depths. In the region north of Cloppenburg, four faults (purple, green, black and blue), highlighted by dashed lines, Fig. 68b) are assumed to be seismogenic.

6.5.3 Syke

a)



b)

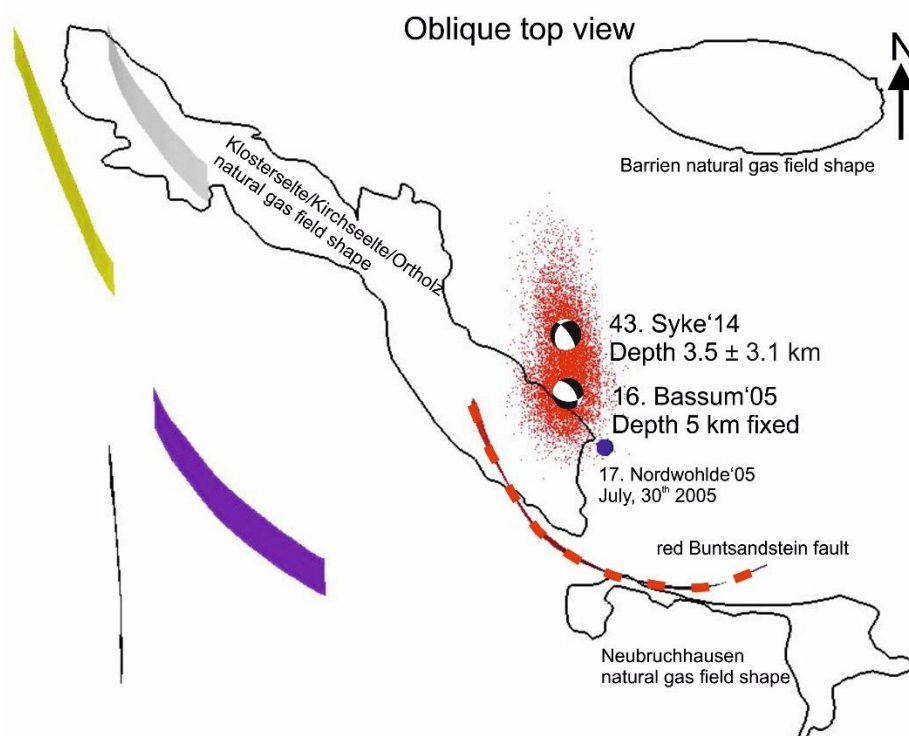


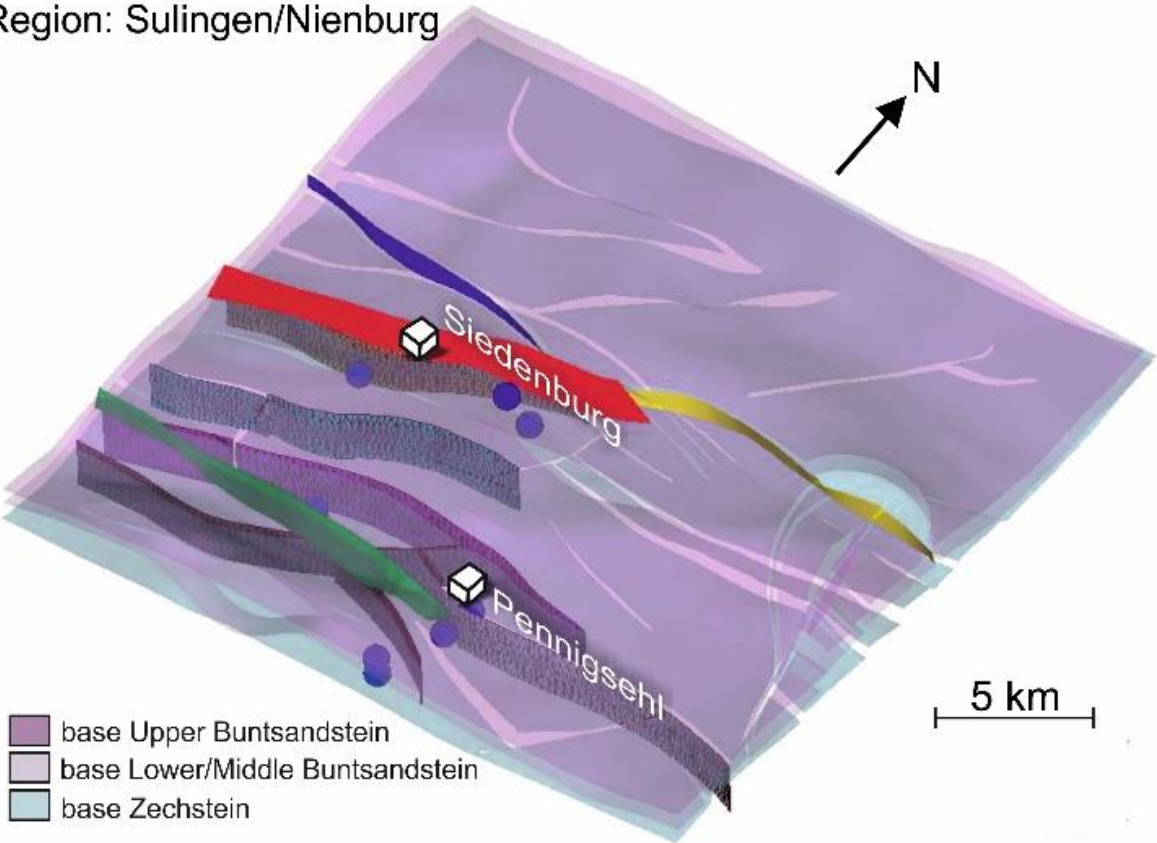
Figure 69. Hypocenter location and fault planes in the region of Syke. **a)** 3-D subsurface model of the base Zechstein (transparent blue), the base Lower/Middle Buntsandstein (transparent light purple), the base Upper Buntsandstein (transparent deep purple) and Permian basement faults in combination with hypocenter locations (blue spheres) are shown. The light grey/green surface defines the inferred top Carboniferous. **b)** Oblique top view of the four modeled Permian basement fault planes and one Buntsandstein fault (red dashed lines) in connection with hypocenters (blue spheres, “beachballs” and the red scatter cloud). The black lines indicate projected natural gas field shapes. More details are described in the text. In addition, details for the labeled seismic events are given in Appendix IV

Figures 69a and b show perspective views with four NNW-SSE trending vertically modeled normal faults below the base Zechstein, one Buntsandstein fault (dark red) as well as three relocated hypocenters (blue spheres). The three events cluster within the region of the Bassum salt pillow (Fig. 57) in the north of a curving Buntsandstein thrust fault (Fig. 69b). The red Buntsandstein fault seems to be the only opportunity to cause earthquakes in this area. This could be the first and only seismogenic active Buntsandstein fault, which is identified in the study area.

6.5.4 Sulingen/Nienburg

a)

Region: Sulingen/Nienburg



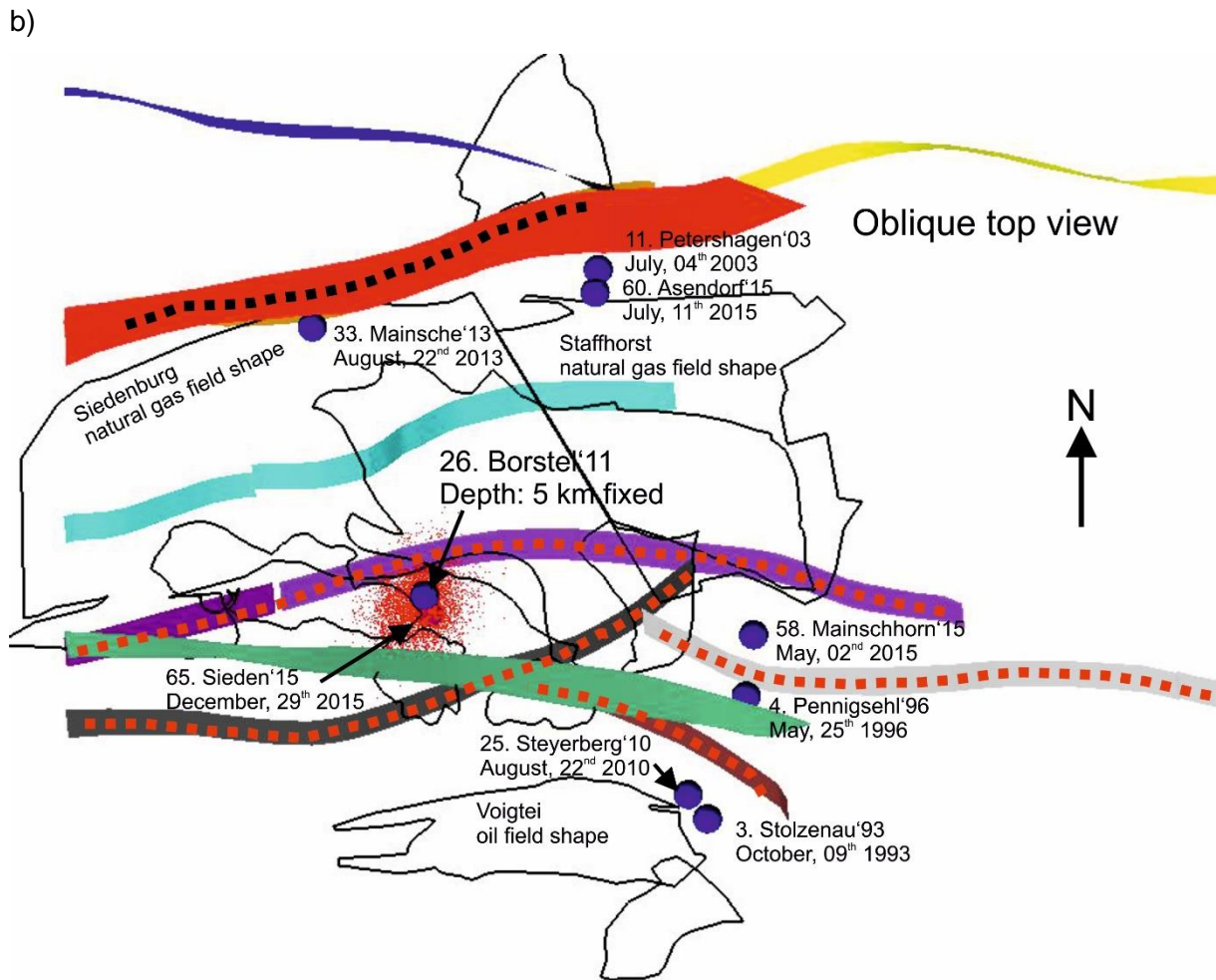
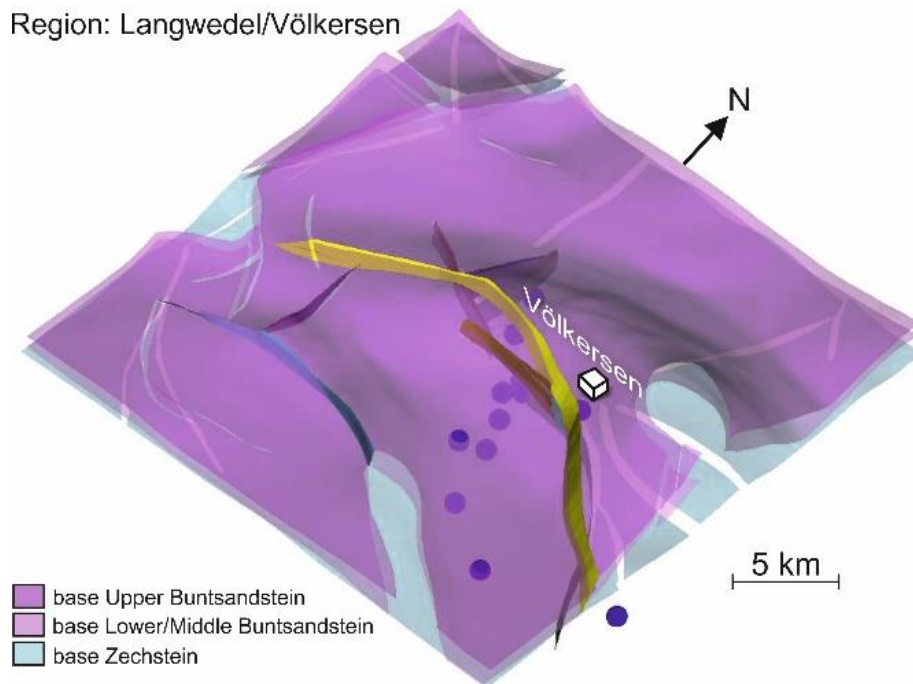


Figure 70. Hypocenter location and fault planes in the region Sulingen/Nienburg. **a)** 3-D geological subsurface model of the base Zechstein (transparent blue), the base Lower/Middle Buntsandstein (transparent light purple), the base Upper Buntsandstein (transparent deep purple) and Permian basement faults in combination with hypocenter locations (blue spheres). **b)** Oblique top view of the six modeled Permian basement fault planes (orange, aqua, purple, black, dark grey and grey) and four Buntsandstein faults (dark blue, red, yellow and dark green) in connection with hypocenters (blue spheres and red scatter cloud). Details are described within the text. In addition, details for the labeled seismic events are given in Appendix IV

Figures 70a and b show perspective views of the Permian basement fault array, four faults in the Buntsandstein layer, as well as nine located seismic events (blue spheres) in the region of Sulingen/Nienburg. Each of these nine seismic events can be assigned to the roughly E-W trending normal faults. The unambiguous allocation of one seismic event to one seismogenic fault is difficult because of greater relocalization uncertainties. However, I assume that the earthquakes were mostly caused by these Permian basement faults based on their hypocenter depth below the base Zechstein. Five possible seismogenic active faults are marked by red and black dashed lines in Figure 70b.

6.5.5 Langwedel/Völkersen

a)



b)

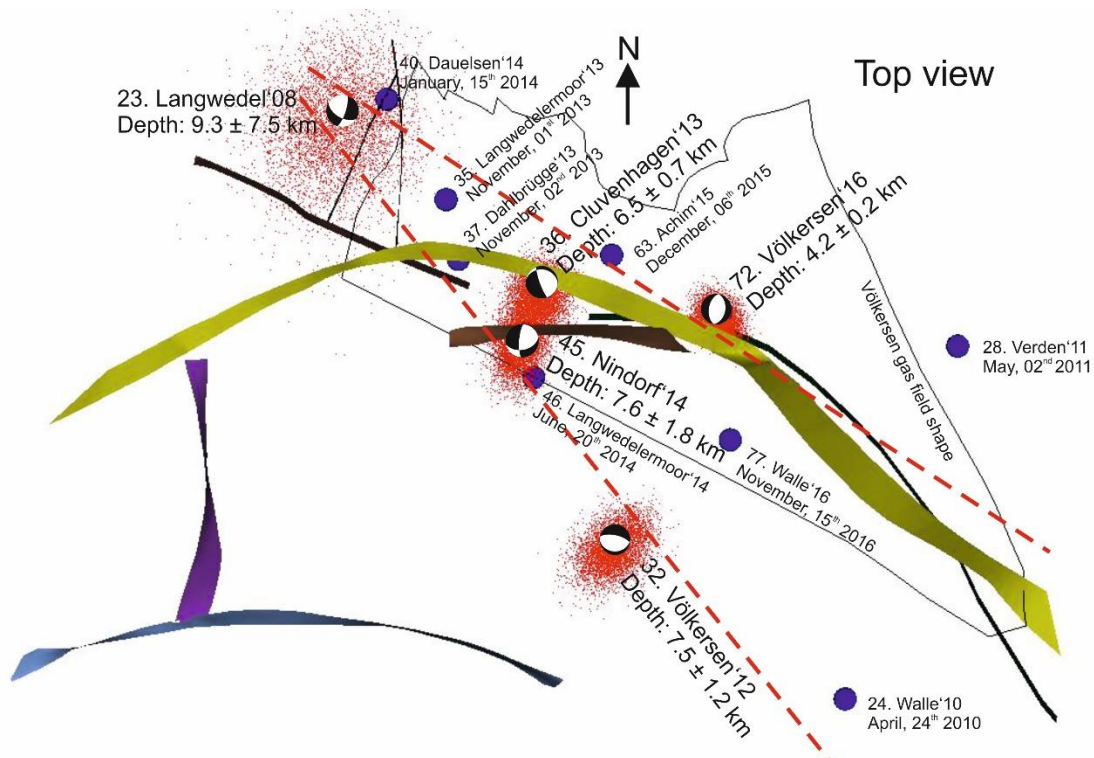


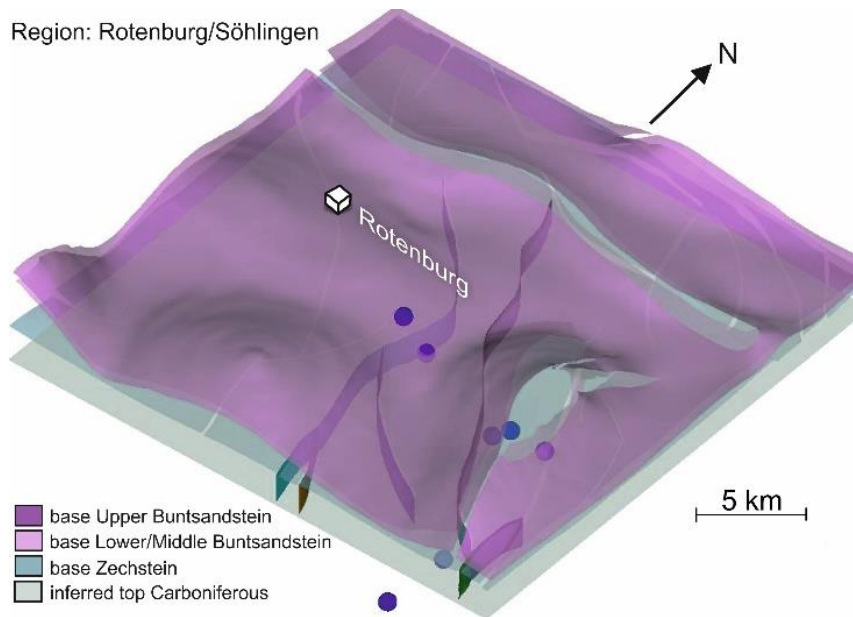
Figure 71. Hypocenter location and fault planes in the region of Langwedel/Völkersen. **a)** 3-D geological subsurface model of the base Zechstein (transparent blue), the base Lower/Middle Buntsandstein (transparent light purple), the base Upper Buntsandstein (transparent deep purple). The modeled fault planes and the hypocenter locations are also shown. The light grey/green surface defines the inferred top Carboniferous. **b)** Top view on the eight modeled fault planes together with hypocenters (blue spheres and “beachballs”) in the region of the Völkersen natural gas field (black shape). Details are described within the text. In addition, details for the labeled seismic events are given in Appendix IV.

Figures 71a and b show an overview of the region Langwedel/Völkersen, with 12 relocated earthquake hypocenters (blue spheres and “beachballs”). In addition to two seismic events, which were fixed in depth of 5 km for the purpose of the 1-D pre-localization, further (3-D relocated) hypocenters are located in depth between 6 and 9 km. Figure 71b displays a simple top view of the major faults (Buntsandstein faults (yellow, purple, blue and brown) and Permian basement faults (black and green)) and hypocenters including five normal fault focal mechanisms. Bischoff et al. (2013) determined a similar normal fault focal mechanism for the Völkersen’12 event (November, 22nd 2012).

The earthquake hypocenters cluster along two theoretical lines (red dashed lines in Figure 71b), trending NW-SE and roughly NNW-SSE. A potential relationship between the hypocenters and modeled faults is difficult to estimate. However, the earthquakes are potentially related to the green and black faults (Fig. 71b), which are located in depth below the base Zechstein. Three events in the south of the green fault (along the southern red dashed line) are located in an area where data about faults lack. There are two potential explanations for the mismatch of faults and hypocenters: (1) relocation uncertainties and/or (2) limited fault data. However, based on the relocated hypocenter depths of more than 6 km, I assume that the earthquakes in this region were mostly caused by Permian basement faults below the base Zechstein. In the region Langwedel/Völkersen, four faults (3x black near the event Langwedel’08 and green) are assumed to be seismogenic.

6.5.6 Rotenburg/Söhlingen

a)



b)

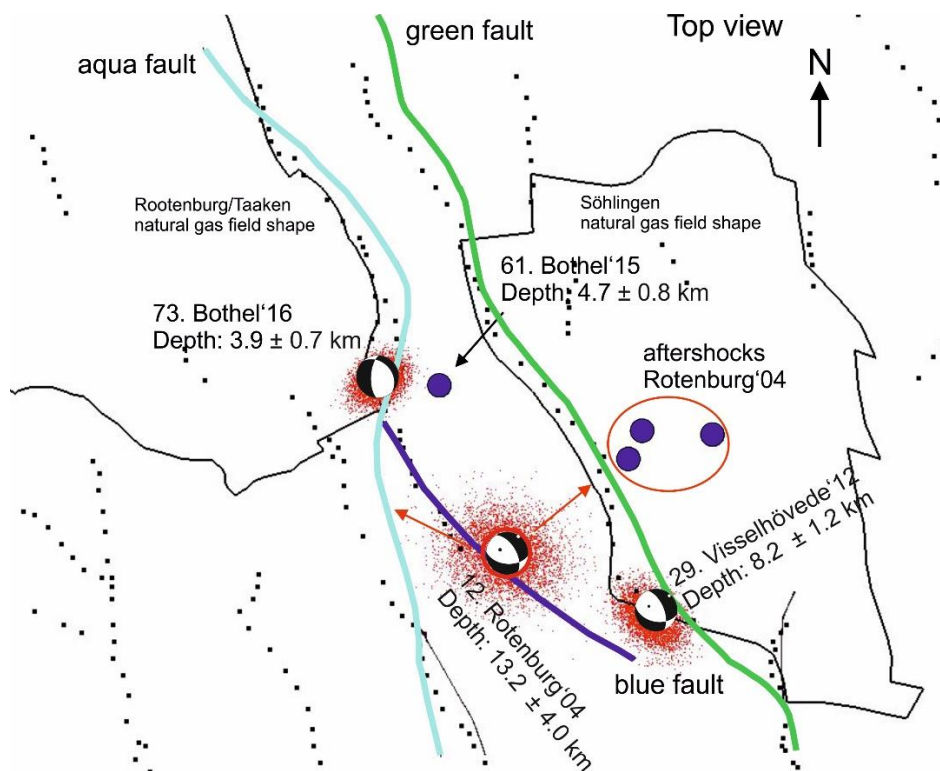


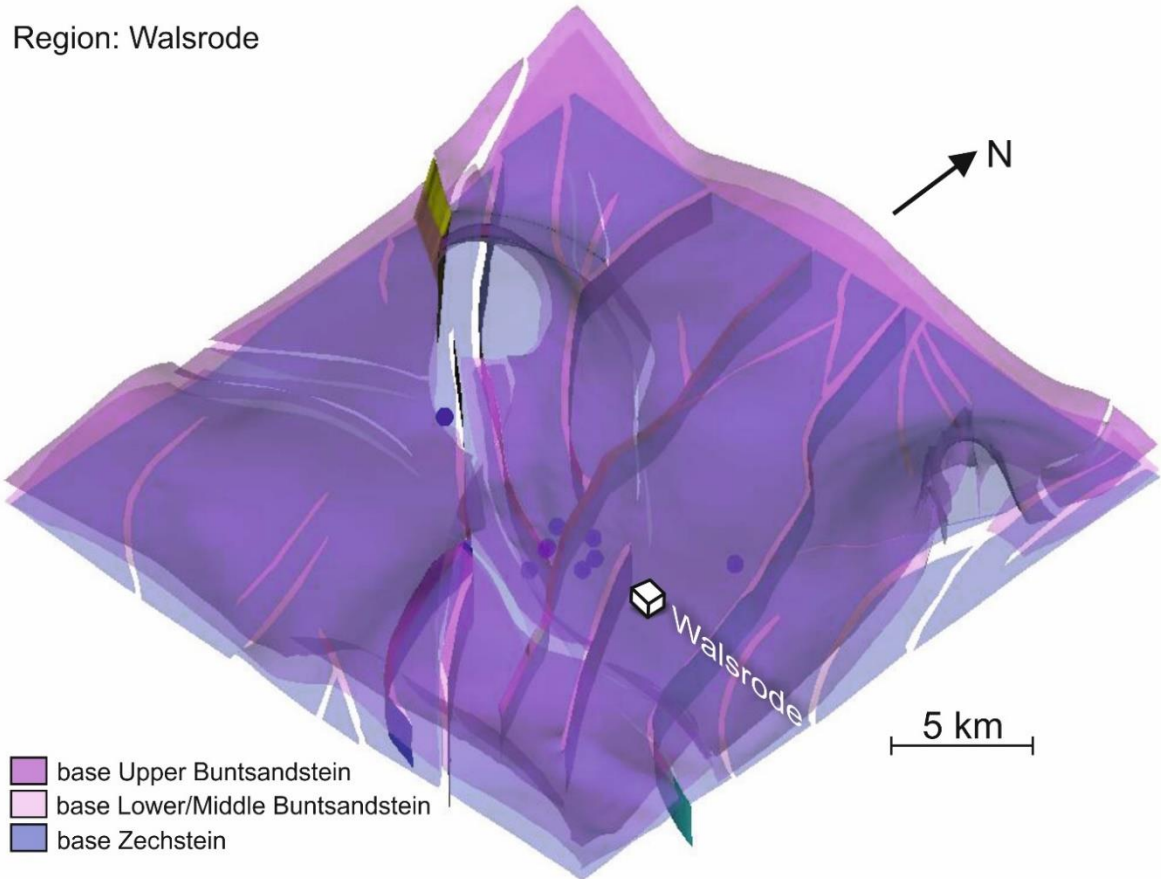
Figure 72. Hypocenter location and fault planes in the region of Rotenburg/Söhlingen. **a)** 3-D geological subsurface of the base Zechstein (transparent blue), the base Lower/Middle Buntsandstein (transparent light purple), the base Upper Buntsandstein (transparent deep purple) and Permian basement faults in combination with hypocenter locations (blue spheres). The light grey/green surface defines the inferred top Carboniferous. **b)** Top view of the six modeled Permian basement fault planes in connection with hypocenters (blue spheres, “beachballs” and related red scatter clouds). The black dashed lines indicate fault traces, which are visible in 3-D seismics provided by industry partners. The black lines highlight projected natural gas field shapes. Details are described within the text. In addition, details for the labeled seismic events are given in Appendix IV.

Figures 72a and b show perspective views of the Permian basement faults as well as six relocated seismic events (blue spheres and three “beachballs”) in the region of Rotenburg/Söhlingen. Each of these six seismic events can be assigned to one of the NNW-SSE trending normal faults. The mainshock of Rotenburg in 2004 ($M_L = 4.3$, highlighted by a red circle in Figure 72b), the strongest seismic event ever recorded in NW Germany, and the seismic event Visselhövede in 2012 ($M_L = 2.9$) were plotted with their determined focal mechanism (chapter 6.2.1). Both show a similar NW-SE trend and a normal faulting focal mechanism. Dahm et al. (2007) determined nearly the same focal mechanism for the Rotenburg mainshock. The relocalization of the hypocenter provides a depth of 13 km. Due to the higher depth and horizontal uncertainties, the Rotenburg mainshock (red arrows in Figure 72b) could be assigned to the green, blue or aqua base Zechstein fault. Similar to the region of Langwedel/Völkersen, I assume that the earthquakes were mostly caused by Permian basement faults below the base Zechstein. In the region Rotenburg/Söhlingen, three faults (green, blue and aqua in Figure 72b) are assumed to be seismogenic.

6.5.7 Walsrode

a)

Region: Walsrode



b)

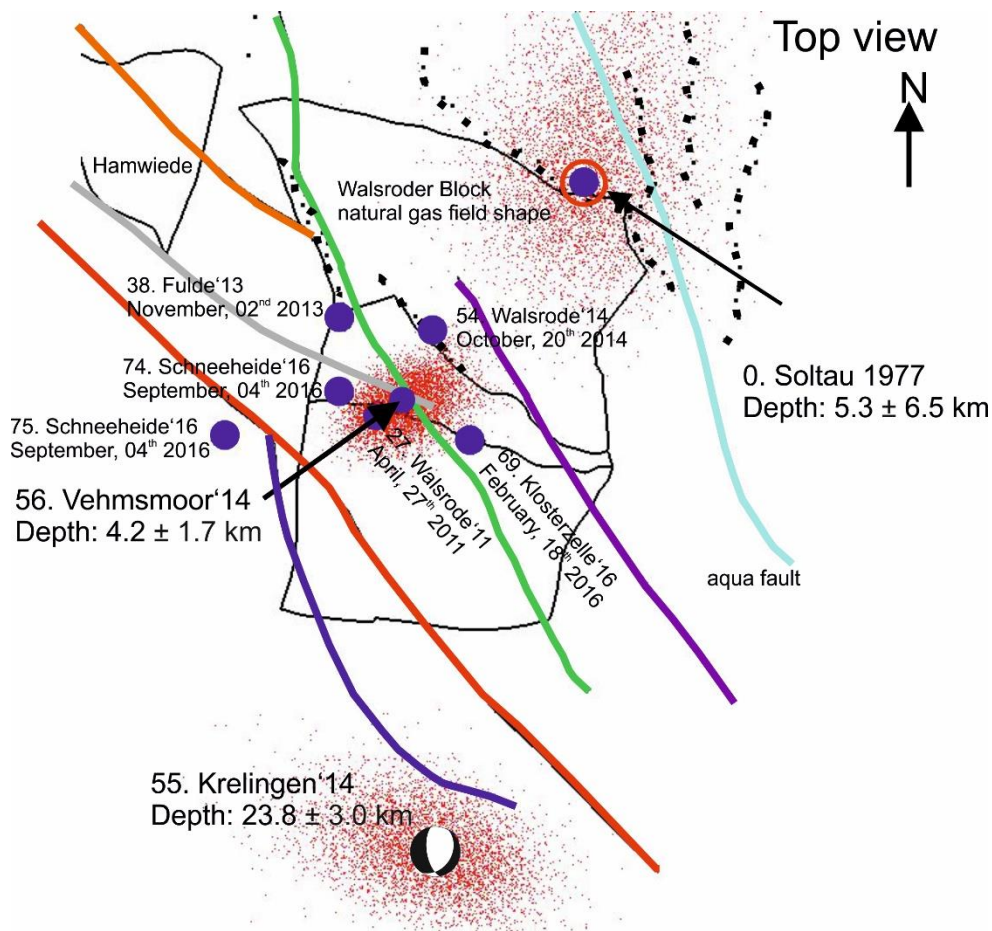


Figure 73. Hypocenter location and fault planes in the region of Walsrode. **a)** 3-D subsurface model of the base Zechstein (transparent blue), the base Lower/Middle Buntsandstein (transparent light purple), the base Upper Buntsandstein (transparent deep purple) and Permian basement faults in combination with hypocenter locations (blue spheres) are shown. **b)** Top view of the seven modeled Permian basement fault planes in connection with hypocenters (blue spheres, “beachball” and related red scatter cloud). The black dashed lines indicate fault traces, which are visible in 3-D seismics provided by industry partners. Details are described within the text. In addition, details for the labeled seismic event are given in Appendix IV.

Figures 73a and b show perspective views with seven NNW-SSE trending vertically modeled normal faults below the base Zechstein as well as five relocated hypocenters (blue spheres). Four events cluster near a fault branch (Fig. 73b). Only one event (the relocated Soltau’77-earthquake, highlighted by a red circle in Figure 73b) is situated at a NNW-striking fault (shown in aqua) in the NW of the area. This aqua colored fault extends to the adjacent area of Rotenburg/Söhlingen in the north, where another seismic event is located. The very deep event Krelingen’14 (November, 02nd 2014, in depths of about 23 km) is shown as determined “beachball” with normal fault focal mechanism.

Based on the relocated hypocenter depths below 5 km, I assume that the earthquakes were mostly caused by Permian basement faults below the base Zechstein. In the region of Walsrode, four faults (green, purple, red and aqua in Figure 73b) can be identified to be seismogenic.

6.6. Glacial isostatic adjustment

On the basis of the identified potential seismogenic active faults obtained from the 3-D subsurface modeling and hypocenter analyses, the numerical simulations of the glacial isostatic adjustment (GIA) are conducted at these seismic event locations. Figure 74 shows the fault pattern in the study area (red lines in the black rectangles) in NW Germany and associated seismic events. GIA-induced stresses were calculated for 31 seismic event locations (yellow dots in Figure 74) using the finite element method of ABACUS©. The detailed description of these numerical simulations is given in chapter 5.7.

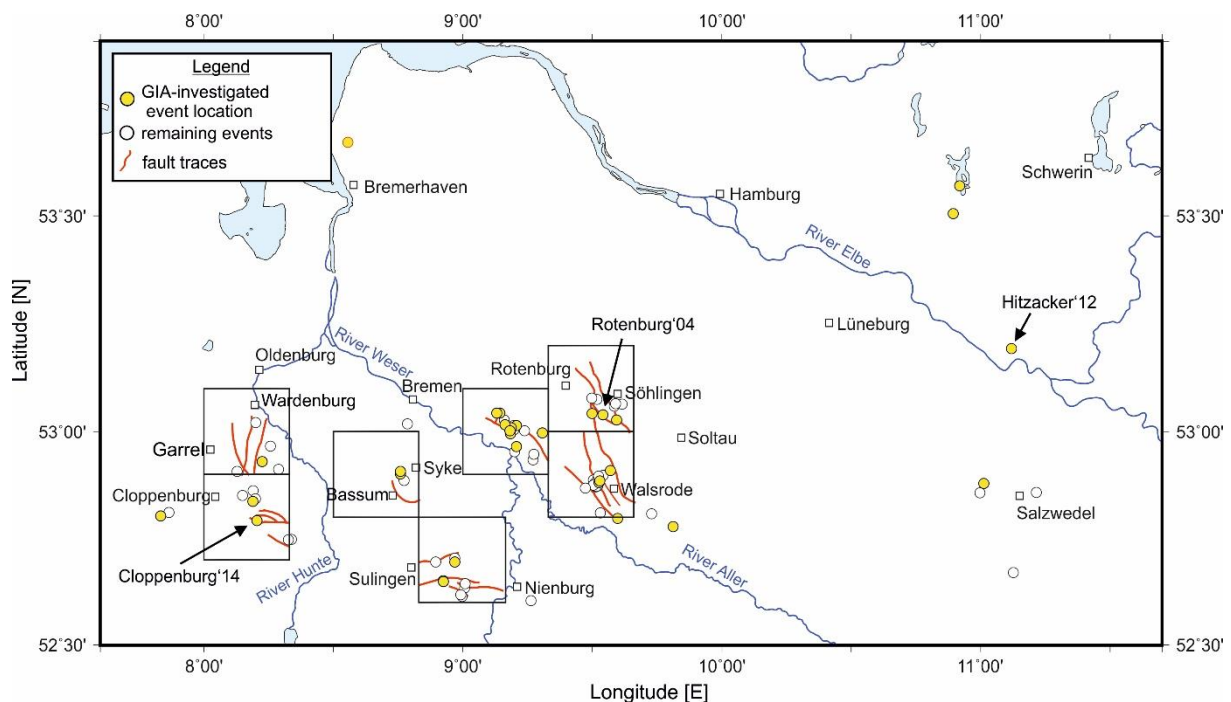


Figure 74. Fault pattern in the study area (black boxes) in NW Germany, which was derived by the relocated hypocenter linking with constructed faults on the basis of the GTA. The 31 GIA-investigated event locations are highlighted by yellow dots. Events, which occurred in the N and NE are relocated in greater depth, where information about faults lack. Therefore, fault modeling could not be performed. Three highlighted seismic events are shown below in Figure 75 and are described in the text in detail.

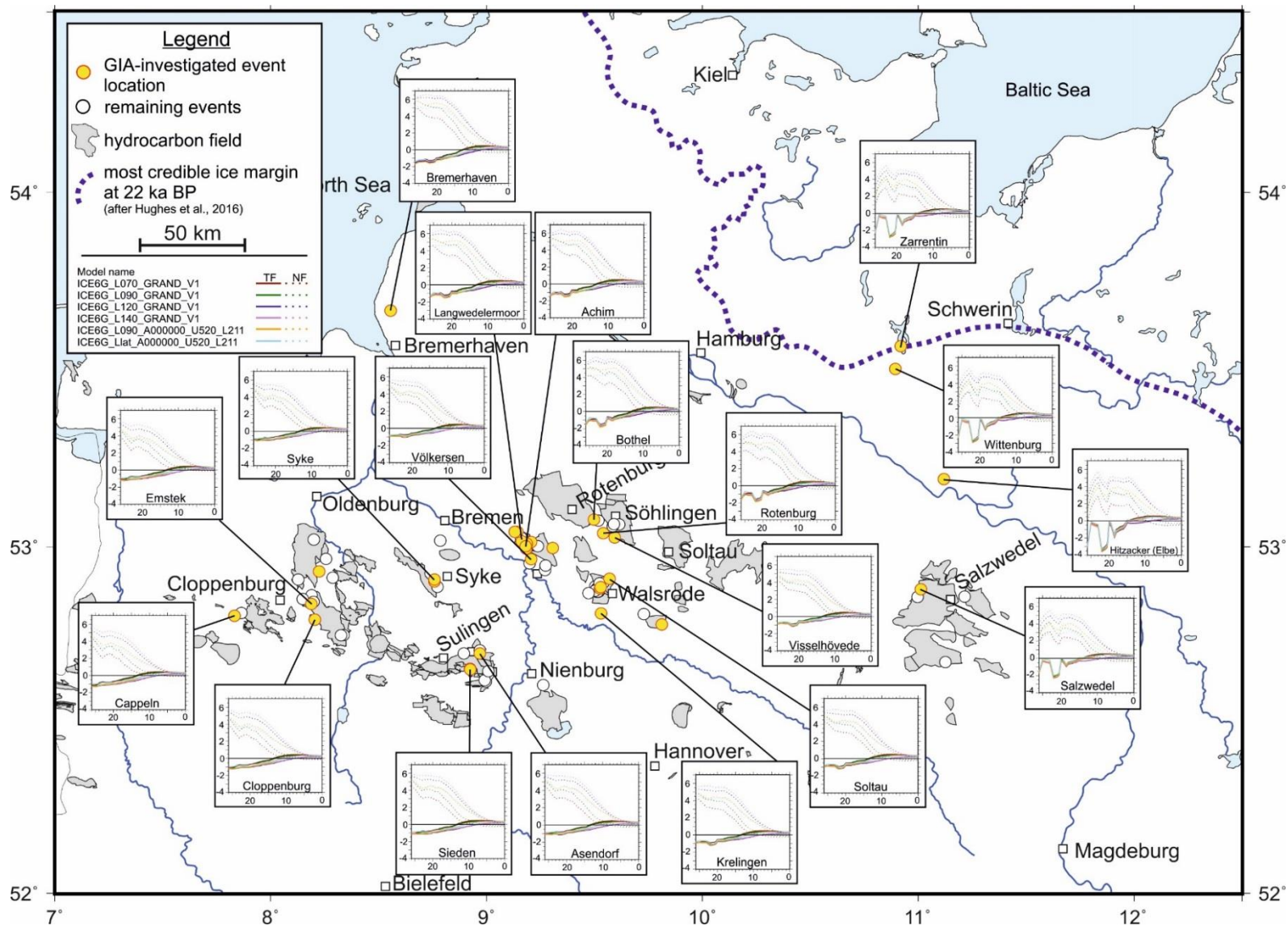


Figure 75. GIA-investigated event location map. 19 out of 31 determined changes in Coulomb Failure Stress (δ CFS) for relocated seismic event locations induced by the last glaciation (Weichselian) are plotted on the map. According to the small sketches, the y-axis defines the δ CFS value in MPa and the x-axis belongs to the time [ka BP] since 26 ka BP up to the present day. Evaluation results of both possible stress regimes, compressional (TF, colored solid lines) and extensional (NF, colored dashed lines) are drawn. For a better visualization, all graphs of δ CFS are given in Appendix VIII.

The map in Figure 75 shows the study area with 19 out of 31 event locations, where changes in the Coulomb Failure Stress (small sketches) for an assumed compressional (colored solid lines) and extensional (colored dashed lines) stress regime were calculated. In addition, the former ice margin at 22 ka BP related to the Weichselian glaciation is also plotted (blue dashed line, Hughes et al., 2016). Results of all 31 GIA-investigated event locations are given in Appendix VIII.

For a better visualization and evaluation of all figures, three simulation results are exemplarily selected, because they show nearly the same curve characteristics concerning their distinct locations in the study area (Fig. 76). The numerical simulations (carried out by Holger Steffen, Landmäteriet, Sweden) were conducted with six different rheology-models. Four models come along with laterally varying viscosities in the upper and lower mantle as well as four fixed lithosphere thicknesses, respectively (see Figure 76: 70 km = red curve; 90 km = green curve; 120 km = blue curve and 140 km = purple curve). The fifth model includes a 90 km thick lithosphere and a 1-D viscosity structure comprising only one viscosity value for each mantle layer, respectively (Fig. 76, yellow curve). The sixth model has also only a 1-D viscosity structure but laterally varying lithosphere thicknesses (Fig. 76, light blue curve) adapted from Wang and Wu (2006).

In the following, the description of the GIA simulation results is divided into two main parts: 6.6.1 GIA in a compressional stress regime (based on Figures 75 and 76, colored lines), 6.6.2 GIA in an extensional stress regime (based on Figures 75 and 76, colored dashed lines).

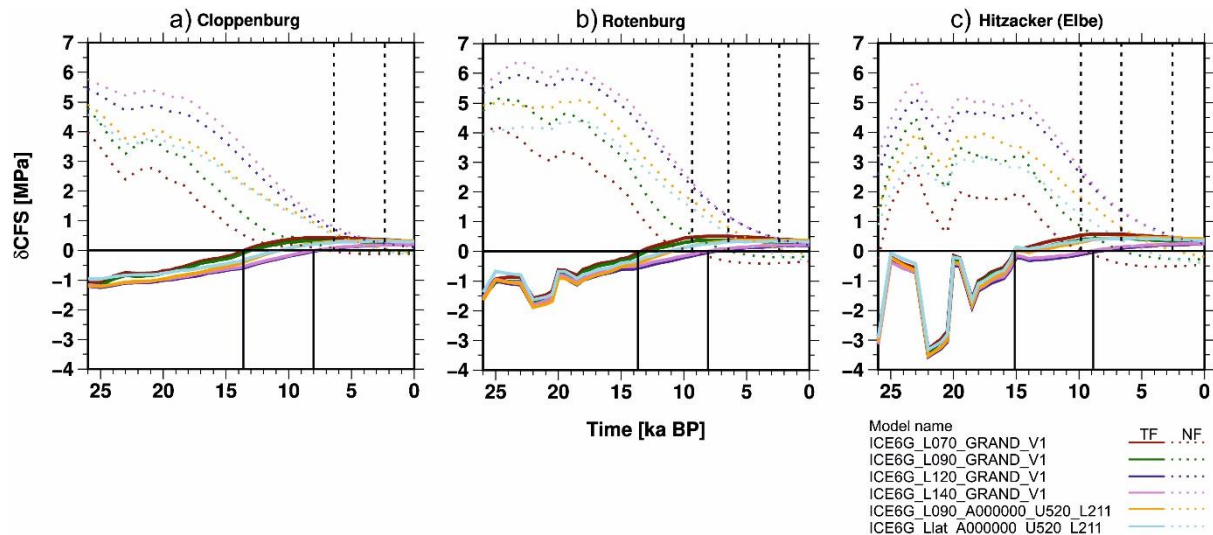


Figure 76. Changes in the Coulomb Failure Stress (δCFS) for three selected locations in NW Germany (highlighted in Figure 75). The stress changes are calculated on the basis of the advance and retreat of the Weichselian glaciation in the past 26 ka for a compressional (TF, colored solid lines) and an extensional stress regime (NF, colored dashed lines). Three examples are exemplarily selected from the 31 determined samples and arranged as they occurred from west to east in the study area. In a thrust fault regime (TF), black lines show the time when $\delta\text{CFS}=0$ is firstly reached and movement along an optimally oriented fault is possible. In a normal fault regime (NF) black dashed lines indicate the time when $\delta\text{CFS}=0$ is firstly reached and stable fault conditions are assumed. In general, negative δCFS values indicate stable fault conditions whereas positive values lead to the possibility of fault movement. The three examples have different approximated distances to the former ice margin. **a)** Cloppenburg'14, distance: 270 km **b)** Rotenburg'04, distance: 125 km **c)** Hitzacker'12, distance: 63 km.

6.6.1 GIA in an assumed compressional stress regime

The results show that some features are evident and applicable to each curve (colored lines Fig. 76): During deglaciation, all graphs show changes in δCFS from negative to positive values. If $\delta\text{CFS}=0$ is reached the possibility exists that movement along the investigated fault occurs. Fault slip and related stress release is not taken into account.

On the basis of the six GIA-models, in general, three different curve shapes for each investigated location can be distinguished. The curves with the lithosphere thickness of 70 and 90 km as well as 120 and 140 km show a very similar trend, respectively. In contrast, the curves of the 1-D viscosity structure model follow first, the course of the greater lithosphere thickness models up to 15 ka BP. It reaches $\delta\text{CFS}=0$ mostly right in the middle between the other model curves. Afterwards, it shows nearly the same shape as the smaller lithosphere thickness models.

The 31 numerical simulation results can be divided into three types showing similar curve characteristics. These summarized three types of differently developed changes in the Coulomb Failure Stress can also be allocated to distinct regions in the study area (Fig. 75). In

the following, these three types are described based on the three exemplarily selected event locations shown in Figure 76.

Type (1) corresponds to the regions Cloppenburg, Syke and Sulingen/Nienburg (Figs. 75 and 76a). After the beginning of deglaciation (about 21 ka BP, relating to the applied ice history of ICE-6G_C, Peltier et al., 2015) each model yields a significant increase of δCFS , especially the models with the thinner lithospheres (70 and 90 km). $\delta\text{CFS}=0$ is mainly reached between 13.5 and 8 ka BP. For the models with the lithosphere thicknesses of 120 and 140 km, $\delta\text{CFS}=0$ is reached at 8 ka BP, while possible fault activation for both models with the thinner lithosphere occur earlier at 13.5 ka BP. The 1-D viscosity structure models (yellow and light blue lines, Fig. 76a) reach $\delta\text{CFS}=0$ at about 10.5 ka BP. Each fault location indicates the possibility of fault movement due to stress changes, which are induced by the deglaciation of the Weichselian ice sheet up to the present day.

Type (2), characteristic for the area of Langwedel/Völkersen and Rotenburg/Söhlingen (Figs. 75 and 76b), is situated about 140 - 170 km away from the former ice margin. In contrast to the more constant increasing course of type 1 (Fig. 76a), the curves of type 2 show a different temporal development, especially in the time range between 26 to 17 ka BP. Thereby, the five models yield a very similar shape up to 18 ka BP. δCFS decreases significantly from 23 ka BP reaching the minimum value of δCFS at 22 ka BP. Between 22 and 19 ka BP a strong increase of δCFS is observed due to the deglaciation directly after a great ice extent at about 21 ka BP. After an interim low at 18 ka BP the six models differ but each exhibit an increase of δCFS until the zero line is reached. Hence, the 3-D viscosity models with lithosphere thicknesses of 70 and 90 km (green and red line) would point to a possible fault activation at about 13.5 ka BP, while the two 3-D viscosity models with thicker lithosphere (120 and 140, blue and purple line) would suggest 8 ka BP as activation time. In contrast, the models with the 1-D viscosity structure (yellow and light blue line, Fig. 76b) crosses the zero line to more instable fault conditions at about 10.5 ka BP. The times, when instable fault conditions were reached are the same compared to these of type 1. At present day, each model approaches nearly the same positive δCFS value. Since no stress release is considered in times of positive δCFS values, each model indicates the potential of fault movements due to GIA-induced stress perturbations at present day.

Type (3) corresponds to the region of Salzwedel and to locations east of the Elbe river (Figs. 75 and 76c). These locations are situated very close to the former ice margin or even below the former ice sheet of the Weichselian glaciation. For the time range between 26 up to 15 ka BP the six models yield a very similar shape. However, in comparison with both types described before, which are more distant to the former ice margin, the six models in Figure 76c exhibit more pronounced variations in δCFS and a different shape. Variations in the ice load or retreat of the continental Weichselian ice sheet cause substantial stronger changes in the Coulomb Failure Stress. Leading to more stable fault conditions, the ice load until 22 ka BP reveals a significant decrease of δCFS down to its minimum in that time range. When the subsequent ice retreat starts, the increase of δCFS is constantly strong. Another ice advance interrupt the increase of δCFS between 20 and 18 ka BP and produce more negative δCFS values. From that point (18 ka BP), an increase of δCFS dominates each model. A possible fault activation for the thinner lithosphere models (1-D and 3-D) is observed at 15 ka BP, about 1,500 years earlier than at any other virtual fault location belonging to type 1 and 2. In addition, the models with the 1-D viscosity structure reach $\delta\text{CFS}=0$ a second time at 13 ka BP. According to type 1 and 2, the models ICE6G_L120 and L140 (purple and blue line) reveal instable fault conditions at 8 ka BP. At present day, each model approaches nearly the same positive δCFS value. Since no stress release is considered in times of positive δCFS values, each model indicates the potential of fault movements due to GIA-induced stress perturbations at present day.

The derived results for the assumed compressional stress regime can be summarized as follows:

- The greater the distance between a fault and the former ice margin, the smaller the effects due to the former ice load on changes in the Coulomb Failure Stress especially before $\delta\text{CFS}=0$ is reached.
- On the basis of the curve characteristics, after reaching the zero line, type 1 and type 2 can be combined. These fault locations are related to the regions between Cloppenburg in the west and Walsrode/Soltau in the east. Considering the most reliable lithosphere thicknesses of 70 or 90 km, both indicate possible fault movements between 14 to 13 ka BP.
- Type 3 reveals a slightly different shape. These locations, which are situated below or right in front of the former ice margin in the east of the study area reach $\delta\text{CFS}=0$ about 1,500 years earlier than the other fault locations mentioned above.
- However, without considering fault slip at $\delta\text{CFS}=0$, each model indicates the potential of fault movements due to GIA-induced stress perturbations at present day.

6.6.2 GIA in an assumed extensional stress regime

In contrast to the model results of the assumed compressional stress regime in northern Germany, the colored dashed lines in Figures 75 and 76a-c show almost exactly the counter development. A classification into three different curve types as previously applied for the compressional stress regime is more complex and is not taken into account in this case. The most significant curve characteristics are described in the following.

Applicable to every curve: During deglaciation, all graphs show changes in δCFS from positive to negative values. If $\delta\text{CFS} < 0$ is reached, stable fault conditions are assumed and movement along the investigated fault is inhibited. Fault slip in the area of positive δCFS values is not considered.

In the region between Cloppenburg in the west and Walsrode/Soltau in the east, the δCFS decreases from positive values until $\delta\text{CFS} < 0$ is reached (Figs. 76a and b). The calculated GIA-models for the locations right in front or below the former ice sheet show a slightly different curve pattern, especially in times between 26 and 15 ka BP (Fig. 76c). During glaciation, an increase of positive δCFS values from 26 to 23 ka BP is observed. Except an interim low at 20,5 ka BP (still positive δCFS) the deglaciation lead to a linear decrease of changes in the Coulomb Failure Stress to 14 ka BP and continue with a higher slope until $\delta\text{CFS} < 0$ is reached at various times concerning the different models.

In case of the models with lithosphere thicknesses between 70 and 90 km, including a 3-D viscosity structure, in the region of Cloppenburg, Syke and Sulingen/Nienburg, fault movement is inhibited since 7 and 5 ka BP, respectively (Fig. 76a). Further east, in the regions of Langwedel/Völkersen, Rotenburg, Salzwedel and north of the Elbe river an inhibition of possible fault movement is observed for 10 and 7 ka BP (Figs. 76b and c).

The models with the 1-D viscosity structure in the regions between Cloppenburg and Walsrode reach $\delta\text{CFS} < 0$ at nearly the same times between 3 and 2 ka BP (Figs. 76a and b). For investigated event locations in front or below the former ice sheet the faults are stable since 5 ka BP (model Llat, Fig. 76c) and 3 ka BP (model L090_A0000..., Fig. 76c).

Only the models with high lithosphere thicknesses (120 km and 140 km) show always positive δCFS values and indicate possible movement along optimally oriented faults up to the present day.

The derived results for the assumed extensional stress regime can be summarized as follows:

- The greater the distance between a fault and the former ice margin, the smaller the effects due to the former ice load on changes in the Coulomb Failure Stress especially before $\delta\text{CFS}=0$ is reached.
- Models with 1-D and 3-D viscosity structures as well as varying lithosphere thicknesses between 70 km and 90 km show stable fault conditions at present day.
- Only models with lithosphere thicknesses of 120 or 140 km indicate the potential of fault movements due to GIA-induced stress perturbations at present day.

7. INTRAPLATE SEISMICITY

The relocated hypocenters in combination with the 3-D subsurface models obtain an extended and enhanced knowledge of the seismicity pattern in the heterogeneous intraplate region of NW Germany. This chapter deals with a qualitative comparison between the seismicity of NW Germany and the seismicity in other intraplate areas to better interpret the controlling factors for the occurrence of seismic events later on in the discussion.

After Talwani and Rajendran (1991) intraplate earthquakes occur away from active plate margins and are generally triggered by the reactivation of pre-existing zones of weakness, mostly in a stress regime, which is oriented parallel to the absolute direction of plate motion. Therefore, the pre-existing stress field is one of the key parameters of intraplate earthquakes. In Central Europe, the intraplate stress is induced by the ongoing collision of the African and Eurasian plate and by the ridge push of the North Atlantic (e.g. Grünthal and Strohmeier, 1992, Heidbach et al., 2010). In the study area, the principal horizontal stress (S_{Hmax}) orientation trends NW to NNW (Müller et al., 1992) whereas the Northwest German Basin trends more likely WNW-ESE (e.g. Lohr et al., 2007). Marotta et al. (2002) compared the stress pattern with a fan in which S_{Hmax} deviates in directions between NW-SE in the western part to NE-SW in the eastern part of northern Germany. Local stress changes in the stress field often lead to the reactivation of pre-existing zones of crustal weakness (e.g. McGarr et al., 2002, Suckale, 2010). In northern Germany, stress perturbations may occur by the presence of local subsurface structures such as salt domes (Brandes et al., 2013) or the hydrocarbon production (Suckale, 2010). Another natural trigger mechanism for changing the local stress field in northern Germany is the glaciation/deglaciation of the Scandinavian ice sheet. These stress changes can lead to the reactivation of pre-existing faults (Brandes et al., 2012, Brandes et al., 2015). In the study area, more or less two possible trigger mechanism are assumed – induced seismicity due to the production of natural gas (and)/or the glacial isostatic adjustment.

7.1 Seismicity of NW Germany in comparison to seismicity in other intraplate regions of the world

In Appendix IX, geological settings and focal parameters of earthquakes, belonging to different intraplate regions distributed all over the world are summarized. On the one hand these regions are subjected to hydrocarbon extraction and on the other hand they are not influenced by anthropogenic treatments. Three regions will be discussed in more detail - The Netherlands, Alberta/Canada and the New Madrid Seismogenic Zone (USA) - to figure out similarities and/or differences. More documented regions are stored within Appendix IX.

northern Germany and northern Netherlands are both located within the Central European Basin System (Littke et al., 2008) and may exhibit a possible comparison of occurring seismicity. Natural tectonic earthquakes with magnitudes up to 5.8 (Roermond earthquake in 1992, Camelbeck and van Eck, 1994) are more or less limited to the region of the Roer Valley Graben in southern Netherlands (Camelbeck et al., 2007). In the north of the Netherlands, hydrocarbon production has been started many decades ago (van Eck et al., 2006). For the formerly low strain area, seismicity is observed after 28 years of ongoing production. The seismicity in the vicinity of hydrocarbon fields in NW Germany, a region also regarded as aseismic (Leydecker and Kopera, 1999), shows a delay time between 10 - 30 years after production has begun. In the Netherlands, for only 16 out of 125 producing fields (in NW Germany: 13 out of 96) seismic activity was registered (van Eijs et al., 2006), whereby three natural gas reservoirs - Groningen, Roswinkel and Bergermeer - exhibit significant seismicity (Dost et al., 2012), which is almost comparable with the NW German setting. However, due to the very large extent of the Groningen field and the seismic event location inside or above this reservoir (Daniel et al., 2016), the Groningen field is unique in the world and difficult to compare with reservoirs in Germany or other regions. Nevertheless, Bergermeer and Roswinkel, show similar seismicity patterns to the seismicity in the regions of Syke and Völkersen, respectively. At Bergermeer (Haak et al., 2001) and Syke a very small number of seismic events occurred with magnitudes up to M_L 3.5. In the regions of Völkersen and Roswinkel (van Eck et al., 2006) a high amount of seismic events with similar magnitudes ($0.5 \geq M_L \geq 3.1$) are observed. In northern Netherlands, the seismic events are located more or less at NW-SE oriented faults at reservoir depth and not deeper than 4 km. In contrast, the relocated earthquakes in NW Germany occurred slightly deeper between 5 and 8 km. These deeper locations may relate to the eastward dipping reservoir horizons (Pasternak, 2015) and the reactivation of Permian basement faults in deeper layers. These faults were identified within the present study.

Another region with active hydrocarbon production is situated in west central Alberta/Canada near Edmonton in front of the Rocky Mountain Front Thrust Belt. Within the so-called Rocky Mountain House area in the NE of the Rocky Mountain Front Thrust Belt, the Strachan sour gas reservoir is located in the Western Canada Sedimentary basin (Eaton and Mahani, 2015) in depth of 3 to 5 km (Wetmiller, 1986). A delay time of nearly 5 years between the onset of production and the start of major seismic activity was observed (Wetmiller, 1986). Therefore, the seismicity shows a shorter delay time than in the above mentioned regions. This faster failure of present faults may result in a higher stress drop (e.g. McGarr and Simpson, 1997, McGarr et al., 2002) related to extensive production in the first years or a stronger initial tension, which takes the fault very close to failure due to the proximity of the Rocky Mountain Front Thrust Belt.

After Wetmiller (1986) only the Strachan sour gas reservoir is seismically active, the other ones remain all aseismic. Eaton and Mahani (2015) derived hypocenter depths between 4 - 6 km, mostly below the Strachan reservoir in a reverse-faulting regime. In contrast, most of the seismic events in NW Germany are located at the margins of the reservoirs and most of the determined fault plane solutions show normal fault movements.

Natural tectonic earthquakes are only located within the thrust belt of the Rocky Mountain Front and seismic activity significantly increased in the Rocky Mountain House area after gas production was established (Wetmiller, 1986). The occurrence of seismic events in this area is therefore regarded as man-made induced due to the depletion of the Strachan hydrocarbon reservoir (Baranova et al., 1999). Further to the NW, the so-called Crooked lake area exhibits episodically seismic activity, which is directly correlated with wastewater injections or extensive hydraulic fracturing stages (Eaton and Mahani, 2015). It is evident that it is important to differentiate between settings which are dominated by either injection or extraction induced seismicity (e.g. Suckale, 2010, Dahm et al., 2010, 2015). Especially, the formerly mentioned delay time or the lack of the delay time serve as indicator for these different possible trigger mechanisms.

Another prominent intraplate region is the New Madrid Seismogenic Zone in Eastern Central United States (Powell and Horton, 2009). The New Madrid Seismogenic Zone is located in a large alluvial valley along the Mississippi river at the corner between Missouri, Arkansas, Tennessee and Kentucky. The extent of the New Madrid Seismogenic Zone is defined by the occurrence of microseismicity ($M \leq 3.0$, Mueller and Pujol, 2001), where, after Johnson et al. (2014) approximately 200 small ($M \geq 0.2$) to moderate earthquakes were registered each year along reactivated basement faults within the ancient failed Reelfoot Rift (McKeown and Diehl, 1994). In comparison, since 2012, in NW Germany only about 10 to 20 seismic events were registered within the study area ($0.5 \geq M_L \geq 3.5$), whereby the vast majority of seismic events rarely exceeds a magnitude of $M_L 3.0$. According to the event bulletin of the United States Geological Survey (time period of the last 2 years) and after McKeown and Diehl (1994), most of the earthquakes in the New Madrid Seismogenic Zone occurred in depth shallower than 15 km. In contrast, each relocated earthquake in NW Germany with undoubted tectonic origin is located deeper than 13 km.

The less destructive microseismicity in the New Madrid Seismogenic Zone is dominated by a 500-year recurrence interval of significant earthquakes yielding high magnitudes of $M \geq 7.0$ (e.g. Hough et al., 2000, Mueller and Pujol, 2001, Arsdale, 2014, Talwani, 2014). These stronger earthquakes are assumed to be triggered by Late Pleistocene erosion (Calais et al., 2010) or induced by bending of the lithosphere due to the glacial unloading of the Laurentide ice sheet in northern parts of the United States (Grollimund and Zoback, 2001). Similar to the

region of the Osning Thrust near Bielefeld (Brandes et al., 2012, Brandes and Winsemann, 2013, Brandes et al., 2015) in Central Germany, the New Madrid Seismogenic Zone was also not covered by ice sheets.

It is difficult to compare regions where several hydrocarbon reservoirs are situated, because each of these fields may exhibit different seismicity patterns, even with close proximity to each other. Thus, basically, each active natural gas field and the relating seismicity has to be considered separately. But some significant similarities are observed for each region, where hydrocarbon production was established. Seismic activity is observed within regions, which are formerly referred to as aseismic. Small-to-moderate magnitude seismic events in the vicinity of active hydrocarbon fields are mostly located at reservoir depth. Whereas natural tectonic intraplate earthquakes occur often slightly deeper and present much higher magnitudes up to 7.5 (New Madrid seismic zone or the Rocky Mountain Front Thrust Belt) or 8.0 in North China (Liu et al., 2014) than the assumed induced seismic events distributed all over the world. For each region with hydrocarbon extraction, a delay time between the beginning of the ongoing production and the onset of seismicity is observed. Although many hydrocarbon fields are in production, only a small amount of active hydrocarbon fields in each region show seismic activity.

In contrast to other regions with hydrocarbon production the seismicity in NW Germany reveals some unique and special features: Only a very limited number of small-to-moderate magnitude seismic events occurred in NW Germany, although production lasted more than 30 years. The presence of salt structures may influence the seismicity (whereby the influence on the seismicity or on the relocalization has not yet been clarified). In addition, deep natural tectonic earthquakes occurred in the region of the assumed induced events.

8. DISCUSSION

Altogether, 77 seismic events were instrumentally registered in northern Germany during the last 25 years. Most of them cluster in areas of ongoing hydrocarbon production. In addition, historical and deep seismic events, mostly of undoubted tectonic origin occurred in this intraplate region of NW Germany. Intraplate earthquakes are different to those at plate margins. Their occurrence, magnitude and location are more difficult to anticipate in contrast to earthquakes, which are connected with plate tectonics (Liu and Stein, 2016). On mid-continental earthquakes (Liu and Stein, 2016), one of the main goal, using seismological analyses is the identification of their causes. The glacial isostatic adjustment and the hydrocarbon production are assumed to cause recent intraplate earthquakes in NW Germany (Dahm et al., 2007, 2015, Brandes et al., 2012, 2015). Both trigger mechanisms may occur side-by-side in the study area.

In NW Germany, the vast majority of seismic events, ranging in depths between 5 to 9 km is located in close proximity to the natural gas fields. Only five earthquakes are located in greater depth (13 – 42 km), mostly in a distance of 70 - 200 km to the gas fields. Most of the shallow seismic events indicate normal fault movement along major Permian basement faults trending NW-SE, NNW-SSE, roughly N-S and in some cases WNW-ESE. A small number of faults, namely 25 were identified to be potentially seismogenic active. Numerical simulations reveal two different szenarios. In a compressional stress regime, optimally oriented faults in the study area indicate potential movement due to GIA-induced stress perturbations at present day. Whereas, in an extensional stress field all faults are stable at present day.

8.1. Quality of the 3-D relocation

8.1.1 Improvement of hypocenter localization

The location of earthquakes is regarded as one of the basic problems in seismology (e.g. Pujol, 2004, Gajewski and Tessmer, 2005) and can be divided into two main parts. I) A forward computation of theoretical travel times and II) an inverse search for the unknown hypocenter parameters (Wittlinger et al., 1993). Over the years, several approaches and tools were developed for hypocenter localization in heterogeneous 3-D media (Moser et al., 1992, Wittlinger et al., 1993, Lomax et al., 2000, Lin et al., 2007, Lin et al., 2010 among others). Nevertheless, there is still the potential to reduce uncertainties during the localization process and to enhance the quality of results for sharpening the seismicity pattern (Lin et al., 2007).

I performed a 3-D probabilistic relocation approach by using two differently scaled 3-D *P*-wave-velocity models and was able to reduce hypocenter uncertainties significantly. The applied technique differs widely from the routinely used 1-D earthquake localization approach of Seismic Handler (Stammler, 1993) in combination with the implemented iterative-linearized algorithm of LocSAT (Bratt and Bache, 1988, Nagy, 1996) and was also hardly comparable with other prominent 1-D localization programs like Hypo71 (Lee and Lahr, 1975), Hypoinverse (Klein, 1978) or Hypoellipse (Lahr, 1980). The direct comparison of 1-D iterative-linearized approaches with the 3-D probabilistic relocation used in this study was difficult, because of great differences in their methodologies.

Wittlinger et al. (1993) already stated the importance of applying new localization methods that incorporate complex 3-D velocity structures as had been observed for subduction zones, volcanoes and regions with hydrocarbon fields. They adapted the finite difference determination method of travel times (Podvin and Lecomte, 1991), which is based on the inverse problem formulation of Tarantola and Valette (1982a, b) to gain new insights into the induced seismicity in the vicinity of the Lacq gas field in France (e.g., Grasso and Wittlinger, 1990, Bardainne et al., 2008). This travel time calculation method, including the formulation of Tarantola and Valette (1982a, b) was integrated within the software package of NonLinLoc (Lomax et al., 2000 and Lomax and Curtis, 2001). NonLinLoc, imprinted with the advantage of a complete description of location uncertainties (Husen et al., 2003) was widely used in many location studies with minimum 1-D velocity models (Husen et al., 2003) and 3-D velocity models (e.g., Husen and Smith, 2004, Bardainne et al., 2008, Diehl et al., 2014, Béthoux et al., 2016, Gaité et al., 2016). All studies used 3-D velocity models to reduce uncertainties for local earthquakes and to improve the seismicity pattern in very heterogeneous crustal regions. For relocating earthquakes in NW Germany, the advantages of NonLinLoc were also taken

into account. However, instead of only one velocity model, a combination of two differently scaled 3-D *P*-wave-velocity models were applied in this study. Advantages and restrictions of the application of NonLinLoc as well as of the two conducted 3-D velocity models will be discussed in the following with respect to (1) the computation time, (2) hypocenter uncertainties and (3) the station network.

(1) The used small fine-meshed 100 m cell size WEG travel time grid consists of more than 96×10^9 cells in a very limited region comprising an area of 96,360 km³. The CRUST1.0 model area encompasses more than 120 Mio. km³, however, composed of cubic cells with 1,000 m edge length. Due to the increase of cell size, the number of cells and the computation time was significantly reduced for the calculation of long travel paths and even more for the subsequent inversion. Another reason for the reduction of computation time was the application of the 100 times faster Oct-Tree importance sampling (Lomax and Curtis, 2001), in contrast to usually used grid-search algorithms. Though Wittlinger et al. (1993) applied only one dense 3-D velocity grid with 10^6 cells (250 m cell size), they also tried to save computation time during their hypocenter location search. Thereby, they adapted a two-scale process from Nelson and Vidale (1990). The first step was to obtain a rough location, where subsequently the fine-meshed travel time grid was applied to search for the final hypocenter. The underlying concept of the applied technique, comprising one coarse grid and one fine-meshed grid in the area of interest is an analog representation of this two-scale process. This two-scale process was meshed within one localization run by combining both differently scaled velocity models. In case of the fast increase of computer power in recent times, the non-linear determination of travel times using 3-D velocity models or the inversion of hypocenters in a dense and large 3-D travel time grid are faster and available for the non-scientific world as well as applicable in routine analysis as it is used for example in Switzerland (Husen et al., 2003). However, new approaches, resulting in the reduction of computation time are still important and necessary, in cases of monitoring seismicity and the location of earthquakes swiftly in regions with high seismic risks for example at Mt. Etna (Mostaccio et al., 2013) or in near real-time tsunami forecast systems (Hanka et al., 2010, Melgar et al., 2016).

(2) In order to classify my derived uncertainty results, they were compared with several recent prominent studies, in which relocalizations were carried out with a 3-D model. Among others, Husen et al. (2003), Lin et al. (2007), Bardainne et al. (2008), Münch et al. (2012), Gaité et al. (2016) had revealed that an optimal relocated hypocenter must have horizontal errors of less than 1.5 km and less than 3 km in focal depth uncertainties. They located earthquakes in Switzerland (Husen et al., 2003), southern California (Lin et al., 2007), at Lacq gas field (France, Bardainne et al., 2008), in southern Germany (Münch et al., 2012) and in Spain (Gaité

et al., 2016), respectively. In this study, earthquake uncertainties were reduced by almost one half. Average uncertainties obtained from the 40 relocated seismic events are ± 0.5 km in horizontal errors and ± 1.0 to ± 1.5 km in focal depth, which is very well suited or even better than in the formerly mentioned high accurate earthquake location studies. Therefore, the 3-D relocalization approach used in this study provides reliable earthquake locations to analyse earthquake origins in detail. Nevertheless, e.g. Lin et al. (2007) applied another prominent and commonly used technique – the waveform cross-correlation approach introduced by Waldhauser and Ellsworth (2000). Lin et al. (2007) located earthquakes in southern California and obtained a very small median of horizontal errors of 0.2 km, and 0.4 km in hypocenter depth. In addition, Gaité et al. (2016) were able to reduce the average horizontal location error from 2.1 ± 1.6 km to 1.5 ± 0.7 km of 550 earthquakes in Spain using the waveform cross-correlation in addition to the relocalization with a 3-D model. Unfortunately, relative locations for earthquakes in northern Germany are not conducted yet. The waveform cross-correlation should be kept in mind for further studies to continue the improvement of the seismicity pattern.

(3) The relocalization of seismic events in NW Germany before 2012 was influenced by a limited station coverage resulting in an earthquake location mostly at margins and outside the seismic network. After e.g. Thurber (1987), Moser et al. (1992), Bondar et al. (2004) or Bai et al. (2006), high accurate hypocenter locations can only be achieved for events that occurred inside a station network. On the basis of the conducted synthetic model tests and results of the relocated events especially after 2012, I assume that the more detailed 3-D travel time grid in the area of Langwedel/Völkersen, Rotenburg/Söhlingen and Walsrode was able to compensate a limited station coverage to a certain extent. Crustal heterogeneities seem to be well resolved within the more complex and detailed 3-D WEG velocity model. The coarse 3-D model (CRUST1.0) in combination with an additional fine-meshed and detailed 3-D model in the area with an estimated hypocenter revealed the real advantage of 3-D models by providing a reliable determination of focal depths, which is one of the key factor to understand the regional seismicity (Deichmann, 2003, Ma and Atkinson, 2006).

As shown before, the application of NonLinLoc in combination with 3-D velocity models is a valuable tool to relocate seismic events in a very heterogeneous crustal region like northern Germany. However, it is evident that the procedure has its limitations (Husen et al., 2003). In case of a limited station coverage including only a few observations, the 3-D velocity models do not have the possibility to compensate these limitations completely. This is clearly documented by the extent of the confidence ellipsoids of seismic events with a quality rating of C or D that are significantly greater than for events with the best ratings of A and B. Relocalization results for all the events also for those of minor quality reveal smaller

uncertainties than those with simple 1-D velocity models. The minor RMS-value and the very small confidence ellipsoids indicate well-constrained hypocenter solutions by using the combination of the two 3-D velocity models.

Influence of V_p/V_s on the focal depth

Since no accurate S-wave-velocity model is available for northern Germany, the selection of the V_p/V_s ratio is one of the main factors for the determination of the hypocenter depth. Most results of the relocation approach show that higher V_p/V_s yields a deeper location (Fig. 77), especially in cases of events with less than 10 observations. In some cases, the increase of the V_p/V_s ratio leads to a shallower location.

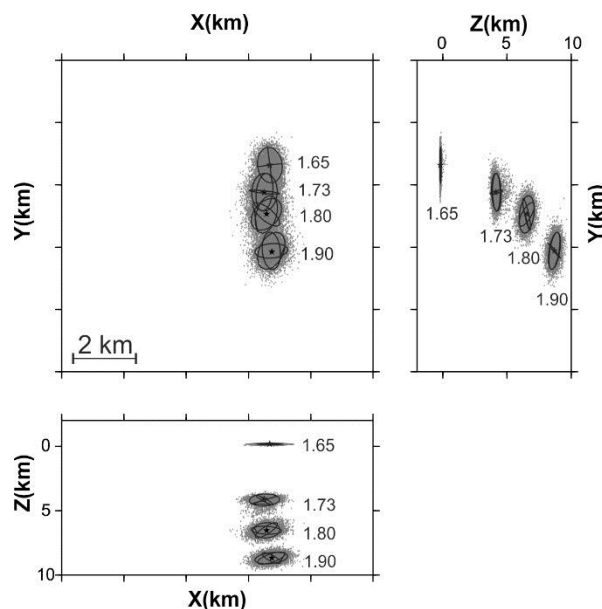


Figure 77. Hypocenter location shift observed for one relocated single seismic event. The different locations are obtained by varying V_p/V_s ratios from 1.65 to 1.90.

During the relocalizations, a V_p/V_s – ratio ranging between 1.65 and 1.95 was investigated and the best-fitting hypocenters, including smallest residuals were achieved for a ratio of about 1.81. This value is slightly higher than the commonly used ratio of 1.73 for locating earthquakes in Germany (SZO, pers. communication). Hamada (2004), Shillington et al. (2008) and Wang et al. (2012) pointed out, that V_p/V_s ratios showed a lateral variability with depth due to the presence/absence of different fluid types (water, oil and gas) in the subsurface. In northern Germany, seismic wave travel paths are only marginally influenced by hydrocarbon fluids. Because the thickness of reservoirs is only in the range between tens to hundred meters (e.g. Schröder et al., 1995 or Bischoff et al., 2015). Further fluids like brines located within the Northwest German Basin (Magri et al., 2008) are able to influence the seismic properties of

rocks (Carcione et al., 2006). To my knowledge, there is no publication, concerning NW Germany, in which a correlation between brines and wave velocities was investigated. However, further studies might be important because e.g. Kraaijpoel and Dost (2013) showed that salt-related effects led to misinterpretation of focal location and mechanism by the example of the Groningen gas field in the Netherlands.

Important controlling factors for the seismic wave propagation are the differing thickness and physical properties of basin fills (Bormann, 2012). In the Northwest German Basin, the cumulative thickness of Permian to Cenozoic sediments of more than 5,000 m (Maystrenko and Scheck-Wenderoth, 2013) lead to a decrease in density and V_s . Thus, a higher V_p/V_s ratio was observed for a long travel time path way and had to be considered during the hypocenter inversion. Similar and slightly higher V_p/V_s values were found in a comparable sedimentary setting within the Los Angeles Basin (Biddle, 1991). Hauksson (2000) generated 3-D V_p and V_p/V_s models and investigated V_p/V_s ratios for distinct sedimentary basins in southern California revealing mostly V_p/V_s of more than 1.75 up to 2.2 in depth less than 5,000 m.

In contrast, lower V_p/V_s ratios were determined for the Vogtland/West Bohemia region, where sediments almost lack and an intrusive body as well as fluid pathways are most likely present in the subsurface (Mousavi et al., 2015). The local swarm earthquakes were relocated with a V_p/V_s value of about 1.67 (e.g. Fischer and Horálek, 2000, Jansky et al., 2000). For earthquake locations in Switzerland, Diehl et al. (2014) determined S-wave velocities from V_p with a V_p/V_s of 1.71.

The best relocalization results for events in northern Germany were achieved with a V_p/V_s ratio of 1.8 and higher. Hence, I recommend to use this value for the relocalization of future events as long as no detailed 3-D S-wave-velocity model for northern Germany is available. It is noticeable that an increase of the V_p/V_s ratio doesn't shift the hypocenter always in one direction. The hypocenter location does not only depend on the V_p/V_s ratio but also on the applied velocity model and on the station configuration. A detailed investigation was beyond the scope of my study.

8.2. Possible trigger mechanisms for intraplate earthquakes in NW Germany

"Recent earthquakes in northern Germany are most likely induced by the natural gas extraction". This statement is used by public authorities (BGR, LBEG, Bischoff et al., 2013, 2014, 2015) and recent publications (e.g. Dahm et al., 2007, 2010, 2015) to classify most of the recent seismic events that occurred in northern Germany.

Davies et al. (1995) developed criteria, which were applied by Dahm et al. (2007, 2010, 2015) to classify seismic events in NW Germany as human-induced seismicity. Main criteria are the previous aseismic character in distinct regions, the time-dependent occurrence of earthquakes after the production was established and the earthquake location in close proximity to hydrocarbon fields.

However, historical events (Intensity up to VII, Leydecker, 2011), recent deep earthquakes (this study) and some seismic events, which occurred away from active hydrocarbon fields (Bock et al., 2002 and this study) yield evidence for a possible natural tectonic driving mechanism. The occurrence of human-induced and natural triggered earthquakes together in a relative small region raises the question, which events are induced and which are of tectonic origin. In particular, is it possible to create unique criteria to discriminate between both types of seismic event causes? In the following, the most probable trigger mechanisms namely stress changes generated either by reservoir depletion due to gas extraction (8.2.1) or by glacial isostatic adjustment (8.2.2) are discussed individually.

8.2.1 Induced seismicity due to reservoir depletion

Seismic activity related to hydrocarbon production is a well-known phenomenon (e.g. Milne and Berry, 1976). During the production procedure, two different ways are known to trigger seismic events. Fluid injection leads to reduction of the effective normal stress in the reservoir, while the shear stress remains constant (Grasso, 1992). This can cause movements almost instantly along pre-existing fractures (Edelmann, 2006, Mukuhira et al., 2013), which may be accompanied by seismic events (Davis and Pennington, 1989). The second trigger mechanism is related to extraction of fluids (Yerkes and Castle, 1976, Segall, 1989). Fluid withdrawal leads to compaction of the reservoir and an alteration of the state of stress (Yerkes and Castle, 1976, Oppenheimer, 1986, Segall, 1989). These poroelastic stress changes are observed inside the reservoir and within the surrounding rocks causing induced earthquakes (Segall, 1989, Segall et al., 1994, Baranova et al., 1999).

In NW Germany, fluid injection like hydraulic fracturing activities at hydrocarbon fields are unrelated to the spatio-temporal occurrence of earthquakes at these fields (Gestermann,

2015). Therefore, the focus in the present study was set on reservoir depletion due to fluid extraction. Suckale (2009, 2010) provides summarized common observations of case studies, referring to induced seismicity by fluid extraction all over the world. Similar observations were adopted to create criteria for identifying human-induced seismicity (Davies et al., 1995, Dahm et al., 2010). In the following, these general observations for induced seismicity are used to classify the relocated seismic events of NW Germany and set them into the context of worldwide induced seismicity.

Magnitude Range: Except two destructive earthquake sequences (Coalinga, USA 1983-1987, McGarr, 1991, McGarr et al., 2002 and Gazli, Uzbekistan 1976-1984, Simpson and Leith, 1985), which are more or less suspected to be connected with hydrocarbon production (Suckale, 2010), induced seismicity only leads to small-to-moderate magnitudes ($M_L \leq 4.5$, Suckale, 2010). The strongest events, which are related to conventional gas production are situated e.g. at the Lacq gas field in France $M_L \sim 4.2$ (Bardainne et al., 2008), in the Netherlands $M_L = 3.6$ in Groningen (van Thienen-Visser and Breunese, 2015) and up to $M_L 3.5$ at the hydrocarbon fields Roswinkel and Bergermeer (van Eck, 2006 and van Eijs, 2006) or at the Strachan sour gas reservoir in the Rocky Mountain House area (Alberta, Canada) with $M_L 3.8$ (Wettmiller, 1986, Eaton and Mahani, 2015). The majority of events in the vicinity of hydrocarbon fields in NW Germany does not exceed a local magnitude of 3.0. Thus, the Rotenburg mainshock from 2004 and the Soltau event from 1977, both with magnitudes $M_L \geq 4.0$ could be two exceptions.

Correlation with production: A direct spatio-temporal correlation between gas production and seismicity is a challenging and difficult task because of the lack of information about production values at distinct wells (Suckale, 2009). However, if production data for reservoirs is available the cumulative production gas volume can be correlated with the cumulative seismic moment released by events in NW Germany (Fig. 78).

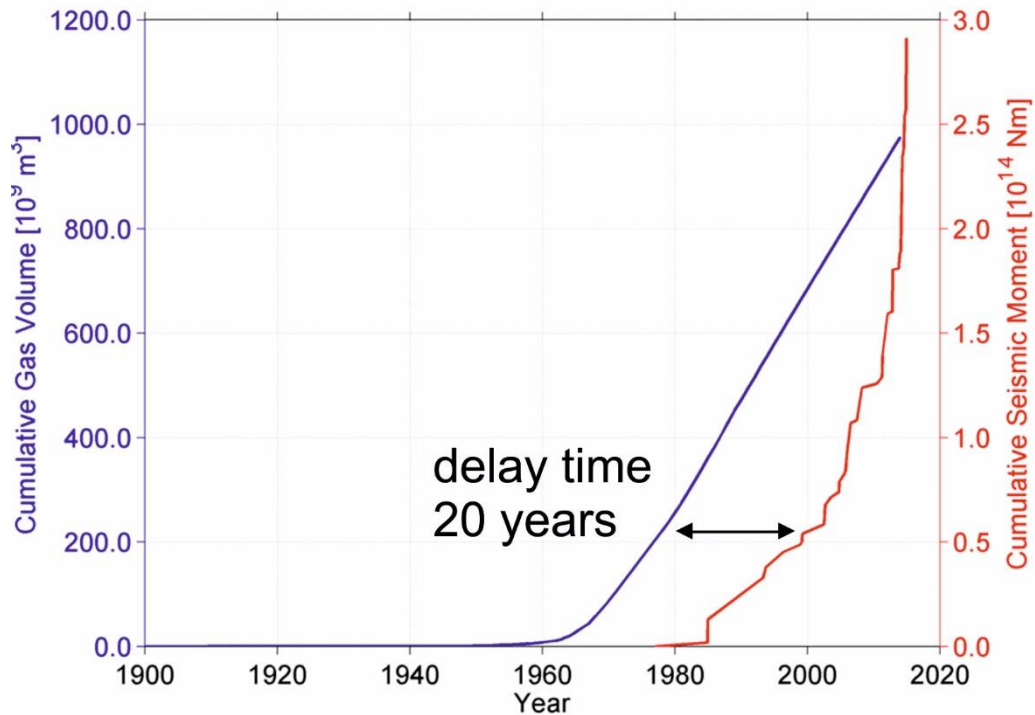


Figure 78. Comparison between the cumulative gas volume of all active gas fields in northern Germany and the cumulative seismic moment released by all instrumentally registered events in northern Germany (Gestermann, 2015).

Figure 78 shows that seismicity was first registered since the production lasted about 20 years. An obvious correlation between gas extraction and the occurrence of seismic events immediately right after the production had commenced cannot be observed. This finding is supported by several studies, which observed seismicity at hydrocarbon fields all over the world (e.g. Wetmiller, 1986, Grasso and Wittlinger, 1990, Baranova et al., 1999, Bardainne et al., 2008). The time delay is later discussed in detail during the observation of temporal patterns for extraction induced seismicity.

Location: Recent studies for Lacq gas field (Bardainne et al., 2008), Strachan sour gas field (Wetmiller, 1986, Eaton and Mahani, 2015) or for gas fields in the Netherlands (van Eck et al., 2006, van Eijs et al., 2006) revealed that the extraction induced seismicity occurs right below or directly above hydrocarbon reservoirs. In NW Germany, the shallow seismic events (between 5 and 9 km) in the vicinity of active hydrocarbon fields are located in reservoir depth or slightly deeper and mostly in the peripheral region. In comparison to results obtained from the routine analysis of the Federal Institute for Geosciences and Natural Resources, the hypocenters of the present study are located on average 3 km deeper. According to the hypocenter location, after a geometrical model of Segall (1989) or a deformation model of Odonne et al. (1999), thrust or reverse faulting was observed for locations above and below the reservoir. In most cases, the peripheral region is dominated by normal fault focal

mechanisms (Segall, 1989, Odonne et al., 1999). This fits very well for most of the shallow seismic events in NW Germany, which exhibit normal fault focal mechanisms mostly at reservoir boundary faults.

Spatial clustering is observed for most of the events in NW Germany. Only four events are located far away from natural gas reservoirs. Earthquake clusters are constrained to regions with ongoing hydrocarbon production. However, the database is very limited (greatest cluster at Völkersen hydrocarbon field, about 19 instrumentally registered events in 25 years) and difficult to compare with regions like Groningen (Dost et al., 2012, van Wees et al., 2014) or Lacq (Bardainne et al., 2008) where induced seismicity occurs forming huge clusters or swarms. Nevertheless, a possible association between recent seismicity and pre-existing faults derived by the 3-D subsurface modeling is observed for most parts in the study area. This finding is also observed for pre-existing faults for example in regions of Valhall and Ekofisk (Zoback and Zinke, 2002, Arrowsmith and Eisner, 2006), Lacq (Bardainne et al., 2008) or Groningen (Dost et al., 2012).

Temporal pattern: General poroelastic modeling (Segall, 1985) and observations, which were made for the temporal pattern of induced seismicity at Strachan sour gas field (Wetmiller, 1986), Cogdell oil field (Davis and Pennington, 1989), Groningen gas field (van Eck et al., 2006), Lacq gas field (Bardainne et al., 2008) or at gas fields in northern Germany reveal a significant delay time between the increase of seismicity and the beginning of hydrocarbon production. With regard to the lack of a seismic monitoring network right after the production had commenced the delay time is between 5 (Strachan, Wetmiller, 1986) and 28 years (Groningen, van Eck et al., 2006). Events in NW Germany occurred between 10 to 20 years after hydrocarbon production was established (Fig. 78, Gestermann, 2015 and present study). Fluid withdrawal leads to pore pressure reduction and reservoir compaction including subsurface subsidence (Yerkes and Castle, 1976, Grasso 1992). If the pore pressure reduction exceeds a threshold of about 10 MPa seismicity can be observed in the close proximity to a reservoir (Segall, 1989). Exact values of pore pressure reduction for hydrocarbon reservoirs in NW Germany are not known. However, there should be a correlation between reservoir characteristics such as pore pressure and time delay. The ambient tectonic stress pattern, which is also a significant factor for the occurrence of intraplate earthquakes is discussed in the next subchapter 8.2.2.

Faulting and source mechanisms: On intraplate seismicity, the recent stress field and crustal weak zones such as pre-existing faults are some of the main controlling factors (e.g. Sykes, 1978, Zoback and Zoback, 1981, Talwani and Rajendran, 1991). The determination of the

recent stress field in northern Germany seems to be difficult. Kaiser et al. (2005) defined the stress regime in northern Central Europe as compressional, whereas Röckel and Lempp (2003) show that the recent regional stress field of the North German Basin is dominated by normal faulting (Röckel and Lempp, 2003), which indicates an extensional stress regime. For most seismic events in the study area, normal fault focal mechanisms were determined. In case of natural, tectonic earthquakes, this supports the assumption of Röckel and Lempp, (2003).

Faulting and seismicity in NW Germany due to hydrocarbon production are only associated with the reactivation of pre-existing faults (Dahm et al., 2007, Bischoff et al., 2013, 2014, 2015) and not related to the formation of new faults. The latter case is only observed for extensive fluid extraction (Suckale, 2009) for example in Texas for Goose Creek (Yerkes and Castle, 1976). Thus, it appears that the fault pattern is one of the key factors to understand faulting and seismicity in northern Germany. Potential seismogenic active normal faults have to be parallel oriented to the maximum horizontal stress direction of the recent regional stress field to gain a high reactivation potential (Wiprut and Zoback, 2000). Marotta et al. (2002) compared the stress pattern with an opened fan in which S_{Hmax} (maximum principle horizontal stress) deviates in directions between NW-SE in the western part to NE-SW in the eastern part of northern Germany. Horst and graben structures of the Rotliegend rift basin (Fig. 79) investigated by Gast (1988) and Gast and Gundlach (2006) show the same fan structure as it was described by Marotta et al. (2002). In good agreement with that, in NW Germany, Permian basement normal faults, which were identified by the geological 3-D modeling, mainly trend NW-SE, NNW-SSE and roughly N-S. Most of the shallow seismic events cluster at these normal faults and show similar strike directions and kinematics of their fault plane solutions (Fig. 79). For the region of Langwedel/Völkersen, some strike directions of derived focal mechanisms differ significantly to superordinate Rotliegend rift basin faults, but still fit to the local fault pattern. In NW Germany, seismic event origins are related to these reactivated Rotliegend rift basin faults.

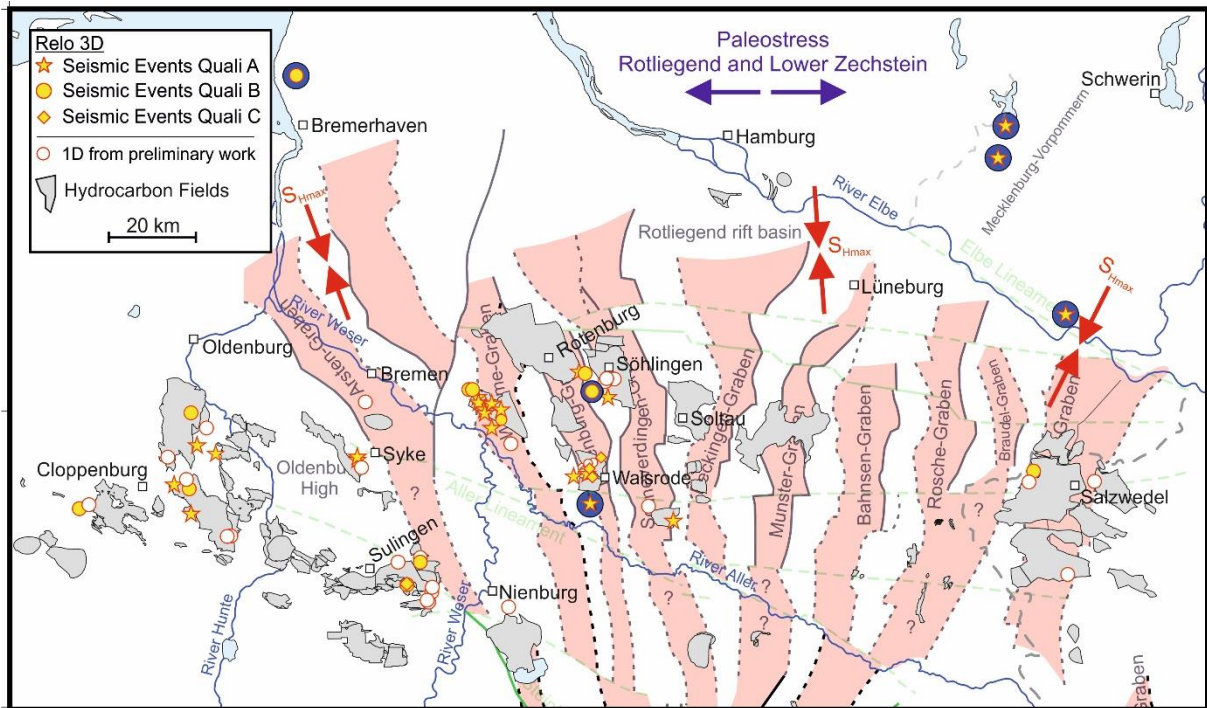


Figure 79. Relocated hypocenter in combination with the Rotliegend rift system in NW Germany. According to potential GIA-induced events, the Soltau 1977 event, the Rotenburg mainshock and the deep earthquakes are highlighted by blue circles. Red arrows indicate the inferred the recent maximum horizontal stress (S_{Hmax}) obtained from Reicherter et al. (2005). S_{Hmax} is based on evaluated subsalt formations by Röckel and Lempp (2003). The blue arrows indicate Rotliegend and Lower Zechstein rift E-W extension which was observed by Lohr et al. (2007). The map is modified after Gast (1988) and Gast and Gundlach (2006).

Most of the previously discussed common observations described by Suckale (2009, 2010) can also be observed for the shallow and small-to-moderate magnitude seismic events ($M_L \leq 3.9$) in northern Germany. A simplified sketch of how fault reactivation may result from gas extraction in northern Germany is shown in Figure 80. Assuming an extensional stress field, an investigated fault is optimally oriented, if its strike direction is almost parallel (or in line) to the maximum horizontal stress (S_{Hmax} , Fig. 80). In addition to that the fault reactivation potential increases if the observed fault indicates normal fault kinematics. The reservoir depletion leads to an additional extensional stress component in the peripheral region of hydrocarbon fields. Thus, the reactivation potential increases and movement along optimally oriented normal faults is possible.

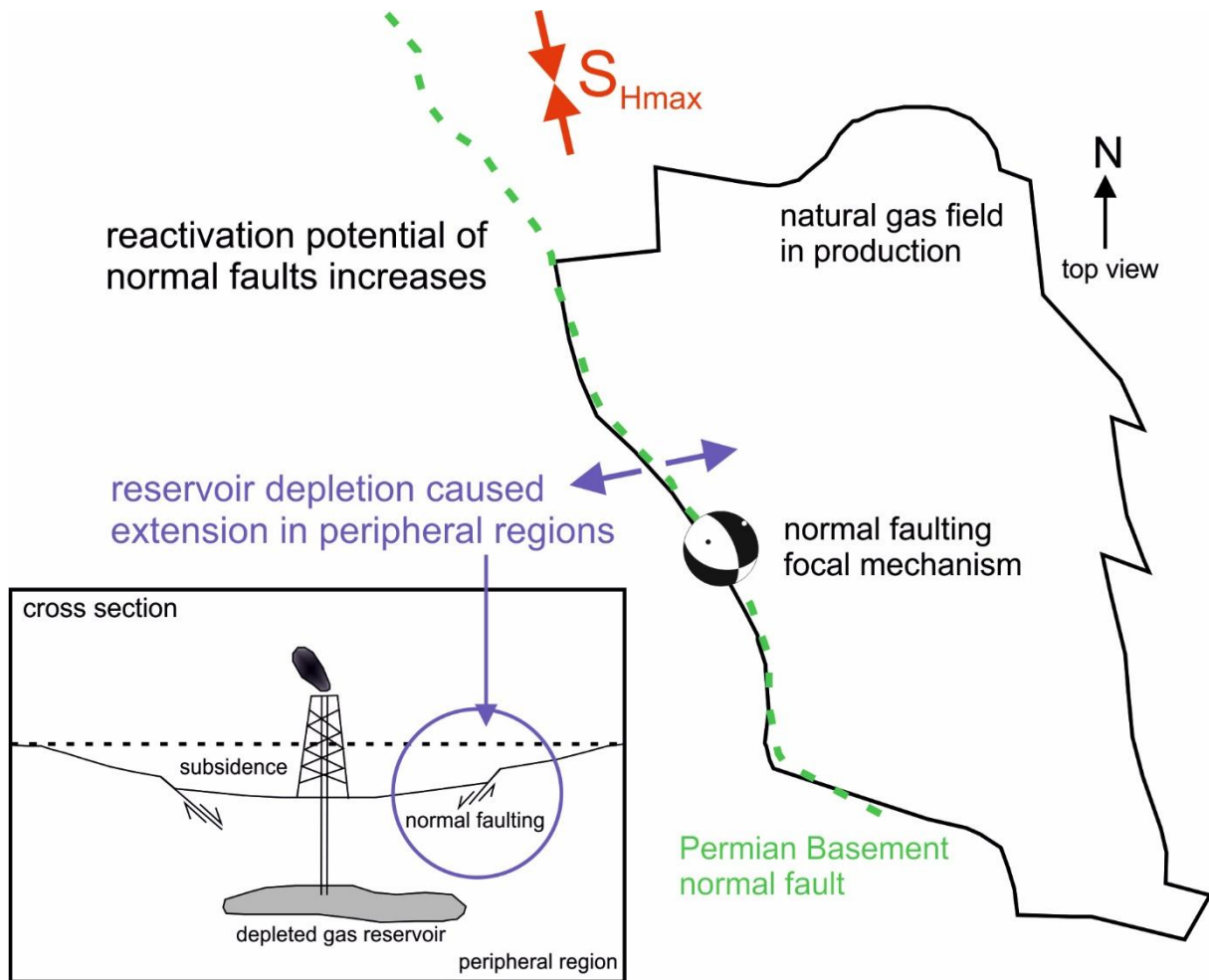


Figure 80. Fault reactivation due to gas extraction. Possible evidence obtained from seismological analyses and 3-D subsurface modeling in combination with the schematic cross section showing surface deformation and faulting (small box) modified after Segall (1989) and Odonne et al. (1999). Red arrows indicate the recent maximum horizontal stress obtained from Marotta et al. (2002).

8.2.2 Glacial isostatic adjustment and stress field

For a compressive stress regime, all investigated event locations in the study area reveal the potential of fault movement due to GIA-induced stress perturbations at nearly parallel to the former ice margin trending faults (WNW-ESE, called optimally oriented faults). Whereby, in an extensional stress regime, only models with high lithospheric thicknesses (more than 120 km) show fault instability, up to the present day. All the other models exhibit stable conditions. In the following, both possible stress regimes are taken into account.

GIA-induced stresses lose their influence on the recent stress field with increasing distance to the former ice margin. Modeling results show that optimally oriented faults in the region between Cloppenburg and Walsrode became unstable between 14 and 13 ka BP in a compressive stress regime. Whereas, optimally oriented faults in the very close proximity to the former ice margin may experience fault movement about 1,500 years earlier. These unstable fault conditions are in good agreement with results obtained from Brandes et al. (2015) for the Osning Thrust (50 km south of the study area) or for reverse faults in the area of the Magdeburger Börde or Altmark area (fault locations see Figure 8, chapter 4.1.3). Brandes et al. (2015) calculated the beginning of possible movement along these WNW-ESE trending Mesozoic reverse faults for times between 16 and 10 ka BP. For favorably oriented thrust faults, which are situated in a compressive stress regime, Late Pleistocene GIA-induced stress perturbations are a possible trigger mechanism in northern Germany. Brandes et al., (2015) also showed that GIA-induced stresses in an extensional stress regime cannot lead to fault reactivation. A finding, which is in good agreement with most observations concerning GIA numerical simulation results of the normal faulting regime in the present study.

After Brandes et al. (2012, 2015), fault and stress field characteristics for a potential postglacial seismicity in northern Germany can be derived (Fig. 81a) and are subsequently applied to recent findings of the seismicity pattern and fault structure in the study area (Fig. 81b). Thus, the possibility of glacially-induced seismic events can be confirmed or neglected. After Brandes et al. (2015) indicators for a high reactivation potential due to GIA-induced stresses for northern Germany are (Fig. 81a):

- faults parallel oriented to the former ice margin
- thrust faults in a compressive stress regime
- recent maximum horizontal stress (S_{Hmax}) almost perpendicular to the thrust faults
- maximum horizontal stress (S_{Hmax}) of the ice sheet-induced stress is in line with the recent maximum horizontal stress

In contrast, Figure 81b shows the assumed lower GIA-induced fault reactivation potential on the basis of the seismicity pattern and fault structure in the study area (Fig. 81b):

- faults with higher angles to the former ice margin
- mostly normal faulting in an extensional stress regime
- recent maximum horizontal stress (S_{Hmax}) almost parallel to the normal faults
- maximum horizontal stress (S_{Hmax}) of the ice sheet-induced stress is almost perpendicular to the Permian basement normal faults

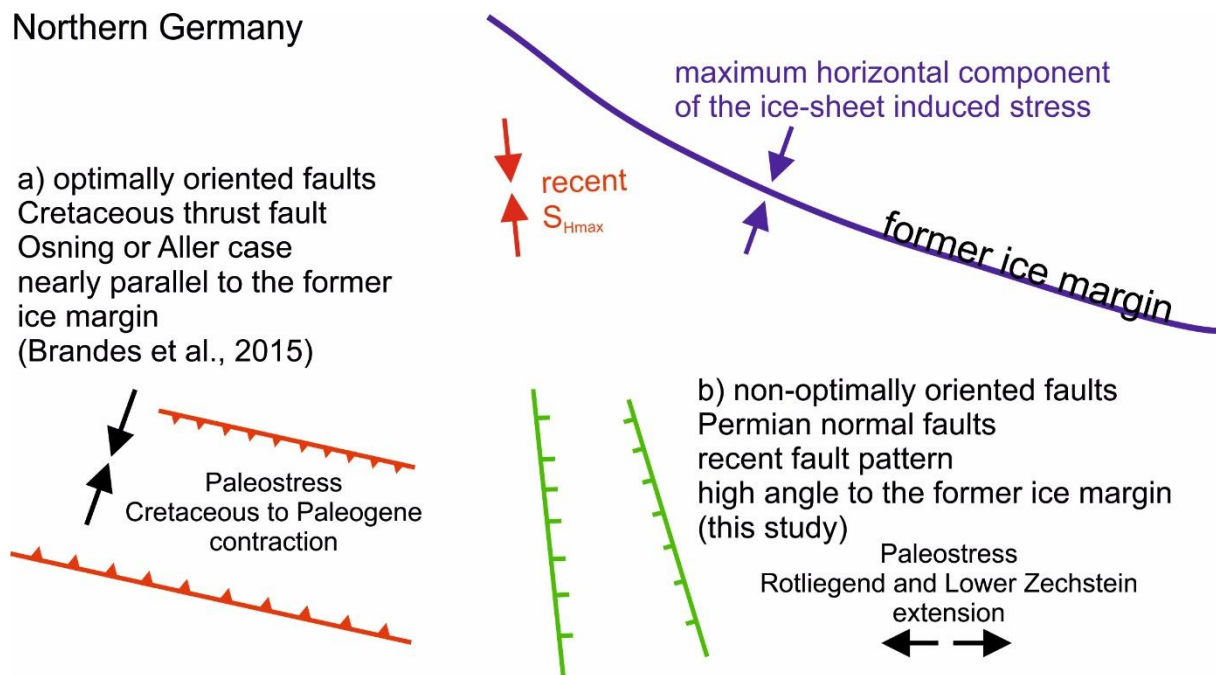


Figure 81. Schematic models of the fault reactivation potential of optimally- and non-optimally oriented faults due to GIA-induced stress perturbations for different fault patterns and stress regimes in northern Germany. **a)** Compressive stress regime and fault orientation obtained from the Osning Thrust investigation by Brandes et al. (2015). This example maintained a high fault reactivation potential due to GIA-induced stress perturbations **b)** Recent situation in the study area, which is compared with a) to reveal the fault reactivation potential due to GIA-induced stress perturbations.

In Late Cretaceous times, NW-SE trending reverse faults formed or were reactivated due to an almost N-S oriented compressional stress regime (Lohr et al., 2007, Kley and Voigt, 2008). Thus, the Cretaceous paleo S_{Hmax} is similarly oriented to the maximum horizontal stress in recent times (Marotta et al., 2002, Kaiser et al., 2005). The Cretaceous thrust faults investigated by Brandes et al. (2015) trend WNW-ESE and are regarded to be optimally oriented, which means nearly parallel to the former ice margin and almost perpendicular to the recent maximum horizontal stress (Brandes et al., 2015). The optimal orientation of these faults and in addition that the direction of the maximum horizontal stress of the Weichselian ice sheet is in-line with the compressive paleo stress orientation (cf. Stewart et al., 2000) lead to a high reactivation potential of these Cretaceous thrust faults induced by GIA stress perturbations (Brandes et al., 2015).

In contrast, almost all identified potential seismogenic active faults in the study area developed in Permian times and indicate normal fault movement with strike directions varying between NW-SE, NNW-SSE or roughly N-S (Fig. 81b). These normal faults show larger angles to the former ice margin. Thus, their reactivation potential decreases (Brandes et al., 2015). Recent seismic events are most probably related to these Permian basement faults below the base Zechstein. The paleo stress field of the Rotliegend and Early Zechstein was dominated by an E-W oriented extension (Lohr et al., 2007) that led to the formation of the Rotliegend rift basin system (Gast, 1988, Gast and Gundlach, 2006). The fan-like present-day S_{Hmax} (Marotta et al., 2002, Kaiser et al., 2005) is more or less perpendicular oriented to the Permian paleo stress direction and thus, trending nowadays nearly parallel to the Permian normal faults. The ice sheet-induced compressive stress direction show larger angles to these faults. Therefore, on the basis of this maximum horizontal component, the ice sheet-induced stress may reduce the reactivation potential of NW-SE, NNW-SSE or roughly N-S striking normal faults.

Due to the orientation of these Permian rift basin normal faults and the recent maximum horizontal stress, the reactivation potential for GIA-induced stresses decreases, while extensional stresses induced by reservoir depletion may increase the reactivation potential (Fig. 80). According to the common induced seismicity observations in chapter 8.2.1, most seismic events in northern Germany, especially shallow and low-to-moderate magnitude events ($M_L \leq 3.9$) in the vicinity of active hydrocarbon fields are most likely triggered by the gas extraction.

However, there are individual, significant earthquakes in the study area such as the Soltau 1977 event, the Rotenburg 2004 mainshock and all of the five deep seismic events (highlighted by a blue circle in Figure 79), which show the potential of being triggered by the glacial isostatic adjustment.

The earthquake near Soltau in 1977 ($M_L \sim 4.0$) is regarded as natural tectonic earthquake (Leydecker et al. 1980, Leydecker, 2011). This earthquake is located in depth between 4 to 13 km (Leydecker et al., 1980). At that time, a relationship with the beginning of gas extraction was not taken into account because hydrocarbon production was still established two years ago at the Munster gas field (Dahm et al., 2007). After Grasso and Wittlinger (1990), this is not enough time to provide a reliable relationship between hydrocarbon production and seismicity. Nevertheless, Dahm et al. (2007) try to find a possible relationship between gas extraction and the Soltau 1977. However, several databases and different localization techniques reveal different localizations of the Soltau 1977 event. It is evident that as long as no reliable location is provided, identifying causes for this earthquake is speculative. Indications for a natural tectonic origin are the low time span after natural gas withdrawal had commenced (after Davies

et al., 1995), a possible depth greater than 10 km and the potential oblique thrust fault focal mechanism (Leydecker et al., 1980). These evidence and the inferred instable fault conditions in the study area due to GIA may lead to a possible GIA-induced tectonic cause for the Soltau earthquake. Nevertheless, this hypothesis should be handled with care.

In recent studies, the mainshock of the strongest event ever recorded in northern Germany – the Rotenburg earthquake from October, 20th 2004 - is discussed with respect to the focal depth, fault plane solutions and possible driving mechanisms (Dahm et al., 2007, 2015). Similar to the Soltau 1977 event, a relative sparse database and the lack of a nearby station lead to higher epicentral and in particular, hypocenter uncertainty domains. For a reliable hypocenter estimation, Dahm et al. (2007) used teleseismic phase modeling (at seismological arrays in Canada and USA) and waveform fits to constrain the focal depth and focal mechanism. They located the mainshock in a depth between 5 and 7 km, which fits very well with the Söhlingen reservoir depth (Dahm et al., 2007). In addition, the determined normal fault focal mechanism in reservoir depth fits very well with theoretical models derived from Segall (1989) and Grasso (1992) to indicate a possible relationship between the Rotenburg earthquake and fluid withdrawal (Dahm et al., 2007). However, on the basis of the relative high magnitude of M_w 4.4, it is possible that more than one driving force is responsible to cause moderate intraplate earthquakes ($M_L \geq 4.0$) in NW Germany, in contrast to the smaller ones. For example, Dahm et al. (2015) used a probabilistic approach to discriminate between human-induced and human-triggered events. According to McGarr and Simpson (1997) and Cesca et al. (2013), triggered seismic events are mostly controlled by the background stress, while the triggering process itself forces the nucleation for only a frictional amount, which is sufficient to initiate movement along a fault. In contrast, human activities in the subsurface are necessary to release energy in form of induced seismicity. Stress changes related to these subsurface operations lead to slip at pre-existing faults (Cesca et al., 2013). For the Rotenburg mainshock, the likelihood of being triggered is predicted with 74 % and a probability of induced is given by 46 % (Dahm et al., 2015). A natural trigger component such as GIA-induced stress perturbations were not included within the evaluation.

Assuming the hypocenter depth of about 13 km (constrained by the evaluation of synthetic seismograms in chapter 6.2.2), the second possible fault plane solution of a thrust fault movement (second solution, see Table 12) and a compressive stress regime in northern Germany, then the possibility exists that the Rotenburg mainshock in 2004 is caused by GIA-induced stress changes. Nevertheless, both, the high potential of being triggered (see Dahm et al., 2015) and the GIA-induced instability of faults in the Rotenburg/Söhlingen region (present study) should be considered together while defining a possible trigger mechanism for the Rotenburg mainshock. Hence, for both stress regimes (compressional and extensional)

GIA is possibly responsible to bring faults very close to failure and only small changes in the stress field e.g. due to reservoir depletion (small pore pressure drop, Segall, 1989) trigger movement along faults. The interaction between a major natural (GIA-induced) and minor trigger component may cause the Rotenburg mainshock in 2004.

In case of five very deep seismic events in the study area, ranging in depth between 13 and 42 km, until now, no reliable trigger mechanism is provided. The database for these depth ranges is very limited, for them GIA-induced stress changes may reveal one possible natural driving force. Human-induced causes are most likely excluded for these depth ranges because each assumed induced seismic event distributed all over the world is more or less concentrated at reservoir depth and restricted to the uppermost 10 km of Earth's crust (Wetmiller, 1986, van Eck, 2006, van Eijs, 2006, Dahm et al., 2007, Bardainne et al., 2008, Bischoff et al., 2013, 2014, 2015).

9. CONCLUSIONS

In the last 25 years, 77 seismic events occurred in the low seismically active region of northern Germany. The majority of these events is concentrated along the hydrocarbon reservoir belt from Cloppenburg in the west to Salzwedel in the east. Therefore, most of them are regarded to be of anthropogenic origin. Historic seismic events and a few recent earthquakes form evidence for a tectonic driving force located side-by-side to the assumed anthropogenic trigger mechanism. In this study, recent earthquakes were investigated in detail to identify their possible causes. The first step was a relocalization using the probabilistic method imprinted within NonLinLoc in combination with a new approach of applying two differently scaled 3-D *P*-wave-velocity models. The 3-D relocalization was of main importance to derive improved hypocenters and thereby a better overview on the seismicity pattern. In the second step, a 3-D geological subsurface modeling was conducted with GOCAD© to link the previously relocated hypocenters with existing fault structures. Subsequently, the earthquake locations were investigated by numerical simulations to reveal their potential of being induced by stress changes resulting from the decay of the Late Pleistocene Scandinavian ice sheet. The main results of the present study are summarized as follows:

For 36 out of 40 relocated events in NW Germany reliable hypocenter locations with high accuracy were derived. Location uncertainties have been reduced by almost 50 % in contrast to usually used 1-D localization procedures. Looking only at the focal depth, the uncertainties were reduced by nearly 40 % to a mean value below 1.2 km. This improvement in the hypocenter locations is attributed to the application of the two differently scaled 3-D velocity models. Due to the newly inferred, more reliable focal depths in combination with very small calculated horizontal uncertainties, the seismic events in northern Germany can now be better associated with subsurface structures to reveal the most probable earthquake causes.

The newly derived epicenters are predominantly pinpointed at the boundaries of the natural gas fields and some of them lie inside. Furthermore, the focal depths of the relocated events are either in the depth horizon of the gas extraction or partially slightly deeper (5 - 9 km), which indicates a correlation between the occurrence of seismic events and the ongoing gas production. Both findings are important because common stress models of Segall (1989) and Odonne et al. (1999) support the assumption of an induced seismicity in reservoir surroundings due to the fluid withdrawal.

Five seismic events are deep (below 13 km). Except one of them, they are located in the north of the study area, in a distance of 70 km - 120 km to the natural gas fields and therefore of

undoubted tectonic origin. The seismic event south of Walsrode (November, 2nd 2014) is this one exception. The 3-D relocalization in the present study yields a reliable focal depth of about 23 km, whereas the 1-D linearized localization technique was not able to determine a reliable hypocenter depth. Since the quality of the observations is good and the uncertainties are small this event must be of lower crustal origin. This Walsrode event is the first well constrained example for a recent tectonic earthquake in the vicinity of hydrocarbon fields in NW Germany.

From the 3-D relocalizations, it turned out that seismic events in northern Germany are mostly concentrated along the NNW-SSE or N-S trending Rotliegend graben faults. In addition, the determined fault plane solutions indicate NW-SE, NNW-SSE, roughly N-S and in some cases WNW-ESE trending normal fault movement, which fits very well with the identified regional fault pattern. Due to the correlation between hypocenters, fault plane solutions and the geological 3-D modeling, 25 potential seismogenic active faults were identified.

Depending on the assumed stress regime, numerical simulations of GIA-induced stress changes related to the melting of the Late Pleistocene ice sheet reveal both, the reactivation or inhibition potential of optimally oriented faults. In a compressional stress regime, GIA-induced stress perturbations are a potential tectonic driving mechanism for earthquakes in the study area as it was also described by Brandes et al. (2015) for historical seismic events at the Osning Thrust (50 km away from the study area), at reverse faults in the Altmark area, at faults in the region of Halle (SE of the study area) and in southern Sweden. Each model indicates the potential of fault movements due to GIA-induced stress perturbations at present day. However, the derived normal fault focal mechanisms for seismic events imply an extensional stress regime in the study area. This leads to the assumption that fault movement is inhibited for most of the applied GIA-models.

The observed similarities to human-induced seismicity distributed all over the world and the spatio-temporal pattern of shallow seismic events (5 – 9 km) in the vicinity of active hydrocarbon fields, yielding magnitudes of $M_L \leq 3.9$ lead to the conclusion that these events are most likely induced by the natural gas extraction. In contrast, origins for deep earthquakes (depth > 13 km) in northern Germany are difficult to derive. However, the results clearly indicate that also GIA-induced stress changes as a result of the melting of the Late Pleistocene ice sheet play a role in case of fault reactivation in the study area.

Except two destructive earthquake sequences (Coalinga, USA 1983-1987, McGarr, 1991, McGarr et al., 2002 and Gazli, Uzbekistan 1976-1984, Simpson and Leith, 1985), which are more or less suspected to be connected with hydrocarbon production and a $M_L \sim 4.2$ event at the Lacq gas field (Bardainne et al., 2008), no seismic event that is related to hydrocarbon

extraction in intraplate regions distributed all over the world exceed the local magnitude of 4. Dahm et al. (2015) determined a high probability that the Rotenburg earthquake is most likely triggered and my determined depth of 13 km including a possible thrust fault focal mechanism indicate a more complex earthquake driver. On this basis, I draw a potential scenario that stronger seismic events ($M_L \geq 4.0$) of greater depth in northern Germany may be related to an interaction between major tectonic-induced stress changes like GIA and a minor depletion triggered component. Nevertheless, for the Rotenburg 2004 mainshock and the Soltau event from 1977 an assessment of causes cannot be finally given. Therefore, further investigations are of great interest, especially on the basis of a reliable risk assessment for the future in northern Germany.

REFERENCES

Ahmadi, O., Juhlin, C., Ask, M. and Lund, B. – Revealing the deeper structure of the end-glacial Pärvie fault system in northern Sweden by seismic reflection profiling. *Solid Earth*, Vol. 6, pp. 621 – 632, (2015).

Ahorner, L. – Present-day stress field and seismotectonic block movements along major fault zones in central Europe. *Tectonophysics*, Vol. 29, pp. 233 – 249, (1975).

Aki, K. – Seismicity and seismological method. Volume 6, Issue 1, pp. 41 – 58, (1968).

Amante, C. and Eakins, B.W. - ETOPO1 1 Arc-Minute Global Relief Model: Procedures, Data Sources and Analysis, (NOAA Technical Memorandum: ESDIS / National Environmental Satellite, Data, and Information Service; NGDC-24), National Geophysical Data Center, National Oceanic and Atmospheric Administration. DOI: <http://doi.org/10.7289/V5C8276M> (2009).

Arrowsmith, S.J. and Eisner, L. – A technique for identifying microseismic multiplets and application to the Valhall field, North Sea. *Geophysics*, Vol. 71, No. 2, pp. V31 – V40, (2006).

Arsdale, R.V. – The New Madrid seismic zone of the Central United States. In *Intraplate Earthquakes*, ed. **Talwani, P.**, Cambridge University Press, New York, 338 p., (2014).

Arvidsson, R. – Fennoscandian earthquakes: Whole crustal rupturing related to postglacial rebound. *Science*, Vol. 274, pp. 744 – 746, (1996).

Bachmann, G.H. and Grosse, S. - Struktur und Entwicklung des Norddeutschen Beckens - geologische und geophysikalische Interpretation einer verbesserten Bouguer-Schwerekarte. *Nds Akad Geowiss Veröfftl.* Vol. 2, pp. 23- 47, (1989).

Bachmann, G.H., Voigt, T., Bayer, U., von Eynatten, H., Legler, B. and Littke, R. – Depositional history and sedimentary cycles in the Central European Basin System. In **Littke, R., Bayer, U., Gajewski, D. and Nelskamp, S.** - Dynamics of complex intracontinental basins. The example of the Central European Basin System.– Springer-Verlag, Berlin-Heidelberg, 519 p. (ISBN: 978-3-540-85084-7), (2008).

Bai, L., Wu, Z., Zhang, T. and Kawasaki, I. – The effect of distribution of stations upon location error: Statistical tests based on the double-difference earthquake location algorithm and the bootstrap method. *Earth Planets Space*, Vol. 58, pp. e9 – e12, (2006).

Baldschuhn, R., Best, G. and Kockel, F. – Inversion tectonics in the north-west German basin. In: Spencer, A.M. (ed) *Generation accumulation and production of Europe's hydrocarbons.* Spec Publ European Ass Petrol Geoscien 1, pp. 149 – 159, (1991).

Baldschuhn, R., Binot, F., Fleig, S. and Kockel, F. - Geotektonischer Atlas von Nordwest-Deutschland und dem deutschen Nordsee-Sektor. *Geol Jb, A*, 153, pp. 3 - 95, (2001).

Baranova, V., Mustaqeem, A. and Bell, S. – A model for induced seismicity caused by hydrocarbon production in the Western Canada Sedimentary Basin. *Can. J. Earth Sci.*, Vol. 36, pp. 47 – 64, (1999).

Bardainne, T., Bubos-Sallée, N., Sénéchal, G., Gaillot, P. and Perroud, H. – Analysis of the induced seismicity of the Lacq gas field (Southwestern France) and model deformation. *Geophys. J. Int.*, Vol. 172, pp. 1151 – 1162, (2008).

Bassin, C., Laske, G. and Masters, G., The Current Limits of Resolution for Surface Wave Tomography in North America, *EOS Trans AGU*, 81, F897, (2000).

Bath, M. – Energy and tectonics of Fennoscandian earthquakes. *Tectonophysics*, Vol. 50, pp 9 – 17, (1978).

Bayer, U., Grad, M., Pharaoh, T.C., Thybo, H., Guterch, A., Banka, D., Lamarche, J., Lassen, A., Lewerenz, B., Schek, M. and Marotta, A.-M. – The southern margin of the East European Craton-new results from seismic sounding and potential fields between the North Sea and Poland. *Tectonophysics*, 360, pp. 301 – 314, (2002).

Berger, A.L. – Long-Term Variations of daily insolation and Quarternary climatic change. *Journal of the Atmospheric Sciences*, Vol. 35, pp. 2362 – 2367, (1978).

Best, G. and Zirngast, M. - Die strukturelle Entwicklung der exhumierten Salzstruktur "Oberes Allertal". *Geologisches Jahrbuch*, A1, 100 p., (2002).

Berglund, M. and Dahlström, N. – Post-glacial fault scarps in Jämtland, central Sweden. *GFF*, Vol. 137, Issue 4, pp. 339 – 343, (2015).

Béthoux, N., Theunissen, T., Beslier, M.-O., Font, Y., Thouvenot, F., Dessa, J.-X., Simon, S., Courrioux, G. and Guillen, A. – Earthquake relocation using a 3D a-priori geological velocity model from the western Alps to Corsica: Implication for seismic hazard. *Tectonophysics*, Vol. 670, pp. 82 – 100, (2016).

Betz, D., Führer, F. Greiner, G. and Plein, E. – Evolution of the Lower Saxony Basin. *Tectonophysics* Vol. 137, pp. 127 – 170, (1987).

Biddle, K.T. – The Los Angeles basin: an overview. *Active margin basins*, pp. 5 - 24, (1991).

Bischoff, M., Bönnemann, C., Ceranna, L., Fritz, J., Gestermann, N., Pasternak, M. and Plenefisch, T. – Kurzbericht zum Erdbeben bei Emstek (Landkreis Cloppenburg) am 19.12.2014 – Seismologische Auswertung, Report, 24 p., (2015).

Bischoff, M., Ceranna, L., Fritz, J., Gestermann, N. and Plenefisch, T. – Untersuchungsergebnisse zum Erdbeben bei Syke (Landkreis Diepholz) am 01.05.2014 – Seismologische Auswertung, Report, 33 p., (2014).

Bischoff, M., Bönnemann, C., Fritz, J., Gestermann, N. and Plenefisch, T. - Untersuchungsergebnis zum Erdbeben bei Völkersen (Landkreis Verden) am 22.11.2012; Report. LBEG / BGR. Hannover, 60 p., (2013).

Blendinger, W., Brack, P., Norborg, A.K. and Wulff-Pedersen, E. – Three-dimensional modelling of an isolated carbonate buildup (Triassic, Dolomites, Italy) – *Sedimentology*, 51, pp. 297 – 314, (2004).

Blundell, D., Freeman, R. and Müller, S. - A continent revealed-The European Geotraverse, Cambridge University Press, Book 275 p., CDROM and Map box, (1992).

Bock, G., Wylegalla, K., Stromeyer, D. and Grünthal, G. – The Wittenburg MW = 3.1 Earthquake of May 19, 2000: an unusual tectonic event in northeastern Germany – In: Korn, W. (Eds.) Ten Years of German Regional Seismic Network (GRSN), Kommission für Geowissenschaftliche Gemeinschaftsforschung (DFG), pp. 220 – 226, (2002).

Bommer, J.J., Dost, B., Edwards, B., Stafford, P.J., van Elk, J., Doornhof, D. and Ntinalexis, M. – Developing an application-specific ground-motion model for induced seismicity. *Bulletin of the Seismological Society of America*, Vol. 106, no. 1, pp. 158 - 173, (2016).

Bondar, I., Myers, S.C., Engdahl, R. and Bergmann, E.A. – Epicentre accuracy based on seismic network criteria. *Geophys. J. Int.*, Vol. 156, pp. 483 – 496, (2004).

Bormann, P. (Ed.) - New Manual of Seismological Observatory Practice (NMSOP-2), IASPEI, GFZ German Research Centre for Geosciences, Potsdam; <http://nmsop.gfz-potsdam.de>; DOI: 10.2312/GFZ.NMSOP-2urn:nbn:de:kobv:b103-NMSOP-2, (2012).

Brandes, C. and Winsemann, J. – Soft-sediment deformation structures in NW Germany caused by Late Pleistocene seismicity. *Int. J. Earth Sci (Geol Rundsch)*, Vol. 102, pp. 2255 – 2274, (2013).

Brandes, C., Schmidt, C., Tanner, D.C. and Winsemann, J. – Paleostress pattern and salt tectonics within a developing foreland basin (north-western Subhercyn Basin, northern Germany. *International Journal of Earth Sciences*, Vol. 102, pp. 2239 – 2254, (2013).

Brandes, C., Steffen, H., Steffen, R. and Wu, P. – Intraplate seismicity in northern Central Europe is induced by the last glacialiation. *Geology*, Vol. 43, Issue 7, 26 May 2015, pp. 611-614, (2015).

Brandes, C., Winsemann, J., Roskosch, J, Meinsen, J., Tanner, D.C., Frechen, M., Steffen, H. and Wu, P. - Activity of the Osning thrust during the Lateglacial: ice-sheet and lithosphere interactions. *Quaternary Science Reviews*, Vol. 38, pp. 49 - 62, (2012).

Bratt, S.R. and Bache, T.C. - Locating events with a sparse network of regional arrays. *Bulletin of the Seismological Society of America*, Vol. 78, Issue 2, pp. 780 - 798, (1988).

Brown, L.D. and Oliver, J.E. – Vertical crustal movements from leveling data and their relation to geologic structure in the Eastern United States. *Reviews of Geophysics and Space Physics*. Vol. 14, no. 1, pp. 13 – 35, (1976).

Bungum, H., Olesen, O., Pascal, C., Gibbons, S., Lindholm, C. and VestØI, O. - To what extent is the present seismicity in Norway driven by post-glacial rebound? *Journal of the Geological Society, London*, Vol. 167, pp. 373 - 384, (2010).

Calais, E., Freed, A.M., van Arsdale, R. and Stein, S. - Triggering of New Madrid seismicity by late-Pleistocene erosion. *Nature* 466, 608, (2010).

Camelbeek, T. and van Eck, T. – The Roer Valley Graben earthquake of 13 April 1992 and its seismotectonic setting. *Terra Nova*, Vol. 6, pp. 291 – 300, (1994).

Camelbeek, T., Vanneste, K., Alexandre, P., Verbeek, K., Petermans, T., Rosset, P., Everaerts, M., Warnant, R. and Van Camp, M. – Relevance of active faulting and seismicity studies to assessments of long-term earthquake activity and maximum magnitude in intraplate northwest Europe between the Lower Rhine Embayment and the North Sea. *GSA Special Papers*, Vol. 425, pp. 193 – 224, (2007).

Carcione, J.M., Picotti, S., Gei, D. and Rossi, G. – Physics and seismic modeling for monitoring CO₂ storage. *Pure appl. geophys.*, Vol. 163, pp. 175 – 207, (2006).

Cesca, S., Dost, B. and Oth, A. – Preface to the special issue “Triggered and induced seismicity: probabilities and discrimination” – *J Seismol*, Vol. 17, pp. 1 – 4, (2013).

Choukroune, P. – Tectonic evolution of the Pyrenees. *Annual Review of Earth and planetary sciences*, Vol. 20, pp. 143 – 158, (1992).

Church, J., Clark, P., Cazenave, A., Gregory, J., Jevrejeva, S., Levermann, A., Merrifield, M., Milne, G., Nerem, R., Nunn, P., Payne, A., Pfeffer, W. and Stammer, D. - Contribution of working group I to the fifth assessment report of the intergovernmental panel on climate change. In: **Stocker, T., Qin, D., Plattner, G.K., Tignor, M., Allen, S., Boschung, J., Nauels, A., Xia, Y., Bex, V. and Midgley, P. (eds)** - *Climate change 2013: the physical science basis*. Cambridge University Press, Cambridge, pp. 1138–1191, (2013).

Clark, P.U., Dyke, A.S., Shakun, J.D., Carlson, A.E., Clark, J., Wohlfarth, B., Mitrovica, J.X., Hosteller, S.W. and McCabe, A.M. – The Last Glacial Maximum. *Science*, Vol. 325, issue 5941, pp. 710 – 714, (2009).

Clark, J.A., Farrell, W.E., Peltier, W.R. - Global changes in postglacial sea level: a numerical calculation. *Quaternary Research*, Vol. 9(3), pp. 265 – 287, (1978).

Clark, D., McPherson, A., and Van Dissen, R. – Long-term behaviour of Australian stable continental region (SCR) faults. *Tectonophysics*, Vol. 566 – 567, pp. 1 – 30, (2012).

Cohen, K.M., Finney, S.C., Gibbard, P.L. and Fan, J.-X. – The ICS International Chronostratigraphic Chart, Episodes 36, pp. 199 – 2004, (2013; updated).

Costain, J.K. – Intraplate seismicity, hydroseismicity, and predictions in hindsight. *Seismological Research Letters*, Vol. 79, no. 4, pp. 579 – 589, (2008).

Costain, J.K., Bollinger, G.A. and Speer, J.A. - Hydroseismicity – A hypothesis for the role of water in the generation of intraplate tectonics. *Geology*, Vol. 15, pp. 618 - 621, (1987).

Costain, J.K. and Bollinger, G.A. - Review: Research results in hydroseismicity from 1987 to 2009. *Bulletin of the Seismological Society of America*, Vol. 100, pp. 1841 - 1858, (2010).

Craven, J. – Paleoseismological study in the New Madrid Seismic Zone using geological and archeological features to constrain ages of Liquefaction Deposits M.S., thesis: Memphis, Tennessee, University of Memphis, 51 p., (1995).

D'Alessandro, A., Luzio, D., D'Anna, G. and Mangano, G. – Seismic network evaluation through simulation: An application to the Italian National Seismic Network. *Bulletin of the Seismological Society of America*, Vol. 101, Issue 3, pp. 1213 – 1232, (2011).

Dahm, T., Krüger, F., Stammer, K., Klinge, K., Kind, R., Wylegalla, K. and Grasso, J.-R. - The 2004 Mw 4.4 Rotenburg, Northern Germany, earthquake and its possible relationship with gas recovery. *Bulletin of the Seismological Society of America*, Vol. 97, Issue 3, pp. 691 – 704, (2007).

Dahm, T., Hainzl, S., Becker, D., Bisschoff, M., Cesca, S., Dost, B., Fritschen, R., Kuhn, D., Lasocki, S., Klose, C. D., Meier, T., Ohrnberger, M., Rivalta, E., Shapiro, S. and Wegler, U. - How to discriminate induced, triggered and natural seismicity, *Proceedings of the Workshop Induced seismicity: November 15 - 17, 2010, Hotel Hilton, Luxembourg, Grand-Duchy of Luxembourg, (Cahiers du Centre Européen de Géodynamique et de Séismologie, 30), Centre Européen de Géodynamique et de Séismologie, 69, (2010).*

Dahm, T., Cesca, S., Hainzl, S., Braun, T. and Krüger, F. - Discrimination between induced, triggered, and natural earthquakes close to hydrocarbon reservoirs: A probabilistic approach based on the modeling of depletion-induced stress changes and seismological source parameters. *J. Geophys. Res. Solid Earth*, Vol. 120, pp. 2491 – 2509, (2015).

Daly, R.A. – Oscillations of level in the belts peripheral to the Pleistocene ice-caps. *Bulletin of the Seismological Society of America*, Vol. 31, pp. 303 – 318, (1920).

Daly, R.A. - The changing world of the ice age. New Haven: Yale University Press, 271p., (1934).

Daniel, G., Fortier, E., Romijn, R. and Oates, S. – Location results from borehole microseismic monitoring in the Groningen gas reservoir, Netherlands. *Conference Paper, 6th EAGE Workshop on Passive Seismic*, pp. 87 – 92, (2016).

Davis, S. D. and Pennington, W. D. - Induced seismic deformation in the Cogdell oil field of West Texas. *Bulletin of the Seismological Society of America*, Vol. 79, pp. 1477 - 1495, (1989).

Davies, S. D., Nyffenegger, P. A. and Frohlich, C. – The 9 April 1993 Earthquake in South-Central Texas: Was It Induced by Fluid Withdrawal? *Bulletin of the Seismological Society of America*, Vol. 85, No. 6, pp. 1888 - 1895, (1995).

Dehls, J.F., Olesen, E., Olsen, L. and Blikra, L.H. – Neotectonic faulting in northern Norway; the Stuuragurra and Nordmannvikdalen postglacial faults. *Quaternary Science Reviews*, Vol. 19, pp. 1447 – 1460, (2000).

Deichmann, N. – Focal depths of earthquakes below Switzerland. Excerpt from Deichmann et al.: Earthquakes in Switzerland and surrounding regions during 1999, *Eclogae Geol. Helv.*, Vol. 93, pp. 395 - 406, (2003).

Deichmann, N., Baer, M., Braunmiller, J., Cornou, C., Fäh, D., Giardini, D., Gisler, M., Huber, S., Husen, S., Kästli, P., Kradolfer, U., Mai, M., Maraini, S., Oprsal, I., Schler, T., Schorlemmer, D., Wiemer, S., Wössner, J. and Wyss, A. - Earthquakes in Switzerland and surrounding regions during 2003. *Eclogae geol. Helv.*, Vol. 97, pp. 447 – 458, (2004).

Diehl, T. and Kissling, E. - Users Guide for Consistent Phase Picking at Local to Regional Scales, 37. p. (2009).

Diehl, T., Clinton, J., Kraft, T., Husen, S., Plenkers, K., Guilhelm, A., Behr, Y., Cauzzi, C., Kästli, P., Haslinger, F., Fäh, D., Michel, C. and Wiemer, S. - Earthquakes in Switzerland and surrounding regions during 2013. *Swiss J Geosci*, Vol. 107: pp. 359 – 375, (2014).

De Kemp, E.A. – 3-D geological modelling supporting mineral exploration. – In: **Goodfellow, W.D.** (ed): Mineral deposits of Canada: a synthesis of major deposit types, district metallogeny, the evolution of geological provinces, and exploration methods. - Spec. Publ., Geol. Assoc. Canada, Mineral Deposits Division, 5, pp. 1051 – 1061, St. John's, (2007).

DMT (German Montane Technology GmbH) – Jahresbericht-Seismisches Messnetz Norddeutschland. Annual report 2015, 13 p., (2016).

Doornebal, H. and Stvenson, A. – Petroleum Geological Atlas of the Southern Permian Basin Area. EAGE Publications BV, 354 p., (2010).

Dost, B., Goutbeek, F., van Eck, T. and Kraaijpoel, D. – Monitoring induced seismicity in the North of the Netherlands-status report 2010. KNMI Scientific Report, WR 2012-13, 46 p., (2012).

Drong, H.-J. – Diagenetische Veränderungen in den Rotliegend Sandsteinen im NW-Deutschen Becken. *Geologische Rundschau*, Vol. 68, issue 3, pp. 1172 – 1183, (1979).

Dziewonski, A.M. and Anderson, D.L. – Preliminary reference Earth model. *Physics of the Earth and Planetary Interiors*, Vol. 25, pp. 297 – 356., (1981).

Eaton, D.W. and Mahani, A.B. – Focal mechanisms of some inferred induced earthquakes in Alberta, Canada. *Seismological Research Letters*, Vol. 86, no. 4, pp. 1078 – 1085, (2015).

Edelmann, I. - An analytical interpretation of liquid injection induced microseismicity in porous reservoirs. *Soil Dynamics and Earthquake Engineering*, Vol. 26, pp. 566 - 573, (2006).

Ehlers, J., Grube, A., Stephan, H.-J. and Wansa, S. – Pleistocene glaciations if North Germany-New results. *Developments in Quaternary Science*, Vol. 15, pp. 149 – 162, (2011).

Ellsworth, W.L. – Injection-Induced Earthquakes. *Science*, Vol. 341, 8 p., (2013).

Elsner, H., - Verbreitung und Ausbildung Elster-zeitlicher Ablagerungen zwischen Elm und Flechtinger Höhenzug. Eiszeitalter und Gegenwart, Vol. 52, pp. 91 – 116 (2003).

Emoto, K., Sato, H. and Nishimura, T. – Synthesis of vector wave envelopes on the free surface of a random medium for the vertical incidence of a phase wavelet based on the Markov approximation. Journal of Geophysical Research, Vol. 115, B08306, 15 p., (2010).

Eulenfeld, T. and Wegler, U. - Measurement of intrinsic and scattering attenuation of shear waves in two sedimentary basins and comparison to crystalline sites in Germany, Geophys. J. Int., Vol. 205 (2), pp. 744 – 757, (2016).

Evans, D., Graham, C., Armour, A. and Bathurst, P. - The Millennium Atlas: Petroleum geology of the central and northern North Sea. Geol Soc Lond, 389 p., (2003).

Farrell, W.E. and Clark, J.A. – On postglacial sea level. Geophys. J. R. astr. Soc., Vol. 46, pp. 647 – 667, (1976).

Feng, F. and Bailer-Jones, C.A.L. – Obliquity and precession as pacemakers of Pleistocene deglaciations. Quaternary Science Reviews, vol. 122, pp. 166 – 179, (2015).

Fischer, T. and Horálek, J. – Refined locations of the swarm earthquakes in the Nový Kostel Focal Zone and Spatial Distribution of the January 1997 swarm in Western Bohemia, Czech Republic. Studia Geophysica et Geodetica, Vol. 44, Issue 2, pp. 210 – 226, (2000).

Fjeldskaar, W. – The amplitude and decay of the glacial forebulge in Fennoscandia. Norsk Geologisk Tidsskrift, Vol. 74, pp. 2 – 8, (1994).

Fjeldskaar, W., Lindholm, C., Dehls, J.F. and Fjeldskaar, I. – Postglacial uplift, neotectonics and seismicity in Fennoscandia. Quaternary Science Reviews, Vol. 19, pp. 14113 – 1422, (2000).

Ford, J. R., Mathers, S. J., Royse, K. R., Aldiss, D. T. and Morgan, D. J. R. - Geological 3D modelling: Scientific discovery and enhanced understanding of the sub-surface, with examples from the UK. British Geological Survey, Keyworth, Report, 22 p., (2010).

Frisch, U. and Kockel, F. - Der Bremen-Knoten im Strukturnetz Nordwest-Deutschlands. BGR Hannover, Hannover, 379 p., (2003).

Fritschen, R. and Kremers, S. – Sensitivitätsstudie des Geschwindigkeitsmodells in Norddeutschland. Report, 33 p., (2013).

Fuchs, K. and Müller, G. – Computation of synthetic seismograms with the reflectivity method and comparison with observations. Geophys. J. R. astr. Soc., Vol. 23, pp. 417 – 433, (1971).

Gagnepain-Beyneix, J. - Evidence of Spatial Variations of Attenuation in the Western Pyrenean Range. Geophys. J. R. astr. SOC., Vol. 89, pp. 681 - 704, (1987).

Gaite, B., Ugalde, A., Villasenor, A. and Blanch, E. – Improving the location of induced earthquakes associated with and underground gas storage in the Gulf of Valencia (Spain). *Physics of the Earth and Planetary Interiors*, Vol. 254, pp. 46 – 59, (2016).

Gajewski, D. and Tessmer, E. – Reverse modelling for seismic event characterization. *Geophys. J. Int.*, Vol. 163, pp. 276 – 284, (2005).

Gast, R. E. – Rifting im Rotliegenden. *Die Geowissenschaften*. 6. Jahrgang, Heft 4, pp. 103 – 136, (1988).

Gast, R. E. and Gundlach, T. – Permian strike slip and extensional tectonics in Lower Saxony, Germany. *Z. dt. Ges. Geowiss.*, 157/1, pp. 41 – 56, (2006).

Gaupp, R., Möller, P., Lüders, V., die Primio, R. and Littke, R. – Fluids in sedimentary basins: an overview. In **Littke, R., Bayer, U., Gajewski, D. and Nelskamp, S.** - Dynamics of complex intracontinental basins. The example of the Central European Basin System.– Springer-Verlag, Berlin-Heidelberg, 519 p. (ISBN: 978-3-540-85084-7), (2008).

Geissler, W.H., Sodoudi, F. and Kind, R. – Thickness of the central and eastern European lithosphere as seen by S receiver funtions. *Geophys. J. Int.*, Vol. 181, pp. 604 – 634, (2010).

Gestermann, N. – Zusammenhang zwischen Seismizität und hydraulischen Gesteinsbestimmungen in Norddeutschland, DGMK/ÖGEW Frühjahrstagung 2015,, Celle, (2015).

Geyh, M.A. and Müller, H. - Numerical ²³⁰Th/U dating and a palynological review of the Holsteinian/Hoxnian Interglacial. *Quatern. Sci. Rev.* Vol. 24, pp- 1861 – 1872, (2005).

Giardini, D., Wössner, J. and Danciu, L – Mapping Europe’s seismic hazard. *EOS, Transactions, American Geophysical Union*, Vol. 95, No. 29, pp. 261 – 262, (2014).

Gibbard, P.L. – Palynological problems and the vegetational sequence of the Pliocene- preglacial Pleistocene of East Anglia. *The Pliocene-Middle Pleistocene of East Anglia. Field Guide*, pp. 42 – 49, (1988).

Glennie, K. W. - Early Permian (Rotliegendes) palaeowinds of the North Sea. *Sed Geol.* Vol. 34 pp. 245 - 265, (1983).

Gomberg, J.S., Shedlock, K.M. and Roecker, S.W. – The effect of S-wave arrival times on the accuracy of hypocenter estimation. *BSSA*, Vol. 8, no. 6., pp. 1605 – 1628, (1990).

Grand, S.P., van der Hilst, R.D. and Widiyantoro, S. – Global seismic tomography: A snapshot of convection in the earth. *GAS Today*, Vol. 7, issue 4, pp. 1- 7, (1997).

Grassmann, S., Cramer, B., Delisle, G., Hantschel, T., Messner, J. and Winsemann, J. - pT-effects of Pleistocene glacial periods on permafrost, gas hydrate stability zones and reservoir of the Mittelplate oil field, northern Germany. *Marine and Petroleum Geology*, Vol. 27, Issue 1, pp. 298 - 306, (2010).

Grasso, J.-R. – Mechanics of seismic instabilities induced by the recovery of hydrocarbons. *PAGEOPH*, Vol. 139, No. 3/4, pp. 507 – 534, (1992).

Grasso, J.R. and Wittlinger, G. – Ten years of seismic monitoring over a gas field. *Bulletin of the Seismological Society of America*, Vol. 80, No. 2, pp. 450 – 473, (1990).

Gregory A.R. - Fluid saturation effects on dynamic elastic properties of sedimentary rocks. *Geophysics*, Vol. 41, pp. 895–921, (1976).

Grollmund, B. and Zoback, M.D. – Did glaciation trigger intraplate seismicity in the New Madrid seismic zone? *Geology*, Vol. 29, pp. 175 – 178, (2001).

Grünthal, G. (Ed.) – European Macroseismic Scale 1998, *Cahiers du Centre Européen de Géodynamique et de Séismologie*, Vol. 15, Conseil de l'Europe, Luxembourg, 99 p., (1998).

Grünthal, G. and Bosse, C. – Seismic hazard assessment for low-seismicity areas-case study: northern Germany. *Nat Hazard* Vol. 14, pp. 127 – 139, (1997).

Grünthal, G. and Stromeyer, D. – The recent crustal stress field in central Europe: trajectories and finite element modeling. *Journal of Geophysical Research*, Vol. 97, issue B8, pp. 11805 – 11820, (1992).

Grünthal, G., Mayer-Rosa, D. and Lenhardt, W.A. – Abschätzung der Erdbebengefährdung für die D-A-CH-Staaten – Deutschland Österreich Schweiz. *Bautechnik*, 10, pp. 753 – 767, (1998)

Guyoton, F., Grasso, J.-R. and Volant, P., - Interrelation between induced seismic instabilities and complex geological structure, *Geophys. Res. Lett.*, Vol. 19, pp. 705–708, (1992).

Gyllencreutz, R., Mangerud, J., Svendsen, J.-I. and Lohne, Ø. – DATED-A Gis-based reconstruction and dating database of the Eurasian deglaciation. *Special Paper of the Geological Survey of Finland*, Vol. 2007, issue 46, pp. 113 – 120, (2007).

Haak, H.W., Dost, B. and Goutbeek, F.W. - Seismische analyse van aardbevingen bij Alkmaar op 9 en 10 september en Bergen op Zee op 10 oktober 2001. *KNMI Report*, TR-239. 24 p., (2001).

Hamada, G.M. – Reservoir fluids identification using Vp/Vs ratio. *Oil & Gas Science and Technology – Rev. IFP*, Vol. 59, No. 6, pp. 649 – 654, (2004).

Hampel, A., Hetzel, R., Maniatis, G. and Karow, T. - Three-dimensional numerical modeling of slip rate variations on normal and thrust fault arrays during ice cap growth and melting. *J. Geophys. Res.*, Vol. 114, 14 p., B08406, (2009).

Hampel, A., Hetzel, R. and Maniatis, G. - Response of faults to climate-driven changes in ice and water volumes on Earth's surface. *Phil. Trans. R. Soc. A*, Vol. 368, pp. 2501 – 2517, (2010a).

Hampel, A., Karow, T., Maniatis, G. and Hetzel, R. - Slip rate variations on faults during glacial loading and post-glacial unloading: implications for the viscosity structure of the lithosphere. *J. Geol. Soc. London*, Vol. 167, pp. 385 – 399, (2010b).

Hanka, W., Saul, J., Weber, B. Becker, J., Harjadi, P., Fauzi and GITEWS Seismology Group – Realtime earthquake monitoring for tsunami warning in the Indian Ocean and beyond - *Nat. Hazards Earth Syst. Sci.*, Vol. 10, pp. 2611 – 2622, (2010)

Hantschel, T. and Kauerauf, A.I. – *Fundamentals of Basin and Petroleum Systems Modeling*, Springer-Verlag Berlin Heidelberg, Book, 475 p., (2009).

Harbor, J., Stroeven, A.P., Fabel, D., Clarhäll, A., Kleman, J., Li, Y., Elmore, D. and Fink, D. – Cosmogenic nuclide evidence for minimal erosion across two subglacial sliding boundaries of the late glacial Fennoscandian ice sheet. *Geomorphology*, Vol. 75, pp. 90 – 99, (2006).

Harris, R.A. - Introduction to Special Section: Stress Triggers, Stress Shadows, and Implications for Seismic Hazard. *J. Geophys. Res.*, Vol. 103, pp. 24347 – 24358, (1998).

Haskell, N.A. – The motion of viscous fluid under a surface load. *Physics*, Vol. 6, pp. 53 – 57, (1935).

Haskell, N.A. – The motion of viscous fluid under a surface load Part II. *Journal of applied Physics*, Vol. 7, pp. 56 – 61, (1936).

Hauksson, E. – Crustal structure and seismicity distribution adjacent to the Pacific and North America plate boundary in southern California. *Journal of Geophysical Research*, Vol. 105, No. B6, pp. 13875 – 13903, (2000).

Hays, J.D., Imbrie, J. and Shackleton, N.J. – Variations in the Earth's Orbit: Pacemaker of the Ice Ages. *Science*, Vol. 194, pp. 1121 – 1132, (1976).

Heidari, M., Nikolinakou, M.A., Hudec, M.R. and Flemings, P.B. – Geomechanical analysis of a welding salt layer and its effects on adjacent sediments. *Tectonophysics*, Vol. 683, pp. 172 – 181, (2016).

Heidbach, O., Tingay, M., Barth, A., Reinecker, J., Kurfeß, D. and Müller, B. – Global crustal stress pattern based on the World Stress Map database release 2008. *Tectonophysics*, Vol. 482, pp. 3 – 15, (2010).

Heine, K., Reuther, A.U., Thieke, H.U., Schulz, R., Schlaak, N., Kubik, P.W. - Timing of Weichselian ice marginal positions in Brandenburg (northeastern Germany) using cosmogenic in situ ¹⁰Be. *Z. Geomorphol. N.F.*, Vol. 53 (4), pp. 433 – 454, (2010).

Hillis, R.R., Sandiford, M., Reynolds, S.D. and Quigley, M.C., - Present-day stresses, seismicity and Neogene-to-Recent tectonics of Australia's 'passive' margins: intraplate deformation controlled by plate boundary forces. In: **Johnson, H., Doré, A.G., Gatliff, R.W., Holdsworth, R., Lundin, E.R. and Ritchie, J.D. (Eds.)**, *The Nature and*

Origin of Compression in Passive Margins: Geological Society of London Special Publication, Vol. 306, pp. 71–90, (2008).

Hobbs, W.H. – The cause of earthquakes; especially those of the eastern United States. In Annual report of the board of regents of the Smithsonian Institution showing the Operations, Expenditures, and conditions of the Institution for the year ending June 30, 1926, pp. 257 – 278, (1927)

Hough, S.E. and Page, M. – A century of induced earthquakes in Oklahoma? Bulletin of the Seismological Society of America, Vol. 105, No. 6, pp. 2863 – 2870, (2015).

Hough, S.E., Armbruster, J.H., Seeber, L. and Hough, J.F. – On the modified Mercalli intensities and magnitudes of the 1811 – 1812 New Madrid, central U.S. earthquakes. Journal of Geophysical Research, Vol. 105, pp. 23,839 – 23,864, (2000).

Huang, J. and Zhao, D. – Crustal heterogeneity and seismotectonics of the region around Beijing, China. Tectonophysics, Vol. 385, pp. 159 – 180, (2004).

Hudec, M.R. and Jackson, M.P.A. – Terra infirma: Understanding salt tectonics. Earth-Science Reviews, 82, pp. 1 – 28, (2007).

Hughes, A.L.C., Gyllencreutz, R., Lohne, Ø.S., Mangerud, J. and Svendsen, J.I. – The last Eurasian ice sheet- a chronological database and time-slice reconstruction, DATED-1, Boreas, Vol. 45, pp. 1–45. 10.1111/ bor.12142. ISSN 0300-9483 (2016).

Husen, S. and Smith, R. B. - Probabilistic Earthquake Relocation in Three-Dimensional Velocity Models for the Yellowstone National Park Region, Wyoming. Bulletin of the Seismological Society of America, Vol. 94, No. 3, pp. 880 - 896, (2004).

Husen, S., Kissling, E., Deichmann, N., Wiemer, D., Giardini, D. and Baer, M. - Probabilistic earthquake location in complex three-dimensional velocity models: Application to Switzerland. Journal of Geophysical Research, Vol. 108, No. 2, pp. ESE 5-1 5 - 5-20, (2003).

Jakobbsen, M., Björck, S., O'Regan, M., Flodén, T., Greenwood; S.L., Swärd, H., Lif, A., Ampel, L., Koyi, H. and Skelton, A. – Major earthquakes at the Pleistocene-Holocene transition in Lake Vättern, southern Sweden. Geology, Vol. 42, no. 5, pp. 379 – 382, (2014).

Jamieson, T.F. - On the history of the last geological changes in Scotland. Q. J. Geol. Soc. London, Vol. 21, pp. 161 – 203, (1865).

Janský, J., Horálek, J., Málek, J. and Boušková – Homogeneous velocity models of the West Bohemian swarm region obtained by grid search. Studia Geophysica et Geodaetica, Vol. 44, Issue 2, pp. 158 – 174, (2000).

Jaritz, W. – Some aspects of the development of NW German salt domes. Geowissenschaftliche Aspekte Endlagerung radioaktiver Abfälle Vorträge, Symposium 19.11.19 Braunschweig, (Deutschen Geologischen Gesellschaft; Zeitschrift, 131(2): Ferdinand Enke), pp. 387 – 408, (1980).

Jaritz, W., Best, G., Hildebrand, G. and Jürgens, U. – Regional Analyse der seismischen Geschwindigkeiten in Nordwestdeutschland. Geologisches Jahrbuch, Reihe E, Band 45, pp. 23 - 57, (1991).

Johnson, G.A., Horton, S.P., Withers, M. and Cox, R. – Earthquake focal mechanisms in the New Madrid seismic zone. Seismological Research Letters, Vol. 85, No.2, pp. 257 – 267, (2014).

Johnston, A.C. - Suppression of earthquakes by large continental ice sheets. Nature, Vol. 330, pp. 467 – 469, (1987).

Johnston, A.C. – Seismic moment assessment of earthquakes in stable continental regions – III: 1811 – 1812 New Madrid, 1886 Charleston and 1755 Lisbon, Geophys. J. Int., Vol. 126 (2), pp. 314 – 344, (1996).

Johnston, P., Wu, P. and Lambeck, K., - Dependence of horizontal stress magnitude on load dimension in glacial rebound models. Geophys. J. Int. 132, pp. 41 – 60, (1998).

Juhlin, C., Dehghannejad, M., Lund, B., Malehmir, A. and Pratt, G. – Reflection seismic imaging of the end-glacial Pärvie Fault system, northern Sweden. Journal of Applied Geophysics, Vol. 70, pp. 307 – 316, (2010).

Junge, F.W. - Die Bändertone Mitteldeutschlands und angrenzender Gebiete. Altenburger Naturwissenschaftliche Forschungen, 9, 210 p., (1998).

Kaiser, A., Reicherter, K., Hübscher, C. and Gajewski, D. – Variation of the present-day stress field within the North German Basin – insights from thin shell FE modeling based on residual GPS velocities. Tectonophysics, Vol. 397, pp. 55 – 72, (2005).

Kenner, S.J. and Segall, P. – A mechanical model for intraplate earthquakes: Application to the New Madrid Seismic Zone. Science, Vol. 289, pp. 2329 – 2332, (2000).

Kennett, B. L. N. - Seismic wave propagation in stratified media, Cambridge University Press, Book, 288 p., First Edition (1983).

Kiden, P., Denys, L. and Johnston, P. – Late Quaternary sea-level change and isostatic and tectonic land movements along the Belgian – Dutch North Sea coast: geological data and model results. Journal of Quaternary Science, Vol. 17 (5-6), pp. 535 – 546, (2002).

Kierulf, H.P., Steffen, H., Simpson, M.J.R., Lidberg, M., Wu, P. and Wang, H. – A GPS velocity field for Fennoscandia and a consistent comparison to glacial isostatic adjustment models. J. Geophys. Res. Solid Earth, Vol. 119, pp. 6613 – 6629, (2014).

King, G.C.P., Stein, R.S. and Lin, J. – Static stress changes and the triggering of earthquakes. Bulletin of the Seismological Society of America, Vol. 84, Issue 3, pp. 935 – 953, (1994).

King, M.A., Altamimi, Z., Boehm, J., Bos, M., Dach, R., Elosegui, P., Fund, F., Hernández-Pajares, M., Lavalée, D., Cerveira, P.J.M., Penna, N., Riva, R.E.M., Steigenberger, P., van Dam, T., Vittuari, L., Williams,

S. and Willis, P. - Improved constraints on models of glacial isostatic adjustment: a review of the contribution of ground-based geodetic observations. *Surv. Geophys.*, 31(5), pp. 465 - 507, (2010).

Klein, F.W. - Hypocenter location program HYPOINVERSE, U.S. Geological Survey Open-File Report 78-694, 113 p., (1978).

Kley, J and Voigt, T. – Late Cretaceous intraplate thrusting in central Europe: effect of Africa-Iberia-Europe convergence, not Alpine collision. *Geology*, Vol. 36, pp. 839 – 842, (2008).

Kockel, F. – Inversion structures in Central Europe – expressions and reasons, an open discussion. *Neth J Geosci* Vol. 82, pp. 367 – 382, (2003).

Kosinowski M., Porth, H. and Sedlacek, R. – Erdöl und Erdgas in Niedersachsen – Entstehung und Vorkommen. Niedersächsische Akademie der Geowissenschaften, Veröffentlichungen, Heft 13, pp. 5 – 19, (1997).

Koupriantchik, D., Hunt, S.P. and Meyers, A.G. – Geomechanical modeling of salt diapirs-A field scale analysis for a 3D salt structure from the North Sea. *Impact of Human Activity on the Geological Environment - Proceedings of the International Symposium of the International Society for Rock Mechanics, Eurock 2005*, pp. 275 – 280, (2005).

Koupriantchik, D., Hunt, S.P., Boulton, P.J. & Meyers, A.G. - Geomechanical modelling of salt diapirs: 3D salt structures from the Officer Basin, South Australia. In: **Munson, T.J. and Ambrose, G.J.** *Proceedings of the Central Australian Basins Symposium (CABS), Alice Springs, Northern Territory, 16–18 August, 2005. Northern Territory Geological Survey, Special Publication 2*, pp. 388 - 396, (2007).

Kraaijpoel, D. and Dost, B. – Implications of salt-related propagation and mode conversion effects on the analysis of induced seismicity. *J Seismol*, Vol. 17, pp. 95 – 107, (2013).

Krawczyk, C.M., McCann, T., Cocks, L.R.M., McBride, J.H. and Wybraniec, S. – Caledonian tectonics. *Geology of Central Europe*, Vol. 1, pp. 303 – 381, (2008).

Krbetschek, M.R., Degering, D., Alexowsky, W. - Infrarot-Radiofluoreszenz-Alter (IR-RF) unter-saalezeitlicher Sedimente Mittel und Ostdeutschlands. *Zeitschrift der Deutschen Gesellschaft für Geowissenschaften*, Vol. 159 (1), pp. 133 – 140, (2008).

Kröner, U., Mansy, J.-L., Mazur, S., Aleksandrowski, P., Hann, H.P., Huckriede, H., Lacquement, F., Lamarche, J., Ledru, P., Pharaoh, T.C., Zedler, H., Zeh, A. and Zulauf, G. – Variscan tectonics. *Geology of Central Europe*, Vol. 1, pp. 599 – 664, (2008).

Kukla, P.A., Urai, J.L. and Mohr, M. – Dynamics of salt structures. In **Littke, R., Bayer, U., Gajewski, D. and Nelskamp, S.** - *Dynamics of complex intracontinental basins. The example of the Central European Basin System.* – Springer-Verlag, Berlin-Heidelberg, 519 p. (ISBN: 978-3-540-85084-7), (2008).

Kvale, A. – Norwegian earthquakes in relation to tectonics. Norwegian Universities Press. (1960).

Lagerbäck, R. - Late Quaternary faulting and paleoseismicity in northern Fennoscandia, with particular reference to the Lansjärv area, northern Sweden. *Geol. Fören. Stockholm Förh.*, Vol. 112, pp. 333 – 354, (1990).

Lagerbäck, R. and Witschard, F. – Neotectonics in northern Sweden-geological investigations. Report – Geological Survey of Sweden, 70 p., (1983).

Lahr, J.C. - HYPOELLIPSE: a computer program for determining local earthquake hypocentral parameters, magnitude and first motion pattern, U.S. Geological Survey Open-File Report 80-59, 59 p., (1980).

Lambeck, K., Purcell, A., Zhao, J. and Svensson, N.-O. – The Scandinavian Ice Sheet: from MIS 4 to the end of the Last Glacial Maximum. *Boreas*, Vol. 39, pp. 410 – 435, (2010).

Lambeck, K., Purcell, A., Funder, S., Kjaer, K.H., Larsen, E. and Möller, P. – Constraints on the Late Saalian to early Middle Weichselian ice sheet of Eurasia from field data and rebound modelling. *Boreas*, Vol. 35, pp. 540 – 575, (2006).

Landolt, H. H. and Börnstein, R. - Zahlenwerte und Funktionen aus Naturwissenschaften und Technik, neue Serie: Geophysik u. Weltraumforschung. Physikalische Eigenschaften d. Gesteine, Band 1, Buch, 795 p., (1982).

Lang, J. Hampel, A., Brandes, C. and Winsemann, J. - Response of salt structures to ice-sheet loading: implications for ice-marginal and subglacial processes. *Quaternary Science Reviews*, Vol. 101, pp. 217 - 233, (2014).

Laske, G., Masters., G., Ma, Z. and Pasyanos, M. - Update on CRUST1.0 - A 1-degree Global Model of Earth's Crust, *Geophys. Res. Abstracts*, 15, Abstract EGU2013-2658, (2013).

LBEG (Landesamt für Bergbau, Energie und Geologie) – Erdöl und Erdgas in der Bundesrepublik Deutschland. Annual report, 73 p., (2016).

Lee, W. H. K. and Lahr, J. C. - HYPO 71 (revised): A computer program for determining hypocenter, magnitude, and first motion pattern of local earthquakes, U.S. Geol. Surv. Open-File Rep., 64 p., (1975).

Lengliné, O., Lamourette, L., Vivin, L., Cuenot, N. and Schmittbuhl, J. - Fluid-induced earthquakes with variable stress drop. *J. Geophys. Res. Solid Earth*, Vol. 119, pp. 8900 – 8913, (2014).

Leydecker, G. – Erbebenkatalog für die Bundesrepublik Deutschland mit Randgebieten für die Jahre 800 bis 2008 (Earthquake catalog for the Federal Republic of Germany and adjacent areas for the years 800 to 2008). *Geologisches Jahrbuch Reihe E*, v. 59, 198 p., (2011).

Leydecker, G. and Kopera, J. R. – Seismological hazard assessment for a site in Northern Germany, an area of low seismicity. *Engineering Geology*, Vol. 52, pp. 293 – 304, (1999).

Leydecker, G., Kaiser, D, Busche, H. and Schmitt, T. – Makroseismische Bearbeitung des Erdbebens vom 20. Okt. 2004 östlich Rotenburg (Wümme) im Norddeutschen Tiefland. Report, Bundesanstalt für Geowissenschaften und Rohstoffe, Hannover, 7 p., (2006).

- Leydecker, G., Steinwachs, M., Seidl, D., Kind, R., Klusmann, J. and Zerna, W.** - Das Erdbeben vom 2. Juni 1977 in der Norddeutschen Tiefebene bei Soltau. *Geologisches Jahrbuch*, E 18: pp. 3 - 18, (1980).
- Lin, G., Shearer, P. M. and Hauksson, E.** - Applying a three-dimensional velocity model, waveform cross correlation, and cluster analysis to locate southern California seismicity from 1981 to 2005. *Journal of Geophysical Research*, Vol. 112, B12309, (2007).
- Lin, G., Thurber, C.H., Zhang, H., Hauksson, E., Shearer, P.M., Waldhauser, F., Brocher, T.M. and Hardebeck, J.** – A California statewide three-dimensional seismic velocity model from both absolute and differential times. *Bulletin of Seismological Society of America*, Vol. 100, No. 1, pp. 225 – 240, (2010).
- Littke, R., Bayer, U., Gajewski, D. and Nelskamp, S.** - Dynamics of complex intracontinental basins. The example of the Central European Basin System.– Springer-Verlag, Berlin-Heidelberg, 519 p. (ISBN: 978-3-540-85084-7), (2008)
- Liu, M., Stein, S.** – Mid-continental earthquakes: Spatiotemporal occurrences, causes, and hazards. *Earth Science Reviews*, Vol. 162, pp. 364 – 386, (2016).
- Liu, L. and Zoback, M.D.** – Lithospheric strength and intraplate seismicity in the New Madrid seismic zone. *Tectonics*, Vol. 16, no. 4, pp. 585 – 595, (1997).
- Liu, M., Wand, H., Ye, J. and Jia, C.** – Intraplate earthquakes in North China. In *Intraplate Earthquakes*, ed. **Talwani, P.**, Cambridge University Press, New York, 338 p., (2014).
- Liu, C., Zhu, B. and Shi, Y.** – Lithospheric rheology and Moho upheaval control the generation mechanism of the intraplate earthquakes in the north China Basin. *Journal of Asian Earth Sciences*, Vol. 121, pp. 153 – 164, (2016).
- Lohr, T., Krawczyk, C.M., Tanner, D.C., Samiee, R., Endres, H., Oncken, O., Trappe, H. and Kukla, P.A.** - Strain partitioning due to salt: insights from interpretation of a 3D seismic data set in the NW German Basin - *Basin Research*, Vol. 19, pp. 579 – 597, (2007).
- Lokhorst, A.** - NW European Gas Atlas, **Lokhorst** (Ed.), Nederlands Institute voor Toegepaste Geowetenschappen TNO, Haarlem (1998) CD-ROM, (1998).
- Lomax, A. and Curtis, A.** - Fast, probabilistic earthquake location in 3D models using oct-tree importance sampling, *Geophys. Res. Abstr.* 3:955 (www.alomax.net/nlloc/octtree), (2001)
- Lomax, A., Virieux, J., Volant, P. and Berge, C.** - Probabilistic earthquake location in 3D and layered models: Introduction of a Metropolis-Gibbs method and comparison with linear locations. pp. 101 - 134, *Advances in Seismic Event Location*. **Thurber CH, Rabinowitz N (eds.)**, Kluwer, Amsterdam, (2000).
- Lomax, A., Zollo, A., Capuano, P. and Virieux, J.** – Precise, absolute earthquake location under Somma-Vesuvius volcano using a new three-dimensional velocity model. *Geophys. J. Int.*, Vol. 146, pp. 313 – 331, (2001).

Lomax, A., Michelini, A. and Curtis, A. - Earthquake Location, Direct, Global-Search Methods, in Complexity In Encyclopedia of Complexity and System Science, Part 5, Springer, New York, pp. 2449 - 2473,(2009)

Lund, B. and Zoback, M.D. – Orientation and magnitude of in situ stress to 6.5 km depth in the Baltic Shield. International Journal of Rock Mechanics and Mining Sciences, Vol. 36, pp. 169 – 190, (1999).

Lundqvist, J. and Lagerbäck, R. - The Pärve Fault: a late-glacial fault in the Precambrian of Swedish Lapland. Geol. Fören. Stockholm Förh., Vol. 98, pp. 45 – 51, (1976).

Lüthgens, C. and Böse, M. – From morphostratigraphy to geochronology – on the dating of ice marginal positions. Quaternary Science Reviews, Vol. 44, pp. 26 – 36, (2012).

Lüthgens, C., Böse, M. and Prfeusser, F. – Age of the Pomeranian ice-marginal position in northeastern Germany determined by Optically Stimulated Luminescence (OSL) dating of glaciofluvial sediments. Boreas, Vol. 40, pp. 598–615, (2011).

Ma, S and Atkinson, G.M. - Focal Depths for Small to Moderate Earthquakes (mN 2.8) in Western Quebec, Southern Ontario, and Northern New York. Bulletin of the Seismological Society of America, Vol. 96, No. 2, pp. 609 – 623, (2006).

Magri, F., Bayer, U., Tesmer, M., Möller, P. and Pekdeger, A. – Salinization problems in the NEGB: results from thermohaline simulations. Int J Earth Sci (Geol Rundschau), Vol. 97, pp. 1075 – 1085, (2008).

Malehmir, A., Andersson, M., Mehta, S., Brodic, B., Munier, R., Place, J., Maries, G., Smith, C., Kamm, J., Bastani, M., Mikko, H. and Lund, B. – Post-glacial reactivation of the Bollnäs fault, central Sweden – a multidisciplinary geophysical investigation. Solid Earth, Vol. 7, pp. 509 – 527, (2016).

Mallet, J.L. – GOCAD: A computer aided design program for geological applications. In: **Turner, A.K.** (ed)-Three-dimensional modeling with geoscientific information systems, Kluwer Academic Publishers, pp. 123 - 141, (1992).

Mallet, J.L. – Geomodeling, Book, Oxford University Press, 601 p., (2002).

Marks, L. – Quaternary glaciations in Poland. Developments in Quaternary Science, Vol. 15, pp. 299 – 303, (2011).

Marotta, A.M., Bayer, U., Thybo, H. and Scheck, M. – Origin of the regional stress in the North German basin: results from numerical modelling. Tectonophysics, Vol. 360, pp. 245 – 264, (2002).

Maystrenko, Y.P. and Scheck-Wenderoth, M. – 3D lithosphere-scale density model of the Central European Basin System and adjacent areas. Tectonophysics, Vol. 601, pp. 53 – 77, (2013).

Maystrenko, Y., Bayer, U. and Scheck-Wenderoth, M. – Structure and evolution of the Glueckstadt Graben due to salt movements. Int. J. Earth Sci (Geol Runsch), Vol. 94, pp. 799 – 814, (2005).

Maystrenko, Y.P., Bayer, U. and Scheck-Wenderoth, M. – Regional-scale structural role of Permian salt within the Central European Basin System. Geological Society, London, Special Publications, Vol. 363, pp. 409 – 430, (2012).

Maystrenko, Y.P., Bayer, U., Brink, H.-J. and Littke, R. – The Central European Basin System – An Overview. In: Eds. Littke, R., Bayer, U., Gajewski, D. and Nelskamp, S. - Dynamics of complex intracontinental basins. The example of the Central European Basin System. Springer-Verlag, Berlin-Heidelberg, 519 p. (ISBN: 978-3-540-85084-7), (2008).

Mazur, S. and Scheck-Wenderoth, M. – Constraints on the tectonic evolution of the Central European Basin System revealed by seismic reflection profiles from Northern Germany. Netherlands Journal of Geosciences, 84, 4, pp. 389 – 401, (2005).

Mazur S., Scheck-Wenderoth, M. and Krzywiec, P. - Different modes of Late Cretaceous-Early Tertiary inversion in the North German and Polish basins. Int J Earth Sci Vol. 94 pp. 782 - 798, (2005).

Mazzotti, S. and Townend, J. – State of stress in central and eastern North American seismic zones. Lithosphere, Vol. 2(2), pp. 76 – 83, (2010).

McCann, T., Pascal, C., Timmerman, M.J., Krzywiec, P., López-Gómez, J., Wetzel, L., Krawczyk, C.M., Rieke, H. and Lamarche, J. – Post-Variscan (end Carboniferous-Early Permian) basin evolution in western and Central Europe. Geological Society, London, Memoirs 2006, v. 32, pp. 355 – 388, (2006).

McCue, K. Wesson, V. and Gibson, G. – The Newcastle, New South Wales, earthquake of 28 December 1989. BMR Journal of Australian Geology & Geophysics, Vol. 11, Issue 4, pp. 559 – 567, (1990).

McGarr, A. - On a possible connection between three major earthquakes in California and oil production. Bull. Seism. Soc. Am. Vol. 81, pp. 948 – 970, (1991).

McGarr, A. and Simpson, D. – A broad look at induced and triggered seismicity. In: "Rockbursts and Seismicity in Mines," pp. 385 - 396, Balkema, (1997).

McGarr, A., Simpson, D. and Seeber, L. - 40 Case histories of induced and triggered seismicity. International Geophysics, Vol. 81, Part A, pp. 647 – 661, (2002).

McKeown, F.A. and Diehl, S.F. - Evidence of contemporary and ancient excess fluid pressure in the New Madrid seismic zone of the Reelfoot rift, central United States. In Investigations of the New Madrid Seismic Zone, U.S. Geol. Surv. Prof. Pap. 1538N, ed. K.M. Shedlock, A.C. Johnston, pp. N1-N24, (1994).

McNamara, D.E., Benz, H.M., Herrmann, R.B., Bergman, E.A., Earle, P., Holland, A., Baldwin, R. and Gassner, A. – Earthquake hypocenters and focal mechanisms in central Oklahoma reveal a complex system of reactivated subsurface strike-slip faulting. Geophys. Res. Lett., 42, pp. 2742 – 2749, (2015).

Meier, R. and Grünthal, G. – Eine Neubewertung des Erdbebens vom 3. September 1770 bei Alfhausen (Niedersachsen). Osnabrücker naturwissenschaftliche Mitteilungen, Vol. 18, pp. 67 – 80, (1992).

Melgar, D., Allen, R.M., Riquelme, S., Geng, J., Bravo, F., Baez, J.C., Parra, H., Barrientos, S., Fang, P., Bock, Y., Bevis, M., Caccamise II, D.J., Vigny, C., Moreno, M. and Smalley Jr., R. – Local tsunami warnings: Perspectives from recent large events. *Geophys. Res. Lett.*, 43, pp. 1109 – 1117, (2016).

Meyer, K.-D. - Das Quartärprofil am Steilufer der Elbe bei Lauenburg. *Eiszeitalter und Gegenwart*, Vol. 16, pp. 47 – 60, (1965).

Mikko, H., Smith, C.A., Lund, B., Ask, M.V.S. and Munier, R. – LiDAR-derived inventory of post-glacial fault scarps in Sweden. *GFF*, Vol. 137, issue 4, pp. 334 – 338, (2015).

Milne, W.G. and Berry, M.J. – Induced seismicity in Canada. *Engineering Geology*, Vol. 10, pp. 219 – 226, (1976).

Milne, G.A., Gehrels, W.R., Hughes, C.W. and Tamisiea, M.E. – Identifying the causes of sea-level change. *Nature Geoscience*, Vol. 2, pp. 471 – 478, (2009).

Mitrovica, J.X. - Haskell [1935] revisited. *Journal of Geophysical Research*, Vol. 101, No. B1, pp. 555 – 569, (1996).

Mitrovica J.X. and Wahr, J. – Ice age earth rotation. *Annual Review of Earth and Planetary Sciences*, Vol. 39, pp. 577 – 616, (2011).

Mitrovica, J.X., Wahr, J., Matsuyama, I., Paulson, A. - The rotational stability of an ice-age earth. *Geophys J Int*, Vol. 161(2), pp. 491 – 506, (2005).

Mohr, M., Kukla, P.A., Urai, J.L. and Bresser, G. - Multiphase salt tectonic evolution in NW Germany: Seismic interpretation and retro-deformation. *Int J Earth Sci* Vol. 94, pp. 917 - 940, (2005).

Mooney, W.D., Laske, G. and Masters, T.G. – CRUST 5.1: A global crustal model at 5° x 5°. *Journal of Geophysical Research: Solid Earth*, Vol. 103, Issue 1, pp. 727 – 747, (1998).

Mörner, N.-A. – Active faults and paleoseismicity in Fennoscandia, especially Sweden. Primary structures and secondary effects. *Tectonophysics*, Vol. 380, pp. 139 – 157, (2004).

Mörner, N.-A. – Paleoseismology: The application of multiple parameters in four case studies in Sweden. *Quaternary International*, Vol. 242, pp. 65 – 75, (2011).

Mörner, N.-A., Tröften, P.E., Sjöberg, R., Grant, D., Dawson, S., Bronge, C., Kvamsdal, O. and Siden, A. - Deglacial paleoseismicity in Sweden: the 9663 BP Iggesund event. *Quat. Sci. Rev.*, Vol. 19, pp. 1461–1468, (2000).

Moser, T.J., van Eck, T. and Nolet, G. – Hypocenter determination in strongly heterogeneous earth models using the shortest path method. *Journal of Geophysical Research*, Vol. 97, No. B5, pp. 6563 – 6572, (1992).

Mostaccio, A., Tuvè, T., Patanè, D., Barberi, G. and Zuccarello, L. – Improving seismic surveillance at Mt. Etna Volcano by probabilistic earthquake location in a 3D model. *Bulletin of the Seismological Society of America*, Vol. 103, No.4, pp. 2447 – 2459, (2013).

Mousavi, S., Bauer, K., Korn, M. and Hejrani, B. – Seismic tomography reveals a mid-crustal intrusive body, fluid pathways and their relation to the earthquake swarms in West/Bohemia/Vogtland. *Geophys. J. Int.*, Vol. 203, pp. 1113 – 1127, (2015).

Mueller, K. and Pujol, J. – Three-dimensional geometry of the Reelfoot blind thrust: implications for moment release and earthquake magnitude in the New Madrid seismic zone. *Bulletin of the Seismological Society of America*, Vol. 63, pp. 1563 – 1573, (2001).

Mueller, K., Champion, J., Guccione, M. and Kelson, K. – Fault slip rates in the modern new Madrid seismic zone. *Science*, Vol. 286, Issue 5442, pp. 1135 – 1138, (1999).

Muir-Wood, R. - A review of the seismotectonics of Sweden. SKB, Technical Report, Vol.13, 225 p., (1993).

Muir-Wood, R. – Deglaciation seismotectonics: a principal influence on intraplate seismogenesis at high latitudes. *Quaternary Science Reviews*, Vol. 19, pp. 1399 – 1411, (2000).

Mukuhira, Y., Asanuma, H., Niitsuma, H. and Häring, M. O. - Characteristics of large-magnitude microseismic events recorded during and after stimulation of a geothermal reservoir at Basel, Switzerland. *Geothermics*. Vol. 45, pp. 1 - 17, (2013).

Müller, B., Zoback, M.L., Fuchs, K., Mastin, L., Gregersen, S., Pavoni, N., Stephansson, O. and Ljunggren, C. – Regional patterns of tectonic stress in Europe. *J. Geophys. Res.*, Vol. 97, pp. 11,783 – 11,803, (1992).

Müller, G. - The reflectivity method: A tutorial. *Journal of Geophysics*, Vol. 58, pp. 153 - 174, (1985).

Münch, T.W., Koch, M. and Schlittenhardt, J. – Relocation of the 5 December 2004 Waldkirch, Germany, Earthquake with regional 1D and 3D seismic velocity models in the presence of upper-mantle anisotropy. *Bulletin of the Seismological Society of America*, Vol. 102, No. 5, pp. 2077 – 2089, (2012).

Nagy, W. – New region-dependent travel-time handling facilities at the IDC; Functionally testing and implementation details, Tech. Rep. 96/1179, SAIC, (1996).

Nansen, F. - The Earth's Crust, its surface-forms, and isostatic adjustment. Det Norske Videnskups-akudemi, matematisk-naturvidenskuplig klasse 12, 122 p., (1928).

Nelson, G. D. and Vidale, J. E. - Earthquake locations by 3D finite-difference travel times, *Bull. seism. SOC. Am.*, Vol. 80, pp. 395 – 410, (1990).

Nyamwandha, C.A., Powell, C.A. and Langston, C.A. – A joint local and teleseismic tomography study of the Mississippi Embayment and New Madrid Seismic Zone. *J. Geophys. Res. Solid Earth*, Vol. 121 pp. 3570 – 3585, (2016).

Odonne, F., Ménard, I., Massonnat, G.J. and Rolando, J.-P. – Abnormal reverse faulting above a depleting reservoir. *Geology*, Vol. 27, Issue 2, pp. 111 – 114, (1999).

Oppenheimer, D.H. – Extensional tectonics at The Geysers geothermal area, California. *Journal of Geophysical Research*, Vol. 91, No. B11, pp. 11,463 – 11,476, (1986)

Palmu, J.-P., Ojala, A.E.K., Ruskeenieni, T., Sutinen, R. and Mattila, J. – LiDAR DEM detection and classification of postglacial faults and seismically-induced landforms in Finland: a paleoseismic database. *GFF*, Vol. 137, Issue 4, pp. 344 – 352, (2015).

Pandey, M.R., Tandukar, R.P., Avouac, J.P., Vergne, J. and Heritier, Th. – Seismotectonics of the Nepal Himalaya from a local seismic network. *Journal of Asian Earth Science*, Vol. 17, pp. 703 – 712, (1999).

Park, J., Lee, J.M., Chio, J.-M., Kim, W. and Kim, W.-Y. – Relocation of earthquakes in the New Madrid Seismic Zone: Estimation of 1D velocity structure and geometry of a seismogenic fault. *Bulletin of the Seismological Society of America*, Vol. 105, No. 2A, pp. 873 – 888, (2015).

Pasternak, M. – Exploration und Produktion von Erdöl und Erdgas in Deutschland 2014. *Erdöl, Erdgas, Kohle*, Vol. 131, Heft 7/8, pp. 258 – 273, (2015).

Pasyanos, M. E., Masters, T. G., Laske, G. and Ma, Z. - LITHO1.0: An updated crust and lithospheric model of the Earth. *J. Geophys. Res. Solid Earth*, Vol. 119, pp. 2153 - 2173, (2014).

Pedlosky, J. – *Geophysical Fluid Dynamics*. Springer, 2nd ed. 1987, 728 p., (1987).

Peltier, W.R. – The impulse response of a Maxwell Earth. *Reviews of Geophysics*. Vol. 12, pp. 649 – 669, (1974).

Peltier, W.R. - Ice age paleotopography. *Science*, Vol. 265, pp. 195 - 201, (1994).

Peltier, W.R. - Mantle viscosity and ice-age ice sheet topography. *Science*, Vol. 273, pp. 1359 – 1364, (1996).

Peltier, W.R. – Global glacial isostasy and the surface of the ice-age Earth: The ICE-5G (VM2) model and GRACE. *Annu. Rev. Earth Planet. Sci.* Vol. 32, pp. 111 – 149, (2004).

Peltier, W.R. and Andrews, J.T. - Glacial–isostatic adjustment – I. The forward problem. *Geophys. J. R. Astr. Soc.* Vol. 46, pp. 605 – 646, (1976).

Peltier, W. and Tushingham, A. - Global sea level rise and the greenhouse effect: might they be connected? *Science* Vol. 244, pp. 806 – 810, (1989).

Peltier, W.R., Argus, D.F. and Drummond, R. – Space geodesy constrains ice age terminal deglaciation: The global ICE-6G_C (VM5a) model. *J. Geophys. Res. Solid Earth*, Vol. 120, pp. 450 – 487, (2015).

Penck, A. – Die Geschiebformation Norddeutschlands. *Z. Geol. Ges.*, Vol. 31, pp. 117 – 203, (1879).

Plag, H.-P., Engen, B., Clark, T.A., Degnan, J.J. and Richter, B. – Post-glacial rebound and present-day three-dimensional deformations. *J. Geodynamics*, Vol. 25, no.3/4, pp. 263 – 301, (1998).

Plein, E. – Rotliegend-Ablagerungen im Norddeutschen Becken, *Z. dt. geol. Ges.*, Band 129, pp. 71 – 97, (1978).

- Podvin, P. and Lecomte, I.** - Finite difference computation of traveltimes in very contrasted velocity models: a massively parallel approach and its associated tools - *Geophys. J. Int.*, Vol. 105, pp. 271 - 284, (1991).
- Pollitz, F.F., Kellogg, L. and Bürgmann, R.** – Sinking mafic body in reactivated lower crust: A mechanism for stress concentration at the New Madrid seismic zone. *BSSA*, Vol. 91, issue 6, pp. 1882 – 1897, (2001).
- Powell, C. and Horton, S.** – Seismotectonics of the New Madrid seismic zone: improved velocity models and fault characterization. Final Technical Report, USGS NEHRP AWARD, #08HQGR0040, 57 p., (2009)
- Pujol, J.** – Earthquake Location Tutorial: Graphical approach and approximate epicentral location techniques. *Seismological Research Letters*, Volume 75, No. 1, pp. 63 – 75, (2004).
- Quinlan, G.** – Postglacial rebound and the focal mechanisms of eastern Canadian earthquakes. *Can. J. Earth Sci.*, Vol. 21, pp. 1018 – 1023, (1984).
- Rajabi, M., Tingay, M. and Heidbach, O.** – The present-day stress field of New South Wales, Australia. *Australian Journal of Earth Sciences*, Vol. 63, No. 1, pp. 1-21, (2016).
- Ranalli, G.** - *Rheology of the Earth*, 2nd ed. Chapman and Hall, London, (1995).
- Reicherter, L., Froitzheim, N., Jarosinski, M., Badura, J., Franzke, H.-J., Hansen, M., Hübscher, C., Müller, R., Poprawa, P., Reinecker, J., Stackebrandt, W., Voigt, T., von Eynatten, H. and Zuchiewicz, W.** – Alpine tectonics north of the Alps. *Geology of Central Europe*, Vol. 2, pp. 1233 – 1285, (2008).
- Reicherter, K., Kaiser, A. and Stackebrandt, W.** – The post-glacial landscape evolution of the North German Basin morphology, neotectonics and crustal deformation. *Int J Earth Sci (Geol Rundsch)*, Vol. 94, pp. 1083 – 1093, (2005).
- Reimer, J.P., Baillie, M.G.L., Bard, E., Bayliss, A., Beck, J.W., Bertrand, C.J.H.** -. *INTCAL04 Terrestrial Radiocarbon Age Calibration, 0–26 Cal KYR BP*. *Radiocarbon*, Vol. 46 (3), pp. 1029 – 1058, (2004).
- Ricard, Y., Spada, G. and Sabadini, R.** – Polar wandering of a dynamic earth. *Geophys. J. Int.*, Vol. 113, pp. 284 – 298, (1993).
- Rinterknecht, V., Börner, A., Boursier, D. and Braucher, R.** – Cosmogenic¹⁰Be dating of ice sheet marginal belts in Mecklenburg-Vorpommern, Wetzern Pommerania (northeast Germany). *Quaternary Geochronology*, Vol. 19, pp. 42 – 51, (2014).
- Röckel, T. and Lempp, C.** – Der Spannungszustand im Norddeutschen Becken – *Erdöl Erdgas Kohle* No. 119, Heft 2, pp. 73 – 80, (2003).
- Roecker, S. W., Tucker, B., King, J. and Hatzfeld, D.** - Estimates of Q in Central Asia as a Function of Frequency and Depth Using the Coda of Locally Recorded Earthquakes. *BSSA*, Vol. 72, No. 1, pp. 129 - 149, (1982).

- Roskosch, J., Tsukamoto, S., Meinsen, J., Frechen, M. and Winsemann, J.** – Luminescence dating of an Upper Pleistocene alluvial fan and aeolian sandsheet complex: The Senne in the Münsterland Embayment, NW Germany. *Quaternary Geochronology*, Vol. 10, pp. 94 – 101, (2012).
- Sandersen, P.B.E. and Jørgensen, F.** – Neotectonic deformation of a Late Weichselian outwash plain by deglaciation-induced fault reactivation of a deep-seated graben structure. *Boreas*, Vol. 44, pp. 413 – 431, (2015).
- Scheck, M. and Bayer, U.** – Evolution of the Northeast German Basin-inferences from a 3D structural model and subsidence analysis. *Tectonophysics*, 313, pp. 145 – 169, (1999).
- Scheck, M., Bayer, U. and Lewerenz, B.** – Salt movement in the Northeast German Basin and its relation to major post-Permian tectonic phases – results from 3D structural modelling, backstripping and reflection seismic data. *Tectonophysics*, Vol. 361, issue 3-4, pp. 277 – 299, (2003a).
- Scheck, M., Bayer, U. and Lewerenz, B.** – Salt redistribution during extension and inversion inferred from 3D backstripping. *Tectonophysics*, 373, pp. 55 – 73, (2003b).
- Scheck-Wenderoth, M., Maystrenko, Y., Hübscher, C., Hansen, M. and Mazur, S.** – Dynamics of salt basins. In **Littke, R., Bayer, U., Gajewski, D. and Nelskamp, S.** - Dynamics of complex intracontinental basins. The example of the Central European Basin System. Springer-Verlag, Berlin-Heidelberg, 519 p. (ISBN: 978-3-540-85084-7), (2008).
- Scholz, C.H.** – The mechanics of earthquakes and faulting. Cambridge University Press, 2002, 2. Ed., 473 p., (2002).
- Schöner, R. and Gaupp, R.** - Contrasting red bed diagenesis: The southern and northern margin of the Central European Basin. *Int J Earth Sci*, Vol. 94, pp. 897 - 916, (2005).
- Schröder, L., Plein, E., Bachmann, G.H., Gast, R.E., Gebhardt, U., Graf, R., Helmuth, H.-J., Pasternak, M., Porth, H. and Süßmuth, S.** – Stratigraphische Neugliederung des Rotliegend im Norddeutschen Becken. *Geologisches Jahrbuch*, Reihe A, Heft 148, pp. 3- 21, 7 Tafeln, (1995).
- Schulz, R., Agemar, T., Alten, A.-J., Kühne, K., Maul, A.-A., Pester, S. and Wirth, W.** – Aufbau eines geothermischen Informationssystems für Deutschland. – *Erdöl Erdgas Kohle*. Vol. 123 (2), pp. 76 – 81, (2007).
- Schulze, M.** – Informations- und Entscheidungshilfesysteme zur oberflächennahen Geothermie in Bayern. – *Korrespondanz Wasserwirtschaft*, 1/09: pp. 25 – 28, Hennef (Ges. Förderung Abwassertechnik), (2009).
- Schwarzer, D. and Littke, R.** – Petroleum generation and migration in the 'Tight Gas' area of the German Rotliegend natural gas play: a basin modeling study. *Petroleum Geoscience*, Vol. 13, pp. 37 – 62, (2007).
- Schweitzer, J.** - HYPOSAT – an enhanced routine to locate seismic events. *Pure and Applied Geophysics*, Vol. 158, Issue 1-2, pp. 277 - 289, (2001).

Segall, P. – Stress and subsidence resulting from subsurface fluid withdrawal in the epicentral region of the 1983 Coalinga Earthquake. *Journal of Geophysical Research*, Vol. 90, No. B8, pp. 6801 – 6816, (1985).

Segall, P. - Earthquakes triggered by fluid extraction. *Geology*, v. 17, pp. 942 - 946, (1989).

Segall, P., Grasso, J.-R. and Mossop, A. – Poroelastic stressing and induced seismicity near the Lacq gas field, southwestern France. *Journal of Geophysical Research*, Vol. 99, Issue B8, pp. 15,423 – 15,438, (1994).

Seton, M., Müller, R.D., Zahirovic, S., Gaina, C., Torsvik, T., Shephard, G., Talsma, A., Gurnis, M., Turner, M., Maus, S. and Chandler, M. - Global continental and ocean basin reconstructions since 200 Ma. *Earth-Science Reviews*, Vol. 113, pp. 212 - 270, (2012).

Shillington, D.J., Minshull, T.A., Piece, C. and O’Sullivan, J.M. – P- and S-wave velocities of consolidated sediments from a seafloor seismic survey in the North Celtic Sea Basin, offshore Ireland. *Geophysical Prospecting*, Vol. 56, pp. 197 – 211., (2008).

Simpson, D.W. and Leith, W. - The 1976 and 1984 Gazli, USSR, earthquakes-were they induced? *Bull. Seism. Soc. m.* Vol. 75, pp. 1465 – 1468, (1985).

Sippel, J., Scheck-Wenderoth, M., Reicherter, K. and Mazur, S. – Paleostress states at the south-western margin off the Central European Basin System – Application of fault-slip analysis to unravel a polyphaser deformation pattern. *Tectonophysics*, Vol. 470, pp. 129 – 146, (2009).

Sirocko, F., Reicherter, K., Lehné, R., Hübscher, Ch., Winsemann, J. and Stackebrandt, W. – Glaciation, salt and the present landscape. In **Littke, R., Bayer, U., Gajewski, D. and Nelskamp, S.** - Dynamics of complex intracontinental basins. The example of the Central European Basin System.– Springer-Verlag, Berlin-Heidelberg, 519 p. (ISBN: 978-3-540-85084-7), (2008).

Slangen, A. - Modelling regional sea-level changes in recent past and future. Ph.D. thesis, Utrecht University, the Netherlands, 150 p., (2012).

Slunga, R. - The Baltic Shield earthquakes. *Tectonophysics*, Vol. 189, pp. 323 - 331, (1991).

Smith, C.A., Sundh, M. and Mikko, H. – Surficial geology indicates early Holocene faulting and seismicity, central Sweden. *Int J Earth Sci (Geol Rundsch)*, Vol. 103, pp. 1711 – 1724, (2014).

Snoke, J. A., Munsey, J. W., Teague, A. G., and Bollinger, G. A. - A program for focal mechanism determination by combined use of polarity and SV-P amplitude ratio data. *Earthquake notes*, 55, (1984).

Snoke, J. A. - FOCMEC: FOCal MECHANism Determinations, Virginia Tech, Blacksburg, Manual, Report, 22 p, (2009).

Spada, G. – Glacial isostatic adjustment and contemporary sea level rise: An Overview. *Surv. Geophys.*, 33 p., (2016).

Spada, G., Ricard, Y. and Sabadini, R. – Excitation of true polar wander by subduction. *Nature*, Vol. 360, pp. 452 – 454, (1992).

Stammler, K. - Seismic Handler - programmable multichannel data handler for interactive and automatic processing of seismological analysis, *Comp. Geosci.*, Vol. 19, 135 p., (1993).

Stammler, K., - Technical aspects of the GRSN, in **Korn, M.** (ed.) – Ten years of German Regional Seismic Network. Report 25, 276 p., (2002).

Steffen, H. and Wu, P. – Glacial isostatic adjustment in Fennoscandia-A review of data and modeling. *Journal of Geodynamics*, Vol. 52, pp. 169 – 204, (2011).

Steffen, H., Kaufmann, G., Wu, P. - Three-dimensional finite-element modelling of the glacial isostatic adjustment in Fennoscandia. *Earth Planet. Sci. Lett.*, Vol. 250, pp. 358 – 375, (2006).

Steffen, H., Wu, P. and Wang, H. – Optimal locations for absolute gravity measurements and sensitivity of GRACE observations for constraining glacial isostatic adjustment on the northern hemisphere. *Geophys. J. Int.*, Vol. 190, pp. 1483 – 1494, (2012).

Steffen, R., Wu, P., Steffen, H. and Eaton, D.W. – On the implementation of faults in finite-element glacial isostatic adjustment models. *Computer & Geosciences*, Vol. 62, pp. 150 – 159, (2014a).

Steffen, R., Steffen, H., Wu, P. and Eaton, D.W. – Stress and fault parameters affecting fault slip magnitude and activation time during a glacial cycle. *Tectonics*, Vol. 33, pp. 1461 – 1476, (2014b).

Steffen, R., Wu, P., Steffen, H. and Eaton, D.W. – The effect of earth rheology and ice-sheet size on fault slip and magnitude of postglacial earthquakes. *Earth and Planetary Science Letters*, Vol. 388, pp. 71 – 80, (2014c).

Stein, S., Cloetingh, S., Sleep, N.H. and Wortel, R. – Passive margin earthquakes, stresses and rheology. In: Gregersen, S. and Basham, P.W. (eds) – *Earthquakes at North-Atlantic Passive Margins: Neotectonics and postglacial rebound*, Kluwer Academic Publishers, pp. 231 – 259, (1989).

Stein, S., Sleep, N.H., Geller, R.J., Wang, S.-C. and Kroeger, G.C. – Earthquakes along the passive margin of eastern Canada – *Geophysical Research Letters*, Vol. 6, issue 7, pp. 537 – 540, (1979).

Steinberg, D.M. and Rabinowitz, N. – Optimal seismic monitoring for event location with application to on site inspection of the comprehensive nuclear test ban treaty. *Metrika*, Vol. 58, Issue 1, pp. 31 – 57, (2003).

Stewart, I.S., Sauber, J. and Rose, J. – Glacio-seismotectonics: ice sheets, crustal deformation and seismicity. *Quaternary Science Reviews*, Vol. 19, pp. 1367 – 1389, (2000).

Stollhofen, H., Bachman, G.H., Barnasch, J., Bayer, U., Beutler, G., Franz, M., Kästner, M., Legler, B., Mutterlose, J. and Radies, D. – Upper Rotliegend to Early Cretaceous basin development, in **Littke, R., Bayer, U., Gajewski, D. and Nelskamp, S.** - Dynamics of complex intracontinental basins. The example of the Central European Basin System.– Springer-Verlag, Berlin-Heidelberg, 519 p. (ISBN: 978-3-540-85084-7), (2008).

- Suckale, J.** – Induced seismicity in hydrocarbon fields. *Advances in Geophysics*, Vol. 51, pp. 55 – 106, (2009).
- Suckale, J.** – Moderate-to-large seismicity induced by hydrocarbon production. *The Leading Edge*, Vol. 29(3), pp. 310 – 319, (2010).
- Sykes, L.R.** – Intraplate seismicity, reactivation of preexisting zones of weakness, alkaline magmatism, and other tectonism postdating continental fragmentation. *Reviews of Geophysics and Space Physics*, Vol. 16, No. 4, pp. 621 – 688, (1978).
- Talbot, C.** – A preliminary structural analysis of the pattern of post-glacial faults in northern Sweden. Technical report, SKB, 41 p., (1986).
- Talwani, P.** – *Intraplate Earthquakes*. Cambridge University Press, New York, 338 p., (2014).
- Talwani, P. and Rajendran, K.** – Some seismological and geometric features of intraplate earthquakes. *Tectonophysics*, Vol. 186, pp. 19 – 41, (1991).
- Tanner, B. and Meissner, R.** – Caledonian deformation upon southwest Baltica and its tectonic implications- Alternatives and consequences. *Tectonics*, Vol. 15., no. 4, pp. 803 – 812, (1996).
- Tanner, D.C., Musmann, O., Wawerzinek, B., Buness, H., Krawczyk, and Thomas, R.** – Salt tectonics of the eastern border of the Leinetal Graben, Lower Saxony, Germany, as deduced from seismic reflection data. *Interpretation*, Vol. 3, pp. 169 – 181, (2015).
- Tarantola, A. and Valette, B.** - Generalized non-linear inverse problems solved using the least squares criterion - *Rev. Geophys. Space Phys.*, 19, No. 2, pp. 159 - 174, (1982a).
- Tarantola, A. and Valette, B.** - Inverse Problems = Quest for Information - *Journal of Geophysics*, Vol. 50, pp. 159 - 170, (1982b).
- Tarbuck, E.J., Lutgens, F.K. and Tasa, D.** – *Earth Science, Global Edition*. Prentice Hall International, 14th edition, 788 p., (2015).
- Thurber, C.H.** – Seismic structure and tectonics of Kilauea volcano. U.S. Geological Survey Professional Paper, 1350, pp. 919 – 934, (1987).
- Toucanne, S., Zaragosi, S., Bourillet, J.F., Gibbard, P.L., Eynaud, F., Giraudeau, J., Turon, J.L., Cremer, M., Cortijo, E., Martinez, P. and Rossignol, L.** – A 1.2 Ma record of glaciation and fluvial discharge from the West European Atlantic margin. *Quaternary Science Reviews*, Vol. 28, pp. 2974 – 2981, (2009).
- Turpeinen, H., Hampel, A., Karow, T. and Maniatis, G.** - Effect of ice growth and melting on the slip evolution of thrust faults. *Earth Planet. Sci. Lett.*, Vol. 269, pp. 230 – 241, (2008).

Tushingham, A.M. and Peltier, W.R. - Ice-3G: a new global model of late Pleistocene deglaciation based upon geophysical predictions of post-glacial relative sea level change. *J. Geophys. Res.*, Vol. 96, pp. 4497 – 4523, (1991).

Tuttle, M.P., Collier, J., Wolf, L.W. and Lafferty III, R.H. – New evidence for a large earthquake in the New Madrid seismic zone between A.D. 1400 and 1670. *Geology*, Vol. 27, Issue 9, pp. 771 – 774, (1999).

Tyagunov, S., Grünthal, G., Wahlström, R., Stempniewski, L. and Zschau, J. – Seismic risk mapping for Germany. *Nat. Hazards Earth Syst. Sci.*, 6, pp. 573 – 586, (2006).

van der Pluijm, B.A. and Marshak, S. – *Earth Structure: An introduction to structural geology and tectonics*. W W Norton & Co Inc. New York, Second Edition, 656 p., (2004).

van Eck, T., Goutbeek, F., Haak, H. and Dost, B. - Seismic hazard due to small-magnitude, shallow-source, induced earthquakes in the Netherlands. *Engineering Geology*, Vol. 87, pp. 105 - 121, (2006).

van Eijs, R. M. H. E., Mulders, F. M. M., Nepveu, M., Kenter, C. J. and Scheffers, B. C. - Correlation between hydrocarbon reservoir properties and induced seismicity in the Netherlands. *Engineering Geology*, Vol. 84, pp. 99 - 111, (2006).

van Thienen-Visser, K. and Breunese, J.N. – Induced seismicity of the Groningen gas field: History and recent developments. *The Leading Edge*, Vol. 34 (6), pp. 664 – 671, (2015).

van Wees, J.D., Buijze, L., Van Thienen-Visser, K., Nepveu, M., Wassing, B.B.T., Orlic, B. and Fokker, P.A. – Geomechanics response and induced seismicity during gas field depletion in the Netherlands. *Geothermics*, Vol. 52, pp. 206 – 219, (2014).

van Wees, J.D., Stephenson, R.A., Ziegler, P.A., Bayer, U., McCann, T., Dadlez, R., Gaupp, R., Narkiewicz, M., Bitzer, F. and Scheck, M. – On the origin of the Southern Permian Basin, Central Europe. *Mar Petrol Geol*, Vol. 17, pp. 43 – 59, (2000).

Vendevile, B.C. and Jackson, M.P.A. – The rise of diapirs during thin-skinned extension. *Marine and Petroleum Geology*, Vol. 9, pp. 331 – 354, (1992).

Vink, A., Steffen, H., Reinhardt, L. and Kaufmann, G. – *Quaternary Science Reviews*, Vol. 26, pp. 3249 – 3275, (2007).

Vogt, J., and Grünthal, G., - Die Erdbebenfolge vom Herbst 1612 im Raum Bielefeld: *Geowissenschaften*, v. 12, pp. 236–240, (1994).

Waldhauser, F. and Ellsworth, W.L. – A double-difference earthquake location algorithm: Method and application to the Northern Hayward fault, California. *Bulletin of the Seismological Society of America*, Vol. 90 (6), pp. 1353 – 1368, (2000).

Wang, H. and Wu, P. – Effects of lateral variations in lithospheric thickness and mantle viscosity on glacially induced surface motion on a spherical, self-gravitating Maxwell Earth. *Earth and Planetary Science Letters*, Vol. 244, pp. 576 – 589, (2006).

Wang, X.-Q., Schubnel, A., Fortin, J., David, E.C., Guéguen, Y. and Ge, H.-K. – High Vp/Vs ratio: Saturated cracks or anisotropy effects? *Geophysical Research Letters*, Vol. 39, L11307, 6 p., (2012).

Wansa, S., - Zur Lithologie und Genese der Elster-Grundmoränen und der Haupt-Drenthe-Grundmoräne im westlichen Elbe-Weser-Dreieck. *Mitteilungen aus dem Geologischen Institut der Universität Hannover*, 34, (1994).

WEG (Wirtschaftsverband Erdöl- und Erdgasgewinnung e.V.) – Sicher und umweltschonend: Erdgas-Produktion in Deutschland, report, 16 p., (2008).

Wetmiller, R.J. – Earthquakes near the Rocky Mountain House, Alberta, and their relationship to gas production facilities. *Can. J. Earth Sci.*, Vol. 23, pp. 172 – 181, (1986).

Williams, M., Dunkerley, D., DeDekker, P., Kershaw, P. and Chappell, J., - Quaternary Environments. Arnold, London, 329 p., (1998).

Winsemann, J., Lang, J., Roskosch, J., Polom, U., Böhner, U., Brandes, C., Glotzbach, C. and Frechen, M. – Terrace styles and timing of terrace formation in the Weser and Leine valleys, northern Germany: Response of a fluvial system to climate change and glaciation. *Quaternary Science Review*, Vol. 123, pp. 31 – 57, (2015).

Wiprut, D. and Zoback, M.D. - Fault reactivation and fluid flow along a previously dormant normal fault in the northern North Sea. *Geology*; Vol. 28, No. 7, pp. 595 – 598, (2000).

Wittlinger, G., Herquel, G. and Nakache, T. – Earthquake location in strongly heterogeneous media. *Geophys. J. int.*, Vol. 115, pp. 759 – 777. (1993)

Woodward, R. - On the form and position of mean sea level. *USGS Bull*, Vol. 48, report, 88 p., (1888).

Worsley, P. - Possible early Devensian glacial deposits in the British Isles. In: **Ehlers, J., Gibbard, P., Rose, J.** (Eds.), *Glacial Deposits in Great Britain and Ireland*. Balkema, Rotterdam, Brookfield, pp. 47 – 51, (1991).

Wu, P. - Deformation of an incompressible viscoelastic flat Earth with power-law creep: a finite element approach. *Geophys. J. Int.*, Vol. 108, pp. 35 – 51, (1992a).

Wu, P. - Viscoelastic versus viscous deformation and the advection of pre-stress. *Geophys. J. Int.*, Vol. 108, pp. 136 – 142, (1992b).

Wu, P. - Will earthquake activity in Eastern Canada increase in the next few thousand years? *Can. J. Earth Sci.*, Vol. 35 (5), pp. 562 – 568, (1998).

Wu, P. - Using commercial Finite element packages for the study of earth deformations, sea levels and the state of stress. *Geophys. J. Int.*, Vol. 158 (2), pp. 401 – 408, (2004).

Wu, P. and Peltier, W.R. - Viscous gravitational relaxation. *Geophys. J. R. Astr. Soc.*, Vol. 70, pp. 435 – 486, (1982).

Wu, P. and Hasegawa, H.S. - Induced stresses and fault potential in Eastern Canada due to a disc load: a preliminary analysis. *Geophys. J. Int.*, Vol. 125, pp. 415 – 430, (1996a).

Wu, P. and Hasegawa, H.S. - Induced stresses and fault potential in Eastern Canada due to a realistic load: a preliminary analysis. *Geophys. J. Int.*, Vol. 127, pp. 215 – 229, (1996b).

Wu, P. and Johnston, P.J. – Can deglaciation trigger earthquakes in N. America? *Geophysical Research Letters*, Vol. 27(9), pp. 1323 – 1326, (2000).

Wu, P., Johnston, P. and Lambeck, K. – Postglacial rebound and fault instability in Fennoscandia. *Geophys. J. Int.*, Vol. 139, pp. 657 – 670, (1999).

Yerkes, R. F. and Castle, R. O. - Seismicity and faulting attributed to fluid extraction. *Engineering Geology*, Vol. 10, pp. 151 - 167, (1976).

Ziegler, P.A. - Geological Atlas of Western and Central Europe. Shell internationale petroleum Maatschappij BV, ISBN 90–6644–125–9, distributed by Geological Society Publishing House, 256 p., (1990).

Ziegler, P.A. – European Cenozoic rift system. *Tectonophysics*, Vol. 208, pp. 91 – 111, (1992).

Ziegler, P.A. and Dèzes, P. – Crustal evolution of western and Central Europe. *Geological Society Memoir*, Vol. 32, pp. 43 – 56, (2006).

Ziegler, P.A., Cloetingh, S. and van Wees, J.-D. – Dynamics of intra-plate compressional deformation: the Alpine foreland and other examples. *Tectonophysics*, Vol. 252, pp. 7 – 59, (1995).

Zijerveld, L., Stephenson, R., Cloetingh, S., Duin, E. and van den Berg, M.W. – Subsidence analysis and modelling of the Roer Valley Graben (SE Netherlands). *Tectonophysics*, Vol. 208, pp. 159 – 171, (1992).

Zoback, M.L. – Stress field constraints on intraplate seismicity in eastern North America. *Journal of Geophysical Research*, Vol. 97, issue B8, pp. 11761 – 11782, (1992).

Zoback, M.D. and Grollmund, B. – Impact of deglaciation on present-day intraplate seismicity in eastern North America and western Europe. *C. R. Acad. Sci. Paris, Sciences de la Terre et des planètes / Earth and Planetary Sciences*, Vol. 333, pp. 23 – 33, (2001).

Zoback, M.D. and Zinke, J.C. – Production-induced normal faulting in the Valhall and Ekofisk Oil Fields. *Pure appl. geophys.* Vol. 159, pp. 403 – 420, (2002).

Zoback, M.D. and Zoback, M.L. – State of stress and intraplate earthquakes in the United States. *Science*, Vol. 213, pp. 96 – 104, (1981).

Zoback, M.D., Hamilton, R.M., Crone, A.J., Russ, D.P., McKeown, F.A. and Brockman, S.R. – Recurrent intraplate tectonism in the New Madrid Seismic Zone. *Science*, Vol. 209, No. 4460, pp. 971 – 976, (1980).

Appendix I. NonLinLoc control-file, including all seismic stations, which were used during the relocation approach. These stations are highlighted without '#' in chapter GTSRCE.

```
# =====
# Sample NonLinLoc programs control file
#
# NonLinLoc Version 6 März 2011
#
# Anthony Lomax <lomax@faille.unice.fr>
#
# See "Control File" and "Running the Sample Location" pages
#   in the NonLinLoc on-line documentation:
#   http://www-geoazur.unice.fr/~lomax/nlloc
# =====
#
#Last Change: 12.05.2016 Uta

# = comment

# non-nested include files allowed, use:
# INCLUDE <include_file_name>

# =====
# =====
# Generic control file statements
# =====

# control (CONTROL message_flag (0:silent,1:few messages,2:verbose,...),
#           RandomNumSeed)
CONTROL 6 54321

# -----
# lat/long to rect grid transformation
# -----

# map projection / transformation
# (TRANS type <params>)
#   (char[])   search_type (SIMPLE, LAMBERT)
#   <params>:
#     SIMPLE LatOrig LongOrig RotCW
#     LAMBERT RefEllipsoid LatOrig LongOrig
#             FirstStdParal SecondStdParal RotCW
#
#   RefEllipsoid choices:
#             WGS-84, GRS-80, WGS-72, Australian, Krasovsky,
#             International, Hayford-1909, Clarke-1880, Clarke-1866,
#             Airy, Bessel, Hayford-1830, Sphere
#
# Lambert III France - IGN (except that origin is arbitrary)

#3D Norddeutschland Crust 1.0 und WEG-Modell (und auch neu CRUST2.0)

#TRANS LAMBERT WGS-84 46.00 4.00 46.00 47.00 0.0
TRANS LAMBERT WGS-84 52.3348 9.00 52.00 53.00 0.0

# maplines (MAPLINE id_num, name, red, green, blue,
#           linestyle (SOLID, DASHED, DOTTED, DASHDOT))
#MAPLINE GMT_LONLAT ./data_geog/map.prov.line 0.0 0.0 0.0 SOLID
```

```

#MAPLINE XY_LONLAT /u/cayman/1/users/lomax/data_geog/maps/france/prov.line 0.0
0.0 0.0 SOLID

# plot grid for GMT
#MAPGRID 20 20 20 -97 94 0.0 1.0 1.0 1.0 PROB_DENSITY
#
#
# =====
# END of Generic control file statements

=====
# Vel2Grid3D control file statements (Ver 03)
#
# =====
#
#
# input filename / type
# (VGINP <input file> <file type> <params>)
# (char[]) filename of the input file
# (char[]) type of the input file (SIMUL2K, FDTOMO)
#
# SIMUL2K - orig_x orig_y orig_z
#
# FDTOMO - orig_x orig_y orig_z num_x num_y num_z d_x d_y d_z
#
# Note: orig_x, orig_y, orig_z are no longer in use for SIMUL2K option
# set to zero
#
#VGINP ./fdtomo.out FDTOMO 0.0 0.0 0.0 10 10 10 6.0 6.0 6.0
#VGINP ./velomodcrust1_50_final.out SIMUL2K 0.0 0.0 0.0
VGINP ./velomodcrust1_50_test.out SIMUL2K 0.0 0.0 0.0

# output filename root
# (VGOUT <output file root>)
#
VGOUT ./mod_crust1_velo/GitterCrust1_TEST_ORIG

# wave type
# (VGTYPE wave_type (P))
#
VGTYPE P

# grid description
# (GRID num_grid_x num_grid_y num_grid_z
# orig_grid_x orig_grid_y orig_grid_z
# d_grid_x d_grid_y d_grid_z
# type
# (float) num_grid_x/y/z : number of nodes along x/y/z axis
# (float) orig_grid_x : x location of grid origin (0,0,0) in km pos east
# (float) orig_grid_y : y location of grid origin (0,0,0) in km pos north
# (float) orig_grid_z : z location of grid origin (0,0,0) in km pos down
# (float) d_grid_x/y/z : grid spacing along x/y/z axis
# (char[]) type :
# VELOCITY = km/s,
# VELOCITY_METERS = m/s,
# SLOWNESS = s/km,
# VEL2 = vel**2,
# SLOW2 = slow**2,
# SLOW_2_METERS = slow**2 ((s/m)**2),

```

```

#          SLOW_LEN = slow*d_grid)
#
#
# Layer 2DGrid (NOTE: num_grid_x must be = 2 for 2D grids
#
# Layer 3D Grids
#

# setup for model Crust 1 Uta Deutschland und Crust2

# VGGRID 1600 1600 47  -800.0 -800.0 -2.0 1.0 1.0 1.0 SLOW_LEN

# TEST Grid

#VGGRID 1400 1400 47  0.0 0.0 -2.0 1.0 1.0 1.0 SLOW_LEN

# setup for Model WEG 3D Erdgasfelder NW-Deutschland
VGGRID 884 733 150  4.150000 31.550000 -0.200000  0.100000 0.100000 0.100000
SLOW_LEN

=====
# END of Vel2Grid3D control file statements
#
=====
# =====
# Grid2Time control file statements
#=====
# Determination of travel-times using the Podvin and Lecomte Eikonal #finite
differences algorithm

# input, output filename root
# (GTFILES <input file root> <output file root> wave_type (P, S))
#
# GTFILES für CRUST1
# GTFILES  ./mod_crust1/GitterCrust1_TEST_ORIG
./time_crust1/GitterCrust1_TEST_ORIG P
# GTFILES  ./mod_crust1/GitterCrust1_FINAL  ./time_crust1_weg/Gitter_FINAL P

GTFILES  ./mod_crust1/GitterCrust1_FINAL  ./time_crust1/GitterCrust1_FINAL P

# GTFILES für WEG-Netz gespeichert im Combination Ordner
#GTFILES  ./mod_weg/GitterWEG  ./time_crust1_weg/Gitter_FINAL P

# GTFILES für WEG-Netz gespeichert im WEG_only Ordner
#GTFILES  ./mod_weg/GitterWEG  ./time_weg/GitterWEG_FINAL P

# time grid modes
# (GTMODE grid_mode, angle_mode)
#   (char[])   grid_mode (GRID3D, GRID2D)
#   (char[])   angle_mode (ANGLES_YES, ANGLES_NO)
#
GTMODE GRID3D ANGLES_YES

# source description (multiple sources can be specified)
# (GTSRCE label x_srce y_srce z_srce elev)
#
#   (char[])   label
#

```

```

#      (char[])   loc type (XYZ, LATLON (+/-dec deg), LATLONDM (deg, dec min))
#  XYZ----- LATLON/LATLONDM-----
#  x_srce : km pos E   or  lat   : pos N
#  y_srce : km pos N   or  long  : pos E
#  z_srce : km pos DN  or  depth : pos DN
#
#      elev : km pos UP
#
# Examples:
#
#GTSRCE STA   XYZ           27.25 -67.78  0.0  1.242
#GTSRCE CALF  LATLON       43.753  6.922  0.0  1.242
#GTSRCE JOU   LATLONDM    43 38.00 N  05 39.52 E   0.0  0.300
#

```

```

GTSRCE A807   LATLON       52.0968 13.4187  0.0  0.000
GTSRCE ABW5S  LATLON       53.1137  9.2241  0.0  0.023
GTSRCE AHRW   LATLON       50.5410  7.0760  0.0  0.000
#GTSRCE AMKTS  LATLON       52.8319 10.0866  0.0  0.055
#GTSRCE ARSA   LATLON       47.2505 15.5232  0.0  0.577
#GTSRCE ASS    LATLON       52.1317 10.6656  0.0 -0.295
GTSRCE ASSE   LATLON       52.1303 10.6729  0.0 -0.318
GTSRCE BFO    LATLON       48.3301  8.3296  0.0  0.589
GTSRCE BGR1   LATLON       52.9948  9.3999  0.0  0.000
GTSRCE BGR3   LATLON       53.0199  9.2473  0.0  0.000
GTSRCE BGR5   LATLON       53.0447  9.5702  0.0  0.000
GTSRCE BGR7   LATLON       52.9572  9.3143  0.0  0.000
#GTSRCE BKL B  LATLON       51.4400  7.2700  0.0  0.000
GTSRCE BKS1   LATLON       52.9948  9.3999  0.0  0.049
GTSRCE BKS B  LATLON       52.9948  9.3999  0.0  0.049
GTSRCE BNS    LATLON       50.9639  7.1756  0.0  0.200
GTSRCE BP3S   LATLON       52.9837  9.8527  0.0  0.069
GTSRCE BRG    LATLON       50.8732 13.9428  0.0  0.296
GTSRCE BSD    LATLON       55.1100 14.9100  0.0  0.000
GTSRCE BSEG   LATLON       53.9353 10.3169  0.0  0.040
#GTSRCE BSHA   LATLON       51.4470  7.2450  0.0  0.000
#GTSRCE BTEZ   LATLON       51.4490  7.2790  0.0  0.000
GTSRCE BUG    LATLON       51.4406  7.2693  0.0  0.085
#GTSRCE BUH    LATLON       48.6755  8.2284  0.0  0.750
GTSRCE CHRS   LATLON       51.6101 10.8186  0.0  0.533
GTSRCE CLL    LATLON       51.3077 13.0026  0.0  0.230
GTSRCE CLNZ   LATLON       52.9423 10.9534  0.0  0.038
GTSRCE CLZ    LATLON       51.8416 10.3724  0.0  0.680
#GTSRCE COP    LATLON       55.6800 12.4300  0.0  0.000
#GTSRCE DAVA   LATLON       47.2867  9.8803  0.0  1.602
GTSRCE DEEL   LATLON       52.9573  9.3143  0.0  0.057
GTSRCE DONN   LATLON       52.9581  8.9796  0.0  0.040
#GTSRCE ELG    LATLON       50.2060  7.3372  0.0  0.132
GTSRCE FBE    LATLON       50.9212 13.3541  0.0  0.234
GTSRCE FAHL   LATLON       52.9082  8.1537  0.0  0.040
GTSRCE FLT1   LATLON       52.3306 11.2372  0.0  0.000
GTSRCE FUR    LATLON       48.1629 11.2752  0.0  0.565
GTSRCE GEC2   LATLON       48.8451 13.7016  0.0  1.132
GTSRCE GOLD   LATLON       52.9220  9.4255  0.0  0.038
GTSRCE GOR1   LATLON       52.9903 11.3075  0.0 -0.278
GTSRCE GOR2   LATLON       53.0661 11.3017  0.0 -0.284
GTSRCE GOR3   LATLON       53.0332 11.4347  0.0 -0.280
GTSRCE GOR4   LATLON       52.9406 11.3996  0.0 -0.276
GTSRCE GOR5   LATLON       52.9228 11.2217  0.0 -0.265
GTSRCE GOR6   LATLON       53.0040 11.1735  0.0 -0.285

```


GTSRCE	GRA1	LATLON	49.6918	11.2217	0.0	0.499
#GTSRCE	GRB4	LATLON	49.4689	11.5608	0.0	0.507
#GTSRCE	GRFO	LATLON	49.6909	11.2203	0.0	0.384
GTSRCE	GPM1S	LATLON	53.0008	9.5369	0.0	0.045
GTSRCE	GRO1S	LATLON	52.9776	9.1842	0.0	0.012
GTSRCE	GROSS	LATLON	53.1093	9.3993	0.0	0.020
GTSRCE	GSH	LATLON	50.7370	6.3798	0.0	0.370
GTSRCE	GTTG	LATLON	51.5464	9.9642	0.0	0.272
#GTSRCE	GTTN	LATLON	51.5464	9.9642	0.0	0.272
GTSRCE	GUNZ	LATLON	50.3635	12.3316	0.0	0.669
GTSRCE	H03BB	LATLON	52.9492	9.4681	0.0	-0.144
GTSRCE	HAM	LATLON	53.4650	9.9247	0.0	0.030
GTSRCE	HAM3	LATLON	53.5655	9.9745	0.0	0.010
GTSRCE	HB6S	LATLON	52.9996	9.0877	0.0	0.028
GTSRCE	HGN	LATLON	50.7640	5.9317	0.0	0.135
GTSRCE	HKWD	LATLON	50.8297	12.2681	0.0	0.232
GTSRCE	HLG	LATLON	54.1847	7.8839	0.0	0.041
#GTSRCE	HOE	LATLON	52.6909	10.2530	0.0	-0.839
#GTSRCE	HOF	LATLON	50.3136	11.8775	0.0	0.566
#GTSRCE	HOK	LATLON	50.9803	7.3122	0.0	0.230
GTSRCE	HOP2S	LATLON	52.8387	9.9215	0.0	0.078
GTSRCE	HWTS	LATLON	50.5923	11.4723	0.0	0.555
GTSRCE	IBBN	LATLON	52.3072	7.7566	0.0	0.140
GTSRCE	IGAD	LATLON	53.2576	8.6904	0.0	0.043
GTSRCE	IO3CB	LATLON	52.9984	9.7825	0.0	-0.119
GTSRCE	KAST	LATLON	51.2050	8.4211	0.0	0.600
#GTSRCE	KLL	LATLON	50.6467	6.3113	0.0	0.400
#GTSRCE	KON	LATLON	52.1914	10.4044	0.0	-1.089
GTSRCE	LANGS	LATLON	52.8609	9.5919	0.0	0.039
GTSRCE	LAWA	LATLON	51.5690	10.7870	0.0	0.265
#GTSRCE	LEIB	LATLON	50.5795	11.1949	0.0	0.000
#GTSRCE	LEIN	LATLON	50.9426	12.4682	0.0	0.236
GTSRCE	LOENS	LATLON	52.9878	9.5827	0.0	0.060
GTSRCE	MANZ	LATLON	49.9862	12.1083	0.0	0.635
GTSRCE	MELL	LATLON	52.2357	8.3901	0.0	0.168
GTSRCE	MLFH	LATLON	50.7898	12.0810	0.0	0.212
#GTSRCE	MOA	LATLON	47.8495	14.2659	0.0	0.572
GTSRCE	MOX	LATLON	50.6447	11.6156	0.0	0.455
GTSRCE	MUD	LATLON	56.4600	9.1700	0.0	0.000
#GTSRCE	MULD	LATLON	50.4118	12.4039	0.0	0.678
#GTSRCE	NEUB	LATLON	51.1942	11.7719	0.0	0.200
GTSRCE	NKC	LATLON	50.2331	12.4480	0.0	0.564
GTSRCE	NRDL	LATLON	52.4943	10.1073	0.0	-0.355
#GTSRCE	OBER	LATLON	47.4069	10.2933	0.0	0.908
#GTSRCE	OGA	LATLON	46.8680	11.0250	0.0	1.934
GTSRCE	PLN	LATLON	50.4867	12.1589	0.0	0.414
GTSRCE	POSS	LATLON	51.3334	10.8669	0.0	0.425
GTSRCE	RAST	LATLON	52.9096	7.7164	0.0	0.037
GTSRCE	RETH	LATLON	52.7378	9.3611	0.0	-0.150
GTSRCE	RETHO	LATLON	52.7381	9.3607	0.0	0.021
GTSRCE	RGN	LATLON	54.5477	13.3214	0.0	0.015
GTSRCE	RJOB	LATLON	47.7372	12.7957	0.0	0.860
#GTSRCE	ROHR	LATLON	50.2340	12.3170	0.0	0.629
GTSRCE	ROTZ	LATLON	49.7669	12.2070	0.0	0.430
GTSRCE	RS52S	LATLON	53.0910	9.4620	0.0	0.030
GTSRCE	RUE	LATLON	52.4759	13.7800	0.0	0.040
GTSRCE	S06AB	LATLON	53.0525	10.2789	0.0	-0.105
#GTSRCE	SCHD	LATLON	50.5351	11.2119	0.0	0.761
GTSRCE	SCHF	LATLON	50.6772	12.4031	0.0	0.435
GTSRCE	SCHUS	LATLON	53.1198	9.7874	0.0	0.087

GTSRCE SEVE	LATLON	52.7994	8.0709	0.0	0.040
#GTSRCE SKMB	LATLON	54.7177	9.4384	0.0	0.031
#GTSRCE STB	LATLON	50.5940	6.8400	0.0	0.270
GTSRCE STF1	LATLON	51.8503	11.5823	0.0	0.112
GTSRCE STU	LATLON	48.7708	9.1933	0.0	0.360
GTSRCE SYKE	LATLON	52.8785	8.8757	0.0	0.042
GTSRCE TANN	LATLON	50.4150	12.4610	0.0	0.836
#GTSRCE TAUT	LATLON	50.9820	11.7111	0.0	0.330
GTSRCE TNS	LATLON	50.2225	8.4473	0.0	0.815
GTSRCE TRFTS	LATLON	52.9812	9.2292	0.0	0.020
GTSRCE TRIB	LATLON	50.3520	12.1370	0.0	0.510
GTSRCE TRIFS	LATLON	52.9166	9.2435	0.0	0.020
GTSRCE UBBA	LATLON	50.8188	10.0001	0.0	-0.526
GTSRCE VITZ	LATLON	50.8883	10.0915	0.0	0.411
GTSRCE VOLK	LATLON	53.0199	9.2473	0.0	0.037
GTSRCE VOR1B	LATLON	53.1961	9.1479	0.0	-0.171
GTSRCE V01EB	LATLON	52.9439	9.1098	0.0	-0.189
#GTSRCE WBSS	LATLON	52.9877	10.0857	0.0	0.076
GTSRCE WEESB	LATLON	52.8309	10.1392	0.0	-0.068
GTSRCE WERD	LATLON	50.4476	12.3064	0.0	0.589
GTSRCE WERN	LATLON	50.2874	12.3761	0.0	0.600
GTSRCE WET	LATLON	49.1440	12.8782	0.0	0.613
GTSRCE WIMM	LATLON	51.5210	11.5050	0.0	-0.030
GTSRCE WIT	LATLON	52.8135	6.6695	0.0	0.017
GTSRCE WLF	LATLON	49.6646	6.1526	0.0	0.295
GTSRCE WTSB	LATLON	51.9663	6.7989	0.0	0.043
GTSRCE ZARR	LATLON	53.5538	10.9175	0.0	0.039
#GTSRCE ZERL	LATLON	51.6210	6.8700	0.0	0.000
GTSRCE ZURM	LATLON	52.9512	9.1687	0.0	0.040

#GTSRCE ALL4S	LATLON	52.69300	8.94197	0.0	0.042
#GTSRCE AME1S	LATLON	52.94382	8.25943	0.0	0.039
#GTSRCE AMP1S	LATLON	52.79663	7.86429	0.0	0.035
#GTSRCE ASP1S	LATLON	52.97098	8.39911	0.0	0.037
#GTSRCE BKP1S	LATLON	52.49756	8.90639	0.0	0.039
#GTSRCE HS49S	LATLON	52.99327	8.79659	0.0	0.010
#GTSRCE K181S	LATLON	53.08667	8.12163	0.0	0.016
#GTSRCE KS19S	LATLON	52.71220	8.50316	0.0	0.035
#GTSRCE MTS2S	LATLON	52.84822	8.72855	0.0	0.043
#GTSRCE PW17S	LATLON	52.72820	8.29145	0.0	0.034
#GTSRCE SLS1S	LATLON	52.50235	9.46304	0.0	0.043
#GTSRCE WS12S	LATLON	52.79838	8.41880	0.0	0.040
GTSRCE BECKB	LATLON	52.88334	8.55777	0.0	0.243
GTSRCE BROKB	LATLON	52.46050	8.44188	0.0	0.062
#GTSRCE ESSNB	LATLON	52.74579	8.01327	0.0	0.030
#GTSRCE HUDEB	LATLON	53.07702	8.43434	0.0	0.017
#GTSRCE MOLBB	LATLON	52.89110	7.97383	0.0	0.050
GTSRCE PENNB	LATLON	52.64451	9.04521	0.0	0.055
GTSRCE SCHWB	LATLON	52.65819	9.63209	0.0	0.027
#GTSRCE SULIB	LATLON	52.67456	8.74439	0.0	0.038
GTSRCE WARDB	LATLON	53.04821	8.15859	0.0	0.007
GTSRCE WOELB	LATLON	52.41191	9.22809	0.0	0.070

```

# Podvin & Lecomte FD params
# Podvin and Lemcomte, 1991, GJI, 105, 271-284.
# (PLFD hs_eps_init message_flag)
#   (float) hs_eps_init : fraction (typically 1.0E-3) defining the toler-
#   ated model inhomogeneity for exact initialization.
#   A tolerance larger than 0.01 will potentially

```

```

#           create errors larger than those involved by the
#           F.D. scheme without any exact initialization.
#   (int) message_flag : Message flag (0:silent,1:few messages,2:verbose)
#           A negative value inhibits "clever"
#           initialization.
#
GT_PLFD 1.0e-3 0
#GT_WAVEFRONT_RAY

## =====
# END of Grid2Time control file statements
# =====
# =====

# =====
# =====
# Time2EQ control file statements
# =====
# The Time2EQ program calculates predicted travel-times between one or more
# synthetic events and one or more stations. Predicted take-off angles at the
# source are also calculated if an event mechanism is given and the corresponding
# take-off angles grids are available
#
# input  grid filenames root, output filename
# (EQFILES <input file root> <output file>)
EQFILES ./time_crust1_weg/Gitter_FINAL ./obs/synthvolk12.obs

# mechanism (MECH mech_type (DOUBLE, NONE), strike(E of N), dip, rake)
# EQMECH  DOUBLE 0.0 90.0 0.0

# mode
# (EQMODE str_mode)
#   SRCE_TO_STA  calc time for single source to multiple stations
#   STA_TO_SRCE  calc time for multiple sources to single station
EQMODE SRCE_TO_STA

# event description
# (EQEVENT label x_event y_event z_event otime
#   (char[]) label
#   (float) x_event : km pos east
#   (float) y_event : km pos north
#   (float) z_event : km pos down
#   (float) otime  : sec
# EQEVENT EQ001  0.0 0.0 10.0  0.0

# source description (multiple sources can be specified)
# (EQSRCE (see GTSRCE)
#
EQSRCE SynthVolk12  LATLON  52.965  9.207  7.51  0.0

# station description (multiple stations can be specified)
# (EQSTA label phase error_type error)
#   (char[]) label
#   (char[]) phase
#   (char[]) calc_error_type
#   (float) calc_error
#   (char[]) report_error_type
#   (float) report__error

```

EQSTA	ABW5S	P	GAU	0.0	GAU	0.0
EQSTA	ABW5S	S	GAU	0.0	GAU	0.0
EQSTA	AHRW	P	GAU	0.0	GAU	0.0
EQSTA	ASSE	P	GAU	0.0	GAU	0.0
EQSTA	BGR1	S	GAU	0.0	GAU	0.0
EQSTA	BGR1	P	GAU	0.0	GAU	0.0
EQSTA	BGR3	S	GAU	0.0	GAU	0.0
EQSTA	BGR3	P	GAU	0.0	GAU	0.0
EQSTA	BGR5	S	GAU	0.0	GAU	0.0
EQSTA	BGR5	P	GAU	0.0	GAU	0.0
EQSTA	BGR7	S	GAU	0.0	GAU	0.0
EQSTA	BGR7	P	GAU	0.0	GAU	0.0
EQSTA	BRG	P	GAU	0.0	GAU	0.0
EQSTA	BSD	P	GAU	0.0	GAU	0.0
EQSTA	BSEG	S	GAU	0.0	GAU	0.0
EQSTA	BSEG	P	GAU	0.0	GAU	0.0
EQSTA	BUG	P	GAU	0.0	GAU	0.0
EQSTA	CHRS	P	GAU	0.0	GAU	0.0
EQSTA	CLL	P	GAU	0.0	GAU	0.0
EQSTA	CLNZ	P	GAU	0.0	GAU	0.0
EQSTA	CLZ	P	GAU	0.0	GAU	0.0
EQSTA	FLT1	P	GAU	0.0	GAU	0.0
EQSTA	GEC2	P	GAU	0.0	GAU	0.0
EQSTA	GOLD	P	GAU	0.0	GAU	0.0
EQSTA	GOR6	P	GAU	0.0	GAU	0.0
EQSTA	GRA1	P	GAU	0.0	GAU	0.0
EQSTA	GROSS	S	GAU	0.0	GAU	0.0
EQSTA	GROSS	P	GAU	0.0	GAU	0.0
EQSTA	GTTG	P	GAU	0.0	GAU	0.0
EQSTA	GUNZ	P	GAU	0.0	GAU	0.0
EQSTA	HB6S	P	GAU	0.0	GAU	0.0
EQSTA	HGN	P	GAU	0.0	GAU	0.0
EQSTA	HLG	P	GAU	0.0	GAU	0.0
EQSTA	IBBN	S	GAU	0.0	GAU	0.0
EQSTA	IBBN	P	GAU	0.0	GAU	0.0
EQSTA	IGAD	P	GAU	0.0	GAU	0.0
EQSTA	KAST	P	GAU	0.0	GAU	0.0
EQSTA	LANGS	S	GAU	0.0	GAU	0.0
EQSTA	LANGS	P	GAU	0.0	GAU	0.0
EQSTA	LOENS	S	GAU	0.0	GAU	0.0
EQSTA	LOENS	P	GAU	0.0	GAU	0.0
EQSTA	MOX	P	GAU	0.0	GAU	0.0
EQSTA	NRDL	P	GAU	0.0	GAU	0.0
EQSTA	POSS	S	GAU	0.0	GAU	0.0
EQSTA	POSS	P	GAU	0.0	GAU	0.0
EQSTA	RETHO	P	GAU	0.0	GAU	0.0
EQSTA	RJOB	P	GAU	0.0	GAU	0.0
EQSTA	ROTZ	P	GAU	0.0	GAU	0.0
EQSTA	SCHUS	S	GAU	0.0	GAU	0.0
EQSTA	SCHUS	P	GAU	0.0	GAU	0.0
EQSTA	TNS	P	GAU	0.0	GAU	0.0
EQSTA	TRIFS	P	GAU	0.0	GAU	0.0
EQSTA	UBBA	P	GAU	0.0	GAU	0.0
EQSTA	VITZ	P	GAU	0.0	GAU	0.0
EQSTA	VOR1B	S	GAU	0.0	GAU	0.0
EQSTA	VOR1B	P	GAU	0.0	GAU	0.0
EQSTA	WERN	P	GAU	0.0	GAU	0.0
EQSTA	WET	P	GAU	0.0	GAU	0.0
EQSTA	WIMM	P	GAU	0.0	GAU	0.0
EQSTA	WTSB	P	GAU	0.0	GAU	0.0

```

# Vp / Vs ratio (overrides any S travel-time grids)
# (EQVPVS VpVs_ratio)
EQVPVS 1.73

# quality to error mapping (for HYP071, etc)
# (EQQUAL2ERR Err0 Err1 Err2 ... )
EQQUAL2ERR 0.1 0.2 0.4 0.8 99999.9

#
#
# =====
# END of Time2EQ control file statements
# =====
# =====

# =====
# =====
# NLLoc control file statements
# =====
#
# signature
# (LOCSIG signature)
LOCSIG Philipp Uta

# comment
# (LOCCOM comment)
LOCCOM Walle 2016 vp/vs = 1.88 both models

# input grid filenames root, output filename
# (LOCFILES <obs file> obs_type <travel-time grid files path/root> <output file
path/root>)
# (char[]) obs_type : (NLLOC_OBS, HYP071, HYPOELLIPSE, RENASS_DEP, SEISAN)
#

# LOCFILES ./obs/cloppenburg93.obs NLLOC_OBS ./time_crust1/GitterCrust1_TEST_ORIG
./loc/cloppenburg93

#LOCFILES ./obs/walle16_bearb.obs NLLOC_OBS ./time_crust1/GitterCrust1_FINAL
./loc/walle16_CRUST1

LOCFILES ./obs/walle16_bearb.obs NLLOC_OBS ./time_crust1_weg/Gitter_FINAL
./loc/walle16_both

# Syn
# LOCFILES ./obs/synthvolk12.obs NLLOC_OBS ./time/layerhan ./loc/synthvolk12_both

# LOCFILES ./obs/voelkersen12_weg.obs NLLOC_OBS ./time_weg/GitterWeg_FINAL
./loc/voelkersen12_FINAL_WEG

# LOCFILES ./obs/mainschhorn15.obs NLLOC_OBS ./time_crust1/GitterCrust1_FINAL
./loc/mainschhorn15_FINAL

# output hypocenter file types
# (LOCHYPOUT type1, type2, ...)
# (char[]) typeN (SAVE_NLLOC_ALL, SAVE_NLLOC_SUM,
# SAVE_HYP071_ALL, SAVE_HYP071_SUM, SAVE_HYPOELL_ALL, SAVE_HYPOELL_SUM,
# SAVE_HYPOINV_SUM, SAVE_NLLOC_OCTREE)
LOCHYPOUT SAVE_NLLOC_ALL SAVE_HYP071_SUM SAVE_HYPOINV_SUM

```

```

# search type
# (LOCSEARCH search_type <params>)
#   (char[])  search_type (GRID, MET (Metropolis), SA (Simulated Annealing))
#   <params>:
#     GRID NumScatterSamples
#     MET  NumSamples NumLearn NumEquil BeginSave NumSkip
#           StepInit StepMin StepFact ProbMin
#     OCT init_num_cells_x, init_num_cells_y, init_num_cells_z,
#           min_node_size, max_num_nodes, num_scatter,
#           use_stations_density (1 = Weights oct-tree cell prob values used for
subdivide decision
#           in proportion to number of stations in oct-tree cell.
#           Gives higher search priority to cells containing
stations,
#           stabilises convergence to local events when global search
used
#           with dense cluster of local stations.),
#           stop_on_min_node_size (1 = stop search when first min_node_size
reached,
#           0 = stop subdividing a given cell when min_node_size
reached.)

#LOCSEARCH  OCT 1 1 1 0.0001 50000 5000 0 1
LOCSEARCH  OCT 8 8 4 0.0001 50000 5000 0 1

#LOCSEARCH  OCT 30 15 10 0.05 50000 1000 2 1 -1.0

#GridSearch#
#LOCSEARCH  GRID 10
#LOCSEARCH  MET 10000 1000 4000 5000 5 -1 0.01 8.0 1.0e-10

# location grids description
# (LOCGRID  num_grid_x  num_grid_y  num_grid_z
#   orig_grid_x  orig_grid_y  orig_grid_z
#   d_grid_x  d_grid_y  d_grid_z
#   type  save_flag
#   (float) num_grid_x/y/z : number of nodes along x/y/z axis
#   (float)  orig_grid_x : x location of grid origin (0,0,0) in km pos east
#   (float)  orig_grid_y : y location of grid origin (0,0,0) in km pos north
#   (float)  orig_grid_z : z location of grid origin (0,0,0) in km pos down
#   (float)  d_grid_x/y/z : grid spacing along  x/y/z axis
#   (char[]) type : (PROB_DENSITY, MISFIT)
#   (char[]) save_flag : (SAVE, NO_SAVE)
# For Grid search, first grid is used for initial search.  Subsequent grids are
# shifted in x/y/z so that they are centered on the minimum misfit hypocenter
# x/y/z of the previous grid if x/y/z < -1.0e20.
#
#LOCGRID  450 450 50 0.0 0.0 -2.0 2.0 2.0 2.0  PROB_DENSITY  SAVE

#LOCGRID  800 800 200 0.0 0.0 -2.0 1.0 1.0 1.0  PROB_DENSITY  SAVE

#Suchraster für ganz Deutschland

#LOCGRID  800 800 47 -400.0 -400.0 -2.0 1.0 1.0 1.0  PROB_DENSITY  SAVE

#Suchraster für Erdgasfelder in Niedersachsen

LOCGRID  884 733 150 4.15000 31.5500 -0.2 0.100 0.100 0.100  PROB_DENSITY  SAVE

# LOCGRID 1400 1400 47 0.0 0.0 -2.0 1.0 1.0 1.0  PROB_DENSITY  SAVE

```

```

#Test Grid

#LOCGRID 800 800 46 -400 -400 -2.0 1.0 1.0 1.0 MISFIT SAVE
#LOCGRID 700 700 40 -350 -350 0.0 1.0 1.0 1.0 MISFIT SAVE
#LOCGRID 400 400 20 -200 -200 5.0 1.0 1.0 1.0 MISFIT SAVE
#LOCGRID 100 100 5 -1.0e30 -1.0e30 -1.0e30 1.0 1.0 1.0 MISFIT SAVE
#LOCGRID 100 100 5 -1.0e30 -1.0e30 -1.0e30 0.1 0.1 0.1 PROB_DENSITY SAVE

#LOCGRID 1600 1600 47 -800.0 -800.0 -2.0 1.0 1.0 1.0 PROB_DENSITY SAVE

# method
# (LOCMETH method)
# (char[]) method (GAU_ANALYTIC, EDT, EDT_OT_WT)
# GAU_ANALYTIC - L2 norm following Tarantola and Valette (1982)
# EDT - Equal Differential Time (see )
# EDT_OT_WT - Weights EDT sum prob by variance of OT estimated over all
pairs of readings.
# Downweights locations with inconsistent OT
estimates.
# (float) maximum_dist_sta_to_grid (use very large value for no max)
# (int) minimum_number_phases for location
# (int) maximum_number_phases for location (-1 for no max)
# (int) minimum_number_S_phases for location (-1 for no min)
# (float) Vp/Vs ratio (< 0.0 to use S travel time grids)
# (int) maximum_number_3D_grids to attempt to read into memory (-1 for no max)
# (float) minimum_dist_sta_to_grid (-1 for no min)
# (int) flag indicating if duplicate arrivals used for location (1=reject,
0=use if time diff < sigma / 2)
# duplicate arrivals have same station label and phase name

LOCMETH GAU_ANALYTIC 9999.0 4 -1 -1 1.88 -1 -1.0 1
#LOCMETH EDT_OT_WT 9999.0 4 -1 -1 1.73 -1 -1.0 1
#LOCMETH EDT_OT_WT 1.0e6 2 -1 -1 1.73 6 -1.0 0

# fixed origin time
# (LOCFIXOTIME year month day hour min sec)
# (int) year month day hour min
# (float) sec
#LOCFIXOTIME 1977 06 02 13 32 21.00

# gaussian model error parameters
# (LOCGAU Sigma_T (s), CorrLen (km))
LOCGAU 0.2 0.0
#LOCGAU 0.1 0.0

# travel-time dependent gaussian model error parameters
# (LOCGAU2 SigmaTfraction, SigmaTmin (s), SigmaTmax (s))
# travel time error is travel_time*SigmaTfraction, with max/min value =
SigmaTmin/SigmaTmax
#LOCGAU2 0.01 0.05 2.0

# phase identifier mapping
# (LOCPHASEID phase phase_id0 phase_id1 ...)
#
# examples for P and S
#LOCPHASEID P P p
#LOCPHASEID S S s

```

```

#
LOCPHASEID P P p G Pn Pg
LOCPHASEID S S s G Sn Sg
#ToIgnoreS#LOCPHASEID S $

# quality to error mapping (for HYP071, etc)
# (LOCQUAL2ERR Err0 Err1 Err2 ... )
#
# the following quality mapping is default from Hypoellipse documentation
LOCQUAL2ERR 0.1 0.5 1.0 2.0 99999.9

# phase statistics parameters
# (LOCPHSTAT RMS_Max, NRdgs_Min, Gap_Max, P_ResMax, S_ResMax)
# (float) RMS_Max : max hypocenter RMS to include in ave res
# (float) NRdgs_Min : min hypocenter num readings to include in ave res
# (float) Gap_Max : max hypocenter gap (deg) to include in ave res
# (float) P_ResMax : max abs(P res) to include in ave res
# (float) S_ResMax : max abs(S res) to include in ave res
# (float) S_ResMax : max abs(S res) to include in ave res
# (float) Ell_Len3_Max : max ellipsoid major semi-axis length to include in
ave res
# (float) Hypo_Depth_Min : min hypo depth to include in ave res
# (float) Hypo_Depth_Max : max hypo depth to include in ave res
LOCPHSTAT 9999.0 -1 9999.0 1.0 1.0 9999.9 -9999.9 9999.9

# station distribution weighting
# (LOCSTAWT flag cutoffDist)
# (int) flag: 0 = no weighting, 1 = apply weighting
# (float) cutoffDist: cutoff distance for distance weighting (-1.0 =
automatic)
LOCSTAWT 0 -1.0

# take-off angles mode & minimum quality
# (LOCANGLES angles_mode, min_quality)
# (char[]) angles_mode (ANGLES_YES, ANGLES_NO)
# (integer) min_quality : minimum quality to use take-off angles
LOCANGLES ANGLES_YES 5

# magnitude calculation method
# (LOCMAG magnitude_type <params>)
# (char[]) magnitude_type (ML_HB (ML, Hutton Boore))
# <params>:
# ML_HB amp_fact n K
LOCMAG ML_HB 1.0 1.110 0.00189
# station/inst/comp parameters (for specifying component specific parameters, i.e.
constants for magnitude calculation)
# (LOCCMP name inst comp amp_fact sta_corr)
# (char[]) name : station identifier (after alias evaluation, without
trailing underscore "_")
# (char[]) name : inst identifier (use '?' for don't care)
# (char[]) name : comp identifier (use '?' for don't care)
# (float) amp_fact: amplitude factor, will be multiplied by amplitude
# (float) sta_corr: magnitude correction
#
# example:
#
#LOCCMP CDR ? ? 1.0 0.0
#
# station name alias (for aliasing sta names, for date validation and for

```



```

# phase time delays)
# (LOCALIAS name alias year mo day year mo day)
# (char[]) name : station identifier on input
# (char[]) alias : station identifier for travel time grid on output
# NOTE: a trailing underscore "_" in aliases will only be
# used for time grid identification, not for output
# (ints) year mo day : start date of validity (0 0 0 = no start date)
# (ints) year mo day : end date of validity (9999 99 99 = no end date)
#
# Note:
# Alias evaluation is applied recursively, beware of infinite recursion!
# P and S delays from last alias only are used!
#
# example:
#
#LOCALIAS ART ART_ 1996 05 29 1996 09 18 0.03 0.08
#
#LOCALIAS SBFX SBF 0 0 0 9999 99 99

# phase exclude
# (LOCEXCLUDE name phase)
# (char[]) name : station identifier after any alias
# (char[]) phase : phase identifier on input
#LOCEXCLUDE TNS S
#LOCEXCLUDE BRG S

# time delays
# (LOCDELAY name phase n_readings p_delay s_delay)
# (char[]) name : station identifier on control file statements
# (char[]) phase : phase identifier
# (int) n_readings : number of residuals used to calc delay
# (float) delay : delay in seconds, subtracted from obs time
# station identifiers are evaluated after aliases has been evaluated!
#
# example:
#
#LOCDELAY NEGI P 1 0.04
#
# time corrections
#LOCDELAY UBBA S 1 8.00
#LOCDELAY BUH P 1 4.00
#LOCDELAY NEGI S 1 0.04
#LOCDELAY MONE P 1 0.04
#LOCDELAY MONE S 1 0.04
#LOCDELAY BSEG P 1 -1.20
#LOCDELAY BSEG S 1 1.00
#LOCDELAY BUG S 1 1.00
#LOCDELAY BFO S 1 -1.00
#LOCDELAY MOX P 1 6.00
#LOCDELAY IBBN S 1 1.50
#LOCDELAY GOR6 P 1 1.50
#LOCDELAY KAST P 1 2.50
#LOCDELAY NRDL P 1 1.90
#LOCDELAY GOR3 P 1 1.80
# =====
# END of NLLoc control file statements
#

```

Appendix II. Quality class determination for 40 relocated seismic events. Len1, Len2, Len3 correspond to the semi-minor, semi-intermediate and semi-major axis, respectively. The green length is attributed to the z-axis (depth uncertainty) and the red value corresponds to the y-axis. Average error and DIFF are calculated as defined in chapter 5.2.5. The blue highlighted rows are the best-fitting hypocenters for each of the 40 evaluated seismic events.

Event	Len1	Len2	Len3	Avr. Error	DIFF	Crit. focal depth
Soltau'77	1,13	1,90	6,47	3,16	1,65	
Wittenburg 2000	0,76	1,01	2,41	1,40	0,04	
Rotenburg'04	0,81	1,25	3,37	1,81	0,11	
Bassum'05	0,83	1,06	1,58	1,15	0,22	
Bremerhaven'05	1,31	4,65	16,34	7,44	0,14	
Cappeln'06	1,00	2,03	3,37	2,13	0,43	
Langwedel'08	1,23	1,53	7,54	3,43	0,29	
Borstel'11	0,72	0,90	1,42	1,01	0,50	
Verden'11	1,05	1,53	2,12	1,57	0,32	x
Visselhövede'12	0,55	0,82	1,20	0,86	0,07	
Hitzacker'12	0,83	1,97	2,71	1,83	0,07	x
Salzwedel'12	0,56	0,82	2,48	1,29	0,10	
Völkersen'12 (only WEG)	0,53	0,72	1,13	0,79	0,03	x
Völkersen'12 (only CRUST)	0,15	0,37	0,45	0,32	0,10	x
Völkersen'12 (both)	0,29	0,32	0,43	0,35	0,09	x
Langwedelermoor'13 (both)	0,94	1,66	2,19	1,60	0,13	x
Langwedelermoor'13 (only CRUST)	1,19	2,64	6,43	3,42	4,87	x
Cluvenhagen'13 (both)	0,47	0,61	0,68	0,59	0,02	x
Cluvenhagen'13 (only CRUST)	0,56	0,76	0,94	0,75	0,03	x
Dahlbrügge'13 (both)	0,70	1,31	1,67	1,23	0,06	x
Dahlbrügge'13 (only CRUST)	0,95	1,97	4,07	2,33	0,89	x
Emstek'13 (only CRUST)	0,72	1,93	2,20	1,62	0,10	
Dauelsen'14 (both)	1,36	1,55	3,30	2,07	0,35	x
Dauelsen'14 (only CRUST)	1,28	1,39	3,77	2,15	2,44	x
Meißenndorf'14 (both)	0,62	1,19	2,47	1,43	0,16	x
Meißenndorf'14 (only CRUST)	0,46	0,63	1,33	0,81	0,44	x
Syke'14 (only CRUST, P)	0,60	0,86	3,00	1,48	0,45	
Nindorf'14 (both)	0,44	0,73	1,03	0,73	0,01	x
Nindorf'14 (only CRUST)	0,54	0,94	1,84	1,11	0,37	x
Langwedelermoor'14 (both)	0,58	0,77	1,34	0,90	0,03	x
Langwedelermoor'14 (only CRUST)	0,75	1,08	1,57	1,14	0,06	x
Zarrentin'14 (only CRUST)	0,60	1,03	1,37	1,00	0,02	x
Cloppenburg'14 (only CRUST)	0,20	0,48	0,78	0,49	0,12	x
Walsrode'14 (both)	0,45	0,93	1,95	1,11	0,53	x
Walsrode'14 (only CRUST)	0,91	1,29	2,19	1,47	1,73	x
Krelingen'14 (both)	0,53	0,84	1,26	0,88	0,67	x
Krelingen'14 (only CRUST)	0,58	1,22	2,99	1,60	0,31	x
Vehmsmoor'14 (both)	0,62	1,12	3,74	1,83	0,75	x

Vehmsmoor'14 (only CRUST)	0,52	0,88	1,68	1,03	0,29	x
Ernstek'14 (only CRUST)	0,54	0,79	1,62	0,98	0,08	x
Döhlen'15 (only CRUST)	0,58	1,18	2,14	1,30	0,18	x
Asendorf'15 (only CRUST)	0,25	0,55	0,82	0,54	0,16	
Bothel'15 (both)	0,51	0,83	0,85	0,73	0,13	x
Bothel'15 (only CRUST)	0,66	1,33	1,76	1,25	0,45	x
Achim'15 (both)	0,48	0,52	0,97	0,66	0,13	x
Achim'15 (only CRUST)	0,57	0,61	1,91	1,03	0,34	x
Sieden'15 (only CRUST)	0,76	0,95	2,62	1,44	0,21	
Wardenburg'16 (only CRUST)	0,63	1,11	1,61	1,12	0,06	
Klosterzelle'16 (both)	0,42	0,48	0,94	0,61	0,05	
Klosterzelle'16 (only CRUST)	0,10	0,53	1,06	0,56	0,07	
Völkersen'16 (both)	0,19	0,37	0,47	0,34	0,04	x
Völkersen'16 (only CRUST)	0,40	0,59	0,62	0,54	0,02	x
Bothel'16 (both)	0,44	0,63	0,74	0,60	0,02	x
Bothel'16 (only CRUST)	0,57	0,61	1,95	1,04	0,33	x
Schneeheide'16 (both)	0,47	0,91	1,17	0,85	0,21	x
Schneeheide'16 (only CRUST)	0,66	0,87	1,59	1,04	0,31	
Großenkneten'16 (only CRUST)	0,46	0,57	1,14	0,72	0,03	x
Walle'16 (both)	0,67	0,78	1,76	1,07	0,69	x
Walle'16 (only CRUST)	0,73	0,82	1,17	0,91	0,09	x

Appendix III. 3-D relocation results with the best-fitting hypocenter solution using the different travel times. The best-fitting hypocenter, which is also drawn on the map (Fig. 35, chapter 6.1.2 are highlighted with a small star *.

Name	Date	Origin Time (UTC)	Lat (N)	Lon (E)	Depth (km)	Magnitude	Type	RMS (sec)	Velo-Mod	Phases	Gap	min. Epi Distance (km)	vp/vs	DIFF (km)	Aver. error (km)	Quality
0. Soltau'77	02.06.1977	13:32:19.350	52.909	9.570	5,28	4.000 MI	ki/ke ?	0.454	CRUST1.0	13P, 2S = 15	157	HAM 66,93	1.74	1,65	3,17	C
8. Wittenburg2000	19.05.2000	19:22:42.770	53.505	10.894	13,57	3.300 MI	ke	0.407	CRUST1.0	11P, 4S = 15	91	BSEG 61,181	1.80	0,04	1,4	A
12. Rotenburg'04	20.10.2004	06:59:17.033	53.039	9.541	13,23	4.300 MI	ki	0.560	CRUST1.0	17P, 2S = 19	83	NRDL 71,750	1.80	0,11	1,81	B
16. Bassum'05	15.07.2005	15:02:50.239	52.901	8.759	-	3.500 MI	ki	0.442	CRUST1.0	18P, 2S = 20	112	IBBN 94,732	1.80	0,22	1,15	A
18. Bremerhaven'05	11.08.2005	05:22:56.587	53.669	8.556	30,59	2.500 MI	ke	0.220	CRUST1.0	5P, 1S = 6	167	HLG 72,455	1.75	0,14	7,44	B
21. Cappeln'06	02.07.2006	14:37:39.414	52.803	7.833	7,89	2.700 MI	ki	0.484	CRUST1.0	13P, 2S = 15	167	IBBN 55,429	1.73	0,43	2,13	B
23. Langwedel'08	03.04.2008	00:06:19.441	53.043	9.131	9,37	2.500 MI	ki	0.442	CRUST1.0	13P, 1S = 14	94	NRDL 89,835	1.80	0,29	3,43	B
26. Borstel'11	16.04.2011	08:47:33.414	52.651	8.924	1,00	2.000 MI	ki	0.540	CRUST1.0	8P, 4S = 12	94	IGAD 69,347	1.78	0,5	1,01	C
28. Verden'11	02.05.2011	02:57:21.479	52.997	9.307	6,75	2.500 MI	ki	0.544	CRUST1.0	9P, 2S = 11	154	GOLD 11,563	1.80	0,32	1,57	A
29. Visselhövede'12	13.02.2012	06:04:32.190	53.027	9.594	8,24	2.600 MI	ki	0.527	CRUST1.0	19P, 8S =27	80	GOLD 16,249	1.76	0,07	0,86	A
30. Hitzacker'12	16.03.2012	20:47:11.114	53.193	11.119	42,01	1.900 MI	ke	0.243	CRUST1.0	6P, 6S = 12	148	GOR2 18,644	1.80	0,1	1,83	B
31. Salzwedel'12	28.10.2012	05:19:23.807	52.879	11.012	4,67	1.600 MI	ki	0.560	CRUST1.0	9P, 5S = 14	95	CLNZ 8,047	1.76	0,03	1,29	B
32. Völkersen'12	22.11.2012	20:38:11.664	52.990	9.245	-	2.850 MI	ki	0.627	CRUST1.0 + WEG	44P, 10S = 54	39	BGR3 3,356	1.74	0,09	0,35	A
32. Völkersen'12	22.11.2012	20:38:10.956	52.974	9.216	-	2.850 MI	ki	0.439	CRUST1.0	44P, 10S = 54	52	BGR3 5,510	1.74	0,1	0,32	A
*32. Völkersen'12	22.11.2012	20:38:11.664	52.965	9.207	7,51	2.850 MI	ki	0.282	WEG	14P, 10S = 24	138	TRIFS 5,937	1.74	0,03	0,79	B
*35. Langwedelermoor'13	01.11.2013	20:15:54.575	53.027	9.160	8,96	0.500 MI	ki	0.149	CRUST1.0 + WEG	5P, 5S = 10	257	GRO1S 5,672	1.73	0,13	1,6	A
35. Langwedelermoor'13	01.11.2013	20:15:54.480	53.041	9.145	-	0.500MI	ki	0.226	CRUST1.0	5P, 5S = 10	274	BGR3 7,241	1.73	4,87	3,42	C
*36. Cluvenhagen'13	01.11.2013	20:17:43.414	53.009	9.187	6,54	1.800 MI	ki	0.528	CRUST1.0 + WEG	15P, 11S = 26	92	GRO1S 3,528	1.80	0,02	0,59	A
36. Cluvenhagen'13	01.11.2013	20:17:44.042	53.001	9.153	7,38	1.800 MI	ki	0.531	CRUST1.0	15P, 11S = 26	91	GRO1S 3,350	1.80	0,03	0,75	A
*37. Dahlbrügge'13	02.11.2013	03:14:45.151	53.016	9.163	8,43	0.750 MI	ki	0.229	CRUST1.0 + WEG	5P, 8S = 13	242	GRO1S 4,529	1.80	0,06	1,23	A
37. Dahlbrügge'13	02.11.2013	03:14:45.462	53.053	9.119	5,77	0.750 MI	ki	0.25	CRUST1.0	5P, 8S = 13	287	BGR3 9,372	1.80	0,89	2,33	C
39. Emstek'13	20.12.2013	19:57:01.264	52.851	8.149	9,48	2.400 MI	ki	0.52	CRUST1.0	13P, 2S = 15	184	IGAD 58,004	1.76	0,1	1,62	A
*40. Dauelsen'14	15.01.2014	13:15:57.049	53.043	9.143	6,85	1.000 MI	ki	0.12	CRUST1.0 + WEG	7P, 3S = 10	306	GRO1S 7,066	1.80	0,35	2,07	B
40. Dauelsen'14	15.01.2014	13:15:57.024	53.030	9.147	-	1.000 MI	ki	0.15	CRUST1.0	7P, 3S = 10	303	GRO1S 6,344	1.80	2,44	2,15	C
*41. Meissendorf'14	09.02.2014	08:51:56.278	52.778	9.812	7,96	1.100 MI	ki	0.21	WEG	6P, 4S = 10	187	HOPS2 9,962	1.80	0,16	1,43	A
41. Meissendorf'14	09.02.2014	08:51:56.188	52.785	9.803	-	1.100 MI	ki	0.25	CRUST1.0	6P, 4S = 10	182	HOP2S 10,038	1.80	0,44	0,81	A
43. Syke'14	01.05.2014	08:29:58.907	52.907	8.759	3,48	3.500 MI	ki	0.38	CRUST1.0	41 P	68	V01EB 23,883	only P	0,45	1,49	A
*45. Nindorf'14	20.06.2014	02:57:47.332	53.002	9.182	7,63	1.500 MI	ki	0.44	CRUST1.0 + WEG	13P, 12S = 25	86	GRO1S 2,670	1.80	0,01	0,73	A
45. Nindorf'14	20.06.2014	02:57:48.174	52.996	9.148	6,69	1.500 MI	ki	0.58	CRUST1.0	13P, 12S = 25	83	GRO1S 3,142	1.80	0,37	1,11	B
*46. Langwedelermoor'14	20.06.2014	02:58:57.473	52.995	9.184	8,52	1.000 MI	ki	0.25	CRUST1.0 + WEG	8P, 7S = 15	79	GRO1S 1,949	1.90	0,03	0,9	A
46. Langwedelermoor'14	20.06.2014	02:58:58.074	52.978	9.156	9,31	1.000 MI	ki	0.34	CRUST1.0	8P, 7S = 15	118	GRO1S 1,900	1.90	0,06	1,14	A
47. Zarrentin'14	20.07.2014	22:34:15.904	53.569	10.919	25,65	1.900 MI	ke	0.44	CRUST1.0	22P, 9S = 31	99	ZARR 1,677	1.80	0,02	1	A
*49. Cloppenburg'14	02.09.2014	00:12:08.944	52.792	8.205	-	2.700 MI	ki	0.42	CRUST1.0	22P, 5S =27	60	SEVE 9,087	1.80	0,12	0,49	A
*54. Walsrode'14	20.10.2014	16:23:17.667	52.885	9.529	-	1.400 MI	ki	0.19	CRUST1.0 + WEG	8P, 5S = 13	93	LANGS 4,993	1.80	1,1	1,1	C
54. Walsrode'14	20.10.2014	16:23:17.921	52.891	9.528	-	1.400 MI	ki	0.22	CRUST1.0	8P	87	LANGS 5,479	only P	1,47	1,47	C
55. Krelingen'14	02.11.2014	11:34:48.004	52.797	9.598	14,70	1.300 MI	ke	0.32	CRUST1.0 + WEG	11P, 6S = 17	95	RETHO 17,297	1.80	0,67	0,88	C
*55. Krelingen'14	02.11.2014	11:34:48.312	52.810	9.531	23,75	1.300 MI	ke	0.33	CRUST1.0	11P, 6S = 17	84	RETHO 13,950	1.80	0,31	1,6	A
56. Vehmsmoor'14	15.11.2014	22:30:53.918	52.873	9.521	4,21	0.700 MI	ki	0.081	CRUST1.0 + WEG	6P, 3S = 9	110	LANGS 4,983	1.90	0,75	1,83	C
*56. Vehmsmoor'14	15.11.2014	22:30:53.845	52.881	9.526	-	0.700 MI	ki	0.056	CRUST1.0	6P, 3S = 9	97	LANGS 4,981	1.90	0,29	1,03	A

57. Emstek'14	19.12.2014	04:12:30.556	52.837	8.189	-	2.900 MI	ki	0.49	CRUST1.0	14P, 5S = 19	65	FAHL 8,323	1.68	0,13	0,5	B
*57. Emstek'14	19.12.2014	04:12:31.858	52.843	8.199	5,53	2.900 MI	ki	0.69	CRUST1.0	14P, 5S = 19	71	FAHL 7,904	1.78	0,08	0,98	B
59. Döhlen'15 (Clopp.)	05.06.2015	06:36:27.742	52.930	8.225	7,08	1.900 MI	ki	0.45	CRUST1.0	10P, 4S = 14	134	FAHL 5,39	1.93	0,18	1,3	A
60. Asendorf'15 (Sulingen)	13.07.2015	08:26:56.916	52.695	8.969	-	2.000 MI	ki	0.55	CRUST1.0	8P, 6S = 14	99	SYKE 21,38	1.79	0,16	0,54	B
*61. Bothel'15	14.08.2015	06:21:51.672	53.042	9.499	4,70	1.700 MI	ki	0.58	CRUST1.0+WEG	10P, 7S = 17	186	BKSB 8,47	1.91	0,13	0,73	B
61. Bothel'15	14.08.2015	06:21:51.824	53.075	9.519	6,48	1.700 MI	ki	0.59	CRUST1.0	10P, 7S = 17	198	BKSB 11,99	1.85	0,45	1,25	B
*63. Achim'15	06.12.2015	13:37:21.799	53.014	9.207	6,14	2.000 MI	ki	0.42	CRUST1.0+WEG	15P, 8S = 23	90	BGR3 2,76	1.78	0,13	0,65	A
63. Achim'15	06.12.2015	13:37:22.645	53.009	9.176	4,44	2.000 MI	ki	0.49	CRUST1.0	15P, 8S = 23	95	GRO1S 3,54	1.78	0,34	1,03	A
65. Sieden'15 (Sulingen)	29.12.2015	20:50:16.613	52.649	8.925	5,35	1.800 MI	ki	0.60	CRUST1.0	11P, 3S = 14	108	SYKE 25,79	1.88	0,21	1,44	B
66. Wardenburg'16 (Clopp)	14.01.2016	14:04:00.051	52.990	8.209	3,99	2.400 MI	ki	0.65	CRUST1.0	14P, 3S=17	130	FAHL 9,82	1.90	0,06	1,11	B
69. Klosterzelle (Walsrode)	18.02.2016	14:57:05.230	52.872	9.552	2,4	1.900 MI	ki	0.90	CRUST1.0+WEG	10P, 5S = 15	168	GOLD 10,14	1.84	0,05	0,61	D
*69. Klosterzelle (Walsrode)	18.02.2016	14:57:04.533	52.867	9.539	-	1.900 MI	ki	0.71	CRUST1.0	10P, 5S = 15	165	GOLD 9,80	1.75	0,07	0,56	D
*72. Völkersen'16	22.04.2016	17:45:31.831	53.002	9.238	4,2	3.000 MI	ki	0.66	CRUST1.0+WEG	36P, 7S = 43	47	BGR3 2,05	1.85	0,04	0,34	B
72. Völkersen'16	22.04.2016	17:45:32.362	52.998	9.213	3,71	3.000 MI	ki	0.49	CRUST1.0	37P, 7S = 44	53	TRFTS 2,19	1.85	0,02	0,54	A
*73. Bothel'16	28.05.2016	21:13:40.852	53.078	9.498	3,91	2.200 MI	ki	0.41	CRUST1.0+WEG	16P, 5S = 21	87	RS52S 2,82	1.86	0,02	0,6	A
73. Bothel'16	28.05.2016	21:13:41.278	53.099	9.515	3,54	2.200 MI	ki	0,39	CRUST1.0	16P, 5S = 21	111	RS52S 3,69	1.89	0,33	1,05	A
*75. Schneeheide'16 (Walsrode)	04.09.2016	18:59:42.487	52.868	9.473	-	1.500 MI	ki	0.33	CRUST1.0+WEG	6P, 3S = 9	126	GOLD 6,77	1.89	0,21	0,85	A
75. Schneeheide'16 (Walsrode)	04.09.2016	18:59:42.391	52.873	9.510	-	1.500 MI	ki	0,24	CRUST1.0	6P, 3S = 9	128	GOLD 7,89	1.89	0,31	1,04	A
76. Großenkneten'16 (Clopp.)	27.10.2016	12:34:13.125	52.912	8.288	-	2.300 MI	ki	0.53	CRUST1.0	10P, 6S = 16	99	FAHL 9,09	1.83	0,03	0,72	A
77. Walle'16 (Langwedel)	15.11.2016	09:27:13.759	52.947	9.274	4,6	2.200 MI	ki	0.86	CRUST1.0+WEG	11P, 4S = 15	137	DEEL 2,97	1.88	0,69	1,07	D
*77. Walle'16 (Langwedel)	15.11.2016	09:27:13.747	52.981	9.240	6,1	2.200 MI	ki	0.66	CRUST1.0	11P, 4S = 15	148	DEEL 5,68	1.89	0,09	0,91	B

Appendix IV. 1-D pre-located and 3-D relocated seismic events in the study area since 1993 plus Soltau 1977. (78 Events).

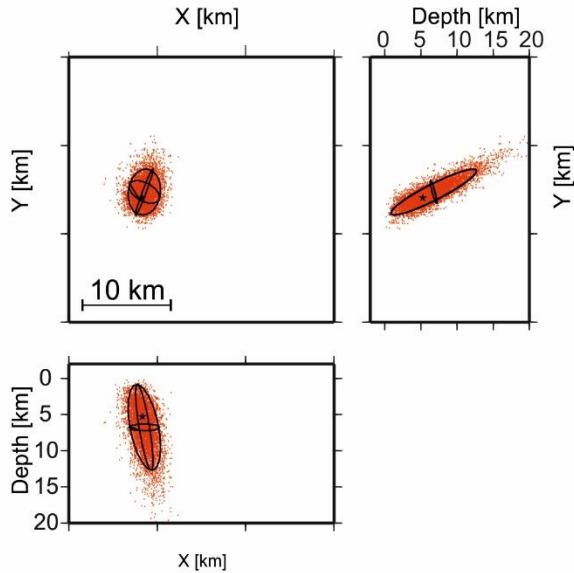
Name	Date	Origin Time (UTC)	Lat (N)	Err Lat (km)	Lon (E)	Err Lon (km)	Depth (km)	Err Depth (km)	Magnitude	Type	RMS [s]	vp/vs	Velo-Mod	No. Of Stations	Phases	Gap	min. Epi. Distance (km)	Selection/Quality
0. Soltau'77*	02.06.1977	13:32:23.500	52.950	N/A	9.950	N/A	7,000f	N/A	4.000 MI	ki/ke								IV
0. Soltau'77	02.06.1977	13:32:19.350	52.909	± 3,2	9.570	± 2,6	5,28	± 6,3	4.000 MI	ki/ke	0,45	1,74	CRUST1.0	12	12P, 2S = 14	157	HAM 66,93	C
1. Cloppenburg'93	07.05.1993	16:19:46.354	52.811	5,96	7.865	4,28	5.000f	N/A	2.500 MI	ki	0,57		DEU	4	3P, 3S = 6	280	BUG 157,99	IV
2. Wustrow'93	21.07.1993	04:22:37.800	52.857	N/A	10.997	N/A	7000,00	N/A	2.100 MI	ki	N/A		DEU	2	2P, 2S = 4			
3. Stolzenau'93	09.10.1993	23:07:59.849	52.614	5,66	8.997	2,69	5.000f	N/A	2.300 MI	ki	0,88		DEU	5	4P, 4S = 8	269	CLZ 127,5	IV
4. Pennigsehl'96	25.05.1996	08:43:33.114	52.634	2,85	9.007	1,95	5.000f	N/A	2.400 MI	ki	0,52		DEU	7	6P, 6S = 12	144	IBBN 92,51	IV
5. Halen'98	10.12.1998	00:21:36.205	52.748	5,75	8.338	4,7	5.000f	N/A	2.400 MI	ki	0,72		DEU	5	5P, 2S = 7	266	IBBN 63,01	IV
6. Klötze'99	18.03.1999	01:48:54.004	52.670	6,1	11.126	3,89	5.000f	N/A	1.800 MI	ki	0,52		DEU	3	3P, 3S = 6	290	CLZ 105,67	IV
7. Visbeck'99	28.03.1999	20:32:50.566	52.747	7,99	8.326	3,43	5.000f	N/A	2.000 MI	ki	0,92		HAN	4	4P, 3S = 7	266	IBBN 62,42	IV
8. Wittenburg'2000	19.05.2000	19:22:41.438	53.487	2,14	10.937	2,74	10.000f	N/A	3.300 MI	ke	0,60		DEU	12	11P, 4S = 15	92	BSEG 64,61	IV
8. Wittenburg'2000	19.05.2000	19:22:42.770	53.505	± 0,7	10.894	± 1,1	13,57	± 2,5	3.300 MI	ke	0,41	1,80	CRUST1.0	12	11P, 4S = 15	91	BSEG 61,18	A
9. Weyhe'02	11.07.2002	21:02:44.724	53.018	6,17	8.786	3,05	5.000f	N/A	2.400 MI	ki	0,57		DEU	5	5P, 3S = 8	261	IBBN 105,49	IV
10. Höltinghausen'02	10.09.2002	23:01:45.763	52.907	3,19	8.128	3,17	5.000f	N/A	2.500 MI	ki	0,57		DEU	4	4P, 2S = 6	153	IBBN 71,4	IV
11. Petershagen'03	04.07.2003	20:16:58.933	52.704	2,65	8.969	1,9	5.000f	N/A	1.900 MI	ki	0,84		DEU	10	9P, 4S = 13	101	NRDL 80,66	IV
12. RotenburgI'04	20.10.2004	06:59:16.020	53.050	1,72	9.569	2,35	5.000f	N/A	4.300 MI	ki	0,76		DEU	17	17P, 5S = 22	82	NRDL 71,79	IV
12. RotenburgI'04	20.10.2004	06:59:17.033	53.039	± 0,8	9.541	± 1,5	13,23	± 3,2	4.300 MI	ki	0,56	1,80	CRUST1.0	17	17P, 2S = 19	83	NRDL 71,75	B
13. RotenburgII'04	20.10.2004	07:47:36.845	53.064	2,07	9.615	3,24	5.000f	N/A	2.100 MI	ki	0,74		DEU	4	3P, 4S = 7	148	NRDL 71,64	IV
14. RotenburgIII'04	20.10.2004	20:05:25.329	53.059	2,09	9.585	3,2	5.000f	N/A	2.000 MI	ki	0,52		DEU	4	3P, 4S = 7	149	NRDL 72,12	IV
15. Ahausen'04	24.10.2004	00:49:35.394	53.065	2,35	9.590	3,36	5.000f	N/A	1.900 MI	ki	0,35		DEU	4	3P, 3S = 6	149	NRDL 72,54	IV
16. Bassum'05 (bei Syke)	15.07.2005	15:02:50.972	52.873	2,53	8.750	2,29	5.000f	N/A	3.500 MI	ki	0,84		DEU	19	19P, 3S = 22	112	IBBN 92,26	IV
16. Bassum'05 (bei Syke)	15.07.2005	15:02:50.239	52.901	± 1,4	8.759	± 0,7	N/A	N/A	3.500 MI	ki	0,44	1,80	CRUST1.0	18	18P, 2S = 20	112	IBBN 94,73	A

17. Nordwohde'05	30.07.2005	22:54:55.449	52.886	2,06	8.773	2,18	5.000f	N/A	2.100 MI	ki	0,87		DEU	7	6P, 5S = 11	111	IBBN 94,39	IV	
18. Bremerhaven'05	11.08.2005	05:22:56.433	53.692	3,78	8.638	4,69	30.000f	N/A	2.600 MI	ke	0,28		DEU	8	7P, 4S = 11	172	HLG 73,96	IV	
18. Bremerhaven'05	11.08.2005	05:22:56.587	53.669	± 3,2	8.556	± 3,9	30,59	± 16,3	2.600 MI	ke	0,22	1,75	CRUST1.0	5	5P, 1S = 6	166	HLG 72,46	B	
19. Pretzier'05	16.10.2005	02:26:37.476	52.858	1,85	11.215	2,03	5.000f	N/A	1.900 MI	ki	0,61		DEU	8	7P, 6S = 13	77	NRDL 85,04	IV	
20. Ellenstedt'05	17.12.2005	11:56:59.113	52.862	7,94	8.190	4,64	5.000f	N/A	2.200 MI	ki	0,59		DEU	4	4P, 3S = 7	261	IBBN 68,44	IV	
21. Cappel'n'06	02.07.2006	14:37:38.758	52.799	1,88	7.863	4,34	5.000f	N/A	2.700 MI	ki	0,55		DEU	13	13P, 4S = 17	166	IBBN 55,25	III	
21. Cappel'n'06	02.07.2006	14:37:39.414	52.803	± 0,9	7.833	± 2,5	7,89	± 3,1	2.700 MI	ki	0,48	1,73	CRUST1.0	13	13P, 2S = 15	166	IBBN 55,43	B	
22. Nienburg'07	27.06.2007	01:45:34.943	52.604	2,09	9.263	2,43	5.000f	N/A	1.900 MI	ki	0,65		DEU	6	6P, 4S = 10	132	NRDL 58,61	III	
23. Langwedel'08	03.04.2008	00:06:18.643	52.996	1,8	9.169	1,84	5.000f	N/A	2.500 MI	ki	1,00		DEU	18	19P, 6S = 25	93	NRDL 84,53	IV	
23. Langwedel'08	03.04.2008	00:06:19.441	53.043	± 1,3	9.131	± 1,3	9,37	± 7,8	2.500 MI	ki	0,44	1,80	CRUST1.0	13	13P, 1S = 14	93	NRDL 89,84	B	
24. Walle'10	24.04.2010	14:10:50.407	52.934	2,49	9.271	13,86	5.000f	N/A	1.500 MI	ki	0,71		DEU	4	4P, 2S = 6	244	GOLD 10,48	IV	
25. Steyerberg'10	22.08.2010	20:14:35.227	52.618	2,44	8.992	2,3	5.000f	N/A	1.300 MI	ki	0,93		DEU	8	7P, 4S = 11	143	GOLD 44,77	III	
26. Borstel'11	16.04.2011	08:47:33.615	52.656	1,8	8.930	1,66	5.000f	N/A	2.000 MI	ki	0,65		DEU	12	11P, 7S = 18	93	IGAD 68,93	IV	
26. Borstel'11	16.04.2011	08:47:33.414	52.651	± 1,0	8.924	± 0,7	N/A	N/A	2.000 MI	ki	0,54	1,78	CRUST1.0	9	8P, 4S = 12	93	IGAD 69,35	C	
27. Walsrode'11	27.04.2011	16:21:14.963	52.871	1,92	9.514	1,73	5.000f	N/A	2.100 MI	ki	0,52		DEU	12	10P, 6S = 16	73	GOLD 8,23	II	
28. Verden'11	02.05.2011	02:57:21.161	52.970	2,18	9.254	1,89	5.000f	N/A	2.500 MI	ki	0,64		DEU	14	13P, 5S = 18	90	GOLD 12,72	II	
28. Verden'11	02.05.2011	02:57:21.479	52.997	± 1,5	9.307	± 1,9	6,75	± 1,4	2.500 MI	ki	0,54	1,80	CRUST1.0	9	9P, 2S = 11	153	GOLD 11,56	A	
29. Visselhövede'12	13.02.2012	06:04:31.630	53.021	1,6	9.612	1,45	5.000f	N/A	2.600 MI	ki	0,67		DEU	25	21P, 11S = 32	79	GOLD 16,70	II	
29. Visselhövede'12	13.02.2012	06:04:32.190	53.027	± 0,7	9.594	± 0,7	8,24	± 1,3	2.600 MI	ki	0,53	1,76	CRUST1.0	23	19P, 8S = 27	80	GOLD 16,25	A	
30. Hitzacker (Elbe)'12	16.03.2012	20:47:12.031	53.195	2,11	11.169	3,6	30.000f	N/A	1.900 MI	ke	0,50		DEU	12	7P, 9S = 16	158	GOR2 16,89	II	
30. Hitzacker (Elbe)'12	16.03.2012	20:47:11.114	53.193	± 1,1	11.119	± 2,1	42,01	± 2,5	1.900 MI	ke	0,24	1,80	CRUST1.0	9	6P, 6S = 12	148	GOR2 18,64	A	
31. Salzwedel'12	28.10.2012	05:19:23.761	52.860	1,55	11.002	2,31	5.000f	N/A	1.600 MI	ki	0,52		DEU	12	12P, 5S = 17	100	CLNZ 9,73	II	
31. Salzwedel'12	28.10.2012	05:19:23.807	52.879	± 0,5	11.012	± 0,7	4,67	± 2,3	1.600 MI	ki	0,56	1,76	CRUST1.0	9	9P, 5S = 14	94	CLNZ 8,05	B	
32. Völkersen'12	22.11.2012	20:38:11.591	52.974	0,98	9.217	1,07	3,45	± 2,04	2.850 MI	ki	0,50		HAN	47	48P, 13S = 61	45	BGR3 5,51	I	
32. Völkersen'12	22.11.2012	20:38:11.664	52.965	± 0,5	9.207	± 0,6	7,51	± 1,2	2.850 MI	ki	0,28	1,74	WEG	14	14P, 10S = 24	137	TRIFS 5,94	A	
33. Mainsche'13	22.08.2013	16:16:35.526	52.695	3,09	8.895	3,66	5.000f	N/A	1.300 MI	ki	1,04		DEU	9	8P, 6S = 14	186	RETH 31,89	III	
34. Westenholz'13	06.09.2013	07:04:05.211	52.808	1,51	9.729	1,34	5.000f	N/A	1.200 MI	ki	0,86		HAN	12	10P, 7S = 17	95	HOP2S 10,96	II	
35. Langwedelermoor'13	01.11.2013	20:15:54.621	53.033	5,93	9.149	4,08	9,20	± 2,75	0.500 MI	ki	0,70		HAN	6	5P, 5S = 10	266	GRO1S 6,61	III	
35. Langwedelermoor'13	01.11.2013	20:15:54.575	53.027	± 1,8	9.160	± 1,0	8,96	± 1,7	0.500 MI	ki	0,15	1,73	CRUST1.0+WEG	6	5P, 5S = 10	256	GRO1S 5,67	A	
36. Cluvenhagen'13	01.11.2013	20:17:43.831	53.001	1,25	9.185	1,2	6,45	± 1,04	1.800 MI	ki	-		HAN	22	18P, 14S = 32	85	GRO1S 2,61	I	
36. Cluvenhagen'13	01.11.2013	20:17:43.414	53.009	± 0,6	9.187	± 0,4	6,54	± 0,5	1.800 MI	ki	0,53	1,80	CRUST1.0+WEG	18	15P, 11S = 26	91	GRO1S 3,53	A	
37. Dahlbrügge'13	02.11.2013	03:14:44.797	53.045	4,45	9.129	3,47	8,80	± 2,55	0.750 MI	ki	-		HAN	9	5P, 8S = 13	280	GRO1S 8,38	IV	
37. Dahlbrügge'13	02.11.2013	03:14:45.151	53.016	± 1,5	9.163	± 0,8	8,43	± 1,3	0.750 MI	ki	0,25	1,80	CRUST1.0+WEG	9	5P, 8S = 13	241	GRO1S 4,53	A	
38. Fulde'13	02.11.2013	20:05:46.594	52.887	1,33	9.504	1,51	5.000f	N/A	0.900 MI	ki	1,17		HAN	10	5P, 8S = 13	75	GOLD 6,57	I - II	
39. Emstek'13	20.12.2013	19:57:00.493	52.854	1,83	8.125	2,37	5.000f	N/A	2.400 MI	ki	0,57		DEU	17	15P, 5S = 20	140	IGAD 58,92	II	
39. Emstek'13	20.12.2013	19:57:01.264	52.851	± 1,5	8.149	± 1,6	9,48	± 1,9	2.400 MI	ki	0,52	1,76	CRUST1.0	14	13P, 2S = 15	184	IGAD 58,00	A	
40. Dauelsen'14	15.01.2014	13:15:58.587	52.957	2,62	9.233	2,14	5.000f	N/A	1.000MI	ki	0,53		HAN	7	7P, 3S = 10	145	TRFTS 2,71	II	
40. Dauelsen'14	15.01.2014	13:15:57.049	53.043	± 2,0	9.143	± 2,3	6,85	± 1,5	1.000MI	ki	0,12	1,80	CRUST1.0+WEG	7	7P, 3S = 10	306	GRO1S 7,07	B	
41. Meißendorf'14	09.02.2014	08:51:56.346	52.770	3,68	9.792	2,1	5.000f	N/A	1.100 MI	ki	0,48		HAN	6	6P, 4S = 10	189	HOP2S 11,62	II	
41. Meißendorf'14	09.02.2014	08:51:56.278	52.778	± 1,2	9.812	± 0,6	7,96	± 2,5	1.100 MI	ki	0,21	1,80	WEG	6	6P, 4S = 10	186	HOP2S 9,96	A	
42. Raum Langwedel	25.04.2014	22:13:34	53.009		9.199				0.900 MI										
43. Syke'14	01.05.2014	08:29:58.225	52.896	1,64	8.750	1,44	5.000f	N/A	3.500 MI	ki	0,58		DEU	44	44P, 8S = 52	67	V01EB 24,80	II	
43. Syke'14	01.05.2014	08:29:58.907	52.907	± 0,7	8.759	± 0,6	3,48	± 3,1	3.500 MI	ki	0,38	only P	CRUST1.0	41	41 P	67	V01EB 23,88	A	
44. Raum Langwedel	16.05.2014	22:26:12	52.953		9.200				0.800 MI										
45. Nindorf'14	20.06.2014	02:57:47.915	53.007	1,36	9.188	0,92	5.000f	N/A	1.500 MI	ki	0,66		HAN	19	16P, 13S = 29	90	GRO1S 3,41	I	
45. Nindorf'14	20.06.2014	02:57:47.332	53.002	± 0,8	9.182	± 0,6	7,63	± 0,8	1.500 MI	ki	0,44	1,80	CRUST1.0+WEG	18	13P, 12S = 25	86	GRO1S 2,67	A	
46. Langwedelermoor'14	20.06.2014	02:58:58.395	53.008	1,45	9.196	1,32	5.000f	N/A	1.000 MI	ki	0,67		HAN	10	8P, 7S = 15	88	GRO1S 3,07	I	
46. Langwedelermoor'14	20.06.2014	02:58:57.473	52.995	± 1,0	9.184	± 0,7	8,52	± 1,0	1.000 MI	ki	0,25	1,90	CRUST1.0+WEG	10	8P, 7S = 15	79	GRO1S 1,95	A	

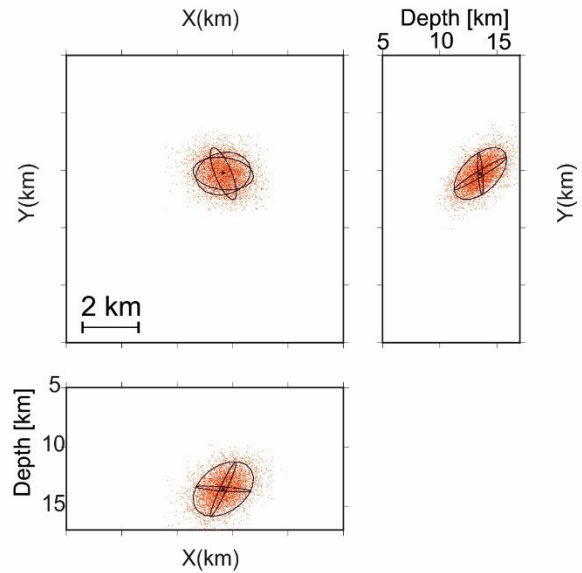
47. Zarrentin'14	20.07.2014	22:34:15.671	53.489	1,53	10.725	2,08	10.000f	N/A	1.900 MI	ke	1,40		DEU	23	23P, 10S = 33	82	ZARR 15,02	II
47. Zarrentin'14	20.07.2014	22:34:15.904	53.569	± 0,7	10.919	± 0,9	25,65	± 0,9	1.900 MI	ke	0,44	1,80	CRUST1.0	22	22P, 9S = 31	98	ZARR 1,677	A
48. Großenkneten'14	28.07.2014	20:03:46.155	52.966	3,64	8.257	2,12	5.000f	N/A	2.000 MI	ki	0,64		HAN	7	7P, 3S = 10	142	RAST 36,92	III
49. Cloppenburg'14	02.09.2014	00:12:09.716	52.802	1,8	8.203	1,33	5.000f	N/A	2.700 MI	ki	0,74		HAN	25	25P, 7S = 32	62	SEVE 8,92	II
49. Cloppenburg'14	02.09.2014	00:12:08.944	52.792	± 1,0	8.205	± 0,5	N/A	N/A	2.700 MI	ki	0,42	1,80	CRUST1.0	23	22P, 5S = 27	60	SEVE 9,09	A
50. Raum Walsrode	15.10.2014	06:42:09	52.892		9.522				1.000 MI									
51. Raum Walsrode	16.10.2014	02:45:00	52.878		9.522				1.200 MI									
52. Raum Walsrode	18.10.2014	07:44:18	52.880		9.510				0.700 MI									
53. Raum Walsrode	20.10.2014	16:17:49	52.898		9.542				1.100 MI									
54. Walsrode'14	20.10.2014	16:23:18.503	52.875	1,45	9.513	1,59	5.000f	N/A	1.400 MI	ki	0,41		HAN	11	9P, 5S = 14	72	LANGS 5,55	I
54. Walsrode'14	20.10.2014	16:23:17.667	52.885	± 0,6	9.529	± 0,7	N/A	N/A	1.400 MI	ki	0,19	1,80	CRUST1.0+WEG	10	8P, 5S = 13	93	LANGS 4,99	C
55. Krelingen'14	02.11.2014	11:34:47.614	52.783	1,6	9.644	1,48	5.000f	N/A	1.300 MI	ke	0,61		HAN	14	12P, 6S = 18	101	RETHO 19,78	II
55. Krelingen'14	02.11.2014	11:34:48.312	52.810	± 1,6	9.531	± 2,0	23,75	± 2,4	1.300 MI	ke	0,33	1,80	CRUST1.0	14	11P, 6S = 17	83	RETHO 13,95	A
56. Vehmsmoor'14	15.11.2014	22:30:54.088	52.866	1,91	9.510	2,17	5.000f	N/A	0.700 MI	ki	0,40		HAN	7	6P, 3S = 9	119	LANGS 5,55	I
56. Vehmsmoor'14	15.11.2014	22:30:53.845	52.873	± 0,6	9.521	± 1,0	4,20	± 3,7	0.700 MI	ki	0,06	1,90	CRUST1.0	7	6P, 3S = 9	97	LANGS 4,98	A
57. Emstek'14	19.12.2014	04:12:31.087	52.833	1,62	8.188	1,68	5,40	± 1,9	2.900 MI	ki	-		HAN	19	16P, 8S = 24	< 45	FAHL 8,69	I
57. Emstek'14	19.12.2014	04:12:31.858	52.843	± 0,9	8.199	± 0,7	5,53	± 1,5	2.900 MI	ki	0,69	1,78	CRUST1.0	14	14P, 5S = 19	70	FAHL 7,90	B
58. Mainschorn'15	02.05.2015	07:25:37.612	52.644	1,78	9.009	1,62	N/A	N/A	1.700 MI	ki	0,65		HAN	14	10P, 8S = 18	96	RETHO 26,01	III
59. Döhlen'15 (Clopp.)	05.06.2015	03:36:26.348	52.921	2,78	8.269	1,48	N/A	N/A	1.900 MI	ki	0,64		HAN	11	11P, 4S = 15	128	FAHL 7,90	II
59. Döhlen'15 (Clopp.)	05.08.2015	03:36:27.742	52.930	± 1,2	8.225	± 1,1	7,08	± 1,6	1.900 MI	ki	0,45	1,93	CRUST1.0	10	10P, 4S = 14	134	FAHL 5,39	A
60. Asendorf'15 (Sulingen)	13.07.2015	08:26:57.347	52.705	1,50	8.976	1,81	3.000f	N/A	2.000 MI	ki	0,71		HAN	10	9P, 6S = 15	99	Syke 20,47	II
60. Asendorf'15 (Sulingen)	13.07.2015	08:26:56.916	52.695	± 0,7	8.969	± 0,8	N/A	N/A	2.000 MI	ki	0,55	1,79	CRUST1.0	10	8P, 6S = 14	99	Syke 21,38	B
61. Bothel'15	14.08.2015	06:21:50.747	53.090	2,51	9.510	1,42	5.000f	N/A	1.700 MI	ki	0,60		HAN	13	11P, 9S = 20	205	BKSB 12,93	III
61. Bothel'15	14.08.2015	06:21:51.672	53.075	± 0,9	9.518	± 0,6	4,70	± 0,8	1.700 MI	ki	0,58	1,91	CRUST1.0+WEG	11	10P, 7S = 17	186	BKSB 8,47	B
62. Raum Walsrode	02.09.2015	17:48:34							0.900 MI									
63. Achim'15 (Langwedel)	06.12.2015	13:37:22.210	53.008	1,19	9.192	1,41	5,15	± 1,33	2.000 MI	ki	0,47		HAN	20	19P, 10S = 29	87	GRO1S 3,43	I
63. Achim'15 (Langwedel)	06.12.2015	13:37:21.799	53.014	± 0,7	9.207	± 0,6	6,14	± 0,6	2.000 MI	ki	0,42	1,78	CRUST1.0+WEG	16	15P, 8S = 23	90	BGR3 2,76	A
64. Raum Langwedel	13.12.2015	18:44:29	53.010		9.199													
65. Sieden'15 (Sulingen)	29.12.2015	20:50:14.942	52.671	2,04	8.958	2,26	N/A	N/A	1.800 MI	ki	0,46		HAN	13	13P, 3S = 16	100	SYKE 23,77	II
65. Sieden'15 (Sulingen)	29.12.2015	20:50:16.613	52.649	± 1,1	8.925	± 0,8	5,35	± 2,2	1.800 MI	ki	0,60	1,88	CRUST1.0	12	11P, 3S = 14	108	SYKE 25,79	B
66. Wardenburg'16 (Clopp.)	14.01.2016	14:04:00.002	53.021	1,92	8.200	2,1	6,79	± 3,1	2.400 MI	ki	0,63		DEU	15	15P, 5S = 20	138	FAHL 12,94	II
66. Wardenburg'16 (Clopp.)	14.01.2016	14:4:00:051	52.990	± 0,8	8.209	± 0,9	3,99	± 1,6	2.400 MI	ki	0,65	1,90	CRUST1.0	14	14P, 3S = 17	130	FAHL 9,82	B
67. Hellwege'16 (Langwedel)	22.01.2016	20:38:20	53.014	4,11	9.196	2,93	5.000f	N/A	1.300 MI	ki	0,29		HAN	4	3P, 3S = 6	282	ZURM 12,65	IV
68. Raum Langwedel	23.01.2016	04:57:31																
69. Klosterzelle'16 (Walsrode)	18.02.2016	14:57:05.167	52.872	1,74	9.516	1,72	5.000f	N/A	1.900 MI	ki	0,72		HAN	13	12P, 5S = 17	164	GOLD 8,80	II
69. Klosterzelle'16 (Walsrode)	18.02.2016	14:57:04.533	52.867	± 0,9	9.539	± 0,8	-	N/A	1.900 MI	ki	0,71	1,75	CRUST1.0	11	10P, 5S = 15	165	GOLD 9,80	D
70. Raum Langwedel	27.02.2016	18:02:40	53.004		9.197													
71. Raum Walsrode	11.03.2016	21:00:14	52.896		9.524				0.900 MI	ki								
72. Völkersen'16	22.04.2016	17:45:31.759	52.998	1,18	9.217	1,14	6,00	± 1,02	3.000 MI	ki	0,51		HAN	37	39P, 7S = 46	40	BGR3 3,18	I
72. Völkersen'16	22.04.2016	17:45:31.830	53.002	± 0,5	9.238	± 0,4	4,20	± 0,2	3.000 MI	ki	0,66	1,85	CRUST1.0+WEG	36	36P, 7S = 43	47	BGR3 2,05	A
73. Bothel'16	28.05.2016	21:13:41.015	53.077	1,38	9.493	1,43	4,80	± 2,34	2.200 MI	ki	0,45		HAN	18	17P, 6S = 23	40	RS52S 2,60	I
73. Bothel'16	28.05.2016	21:13:40.852	53.078	± 0,5	9.498	± 0,5	3,91	± 0,7	2.200 MI	ki	0,41	1,86	CRUST1.0+WEG	17	16P, 5S = 21	83	RS52S 2,80	A
74. Schneeheide'16 (Vorbeben?)	04.09.2016	17:38:19.264	52.875	2,02	9.504	4,31	5.000f	N/A	1.200 MI	ki	0,17		HAN	4	4P, 2S = 6	197	GOLD 7,40	III
75. Schneeheide'16 (Walsrode)	04.09.2016	18:59:42.342	52.865	1,50	9.513	2,25	5.000f	N/A	1.500 MI	ki	0,26		HAN	6	6P, 4S = 10	128	GOLD 8,66	I
75. Schneeheide'16 (Walsrode)	04.09.2016	18:59:42.487	52.868	± 0,4	9.473	± 1,2	-	N/A	1.500 MI	ki	0,33	1,89	CRUST1.0+WEG	6	6P, 3S = 9	126	GOLD 6,77	A
76. Großenkneten'16	27.10.2016	12:34:14.033	52.965	2,86	8.234	1,93	10,60	± 3,5	2.300 MI	ki	0,58		HAN	12	12P, 6S = 18	100	FAHL 8,32	II
76. Großenkneten'16	27.10.2016	12:34:13.125	52.912	± 1,1	8.288	± 0,5	-	N/A	2.300 MI	ki	0,53	1,83	CRUST1.0	11	10P, 6S = 16	99	FAHL 9,09	A
77. Walle'16	15.11.2016	09:27:14.086	52.973	2,15	9.261	2,4	7,30	± 2,2	2.200 MI	ki	-		HAN	14	13P, 5S = 18		DEEL 3,99	II
77. Walle'16	15.11.2016	09:27:13.747	52.981	± 0,7	9.240	± 0,8	6,10	± 0,8	2.200 MI	ki	0,66	1,89	CRUST1.0	11	11P, 4S = 15	148	DEEL 5,68	B

Appendix V. Confidence ellipsoide of the 40 relocated seismic events.

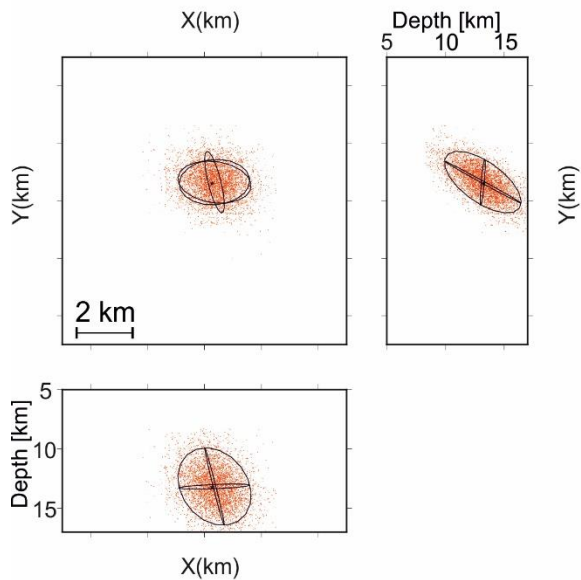
Soltau 1977 June, 02nd 1977
 velomod: only CRUST1.0
 52.909N; 9.569E; Depth 5,275 km
 RMS: 0.454 s; Gap: 157.785°, 14 obs
 Dist: 66.256 km (HAM); vp/vs = 1.74
 aver. error: 3,16 km; DIFF: 1,65 km



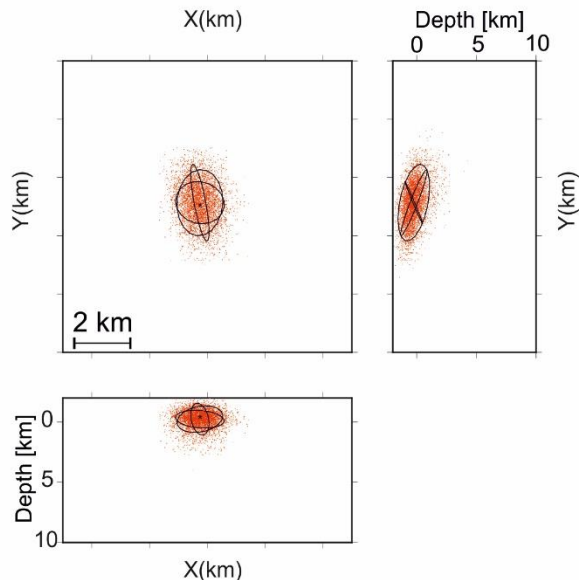
Wittenburg 2000 May, 19th 2000
 velomod: only CRUST1.0
 53.505N; 10.894E; Depth: 13,56
 RMS: 0.407 s; Gap: 91°, 15 obs
 Dist: 61,181 km (BSEG); vp/vs = 1.80
 aver. error: 1,40 km; DIFF: 0,04 km



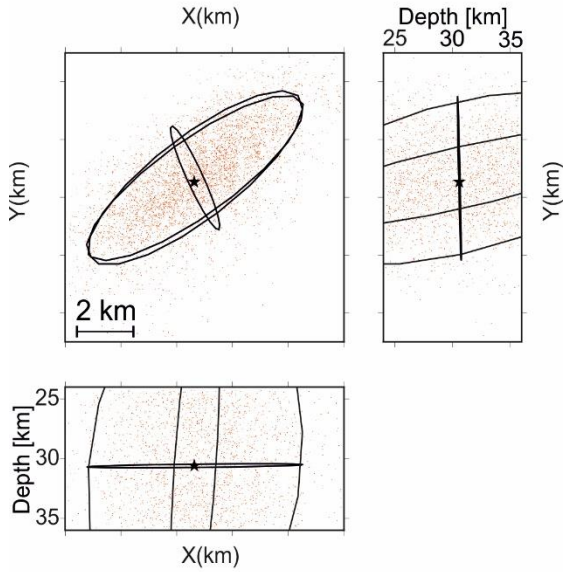
Rotenburg'04 October, 20th 2004
 velomod: only CRUST1.0
 53.039N; 9.541E; Depth: 13,23 km
 RMS: 0.560 s; Gap: 83°, 19 obs
 Dist: 71,750 km (NRDL); vp/vs = 1.80
 aver. error: 1,81 km; DIFF: 0,11 km



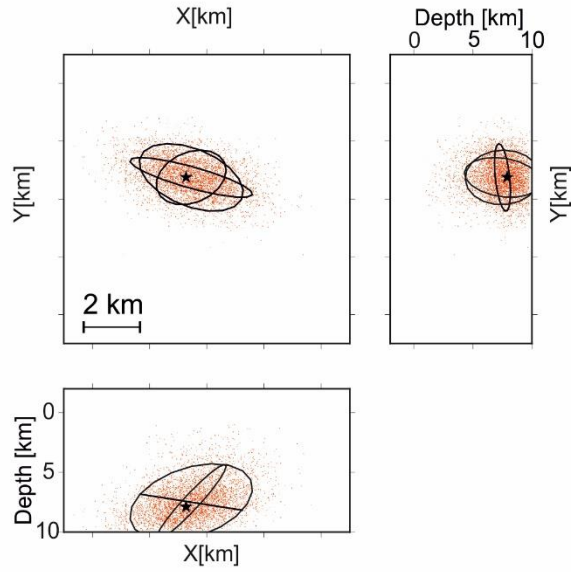
Bassum'05 July, 15th 2005
 velomod: only CRUST1.0
 52.901N; 8.759E; Depth: -
 RMS: 0.442 s; Gap: 112°, 20 obs
 Dist: 94,732 km (IBBN); vp/vs = 1.80
 aver. error: 1,15 km; DIFF: 0,22 km



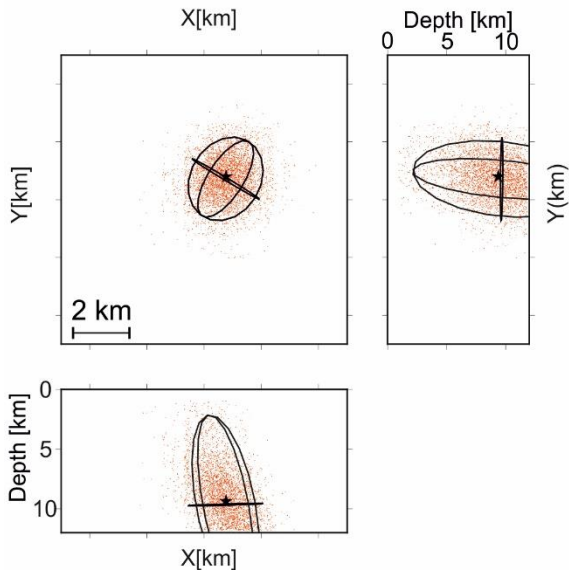
Bremerhaven'05 August, 11th 2005
 velomod: only CRUST1.0
 53.669N; 8.556E; Depth: 30,59 km
 RMS: 0.220 s; Gap: 166°, 6 obs
 Dist: 72,455 km (HLG); vp/vs = 1.75
 aver. error: 7,44 km; DIFF: 0,14 km



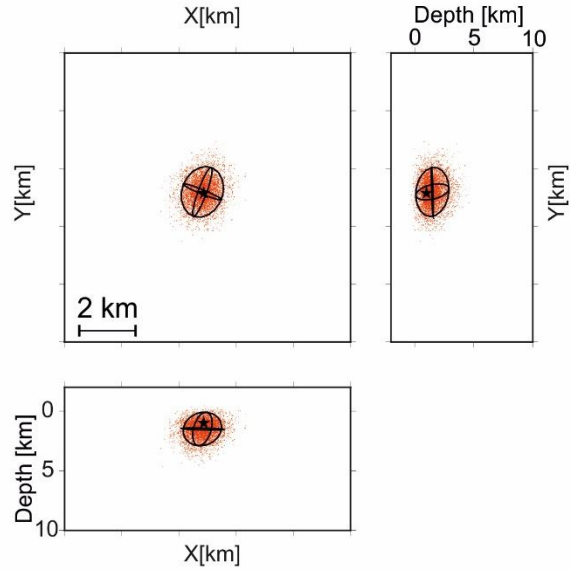
Cappeln'06 July, 02nd 2006
 velomod: only CRUST1.0
 52.803N; 7.833E; Depth: 7,89 km
 RMS: 0.484 s; Gap: 166°, 15 obs
 Dist: 55,429 km (IBBN); vp/vs = 1.73
 aver. error: 2,13 km; DIFF: 0,43 km



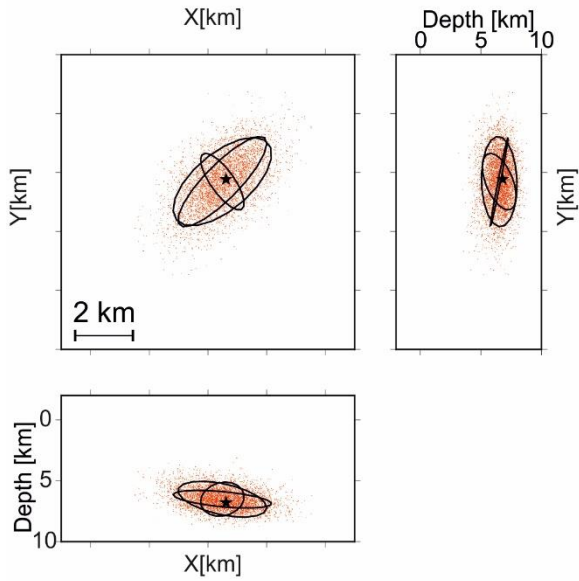
Langwedel'08 April, 03rd 2008
 velomod: only CRUST1.0
 53.043N; 9.131E; Depth: 9,38 km
 RMS: 0.442 s; Gap: 94°, 14 obs
 Dist: 89,835 km (NRDL); vp/vs = 1.80
 aver. error: 3,43 km; DIFF: 0,29 km



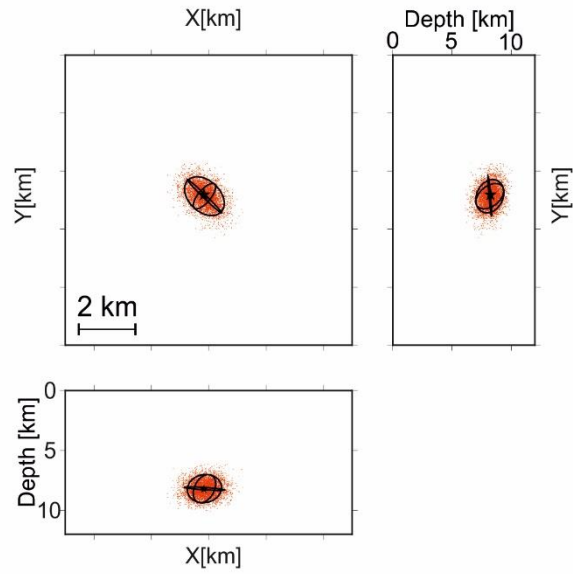
Borstel'11 April, 16th 2011
 velomod: only CRUST1.0
 52.691N; 8.924E; Depth: -
 RMS: 0.540 s; Gap: 94°, 12 obs
 Dist: 69,347 km (IGAD); vp/vs = 1.78
 aver. error: 1,01 km; DIFF: 0,50 km



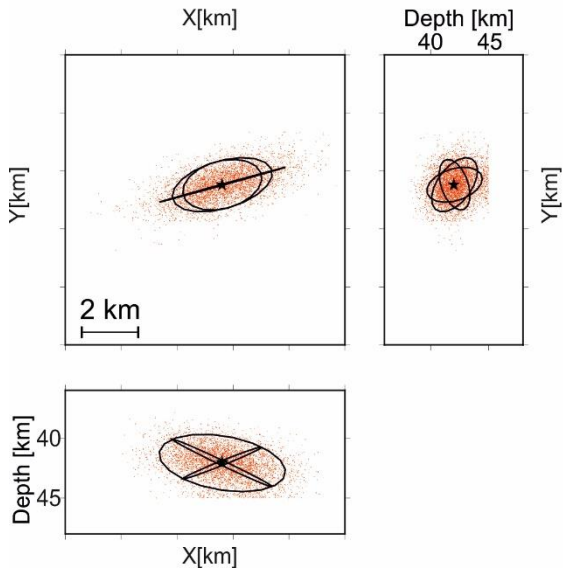
Verden'11 May, 02nd 2011
 velomod: only CRUST1.0
 52.997N; 9.307E; Depth: 6,75 km
 RMS: 0.544 s; Gap: 154°, 11 obs
 Dist: 11,563 km (GOLD); vp/vs = 1.80
 aver. error: 1,57 km; DIFF: 0,32 km



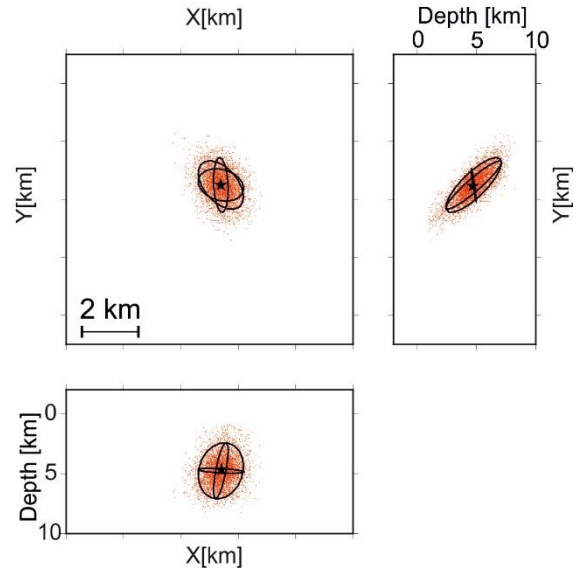
Visselhövede'12 February, 12th 2012
 velomod: only CRUST1.0
 53.027N; 9.594E; Depth: 8,24 km
 RMS: 0.527 s; Gap: 80°, 27 obs
 Dist: 16,249 km (GOLD); vp/vs = 1.76
 aver. error: 0,86 km; DIFF: 0,07 km

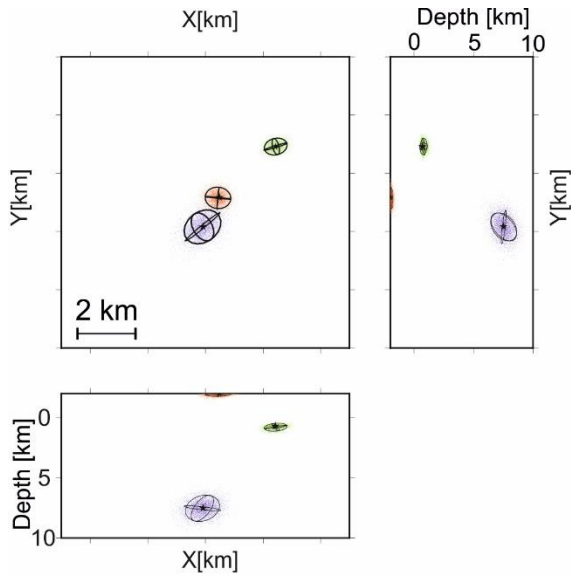


Hitzacker'12 March, 16th 2012
 velomod: only CRUST1.0
 53.193N; 11.119E; Depth: 42,01 km
 RMS: 0.243 s; Gap: 148°, 12 obs
 Dist: 18,644 km (GOR2); vp/vs = 1.80
 aver. error: 1,83 km; DIFF: 0,10 km



Salzwedel'12 October, 28th 2012
 velomod: only CRUST1.0
 52.879N; 11.012E; Depth: 4,67 km
 RMS: 0.560 s; Gap: 95°, 14 obs
 Dist: 8,047 km (CLNZ); vp/vs = 1.76
 aver. error: 1,29 km; DIFF: 0,03 km





Völkersen'12 November, 22nd 2012
 Red: only CRUST1.0
 52.974N; 9.216E; Depth: -
 RMS: 0.439 s; Gap: 51°, 54 obs
 Dist: 5,510 km (BGR3); vp/vs = 1.74
 aver. error: 0,32 km; DIFF: 0,10 km

Green: CRUST1.0 and WEG
 52.990N; 9.245E; Depth: -
 RMS: 0.627 s; Gap: 39°, 54 obs
 Dist: 3,356 km (BGR3); vp/vs = 1.74
 aver. error: 0,35 km; DIFF: 0,09 km

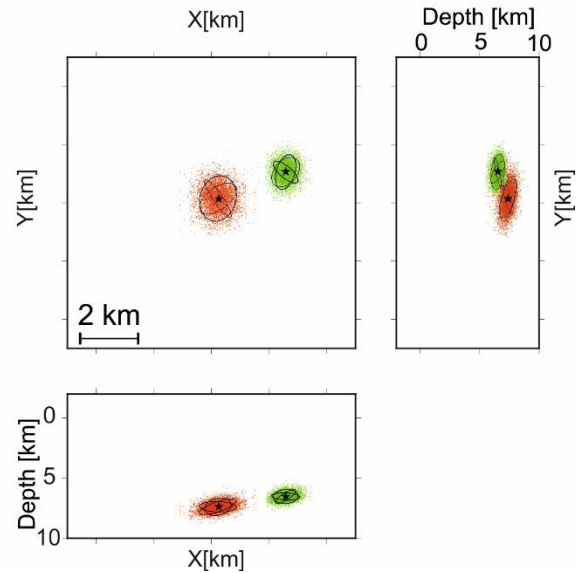
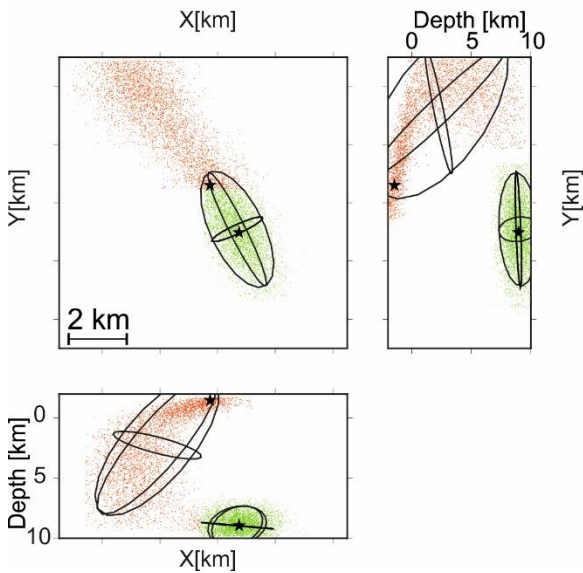
Blue: only WEG model
 52.965N; 9.207E; Depth: 7,51
 RMS: 0.282 s; Gap: 137°, 24 obs
 Dist: 5,937 km (BGR3); vp/vs = 1.74
 aver. error: 0,79 km; DIFF: 0,03 km

Langwedelermoor'13 November, 01st 2013
 Red: only CRUST1.0
 53.041N; 9.145E; Depth: -
 RMS: 0.226 s; Gap: 274°, 10 obs
 Dist: 7,241 km (BGR3); vp/vs = 1.73
 aver. error: 3,42 km; DIFF: 4,87 km

Green: CRUST1.0 and WEG
 53.027N; 9.160E; Depth: 8,96 km
 RMS: 0.149 s; Gap: 257°, 10 obs
 Dist: 5,672 km (GRO1S); vp/vs = 1.73
 aver. error: 1,60 km; DIFF: 0,13 km

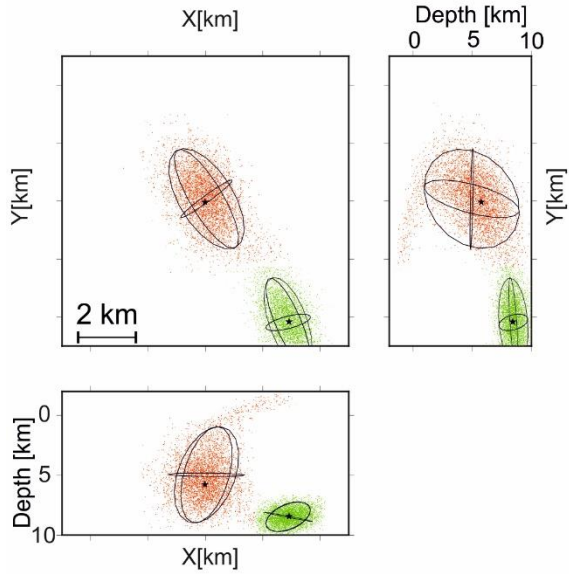
Cluvenhagen'13 November, 01st 2013
 Red: only CRUST1.0
 53.001N; 9.153E; Depth: 7,38 km
 RMS: 0.531 s; Gap: 91°, 26 obs
 Dist: 3,350 km (GRO1S); vp/vs = 1.80
 aver. error: 0,75 km; DIFF: 0,03 km

Green: CRUST1.0 and WEG
 53.009N; 9.187E; Depth: 6,54 km
 RMS: 0.528 s; Gap: 92°, 26 obs
 Dist: 3,528 km (GRO1S); vp/vs = 1.80
 aver. error: 0,59 km; DIFF: 0,02 km

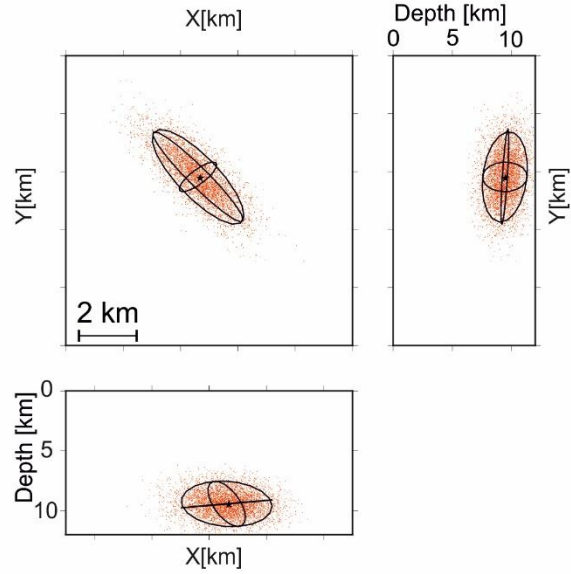


Dahlbrügge'13 November, 02nd 2013
 Red: only CRUST1.0
 53.053N; 9.119E; Depth: 5,77 km
 RMS: 0.250 s; Gap: 287°, 13 obs
 Dist: 9,372 km (GRO1S); vp/vs = 1.80
 aver. error: 2,33 km; DIFF: 0,89 km

Green: CRUST1.0 and WEG
 53.016N; 9.163E; Depth: 8,43 km
 RMS: 0.229 s; Gap: 242°, 26 obs
 Dist: 4,529 km (GRO1S); vp/vs = 1.80
 aver. error: 1,23 km; DIFF: 0,06 km

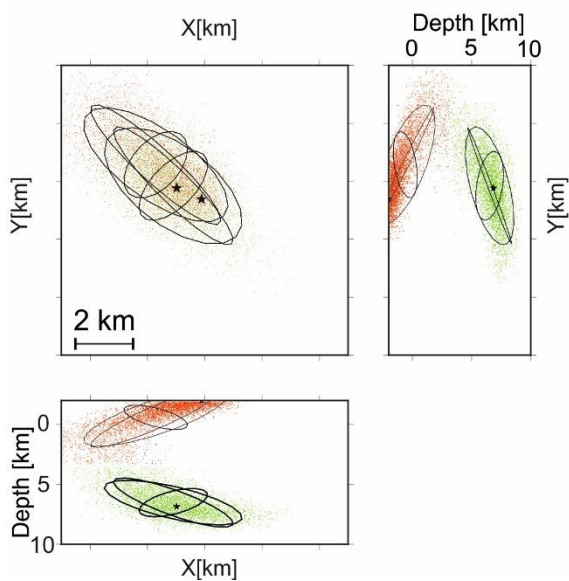


Emstek'13 November, 02nd 2013
 Red: only CRUST1.0
 52.851N; 8.149E; Depth: 9,48 km
 RMS: 0.520 s; Gap: 184°, 15 obs
 Dist: 58,004 km (IGAD); vp/vs = 1.76
 aver. error: 1,62 km; DIFF: 0,10 km



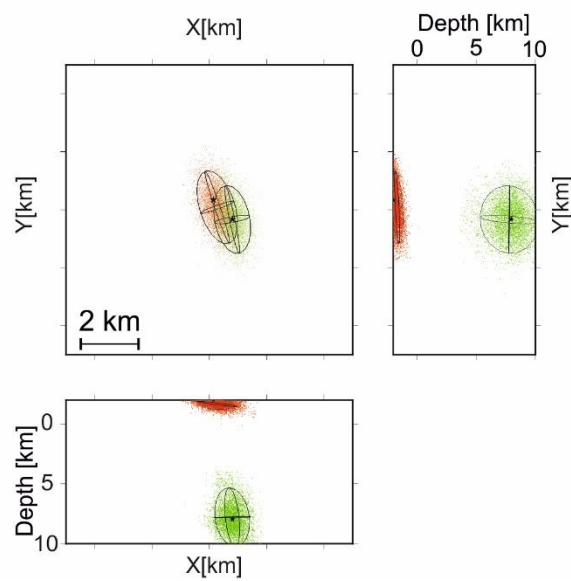
Dauelsen'14 January, 15th 2014
 Red: only CRUST1.0
 53.030N; 9.147E; Depth: -
 RMS: 0.150 s; Gap: 303°, 10 obs
 Dist: 6,344 km (GRO1S); vp/vs = 1.80
 aver. error: 2,15 km; DIFF: 2,44 km

Green: CRUST1.0 and WEG
 53.043N; 9.143E; Depth: 6,85 km
 RMS: 0.120 s; Gap: 306°, 10 obs
 Dist: 7,066 km (GRO1S); vp/vs = 1.80
 aver. error: 2,07 km; DIFF: 0,35 km

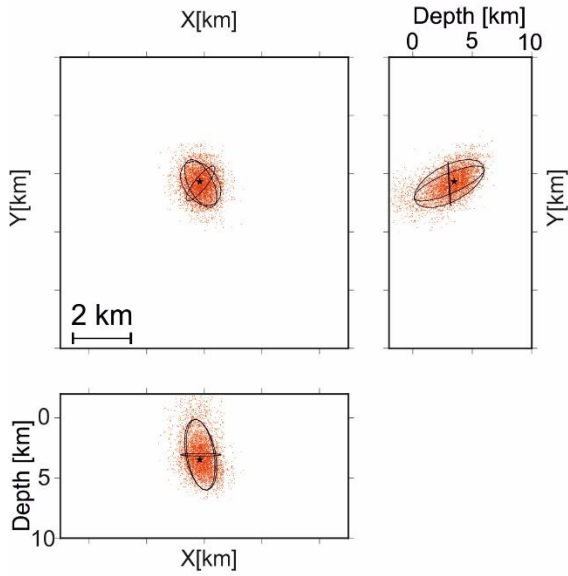


Meissendorf'14 February, 09th 2014
 Red: only CRUST1.0
 52.785N; 9.803E; Depth: -
 RMS: 0.250 s; Gap: 182°, 10 obs
 Dist: 10,038 km (HOPS2); vp/vs = 1.80
 aver. error: 0,81 km; DIFF: 0,44 km

Green: CRUST1.0 and WEG
 52.778N; 9.812E; Depth: 7,96 km
 RMS: 0.210 s; Gap: 187°, 10 obs
 Dist: 9,962 km (HOPS2); vp/vs = 1.80
 aver. error: 1,43 km; DIFF: 0,16 km

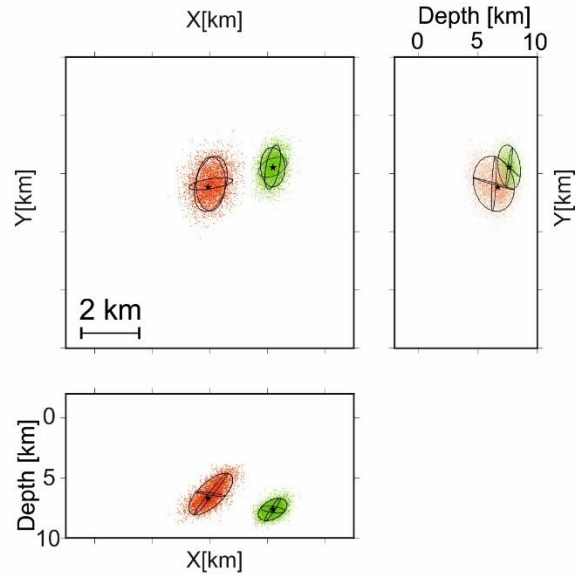


Syke'14 May, 01st 2014
 velomod: only CRUST1.0
 52.907N; 8.759E; Depth: 3,48 km
 RMS: 0.380 s; Gap: 68°, 41 obs
 Dist: 23,883 km (V01EB); vp/vs = only P
 aver. error: 0,73 km; DIFF: 0,01 km



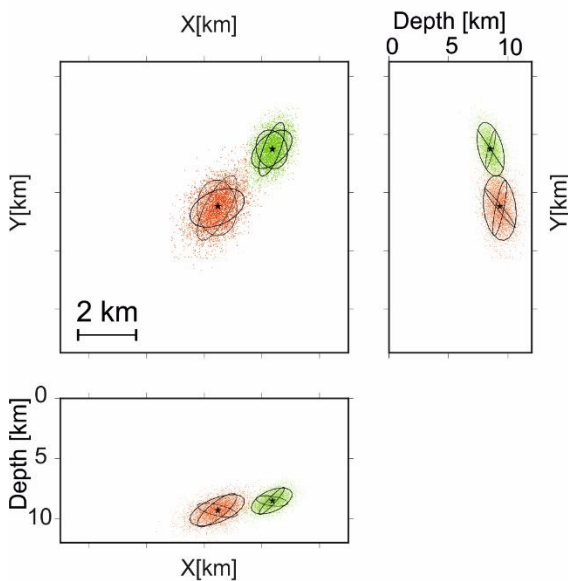
Nindorf'14 June, 20th 2014
 Red: only CRUST1.0
 52.996N; 9.148E; Depth: 6,69 km
 RMS: 0.580 s; Gap: 83°, 25 obs
 Dist: 3,142 km (GRO1S); vp/vs = 1.80
 aver. error: 1,11 km; DIFF: 0,06 km

Green: CRUST1.0 and WEG
 53.003N; 9.182E; Depth: 7,63 km
 RMS: 0.440 s; Gap: 86°, 25 obs
 Dist: 2,670 km (GRO1S); vp/vs = 1.80
 aver. error: 0,73 km; DIFF: 0,01 km

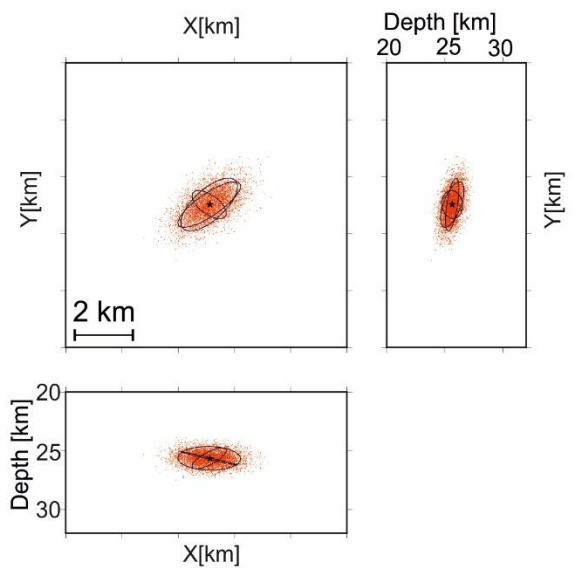


Langwedelermoor'14 June, 20th 2014
 Red: only CRUST1.0
 52.978N; 9.156E; Depth: 9,31 km
 RMS: 0.340 s; Gap: 118°, 15 obs
 Dist: 1,900 km (GRO1S); vp/vs = 1.90
 aver. error: 1,14 km; DIFF: 0,06 km

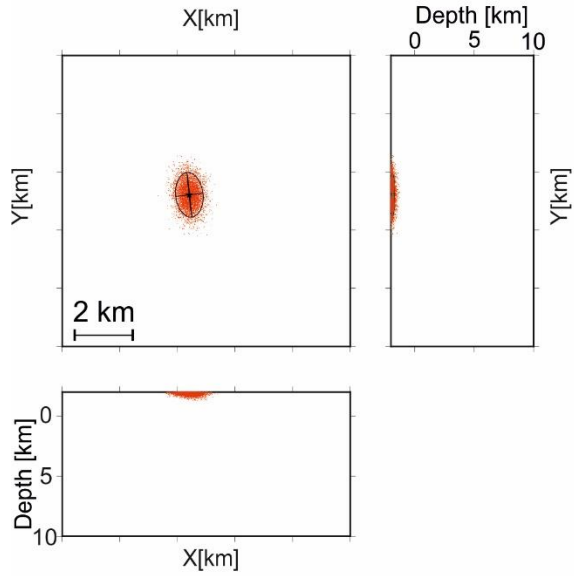
Green: CRUST1.0 and WEG
 52.995N; 9.184E; Depth: 8,52 km
 RMS: 0.250 s; Gap: 79°, 15 obs
 Dist: 1,949 km (GRO1S); vp/vs = 1.90
 aver. error: 0,90 km; DIFF: 0,03 km



Zarrentin'14 July, 20th 2014
 velomod: only CRUST1.0
 53.569N; 10.919E; Depth: 25,65 km
 RMS: 0.44 s; Gap: 99°, 31 obs
 Dist: 1,677 km (ZARR); vp/vs = 1.80
 aver. error: 1,00 km; DIFF: 0,02 km

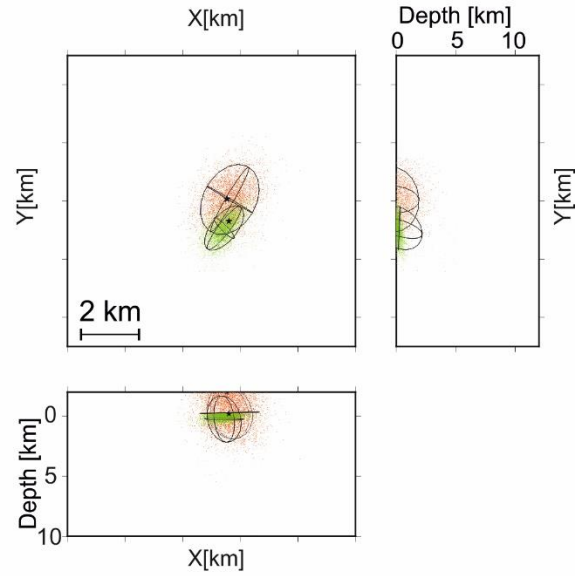


Cloppenburg'14 September, 02nd 2014
 velomod: only CRUST1.0
 52.792N; 8.205E; Depth: -
 RMS: 0.420 s; Gap: 60°, 27 obs
 Dist: 9,087 km (SEVE); vp/vs = 1.80
 aver. error: 0,49 km; DIFF: 0,12 km



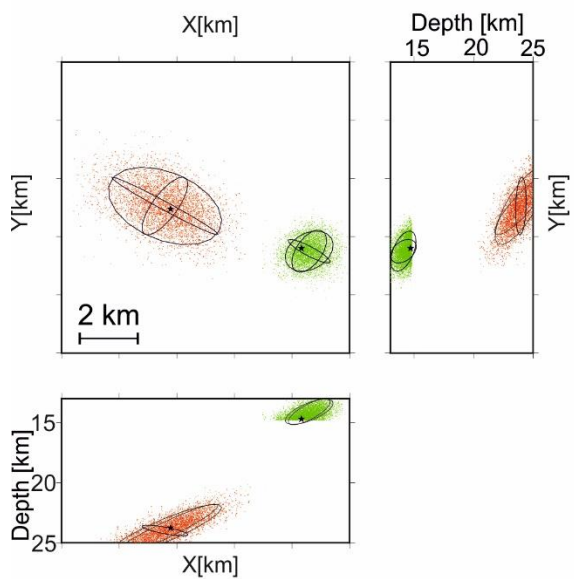
Walsrode'14 October, 20th 2014
 Red: only CRUST1.0
 52.891N; 9.528E; Depth: -
 RMS: 0.220 s; Gap: 87°, 8 obs
 Dist: 5,479 km (LANGS); vp/vs = 1.80
 aver. error: 1,47 km; DIFF: 1,47 km

Green: CRUST1.0 and WEG
 52.885N; 9.529E; Depth: -
 RMS: 0.190 s; Gap: 93°, 13 obs
 Dist: 4,993 km (LANGS); vp/vs = 1.80
 aver. error: 1,10 km; DIFF: 1,10 km



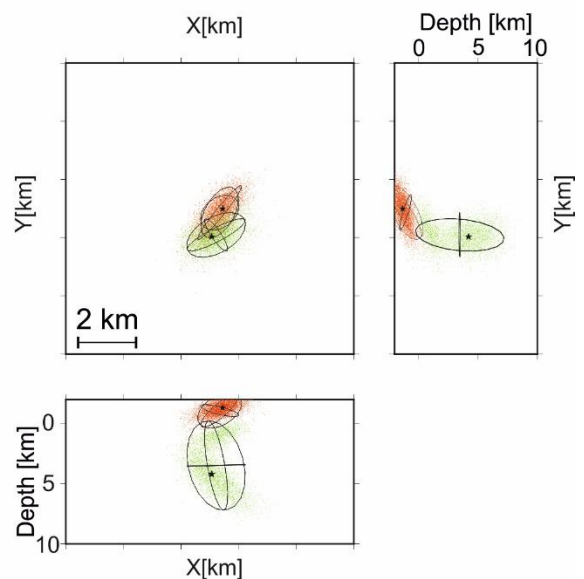
Krelingen'14 November, 02nd 2014
 Red: only CRUST1.0
 52.810N; 9.531E; Depth: 23,75 km
 RMS: 0.330 s; Gap: 84°, 17 obs
 Dist: 13,950 km (RETHO); vp/vs = 1.80
 aver. error: 1,60 km; DIFF: 0,31 km

Green: CRUST1.0 and WEG
 52.797N; 9.598E; Depth: 14,70 km
 RMS: 0.320 s; Gap: 95°, 17 obs
 Dist: 17,297 km (RETHO); vp/vs = 1.80
 aver. error: 0,88 km; DIFF: 0,67 km

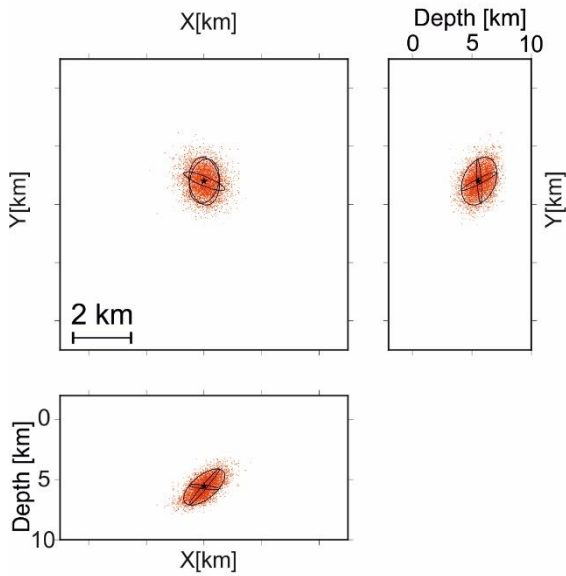


Vehmsmoor'14 November, 11th 2014
 Red: only CRUST1.0
 52.881N; 9.526E; Depth: -
 RMS: 0.056 s; Gap: 97°, 9 obs
 Dist: 4,981 km (LANGS); vp/vs = 1.90
 aver. error: 1,03 km; DIFF: 0,29 km

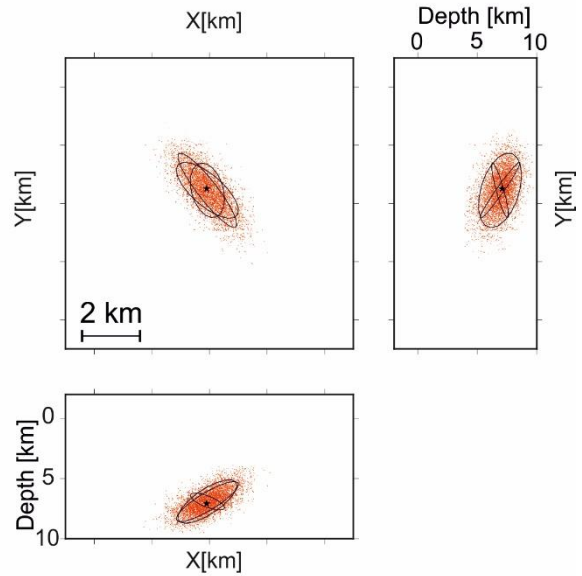
Green: CRUST1.0 and WEG
 52.873N; 9.521E; Depth: 4,21 km
 RMS: 0.081 s; Gap: 110°, 9 obs
 Dist: 4,983 km (LANGS); vp/vs = 1.90
 aver. error: 0,75 km; DIFF: 1,83 km



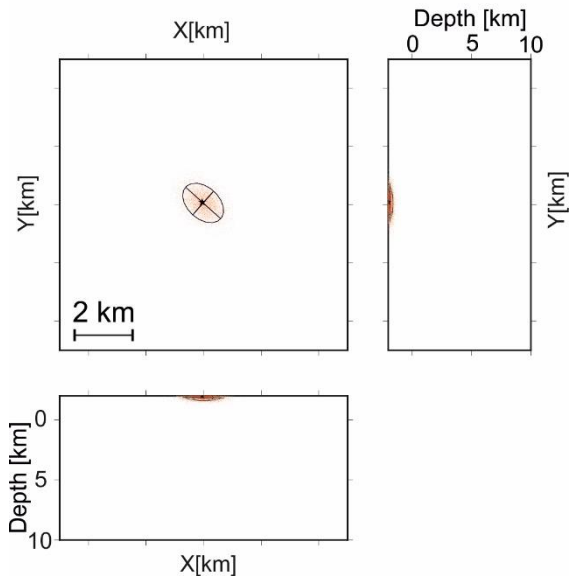
Emstek'14 December, 19th 2014
 velomod: only CRUST1.0
 52.843N; 8.199E; Depth: 5,53 km
 RMS: 0,69 s; Gap: 71°, 19 obs
 Dist: 7,904 km (FAHL); vp/vs = 1.78
 aver. error: 0,98 km; DIFF: 0,08 km



Döhlen'15 June, 05th 2015
 velomod: only CRUST1.0
 52.930N; 8.225E; Depth: 7,08 km
 RMS: 0,450 s; Gap: 134°, 14 obs
 Dist: 5,39 km (FAHL); vp/vs = 1.93
 aver. error: 1,30 km; DIFF: 0,18 km

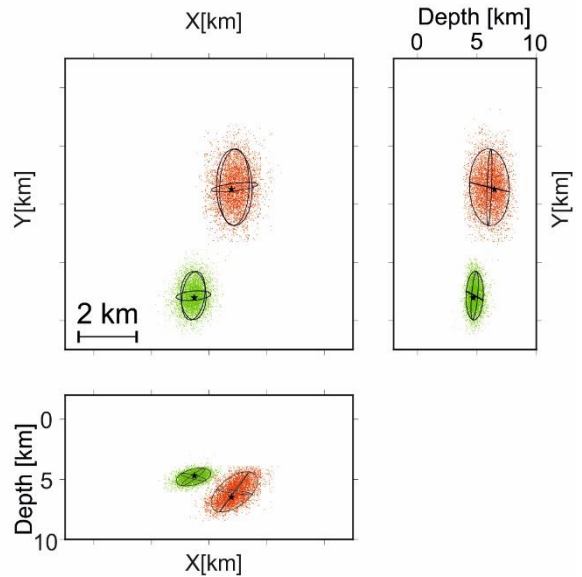


Asendorf'15 July, 13th 2015
 velomod: only CRUST1.0
 52.695N; 8.969E; Depth: -
 RMS: 0,55 s; Gap: 99°, 14 obs
 Dist: 21,38 km (SYKE); vp/vs = 1.79
 aver. error: 0,54 km; DIFF: 0,16 km



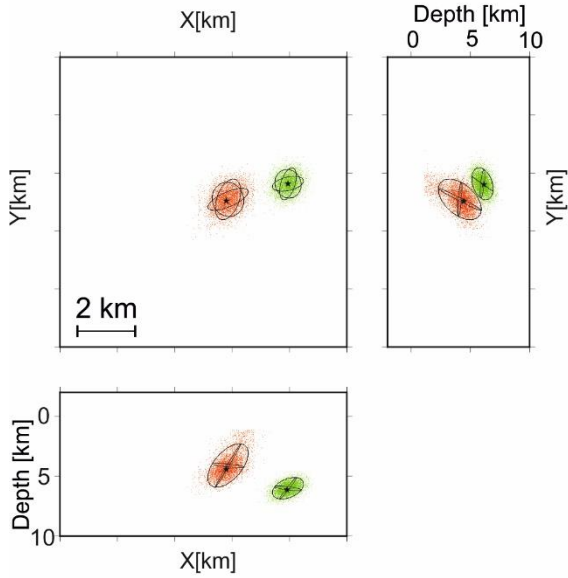
Bothel'15 August, 14th 2015
 Red: only CRUST1.0
 53.075N; 9.519E; Depth: 6,48 km
 RMS: 0,59 s; Gap: 198°, 17 obs
 Dist: 11,990 km (BKSB); vp/vs = 1.85
 aver. error: 1,25 km; DIFF: 0,45 km

Green: CRUST1.0 and WEG
 53.042N; 9.499E; Depth: 4,70 km
 RMS: 0,580 s; Gap: 186°, 17 obs
 Dist: 8,470 km (BKSB); vp/vs = 1.91
 aver. error: 0,73 km; DIFF: 0,13 km

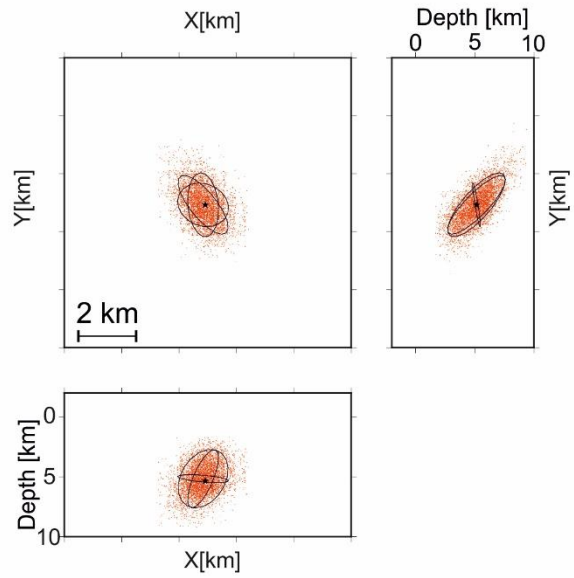


Achim'15 December, 06th 2015
 Red: only CRUST1.0
 53.009N; 9.176E; Depth: 4,44 km
 RMS: 0.49 s; Gap: 95°, 23 obs
 Dist: 3,540 km (GRO1S); vp/vs = 1.78
 aver. error: 1,03 km; DIFF: 0,34 km

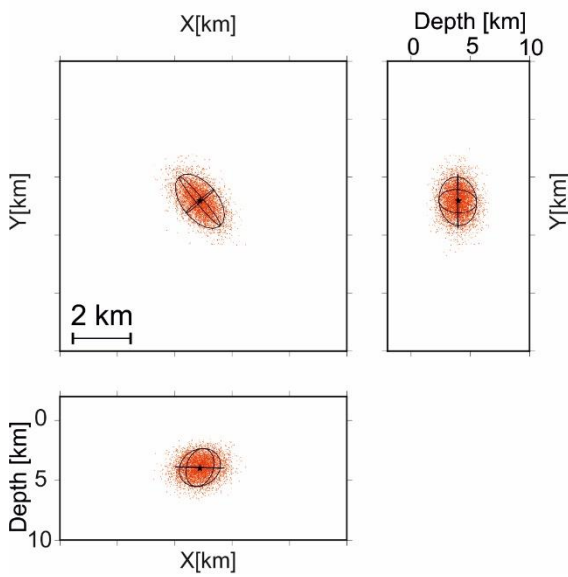
Green: CRUST1.0 and WEG
 53.014N; 9.207E; Depth: 6,14 km
 RMS: 0.420 s; Gap: 90°, 23 obs
 Dist: 2,760 km (BGR3); vp/vs = 1.78
 aver. error: 0,65 km; DIFF: 0,13 km



Sieden'15 December, 29th 2015
 velomod: only CRUST1.0
 52.649N; 8.925E; Depth: 5,35
 RMS: 0.60 s; Gap: 108°, 14 obs
 Dist: 25,79 km (SYKE); vp/vs = 1.88
 aver. error: 1,44 km; DIFF: 0,21 km

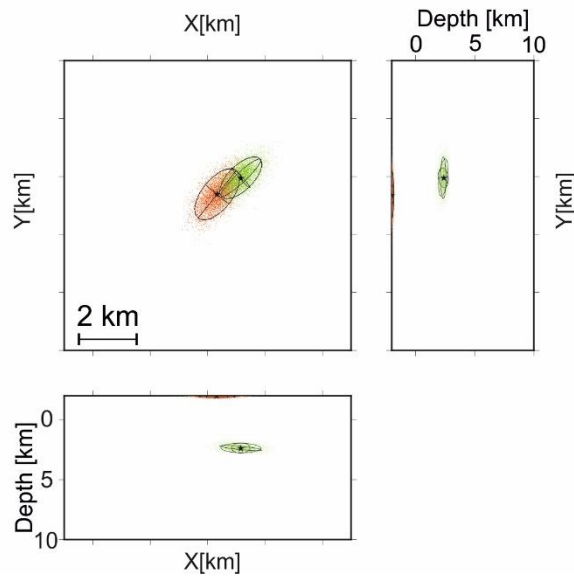


Wardenburg'16 January, 14th 2016
 velomod: only CRUST1.0
 52.990N; 8.209E; Depth: 3,99 km
 RMS: 0.65 s; Gap: 130°, 17 obs
 Dist: 9,82 km (FAHL); vp/vs = 1.90
 aver. error: 1,11 km; DIFF: 0,06 km



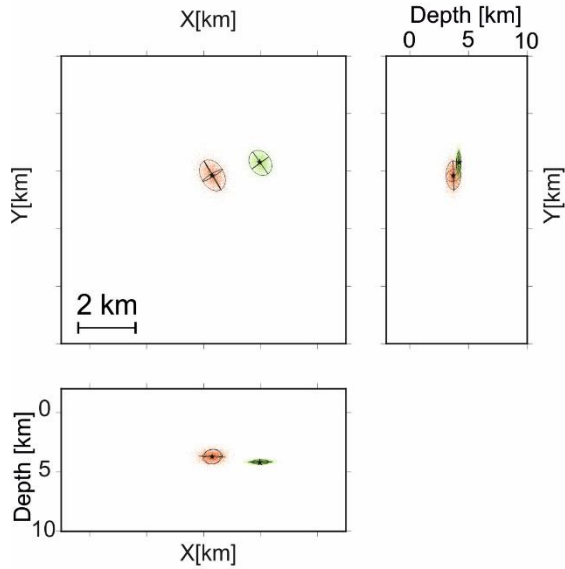
Klosterzelle'16 February, 18th 2016
 Red: only CRUST1.0
 52.867N; 9.539E; Depth: -
 RMS: 0.71 s; Gap: 165°, 15 obs
 Dist: 9,80 km (GOLD); vp/vs = 1.75
 aver. error: 0,56 km; DIFF: 0,07 km

Green: CRUST1.0 and WEG
 52.872N; 9.552E; Depth: 2,40 km
 RMS: 0.580 s; Gap: 168°, 15 obs
 Dist: 10,14 km (GOLD); vp/vs = 1.84
 aver. error: 0,61 km; DIFF: 0,05 km



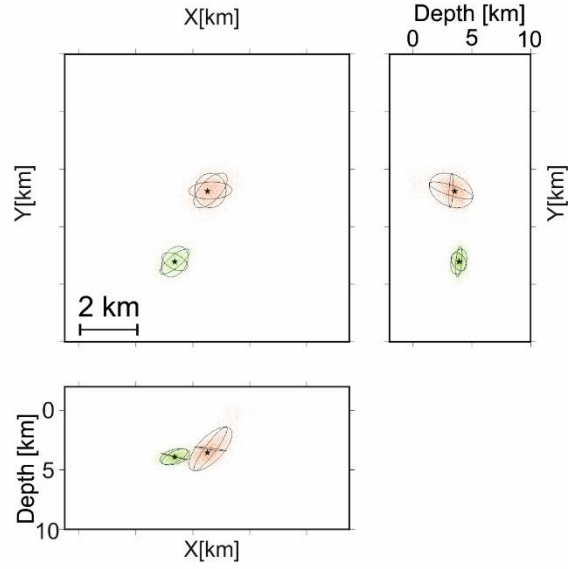
Völkersen'16 April, 22nd 2016
 Red: only CRUST1.0
 52.998N; 9.213E; Depth: 3,71 km
 RMS: 0.49 s; Gap: 53°, 44 obs
 Dist: 2,190 km (TRFTS); vp/vs = 1.85
 aver. error: 0,54 km; DIFF: 0,02 km

Green: CRUST1.0 and WEG
 53.002N; 9.238E; Depth: 4,20 km
 RMS: 0.660 s; Gap: 47°, 43 obs
 Dist: 2,05 km (BGR3); vp/vs = 1.85
 aver. error: 0,34 km; DIFF: 0,04 km



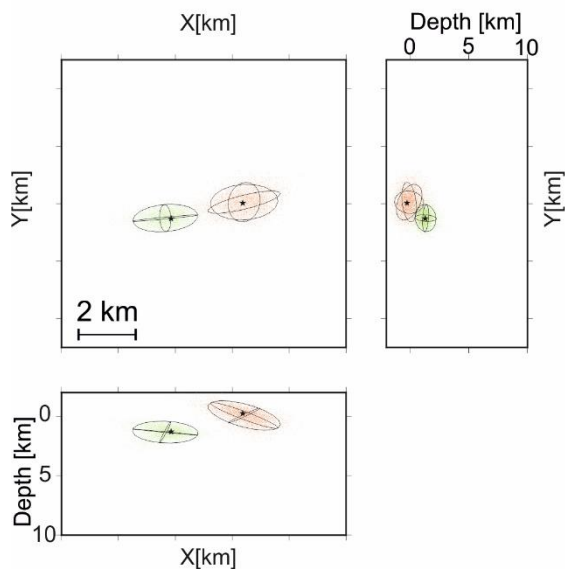
Bothel'16 May, 28th 2016
 Red: only CRUST1.0
 53.099N; 9.515E; Depth: 3,54 km
 RMS: 0.39 s; Gap: 111°, 21 obs
 Dist: 3,69 km (RS52S); vp/vs = 1.89
 aver. error: 1,05 km; DIFF: 0,33 km

Green: CRUST1.0 and WEG
 53.078N; 9.498E; Depth: 3,91 km
 RMS: 0.41 s; Gap: 87°, 21 obs
 Dist: 2,82 km (RS52S); vp/vs = 1.86
 aver. error: 0,60 km; DIFF: 0,02 km

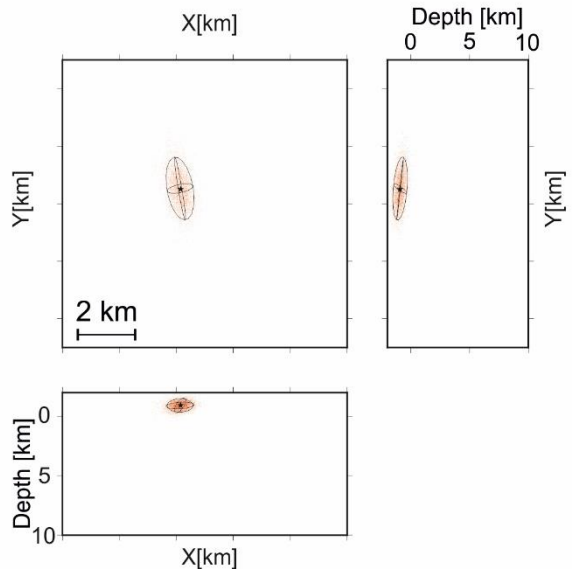


Schneeheide'16 September, 04th 2016
 Red: only CRUST1.0
 52.873N; 9.510E; Depth: -
 RMS: 0.24 s; Gap: 128°, 9 obs
 Dist: 7,89 km (GOLD); vp/vs = 1.89
 aver. error: 1,04 km; DIFF: 0,31 km

Green: CRUST1.0 and WEG
 52.868N; 9.473E; Depth: -
 RMS: 0.33 s; Gap: 126°, 9 obs
 Dist: 6,77 km (GOLD); vp/vs = 1.89
 aver. error: 0,85 km; DIFF: 0,21 km

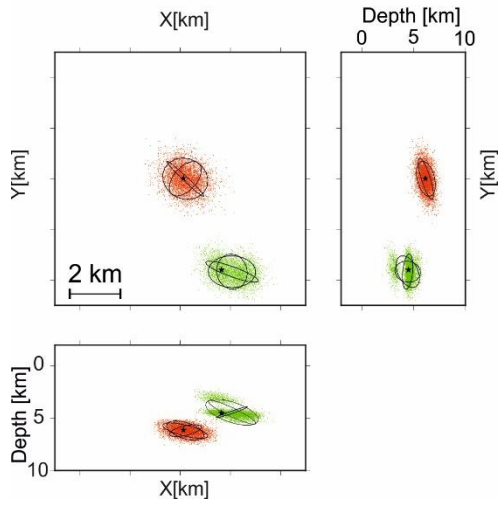


Großenkneten'16 October, 27th 2016
 Red: only CRUST1.0
 52.912N; 8.288E; Depth: -
 RMS: 0.53 s; Gap: 99°, 16 obs
 Dist: 9,09 km (FAHL); vp/vs = 1.83
 aver. error: 0,72 km; DIFF: 0,03 km

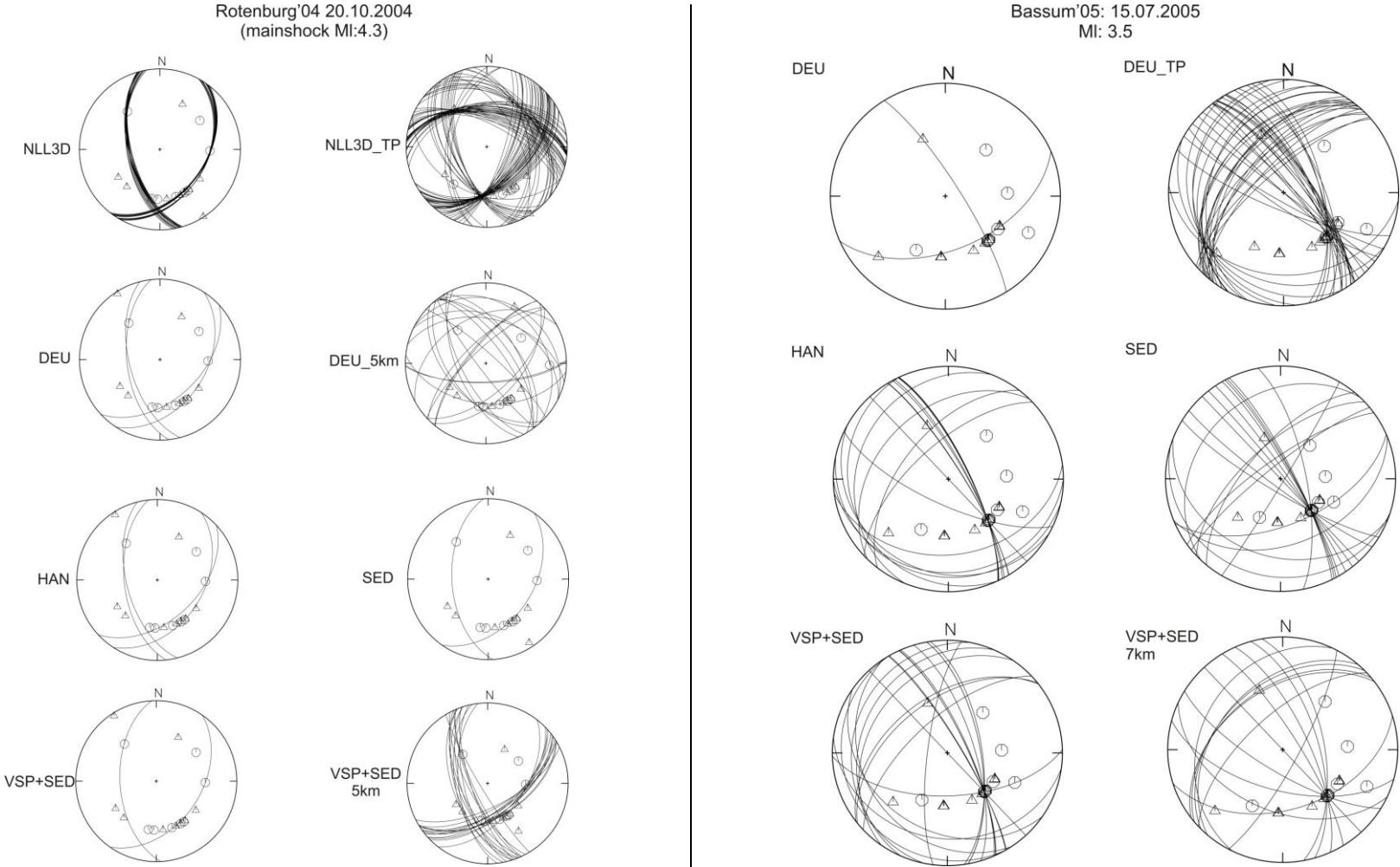


Walle'16 November, 15th 2016
Red: only CRUST1.0
52.981N; 9.240E; Depth: 6,1 km
RMS: 0,66 s; Gap: 148°, 15 obs
Dist: 5,68 km (DEEL); vp/vs = 1.89
aver. error: 0,91 km; DIFF: 0,09 km

Green: CRUST1.0 and WEG
52.947N; 9.274E; Depth: 4,60
RMS: 0,86 s; Gap: 137°, 15 obs
Dist: 2,97 km (DEEL); vp/vs = 1.88
aver. error: 1,07 km; DIFF: 0,69 km

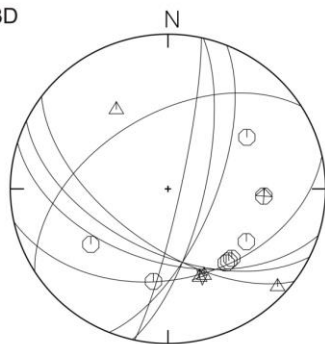


Appendix VI. Fault plane solutions for the 18 selected seismic events. Wittenburg 2000 and Bremerhaven'05 are missing because too many solutions were carried out. Labeled velocity models on the left side of the focal sphere referred to the applied velocity models (Fig. 23).

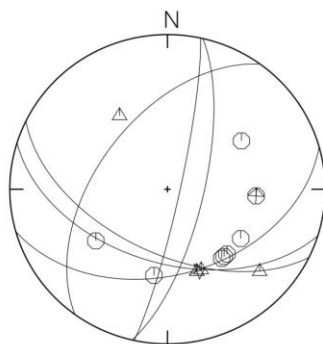


Langwedel'08: 03.04.2008
MI: 2.5

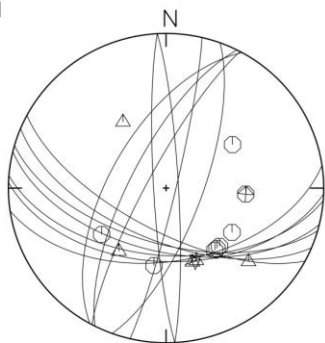
NLL3D



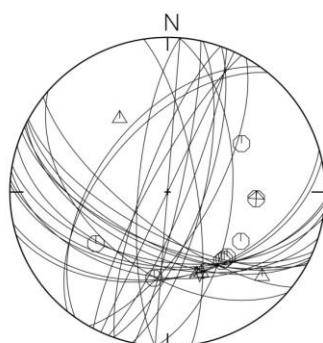
DEU



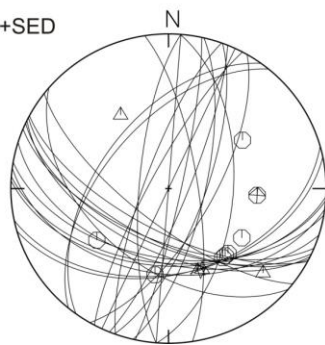
HAN



SED

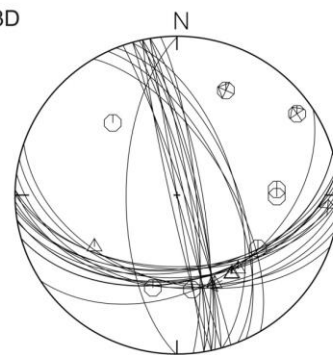


VSP+SED

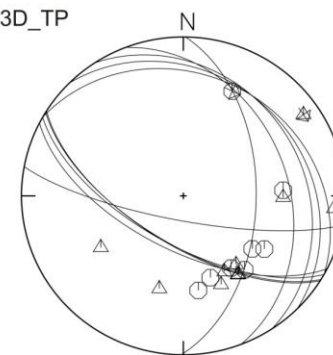


Visselhövede'12: 13.02.2012
MI: 2.6

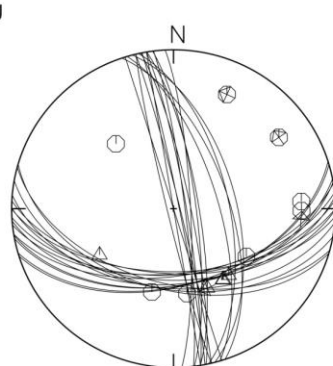
NLL3D



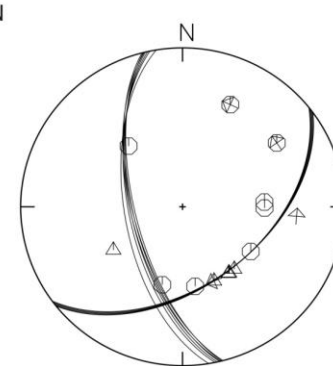
NLL3D_TP



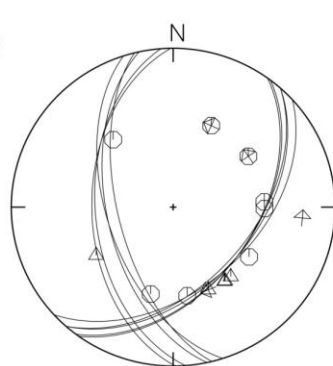
DEU



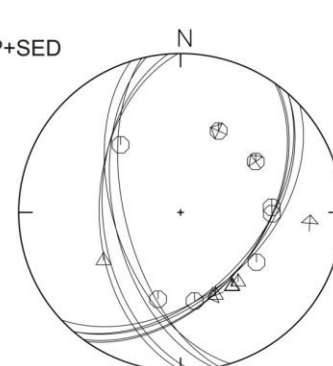
HAN



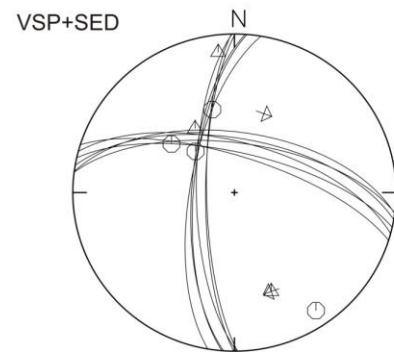
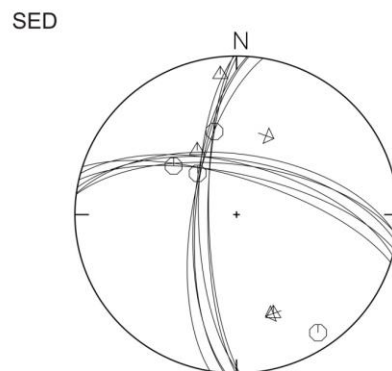
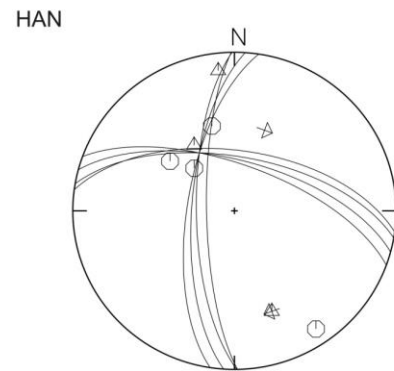
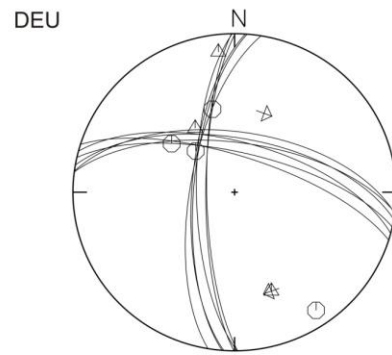
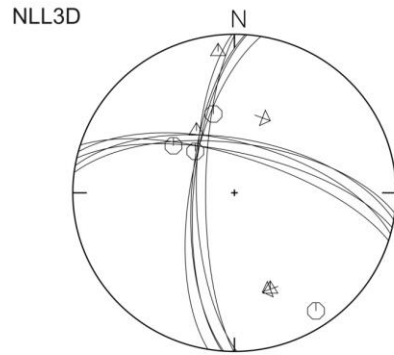
SED



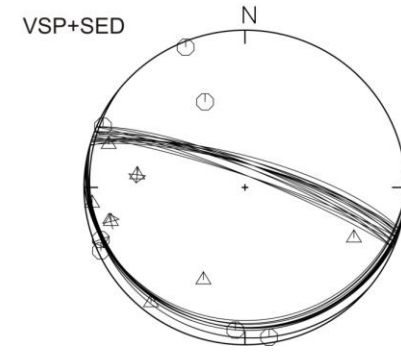
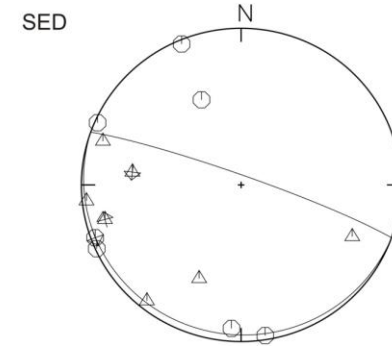
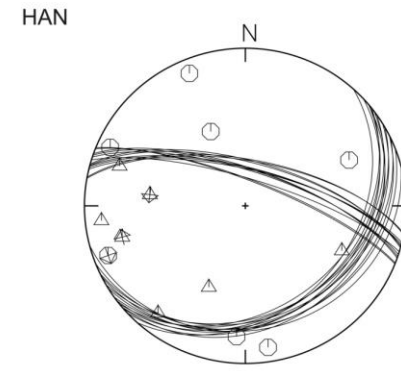
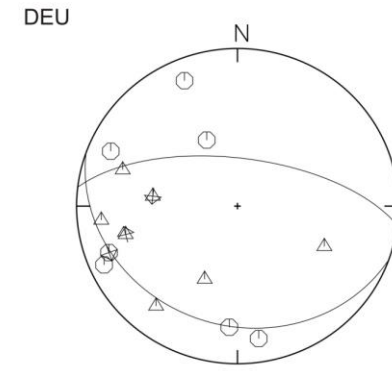
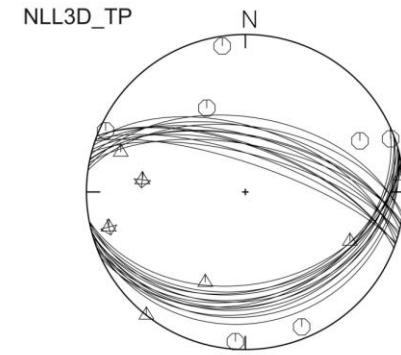
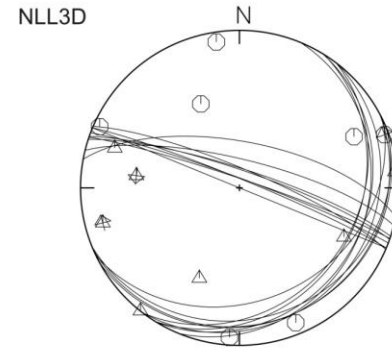
VSP+SED



Hitzacker'12: 16.03.2012
MI: 1.9

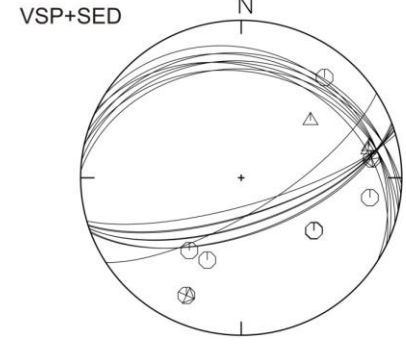
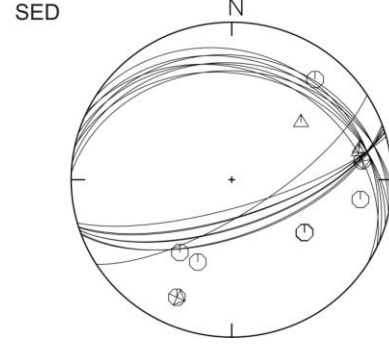
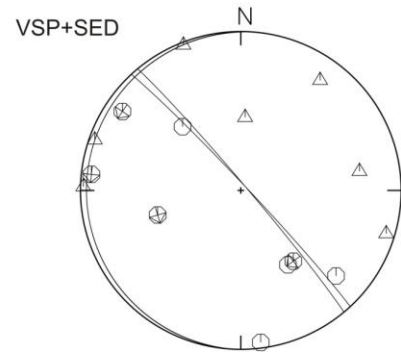
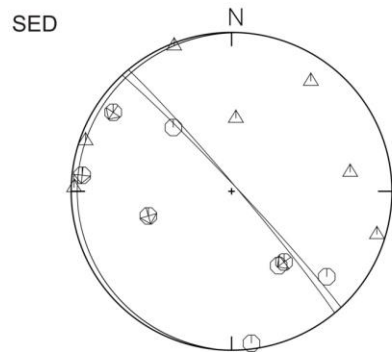
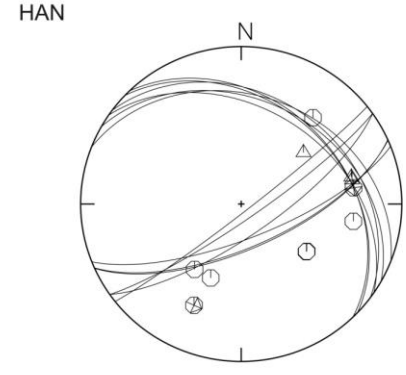
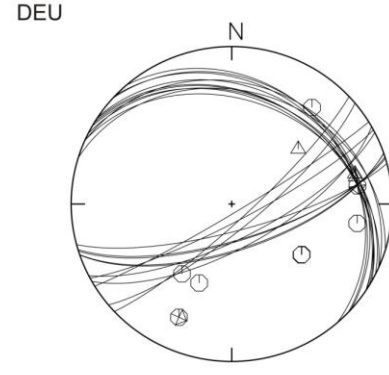
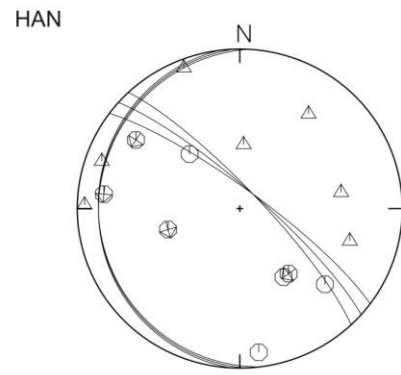
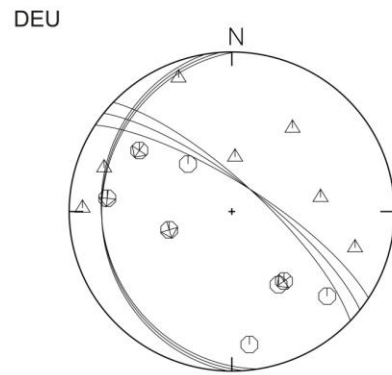
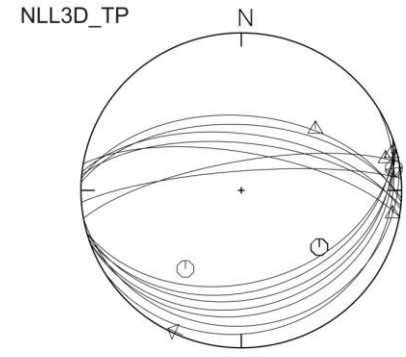
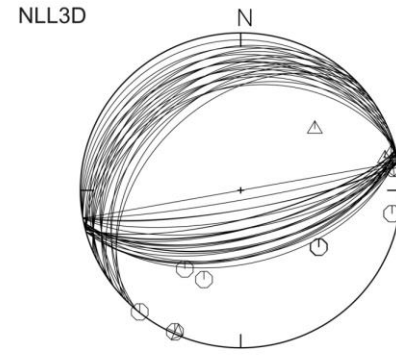
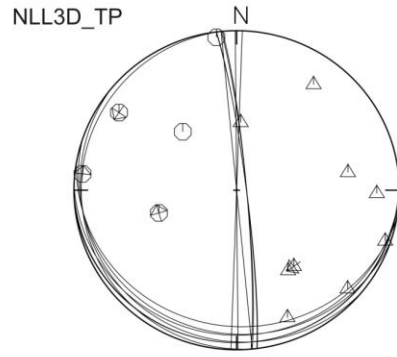
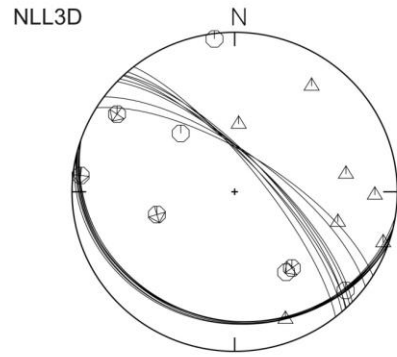


Völkersen'12: 22.11.2012
MI: 2.85



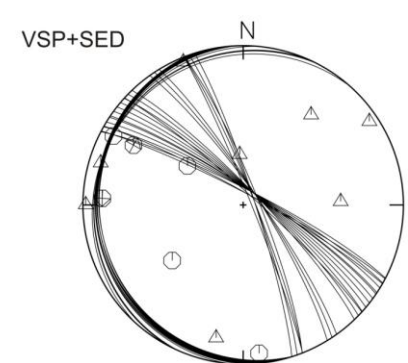
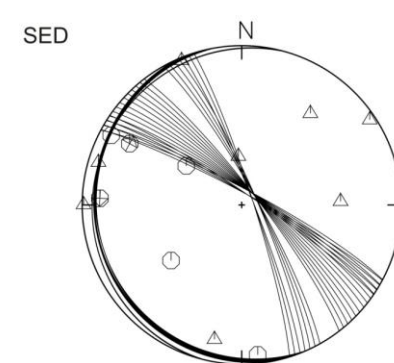
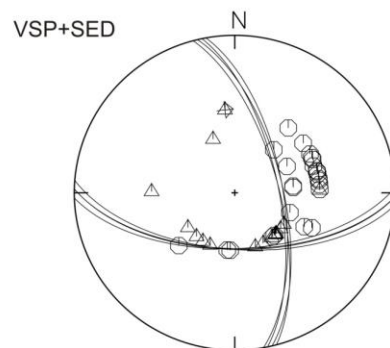
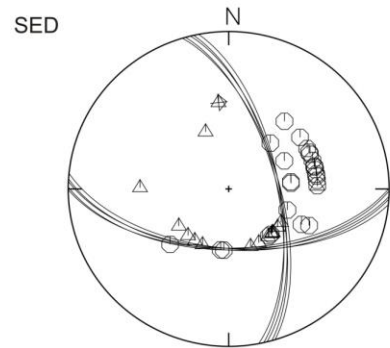
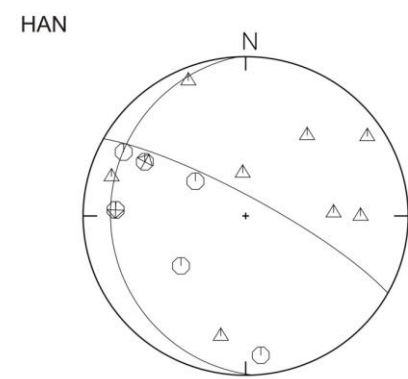
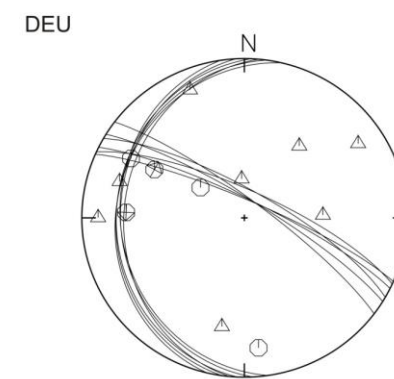
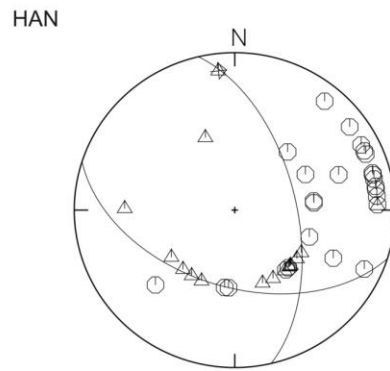
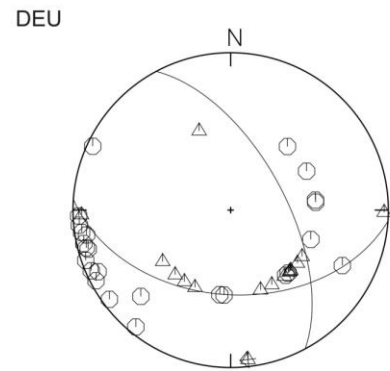
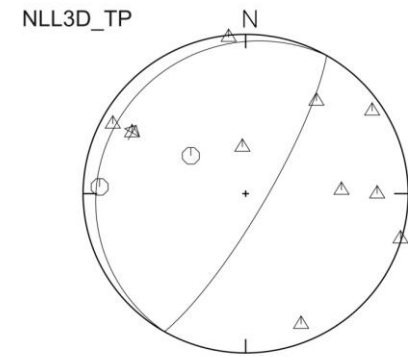
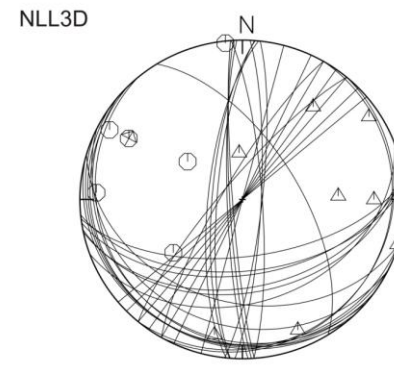
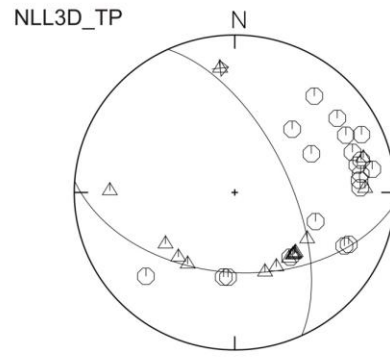
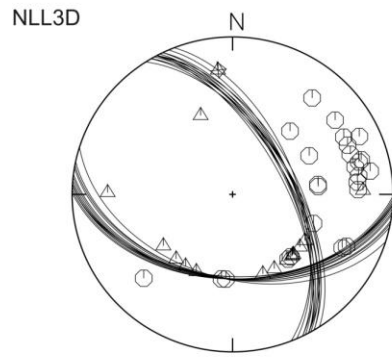
Cluvenhagen'13: 01.11.2013
MI: 1.8

Emstek'13: 20.12.2013
MI: 2.4



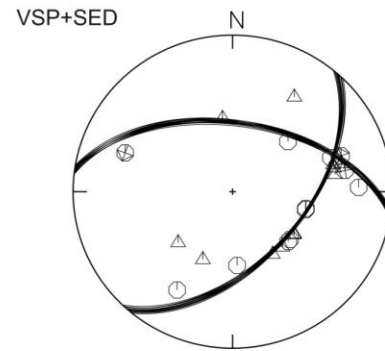
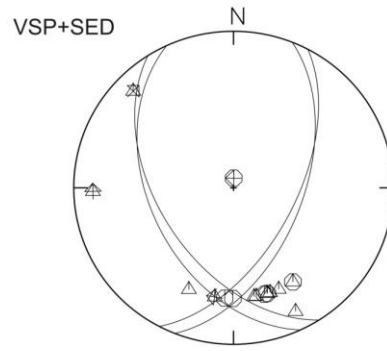
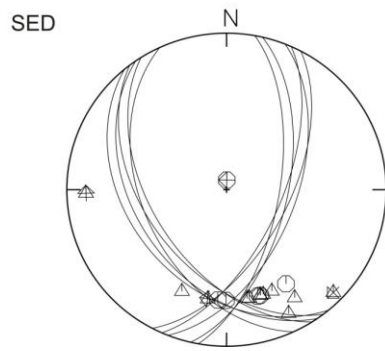
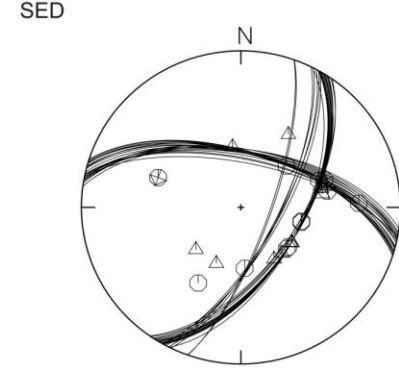
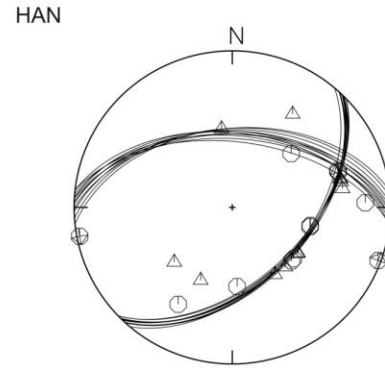
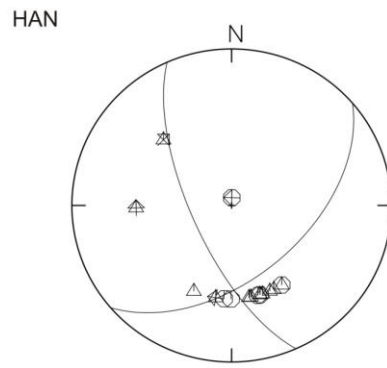
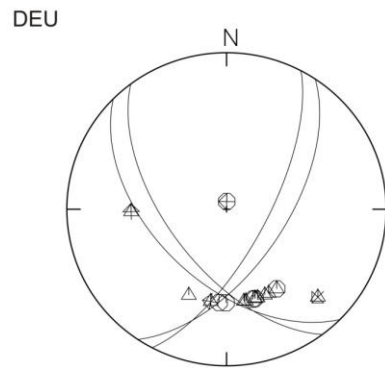
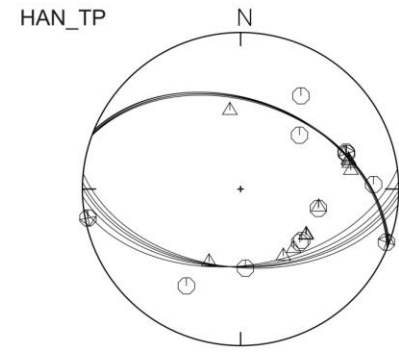
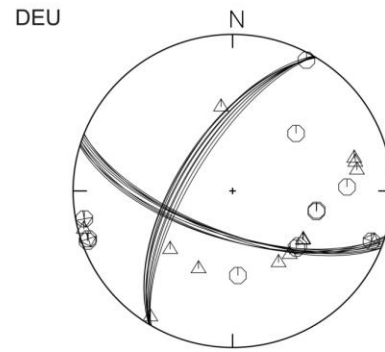
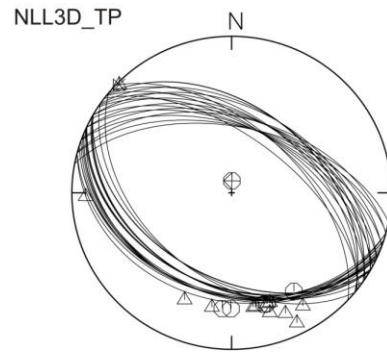
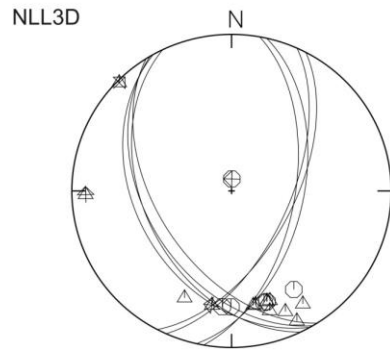
Syke'14: 01.05.2014
MI: 3.5

Nindorf'14: 20.06.2014
MI: 1.5



Schwerin'14: 20.07.2014
MI: 1.9

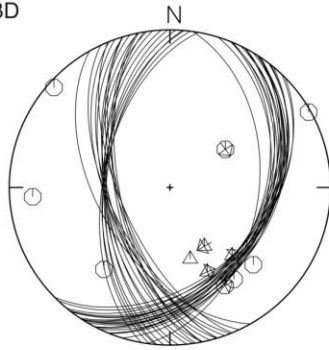
Cloppenburg'14: 02.09.2014
MI: 2.7



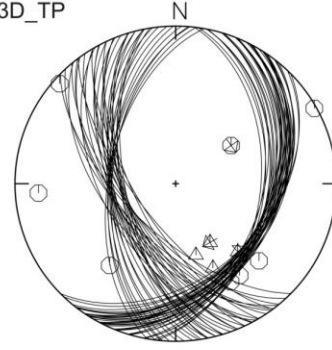
Krelingen'14: 02.11.2014
MI: 1.3

Emstek'14: 19.12.2014
MI: 2.9

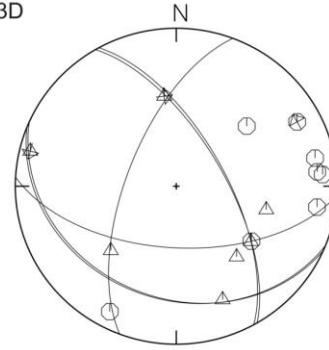
NLL3D



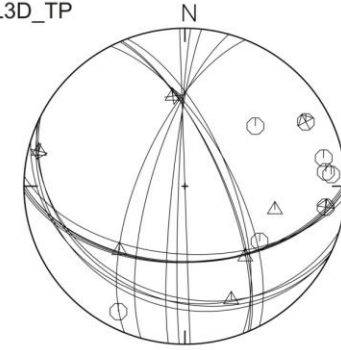
NLL3D_TP



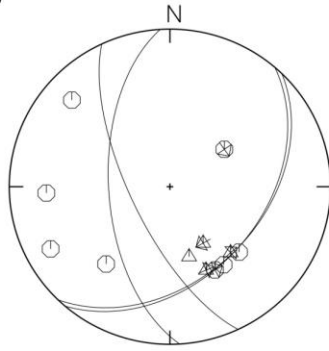
NLL3D



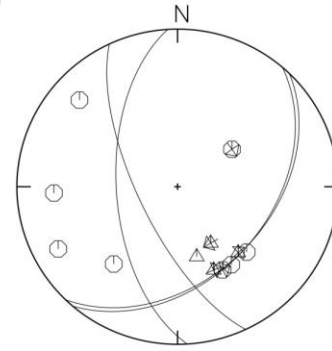
NLL3D_TP



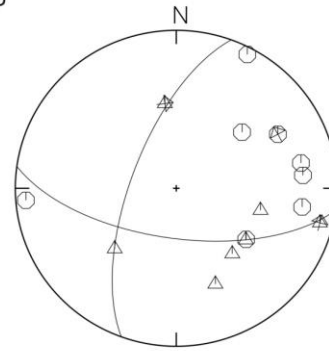
DEU



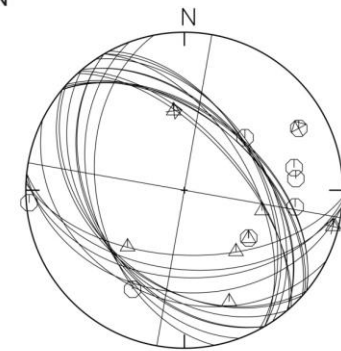
HAN



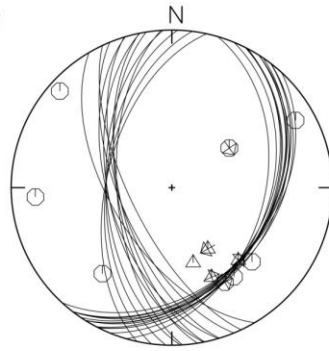
DEU



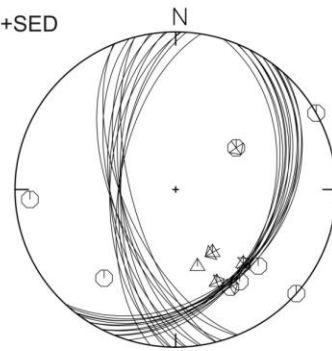
HAN



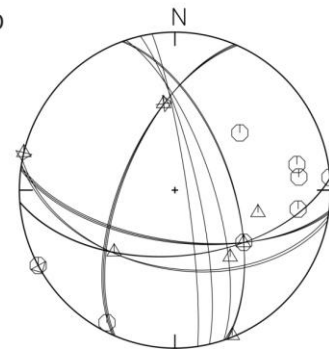
SED



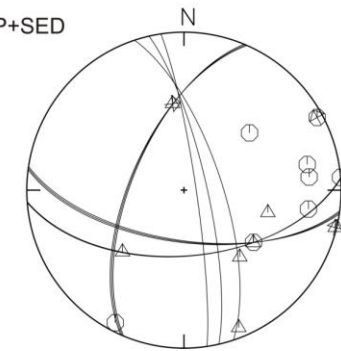
VSP+SED



SED



VSP+SED

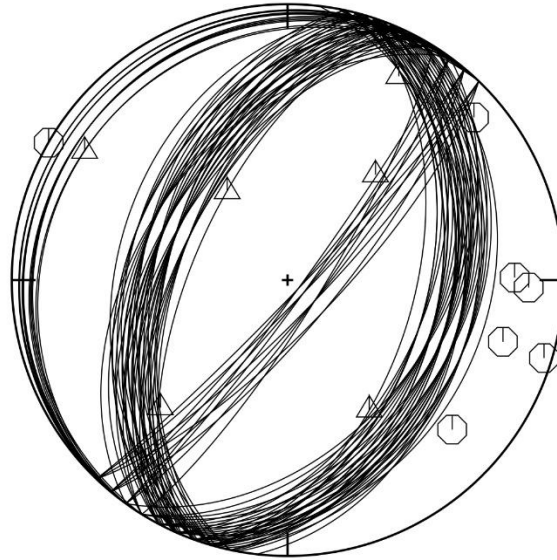


Völkersen'16: 22.04.2016

Ml: 3.0

NLL 3D

N

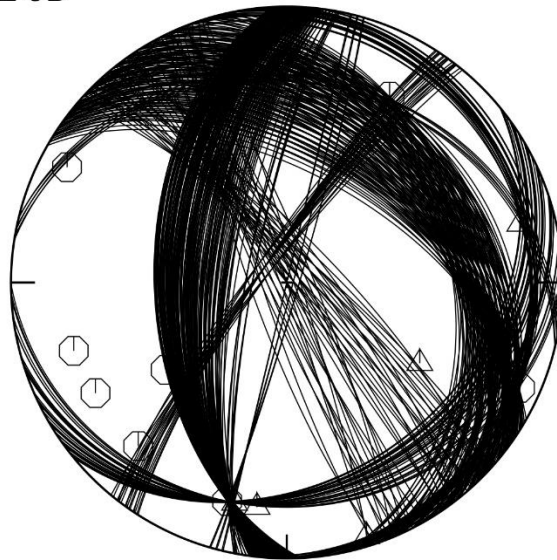


Bothel'16: 28.05.2016

Ml: 2.2

NLL 3D

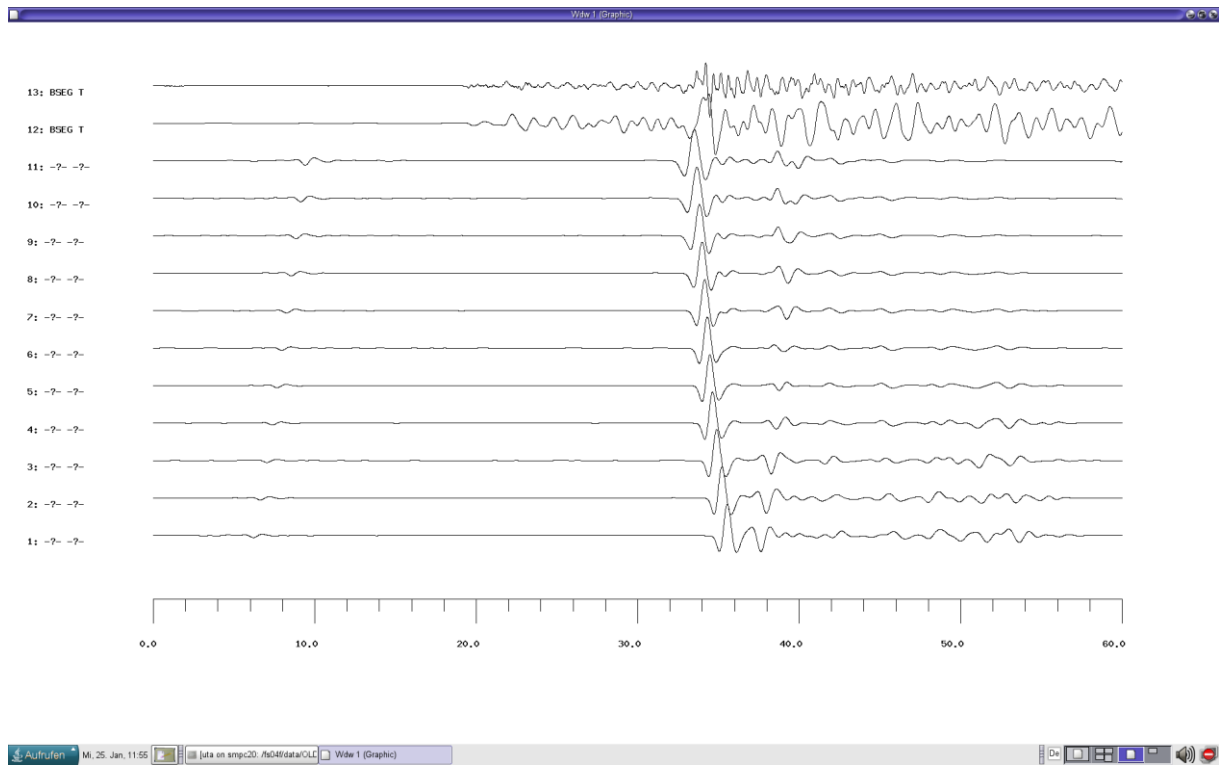
N



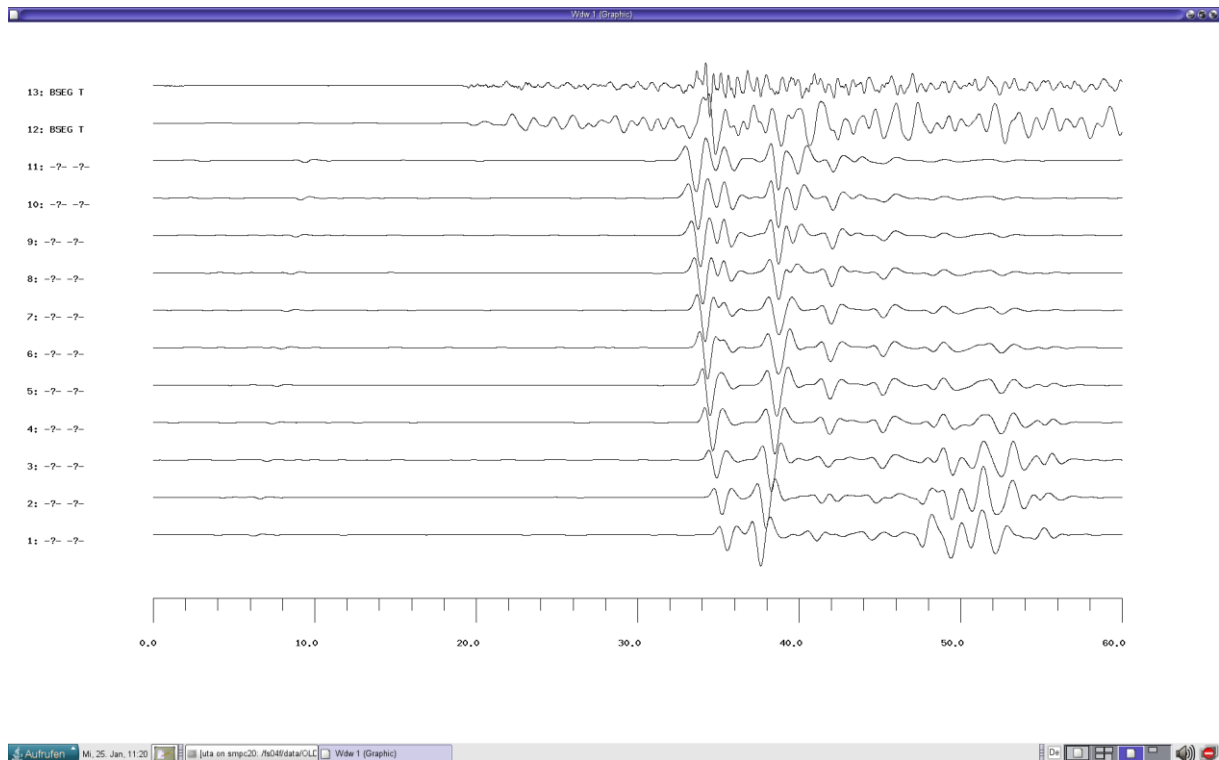
For the events Völkersen'16 and Bothel'16 fault plane solutions were determined using only the take-off angles, which were derived by NonLinLoc and the 3-D velocity models.

Appendix VII. Synthetic Seismograms

Seismic Event Rotenburg'04. Calculated synthetic seismograms at the station BSEG for the thrust fault focal mechanism on the transversal component:

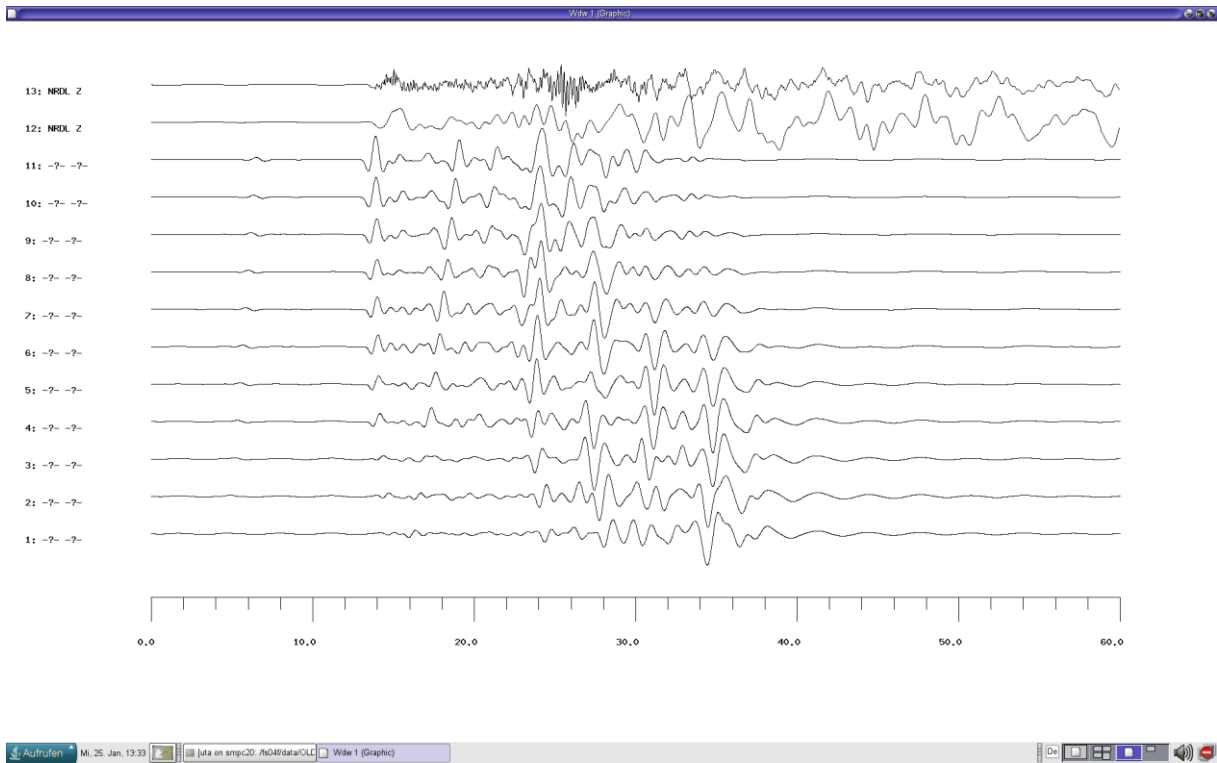


For the normal fault focal mechanism:

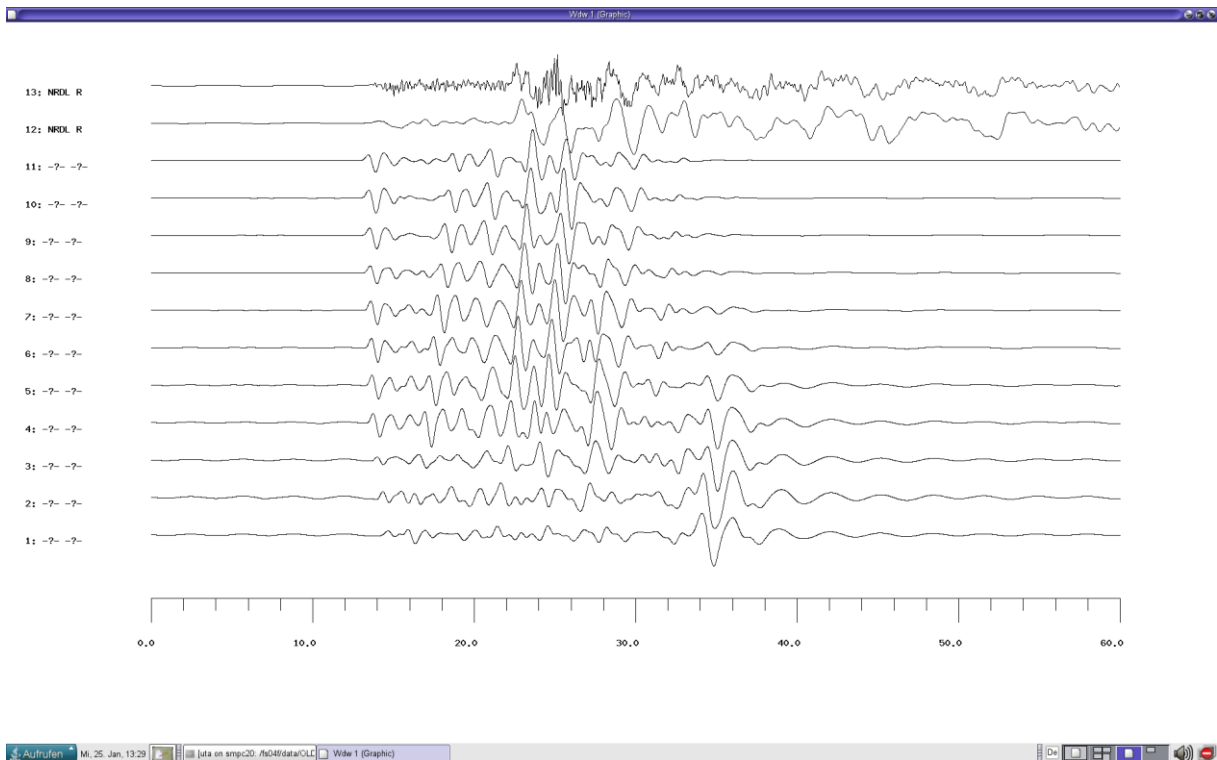


Seismic Event Rotenburg'04. Calculated synthetic seismograms at the station NRDL for the thrust fault focal mechanism on all three components.

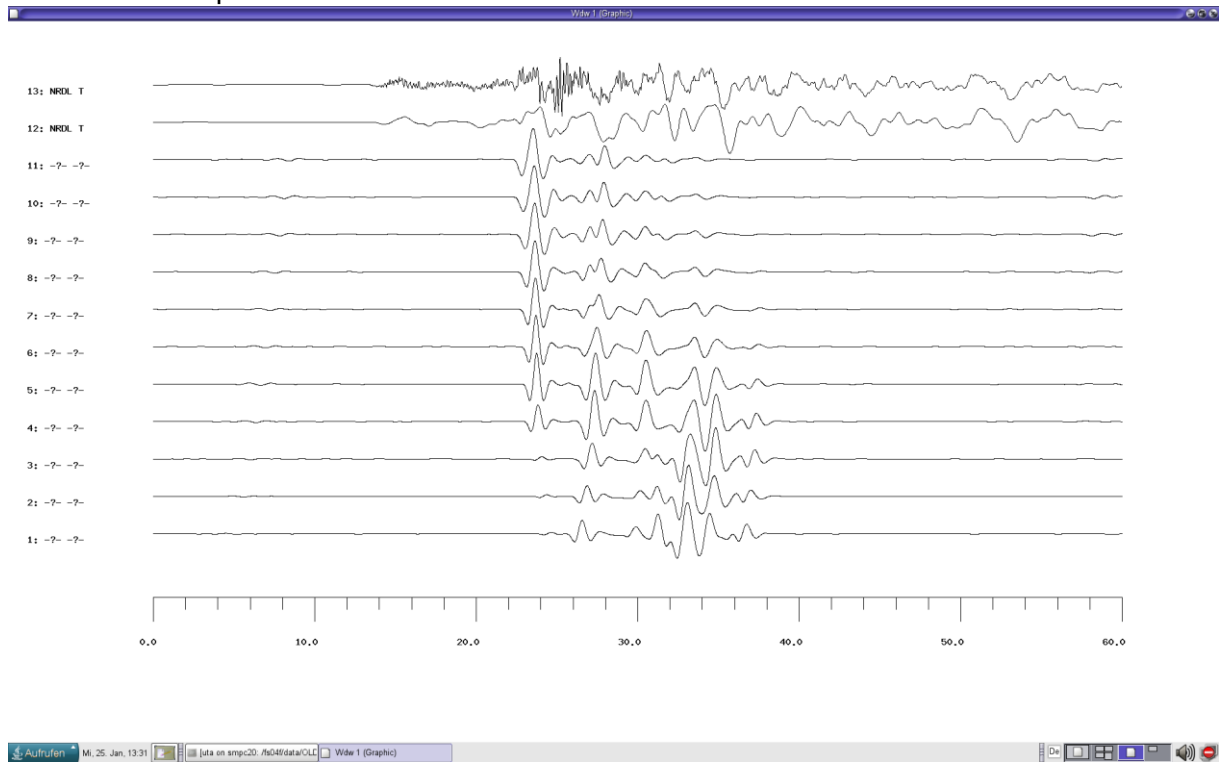
z-component:



radial component:

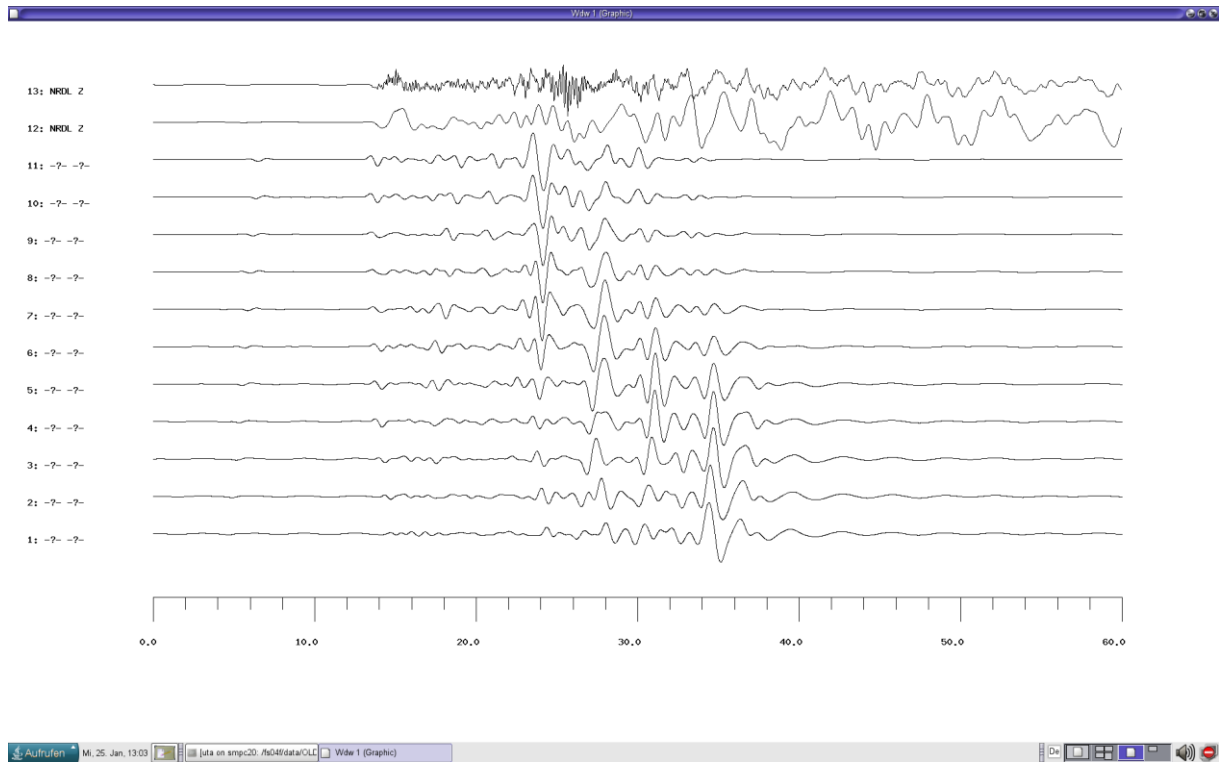


transversal component:

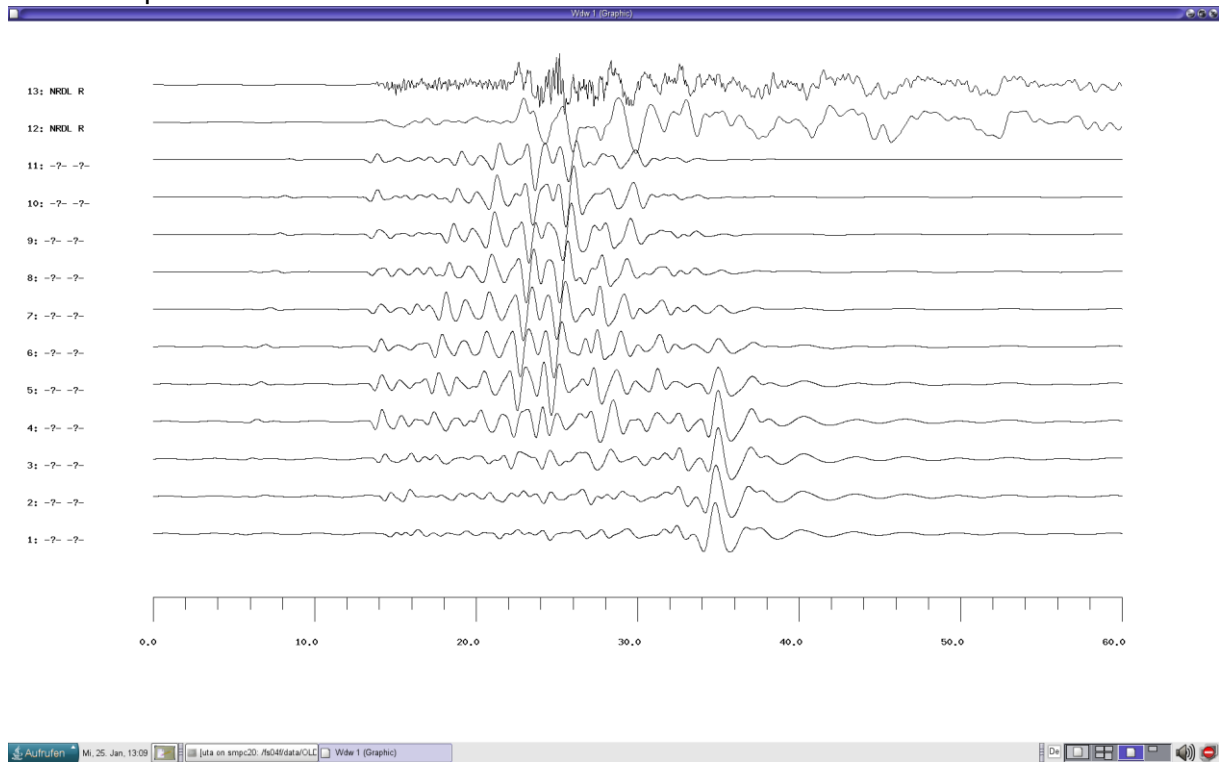


Seismic Event Rotenburg'04. Calculated synthetic seismograms at the station NRDL for the normal fault focal mechanism on all three components.

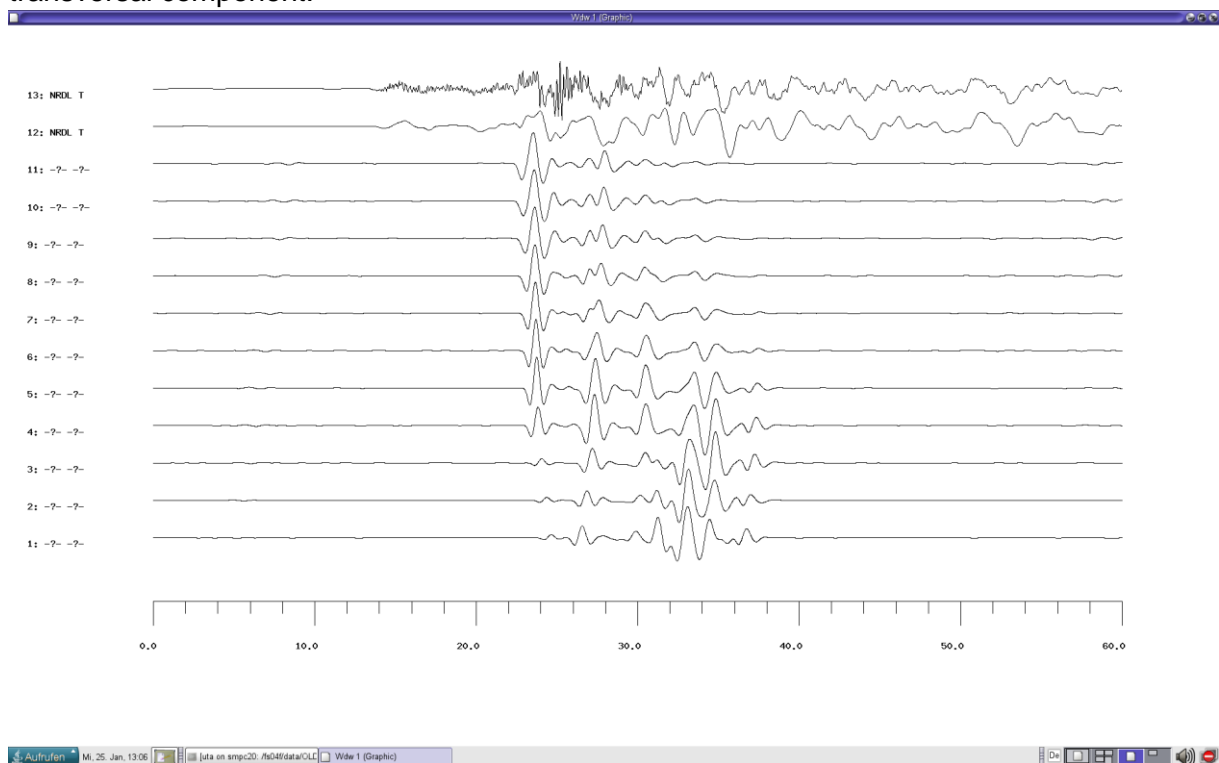
z-component:



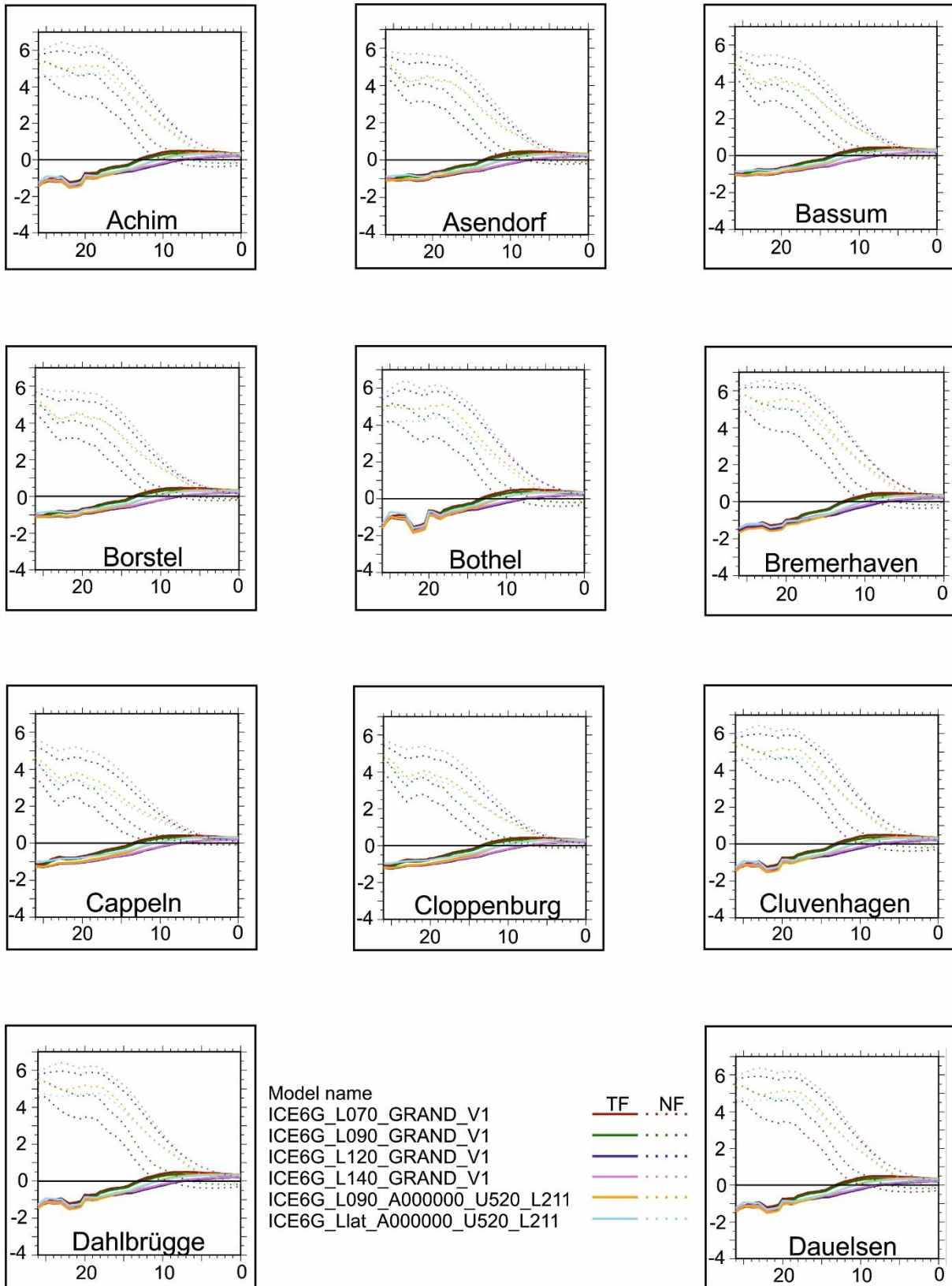
radial component:

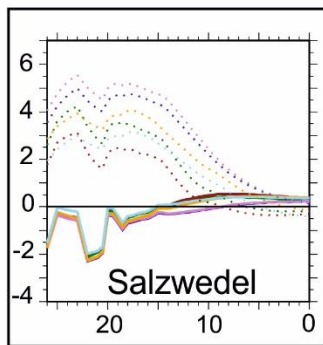
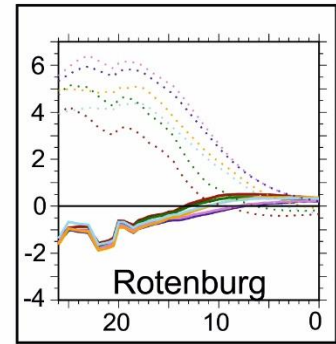
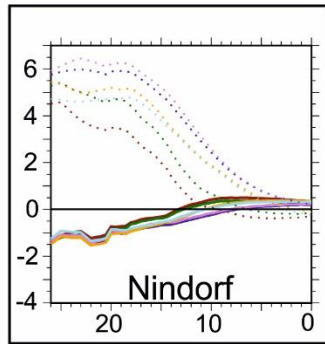
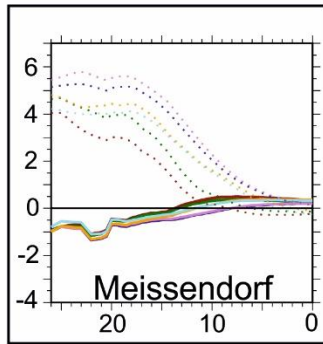
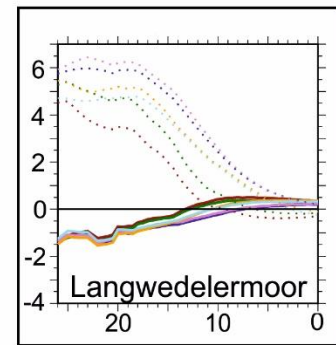
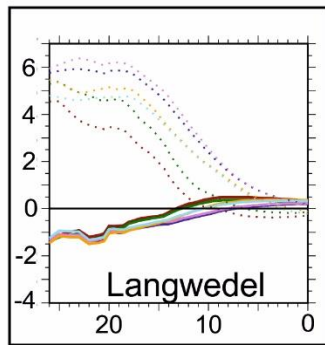
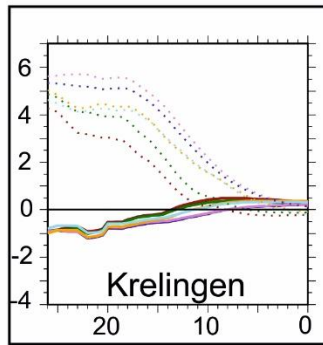
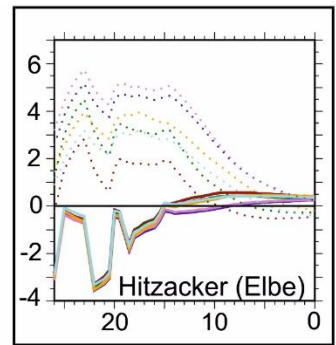
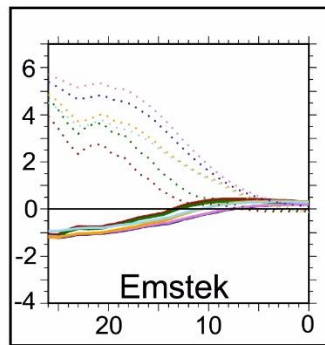
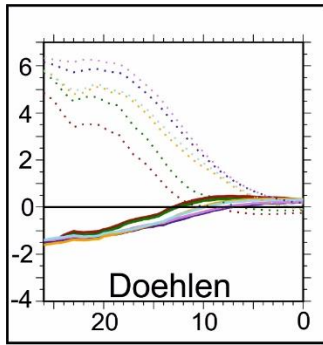


transversal component:



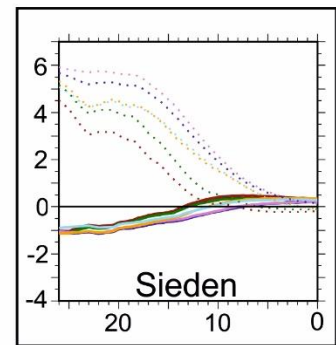
Appendix VIII. Results of the GIA modeling. 31 GIA-investigated locations are shown here. The y-axis defines the δCFS value in MPa and the x-axis belongs to the time [ka BP] 26 ka BP, up to the present day. TF = thrust fault regime, NF = normal fault regime.

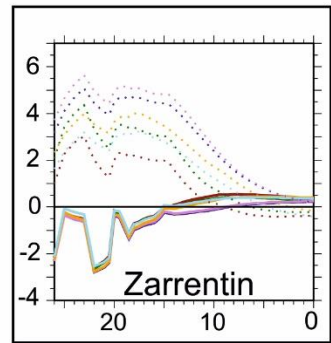
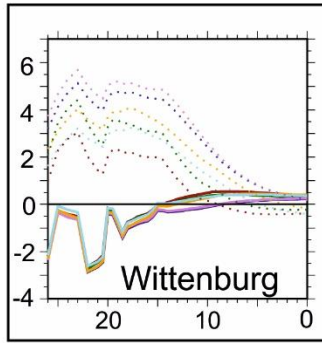
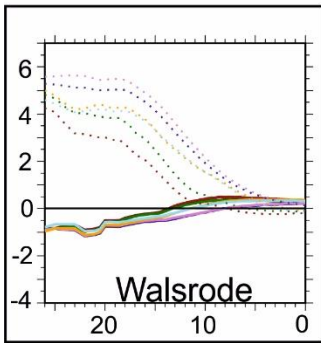
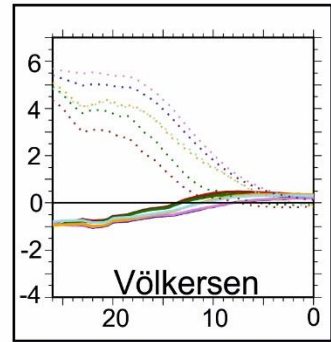
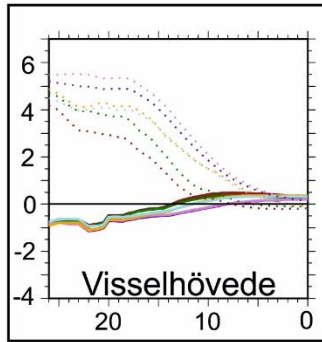
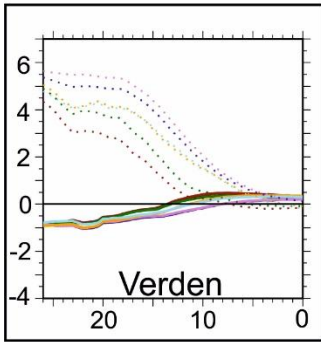
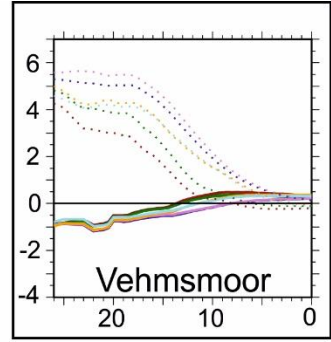
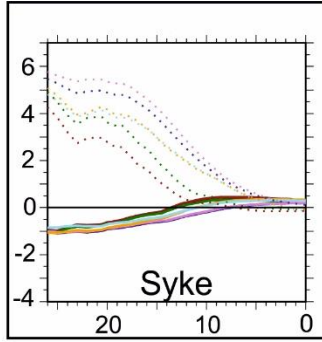
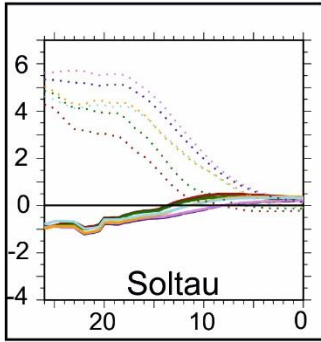




Model name
 ICE6G_L070_GRAND_V1
 ICE6G_L090_GRAND_V1
 ICE6G_L120_GRAND_V1
 ICE6G_L140_GRAND_V1
 ICE6G_L090_A000000_U520_L211
 ICE6G_Llat_A000000_U520_L211

TF NF





Model name

ICE6G_L070_GRAND_V1	TF	NF
ICE6G_L090_GRAND_V1	—
ICE6G_L120_GRAND_V1	—
ICE6G_L140_GRAND_V1	—
ICE6G_L090_A000000_U520_L211	—
ICE6G_Llat_A000000_U520_L211	—

Appendix IX. Table of summarized studies concerning prominent intraplate seismicity.

Region/Country	Setting (special features)	Time period; Important dates	Number of earthquakes	Spatial distribution; Focal mechanism	Magnitude range; Strongest events	Hydrocarbon production?	Assumed causes
Northwest Germany (mostly own investigation)	<ul style="list-style-type: none"> - CEBS, SPB, Northwest German Basin and Lower Saxony Basin (LSB) - Salt structures - dominated by sedimentary basins - formerly regarded as a low seismicity region - Faults, NW-SE, NNW-SSE or roughly N-S oriented - rare historical earthquakes 	<p>1991 – December 2016</p> <p>Since 1991 the German Regional Seismological Network is operated by the BGR</p> <p>First instrumentally registered event in 1977 near Soltau</p> <p>Delay time between first assumed induced event and production about 10 to 20 years</p>	73 instrumentally registered events	<ul style="list-style-type: none"> -Shallow events: 5 – 8 km -Mostly below hydrocarbon reservoir -Clustering in distinct regions -And more or less at the margins and not inside -Deep earthquakes: 13 – 42 km, beside one event, each is located far away from natural gas fields 	<p>0.5 < M_L < 4.3</p> <p>Soltau'77 = 4.0 Rotenburg 2004 = 4.3 Bassum and Syke = 3.5 Völkersen'16 = 3.0</p>	<p>Yes, in a E-W trending belt from Cloppenburg to Salzwedel Reservoir depth dipping from West to east, 4000 – 6000 m</p> <p>Carbon – Zechstein Rotliegend – Buntsandstein Reservoirs</p>	<p>Man-made induced (more or less accepted) hydrocarbon extraction and/or GIA (new natural trigger theory) side-by-side</p>

Region/Country	Setting (special features)	Time period; Important dates	Number of earthquakes	Spatial distribution; Focal mechanism	Magnitude range; Strongest events	Hydrocarbon production?	Assumed causes
northern Netherlands (after van Eck et al., 2006, van Eijs et al., 2006)	-CEBS, SPB, evolution similar to NW Germany - dominated by sedimentary basins Groningen High, LSB, Broad Fourteens Basin - NW-SE normal faults, form mostly significant reservoir boundaries (Bergermeer und Roswinkel) - formerly also low strain area - salt tectonics	Until 2006 First induced event in 1986 in Assen (van Eck et al., 2006) -delay time at Groningen: 28 years after production began	Roughly 340 induced events were recorded - at Bergermeer: only generated four events - Roswinkel showed more than 36 events	- for Groningen Shallow events: mostly around 2.5 km in the northwestern part of the field, no event occurred deeper than 4 km - for Bergermeer - for Roswinkel	-0.8 < M _L < 3.5 - in Groningen up to 3.0 - Bergermeer and Roswinkel events M _L 3.4 and 3.5	Yes, gas fields with prominent seismicity pattern Groningen – Upper Rotliegend reservoir ranging in depth between 3150 and 2600 m (largest in Europe), Bergermeer: Rotliegend at depth of 2100m and Roswinkel in the Buntsandstein 2000 – 2400 m - both latter fields are approaching the end of their production cycle	Man-made induced Hydrocarbon extraction Accepted Reactivation of NW-SE trending normal faults at reservoir depth
Southern Netherlands (and very surroundings like Germany or Belgium) (after Camelbeek and van Eck, 1993)	-dominated by the NW-SE trending Roer Valley Graben situated in the Lower Rhine Embayment -Part of the European Cenozoic rift system (Ziegler, 1992) -Extensional deformation, still active extension of the Graben (Ahorner, 1975) - increased rate of subsidence since the Late Pleistocene (Zijerveld et al., 1992) -Normal fault structures limited the flanks of the Graben, Peel Boundary (NE) and Feldbiss (SW) fault	Since 1755	- Seven earthquakes with M _s > 5 with a return period in this region of 50 – 60 years - At least 5 earthquakes in the 19 th century with magnitude M _s > 4 - Roermond mainshock and more than 200 aftershocks	Roermond earthquake about 17 km deep - seismic activity is more or less limited to the northwestern flank of the Graben, the Peel Boundary fault - along NW-SE striking faults	-0.1 < M _L < 5.8 Uden (Ned) 1932 = M _s = 4.5 Liege (Belgium) 1983 = 4.6 Roermond (Ned) 1992 = 5.8	No hydrocarbon production	- Natural cause - Subsidence and NE-SW oriented extension - active normal faulting - Houtgast et al., 2005: glacial unloading may have triggered an increase of fault activity around 10 – 15 ka B.P - therefore recent events may occur because of stress changes in the subsurface due to GIA

Region/Country	Setting (special features)	Time period; Important dates	Number of earthquakes	Spatial distribution; Focal mechanism	Magnitude range; Strongest events	Hydrocarbon production?	Assumed causes
France Southwest – Lacq area (Bardainne et al., 2008)	<p>-Located north of the North Pyrenean Frontal Thrust, 30 km from the Pyrenean seismicity area</p> <p>-Limited in the North by the Aquitan Basin and in the south by the Pyrenean Zone (Choukroune, 1992)</p>	<p>Hydrocarbon production began in 1957</p> <p>From 1974 to 1997 a seismic network monitored the region</p> <p>First felt event in 1969 after a depletion of 30 MPa</p> <p>Delay time between first event and production 12 years</p>	<p>More than 2000 instrumentally registered in the time period in which the station network had been operated</p>	<p>Most of these events had been located below the reservoir (Guyoton et al., 1992), new insights show a location above the reservoir</p> <p>Different clusters within the field were observed</p> <p>Depth < 10 km ~2.5 to 6.0 km Within or in the vicinity of the field</p> <p>No event was registered in the western part of the field</p>	<p>1.5 < M_L < 4.2</p>	<p>Yes</p> <p>The Lacq gas field is a WNW-ESE oriented about 20 km long anticlinal reservoir at depth of 3200 m</p> <p>Situated below a 600 m deep oil field</p>	<p>Induced seismicity, man-made due to the gas extraction and resulting reservoir compaction</p> <p>One small cluster had been likely induced by an accidental fluid injection (Bardainne et al. 2006)</p> <p>Correlation between pre-existing WNW-ESE oriented faults and the location of the seismic activity</p>

Region/Country	Setting (special features)	Time period; Important dates	Number of earthquakes	Spatial distribution; Focal mechanism	Magnitude range; Strongest events	Hydrocarbon production?	Assumed causes
<p>New Madrid seismic zone (NMSZ)/eastern central United States</p> <p>(ref.: van Arsdale, 2014 aus Intraplate Earthquakes, ed. Pradeep Talwani...2014)</p>	<p>- Located in a large alluvial valley along the Mississippi at the corner between Missouri, Arkansas, Tennessee and Kentucky within the Reelfoot rift in presence of a lower crustal mafic rift pillow</p> <p>- extensional features developed during the breakup of Rodinia in Early Cambrian</p> <p>- It is an ancient failed intraplate rift zone (aulacogen), active during latest Precambrian and/or early Paleozoic time (McKeown, 1982)</p> <p>- Also an episode of Cretaceous magmatic activity is observed (hot-spot) (Zoback et al., 1980)</p> <p>- Three prominent faults were identified to be responsible for faulting at the surface: Reelfoot fault, strike-slip New Madrid North fault and Bootheel fault</p>	<p>Three most recent events occurred in winter of 1811-1812 (Tuttle et al., 1999)</p> <p>4 prehistoric earthquakes have been dated A.D. 1450, 900, 300 and 2350 B.C. (estimations using paleoliquifactions, Craven, 1995)</p> <p>Greatest intensity in the past 2000 years (Müller et al., 1999)</p>	<p>Three events in winter 1811 – 1812 with thousands of aftershocks</p> <p>Two more significant earthquakes occurred in 1843 and 1895 with moment magnitudes > 6 and eight events between magnitude 5 and 6</p> <p>Microseismicity with $M \leq 3.0$ is abundant, more than 200 per year $M > 0.2$</p> <p>Repeat time for earthquakes $M > 7$ of about 500 years</p>	<p>Earthquakes (1811 – 1812) are mostly located within the Reelfoot rift along the assumed Bootheel lineament</p> <p>The microseismicity defines the NMSZ</p> <p>Generalized focal solutions show two NE oriented dextral strike-slip fault zone segments and a NW oriented left-stepping restraining-bend thrust</p> <p>Along reactivated basement faults within the Reelfoot rift (Arsdale, 2014)</p> <p>shallow earthquakes < 13 km, mostly < 10 km (USGS, last 2 years)</p> <p>shallower than 15 km (Park et al., (2015)</p>	<p>Estimated moment magnitudes between 7 – 8 for the earthquake sequence in 1811 - 1812 (Johnston, 1996)</p> <p>A reexamination suggests a magnitude from 7.0-7.5 (Hough et al., 2000)</p> <p>See also number of earthquakes</p>	<p>No hydrocarbon production</p>	<p>-Natural trigger, most of the earthquakes are linked to the tectonic processes, which formed the Mississippi embayment, especially in Mid-Cretaceous times the so-called Bermuda hot spot (Cox and Van Arsdale (1997)</p> <p>- For the large earthquakes: bending of the lithosphere associated with glacial unloading (Grollimund and Zoback, 2001).</p> <p>-The seismic zone is located in front of the ice sheet, see also Osning or our study area.</p> <p>- driving mechanisms are proposed and summarized by Powell and Horton (2009) or Nyamwandha et al., 2016</p>

Region/Country	Setting (special features)	Time period; Important dates	Number of earthquakes	Spatial distribution; Focal mechanism	Magnitude range; Strongest events	Hydrocarbon production?	Assumed causes
Alberta/Canada (see Eaton and Mahani (2015) Or Wettmiller (1986))	<p>-West-central Alberta</p> <p>-In the west of Edmonton</p> <p>-Located in the Crooked lake (CL) area and within the Rocky Mountain House (RMH) area</p> <p>RMH – sour gas reservoir, Devonian-aged limestone reef complex in a section of nearly flat-lying unfaulted sediments</p> <p>- both clusters in the Western Canada sedimentary basin</p> <p>-East of the Rocky Mountain Front Thrust belt (RMFTB)</p> <p>- most of Alberta is relatively aseismic (Wettmiller, 1986)</p>	<p>- RMFTB – since records began in Alberta (1960s)</p> <p>CL – since December 2013</p> <p>- RMH - seismic activity since the late 1970s (1974)</p> <p>- 5 year delay time between the start of major seismic activity and the onset of production</p>	<p>RMFTB: low magnitude earthquakes activity</p> <p>CL: episodically active</p> <p>- RMH: since 1974 more than 350 seismic events</p> <p>-No seismic activity before production was established</p>	<p>- RMFTB: the vast majority of seismic events in Alberta are concentrated at this deformation front</p> <p>- CL:</p> <p>- RMH: east the RMFTB, in depths between 4-6 km Wettmiller (1986), seismic events are mostly located below or within the Strachan D3-A sour gas reservoir</p> <p>- the faulting may be associated with the Precambrian – Paleozoic contact below the reservoir</p>	<p>RMFTB: low magnitude events, but also up to $M \geq 7$, normal faulting?</p> <p>CL: strongest event 4.4, oblique normal fault with significant strike-slip component</p> <p>RMH - August, 09th 2014 the largest recent event with M_w 3.8 occurred, reverse-faulting regime</p>	<p>Yes, Crooked lake – Oil and gas recovery with numerous hydraulic fracturing stages</p> <p>RMH – natural gas extraction (Strachan D3-A pool and more fields)</p> <p>-only the Strachan sour gas reservoir is seismically active, the other ones remain all aseismic (Wettmiller, 1986)</p>	<p>RMFTB – tectonic earthquakes, orogenesis of the Rocky Mountains</p> <p>CL - Injection of fluids and extraction of oil and gas, direct correlation without delay of man-made encroachments into the subsurface</p> <p>RMH – extraction of natural gas, man-made induced seismicity triggered by poroelastic stress changes also surface subsidence, only for the Strachan field</p> <p>- not known to be associated with any hydraulic fracturing activity</p> <p>-however another recent cluster farther east is observed in 2014 – not know origin</p>

Region/Country	Setting (special features)	Time period; Important dates	Number of earthquakes	Spatial distribution; Focal mechanism	Magnitude range; Strongest events	Hydrocarbon production?	Assumed causes
<p>New South Wales (NSW)/Australia</p> <p>South east Seismic Zone (SESZ)</p> <p>(ref.: Rajabi et al., 2016)</p>	<ul style="list-style-type: none"> - consists of different sedimentary basins - SESZ covers west and south of NSW and is located in the Darling Basin - maximum horizontal stress is variable across the state - in the Darling Basin S_{Hmax} oriented mostly E-W to ESE-WNW -Tasman orogenic system – contains three major tectonic belts from early Paleozoic to early Mesozoic - from late Paleozoic to Holocene sedimentary cover deposits and volcanic rocks (resulting from Gondwana break-up) 	<ul style="list-style-type: none"> - Newcastle event in 1989, most damaging event in Australia - Australia bulletin since 1910 - earliest event in the catalogue near Sydney in June 1788 	<ul style="list-style-type: none"> - relatively high level of seismicity and neotectonic activity (Clark et al., 2012, Hillis et al., 2008) -throughout Australia 17000 mainshocks in the catalogue - steady seismicity since the last 100 years in the NSW 	<ul style="list-style-type: none"> - seismicity mostly occur in the south-eastern part of NSW, the South east seismic zone - located at the east coast near the Tasman sea in the Lachlan orogeny; highest topography in Australia - focal depth range from < 4 km to > 17 km - mostly thrust or reverse focal mechanism (Rajabi et al., 2016) - hypocentral depth of earthquakes in Australia range between 8 – 18 km -however in the southwest typically shallower than 5 km 	<ul style="list-style-type: none"> - main shocks typically have numerous aftershocks - up to $M_L = 5.6$ (see Newcastle event, McCue et al., 1990) 	<p>No,</p> <ul style="list-style-type: none"> -only coal-seam gas exploration in several basins of NSW - in particular the potential of exploring petroleum and geothermal energy in the Darling Basin, central west NSW 	<ul style="list-style-type: none"> - natural tectonic causes, - intraplate deformation controlled by plate boundary forces (Hillis et al., 2008)

Region/Country	Setting (special features)	Time period; Significant dates	Number of earthquakes	Spatial distribution; Focal mechanism	Magnitude range; Strongest events	Hydrocarbon production?	Assumed causes
North China (ref.: Liu et al., 2016)	<ul style="list-style-type: none"> - North China Basin (NCB) - an epi-continental basin, which is underlain by the North China craton and characterized by alternate uplift and depression zones - show a complex system of basement faults hidden beneath a thick Quaternary cover - mountains, structures and faults trending mostly NE-SW - Moho depth decreases from about 43 km to 28 km - crust is divided into upper, middle and lower crust - lithosphere thickness varies from 120 km to 80 km (W – E) - the NCB is dominated by a compressional environment - four seismic zones (Huang and Zhao, 2004) 	<ul style="list-style-type: none"> - earthquake catalogue nearly complete for M > 6 events since A.D.1300 - last 1000 years - devastating earthquakes frequently occurred in the NCB 	<ul style="list-style-type: none"> - last 1000 years more than 100 earthquakes with M>5 - apparently increased seismicity in the past century 	<ul style="list-style-type: none"> - most of the largest events occurred along the NE striking Sanhe-Laishui and Tangshan... faults - the mainshocks are located at the bottom of the upper crust in depths between 9 to 15 km or sometimes deeper – 30 km - and aftershocks ranging between 5 to 25 km, in the upper crust and part of the middle crust - more or less right lateral strike-slip faulting for the large ones - or normal faulting with large strike-slip components 	<ul style="list-style-type: none"> - in 1679 M 8.0 earthquake in the Sanhe county of Beijing - two devastating events: 1966 Ms 7.2 – Xingtai; 1976 Ms 7.8 – Tangshan - in this decade destructive earthquakes with 6.3 < Ms 7.8 occurred 	No	<ul style="list-style-type: none"> - natural tectonic cause - stress concentrations with high rates appear in regions where Moho upheaval - large earthquakes are related to Moho undulating - fluid causing the weakening of the seismogenic layer in the upper and middle crust - lithospheric rheology differences: brittle upper crust, brittle-ductile transition in the middle crust and ductile lower crust

Region/Country	Setting (special features)	Time period; Significant dates	Number of earthquakes	Spatial distribution; Focal mechanism	Magnitude range; Strongest events	Hydrocarbon production?	Assumed causes
Oklahoma / USA (Ref.: Ellsworth, 2013 and Hough and Page, 2015, McNamara et al., 2015))	<p>-Central Oklahoma (CO), dominated by the Nemaha (NNW-SSE) and Wilzetta Fault (NE-SW, NNE-SSW) Zone</p> <p>- these fault systems bound a broad region of uplift in CO that was originally formed as a result of the Ancestral Rocky Mountains during the Late Carboniferous (McNamara et al., 2015).</p> <p>- NW-SE Meers fault, the only fault with documented surface rupture, evidences of two earthquakes of M_w 6.5 – 7 in the past 3400yr</p> <p>- recent seismicity rates are extremely low</p> <p>- in southeastern Oklahoma low level tectonic seismicity is observed, which is associated with the Ouachita structural belt, commonly considered to be an extension of the Appalachian</p>	<p>-historical catalogue back to 1882</p> <p>- October 1882: Choctaw Nation earthquake, Ouachita</p> <p>-from 2009 - 2014</p>	<p>- seismicity rate increased during times of oil booms in distinct areas</p> <p>- evolving seismicity - since 2009 a really sharp increase of seismicity rate</p> <p>- catalogue by McNamara et al., 2015 – 3639 earthquakes in central Oklahoma, magnitude complete to 2.5</p>	<p>- well-defined correlation between injection wells, rates and volumes with hypocenters since 2009</p> <p>- shallow seismic events near injection wells</p> <p>- hypocenters are located in depth between 2 to 10 km, average depth of 6 km ($M > 3$ for 2014, Deflandre 2016</p> <p>- McNamara et al, 2015: the majority of earthquakes occur on near-vertical optimal oriented (NE-SW, NW-SE) strike-slip faults in the shallow crystalline basement in CO < 6 km</p> <p>- fault lengths mostly 1 – 3 or more than 10 km</p> <p>- mostly along longer fault structures</p>	<p>- 1882: Choctaw Nation earthquake M_w 4.8</p> <p>- besides Choctaw, all $M \geq 4$ occurred either during the oil boom times or since 2009</p> <p>- in 2014, 17 events with $M > 4$ occurred</p>	<p>- Yes</p> <p>- Oil exploration began at the end of the 19th century</p> <p>- first drilling boom in 1907</p> <p>- by the 1950s fields were being depleted faster than new fields were being discovered</p> <p>- enhanced wastewater disposal began in the 1930s</p> <p>- oil and gas extraction</p>	<p>- most of the significant earthquakes in Oklahoma (20th century) were likely induced by oil production activities</p> <p>- however, low level tectonic activity in southeastern Oklahoma is observed and associated with the Ouachita structural belt</p> <p>- reactivated subsurface fault systems</p>

ACKNOWLEDGEMENTS

I wish to thank various people for their contribution to this thesis. I would like to express my very great appreciation to Prof. Dr. Jutta Winsemann, Institut für Geologie, Leibniz Universität Hannover, my thesis supervisor, for her advice and constructive critiques of this research work. I would also like to thank Prof. Dr. Manfred Joswig, Institut für Geophysik, Universität Stuttgart for his time to review my work as co-referee and his enthusiastic discussions especially about the seismological analyses in this work.

I owe a deep sense of gratitude to Dr. Christian Brandes, Institut für Geologie, Universität Hannover and Dr. Thomas Plenefisch, Federal Institute for Geosciences and Natural Resources for their support and constructive suggestions during the planning and development of this research work. I would like to thank both for countless meetings and critical but very useful discussions about my topic. Their willingness to give their time so generously has been very much appreciated. I would also like to thank Dr. Christian Brandes that he gave me the opportunity to participate at the AGU2015 in San Francisco. This was an outstanding experience. Christian and Thomas, words can never be enough to thank your kindness.

My grateful thanks are also extended to Dr. Christian Bönemann, Federal Institute for Geosciences and Natural Resources, for his valuable advice and support during my research work.

I would like to offer my special thanks to Dr. Holger Steffen, Landmåteriet, Gävle, Sweden for the determination of the glacial isostatic adjustment and also Dr. Rebekka Steffen for a nice and very interesting week in Sweden to learn more about postglacial uplift.

I wish to acknowledge the help provided by Dr. Lars Ceranna for guiding me through MATLAB© and for the application of PSWELLdLC to calculate synthetic seismograms.

I would like to thank Dr. Jörg Lang for his experiences and advice by using GOCAD©.

This thesis is based on the DGMK project 773. The project was funded by Deutsche wissenschaftliche Gesellschaft für Erdöl, Erdgas und Kohle e.V. (DGMK), DEA Deutsche Erdoel AG, ENGIE Deutschland, ExxonMobil Production Deutschland GmbH and Wintershall Holding GmbH. Special thanks should be given to all company representatives for inspiring discussions and critical questions at many meetings and project workshops. Thereby, my special thanks are extended to the staff of the DGMK 761 and DGMK 776 working groups for very interesting discussions and helpful comments for my research work.

Finally, I wish to thank my parents, Dagmar and Burkhard, my brother Alex, his wife Hannah and the very little man Emil for their love, support and encouragement throughout my study. Lastly, and most of all, I would like to thank Madlen for her love. Words can never be enough to describe my love to you.

CURRICULUM VITAE

Personal information

Name: Philipp Uta
Address: Altenbrückerdamm 9a, 21337 Lüneburg
E-Mail: philipp.uta@gmail.com
Nationality: German
Date of Birth: July, 8th 1986

Education

03/2013: Master of Science in Geosciences, Universität Hannover
10/2010: Bachelor of Science in Geosciences, Universität Hannover
06/2006: School-leaving exam, Gymnasium Alfeld/Leine

Academic and professional background

since 03/2014 PhD student at the Institut für Geologie, Universität Hannover
Project title: Active Tectonics in NW Germany: Glacial Isostatic Adjustment and/or a Consequence of Hydrocarbon Production.

10/2010 - 03/2013 Master of Science in Geosciences, Universität Hannover
M.Sc. Thesis: NonLinLoc - Relokalisierung deutscher Erdbebenereignisse mit Hilfe eines 3D - Lokalisierungsprogramms.

06/2011 - 08/2011 Scientific researcher at the Institut für Mineralogie, Universität Hannover; Project title: Analyse verschiedener Syntheseansätze von BH4-Sodalithen zur Bestimmung des Wassergehaltes in ihrer Struktur.

10/2007 - 10/2010 Bachelor of Science in Geosciences, Universität Hannover
B.Sc. Thesis: Der Erdbebenschwarm von Oktober 2008 in der Region Vogtland / NW-Böhmen - Berechnung von Herdflächenlösungen für ausgewählte Beben des Schwarmes.

11/2009 - 09/2010 Scientific researcher at the Federal Institute for Geosciences and Natural Resources, BGR, Hannover B4.3-Seismologisches Zentralobservatorium und Kernwaffenteststopp